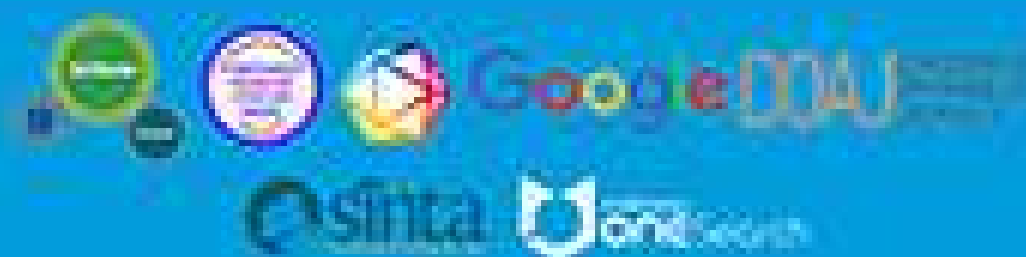
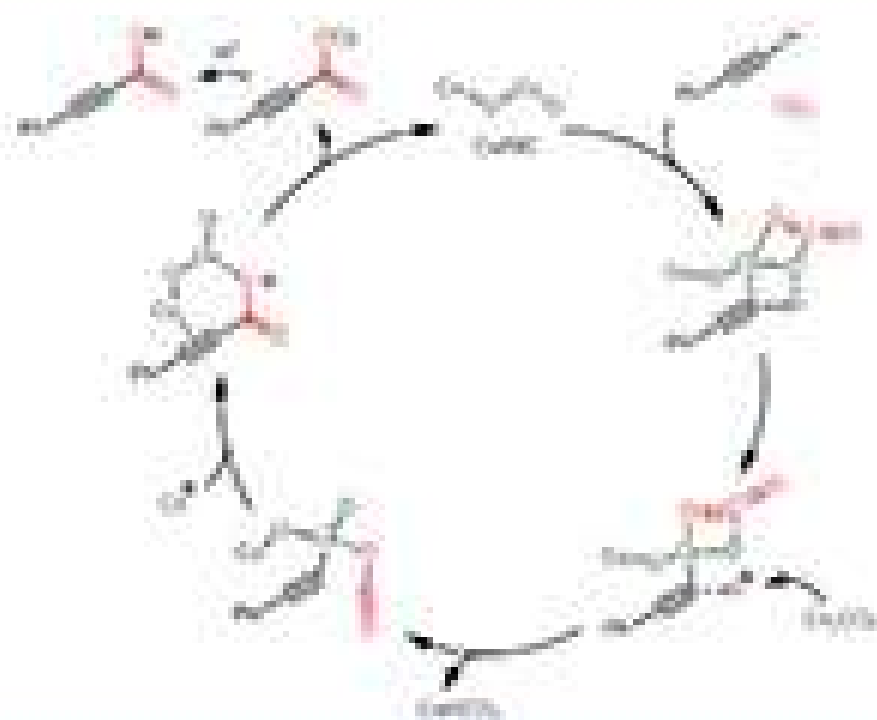


ISSN: 1411-8925 (print) | 2455-1178 (online)

Indonesian Journal of Chemistry

Vol. 21, No. 1, February 2021



Approved by ICAK
No. 10244/1/2020

Hydrothermal Synthesis: Low-Temperature Subcritical Water for Ceria-Zirconia Mixed Oxides Preparation

Siti Machmudah^{1,*}, Widiyastuti¹, Wahyudiono², Sugeng Winardi¹, Hideki Kanda², and Motonobu Goto²

¹Department of Chemical Engineering, Faculty of Industrial Technology, Institut Teknologi Sepuluh Nopember, Surabaya 60111, Indonesia

²Department of Materials Process Engineering, Graduate School of Engineering, Nagoya University, Nagoya 464-8603, Japan

* **Corresponding author:**

email: machmudah@chem-eng.its.ac.id

Received: July 5, 2019

Accepted: April 14, 2020

DOI: 10.22146/ijc.47357

Abstract: A low-temperature hydrothermal synthesis technique was employed as a medium to produce ceria-zirconia mixed oxides particles at temperatures of 200–300 °C and pressure of 10 MPa in a batch process. At these conditions, the average crystallite sizes of ceria-zirconia mixed oxides increased slightly with increasing reaction temperature when the feed solution containing ceria and zirconia with a ratio of 1:1 was fed. SEM images illustrated that the morphologies of the ceria-zirconia mixed oxides particles were spherical and spherical-like with a diameter of around 100 nm. The EDX spectrum indicated that the signal corresponding to the ceria and the zirconia elements at 5 and 2 keV, respectively, were strongly detected in the products. The XRD pattern revealed that the mixed metal oxides particle products that comprised of cerium and zirconium oxides particles with cubic and monoclinic structures, respectively, were affected by their molar content in the feed solution.

Keywords: ceria-zirconia oxides; metal oxides; hydrothermal; subcritical; synthesis

■ INTRODUCTION

Ceria-based materials have been known as one of the most attractive materials for environmental and energy applications due to their distinct defect chemistry. From an environmental point of view, ceria has been used as a key component in composite catalysts due to how relatively easy it can change between its two stable oxidation states. This cerium(IV) oxide-cerium(III) oxide cycle activity allows switching from cerium(IV) oxide under oxidizing conditions to cerium(III) oxide under net declining conditions and vice versa. The highly mobile oxygen vacancies in high concentrations of cerium may promote the rapid change of the oxidation state and may result in its ability to store and release oxygen. This phenomenon resulted in beneficial effects and was an important factor for its catalytic activity [1-4]. Regarding energy applications, ceria-based materials have been known to have the highest ionic and electronic

conductivity by reducing the partial pressure of oxygen at environment temperatures below 1000 °C [5].

Despite the fact that cerium oxide is an attractive rare earth oxide and has been widely investigated for many applications, the sintering of this oxide can occur at high temperatures (over 1000 °C) via a redox reaction. This sintering process may decrease the catalytic activity and the capacity of oxygen storage and release significantly [6-7]. To avoid the effect of the sintering process when cerium oxide is employed at high temperatures, it is very important to stabilize the cerium oxide by addition or modification using different elements. In the current study, cerium oxide is modified by adding zirconium oxide and prepared by hydrothermal treatment in a batch process. Zirconia (zirconium dioxide, ZrO₂) possesses several unique properties that have proven to be superior to other ceramic elements. It is known to be able to improve morphological and redox stability at high temperatures.

Zirconia has good mechanical strength, good resistance against crack propagation, good thermal resistance, relatively high thermal expansion coefficient, and low thermal conductivity at high temperatures (over 1000 °C) [8-11]. Due to these properties, zirconia was used in many industrial applications as ceramic bodies and was also used as reinforcement in various composite materials to improve their mechanical properties.

It is widely known that ceramic nanoparticles can be prepared and synthesized by various approaches. In general, the applied techniques for the synthesis of ceramic nanoparticles can be classified into two types of techniques: chemical and physical [12]. Each technique possesses its own advantages and disadvantages; however, whichever technique is applied, it is important to focus on attaining monodispersity or long-term stability of the particle products. In this work, the hydrothermal synthesis technique, as one of the wet-chemical synthesis techniques, was employed as a media to generate ceria-zirconia mixed oxides nanoparticles from cerium and zirconium oxides. This technique is inexpensive and less hazardous, therefore environmentally friendly, and only requires the use of simple equipment. The hydrothermal synthesis technique can be referred to as crystal growth or heterogeneous crystal synthesis in the presence of aqueous media or mineralizers under high temperature and pressure conditions from materials that are insoluble under ordinary conditions (< 100 °C, < 1 atm) [13].

Regarding ceramic particle generation, the hydrothermal synthesis technique has several advantages, such as how the size and morphology of the particle products are easily managed by varying the synthesis conditions. Allowing the generation of materials with an elemental oxidation state, the synthesis process can be directly applied to many materials to produce the desired crystalline phase at low operating temperatures [14-15]. Furthermore, it is important to judge the conditions of hydrothermal synthesis with water media. In this case, subcritical synthesis conditions would be applied as a media for the synthesis process, where the temperature of the water is increased to above its boiling point (between 100 and 374 °C). However, the pressure is required to be tuned to maintain water in its liquid form. Under these

conditions, the physical and chemical properties of water change quite dramatically, including the ionic product (K_w), density, and dielectric constant of water. Hence, water at subcritical conditions gives a favorable reaction medium for particle generation, owing to the promoted reaction rate. According to the nucleation theory, the high degree of supersaturation is caused by declined solubility [13-16].

■ EXPERIMENTAL SECTION

Materials

The commercial cerium(III) nitrate hexahydrate ($Ce(NO_3)_3 \cdot 6H_2O$, product no. 035-09735) and zirconium nitrate oxide dehydrate ($ZrO(NO_3)_2 \cdot 2H_2O$, product no. 265-00915) were used as starting materials. They were purchased from Wako Pure Chemical Industries Ltd. (Japan), with purities of more than 97.0%. Nitrogen gas obtained from Samator PT (Gresik, Indonesia) was used to purge air during experimental preparation. During preparation, the cerium or zirconium solution was prepared by dissolving cerium(III) nitrate hexahydrate or zirconium nitrate oxide dehydrate in a flask with deionized water. The concentration of each specimen was 0.06 M.

Instrumentation

The experiments were performed in batch type reactors made of SUS-316 and comprised of a tube body and cap (AKICO Co. Ltd., Japan; 8.8 mL). This reactor was operated at 300 °C and 35 MPa. The electric furnace (Linn High Therm GmbH, model VMK 1600, Germany) was used to heat the reactors. The particle products were characterized using a scanning electron microscope (SEM, JEOL JSM-6390LV, Japan), particle size analysis (PSA, a Malvern Zetasizer nanoseries, Germany), energy dispersive X-ray (EDX) spectroscopy equipped in a Zeiss EVO MA 10 scanning electron microscope (SEM) from Bruker, thermogravimeter (TG-50, Shimadzu, Japan), and BET (Brunauer-Emmett-Teller, Nova 1200, Quantachrome, USA).

Procedure

An aqueous solution containing zirconium and cerium substances with different molar ratios was loaded

into the reactor and sealed tightly. The given amounts of solution corresponded to $0.71\text{--}0.87\text{ g mL}^{-3}$ water density. Before closing the reactor, nitrogen gas was introduced to the reactor to purge the air. Next, the reactor was put in the electric furnace and quickly heated to $200\text{--}300\text{ }^{\circ}\text{C}$. The temperature in the reactor was determined by a thermocouple (K-type), and the pressure was determined from the water densities. After 2 h (including the heating time of about 15 min) [13], the reactor was taken out from the electric furnace and quickly quenched in a water bath at room temperature. The collected products were dried and calcined. Fig. 1 shows the general process of the particle synthesis by hydrothermal technique.

The morphologies of the calcined powder products were observed using a scanning electron microscope after gold coating. The size was determined by using particle size analysis (PSA). The elemental analysis of the particle products was investigated by using energy dispersive X-ray (EDX) spectroscopy, which was equipped in a Zeiss EVO MA 10 scanning electron microscope (SEM). X-ray diffraction (XRD) patterns were employed to confirm that

the crystal structure of ceria-zirconia was generated through this hydrothermal synthesis method. The capacity of oxygen storage of the ceria-zirconia particle product was determined by using a thermogravimeter [17-18]. The surface area of the ceria-zirconia particle products was determined by using the BET method.

RESULTS AND DISCUSSION

Fig. 2 and 3 show the typical SEM images of synthesized particles from cerium or zirconium solution under hydrothermal conditions at various operating temperatures with 2 h synthesis time. These results reveal that ceria or zirconia particles can be produced easily in water at the applied reaction temperatures. At subcritical conditions, the water turns into a solvent with weak polarity and possesses both acidic and basic properties. These beneficial properties may result in faster and easier particle generation via synthesis reaction. The water molecules underwent dissociation into H^+ and OH^- , which were illustrated as ion products. These ion products rose as the environmental temperature was increased and achieved the highest value when the environment temperature was around $300\text{ }^{\circ}\text{C}$. Simultaneously, the dielectric constant of water also changed. At ordinary conditions, the dielectric constant of water is around 78; thus, water becomes favorable to dissolve the inorganic salts.

When the environment temperature was increased to 200 or $300\text{ }^{\circ}\text{C}$, the values of the water dielectric constants decreased to 35 or 21. This means that water was still favored to dissolve non-polar organic compounds and to serve a homogenous phase for reactions. The solubility of ionic inorganic salts became lower and was able to promote the solute precipitation to generate fine particles via hydrolysis reaction. At the same time, the change of water properties (acid-base characters) can enhance inorganic salts hydrolysis to obtain hydroxides without the presence of catalysts [13,15-16,19]. Therefore, based on benefits such as the reaction rate enhancement and the reduction of solubility that causes a high degree of supersaturation, subcritical water conditions serve as a comfortable reaction media for particle generation.

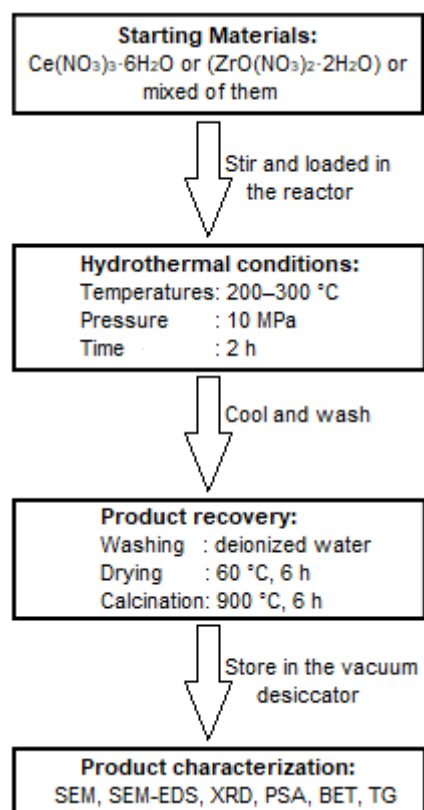


Fig 1. Flowchart summary of the hydrothermal synthesis

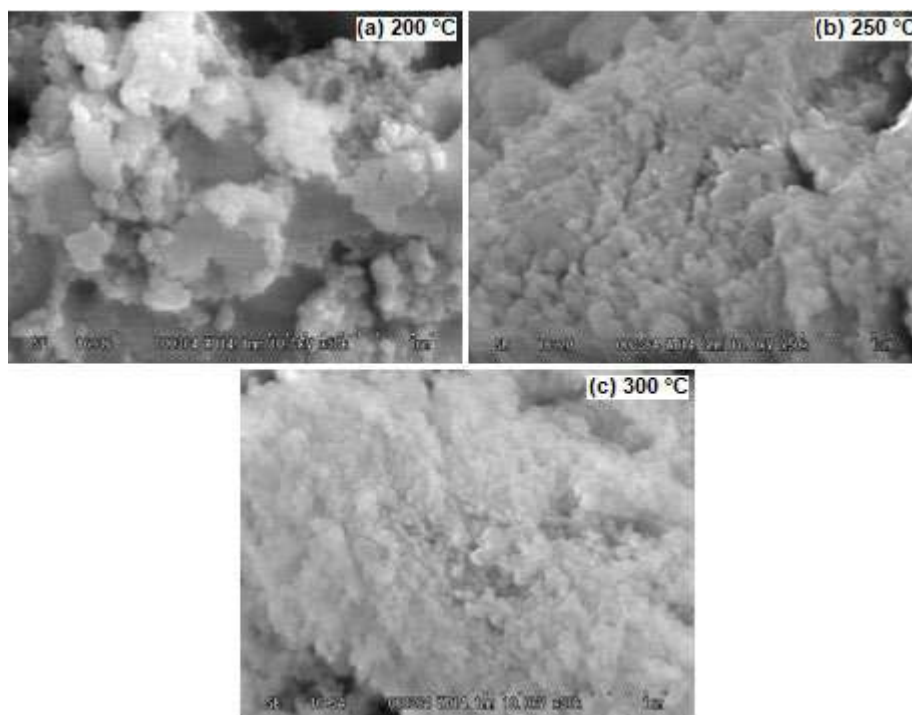


Fig 2. SEM images of ceria particle products

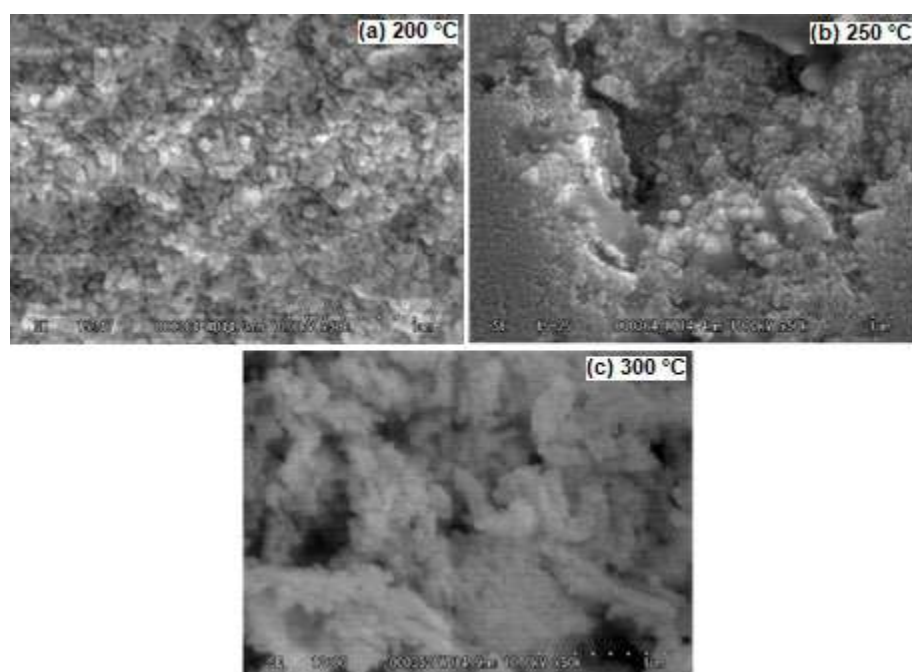


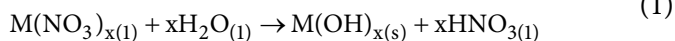
Fig 3. SEM images of zirconia particle products

Adschiri et al. [20] reported that there were two reaction steps for particle generation in hydrothermal conditions from inorganics salts as starting materials, namely, hydrolysis and dehydration reaction. In brief, the

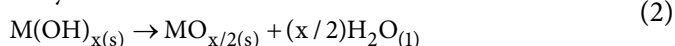
metal salt in the aqueous solution was hydrolyzed into metal hydroxide. Next, the precipitation of metal oxide crystals in nano- or micro-sized particles from solution occurs via dehydration reaction to form particle products.

The formation mechanism of metal oxide particles from the metal nitrate solution was as follows [20-21]:

Hydrolysis



Dehydration



where M is a metal.

As displayed in Fig. 2 and 3, most of the generated ceria and zirconia particles appeared to have spherical morphologies with a diameter of less than 100 nm. The reason for these results may be due to the good solubility of cerium(III) nitrate hexahydrate, and zirconium nitrate oxide hydrate in aqueous media, while the nitrate component from the starting materials may have prevailed as a surfactant to promote the generation of micelles. Similar to other anions that are employed as a coprecipitator, nitrate anions and water are able to surround the surface of cerium or zirconium, which would lead to the generation of fine particles. Due to this phenomenon, the shapes of the generated metal oxide particles, including ceria and zirconia, seemed to have spherical or spherical-like morphologies when the synthesis reaction was carried out in hydrothermal conditions [21-24].

The morphologies of the samples did not shift with the increase in operating temperatures and reaction time. This indicated that the different crystallographic planes of ceria or zirconia particles might have a similar growth rate at these conditions. As a result, the ceria or zirconia particle products that were generated at different temperatures or different reaction times had similar morphology. The results also indicated that hydrothermal reaction conditions are convenient and enough to initiate the formation of fine particles from cerium nitrate or zirconium nitrate solution through hydrolysis and dehydration reactions. Hayashi and Hakuta [13] reported that the hydrothermal synthesis technique involves heterogeneous particle synthesis or particle growth in the existence of liquid media under temperatures (below 300 °C) high enough to start chemical reactions for several hours (h). Afterwards, the hydrothermal synthesis technique for the generation of ceria-zirconia mixed

oxides nanoparticles was set at 2 h reaction time.

Fig. 4 shows the XRD spectra of (a) ceria and (b) zirconia particles obtained by hydrothermal synthesis when the experiments were performed at 300 °C with a reaction time of 2 h. XRD has been applied and mainly relied on for the identification of monoclinic, tetragonal, and cubic phases in materials [25-26]. As shown in Fig. 4(a), the diffraction peaks at 28.5, 33.2, 47.4, 56.5, 59.0, and 69.5° were found clearly on the XRD pattern of the ceria particle products, and can be attributed to the (111), (200), (220), (311), (222), and (400) crystalline faces (JCPDS ICDD PDF card 00-043-1002), respectively. These features revealed that the ceria particle products seemed to have a cubic fluorite-type structure [27-29], where each cerium atom was surrounded by eight oxygen atoms in a face-centered cubic order. This cubic fluorite structure is stable from room temperature to its melting point at around 2400 °C. In addition, ceria particles are also known to be generated by the hydrothermal synthesis method at low operating temperatures.

Tok et al. [27] conducted an experiment for ceria nanocrystalline particles by using a hydrothermal synthesis method at low operating temperatures. They found that ceria particle products containing cubic-fluorite structures were easily generated with relatively good crystallinity at a temperature of around 250 °C. They also reported that increasing the reaction time did not give influence to the properties of the ceria particle products. A similar result was also found when the zirconia particle products were subjected to the X-ray diffraction device (see Fig. 4(b)). The monoclinic, tetragonal, and cubic structures were found in the zirconia particle products; however, the monoclinic structure was found dominantly in the zirconia particle products compared to tetragonal or cubic structures. Hence, the X-ray diffraction patterns for tetragonal or cubic structures were not presented.

The same results were found when Machmudah et al. [15] conducted experiments for hydrothermal synthesis to produce zirconia particles at temperatures of 200-300 °C. They explained that the zirconia particle

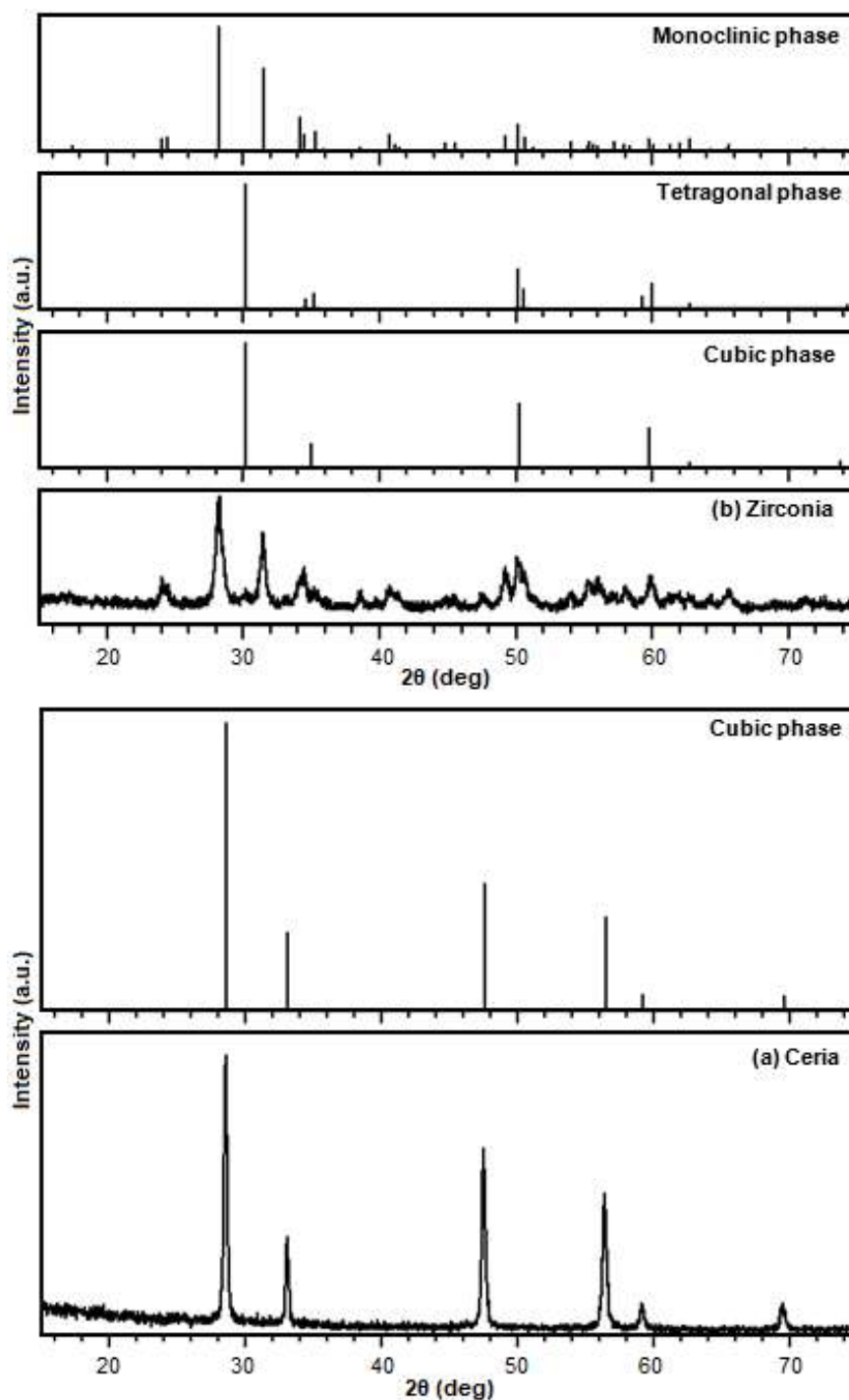


Fig 4. X-ray diffraction spectra of (a) ceria and (b) zirconia particles

products with the monoclinic structure were generated through a dissolution or precipitation process followed by the formation of the tetragonal and cubic structures under subcritical water conditions. As a result, the hydrothermal synthesis products from the zirconium nitrate solution

via the hydrolysis and the dehydration reactions under subcritical water conditions would predominantly be monoclinic zirconia particles. Thus, it can be concluded that the ceria particles with a cubic fluorite-type structure and the monoclinic zirconia particles were

successfully generated from cerium nitrate and zirconium nitrate solutions under hydrothermal conditions.

Fig. 5 shows the typical SEM images and XRD spectra of synthesized particle products from ceria–zirconia solution in a 1:1 ratio at various reaction temperatures with 2 h reaction time. Similar to the pure ceria or pure zirconia particle products, the collected particle products from ceria–zirconia mixed oxides solution seemed to have spherical or spherical-like (oval) shapes at every reaction temperature. Apparently, at these

ranges of temperature, the shapes of the ceria–zirconia particles were dominantly affected by the composition of feed solution that was loaded in the SUS reactor [30–34].

Phokha et al. [30] conducted experiments for the production of monodisperse ceria particles in nano-sphere shapes under hydrothermal conditions. They reported that the feed composition containing cerium nitrate as a cerium source had a significant influence on the morphology of the final product. They also found that the cerium source from cerium nitrate is most favorable

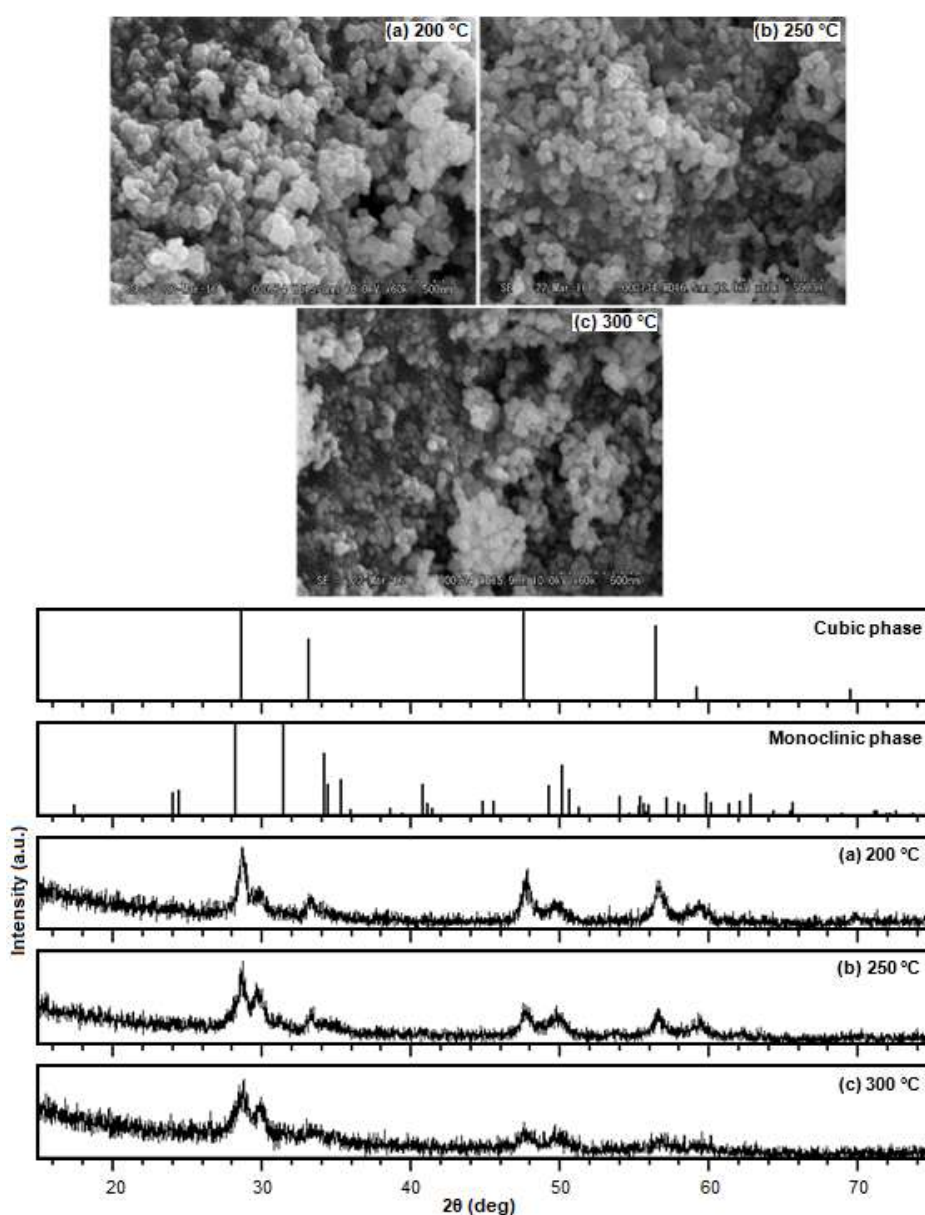


Fig 5. SEM images and X-ray diffraction spectra of ceria–zirconia particle products with 1:1 ratio at various reaction temperatures

for the generation of ceria particles with spherical or spherical-like shapes. Zhang et al. [32] also found the spherical or spherical-like shapes of ceria-zirconia particles when they performed the hydrothermal synthesis of ceria-zirconia nanocomposites from a feed solution containing cerium(III) nitrate hexahydrate and zirconium nitrate hexahydrate. Furthermore, they also reported that the morphologies of the ceria-zirconia nanocomposites did not shift after the calcination process.

When the particles produced from a feed solution containing cerium and zirconium were submitted into the XRD apparatus, the peaks of ceria and zirconia were detected clearly in the XRD patterns at each reaction temperature. Although the hydroxylation of metal ions, including cerium and zirconium, can be significantly stimulated by elevating the reaction temperature at hydrothermal conditions, the characteristic peaks of ceria-zirconia did not seem to shift with increasing reaction temperature. It is well known that the hydrolysis reaction may facilitate and promote complex precursor generation to metal oxide nucleation at hydrothermal conditions (200–300 °C) [13].

Hayashi and Hakuta [13] proposed the mechanism of metal oxide particle generation from metal nitrate solution under hydrothermal conditions. In brief, the hydrated metal ions were hydrolyzed to metal hydroxide. In the next step, the metal hydroxides proceeded to precipitate as metal oxides via dehydration reaction. Due to this phenomenon, the size of the metal oxide particle products was strongly affected by the rate of hydrolysis and the metal oxide solubility in the solvent media. In this work, by using the Scherrer equation, the average crystallite size of ceria-zirconia particle products was estimated from the diffraction peak width at half the peak height (full width half maximum, FWHM). Approximately, the average crystallite sizes of ceria-zirconia particle products at 200, 250, and 300 °C were 7.9, 8.54, and 10.12 nm, respectively. It seemed that the average crystallite sizes slightly increased with the increase in reaction temperature.

In order to accomplish the ceria-zirconia particle analysis, the characterization of the particle products was also carried out by using energy dispersive X-ray (EDX)

analysis, which was attached to the SEM apparatus system. This analysis technique is the general type of X-ray spectroscopy that is simple, non-destructive, and applicable to a small amount of sample. As presented in Fig. 6, the EDX spectrum describes a strong signal corresponding to the ceria and the zirconia elemental regions at around 5 and 2 keV, respectively [35-36]. The peaks that correspond to the existence of ceria and zirconia elements were also found in the regions around 0.2 and 0.9 keV, respectively. It seemed that the ceria and the zirconia elements were a major component compared to oxygen. This is, of course, good news in terms of ceria-zirconia particles formation from cerium(III) nitrate hexahydrate and zirconium nitrate hexahydrate solutions.

The oxygen might have originated from the solvent and/reactants that were bound to the surface of the ceria-zirconia particles. A similar spectrum was also obtained when the ceria-zirconia particles generated from the 200 and 300 °C reaction temperatures were submitted to the EDX device system. Thus, the EDX data for these mixed metal oxide products after hydrothermal treatment at temperatures of 200 and 300 °C are not presented. Judging the results, it can be concluded that the formation of ceria-zirconia particles from the feed solution containing cerium and zirconium elements were successfully performed under hydrothermal conditions at temperatures of 200–300 °C.

Fig. 7 shows the XRD patterns for a series of ceria-zirconia products obtained via hydrothermal reactions at a temperature of 250 °C and 2 h of reaction time with varying molar ratios. As explained above, the composition of the feed solution has an extraordinary influence on the nature and properties of the mixed oxides particles. Proportionally, when cubic fluorite ceria oxides and monoclinic zirconia oxides (see Fig. 4) was fed as the starting materials to produce particles via hydrothermal process, the precipitated particle products with a similar composition to the feed solution can be obtained.

As shown in Fig. 7, when the molar content of ceria oxide in the feed solution was over 50%, the particle products seemed to have a cubic structure. Otherwise, they

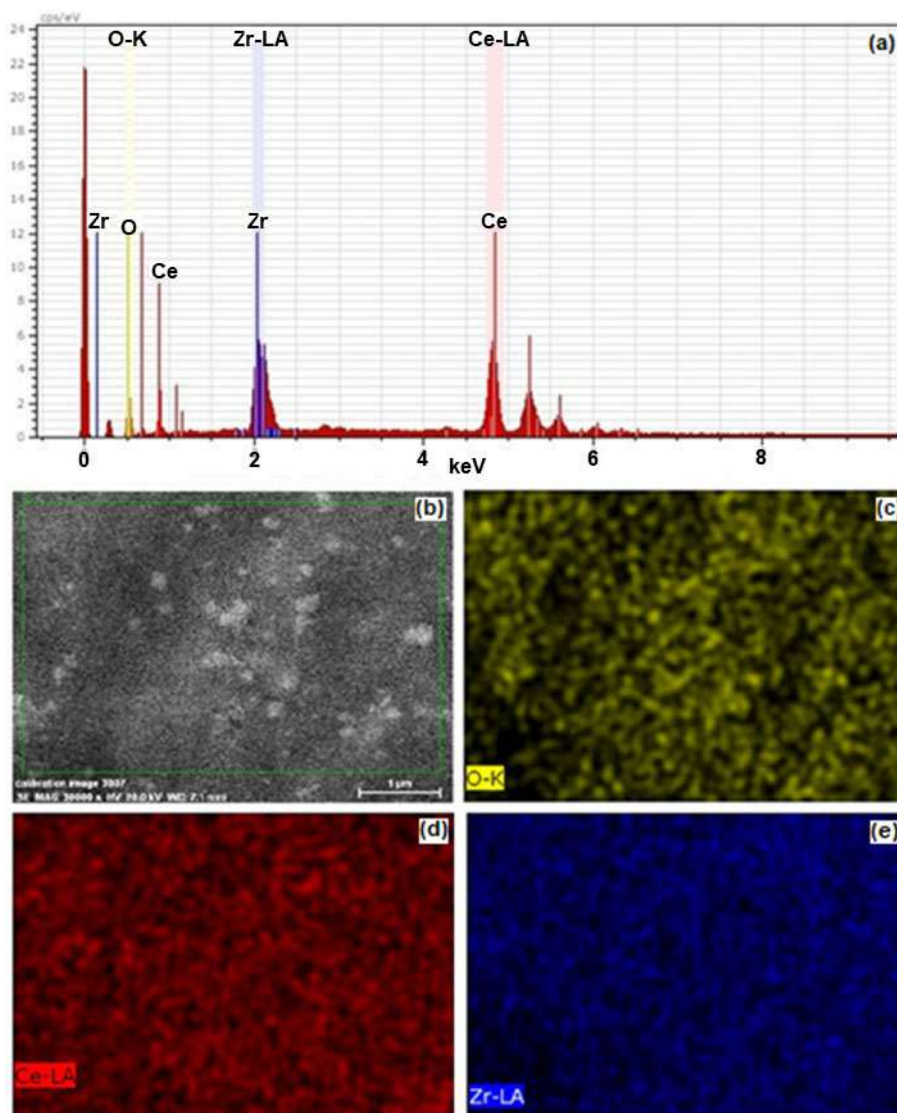


Fig 6. EDX spectrum (a) and dark-field SEM image of ceria-zirconia particles (b) with the corresponding EDX maps for oxygen (c), ceria (d), and zirconia (e) elements (reaction temperature: 250 °C; ceria-zirconia ratio: 1:1; time: 2 h)

appeared as monoclinic structures the same as that of zirconia. The zirconia phase intensity was very weak when the feed solution ratio of ceria to zirconia was 2:1 and 4:1. This result was in agreement with the low amounts of zirconia in the feed solution (ceria-rich feed solution). By increasing the content of zirconia in the starting materials, gradually the shifting of the diffraction lines at 111, 220, and 311, that are attributed to the cubic fluorite-type structure of ceria, was observed [29,37]. Other than that, there were no other diffraction peaks on the XRD patterns of the mixed ceria-zirconia particle products.

It can be assumed that the structure of the ceria-zirconia particle products had uniform distribution. When these particle products were submitted in the particle size analysis (PSA) device, the diameter size of the particles was found at around 100 nm. Note that the particle size distribution was not determined during this study due to the limitation of the analytical equipment. On average, the mean diameter size of the particles was observed at around 99, 125, 92, 118, and 116 nm when the ceria to zirconia ratios of the feed solution was 4:1, 2:1, 1:1, 1:2, and 1:4, respectively. However, by using the Scherrer equation, the estimated

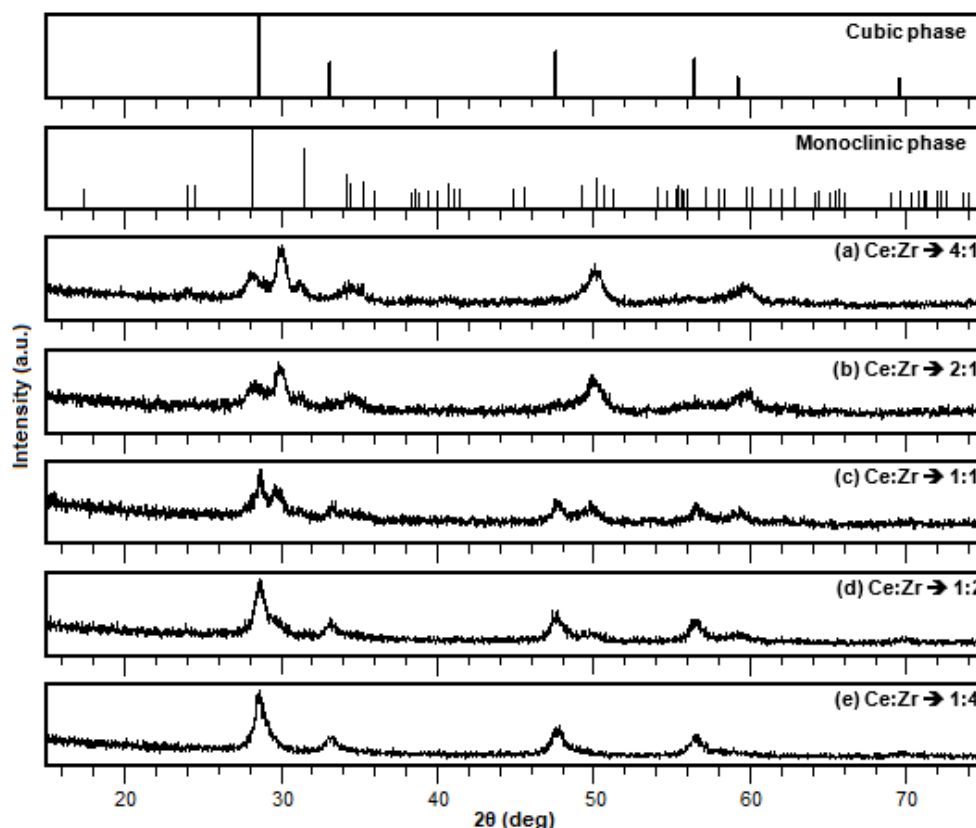


Fig 7. X-ray diffraction spectra of ceria-zirconia particle products at 250 °C with varying molar ratios

crystallite sizes of the ceria-zirconia particles were found at around 10.47, 8.96, 8.54, 5.2, and 7.03 nm on average when the ratios of ceria to zirconia in the starting materials were 4:1, 2:1, 1:1, 1:2, and 1:4, respectively.

It is well known that cerium oxide is the main substance in the three-way catalysis due to its high oxygen storage capacity. This property is associated with the ability of cerium oxide to undergo a rapid reduction-oxidation cycle (between Ce^{4+} and Ce^{3+}). When cerium ion is reduced to Ce^{3+} , the materials release oxygen, and when cerium ion is oxidized to Ce^{4+} , the materials store oxygen. Nevertheless, pure cerium oxide is not widely applicable due to its poor thermal stability and low oxygen storage capacity [6-7].

In this work, when the ceria particles obtained from hydrothermal treatment at a temperature of 250 °C with 2 h reaction time was submitted into the thermogravimeter device to measure its oxygen storage capacity, the amount of oxygen adsorbed was found at around 112.66 $\text{mmol-O}_2/\text{g}$ of sample. By adding zirconia,

the oxygen storage capacity of ceria and the thermal stability were significantly improved. The amounts of oxygen adsorption were 544.48, 652.39, 532.34, 614.71, and 447.38 $\text{mmol-O}_2/\text{g}$ of sample when the ratios of ceria to zirconia in the starting materials were 4:1, 2:1, 1:1, 1:2, and 1:4, respectively. The specific surface area of these samples was around 86.73, 90.98, 92.03, 116.41, and 110.01 m^2/g of sample. It seemed that the values of the oxygen storage capacity were affected by the feed composition of the starting materials. This indicated that the surface area of the ceria-zirconia particles and its oxygen storage capacity were not strongly correlated. The value of the oxygen storage capacity increased with increasing amount of zirconia in the feed solution.

However, increasing zirconia content in the feed solution to over 50% did not significantly affect the oxygen storage capacity of the ceria-zirconia mixed oxides. On the contrary, the oxygen storage capacity value seemed to decrease to 447.38 $\text{mmol-O}_2/\text{g}$ of sample when the mol% ratio of zirconia in the feed

solution was 80%. This indicated that the oxygen storage capacity was not dependent on the surface area of the materials, but they might have been controlled by the thermodynamic equilibrium of the redox reaction of the cerium oxide ions [5,37-42].

Cui et al. [40] investigated the influence of precipitation temperature on the properties of the ceria-zirconia solid solution composite. They reported that the increasing amount of zirconia in the ceria-zirconia solid solution composite did not improve the oxygen storage capacity. Furthermore, they pointed out that the lower amount of zirconia in the ceria-zirconia solid solution composite caused larger oxygen storage capacity. In addition, Cui et al. explained that the decline of textural properties and the shift of composition of the ceria-zirconia composites resulted in the decrease of oxygen storage capacity. Yin et al. [41] confirmed that the high oxygen storage capacity of the ceria-zirconia mixed oxides was associated with the addition of the zirconia substance. However, they also informed that due to the shift of the oxygen mobility in the ceria-zirconia mixed oxides, the higher amount of zirconia in the ceria-zirconia mixed oxides also resulted in lower oxygen storage capacity.

■ CONCLUSION

Ceria-zirconia mixed oxides particles were synthesized via hydrothermal technique at subcritical conditions, at temperatures of 200–300 °C and pressure of 10 MPa. At these conditions, water provides a favorable reaction medium for mixed metal oxides particles formation owing to the adjustability of the thermodynamics and transport properties via pressures and/or temperatures. The SEM images showed that the shapes or morphologies of the ceria-zirconia mixed oxides particles were spherical and spherical-like with a diameter of around 100 nm. The EDX spectrum showed that the signal corresponding to ceria (5 keV) and zirconia (2 keV) were strongly detected in the particle products. The XRD pattern revealed that the mixed metal oxide particles were comprised of cerium and zirconium oxide particles with cubic and monoclinic structures, respectively. Based on the results, this process can be considered as a feasible

technique to produce metal oxide and mixed metal oxides from other types of metals.

■ ACKNOWLEDGMENTS

This research was supported by the Directorate General of Science, Technology and Higher Education, Ministry of Research, Technology and Higher Education of the Republic of Indonesia through the research grant “*Penelitian Dasar Unggulan Perguruan Tinggi*” 2018–2019 contract No. 925/PKS/ITS/2018 and 889/PKS/ITS/2019.

■ REFERENCES

- [1] Trovarelli, A., 1996, Catalytic properties of ceria and CeO₂-containing materials, *Catal. Rev. Sci. Eng.*, 38 (4), 439–520.
- [2] Montini, T., Melchionna, M., Monai, M., and Fornasiero, P., 2016, Fundamentals and catalytic applications of CeO₂-based materials, *Chem. Rev.*, 116 (10), 5987–6041.
- [3] Li, C., Sun, Y., Djerdj, I., Voepel, P., Sack, C.C., Weller, T., Ellinghaus, R., Sann, J., Guo, Y., Smarsly, B.M., and Over, H., 2017, Shape-controlled CeO₂ nanoparticles: Stability and activity in the catalyzed HCl oxidation reaction, *ACS Catal.*, 7 (10), 6453–6463.
- [4] Li, P., Chen, X., Li, Y., and Schwank, J.W., 2019, A review on oxygen storage capacity of CeO₂-based materials: Influence factors, measurement techniques, and applications in reactions related to catalytic automotive emissions control, *Catal. Today*, 327, 90–115.
- [5] Trovarelli, A., and Fornasiero, P., 2013, *Catalysis by Ceria and Related Materials*, 2nd Ed., Imperial College Press, London, UK, p. 329, 666, 735.
- [6] Ragurajan, D., Satgunam, M., and Golieskardi, M., 2014, The effect of cerium oxide addition on the properties and behavior of Y-TZP, *Int. Sch. Res. Notices*, 2014, 828197.
- [7] Huang, H., Liu, J., Sun, P., Ye, S., and Liu, B., 2017, Effects of Mn-doped ceria oxygen-storage material on oxidation activity of diesel soot, *RSC Adv.*, 7 (12), 7406–7412.

- [8] Manicone, P.F., Iommetti, P.R., and Raffaelli, L., 2007, An overview of zirconia ceramics: Basic properties and clinical applications, *J. Dent.*, 35 (11), 819–826.
- [9] Zhang, Y., Malzbender, J., Mack, D.E., Jarligo, M.O., Cao, X., Li, Q., Vaßen, R., and Stöver, D., 2013, Mechanical properties of zirconia composite ceramics, *Ceram. Int.*, 39 (7), 7595–7603.
- [10] Daou, E.E., 2014, The zirconia ceramic: Strengths and weaknesses, *Open Dent. J.*, 8, 33–42.
- [11] Sen, N., and Isler, S., 2020, Microstructural, physical, and optical characterization of high-translucency zirconia ceramics, *J. Prosthet. Dent.*, 123 (5), 761–768.
- [12] Kumar, A., Mansour, H.M., Friedman, A., and Blough, E.R., 2013, *Nanomedicine in Drug Delivery*, 1st Ed., CRC Press, Boca Raton, Florida, USA, p. 25.
- [13] Hayashi, H., and Hakuta, Y., 2010, Hydrothermal synthesis of metal oxide nanoparticles in supercritical water, *Materials*, 3 (7), 3794–3817.
- [14] Kaya, C., He, J.Y., Gu, X., and Butler, E.G., 2002, Nanostructured ceramic powders by hydrothermal synthesis and their applications, *Microporous Mesoporous Mater.*, 54 (1-2), 37–49.
- [15] Machmudah, S., Prastuti, O.P., Widiyastuti, Winardi, S., Wahyudiono, Kanda, H., and Goto, M., 2016, Macroporous zirconia particles prepared by subcritical water in batch and flow processes, *Res. Chem. Intermed.*, 42 (6), 5367–5385.
- [16] Pu, Y., Wang, J.X., Wang, D., Foster, N.R., and Chen, J.F., 2019, Subcritical water processing for nano pharmaceuticals, *Chem. Eng. Process. Process Intensif.*, 140, 36–42.
- [17] Zhang, J., Kumagai, H., Yamamura, K., Ohara, S., Takami, S., Morikawa, A., Shinjoh, H., Kaneko, J., Adschiri, T., and Suda, A., 2011, Extra-low-temperature oxygen storage capacity of CeO₂ nanocrystals with cubic facets, *Nano Lett.*, 11 (2), 361–364.
- [18] Demizu, A., Beppu, K., Hosokawa, S., Kato, K., Asakura, H., Teramura, K., and Tanaka, T., 2017, Oxygen storage property and chemical stability of SrFe_{1-x}Ti_xO_{3-δ} with robust perovskite structure, *J. Phys. Chem. C*, 121 (35), 19358–19364.
- [19] Adschiri, T., and Yoko, A., 2018, Supercritical fluids for nanotechnology, *J. Supercrit. Fluids*, 134, 167–175.
- [20] Adschiri, T., Kanazawa, K., and Arai, K., 1992, Rapid and continuous hydrothermal crystallization of metal oxide particles in supercritical water, *J. Am. Ceram. Soc.*, 75 (4), 1019–1022.
- [21] Lane, M.K.M., and Zimmerman, J.B., 2019, Controlling metal oxide nanoparticle size and shape with supercritical fluid synthesis, *Green Chem.*, 21 (14), 3769–3781.
- [22] Adschiri, T., Hakuta, Y., and Arai, K., 2000, Hydrothermal synthesis of metal oxide fine particles at supercritical conditions, *Ind. Eng. Chem. Res.*, 39 (12), 4901–4907.
- [23] Zhang, Y., Zhang, L., Deng, J., Dai, H., and He, H., 2009, Controlled synthesis, characterization, and morphology-dependent reducibility of ceria-zirconia-yttria solid solutions with nanorod-like, microspherical, microbowknot-like, and micro-octahedral shapes, *Inorg. Chem.*, 48 (5), 2181–2192.
- [24] Yang, Y., Wu, Q., Wang, M., Long, J., Mao, Z., and Chen, X., 2014, Hydrothermal synthesis of hydroxyapatite with different morphologies: Influence of supersaturation of the reaction system, *Cryst. Growth Des.*, 14 (9), 4864–4871.
- [25] Hosokawa, M., Nogi, K., Naito, M., and Yokoyama, T., 2007, *Nanoparticle Technology Handbook*, 1st Ed., Elsevier, Amsterdam, Netherlands, p. 270–272.
- [26] Machmudah, S., Zulhijah, R., Wahyudiono, Setyawan, H., Kanda, H., and Goto, M., 2015, Magnetite thin film on mild steel formed by hydrothermal electrolysis for corrosion prevention, *Chem. Eng. J.*, 268, 76–85.
- [27] Tok, A.I.Y., Boey, F.Y.C., Dong, Z., and Sun, X.L., 2007, Hydrothermal synthesis of CeO₂ nanoparticles, *J. Mater. Process. Technol.*, 190 (1-3), 217–222.
- [28] Kaminski, P., Ziolk, M., and van Bokhoven, J.A., 2017, Mesoporous cerium-zirconium oxides modified with gold and copper – Synthesis, characterization and performance in selective oxidation of glycerol, *RSC Adv.*, 7 (13), 7801–7819.

- [29] Parimi, D., Sundararajan, V., Sadak, O., Gunasekaran, S., Mohideen, S.S., and Sundaramurthy, A., 2019, Synthesis of positively and negatively charged CeO₂ nanoparticles: Investigation of the role of surface charge on growth and development of *Drosophila melanogaster*, *ACS Omega*, 4 (1), 104–113.
- [30] Phokha, S., Pinitsoontorn, S., Chirawatkul, P., Poo-arporn, Y., and Maensiri, S., 2012, Synthesis, characterization, and magnetic properties of monodisperse CeO₂ nanospheres prepared by PVP-assisted hydrothermal method, *Nanoscale Res. Lett.*, 7, 425.
- [31] Alammar, T., Noei, H., Wang, Y., Grünert, W., and Mudring, A.V., 2015, Ionic liquid-assisted sonochemical preparation of CeO₂ nanoparticles for CO oxidation, *ACS Sustainable Chem. Eng.*, 3 (1), 42–54.
- [32] Zhang, X., Wang, Q., Zhang, J., Wang, J., Guo, M., Chen, S., Li, C., Hu, C., and Xie, Y., 2015, One step hydrothermal synthesis of CeO₂-ZrO₂ nanocomposites and investigation of the morphological evolution, *RSC Adv.*, 5 (109), 89976–89984.
- [33] Darr, J.A., Zhang, J., Makwana, N.M., and Weng, X., 2017, Continuous hydrothermal synthesis of inorganic nanoparticles: Applications and future directions, *Chem. Rev.*, 117 (17), 11125–11238.
- [34] Devaiah, D., Reddy, L.H., Park, S.E., and Reddy, B.M., 2018, Ceria-zirconia mixed oxides: Synthetic methods and applications, *Catal. Rev. Sci. Eng.*, 60 (2), 177–277.
- [35] Prasad, D.H., Park, S.Y., Ji, H., Kim, H.R., Son, J.W., Kim, B.K., Lee, H.W., and Lee, J.H., 2012, Effect of steam content on nickel nano-particle sintering and methane reforming activity of Ni-CZO anode cermets for internal reforming SOFCs, *Appl. Catal., A*, 411-412, 160–169.
- [36] Zaytseva, Y.A., Panchenko, V.N., Simonov, M.N., Shutilov, A.A., Zenkovets, Renz, M., Simakova, I.L., and Parmon, V.N., 2013, Effect of gas atmosphere on catalytic behaviour of zirconia, ceria and ceria-zirconia catalysts in valeric acid ketonization, *Top. Catal.*, 56 (9), 846–855.
- [37] Uzunoglu, A., Zhang, H., Andreescu, S., and Stanciu, L.A., 2015, CeO₂-MO_x (M: Zr, Ti, Cu) mixed metal oxides with enhanced oxygen storage capacity, *J. Mater. Sci.*, 50 (10), 3750–3762.
- [38] Hirano, M., and Suda, A., 2003, Oxygen storage capacity, specific surface area, and pore-size distribution of ceria-zirconia solid solutions directly formed by thermal hydrolysis, *J. Am. Ceram. Soc.*, 86 (12), 2209–2211.
- [39] Suda, A., Yamamura, K., Hideo, S., Ukyo, Y., Tanabe, T., Nagai, Y., and Sugiura, M., 2004, Effect of the amount of Pt loading on the oxygen storage capacity of ceria-zirconia solid solution, *J. Jpn. Soc. Powder Powder Metall.*, 51 (11), 815–820.
- [40] Cui, Y., Fang, R., Shang, H., Shi, Z., Gong, M., and Chen, Y., 2015, The influence of precipitation temperature on the properties of ceria-zirconia solid solution composites, *J. Alloys Compd.*, 628, 213–221.
- [41] Yin, K., Davis, R.J., Mahamulkar, S., Jones, C.W., Agrawal, P., Shibata, H., and Malek, A., 2017, Catalytic oxidation of solid carbon and carbon monoxide over cerium-zirconium mixed oxides, *AIChE J.*, 63 (2), 725–738.
- [42] Wang, L., Chen, S., Hei, J., Gao, R., Liu, L., Su, L., Li, G., and Chen, Z., 2020, Ultrafine, high-loading and oxygen-deficient cerium oxide embedded on mesoporous carbon nanosheets for superior lithium-oxygen batteries, *Nano Energy*, 71, 104570.

Antifungal Activity of TiO₂/Ag Nanoparticles under Visible Light Irradiation

Nahzim Rahmat*, Endang Tri Wahyuni, and Adhitasari Suratman

Department of Chemistry, Faculty of Mathematics and Natural Sciences, Universitas Gadjah Mada, Sekip Utara, Yogyakarta 55281, Indonesia

* **Corresponding author:**

tel: +62-87845650024

email: nahzim.rahmat@mail.ugm.ac.id

Received: August 30, 2019

Accepted: September 4, 2020

DOI: 10.22146/ijc.49150

Abstract: The doping of TiO₂ by Ag(I) from [Ag(S₂O₃)₂]³⁻ contained in radiophotography wastewater by photoreduction method has been performed. TiO₂/AgNPs photocatalyst was examined for its activity as an antifungal material for the inhibition of *C. albicans* in water under visible light irradiation. In the doping process, the weight of TiO₂ was varied to obtain TiO₂/AgNPs with different amounts of Ag. The TiO₂/AgNPs samples were characterized by using FTIR, SRUV, TEM, SEM-EDX, and XRD methods. The antifungal test was carried out by disc diffusion method under visible light irradiation, wherein the amount of Ag-doped on TiO₂, the dose of TiO₂/AgNPs, and the irradiation time were optimized. The research results indicated that the antifungal activity of TiO₂/AgNPs in inhibiting *C. albicans* has been successfully prepared. The highest inhibition was achieved by using 0.5 g/L of TiO₂/AgNPs (I), at 5 h of irradiation time.

Keywords: TiO₂/Ag; antifungal; *C. albicans*; visible light; nanoparticle

■ INTRODUCTION

Yeast is a significant component of the microbiota of most natural aquatic ecosystems. The majority of these organisms have no known human health effects. However, a small number of species, primarily within the anamorphic genus *Candida*, are important opportunistic pathogens. *Candida albicans* (*C. albicans*) is an opportunistic pathogen that has a potential impact to increase the risks of waterborne diseases. The presence of *C. albicans* in recreational water and public pools [1-2] requires inclusive attention due to the high risk of infection by the carrier to the human body.

Various methods have been carried out to disinfect water from *C. albicans*, such as conventional methods, ozone water treatment, photo-Fenton, and photocatalysis using TiO₂ under UV light irradiation. The conventional method is a simple method that involves the addition of hypochlorite [Ca(OCl)₂]. This chemical is only effective at pH 7 and temperatures of 23–25 °C. The residue of this chemical has mutagenic and carcinogenic properties when it enters the human digestive tract [3].

The ozone water treatment method is quite effective in killing *C. albicans*, but the operational and installation

costs are expensive [4]. The photo-Fenton method has been proven to kill the *Fusarium solani* fungus [5], but this method still uses UV as a source of radiation, even though the sun only has 3–4% of UV radiation. Photocatalysis using TiO₂ under UV light irradiation has been proven by Tathdil et al. [6] to eradicate *C. albicans*, but the use of TiO₂ was ineffective in visible light regions.

Ag-doped TiO₂ has been proven to increase TiO₂ activity in the visible region by the photoreduction method [7]. Radiophotography wastewater has been reported as a cheap source of Ag(I) that contains [Ag(S₂O₃)₂]³⁻ [8]. The effort to replace expensive AgNO₃ as an Ag precursor, as well as to convert the toxic [Ag(S₂O₃)₂]³⁻ in wastewater into more valuable material, is proposed in this work. On the other hand, radiophotography wastewater was chosen as the source of Ag(I) to support sustainable development goals as well. The synergistic effect between Ag nanoparticles and OH radicals that are produced by TiO₂ after irradiation of UV light increases the antifungal ability of TiO₂/AgNPs.

The ability of TiO₂/Ag nanoparticles (TiO₂/AgNPs) to eradicate microorganisms has not been tested yet on *C. albicans*. Therefore, this study aims to determine the

inhibition of TiO₂/AgNPs on the growth of *C. albicans* by disc diffusion method. In this study, photocatalyst dosage optimization and variation of visible light irradiation time were carried out.

■ EXPERIMENTAL SECTION

Materials

The radiophotography wastewater was collected from the Mitra Paramedika Hospital of Yogyakarta, Indonesia, and was used as a source of Ag(I). The silver standard solution, TiO₂ powder, Nutrient Broth (NB) powder, and Sabouraud Dextrose Agar (SDA) powder were purchased from Merck. Liquid cultures of *Candida albicans* ATCC® 10231 were obtained from the Laboratory of the Microbiology Department, Faculty of Medicine, UGM.

Instrumentation

A set of the photoreduction apparatus with UV Lamp (Black Light Blue 40 W, 220 V, intensity = 0.040 lx) was used for TiO₂/Ag preparation by following the procedure previously reported [8]. Atomic Absorption Spectroscopy/AAS (Perkin-Elmer type 3110), Infra-Red/IR (Shimadzu Prestige 21), Specular Reflectance Ultra Violet/SRUV (Pharmaspec UV 1700), Transmission Electron Microscopy/TEM (JEOL JEM-1400), SEM-EDX (JEOL JSM-6510LA) and X-ray Diffraction/XRD (Shimadzu 6000D) machines were applied for the analysis and characterization of the photocatalyst products. A set of irradiation reactor with a UV lamp (Philips TLD 18 W, 220 V cool daylight, intensity 4750 lx) and visible lamp (Philips TLD 18 W, 220 V cool daylight, intensity = 4750 lx) with wavelengths of 350–400 nm, calliper, autoclave (Hirayama HA-300 MD), micropipette (Socorex), lux meter (mobiken illuminance meter LX2), and incubator (Thelco Oven 4-E-2 Cat No. 31483) were applied for the analysis and assay of the antifungal activity.

Procedure

Analysis of the radiophotography wastewater sample

The Ag(I) content in the sample before and after photoreduction was determined by AAS method. The

amount of Ag reduced and incorporated on TiO₂ structure was calculated using the following formula:

$$C_r = \frac{C_0 - C_{ur}}{W} \times V$$

C_r = The amount of Ag(I) reduced (mg g⁻¹)

C_0 = The concentration of Ag(I) in the wastewater before photoreduction (mg L⁻¹)

C_{ur} = The concentration of Ag(I) in the wastewater after photoreduction (mg L⁻¹)

W = The weight of TiO₂ used in photoreduction (mg)

V = The volume of wastewater (L)

From the AAS analysis, it was found that the concentration of Ag(I) in the radiophotography wastewater was 1502 mg/L.

Preparation of TiO₂/AgNPs photocatalyst

TiO₂ with the weight of 150, 300, and 450 mg were added to separate flasks. Every flask contained 50 mL of radiophotography wastewater and was diluted until 250 mL. The flasks were placed into a sonicator for 1 h and then placed in the photoreduction apparatus. The flasks were exposed to a 40 W UV lamp and were kept stirred with magnetic stirrers at a spin rate of 1500 rpm for 24 h. The product of this process was filtered by using Whatman #42 filter paper to get the solid and filtrate products. The solids were dried at 60 °C and labeled as TiO₂/Ag(150), TiO₂/Ag(300), and TiO₂/Ag(450), corresponding to the weight of TiO₂ that was used. The filtrates were analyzed using AAS to determine the Ag(I) content in the wastewater sample before and after photoreduction.

Characterization of the prepared TiO₂/AgNPs photocatalyst

The photocatalysts produced were characterized by FTIR, SRUV, XRD, SEM-EDX, and TEM. For FTIR analysis, the solids were made into pellets with KBr and were scanned from 400 to 4000 cm⁻¹. The SRUV spectra were taken from the wavelength of 200 to 880 nm. The XRD patterns were recorded using Cu-Kα as the source of radiation with a step of 0.017° and scanning from 5 to 90° (2-theta). The TEM images were shot using copper grids by loading the aqueous suspension at a suitable concentration. The EDX spectra were recorded on JSM-

6510LA (JEOL), equipped with EDX JEOL detector and Analysis Station Software (JEOL).

Antifungal assay by TiO₂/AgNPs photocatalyst

The antifungal assay by one of the TiO₂/AgNPs photocatalyst was carried out by in vitro agar disc diffusion method. All apparatus used were sterilized. A few of the liquid cultures of *C. albicans* were diluted and regrown in nutrient broth (NB) and then incubated for 24 h at 37 °C. The Sabouraud Dextrose Agar 14% with the weight of 6.5 g was dissolved in 100 mL distilled water and then placed into an autoclave to be sterilized at 121 °C and 15 psi for 15 min. The solution was poured into a petri dish then cooled to obtain an agar form. NB was applied and covered on the whole surface area of the agar media (test media) using a sterile cotton swab. The sample (20 µL, 0.3 g/L), sterile distilled water as a negative control which was irradiated for 1 h, and ampicillin disc as a positive control (10 µg) were applied to the test media. This petri dish was incubated for 24 h at 37 °C. The diameter of the inhibition zone was measured using callipers to determine the antifungal activity. The inhibition zone was measured by reducing the overall diameter (paper disc + inhibition zones) with the paper disc diameter. The same procedure was carried out for the visible light irradiation time (1, 3, 5, 7, and 10 h) and the dose variation of TiO₂ and TiO₂/AgNPs (0.1, 0.3, 0.5, 0.7, and 1 g/L),

RESULTS AND DISCUSSION

The photodecomposition of the thiosulfate complex [Ag(S₂O₃)₂]³⁻ can be proceeded through photoreduction under UV light irradiation. This process is catalyzed by the TiO₂ photocatalyst. When TiO₂ absorbs UV light, one electron (e⁻) is excited from the valence band into the conduction band while leaving a hole (h⁺) which is a positively charged radical [13]. The excited electron can react with Ag⁺ which would then be reduced to form Ag⁰ [10]. The reactions are represented by Eq. (1), (2), and (3). At the same time, the hole (h⁺) can react with a water molecule to form a hydroxide radical (•OH) and a proton (H⁺) (Eq. (4)). [Ag(S₂O₃)₂]³⁻ was believed to be oxidized by •OH to form S⁰ and SO₄²⁻ as seen in Eq. (5) [14].

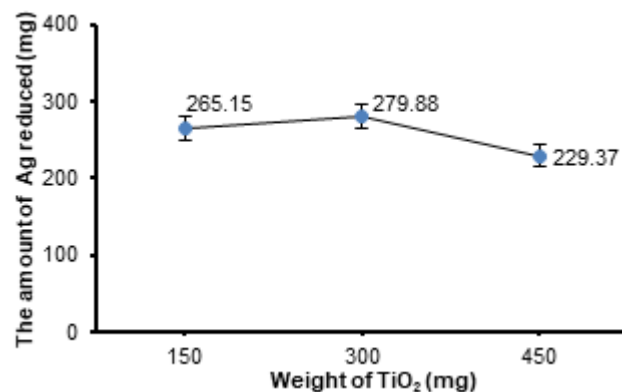
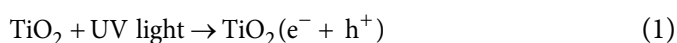
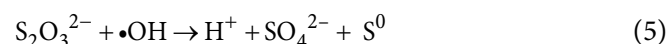
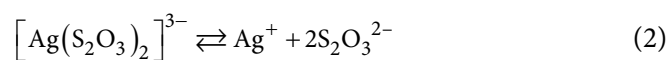


Fig 1. The influence of the TiO₂ weight on the amount of Ag⁰ formed in TiO₂/AgNPs



In this research, the study on the effect of TiO₂ weight toward the amount of Ag⁰ formed in the TiO₂/AgNPs photocatalyst was carried out. Fig. 1 exhibits the amount of Ag(I) reduced from wastewater to form Ag⁰ that was incorporated in the TiO₂/AgNPs photocatalyst, in which the amount of TiO₂ introduced was varied. In Fig. 1, a considerable increase of Ag(I) reduced on the TiO₂ surface was observed when the initial amount of TiO₂ was raised from 150 to 300 mg. This phenomenon was well accepted due to the increased amount of Ag(I) when it captured the release of more electrons which originated from TiO₂, eventually causing the increase of the reduced Ag(I). However, when the weight of TiO₂ was increased, the amount of reduced Ag(I) decreased. Apparently, the larger amount of TiO₂ which exceeded 450 mg, had implicated the turbidity level of the mixture, thereby inhibiting UV light entering the mixture. Consequently, the contact opportunity between UV light and Ag⁺ decreased, thereby decreasing the amount of Ag(I) reduced.

Characterization of TiO₂/AgNPs Photocatalyst

FTIR

Fig. 2 shows the FTIR spectra of TiO₂/AgNPs with various amounts of reduced Ag(I) (279.88, 265.15, and

229.37 mg) prepared by using different TiO_2 weights (150, 300, and 450 mg). For the amount of reduced Ag(I) of 279.88 mg, the notation used was $\text{TiO}_2/\text{AgNPs}$ (I), while $\text{TiO}_2/\text{AgNPs}$ (II) and $\text{TiO}_2/\text{AgNPs}$ (III) denoted the amount of reduced Ag(I) of 265.15 mg, and 229.37 mg, respectively. The strong peaks of anatase TiO_2 were seen at 532, 678, 1635, and 3433 cm^{-1} , which corresponds to the Ti–O–Ti stretching, Ti–O–Ti bending, O–H bending of water, and O–H stretching of Ti–O–H, respectively [8,12]. The spectra for all $\text{TiO}_2/\text{AgNPs}$ samples showed similar peaks with some observable shifts. The peak shifted from 532 to 524 cm^{-1} , 678 to 671 and 655 cm^{-1} , as well as from 1635 to 1627 cm^{-1} . This may be caused by the interaction between Ti–O with Ag ions. According to the fundamental transverse optical phonon mode [13-14], the loading of Ag nanoparticles on the surface of TiO_2 should result in downward shifts of the peaks.

XRD data

The structure and the crystallization of TiO_2 and $\text{TiO}_2/\text{AgNPs}$ were confirmed by using X-ray powder diffraction (XRD, Fig. 3). The XRD patterns of TiO_2 and $\text{TiO}_2/\text{AgNPs}$ was taken in the range of 3–80°. The characteristic peaks of anatase TiO_2 appeared at 2θ values of 25.13°, 37.59°, 47.86°, 53.69°, 54.90°, 62.54°, 68.59°, 70.16° and 74.88°, and are shown in Fig. 3(a). These peaks were confirmed with JCPD Card No. 21-1272 that were

attributed to the diffraction of anatase TiO_2 [9].

Generally, the XRD patterns of $\text{TiO}_2/\text{AgNPs}$ samples with different Ag loads were seen to be almost the same as that of pure TiO_2 , however, Fig. 3(b), 3(c), and 3(d) show that the peak intensities of the $\text{TiO}_2/\text{AgNPs}$ samples were lower than pure TiO_2 (Fig. 3(a)). This indicates that Ag^0 loading only had a small influence (there was almost no effect) [4,15]. The low intensity shown in Fig. 3(b), represented the $\text{TiO}_2/\text{AgNPs}$ (I) sample that had the highest Ag^0 content.

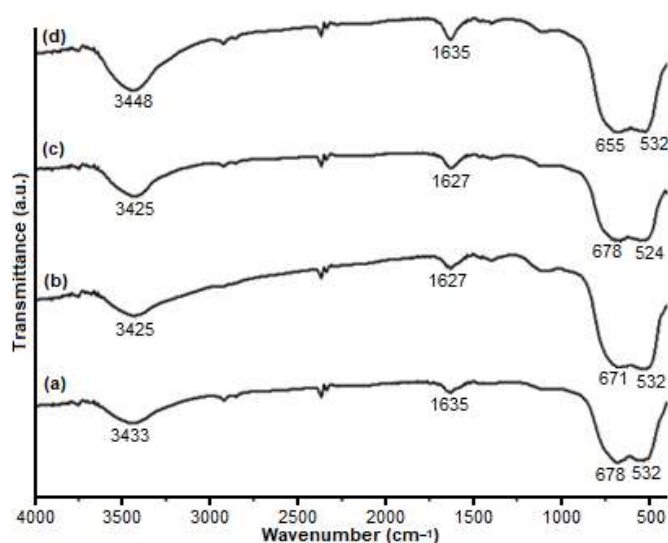


Fig 2. FTIR spectra of (a) TiO_2 , (b) $\text{TiO}_2/\text{AgNPs}$ (III), (c) $\text{TiO}_2/\text{AgNPs}$ (II), and (d) $\text{TiO}_2/\text{AgNPs}$ (I)

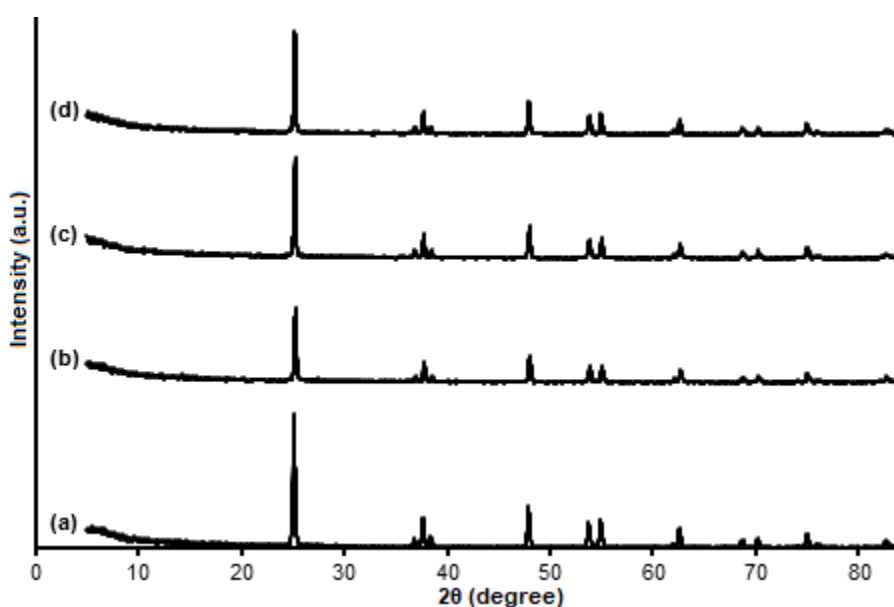


Fig 3. XRD patterns of (a) TiO_2 , (b) $\text{TiO}_2/\text{AgNPs}$ (I), (c) $\text{TiO}_2/\text{AgNPs}$ (II), and (d) $\text{TiO}_2/\text{AgNPs}$ (III)

This indicated that Ag⁰ had covered most of the surface of TiO₂, reducing the intensity of the X-ray diffraction.

The TEM images

The TEM images of TiO₂ and TiO₂/AgNPs samples with various Ag⁰ content are displayed in Fig. 4. Fig. 4(a) shows that the TiO₂ surface was clean and mostly grey [12]. Fig. 4(b), 4(c), and 4(d) show the presence of dark layers in the form of small spheres on the surface of TiO₂ which was likely Ag [11,16-19]. These images also show that the Ag loaded on the surface of TiO₂ were already in nanoparticle size.

EDX data analysis was performed on TiO₂ and TiO₂/AgNPs to determine the content and composition of the elements before (TiO₂) and after loading (TiO₂/Ag). Based on the EDX data analysis, as shown in Table 1, it can be seen that there was a mass of Ag after the loading process. This indicates that the loading of Ag on the surface of TiO₂ was successful. This data can be used to support the TEM images and confirm that the darkest layer in the form of small spheres that appeared on the surface of TiO₂ was likely to be Ag [20]. TiO₂/AgNPs (I) photocatalyst had a higher Ag⁰ content compared to the

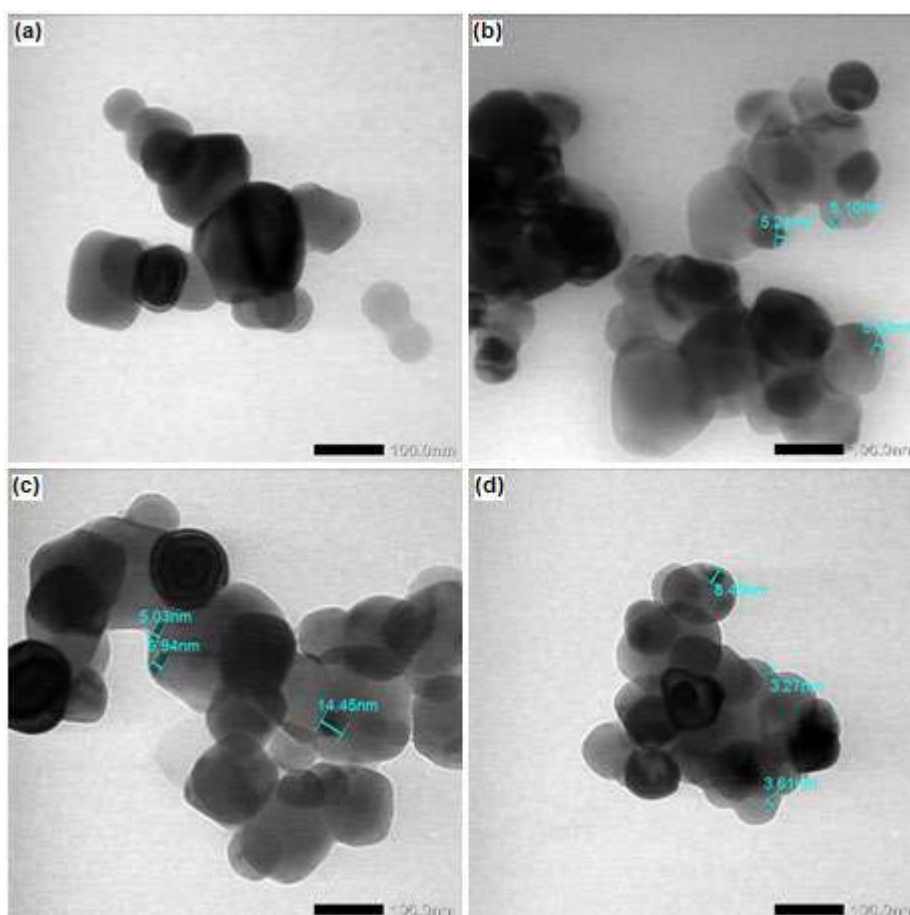


Fig 4. TEM images of (a) TiO₂, (b) TiO₂/AgNPs (I), (c) TiO₂/AgNPs (II), and (d) TiO₂/AgNPs (III)

Table 1. EDX data analysis of TiO₂, TiO₂/AgNPs (I), TiO₂/AgNPs (II), and TiO₂/AgNPs (III)

Element	TiO ₂ (Mass %)	TiO ₂ /AgNPs (I) (Mass %)	TiO ₂ /AgNPs (II) (Mass %)	TiO ₂ /AgNPs (III) (Mass %)
O	52.28	48.45	51.67	53.03
Ti	47.72	44.75	43.79	43.92
Ag	-	6.80	4.54	3.04

other photocatalysts. These results are in agreement with the FTIR and XRD results.

SRUV spectra

The SRUV spectra of the prepared photocatalysts are shown in Fig. 5. The peak absorbance of TiO₂ was found at 381.94 nm, which is in the UV region. Meanwhile, the peak absorbance of the TiO₂/AgNPs samples shifted into the visible region. Calculation using the peak absorbance of the SRUV data provided band gap energies as presented in Table 2.

The band gap energies of TiO₂/AgNPs became lower than TiO₂. This indicated that Ag nanoparticles were loaded on the surface of TiO₂, so that the gap between the valence and conduction bands was narrowed. The photocatalyst TiO₂/AgNPs (I) had the smallest band gap energy compared to the other photocatalysts. This implied that the size of the Ag⁰ particles was small and had the best particle distribution, so they can ideally be loaded on the surface of TiO₂. The band gap energy of TiO₂/AgNPs (II) was slightly greater than TiO₂/AgNPs (I) due to less Ag⁰ content [21]. For TiO₂/AgNPs (III), the band gap energy was higher than the others. This indicates that the amount of Ag⁰ loaded on the surface of TiO₂ was less than the other photocatalysts.

Antifungal Activity of TiO₂/AgNPs

Antifungal activity of TiO₂ and TiO₂/AgNPs under visible and UV light

Based on the results of the SRUV analysis, the lowest band gap energy was owned by TiO₂/AgNPs (I).

Therefore, this photocatalyst was tested for its antifungal activity. Fig. 6(a) shows that the TiO₂/AgNPs was active under visible light. This can be seen from the inhibition zone diameter, although it was still categorized as weak [22]. This barrier was probably derived from Ag⁰ which

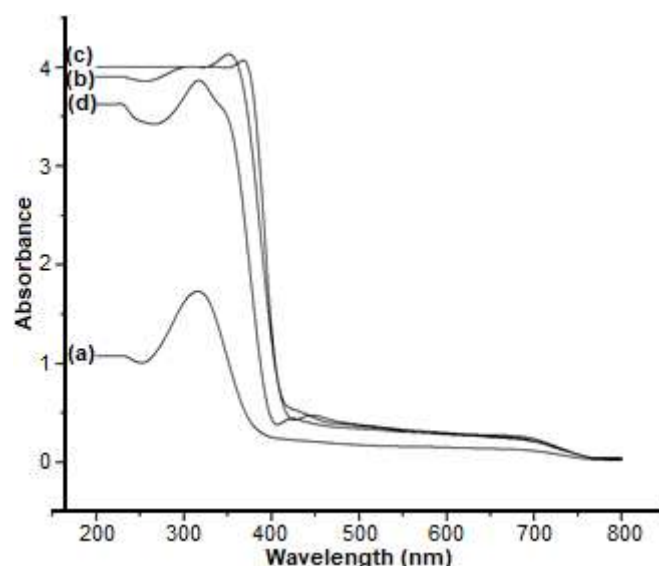


Fig 5. SRUV spectra of (a) TiO₂, (b) TiO₂/AgNPs (I), (c) TiO₂/AgNPs (II), and (d) TiO₂/AgNPs (III)

Table 2. The band gap energy of the titania-based photocatalysts

Photocatalyst	λ_m (nm)	E _g (eV)
Un-doped TiO ₂	381.94	3.25
TiO ₂ /AgNPs (I)	412.70	3.00
TiO ₂ /AgNPs (II)	410.36	3.02
TiO ₂ /AgNPs (III)	397.31	3.12

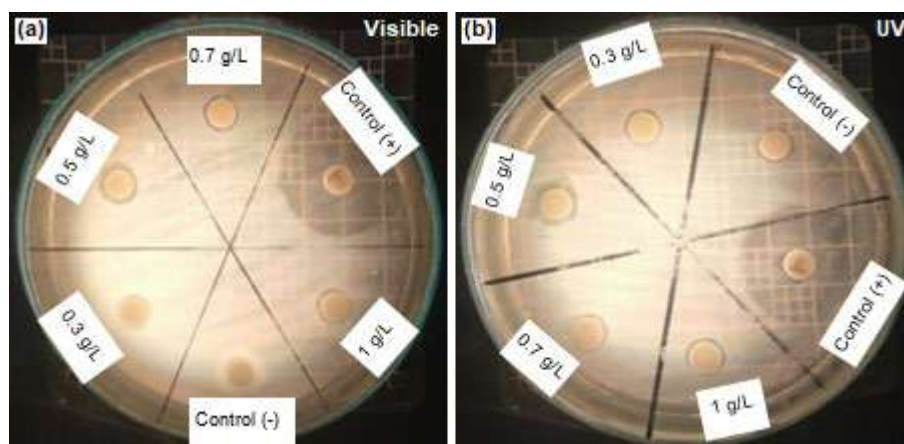


Fig 6. The inhibition zone of TiO₂/AgNPs in UV and visible light irradiation for 5 h on the *C. albicans*

damaged the fungal cell wall. TiO_2 photocatalysts are inactive under visible light because the visible light energy is lower than the energy gap of the TiO_2 band.

The antifungal activity of $\text{TiO}_2/\text{AgNPs}$ was also tested under UV light (Fig. 6(b)) which showed a medium categorized inhibition zone diameter [22]. This suggests that the diameter of the inhibition zone under UV irradiation was wider than under visible light because there were some inhibitory mechanisms that occurred, namely those derived from OH radicals and Ag^0 that damaged the fungal cell wall [23]. TiO_2 is active under UV light. This was indicated from the presence of the inhibition zone diameters, although they were still categorized as weak [22]. This barrier was probably derived from the reaction mechanisms of OH radicals that damaged the fungal cell wall. Observational data are presented in Fig. 7.

The 0.5 g/L dose was chosen for further experiments due to its antifungal activity. Actually, the other samples (0.3, 0.7, and 1 g/L) under visible light (except TiO_2 sample) and UV light also had inhibition activity. However, the most significant inhibition activity was at the dose of 0.5 g/L. This meant that 0.5 g/L was the ideal dose in this experiment. At a dose of 0.1 g/L, there was no inhibition zone, but at higher doses (0.3–1 g/L) the antifungal activity was independent of the catalyst concentration, due to the screening effect produced by the excess of suspended particles which resulted in an inefficient absorption of light by the photocatalyst [8,21].

Various irradiation times (1–10 h) were carried out in this research. At more than 5 h of irradiation, the antifungal activity was no longer dependent on the time irradiation, due to the saturation of the photocatalyst solution which resulted in an inefficient absorption of light [8]. Meanwhile, the irradiation time of 1 and 2 h were observed as well, yet there was no inhibition zone at all. Therefore, the optimum irradiation time was determined at 5 h.

The effect of irradiation time on the antifungal effectiveness of $\text{TiO}_2/\text{AgNPs}$

The effect of irradiation time using visible and UV light on the antifungal activity of $\text{TiO}_2/\text{AgNPs}$ at a dose of 0.5 g/L is shown in Fig. 8. At a dose of 0.5 g/L, the

irradiation intensity that enters the mixture, in both the UV light and the visible light, was sufficient. On the other hand, the availability of OH radicals and Ag nanoparticles to target the large number of fungi was significant. The longer the irradiation time, the wider the diameter of the inhibition zone that occurs. A shorter irradiation time formed only a small amount of OH radicals, so contact with the fungal wall became less effective and the ability to eradicate the fungus decreased.

For a relatively longer time, the production of OH radicals reached optimum results, in which more OH radicals came in contact with *C. albicans*. This fact was indicated by the widening of the diameter of the inhibition zone. However, when the irradiation time was

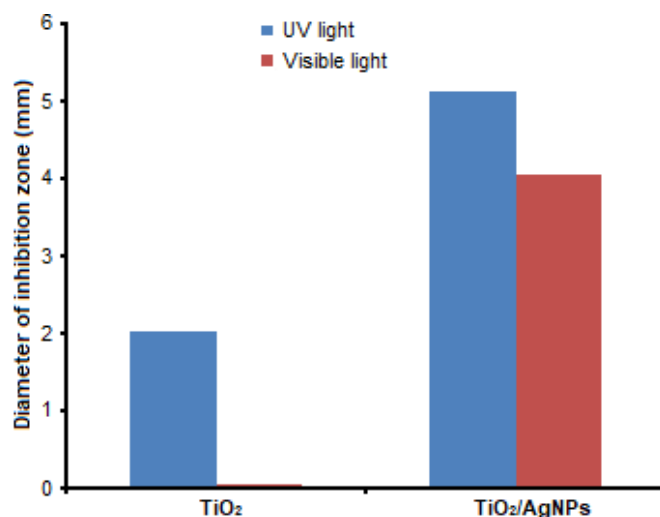


Fig 7. Antifungal activity of TiO_2 and $\text{TiO}_2/\text{AgNPs}$ with 0.5 g/L of the doses on the irradiation for 5 h

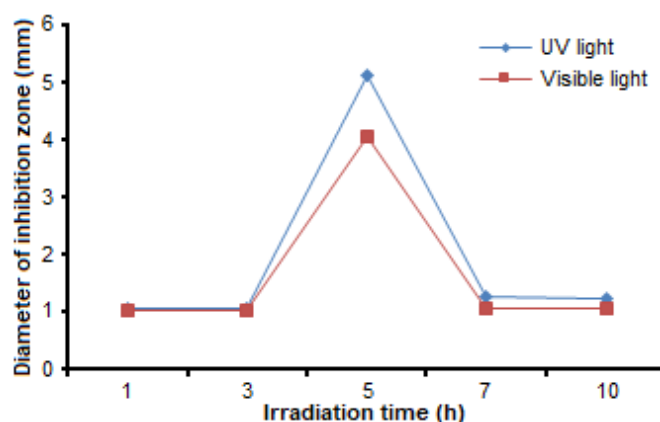


Fig 8. The effect of irradiation time on the antifungal activity of $\text{TiO}_2/\text{AgNPs}$ with 0.5 g/L of the doses

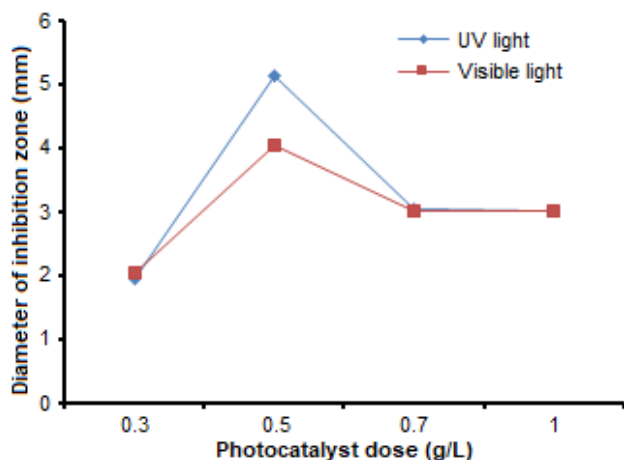


Fig 9. The effect of TiO₂/AgNPs photocatalyst dosage on antifungal activity of *C. albicans* with irradiation time for 5 h

further increased, the antifungal activity decreased as indicated by the decrease in the inhibition zone diameter. This phenomenon was caused by the occurrence of saturation on the surface of the photocatalyst, thereby reducing the ability of the photocatalyst to inhibit fungal growth [8]. The inhibition zone diameter under UV light appeared wider than under the visible light since it was not only Ag⁰ that attacked the fungal cell wall, but also joined by OH radicals. Thus, there was a synergistic effect between Ag⁰ and OH radical which increased the antifungal activity of TiO₂/AgNPs photocatalyst under UV light.

The effect of the photocatalyst dose on the antifungal effectiveness of TiO₂/AgNPs

The effect of the photocatalyst dose on the antifungal activity of TiO₂/AgNPs under 5 h of irradiation is shown in Fig. 9. When the dosage of the photocatalyst was higher, the diameter of the inhibition zone was wider. At low doses, the availability of Ag⁰ was small. This caused the photocatalyst contact with *C. albicans* to be less effective, so the ability to eradicate the *C. albicans* was low. When the dose was increased, the amount of Ag⁰ also increased; so that contact between the photocatalyst and *C. albicans* was more effective and the antifungal activity became higher. This was indicated by the widening of the inhibition zone diameter compared to the previous dose.

At higher photocatalyst dose, the number of photocatalyst particles in the solution also increased. This caused the solution to become turbid, causing obstruction

of visible radiation or UV light that enter the solution [8]. This phenomenon is known as the shadowing or screening effect [21,24]. This effect resulted in the inactivation of the photocatalyst particles thereby reducing its antifungal ability. These results are similar to the research of Wahyuni et al. [8] in which shadowing or screening effect also caused the antibacterial ability of TiO₂/AgNPs in killing *E. coli* to be reduced.

■ CONCLUSION

It can be concluded that the Ag⁰ nanoparticles had been successfully loaded on TiO₂ by photocatalytic reduction of [Ag(S₂O₃)₂]³⁻ contained in the radiophotography wastewater under UV light. AgNPs-doped TiO₂ was found to lose crystallinity and at the same time shifted the optical absorption into visible light. The highest inhibition was achieved by using 0.5 g/L of TiO₂/AgNPs (I), with 5 h of irradiation time.

■ ACKNOWLEDGMENTS

We greatly thank the Ministry of Research and Technology for Higher Education (*Kemristek Dikti*) for the financial support through the PTM research project with the contract number of 2859/UN.1/DIT-LIT/LT/2019.

■ REFERENCES

- [1] Amala, S.E., and Aleru, C.P., 2016, Bacteriological quality of swimming pools water in Port Harcourt Metropolis, *Nat. Sci.*, 8 (3), 79–84.
- [2] Brinkman, N.E., Haugland, R.A., Wymer, L.J., Byappanahalli, M., Whitman, R.L., and Vesper, S.J., 2003, Evaluation of a rapid, quantitative real-time PCR method for enumeration of pathogenic *Candida* cells in water, *Appl. Environ. Microbiol.*, 69 (3), 1775–1782.
- [3] Lubbers, J.D., Chauhan, S., and Bianchine, J.R., 1982, Controlled clinical evaluations of chlorine dioxide, chlorite, and chlorate in man, *Environ. Health Perspect.*, 46, 57–62.
- [4] Cesar, J., Sumita, T.C., Junqueira, J.C., Jorge, A.O.C., and do Rego, M.A., 2012, Antimicrobial effects of ozonated water on the sanitization of dental instruments contaminated with *E. coli*, *S.*

- aureus*, *C. albicans*, or the spores of *B. atrophaeus*, *J. Infect. Public Health*, 5 (4), 269–274.
- [5] Polo-López, M.I., Castro-Alfárez, M., Oller, I., and Fernández-Ibáñez, P., 2014, Assessment of solar photo-Fenton, photocatalysis, and H₂O₂ for removal of phytopathogen fungi spores in synthetic and real effluents of urban wastewater, *Chem. Eng. J.*, 257, 122–130.
- [6] Tatlıdil, I., Sökmen, M., Breen, C., Clegg, F., Buruk, C.K., and Bacaksiz, E., 2011, Degradation of *Candida albicans* on TiO₂ and Ag-TiO₂ thin films prepared by sol-gel and nanosuspensions, *J. Sol-Gel Sci. Technol.*, 60 (1), 23–32.
- [7] Wahyuni, E.T., Roto, R., and Prameswari, M., 2019, Antibacterial activity of TiO₂/Ag-nanoparticle under visible light, *Mater. Sci. Forum*, 948, 33–42.
- [8] Wahyuni, E.T., Roto, R., Novarita, D., Suwondo, K.P., and Kuswandi, B., 2019, Preparation of TiO₂/AgNPs by photodeposition method using Ag(I) present in radiophotography wastewater and their antibacterial activity in visible light irradiation, *J. Environ. Chem. Eng.*, 7 (4), 103178.
- [9] Abbad, S., Guergouri, K., Gazaout, S., Djebabra, S., Zertal, A., Barille, R., and Zaabat, M., 2020, Effect of silver doping on the photocatalytic activity of TiO₂ nanopowders synthesized by the sol-gel route, *J. Environ. Chem. Eng.*, 8 (3), 103718.
- [10] Huang, M., Tso, E., Datye, A.K., Prairie, M.R., and Stange, B.M., 1996, Removal of silver in photographic processing wastewater by TiO₂-based photocatalysis, *Environ. Sci. Technol.*, 30 (10), 3084–3088.
- [11] Sontakke, S., Mohan, C., Modak, J., and Madras, G., 2012, Visible light photocatalytic inactivation of *Escherichia coli* with combustion synthesized TiO₂, *Chem. Eng. J.*, 189–190, 101–107.
- [12] Pelaez, M., Nolan, N.T., Pillai, S.C., Seery, M.K., Falaras, P., Kontos, A.G., Dunlop, P.S.M., Hamilton, J.W.J., Byrne, J.A., O’Shea, K., Entezari, M.H., and Dionysiou, D.D., 2012, Review on the visible light active titanium dioxide photocatalysts for environmental applications, *Appl. Catal., B*, 125, 331–349.
- [13] Suwarnkar, M.B., Dhabbe, R.S., Kadam, A.N., and Garadkar, K.M., 2014, Enhanced photocatalytic activity of Ag doped TiO₂ nanoparticles synthesized by a microwave assisted method, *Ceram. Int.*, 40 (4), 5489–5496.
- [14] Kernazhitsky, L., Shymanovska, V., Gavrillko, T., Naumov, V., Fedorenko, L., Kshnyakin, V., and Baran, J., 2014, Room temperature photoluminescence of anatase and rutile TiO₂ powders, *J. Lumin.*, 146, 199–204.
- [15] Lenzi, G.G., Fávero, C.V.B., Colpini, L.M.S., Bernabe, H., Baesso, M.L., Specchia, S., and Santo, O.A.A., 2011, Photocatalytic reduction of Hg(II) on TiO₂ and Ag/TiO₂ prepared by the sol-gel and impregnation methods, *Desalination*, 270 (1-3), 241–247.
- [16] Susanthy, D., Santosa, S.J., and Kunarti, E.S., 2020, Antibacterial activity of silver nanoparticles capped by *p*-aminobenzoic acid on *Escherichia coli* and *Staphylococcus aureus*, *Indones. J. Chem.*, 20 (1), 182–189.
- [17] Susanthy, D., Santosa, S.J., and Kunarti, E.S., 2018, The synthesis and stability study of silver nanoparticles prepared using *p*-aminobenzoic acid as reducing and stabilizing agent, *Indones. J. Chem.*, 18 (3), 421–427.
- [18] Roto, R., Marcelina, M., Aprilita, N.H., Mudasar, M., Natsir, T.A., and Mellisani, B., 2017, Investigation on the effect of addition of Fe³⁺ ion into the colloidal AgNPs in PVA solution and understanding its reaction mechanism, *Indones. J. Chem.*, 17 (3), 439–445.
- [19] Roto, R., Rasydta, H.P., Suratman, A., and Aprilita, N.H., 2018, Effect of reducing agents on physical and chemical properties of silver nanoparticles, *Indones. J. Chem.*, 18 (4), 614–620.
- [20] Zhao, Y., Sun, L., Xi, M., Feng, Q., Jiang, C., and Fong, H., 2014, Electrospun TiO₂ nanofelt surface-decorated with Ag nanoparticles as sensitive and UV-cleanable substrate for surface enhanced Raman scattering, *ACS Appl. Mater. Interfaces*, 6 (8), 5759–5767.

- [21] Albiter, E., Valenzuela, M.A., Alfaro, S., Valverde-Aguilar, G., and Martinez-Pallares, F.M., 2015, Photocatalytic deposition of Ag nanoparticles on TiO₂: Metal precursor effect on the structural and photoactivity properties, *J. Saudi Chem. Soc.*, 19 (5), 563–573.
- [22] Flanagan, J.N., and Steck, T.R., 2017, The relationship between agar thickness and antimicrobial susceptibility testing, *Indian J. Microbiol.*, 57 (4), 503–506.
- [23] Fujii, G., Chang, J.E., Coley, T., and Steere, B., 1997, The formation of amphotericin B ion channels in lipid bilayers, *Biochemistry*, 36 (16), 4959–4968.
- [24] Mei, S., Wang, H., Wang, W., Tong, L, Pan, H., Ruan, C., Ma, Q., Liu, M., Yang, H., Zhang, L., Cheng, Y., Zhang, Y., Zhao, L., and Chu, P.K., 2014, Antibacterial effects and biocompatibility of titanium surfaces with graded silver incorporation in titania nanotubes, *Biomaterials*, 35, 4255–4265.

Performance Improvement of Tetraethylorthosilicate Consolidated Andesite Rock by Adding Titanium Tetraisopropoxyde and Silica Particles

Nahar Cahyandaru^{1,2}, Endang Tri Wahyuni², and Nuryono^{2,*}

¹Borobudur Conservation Office, Ministry of Education and Culture, Jl. Badrawati Borobudur, Magelang 56553, Indonesia

²Department of Chemistry, Faculty of Mathematics and Natural Sciences, Universitas Gadjah Mada, Sekip Utara, Yogyakarta 55281, Indonesia

* **Corresponding author:**

email: nuryono_mipa@ugm.ac.id

Received: September 18, 2019

Accepted: March 31, 2020

DOI: 10.22146/ijc.49786

Abstract: A study to improve the performance of andesite mortar and rock consolidated with tetraethylorthosilicate (TEOS) sol and a solvent of ethanol in the presence of titanium tetraisopropoxyde (TTIP) and silica particles has been conducted. The improvements include minimizing the shrinkage using silica particles from rice husk ash, rheological property suitability of the consolidant, and mechanical properties of the consolidated mortar and rock. The effect of TTIP concentration, ethanol volume, and addition of the silica particles on rheological properties of TEOS-based consolidant, and also mechanical properties of the consolidated mortar and rock were evaluated. The results showed that the increase of TTIP content in the consolidant shortens the gelling time, and the weight percentage ratio of TTIP:TEOS:ethanol of 5%:55%:40% was the optimum composition for the consolidation. Consolidation of andesite block using that composition significantly increased the compressive strength up to 57.61% (0.58 kgf/mm²). The addition of 2% of silica particles into the consolidant decreased the gel shrinkage and increased the Young modulus of the mortar. The presence of water in the andesite matrix reduced the consolidation performance, and 0.5% was the maximum percentage of water content acceptable for the consolidation.

Keywords: andesite; consolidant; silica-titania; composite

■ INTRODUCTION

Consolidants widely used in rock conservation for many purposes are not only for consolidation of the deteriorated rock but also for repairing mortars. Andesite rock is commonly used for heritage buildings in Southeast Asia, especially in Indonesia. However, the study on the consolidation of andesite rock is still limited. Alkoxysilane based consolidants are the most widely used materials for rock consolidation. Those penetrate easily into porous materials and give less impact compared to other organic-based consolidants. Organic-based consolidants will decrease water and vapor permeability of the consolidated rock and has a glossy appearance. Two compounds, namely tetraethoxysilane (TEOS) and methyltrimethoxysilane (MTMS), are generally used in oligomer form. In the application, those consolidants are adsorbed by a rock to be consolidated, hydrolyzed by water to form silanols, and

followed with condensation to form polymer leading to increase strength [1-2]. Many types of heritage rock, such as sedimentary stone [2], sandstone [3], limestone [4], and calcarenite [5], were conserved with TEOS-based consolidant, but a limited study on andesite rock consolidation was reported.

Consolidation is induced by hydrolysis and condensation reactions of TEOS in the presence of water and catalyst. The hydrolysis of TEOS is generally carried out under acid or alkaline conditions. The acid hydrolysis procedure is commonly employed for the production of silica coating and binder. The quantity of water and acid catalyst used for partial hydrolysis reaction is an important factor for formulating an ethyl silicate binder system. The relatively short shelf life of acid hydrolyzed ethyl silicate solution leads to difficulty in the application [6]. Therefore, the consolidant sol

with a non-aqueous catalyst is developed for the deteriorated rock consolidant to make shelf life longer.

One of the widely used catalysts is dibutyltin dilaurate (DBTDL). This catalyst is used for a TEOS-based consolidant to accelerate the consolidation [7]. The consolidation of TEOS into the rock substrate depends on the gelling time. Typically, TEOS hydrolysis and condensation rate is very slow. The presence of DBTDL in the initial sol increases the rate of hydrolysis, and DBTDL undergoes before hydrolysis to initiate polycondensation reactions [8]. The use of DBTDL as the catalyst in consolidation has been developed to evaluate the effect of a particle on the consolidant performance [2,6-7].

Due to the toxicity of organotin compounds, the application of DBTDL in industrial sectors tends to be decreased to reduce the risk of the negative effects [9]. Organotin compounds are environmental pollutants and endocrine disruptors [10]. Organotin compounds, even in low concentrations, may result in harmful effects on living organisms in the environment [11]. The development of a consolidant without DBTDL catalyst is currently a challenge.

The deficiency of the alkoxy silane-based consolidant is the tendency to crack and shrink during aging. Several studies have modified consolidant by introducing particles into TEOS-based consolidant, a so-called particle modified consolidant (PMC) to minimize the shrinkage. Two types of particles that have been studied as modifiers are nanoparticle silica [2,7] and titania [6].

The consolidation is effective in improving the physical property of deteriorating rock when it can penetrate the rock pores [3]. Therefore, rheological properties such as viscosity, density, and surface tension of the sol are important parameters for consolidant development. It is generally accepted that the penetration of the consolidant mainly depends on its viscosity [8]. An appropriate solvent is added to decrease the viscosity of the mixture to achieve the optimum penetration into the rock pores. However, the solvent addition should be limited since the higher content (34%) of silica gel in the consolidant mixture is necessary [1].

The study reported here is the improvement of TEOS-based consolidant performance by adding silica particles and titanium tetraisopropoxyde (TTIP). Silica particles added into the system acts as a filler in generating particle reinforced composite to reduce gel shrinkage during aging in the consolidation. Silica particles produced from rice husk ash are chosen since, as agricultural solid waste, it has been commonly reported as the precursor for silica particle production [12]. TTIP is used to replace toxic DBTDL as a catalyst to increase the hydrolysis rate and shorten the gelling time [13].

■ EXPERIMENTAL SECTION

Materials

Tetraethylorthosilicate (TEOS, analysis grade with > 99% purity), ethanol (absolute pro analysis grade) were purchased from Merck and used as the consolidant precursor and solvent, respectively. Titanium tetraisopropoxyde (TTIP, pro analysis grade with > 99% purity) used as a titania source was purchased from Aldrich. Silica particles were extracted from rice husk ash in the laboratory of Borobudur Conservation Office using a procedure reported by Zulfiqar et al. [14]. Andesite rock similar to the material used as heritage temples was collected from Magelang, Central Java, Indonesia.

Instrumentation

The instruments used for the analysis included a viscometer Amtast Type NDJ-55, SEM (JEOL 8000-upgraded with Semaphor Image processor) and Image-J software, XRF (Handheld type, Olympus DP-2000), FTIR spectrophotometer (Shimadzu 8201 PC), X-Ray Diffraction (Philips, Ultrasound velocity instrument, Geotron Elektronik type USG40, and Lighthouse DW Ver. 1.3 software for data processing), and Universal Testing Machines (UTM, Comotech model QC-508).

Procedure

Preparation of TEOS/TTIP based consolidant

TEOS/TTIP-based consolidants were prepared by mixing the TEOS, TTIP, and ethanol in various compositions, as presented in Table 1.

The effect of solvent and TTIP concentration on the rheological properties were evaluated from the consolidants C1-C4 and C5-C10, respectively. These rheological properties include viscosity (using viscometer Amtast Type NDJ-55), density, surface tension with capillary method [15], the capillary rate on andesite specimen, and density measured with the gravimetric method using a 25 mL pycnometer.

The surface tension (σ) was calculated using the following formula [15]:

$$\sigma = 0.5\rho ghr [N/m]$$

where ρ = liquid density [kg/m^3], g = gravitational acceleration (9.80665 m/s^2), h = average height of liquid column in capillary [m], and r = capillary radius [m]. The capillary rate was performed on a prismatic andesite specimen of $2.5 \times 2.5 \times 5.0 \text{ cm}$ [1]. One face of $2.5 \times 2.5 \text{ cm}$ was placed in contact with a thin layer of the consolidant sol in a jar to minimize the solvent evaporation during observation. The capillary rate was calculated based on the time needed by consolidant to diffuse completely in the specimen. The gelling time of the sample was observed visually in an interval time of 6 h. The gelling time is equal to the time needed for a consolidant to stop flowing [13].

Consolidation of andesite mortar and rock with TEOS/TTIP consolidants

Andesite powder used for mortar was made from rock block. The sample was grounded with crusher and separated into different sizes by particle siever. The particle size of the andesite powder used for the mortar test followed Fuller law with a maximum size of 2 mm. The particle size distribution of andesite powder tested in this investigation is shown in Table 2.

Consolidation was performed by mixing the 3 mL of consolidant sample to 100 g of andesite powder and put the mixture in a $1.5 \times 1.5 \times 5 \text{ cm}$ cast. After two weeks, the solidification of mortar samples was observed. The result was noted with “negative (-)” if the substrate was still in powder form, positive (+) if the mortar became solid but

fragile, (++) if the mortar became solid but not compact, and (+++) if the mortar became solid and compact.

The consolidation effectivity test of the andesite rock was performed using andesite prism samples with a size of $1.5 \times 1.5 \times 3 \text{ cm}$. The samples were immersed in the consolidant and then air-dried for three weeks for consolidation reaction. The compressive strength of the samples was measured with UTM.

Addition of silica particles in Consolidation

Preparation of silica particles from rice husk ash.

Silica particles were prepared from rice husk ash (RHA) using sodium hydroxide solution followed with a sol-gel process. The rice husk sample was washed with deionized water and dried at $110 \text{ }^\circ\text{C}$ for 2–3 h [9]. The dried sample was powdered by mortar grinding and sieved for 60 mesh [16]. Approximately 25 g of the sample was mixed with 150 mL of 10% citric acid solution and transferred into an autoclave and maintained at $120 \text{ }^\circ\text{C}$ for 2 h. The acid pretreated rice husk was washed several times with distilled water to remove citric acid. The residue of rice husk was dried and incinerated at $650 \text{ }^\circ\text{C}$ for 1 h in a muffle furnace [17-18] to produce RHA. The produced ash was mixed with 100 mL of 2 M NaOH solution, and the mixture was heated at $90 \text{ }^\circ\text{C}$ with continuous stirring

Table 1. The various compositions of prepared consolidants

Consolidant code	Composition (g)		
	TTIP	TEOS	Ethanol
C1(7.3:72.7:20)	7.3	72.7	20
C2(6.4:63.6:30)	6.4	63.6	30
C3(4.5:45.5:50)	4.5	45.5	50
C4(3.6:36.4:60)	3.6	36.4	60
C5(1:59:40)	1	59	40
C6(2:58:40)	2	58	40
C7(3:57:40)	3	57	40
C8(4:56:40)	4	56	40
C9(5:55:40)	5	55	40
C10(6:54:40)	6	54	40

Table 2. Particle size distribution of andesite rock powder 100 g used for mortar consolidation

Particle size (mm)	< 0.063	0.063–0.125	0.125–0.25	0.25–0.5	0.5–1	1–2
Weight (g)	35.44	8.09	10.06	12.39	15.25	18.77

for 2 h to obtain silicate solution. To obtain the desired particle size of silica, the concentration variation of silicate in the solution was 0.05, 0.1, 0.2, 0.3, and 0.4 M, and 10 mL ethanol was added as co-solvent [19]. The silicate solution with various concentrations was then neutralized with 1 M HCl under continuous stirring to allow the gel to be formed. The suspension was centrifuged, and the silica particles were separated, washed with hot water, and dried [8]. The powder was put into crucible porcelain and was pre-heated to 15–200 °C, heated to 650 °C for 2.5–3 h. The silica was grounded in an agate mortar. Ethanol was added and followed with an ultrasonic fragmentation for 2 h. The mixture was left for 10 min at room temperature and centrifuged at 7000 rpm for 5 min. The deposit was refrigerated for 1–2 h, and the silica particles were obtained. Particle size was determined based on the data observation measured with SEM (JEOL 8000-upgraded with Semaphor Image processor). Image-J software was used for the SEM data processing to determine the particle size, and the silica purity of the samples was analyzed with XRF (Handheld type, Olympus DP-2000), and the effect of silicate concentration on particle size was evaluated.

Effect of silica particle addition on the silica-titania gel properties. Silica particle modified silica-titania gel was prepared by adding silica particles to the consolidant C9 (TEOS/TTIP sol with the composition of 55% TEOS,

40% ethanol, and 5% TTIP) at various percentages (0, 1, 2, 3, and 4% (w/w)). The mixtures were put in the open petri dish and located in the open space at room temperature. After 48 h, the solid deposit was obtained, and the shrinkage and crack were observed visually. Additionally, the deposit was characterized by XRD and FTIR spectrophotometer to identify crystallinity and the presence of the functional groups, respectively.

Effect of silica particles on andesite rock consolidation. Analog to the previous work, the mortar was made by mixing 100 g andesite powder and 3 mL consolidant at various percentages of silica particles (0, 1, 2, 3, and 4% (w/w)). The mixture was in a 1.5 × 1.5 × 5 cm cast. The composition of the consolidant sol used for this test was C9. After two weeks, the mortars were characterized by measuring ultrasonic velocity and Young Modulus with Geotron Elektronik type USG40 and Lighthouse DW Ver. 1.3 software for data processing.

■ RESULTS AND DISCUSSION

Rheological Properties of TEOS/TTIP Consolidant

The rheological analysis results of the consolidants, including viscosity, density, surface tension, and capillary rate, are shown in Table 3. In addition, the gelling time and consolidation results are also shown in this table. The mortar samples produced from the consolidation are visually displayed in Fig. 1.

Table 3. Rheological properties of the consolidants with different composition

Sample	Rheological properties					Qualitative result on mortar
	Gelling time (d)	Viscosity (mPa s)	Density (g/cm ³)	Surface tension (Nm)	Capillary rate (cm/s)	
C1(7.3:72.7:20)	3 d 18 h	2.2760	0.8755	0.0314	0.2021	+++
C2(6.4:63.6:30)	3 d 18 h	2.2138	0.8601	0.0323	0.2136	+++
C3(5:55:40)	3 d 18 h	2.1814	0.8410	0.0332	0.2265	+++
C4(4.5:45.5:50)	3 d 18 h	2.1022	0.8318	0.0343	0.2298	+++
C5(3.6:36.4:60)	3 d 18 h	2.0784	0.8145	0.0355	0.2312	+++
C6(1:59:40)	5 d 18 h	2.1811	0.8406	0.0329	0.2253	-
C7(2:58:40)	4 d 18 h	2.1816	0.8409	0.0329	0.2257	-
C8(3:57:40)	4 d	2.1812	0.8408	0.0332	0.2265	+
C9(4:56:40)	3 d 18 h	2.1815	0.8412	0.0332	0.2259	++
C10(5:55:40)	3 d 12 h	2.1820	0.8411	0.0335	0.2264	+++
C11(6:54:40)	3 d 6 h	2.1821	0.8415	0.0335	0.2260	+++

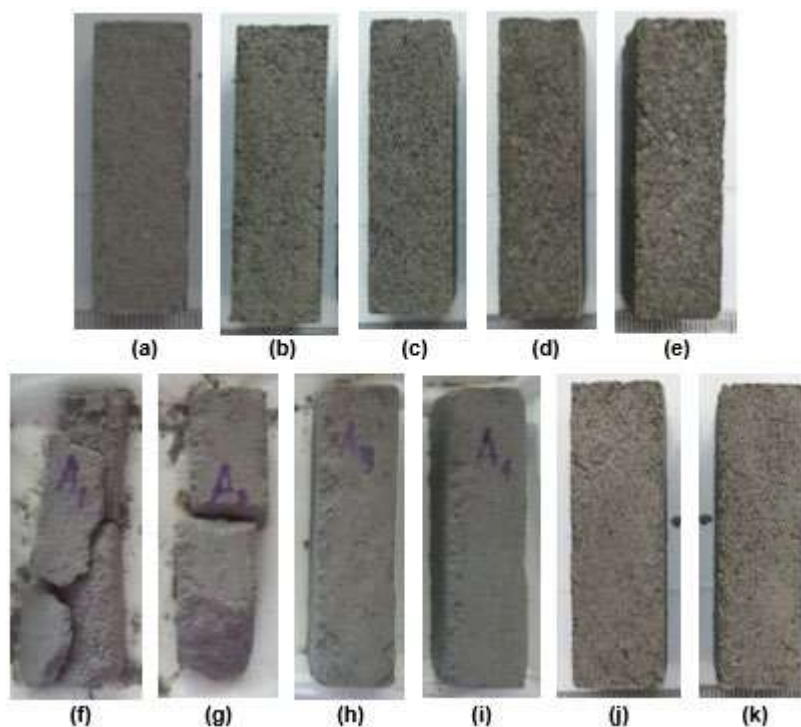


Fig 1. The mortar form andesite and TEOS-base binder with different percentage of TTIP (a) 1%, (b) 2%, (c) 3%, (d) 4%, (e) 5%, and (f) 6%

The rheological data of the samples shows that the increase in ethanol content (C1-C5) decreases the viscosity and density, but increases the surface tension and the capillary rate of the sol to andesite rock particles. A high capillary rate of consolidant is expected to ensure the penetration of consolidant material into the rock pore. The consolidant shows different capillary rates in different types of rock, mainly due to the different microstructural characteristics of rock [6]. Andesite rock is a porous material that easily allows the consolidant to penetrate deeply into the porous structure.

From this data, all samples show good rheological properties. The sol can penetrate easily and saturated the andesite rock. In this variation, there is no optimum point since all viscosities are shown in an acceptable range. According to Li et al., commercial consolidant has a viscosity range between 2–3.3 mPa s [8]. Higher ethanol content increases the capillary rate, but the silica content in the mixture is low and not sufficient to attach andesite inter-particles. According to Pinto and Rodrigues, the minimum of silica gel content in the consolidant mixture is 34% [1].

The optimum mixture of the consolidant was observed from the consolidation result. The effective consolidation was obtained at the high content of TTIP, from sample C7 to C8. The low TTIP content (sample C5 and C6) shows negative consolidation, there is no consolidation, and the substrate remains in powder form. The minimum content of TTIP composition in the consolidant sample is 5% (with 55% TEOS and 40% ethanol) represented by sample C9. This sample also shows acceptable viscosity (2.1820 mPa s) and capillary rate (0.2265 cm/s).

The consolidation effectiveness relates to the gelling time. Hydrolysis and condensation rates of TEOS are typically low. The consolidation occurs with the high hydrolysis and condensation rate, commonly by catalyst addition. In this study, the increase of hydrolysis and condensation rates due to the addition of TTIP. The TTIP hydrolysis rate is faster than TEOS. The increase of TTIP concentration inclines the hydrolysis and condensation rates and decreases the gelling time. There is no significant effect of the ethanol content on the gelling time.

Silica Particles

Silica particles were extracted from RHA by destructing the sample with sodium hydroxide solution and being followed with the sol-gel process. The silica particle size depends on several factors, including the presence of templates, type of solvent, and concentration of precursor [14]. In this research, the effect of silicate concentration

on the particle size was evaluated based on the SEM (with 10.000× magnification) image and measured with Image-J software. The result is shown in Fig. 2.

Based on the Image-J software analysis, the particle size of silica can be determined. The results, including the yield and purity percentages analyzed with XRF, are presented in Table 4.

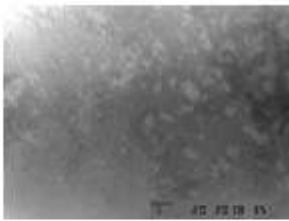
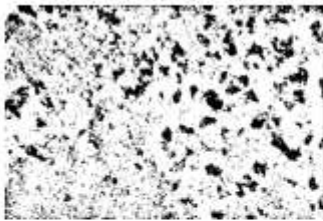
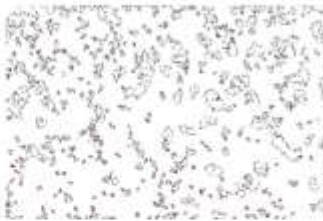
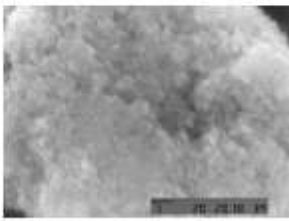
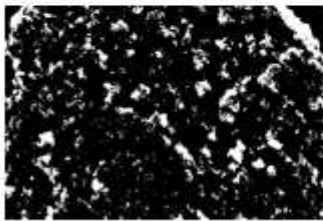

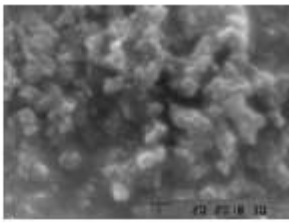
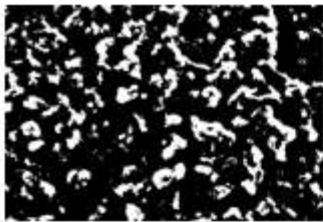

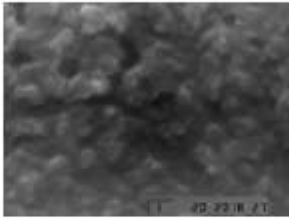
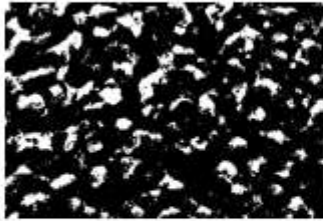

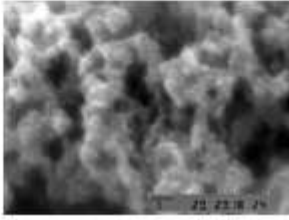


Concentration (M)	Analysis result with Image-J software		
	SEM image	Threshold	Outline
0.05			
0.1			
0.2			
0.3			
0.4			

Fig 2. SEM image, threshold, and outline of silica particles extracted from RHA processed with Image-J software at various silicate concentrations

Table 4. Yield, purity, and particle size of silica particles extracted from RHA at various silicate concentrations

Concentration of silicate solution (M)	Yield (%)	Purity (%)	Size (nm)
0.05	55.74	98.99	109 ± 56
0.10	58.05	98.73	119 ± 83
0.20	59.48	99.01	150 ± 88
0.30	62.64	97.87	197 ± 73
0.40	68.91	98.89	211 ± 81

The particle size of the silica is influenced by the concentration of silicate in the solution during the precipitation. The increase in silicate concentration increases the particle size and the yield of the silica. A silicate concentration of 0.05 M shows the smallest particle size with the narrow particle size distribution (109 ± 56 nm). For that reason, this silica particle resulted from silicate solution 0.05 M was chosen as modifier particles in the TEOS/TTIP consolidant for the next step of this study. This particle size is chosen based on previous researches of the particle modified consolidant studies. Liu et al. used silica commercial silica particles with

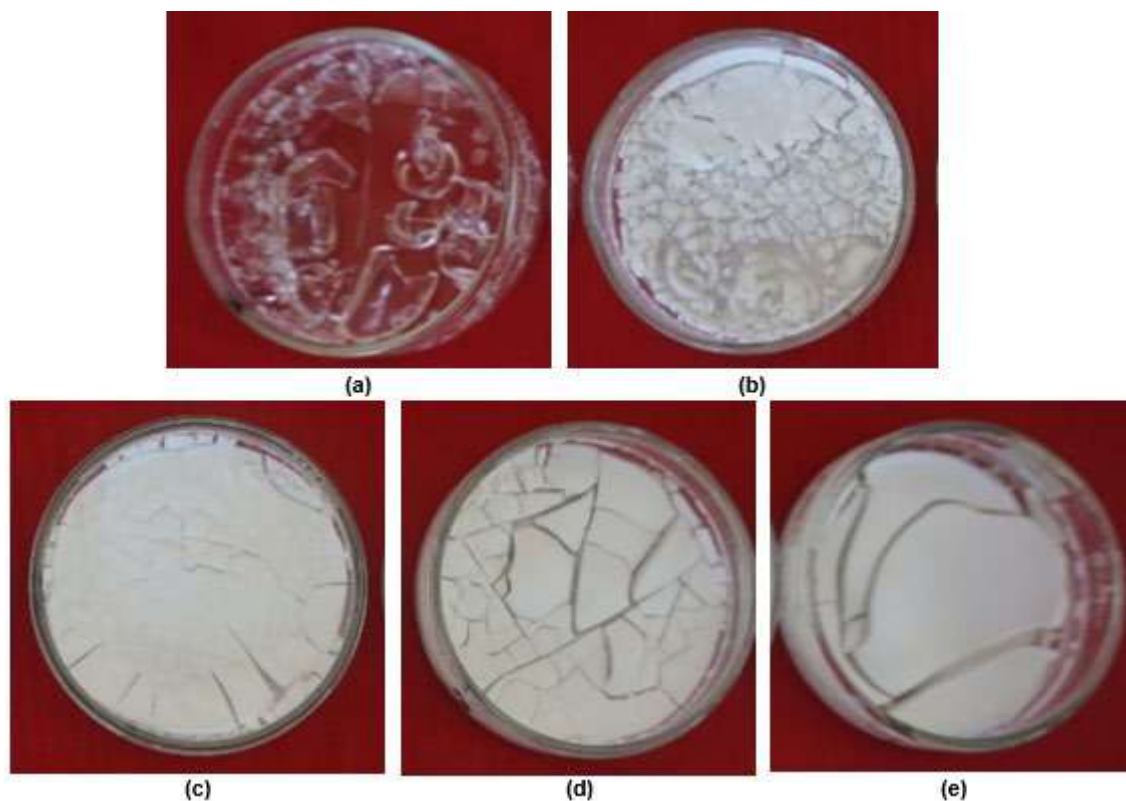
100 nm size [7], while Ksinopoulou et al. used 150 nm commercial titania particles as modifiers [6].

Effect of the Silica Particle Addition on the Gel Properties

Crack and shrinkage level

The effect of silica particle addition on crack and shrinkage levels can be evaluated from the images of the gel formed from consolidants. Fig. 3 shows the images of the gel formed from TEOS/TTIP consolidant with various additions of silica particles. The gel is formed through hydrolysis and condensation reactions. The hard silica gel is obtained after the condensation of silanols. The silica/titania gel formation tends to shrink and crack, as shown in Fig. 3(a), and the crack decreases with the addition of the silica particles (Fig. 2(b-e)).

Fig. 3 indicates that qualitatively, the optimum percentage of the silica particle addition was 2%. There is a significant decrease in crack formation with increasing the percentage up to 2%, and the crack tends to decrease with increasing the percentage up to 4%.

**Fig 3.** Images of silica-titania gel formed by TEOS/TTIP consolidant with addition of silica particle (a) 0%, (b) 1%, (c) 2%, (d) 3%, and (e) 4%

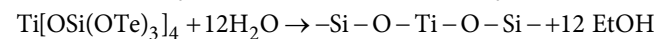
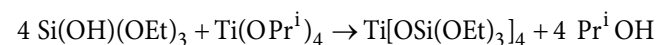
Functional groups of silica-titania gel

Fig. 4 shows the FTIR spectra of the gel formed from various consolidants.

The FTIR spectra of the silica, both extracted from RHA (Fig. 4(d)) and from TEOS (Fig. 4(e)), shows the peaks indicating characteristic bonds in silica. The peaks at 802 and 462 cm^{-1} indicate Si-O symmetric bending and rocking, respectively. Peaks at 1103 and 802 cm^{-1} indicate the presence of Si-O-Si bond [20], and the broad band around 3433 cm^{-1} is assigned to the superposition of the Si-OH bond stretching [21]. In the FTIR spectra of titania (Fig. 4(c)), peaks at 648 and 1080 cm^{-1} indicate the Ti-O-Ti and Ti-O-C bond, respectively [22-23]. A peak at 941 cm^{-1} in the FTIR spectra of silica-titania (Fig. 4(a)) represents a vibration of Si-O-Ti bond [20-21].

There are two types of interaction between TiO_2 and SiO_2 , namely physical (with interaction forces weaker than Van der Waals forces) and chemical (by the formation of Ti-O-Si linkages) interaction. Among the various preparation methods, sol-gel hydrolysis is most widely used due to its possible capability in controlling the textural and surface properties of the mixed oxides. In sol-gel processes, the formation occurs due to the differences in the hydrolysis and the condensation rates of Ti- and Si- alkoxides [13]. According to Marimuthu et al. [24], the formation of Si-Ti mixed oxides through hydrolysis and condensation from TEOS ($(\text{SiOC}_2\text{H}_5)_4$) and TTIP

($\text{Ti}(\text{OPr}^i)_4$) mixture can be presented in the following reaction.



The crystallinity of silica-titania gel

Fig. 5 shows the XRD pattern of the silica-titania gel modified with and without silica particles, in comparison to titania (from TTIP), and silica (from TEOS and rice husk ash).

The samples used for the measurement is in the same amount. From the diffraction pattern, the amorphous silica is shown by the reflection at around 22.5° [25]. This reflection also occurs at the diffraction of the silica-titania gel samples. The addition of silica particles improves the intensity of the specific peak of amorphous silica. The diffraction pattern of the titania shown in Fig. 5(e) suggests that mainly the anatase phase is obtained [26]. The characteristic reflection corresponding to this phase is observed at 2θ of 25.5°, 38.2°, 48.2°, and 54.3°. This reflection also occurs in the pattern of the silica-titania gel (Fig. 5(a)) and silica-titania gel modified with silica particles (Fig. 5(b)) with a lower intensity. The decrease in the intensity of the titania reflection is due to the lower concentration in the gel. Silica can inhibit the formation of TiO_2 by impeding

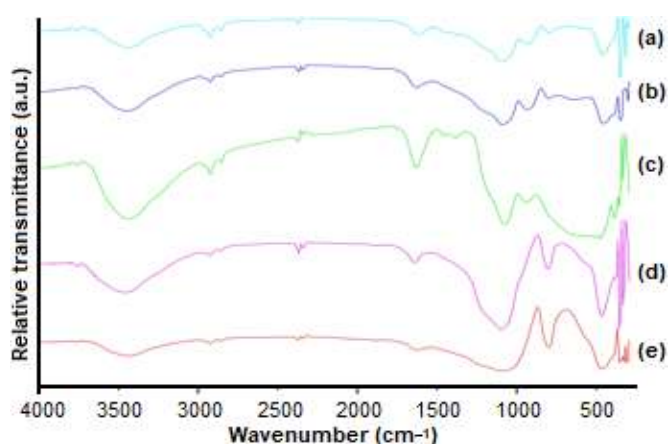


Fig 4. FTIR spectra of (a) silica-titania, (b) silica-titania gel modified with silica particles, (c) titania from TTIP, (d) silica from RHA, and (e) silica from TEOS

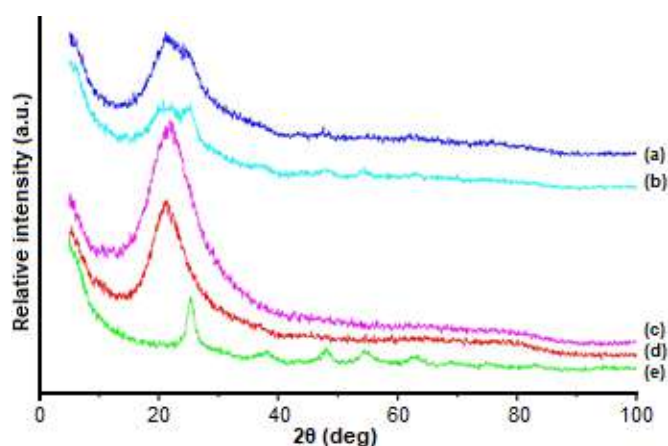


Fig 5. XRD pattern of (a) silica-titania gel, (b) silica-titania gel modified with silica particle, (c) silica gel from TEOS, (d) silica gel from RHA, and (e) titania

direct contact between TiO_2 particles by forming the Ti-O-Si bonding [27].

Consolidation of Andesite Rock

Preparation of TEOS-base consolidant without an organotin catalyst is the main objective of this study. Titanium tetraisopropoxide (TTIP) was tested as a catalyst component on the formation of silica chain during consolidation. Ethanol was used for the solvent to increase the penetration degree of the mixture into the rock pores. The variation of the TTIP percentage in the mixtures were tested to consolidate. Fig. 5 shows the mortar result in consolidation after aging for two weeks at room temperature. The figure shows that mortar consolidation starts from 4% of TTIP, while no effective consolidation occurs at a lower percentage. This relatively higher result, comparing to organotin (normally used at 1%) [28], is due to the double roles of the TTIP in the mixture, acting as a catalyst and being involved in the polymer formation.

Ultrasound velocity measurement of the samples was performed to evaluate the consolidation effectiveness of the sample quantitatively. Table 4 shows the result of ultrasound velocity and the Young modulus data of the samples. Young modulus was one of the important parameters to evaluate the hardness of materials, including rocks [22]. Consolidation is a process of increasing the hardness of the accelerated materials. Therefore, Young modulus could express the effectiveness of the consolidation. The Young modulus data was calculated based on the ultrasound velocity and the density of the samples [21].

At the low percentage of TTIP (1 and 2%, presented with formula C5, and C6, respectively), the consolidation of the mortars is not effective, the hydrolysis and condensation of TEOS to create silica bridging system

were not obtained. The consolidation occurs at 3% and increases with the increase of TTIP up to 5% and to be constant at 6%. The hydrolysis TTIP has a higher hydrolysis rate than TEOS. By mixing TTIP and TEOS, the hydrolysis rate is between TEOS and TTIP ones. Consolidation occurs when hydrolysis and condensation of the mixture are able to bond inter-particles effectively. This inter-particle bonding increases the cohesion between particles and leads to strengthening the material presented with modulus elasticity.

Water is an essential agent in the consolidation process with a TEOS-based consolidant that involves hydrolysis. In consolidation with TEOS-based consolidant using an acid catalyst, few portions of water are added to hydrolyze TEOS to form a silica oligomer. The quantity of water and acid catalysts used for partial hydrolysis is also an important factor in this consolidant formula. The higher presence of water in the consolidant shortens the shelf life of the solution leading to difficulties in application [29].

The hydrolysis reaction rate of TEOS depends on the amount of water in the system. Therefore, the specific and low concentration of water is needed for the next simultaneous step with the condensation reaction of silica. On the other hand, the high water content will accelerate the reaction before contact with the stone and disturb the consolidation process. The consolidation effectiveness of the andesite block sample represents the condition of field implementation. The result of the consolidation effect of different consolidation formula is shown in Table 5.

Compressive strength is an appropriate parameter to understand the effectiveness of the consolidation. An effective consolidant can increase the compression strength of the deteriorated andesite. According to

Table 4. Ultrasound velocity and Young Modulus of mortars produced from consolidation with various concentrations of TTIP in consolidant

	Consolidant sample code					
	C5	C6	C7	C8	C9	C10
Ultrasound velocity (km/s)	*	*	0.868	1.067	1.555	1.565
Raw density (g/cm^3)	*	*	1.52	1.56	1.68	1.674
Young Modulus (N/m^2)	*	*	0.939	1.645	3.786	3.715

* Unmeasurable due to very low consolidation performance, the samples were very fragile

Table 5. Compressive strength of andesite rock sample consolidated using consolidants with different TTIP concentration

	Untreated andesite	Consolidant sample code					
		C5	C6	C7	C8	C9	C10
Compressive strength (kgf/mm ²)	0.368	0.38	0.402	0.474	0.519	0.58	0.589
% Strength increase *		3.26	9.24	28.80	41.03	57.61	60.05

* Based on the comparison with untreated deteriorated andesite from the same block

Clifton [30], effective consolidant increases the compressive strength at a minimum of 10%. This result shows the high increase of andesite compressive strength at more than 3% of the consolidant formula. This result is consistent with the result of the andesite mortar test.

In this study, the effect of water content in the matrix on the consolidation was also evaluated. Table 6 shows mortar performance resulted from consolidation in the various contents of water. The result shows that the consolidation does not work in the presence of water more than 0.75%. The dry matrix is the best condition for the consolidation, and 0.5% of water content is still acceptable for the consolidation.

This result is very important to understand the sensitivity of the formula to the water content. Andesite is commonly used as the heritage materials in Southeast Asian countries, such as Indonesia, Malaysia, and Thailand, located in tropical areas with relatively high humidity. The heritage materials are typically found in the open area. Therefore, the conservation of rock heritages

containing water is still a challenge. All of the TEOS-based consolidants are sensitive to water. This study reveals that the water content limits in the matrix to be conserved and the selection of consolidants used in wet matrixes are important.

Effect of silica particle addition

The influence of silica particle modifier on the mortar parameters by measuring the ultrasound velocity and Young modulus was evaluated, and the result is expressed in Table 7. The data shown in the table corresponds to the qualitative observation of the gel shrinkage, as presented in Fig. 2. Ultrasound velocity and Young modulus of the sample increase in accordance with the percentage of added silica particles. The significant increase in the addition of 1 and 2% is observed, and the addition of more than 2% of the values tends to be constant. Therefore, the optimum addition of the silica particles was at 2%, and higher addition may lead to change the color in the application [6].

Table 6. Ultrasound velocity and Young modulus of mortars made of andesite rock powder with different water content

Parameters	Water content in the mortar (%)				
	0	0.25	0.5	0.75	1
Ultrasound velocity (km/s)	1.565	1.426	1.44	*	*
Raw density (g/cm ³)	1.74	1.78	1.66	*	*
Young Modulus (N/m ²)	3.715	3.253	3.182	*	*

* Unmeasurable due to very low consolidation result, the samples were very fragile

Table 7. Ultrasound velocity and Young modulus of mortars made from a different percentage of silica particle modifiers in the consolidant

	Silica particle addition (%)				
	0	1	2	3	4
Ultrasound velocity (km/s)	1.486	1.517	1.574	1.613	1.609
Raw density (g/cm ³)	1.61	1.59	1.76	1.76	1.76
Young Modulus (N/m ²)	3.407	3.56	4.156	4.327	4.015

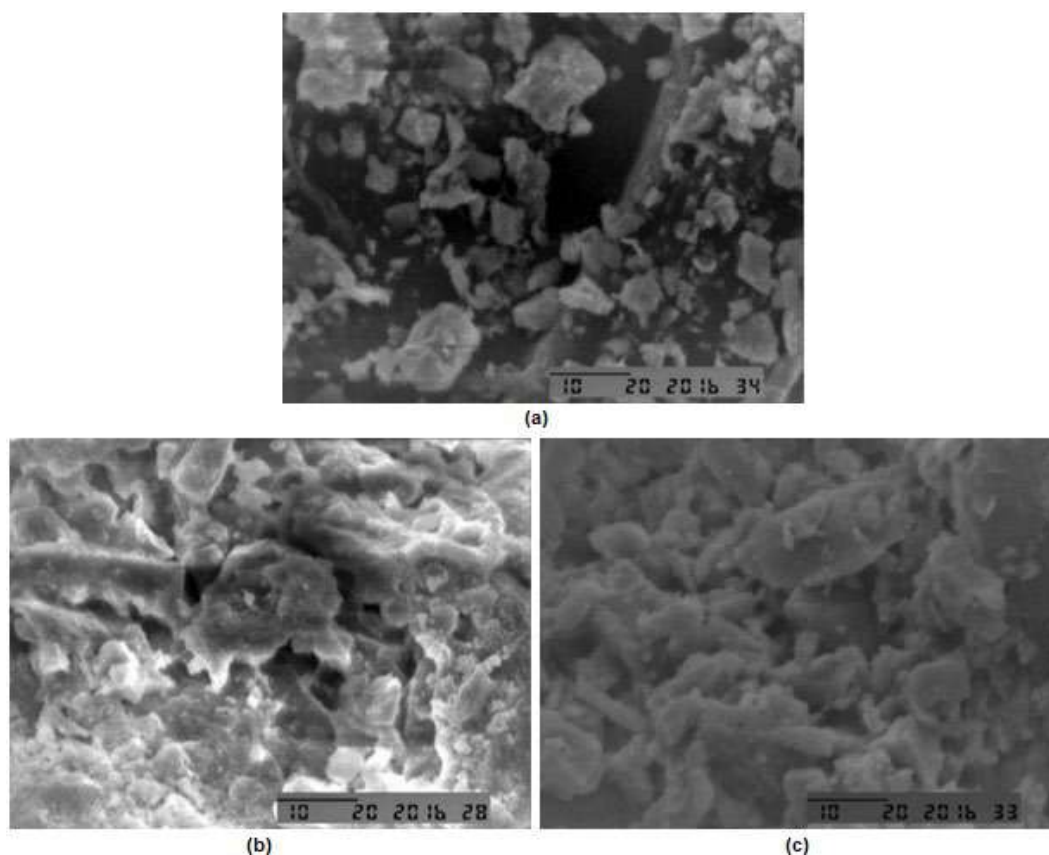


Fig 6. The SEM analysis (2.000× magnification) of (a) andesite powder before consolidation, (b) andesite mortar with silica-titania composite consolidant, and (c) andesite mortar using silica-titania consolidant modified with silica particles

Fig. 6 shows the SEM image of the mortar samples compared to the andesite powder before consolidation. This SEM result indicates the role of the consolidant as a binder between andesite particles. Andesite powders before consolidation appear separate from one another, while the particles in the mortar after consolidation becomes solid and connects each other. There is no significant difference in the appearance between mortar with and without silica particle addition. It occurs probably due to the similar appearance of andesite powder and silica particles.

■ CONCLUSION

The performance of the TEOS-based consolidant was successfully improved by the addition of TTIP and silica particles for andesite rock consolidation. The optimum consolidant composition of TTIP 5%, TEOS 55%, and ethanol 40% significantly increased the

compressive strength up to 57.61% (0.58 kgf/mm^2) of the consolidated andesite rock, which is comparable to that of the fresh one. The water content in the rock matrix reduced the consolidation performance using TEOS-based consolidant, and 0.5% was the maximum water content allowed to maintain the consolidated rock performance. The addition of silica particles 2% to the TEOS consolidant decreased the gel shrinkage and increased the hardness of the consolidated mortar.

■ ACKNOWLEDGMENTS

The first author acknowledges the Indonesian Endowment Fund for Education (LPDP-Ministry of Finance Republic of Indonesia) for the financial support of this study. The authors acknowledge Universitas Gadjah Mada through *Rekognisi Tugas Akhir* (RTA) program for partly financial support and the Borobudur Conservation Office Laboratory Staff for technical

support. The authors also acknowledge Prof. Hans Leisen and Dr. Esther von Plehwe Leisen (Cologne Institute for Applied Sciences/German-APSARA Conservation Project in Angkor) for the support on ultrasound velocity measurement and their encouragement, and Dr. Eberhard Wendler (Fachlabor für Konservierungsfragen in der Denkmalpflege, München) for his field experience information.

■ REFERENCES

- [1] Pinto, A.P.F., and Rodrigues, J.D., 2008, Stone consolidation: The role of treatment procedures, *J. Cult. Heritage*, 9 (1), 38–53.
- [2] Franzoni, E., Sassoni, E., Graziani, G., 2014, Comparison of porous sedimentary stone consolidation by a new hydroxyapatite-based treatment and by TEOS, *VIII Congresso Nazionale di Archeometria Scienze e Beni Culturali*, Bologna.
- [3] Gupta, S.P., 2011, Modification of the physical properties of deteriorated stone by chemical consolidation treatment, *Int. J. Conserv. Sci.*, 2 (4), 229–234.
- [4] Franzoni, E., Graziani, G., Sassoni, E., Bacilieri, G., Griffo, M., and Lura, P., 2015, Solvent-based ethyl silicate for stone consolidation: Influence of the application technique on penetration depth, efficacy, and pore occlusion, *Mater. Struct.*, 48 (11), 3503–3515.
- [5] Zornoza-Indart, A., Lopez-Arce, P., Leal, N., Simão, J., and Zoghlami, K., 2016, Consolidation of a Tunisian bioclastic calcarenite: From conventional ethyl silicate products to nanostructured and nanoparticle-based consolidants, *Constr. Build. Mater.*, 116, 188–202.
- [6] Liou, T.H., and Yang, C.C., 2011, Synthesis and surface characteristics of nanosilica produced from alkali-extracted rice husk ash, *Mater. Sci. Eng., B*, 176 (7), 521–529.
- [7] Liu, R., Han, X., Huang, X., Li, W., and Luo, H., 2013, Preparation of three-component TEOS-based composite for stone conservation by sol-gel process, *J. Sol-Gel Sci. Technol.*, 68, 19–30.
- [8] Li, D., Xu, F., Liu, Z., Zhu, J., Zhang, Q., and Shao, L., 2013, The effect of adding PDMS-OH and silica nanoparticle on sol-gel properties and effectiveness in stone protection, *Appl. Surf. Sci.*, 266, 368–374.
- [9] Graceli, J.B., Sena, G.C., Lopes, P.F.I., Zamprogno, G.C., da Costa, M.B., Godoi, A.F.L., dos Santos, D.M., de Marchi, M.R.R., and dos Santos Fernandez, M.A., 2013, Organotin: A review of their reproductive toxicity, biochemistry, and environmental fate, *Reprod. Toxicol.*, 36, 40–52.
- [10] Milton, F.A., Lacerda, M.G., Sinoti, S.B.P., Masquita, P.G., Prakasan, D., Coelho, M.S., de Lima, C.L., Martini, A.G., Pazzino, G.T.P., Borin, M.F., Amato, A.A., and Neves, F.A.R., 2017, Dibutyltin compounds effects on PPAR/RXR activity, adipogenesis, and inflammation in mammalian cells, *Front. Pharmacol.*, 8, 507.
- [11] Sunday, A.O., Alarafa, B.A., and Oladele, O.G., 2012, Toxicity and speciation analysis of organotin compounds, *Chem. Speciation Bioavailability*, 24 (4), 216–226.
- [12] Yuvakkumar, R., Nathanael, A.J., Rajendran, V., and Hong, S.I., 2014, Rice husk ash nanosilica to inhibit breast cancer cell line (3T3), *J. Sol-Gel Sci. Technol.*, 72 (1), 198–205.
- [13] Ulatovska-Jarza, A., Holowacs, I., Wysocka, K., and Podbielska, H., 2009, Silica-bases versus silica-titania sol-gel materials comparison of the physical properties: Surface tension, gelation time, refractive index and optical transmittance, *Opt. Appl.*, 39 (1), 211–220.
- [14] Zulfiqar, U., Subhani, T., and Husain, S.W., 2015, Toward tunable size of silica particles from rice husk, *J. Non-Cryst. Solids*, 429, 61–69.
- [15] Trompette, J.L., and Meireles, M., 2003, Ion-specific effect on the gelation kinetics of concentrated colloidal silica suspensions, *J. Colloid Interface Sci.*, 263 (2), 522–527.
- [16] Gu, S., Zhou, J., Yu, C., Luo, Z., Wang, Q., and Shi, Z., 2015, A novel two-stages thermal synthesis method of generating nanosilica from rice husk via pre-pyrolysis combined with calcination, *Ind. Crops Prod.*, 65, 1–6.
- [17] Athinarayanan, J., Periasamy, V.S., Alhazmi, M., Alataiah, A.K., and Alshatwi, A.A., 2015, Synthesis of

- biogenic silica nanoparticles from rice husks for biomedical applications, *Ceram. Int.*, 41 (1), 275–281.
- [18] Carmona, V.B., Oliveira, R.M., Silva, W.T.L., Mattoso, L.H.C., and Marconcini, J.M., 2013, Nanosilica from rice husk: Extraction and characterization, *Ind. Crops Prod.*, 43, 291–296.
- [19] Gu, S., Zhou, J., Luo, Z., Wang, Q., and Ni, M., 2013, A detailed study of the effect of pyrolysis temperature and feedstock particle size on the preparation of nanosilica from rice husk, *Ind. Crops Prod.*, 50, 540–549.
- [20] Verma, J., and Bhattacharya, A., 2018, Development of coating formulation with silica-titania core-shell nanoparticles against pathogenic fungus, *R. Soc. Open Sci.*, 5 (8), 180633.
- [21] Yu, Y., Zhu, M., Liang, W., Rhodes, S., and Fang, J., 2015, Synthesis of silica-titania composite aerogel beads for the removal of Rhodamine B in water, *RSC Adv.*, 5 (89), 72437–72443.
- [22] Zárraga, R., Cervantes, J., Salazar-Hernández, C., and Wheeler, G., 2010, Effect of the addition of hydroxyl-terminated polydimethylsiloxane to TEOS-based stone consolidants, *J. Cult. Heritage*, 11 (2), 138–144.
- [23] Vasconcelos, D.C.L., Costa, V.C., Nunes, E.H.M., Sabioni, A.C.S., Gasparon, M., and Vasconcelos, W.L., 2011, Infrared spectroscopy of titania sol-gel coatings on 361L stainless steel, *Mater. Sci. Appl.*, 2 (10), 1375–1382.
- [24] Marimuthu, T., Mohammad, S., and Alias, Y., 2014, Synthesis and characterization of new silica-titania mixed oxide in the presence of 1-butyl-3-methylimidazolium bis(trifluoromethylsulfonyl) imide by sol-gel technique, *J. Sol-Gel Sci. Technol.*, 70, 104–110.
- [25] Fatimah, I., Said, A., and Hasanah, U.A., 2015, Preparation of TiO₂-SiO₂ using rice husk ash as silica source and the kinetics study as photocatalyst in methyl violet decolorization, *Bull. Chem. React. Eng. Catal.*, 10 (1), 43–49.
- [26] Wu, Y., Li, M., Wang, X., and Wang, L., 2016, Preparation and characterization of titania-silica composite particles by Pechini sol-gel method, *MATEC Web Conf.*, 67, 03049.
- [27] Manurung, P., Situmeang, R., Ginting, E., and Pardede, I., 2015, Synthesis and characterization of titania-rice husk silica composite as photocatalyst, *Indones. J. Chem.*, 15 (1), 36–42.
- [28] Briffa, S.M., Sinagra, E., and Vella, D., 2012, TEOS based consolidant for maltese globigerina limestone: Effect of hydroxyl conversion treatment, *12th International Congress on the Deterioration and Conservation of Stone*, Columbia University, New York, 21-25 October 2012.
- [29] Ksinopoulou, E., Bakolas, A., Kartsonakis, I., Charitidis, C., and Moropoulou, A., 2012, Particle modified consolidants in the consolidation of porous stones, *12th International Congress on the Deterioration and Conservation of Stone*, Columbia University, New York, 21-25 October 2012.
- [30] Clifton, J.R., 1980, *Stone consolidating materials – A status report*, Volume 1118 of NBS Technical Note, National Bureau of Standards, United States.

Acid-Alkaline Treatment of Mordenite and Its Catalytic Activity in the Hydrotreatment of Bio-Oil

Febi Yusniyanti¹, Wega Trisunaryanti², and Triyono^{2,*}

¹Department of Chemistry, Islamic State University Maulana Malik Ibrahim, Jl. Gajayana No. 50, Dinoyo, Lowokawaru, Malang 65144, Indonesia

²Department of Chemistry, Faculty of Mathematics and Natural Sciences, Universitas Gadjah Mada, Sekip Utara, Yogyakarta 55281, Indonesia

* **Corresponding author:**

tel: +62-8157950957

email: triyn102@ugm.ac.id

Received: November 14, 2019

Accepted: May 4, 2020

DOI: 10.22146/ijc.51496

Abstract: Acid-alkaline treatment using acetic acid and sodium hydroxide (NaOH) were applied on mordenite (MOR) to increase the Si/Al ratio and surface area properties. Various time treatment (3, 6, and 9 h) and concentration of acetic acid (6, 9, and 12 M) were used to treat MOR, and followed by the treatment with NaOH (0.1 M) under room temperature. The MOR and treated mordenite were applied as a catalyst for hydrotreatment of cellulose-derived bio-oil. The acetic acid treatment caused the increase of the Si/Al ratio of mordenite up to 27.03. The Si/Al ratio was determined using ICP-AES analysis which was also confirmed using FT-IR analysis. The acidity was determined using NH₃ vapors adsorption. The acidity test revealed that as the Si/Al ratio increased the acidity of mordenite decreased. The advantage of using acetic acid for acid treatment was that the XRD patterns of mordenite can be preserved with a little decrease of the intensity. On the other hand, the NaOH treatment under room temperature decreased the crystallinity down to 68%, which was calculated using XRD. The acid-alkaline treatment of mordenite succeeded to increase the surface area 2 times larger than the parent mordenite. The surface area was obtained from BET analysis. The acid-alkaline treated mordenite exhibited better catalytic activity upon hydrotreatment of biomass-derived bio-oil compared to the parent mordenite which corresponded to its highest surface area.

Keywords: acetic acid; bio-oil; dealumination; hydrotreatment; mordenite

■ INTRODUCTION

Mordenite is a microporous aluminosilicate crystalline which belong to a large-pore zeolite family [1-2]. It consists of a 12-membered ring (MR) pore channels of 0.67 × 0.70 nm, interconnected by 8-MR pores of 0.34 × 0.48 nm [3-4]. Mordenite is one of the zeolites that can be employed as a catalyst in industrial processes such as alkylation and hydroisomerization [1,5-6]. The wide range application of mordenite is due to the mechanic and thermal stability of the mordenite structure [1]. High surface area, high Brønsted acidity, and flexible framework are unique properties of mordenite that also contributes to its extensive use [2,7-8]. Despite the immense use of mordenite as a catalyst, there are some

drawback of mordenite. Mordenite has high aluminum content causing it to be undesired to be used as a catalyst. Aluminum can easily leach in the presence of water and acid which affects the chemical stability of mordenite as a catalyst [9-10]. In addition, it is reported that mordenite undergoes rapid deactivation due to the limited mass transfer between product and reactant [3,8].

Several ways to overcome the disadvantages of mordenite has been reported by many researchers. The most sought after method is post-synthesis treatment using acid and alkaline solution [11-12]. The acid and alkaline treatment can enhance the mordenite properties by magnifying mass transfer and catalytic

activity [12-15]. Strong acid treatment affects the structure of mordenite. It is reported that employing strong acid on mordenite causes a partial loss in mordenite structure [8,13]. On the other hand, employing weak acids such as oxalic acid and acetic acid can preserve the structure of mordenite [4,8]. Throughout the acid treatment, the aluminum atoms are removed from the mordenite framework and extra-framework aluminum (EFAI) are formed [16]. The EFAI contributes to the addition of acid sites on the mordenite surface which increase the catalytic activity [16]. The utilization of strong acid and oxalic acid can completely remove the EFAI during the acid treatment, hence these acids are undesired to be used in treatment of mordenite.

Alkaline treatment is another way to increase zeolite properties such as mordenite. This treatment is mostly done using sodium hydroxide (NaOH). A low concentration of NaOH (0.1–0.5 M) can be used for alkaline treatment and can maintain the crystallinity of zeolite [17]. Alkaline treatment is mostly done at high temperature, however it can cause severe decrease in the crystallinity of zeolite. Interestingly, strong acid sites were formed during the alkaline treatment and the treated zeolite exhibited better catalytic activity than the parent zeolite [18]. A recent report on the low temperature of alkaline treatment caught attention of many researchers. This process removed the Si atom up to 78% from zeolite structure [19]. However, this caused the amorphization of zeolite. Therefore, controlling the concentration of NaOH is important to sustain mordenite structure.

In this work, mordenite was treated using acetic acid and NaOH. Various concentrations and condition time of acetic acid treatment were performed to obtain the effective condition to remove the Al atom from mordenite. The treated mordenite was used as a catalyst in the hydrotreatment of bio-oil to investigate its catalytic activity.

■ EXPERIMENTAL SECTION

Materials

Ca-Mordenite (HSZ-642NAA) was purchased from Tosoh Co. Glacial acetic acid (CH_3COOH), sodium hydroxide (NaOH), ammonium chloride (NH_4Cl), silver

nitrate (AgNO_3), nitric acid 65% (HNO_3), hydrochloric acid 37% (HCl), hydrofluoric acid 40% (HF) and ammonia solution 25% (NH_3) were purchased from Merck. All chemicals were of analytical grade. N_2 gas and H_2 gas were purchased from Samator Ltd., and distilled water was used during the experiments.

Instrumentation

Inductively coupled plasma-atomic emission spectrometer (ICP-AES) Shimadzu model ICPE-9820, Fourier transform-infrared (FTIR) spectrophotometer Thermo Nicolet iS10, X-Ray Diffractometer (XRD) Rigaku Miniflex 600, Gas Sorption Analyzer Quantachrome Touchwin Series, Gas Chromatography-Mass Spectroscopy (GC-MS) Shimadzu QP2010S, and other supporting instrumentations, were used in this research.

Procedure

Preparation of H-mordenite

Ca-mordenite (denoted as MOR) was calcined at a temperature of 550 °C for 5 h. Afterwards, the Ca-MOR was introduced into 1 M of NH_4Cl solution accompanied by stirring at 70–75 °C for 2 h. The mixture was then filtered and the solid phase was washed until there was no chloride ion in the liquid phase which was confirmed using AgNO_3 solution. The solid phase was then dried at 100 °C and calcined at 550 °C for 5 h. The obtained solid from this process was named H-mordenite (denoted as HMOR).

Acid-alkaline treatment of HMOR

This procedure followed the procedures done by Chung [8] and Yusniyanti [9]. H-MOR was treated using 6 M of CH_3COOH solution (1 g of HMOR in 30 mL of CH_3COOH solution) for 3, 6 and 9 h at 90–95 °C. The solid phase was then filtered, washed and dried. Afterwards, the solid material was subsequently calcined at 550 °C for 5 h (with a temperature rate of 10 °C min^{-1}) to produce acid treated mordenite. The solids obtained from this step were denoted as HMOR(6-x), in which x stood for reflux time variation. In addition, the optimum concentration of CH_3COOH solution was also investigated using the same procedures under 9 h of

reflux. The concentrations of CH₃COOH solution used in this step were 6, 9 and 12 M. The solids obtained from this step were denoted as HMOR(y-9), in which y stood for acid concentration variation.

The acid treatment of mordenite was then followed by alkaline treatment. The acid-treated mordenite was added into 0.1 M of NaOH solution for 30 min at room temperature under constant stirring. Afterwards, the mixture was filtered, dried at 100 °C for 3 h and later refluxed using 1 M of NH₄Cl. The solid obtained was calcined at 550 °C for 5 h and denoted as DHMOR(y-x).

All the samples were destructed using concentrated HNO₃, HCl and HF. Afterwards, the samples were characterized using ICP-AES to measure the Si/Al ratio. Further analysis is needed to confirm the effect of acid-alkaline treatment. The samples were characterized using XRD to determine the change of the structure and the crystallinity of the mordenites. The crystallinity of the samples was measured using Eq. (1). HMOR, HMOR(6-9) and DHMOR(6-9) was further investigated to determine the surface area using a Gas Sorption Analyzer which is also well known as the N₂ adsorption-desorption.

$$\% \text{Crystallinity} = \frac{\text{Area under } 2\theta: 5 - 40^\circ \text{ of Samples}}{\text{Area under } 2\theta: 5 - 40^\circ \text{ of MOR}} \times 100\% \quad (1)$$

Catalytic activity test on the hydrotreatment of bio-oil

The bio-oil used in this research was produced from the pyrolysis of α -cellulose. The pyrolysis of α -cellulose was done in a semi-batch reactor at temperature of 600 °C under N₂ gas flow (flow rate was 20 mL min⁻¹) for 2 h. The liquid obtained from this process was characterized by GC-MS to determine its composition. The hydrotreatment of bio-oil was done to improve the bio-oil properties. The process was carried out in a semi-batch reactor under H₂ gas flow (flow rate was 20 mL min⁻¹) for 2 h at temperature of 450 °C in the presence of a catalyst. The catalysts used in this process were HMOR, HMOR(6-9), and DHMOR(6-9). The weight ratio between catalyst and bio-oil as the feed was 1:30. The thermal treatment of bio-oil was also done in the same condition without a catalyst. The liquid produced from the hydrotreatment and thermal treatment processes was characterized by GC-MS.

Acidity test

The acidity of the samples were tested by the gravimetric method using adsorption of ammonia vapor. In porcelain crucible, 0.002 g of the sample was added and placed in a desiccator. The weight of the porcelain crucible before and after the addition of the samples were measured. The desiccator was vacuumed and NH₃ vapor was flowed into the desiccator for 30 min by heating the 25% ammonia solution until bubbles were formed. Afterwards, the samples were settled for 24 h in the desiccator. After 24 h, the samples were taken out from the desiccator and the weight of the porcelain crucible with the sample after ammonia adsorption was measured. The acidity of the samples were calculated using Eq. (2).

$$\text{Acidity (mmol / g)} = \frac{W_2 - W_1}{(W_1 - W_0) \times MW} \times 1000 \quad (2)$$

where, W₀: the weight of the empty porcelain crucible (g); W₁: the weight of the porcelain crucible + sample before adsorption (g); W₂: the weight of the porcelain crucible + sample after adsorption (g); MW: molecular weight of NH₃ (mmol/g)

RESULTS AND DISCUSSION

Characterization of the Acid-Alkaline Treated Mordenite

Acid-treated mordenite

In the acid treatment of zeolite, the acid removes aluminum atoms from the zeolite framework causing an increase in the Si/Al ratio of the zeolite. This process is well known as the dealumination process. This process hydrolyzes Si-O-Al bonds, resulting in -Si-OH and -Al-OH, and initiates the formation of vacant sites in the zeolite framework [7]. It is reported that mordenites with Si/Al ratio between 25 and 50 exhibit higher stability than mordenites with Si/Al ratio below that range (25-50) [3]. Moreover, this Si/Al ratio range is also needed to carry out effective silicon removal in alkaline treatment [15].

Since the use of acetic acid is rarely reported for acid treatment of mordenite, it is necessary to evaluate the optimum time and acetic acid concentration required for the treatment. The Si/Al ratios of the

mordenites are listed in Table 1. The highest Si/Al ratio was obtained using 6 M of acetic acid for 9 h of treatment. This condition is required to effectively remove silicon from mordenite. The change in Si/Al ratio can also be proven using FT-IR characteristics. When the Si/Al ratio increases, the T–O–T band (T=Si or Al) tends to shift to a

higher wavenumber. This is due to the difference in bond strength between Al–O and Si–O.

The infrared spectra of acid-treated mordenite are depicted in Fig. 1(a) and (b). The band assigned to the T–O asymmetric stretching shifted to higher wavenumbers of 1075, 1088, 1087 and 1089 cm^{-1} for

Table 1. The Si/Al ratio of acid-alkaline treated mordenite

Sample	Conc. Si (mmol/L)	Conc. Al (mmol/L)	Si/Al Ratio	Acidity (mmol/g)
HMOR	1.31	0.21	11.33	25.88
HMOR(6-3)	3.30	0.25	13.02	20.01
HMOR(6-6)	1.94	0.11	17.87	14.17
HMOR(6-9)	2.88	0.11	27.05	16.59
HMOR(9-9)	1.49	0.08	19.08	17.65
HMOR(12-9)	1.58	0.08	18.58	10.94
DHMOR(6-9)	1.48	0.07	21.65	12.03
DHMOR(9-9)	1.47	0.08	18.94	10.87
DHMOR(12-9)	1.38	0.07	20.37	9.25

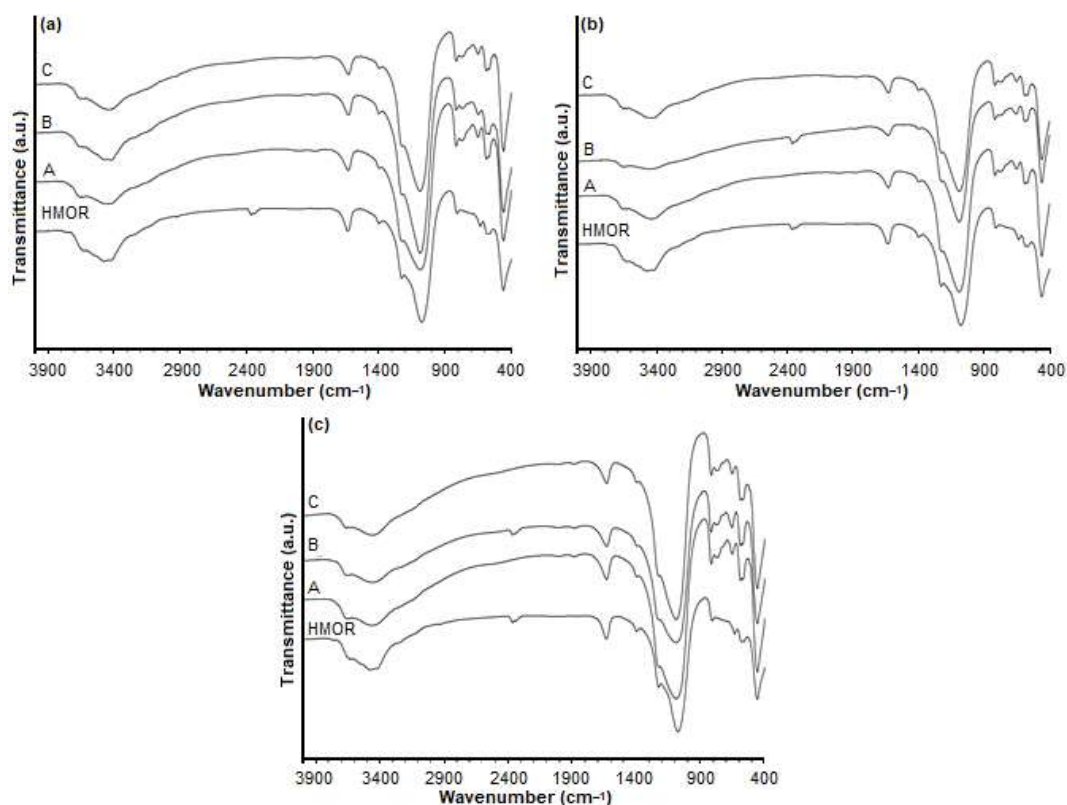


Fig 1. Infrared spectra treated mordenite (a) Treated mordenite using acetic acid 6 M in various treatment time (A. HMOR(6-3), B. HMOR(6-6) and C. HMOR(6-9)), (b) Treated mordenite using the various concentration of acetic acid in 9 h, (A. HMOR(6-9), B. HMOR(9-9) and C. HMOR(9-12)) and (c) Acid-alkaline treated mordenite for various acetic acid concentration (A. DHMOR(6-9), B. DHMOR(9-9) and C. DHMOR(12-9))

Table 2. Interpretation of infrared spectra of mordenites

Type of vibration	Wavenumber (cm ⁻¹)								
	HMOR	HMOR (6-3)	HMOR (6-6)	HMOR (6-9)	HMOR (9-9)	HMOR (12-9)	DHMOR (6-9)	DHMOR (9-9)	DHMOR (12-9)
T-O bending	458	457	457	457	482	457	457	457	457
T-O Sym. stretching	632	650	648	649	649	649	652	652	651
T-O Asym. stretching	1075	1088	1087	1089	1089	1088	1089	1089	1090
O-H bending	1635	1630	1628	1629	1630	1628	1631	1631	1630
O-H stretching	3474	3454	3421	3437	3453	3426	3455	3453	3453
EFAl	3650	3654	3653	3654	3654	3654	3654	3655	3655

HMOR, HMOR(6-3), HMOR(6-6) and HMOR(6-9) respectively (Table 2). This result is in good agreement with Sandoval-Díaz and co-workers [20].

Throughout the acid treatment, the EFAl can be formed as the result of incomplete removal of Al atom [16]. The EFAl on the mordenite framework can be detected in FTIR spectra at wavenumbers around 3650 cm⁻¹ which corresponds to the OH group attached to EFAl species [21]. It is shown in Fig. 1(a) that the band around 3650 cm⁻¹ can be seen in the HMOR and after acid

treatment. The wavenumber corresponds to the EFAl listed in Table 2.

The XRD patterns of the acid-treated mordenites were found to be almost identical (Fig. 2). However, the peak intensities slightly decreased which correspond to the crystallinity of the acid-treated mordenites. The crystallinity of the acid-treated mordenites changed from 100% to 68%, 74% and 88% for acid-treatment using acetic acid 6 M (Fig. 2(c)), 9 M (Fig. 2(d)) and 12 M (Fig. 2(e)) respectively. It clearly shows that acetic acid

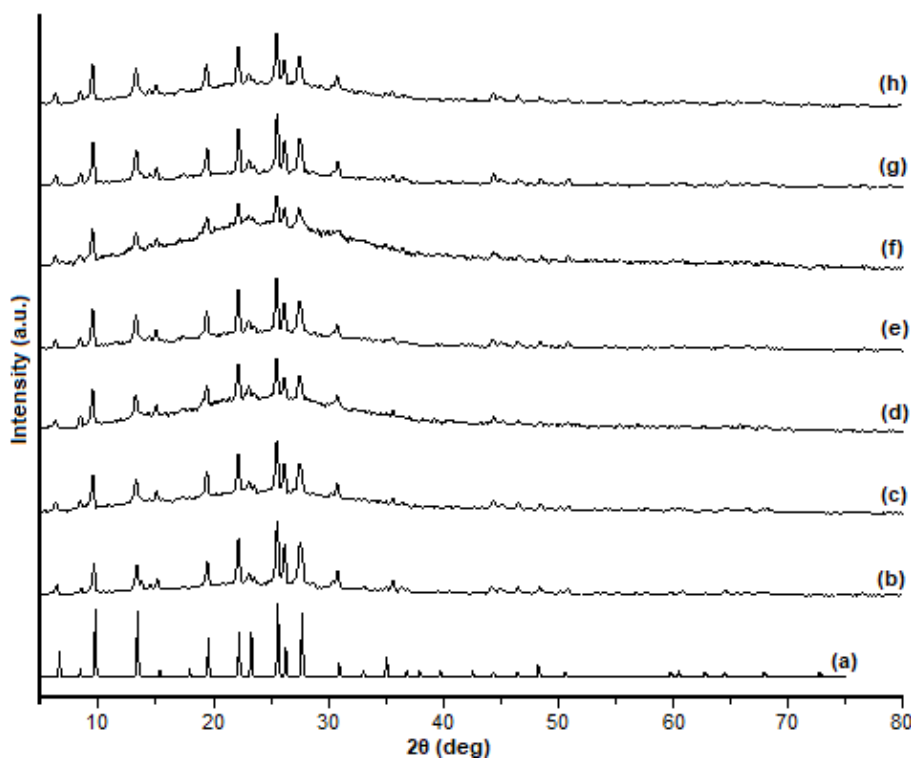


Fig 2. The diffractogram of acid-alkaline treated mordenite (a) JCPDS card 011-0155, (b) HMOR, (c) HMOR(6-9), (d) HMOR(9-9), (e) HMOR(12-9), (f) DHMOR(6-9), (g) DHMOR(9-9) and (h) DHMOR(12-9)

12 M does not cause more damage than acetic acid 9 M. It can be suggested that acetic acid 12 M removed the Al atoms from the mordenite framework, hence the EFAl was not completely formed during the acid treatment process. The EFAl species contributes to the amorphous nature of zeolites hence it can decrease the crystallinity of zeolites.

The uncompleted formation of EFAl on the mordenite framework is also supported by the Si/Al ratio and the acidity of mordenite after acid treatment (Table 1). Table 1 shows that the acidity of HMOR(12-9) is the lowest for acid-treated mordenite. However, the Si/Al ratio is not the highest. This indicates that EFAl in acid-treated mordenite using 12 M of acetic acid is not completely formed during the acid treatment. When the acetic acid concentration is raised, it is expected that the Si/Al ratio will increase. However the result shows that the Si/Al ratio cannot exceed 25 (Table 1). The possible explanation for this is that a large number of aluminum atoms were extracted from the mordenite framework causing the framework to collapse (Fig. 2(c-e)). Hence, the silicon atoms were also removed from the mordenite framework and resulted in the lowering of the Si/Al ratio.

Acid-alkaline treated mordenite

Alkaline treatment of zeolites cause the removal of Si sites on the mordenite framework. This process is well known as desilication. It can lead to the decrease of the Si/Al molar ratio of mordenite. Zeolite framework contains more silicon than aluminum atom. Hence it would be easy to create mesopores upon alkaline treatment. However, it is reported that there is an optimal Si/Al ratio to create the mesoporosity of zeolite after alkaline treatment [15]. Above the optimum ratio, the Al atoms prevented the removal of Si from mordenite. This resulted in the limitation of mesopore formation. The optimal Si/Al ratio was 25. When the Si/Al molar ratio > 25 , the alkaline treatment caused a decrease in the Si/Al molar ratio (as seen in the case of the alkaline treatment of HMOR(6-9)). However, when the Si/Al molar ratio < 25 , the Si/Al molar ratio increased after alkaline treatment (as seen in the case of the alkaline treatment of HMOR(12-9)). When HMOR(9-9) (Si/Al = 19.08) was treated with alkaline, the Si/Al molar ratio decreased. This is due to the removal of EFAl or maybe further dealumination that occurred on

the mordenite framework, that caused the decrease of Al content on DHMOR(9-9).

We can see that the alkaline treatment of HMOR(6-9) decreased the crystallinity of mordenite down to 65%. However, the characteristic peak of HMOR still appeared on the XRD pattern of DHMOR(6-9). When HMOR(9-9) was treated with sodium hydroxide, there was no significant change in the diffractogram of the mordenite (Fig. 2(d) and 2(g)). The crystallinity of HMOR(9-9) increased after alkaline treatment (DHMOR(9-9)) from 74 to 97%. This indicates that the EFAl was removed from HMOR(9-9). However, the removal of Si atoms is more likely to occur than the removal of EFAl. This is supported by the Si/Al molar ratio and the acidity of DHMOR(9-9) (Table 1).

The increase of mordenite crystallinity after alkaline treatment also occurred on the DHMOR(12-9). The crystallinity of HMOR(12-9) was 88%. After alkaline treatment, the crystallinity increased up to 93% (DHMOR(12-9)). This shows that the existence of EFAl or Al atoms prevents the removal of silicon atoms from HMOR(12-9). This result is in good agreement with the previous work of Shilagi et al. [15]. This result is also supported by the Si/Al molar ratio of HMOR(12-9) after the alkaline treatment. There was an increase in the Si/Al molar ratio (Table 1), which indicates that there was the removal of Al atoms either in the mordenite framework or EFAl. This result is also supported by the acidity of DHMOR(12-9).

N₂ Adsorption-Desorption

Fig. 3 depicts the adsorption-desorption isotherm curve of mordenite. In general, the hysteresis loop of adsorption-desorption isotherm curve should close. However in Fig. 3, it can be seen that the hysteresis loop does not close. Usually, the loop that does not close is well known as low-pressure hysteresis loop. The low-pressure hysteresis loop could occur because of the swelling of the adsorbent during the adsorption process or when there is a chemisorption process together with physical adsorption [22]. However, in this case, the loop that does not close is not because of the low-pressure hysteresis loop. In the low-pressure hysteresis loop, in the

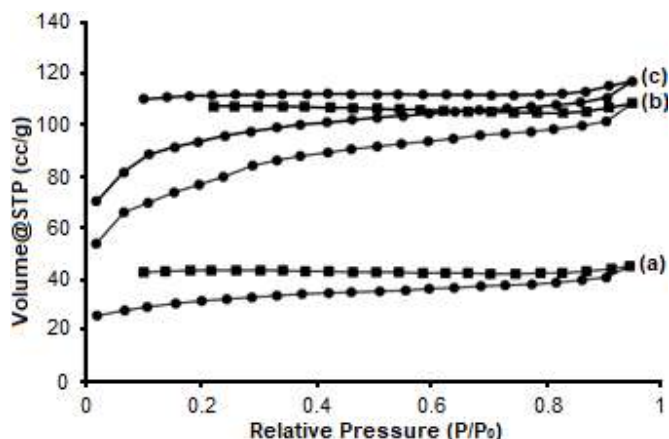


Fig 3. N₂ Adsorption-desorption of (a) HMOR, (b) HMOR(6-9), and (c) DHMOR(6-9)

desorption process, the amount of adsorbate decreases as the relative pressure decreases. In this case, as the relative pressure decreases, the amount of the adsorbate increases. This shows that the desorption process releases more gases than the amount of gases in the adsorption process. This can be due to the incomplete degassing process [23].

Mordenite is well known as a porous material. Acid and Alkaline treatment would change the porosity of mordenite. Table 3 shows the pore characteristic of mordenite before and after the treatments. It can be seen that after acid and alkaline treatment, the BET surface area increased. This increase indicates the removal of Al

atoms and Si atoms from the mordenite framework. The acid treatment removed Al atoms from the mordenite and rose the uniformity of the Si atoms in the mordenite. Zeolites with high Si/Al ratio would have higher surface area than zeolites with low Si/Al ratio [24]. In accordance to Stefanidis et al., it was also reported that acid treatment of mordenite caused the increase of pore volume [14]. It was also reported that the combination of acid and alkaline treatment of mordenite caused the increase of surface area [25].

The Catalytic Activity of Treated Mordenite

Based on Table 4, it can be seen that a catalyst can increase the liquid fraction on the hydrotreatment product. The liquid fraction of HMOR(6-9) was lower than HMOR. Even though the specific surface area of HMOR(6-9) was higher than HMOR, the acidity of HMOR(6-9) was lower than that of HMOR. This result is in good agreement with Boveri et al. [13]. Boveri reported that mordenite after acid treatment showed less catalytic activity due to the elimination of the acid sites [13]. In the case of DHMOR(6-9), the result shows that DHMOR(6-9) had the highest liquid fraction of hydrotreatment product among all of the catalysts. Although the acidity of DHMOR(6-9) was lower than HMOR(6-9) and HMOR, the high specific surface area

Table 3. The pore characteristic of parent mordenite, acid-treated and acid-alkaline treated mordenite

Parameter	Sample		
	HMOR	HMOR (6-9)	DHMOR (6-9)
Average pore size (nm)	2.72	2.56	2.37
Surface area (m ² g ⁻¹) ^a	102.31	262.07	306.14
Total pore volume (mL g ⁻¹) ^b	0.07	0.17	0.18

Note: ^aBET surface area determined using BET method

^bPore volume determined at P/P₀ = 0.95

Table 4. The distribution of hydrotreatment product

Catalyst	Surface Area (m ² g ⁻¹)	Acidity (mmol g ⁻¹)	Hydrotreatment product	
			Liquid Fraction (wt.%)	Gas Fraction (wt.%)
Thermal	-	-	47.08	52.92
HMOR	102.31	25.88	74.40	25.60
HMOR(6-9)	262.07	16.59	66.66	33.16
DHMOR(6-9)	306.14	12.03	81.00	19.00

of DHMOR(6-9) (Table 4) caused the liquid product to be improved. It clearly shows that the activity of the catalyst toward hydrotreatment was affected by the acidity and the surface area of the catalyst.

■ CONCLUSION

Acetic acid as a weak acid can be applied for acid treatment of mordenite which is proven by the increase of Si/Al ratio. The optimum condition for acid treatment of mordenite using acetic acid is 9 h using 6 M of acetic acid under reflux method. On the other hand, alkaline treatment can be carried out at room to temperature, using a low concentration of NaOH. The acid-alkaline treatment was able to increase the surface area of mordenite and also increase the catalytic activity upon hydrotreatment of biomass-derived bio-oil.

■ ACKNOWLEDGMENTS

This research was conducted under the research grant of PTUPT 2020 Universitas Gadjah Mada (Contract No.: 2876/UN1.DITLIT/DIT-LIT/PT/2020). Therefore, the authors would like to thank The Ministry of Research, Technology and Higher Education, the Republic of Indonesia for the financial support.

■ REFERENCES

- [1] Paixão, V., Carvalho, A.P., Rocha, J., Fernandes, A., and Martins, A., 2010, Modification of MOR by desilication treatments: Structural, textural and acidic characterization, *Microporous Mesoporous Mater.*, 131 (1-3), 350–357.
- [2] Huang, S., Liu, X., Yu, L., Miao, S., Liu, Z., Zhang, S., and Xie, S., 2014, Preparation of hierarchical mordenite zeolites by sequential steaming-acid leaching-alkaline treatment, *Microporous Mesoporous Mater.*, 191, 18–26.
- [3] Groen, J.C., Sano, T., Moulijn, J.A., and Pérez-Ramírez, J., 2007, Alkaline-mediated mesoporous mordenite zeolites for acid-catalyzed conversions, *J. Catal.*, 251 (1), 21–27.
- [4] Pastvova, J., Kaucky, D., Moravkova, J., Rathousky, J., Sklenak, S., Vorokhta, M., Brabec, L., Pilar, R., Jakubec, I., Tabor, E., Klein, P., and Sazama, P., 2017, Effect of enhanced accessibility of acid sites in microporous mordenite zeolites on hydroisomerization of *n*-hexane, *ACS Catal.*, 7 (9), 5781–5795.
- [5] Chaouati, N., Soualah, A., Hussein, I., Comparot, J.D., and Pinard, L., 2016, Formation of weak and strong Brønsted acid sites during alkaline treatment on MOR zeolite, *Appl. Catal., A*, 526, 95–104.
- [6] Chen, C.Y., Ouyang, X., Zones, S.I., Banach, S.A., Elomari, S.A., Davis, T.M., and Ojo, A.F., 2012, Characterization of shape selective properties of zeolites via hydroisomerization of *n*-hexane, *Microporous Mesoporous Mater.*, 164, 71–81.
- [7] Baran, R., Millot, Y., Onfroy, T., Krafft, J.M., and Dzwigaj, S., 2012, Influence of the nitric acid treatment on Al removal, framework composition and acidity of BEA zeolite investigated by XRD, FTIR and NMR, *Microporous Mesoporous Mater.*, 163, 122–130.
- [8] Chung, K.W., 2008, Dealumination of mordenites with acetic acid and their catalytic activity in the alkylation of cumene, *Microporous Mesoporous Mater.*, 11 (1-3), 544–550.
- [9] Yusniyanti, F., 2018, Acid-alkaline treatment of mordenite as MoO₃ support and its catalytic activity on the hydrotreatment of cellulose-derived bio-oil, *Thesis*, Department of Chemistry, Universitas Gadjah Mada, Yogyakarta.
- [10] Ong, L.H., Dömök, M., Olindo, R., van Veen, A.C., and Lercher, J.A., 2012, Dealumination of HZSM-5 via steam-treatment, *Microporous Mesoporous Mater.*, 164, 9–20.
- [11] Verboekend, D., Vilé, G., and Pérez-Ramírez, J., 2012, Hierarchical Y and USY zeolites designed by post-synthetic strategies, *Adv. Funct. Mater.*, 22 (5), 916–928.
- [12] Ahmed, M.H.M., Muraza, O., Yoshioka, M., and Yokoi, T., 2017, Effect of multi-step desilication and dealumination treatments on the performance of hierarchical EU-1 zeolite for converting methanol to olefins, *Microporous Mesoporous Mater.*, 241, 79–88.
- [13] Boveri, M., Márquez-Álvarez, C., Laborde, M.Á., and Sastre, E., 2006, Steam and acid dealumination

- of mordenite Characterization and influence on the catalytic performance in linear alkylbenzene synthesis, *Catal. Today*, 114 (2-3), 217–225.
- [14] Stefanidis, S., Kalogiannis, K., Iliopoulou, E.F., Lappas, A.A., Triguero, J.M., Navarro, M.T., Chica, A., and Rey, F., 2013, Mesopore-modified mordenites as catalysts for catalytic pyrolysis of biomass and cracking of vacuum gasoil processes, *Green Chem.*, 15 (6), 1647–1658.
- [15] Silaghi, M.C., Chizallet, C., and Raybaud, P., 2014, Challenges on molecular aspects of dealumination and desilication of zeolites, *Microporous Mesoporous Mater.*, 191, 82–96.
- [16] Almutairi, S.M.T., Mezari, B., Filonenko, G.A., Magusin, P.C.M.M., Rigutto, M.S., Pidko, E.A., and Hensen, E.J.M., 2013, Influence of extraframework aluminum on the Brønsted acidity and catalytic reactivity of faujasite zeolite, *ChemCatChem*, 5, 452–466.
- [17] Li, J., Li, X., Zhou, G., Wang, W., Wang, C., Komarneni, S., and Wang, Y., 2014, Catalytic fast pyrolysis of biomass with mesoporous ZSM-5 zeolites prepared by desilication with NaOH solutions, *Appl. Catal., A*, 470, 115–122.
- [18] Bertrand-Drira, C., Cheng, X., Cacciaguerra, T., Trens, P., Melinte, G., Ersen, O., Minoux, D., Finiels, A., Fajula, F., and Gerardin, C., 2014, Mesoporous mordenites obtained by desilication: Mechanistic considerations and evaluation in catalytic oligomerization of pentene, *Microporous Mesoporous Mater.*, 213, 142–149.
- [19] Gackowski, M., Tarach, K., Kuterasiński, Ł., Podobiński, J., Jarczewski, S., Kuśtrowski, P., and Datka, J., 2018, Hierarchical zeolites Y obtained by desilication: Porosity, acidity and catalytic properties, *Microporous Mesoporous Mater.*, 263, 282–288.
- [20] Sandoval-Díaz, L.-E., González-Amaya, J.-A., and Trujillo, C.-A., 2015, General aspects of zeolite acidity characterization, *Microporous Mesoporous Mater.*, 215, 229–243.
- [21] Agudelo, J.L., Hensen, E.J.M., Giraldo, S.A., and Hoyos, L.J., 2015, Influence of steam-calcination and acid leaching treatment on the VGO hydrocracking performance of faujasite zeolite, *Fuel Process. Technol.*, 133, 89–96.
- [22] Kruk, M., and Jaroniec, M., 2001, Gas adsorption characterization of ordered organic-inorganic nanocomposite materials, *Chem. Mater.*, 13 (10), 3169–3183.
- [23] Silvestre-Albero, A.M., Juárez-Galán, J.M., Silvestre-Albero, J., and Rodríguez-Reinoso, F., 2012, Low-pressure hysteresis in adsorption: An artifact?, *J. Phys. Chem. C*, 116 (31), 16652–16655.
- [24] Vu, X.H., Eckelt, R., Armbruster, U., and Martin, A., 2014, High-temperature synthesis of ordered mesoporous aluminosilicates from ZSM-5 nanoseeds with improved acidic properties, *Nanomaterials*, 4 (3), 712–725.
- [25] Góra-Marek, K., Tarach, K., Tekla, J., Olejniczak, Z., Kuśtrowski, P., Liu, L., Martinez-Triguero, J., and Rey, F., 2014, Hierarchical mordenite dedicated to the fluid catalytic cracking process: Catalytic performance regarding textural and acidic properties, *J. Phys. Chem. C*, 118 (48), 28043–28054.

Polynomial Regression Analysis for the Removal of Heavy Metal Mixtures in Coagulation/Flocculation of Electroplating Wastewater

Siti Wahidah Puasa^{1,2,*}, Kamariah Noor Ismail², Muhammad Amarul Aliff Mahadi², Nur Ain Mohd Zainuddin^{1,2}, and Mohd Nazmi Mohd Mukelas²

¹Integrated Separation Technology Research Group (i-STRonG), Faculty of Chemical Engineering, Universiti Teknologi MARA, 40450 Shah Alam, Selangor, Malaysia

²Faculty of Chemical Engineering, Universiti Teknologi MARA, 40450 Shah Alam, Selangor, Malaysia

* **Corresponding author:**

tel: +603-55436327

email: sitiwahida@uitm.edu.my

Received: December 6, 2019

Accepted: May 11, 2020

DOI: 10.22146/ijc.52251

Abstract: Wastewater produced from the electroplating industry generally consists of heavy metal mixture and organic materials that need to be treated before it can be discharged to the environment. Thus, the present investigation was focused on the selective removal of heavy metal mixtures that consist of Copper (Cu), Cadmium (Cd), and Zinc (Zn). Several operating conditions, including the effect of pH and coagulant (FeCl₃) dosage, were varied to find the best performance of heavy metal removal. Results showed that the efficiency of heavy metals removal for 2 types of wastewaters were both approximately 99%. The experimental data on the treatment of synthetic wastewater was plotted using polynomial regression (PR) via Excel software. The value of the adjusted R² obtained for the final concentration of Cu, Zn, and Cd after treatment were 0.6884, 0.9676, and 0.9283, respectively, which showed that the data were acceptably fitted for Cu and very well fitted for Zn and Cd. The coagulation/flocculation process performed on actual wastewater showed that the lowest final concentration of Cu, Zn, and Cd after treatment were 0.487, 1.232, and 0 mg/L respectively, at pH 12.

Keywords: hydroxide precipitation; metal removal; coagulation-flocculation; electroplating wastewater; polynomial regression

■ INTRODUCTION

The fast emergence of urbanization and the development of industrial sectors, including metal coating manufacturing and electroplating industries, have led to environmental degradation in terms of industrial pollution. Wastewater produced from these industrial activities may consist of a variety of toxic substances, hence, becoming major environmental concerns if it is not properly treated [1-5]. The subsequent water from the acid pickling process, alkaline cleaning, plating, and rinsing activities are discharged in large quantities as wastewater, which contains heavy metals at high concentrations [6-7]. The metallic ions discharged from industries will remain suspended in water for an extended time [8]. The most common toxic heavy metals that are of concern in the treatment of industrial wastewater are zinc

(Zn), copper (Cu), mercury (Hg), nickel (Ni), cadmium (Cd), lead (Pb), and chromium (Cr) [9-14]. These heavy metals are toxic to the environment and may cause illness if consumed even at low concentrations. Each of these heavy metals is known to have significant effects on the health of individuals as well as impacts on the neurological system, and some of them are even carcinogenic [15]. The consequences are also severe to the aquatic ecosystem, even at low concentrations, because heavy metals are not degradable and will remain in the water for a long period of time [16-17]. Industries are facing challenges in treating their wastewater as the Department of Environment (DOE) is stringent on discharge concentration of heavy metals in wastewater via regulation, namely the Environmental Quality (Industrial Effluents) Regulation 2009 under the Environmental Quality Act (EQA) 1974 [18].

The nature of wastewater is a crucial consideration in suggesting the suitable treatment method for heavy metal removal from wastewater [13]. Researchers have explored several treatment technologies to remove heavy metals from industrial wastewater. These treatment approaches can be classified into three main categories: physical, chemical, and biological treatment, which includes adsorption [19-20], membrane filtration [21-22], ion exchange [23], coagulation-flocculation [24], up-flow anaerobic sludge blanket (UASB) [25], and electrochemical treatment technologies [26-28].

Hydroxide precipitation is a common method used for chemical precipitation [29]. Hydroxide precipitation is a process of removal of soluble metal ions from solution in the form of metal hydroxide precipitate. Metal hydroxide is formed when hydroxide ion (OH^-) bonds to the metal ion (Me^{2+}) in the solution at a specific pH. The reaction involved in hydroxide precipitation is [30]:



The optimum pH for metal precipitation is selected at a minimum solubility concentration of the heavy metals [31-32]. Generally, metals such as Ag, Cd, Cu, Ni, Pb, and Zn are soluble in acidic conditions, but their solubility decrease towards alkaline pH. The optimum pH at minimum solubility is different for each of the heavy metals.

The coagulation/flocculation process was typically performed along with metal precipitation to enhance the destabilization of the suspended solid and enable the co-precipitation of heavy metals to create larger agglomerates or flocs. Thus, additional chemicals including ferric chloride (FeCl_3) or alum (PAC) as coagulants and surface charged polymers such as polyacrylamide (PAM) as flocculants are required to initiate the sedimentation of sludge containing heavy metals [33]. In coagulation/flocculation treatment, a coagulant is mainly used to destabilize colloids and form micro flocs, while flocculants function as a bridging agent for the micro flocs to form bigger flocs, dense enough to be able to settle in the sedimentation process [13,34]. This treatment process was found to be cost-efficient, easy to operate, and requires less energy compared to other treatment methods [35-36].

Recent studies mainly focus on single metal removal from synthetic wastewater via the coagulation/flocculation process. Results showed that an excellent removal rate was achieved via this treatment method [37]. However, actual wastewater typically consists of multi-metals. Since the optimum pH at minimum solubility is different for each of the heavy metals [38], it is a challenge to determine the optimum pH for the metal precipitation process. Several researchers have worked on the removal of heavy metal mixture from wastewater by metal precipitation [39]. Generally, the actual wastewater is substantially challenging to treat since the heavy metal content in the waste usually fluctuates as the industrial processes are being altered [40]. Therefore, some significant controls are necessary for the treatment process to achieve maximum removal of heavy metals.

Statistical analysis approaches such as polynomial regression (PR) can predict the effectiveness of a treatment process through mathematical equations [41]. These equations can generate the expected value of response in regards to the interrelated data of the treatment parameter [41-42]. This method has been implemented mostly in the chemical industries and other fields such as physics, engineering, biology [42]. Therefore, a statistical analysis study is important to verify the significant factor that influences the treatment of heavy metal mixture in actual wastewater. The optimization of the coagulation-flocculation process can be initiated by polynomial regression. By implementing statistical analysis, the time consumed on experimental work can be reduced, improving the cost of operation. Optimum conditions can be achieved after simulating the relationship between parameters such as initial pH of wastewater, initial heavy metal concentration, coagulant dosage, alkaline dosage, and flocculant dosage.

A study on synthetic wastewater is introduced to analyze the effect of parameters without the presence of any interference substance that can affect the statistical analysis. This study was performed to evaluate the performance of heavy metal mixture removal using hydroxide precipitation with co-precipitation via the coagulation/flocculation treatment process. The

treatment was performed for synthetic wastewater and actual wastewater. The synthetic wastewater was an imitation of wastewater from electroplating industries, which consists of heavy metal mixtures of Cu, Zn, and Cd. The parameter studies involved were the effect of metal concentration, operating pH, and coagulant dosage on the performance of multi-metals removal. Polynomial regression (PR) analysis via Excel Software was used to analyze and verify the relationship between the percentage of metal removal response with parameters studied for the treatment of synthetic wastewater. The predicted results obtained from PR analysis were compared with the treatment of actual wastewater to evaluate the reliability of the mathematical expression in predicting the removal of heavy metals from wastewater.

■ EXPERIMENTAL SECTION

Materials

The actual wastewater was collected from the raw wastewater of the electroplating industry. The synthetic wastewater was prepared from metal salts such as Cadmium(II) Nitrate Tetrahydrate ($\text{CdN}_2\text{O}_6 \cdot 4\text{H}_2\text{O}$), Copper(II) Nitrate Trihydrate ($\text{CuN}_2\text{O}_6 \cdot 3\text{H}_2\text{O}$), and Zinc(II) Nitrate Hexahydrate ($\text{ZnN}_2\text{O}_6 \cdot 6\text{H}_2\text{O}$) purchased from Sigma Aldrich, Malaysia. The other reagents used were the industrial grade of Ferric Chloride (FeCl_3), Polyacrylamide (PAM), Sodium Hydroxide (NaOH), and Sulfuric Acid (H_2SO_4).

Instrumentation

The metal concentration was analyzed using Furnace Atomic Absorption Spectroscopy (Model HITACHI Z-2000). The percentage of the removal of heavy metals (%R) can be calculated by using the equation:

$$\%R = \frac{(C_0 - C_f)}{C_0} \times 100\% \quad (2)$$

where C_0 is the initial concentration of heavy metal and C_f is the final concentration of heavy metal after treatment.

Procedure

Sample collection and characterization

The characterization of actual wastewater was collected at two different interval dates to determine the

fluctuation of heavy metals in actual wastewater. Then, these samples were characterized for the heavy metal concentration, specifically focused on Cu, Zn, and Cd. The pH condition of both samples of actual wastewater was also checked simultaneously.

Preparation of synthetic wastewater

Characterization results from actual wastewater were the basis for the preparation of synthetic wastewater. The synthetic wastewater containing Cu, Zn, and Cd were prepared by dissolving the respective heavy metal salts, namely cadmium(II) nitrate tetrahydrate ($\text{CdN}_2\text{O}_6 \cdot 4\text{H}_2\text{O}$), copper(II) nitrate trihydrate ($\text{CuN}_2\text{O}_6 \cdot 3\text{H}_2\text{O}$), and zinc(II) nitrate hexahydrate ($\text{ZnN}_2\text{O}_6 \cdot 6\text{H}_2\text{O}$) in deionized water. The pH and metals concentration were prepared based on results obtained from the characterization of actual wastewater.

Jar test

The jar test experiments were carried out at room temperature. The initial pH was adjusted by using H_2SO_4 . The jar test was set at 120 rpm and 5 min for rapid mixing; 60 rpm and 15 min for slow mixing. The hydroxide precipitation was conducted by adjusting operating pH via the addition of NaOH in the range of 8 to 12 with an interval of 0.5. Next, the coagulation process was done by adding FeCl_3 coagulant into the solution until pH 8 was obtained. Both the hydroxide precipitation and coagulation process were performed under rapid mixing. For the flocculation process, PAM at a concentration of 40 mg/L was added into the solution under slow mixing to promote the formation of larger flocs. Residual metal concentration was determined after settling for 40 to 60 min. Fig. 1 presents a flowchart of the treatment process.

The jar test experiments were conducted for synthetic and actual wastewater. For synthetic wastewater, two sets of samples were prepared according to the characterization results of actual wastewater obtained during sample collection and characterization.

Polynomial regression via excel software

Polynomial regression was performed to analyze and verify the relationship between the final concentration of heavy metals as response and the studied

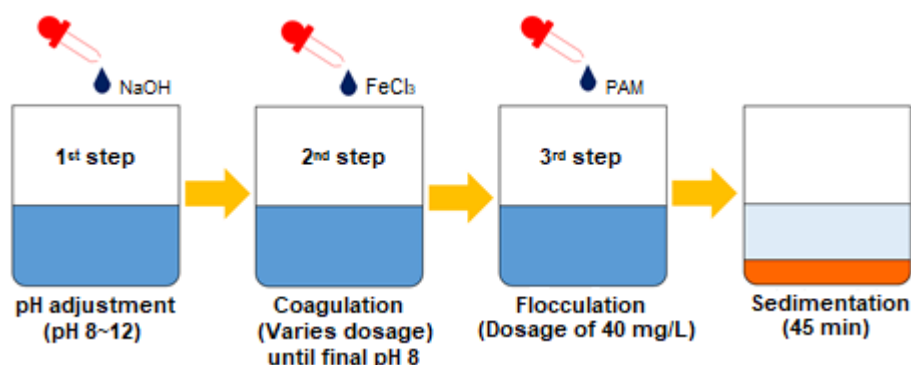


Fig 1. Flowchart of the treatment process

parameter as factor. The factors and responses are listed as follows:

- y_1 = Final concentration of Cu (mg/L)
- y_2 = Final concentration of Zn (mg/L)
- y_3 = Final concentration of Cd (mg/L)
- x_1 = Initial concentration of Cu (mg/L)
- x_2 = Initial concentration of Zn (mg/L)
- x_3 = Initial concentration of Cd (mg/L)
- x_4 = pH for hydroxide precipitation
- x_5 = volume of FeCl_3 (mL)

■ RESULTS AND DISCUSSION

Characterization of Actual Wastewater

The samples obtained at two different interval dates were labeled as Sample 1 (S1) and Sample 2 (S2). Table 1 presents the characteristics of the actual wastewater for both samples. From this table, the actual wastewater was determined to be acidic and consisted of a high concentration of Cu, followed by Zn and Cd, which exceeded the allowable discharge limit as stipulated in IER2009.

Effect of the pH of Hydroxide Precipitation on Heavy Metals Removal

The removal of Cu, Zn, and Cd from two sets of synthetic wastewater (S1 and S2) via hydroxide

precipitation followed by coagulation/flocculation process was conducted by adjusting the pH of the hydroxide precipitation between 8 to 12 through the addition of NaOH and reduced to neutral pH of 7.5 to 8 by addition of FeCl_3 as co-precipitator and coagulant. The results are presented in Fig. 2. It is observed that Cu achieved the highest percentage removal, followed by Zn and Cd for both S1 and S2. This is due to the capability of metal mixtures to produce metal hydroxide precipitates at a certain pH. The tendency of a metal to produce precipitate via hydroxide precipitation increase with the decrease of metal solubility concentration. The metal solubility concentration decreased in the sequence of $\text{Cu} < \text{Zn} < \text{Cd}$ as the pH increased from 9 to 10.5 [38]. Therefore, the tendency of Cu to form hydroxide precipitation is higher than Zn and Cd, hence resulting in the highest removal of Cu as compared to Cd and Zn. The removal of metal mixtures for S1 at pH 9 was 99.56% for Cu, 88.58% for Zn, and 99.34% for Cd. As for S2, the Cu removal was 99.34%, followed by Zn (78.60%) and Cd (30.37%).

Theoretically, the solubility concentration of metal hydroxide decreases as pH increases until it achieves its minimum solubility concentration. Further increase of pH will cause the metal hydroxide to resolubilize, hence increase the metal solubility concentration in aqueous

Table 1. Characteristics of actual wastewater

Sample	Initial pH of solution	Initial COD value (mg/L)	Initial TSS Value (mg/L)	Turbidity (mg/L)	Concentration of heavy metal (mg/L)		
					Cu	Zn	Cd
Sample 1 (S1)	1.5	318	9.5	4.8	80	10	1
Sample 2 (S2)	1.5	276	8.2	4.1	40	20	2
Standard B*	5.5–9.0	200	100	-	1.0	2.0	0.02

*Allowable Discharge Limit by DOE [14]

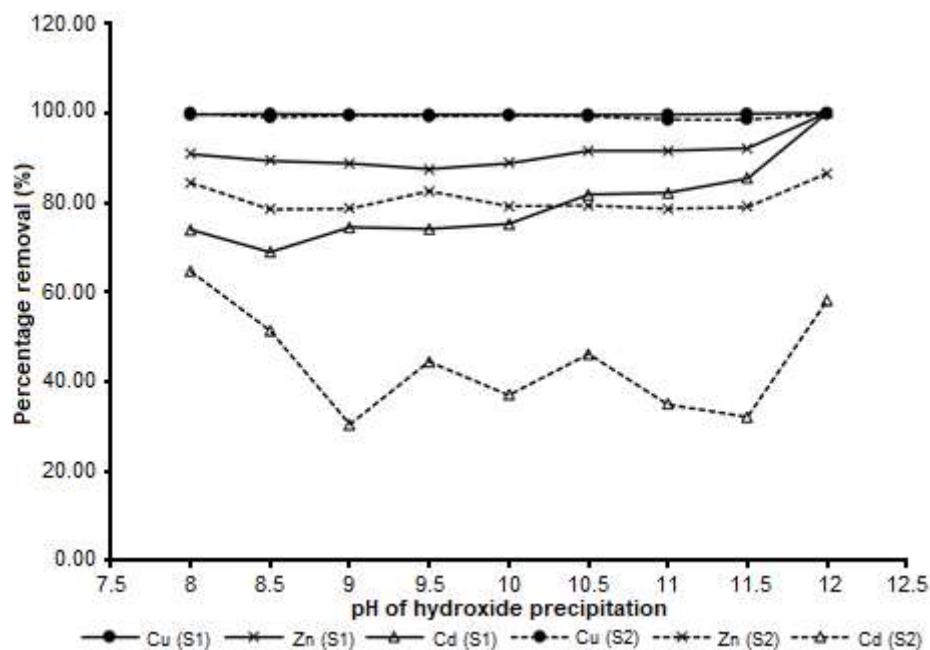


Fig 2. Percentage removal of Cu, Zn, and Cd for S1 and S2

solution. The metal solubility concentration decreased in the sequence of $\text{Cd} < \text{Cu} < \text{Zn}$ as the pH increased from 10.8 to 12 [38]. It is theoretically predicted that Cd would achieve higher removal compared to Cu and Zn at pH between 11 to 12. However, Fig. 2 shows that Cu obtained the highest removal at pH 8 to 12 for both S1 and S2. This finding is resulted from the competitive hydroxide precipitation between Zn and Cd with the hydroxide ion due to the ionization energy factor. The ionization energy of different metals shows different reactivity that attributable to the removal of an electron from its outer orbital [43]. The reactivity of elements in removing electrons to produce stable compounds increases with the decrease of the first ionization energy. The first ionization energy increase in the sequence of $\text{Cu} > \text{Cd} > \text{Zn}$ at 745, 868, and 906 kJ/mol, respectively [43]. The hydrolysis of Cu, Cd, and Zn in aqueous solution creates competition with hydroxide ions (OH^-) for the precipitation of metal ions at certain pH. Thus, the efficiency of selective metal removal depends on the relative concentration of the anions (OH^-) in the solution and is consequently pH-dependent [44]. In this study, Cu has the lowest ionization energy compared to Cd and Zn; hence tends to form hydroxide precipitate better than Zn and Cd. Also, the concentration of Cu was 80 and 20 times higher than the

concentration of Cd for S1 and S2, respectively. The presence of a high concentration of Cu will hinder the Cd ion from reacting with hydroxide ion, hence decreasing the potential for Cd ions to produce $\text{Cd}(\text{OH})_2$, even at its optimum pH of hydroxide precipitation. The highest removal of metal mixtures was obtained at pH 12 for both S1 and S2. The removal of Cu, Zn, and Cd was 99.91%, 99.91%, and 99.97%, respectively for S1. For S2, the sequence of metal removal was $\text{Cu} (99.71\%) > \text{Zn} (86.45\%) > \text{Cd} (58.11\%)$. Johnson et al. [45] and Hargreaves et al. [16] observed similar findings where the removal of Cu was higher than Zn by using FeCl_3 as the coagulant.

It was also observed that the removal of metal mixture for S1 was higher than S2. This phenomenon is due to the different initial metal concentrations used in the experiments. The concentration ratio for $\text{Cu}:\text{Zn}:\text{Cd}$ was 80:10:1 and 20:10:1 for S1 and S2, respectively. The presence of a high concentration of Cu in S1 required a high amount of NaOH for pH adjustment. This resulted in a higher concentration of hydroxide ion in S1, hence increasing the tendency of more metal ions to form hydroxide precipitate compared to S2.

Fig. 3 presents the comparison of metal concentration after the coagulation/flocculation process

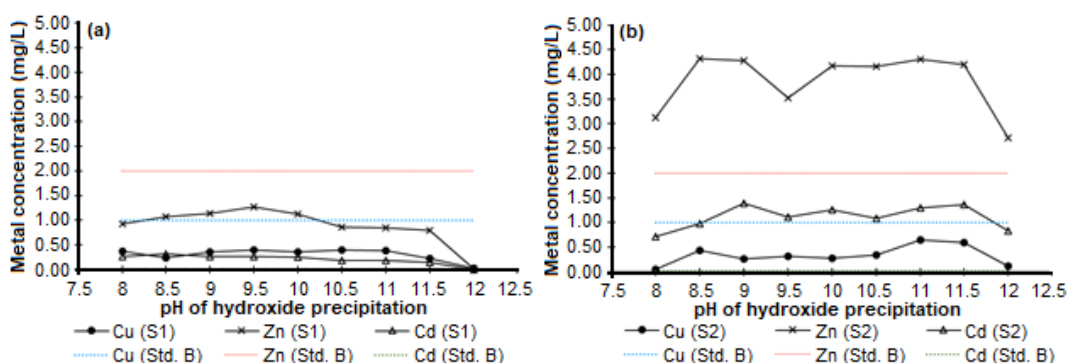


Fig 3. Comparison of metal concentration for (a) S1, and (b) S2 after the coagulation/flocculation process with Standard B of IER 2009

with Standard B of IER 2009 under EQA 1974 for S1 and S2. It can be observed that the concentration of Cu and Zn complied with Standard B. Meanwhile, the Cd concentration only complied at pH 12 for S1. From these findings, it can be concluded that the metal precipitation for multi-metals is influenced by metal solubility concentration and adequate dosing of NaOH to ensure complete hydroxide precipitation of multi-metals in aqueous solution. Therefore, a study on data verification using a mathematical model is useful in predicting the concentration of metals after coagulation/flocculation treatment at various initial metal concentrations.

Polynomial Regression Analysis on Heavy Metals Removal

A polynomial regression analysis via Excel Software was used to analyze and verify the relationship between the final concentration (Cu (y_1), Zn (y_2), and Cd (y_3)) and the parameters studied in this research. The selected parameters were the initial concentration (Cu (x_1), Zn (x_2), and Cd (x_3)), pH for hydroxide precipitation (x_4), and volume of FeCl_3 (x_5).

The best mathematical expression obtained for the prediction of the final concentration of metals Cu (y_1), Zn (y_2), and Cd (y_3) can be expressed as:

$$y_1 = (8.620 \times 10^{-2})x_4^3 - 2.427x_4^2 + 0.139x_5^2 + (7.549 \times 10^{-3})x_2^2x_5 - (4.356 \times 10^{-2})x_4^2x_5 + (2.843 \times 10^{-2})x_1x_2x_4 + (4.67 \times 10^{-3})x_1x_4x_5 - 70.647 \quad (3)$$

$$y_2 = (2.863 \times 10^{-2})x_5^3 - (2.85 \times 10^{-3})x_4^2x_1 - (7.83 \times 10^{-3})x_4^2x_2 - (4.885 \times 10^{-2})x_5^2x_2 + (6.592 \times 10^{-3})x_1x_2x_4 + (2.762 \times 10^{-3})x_1x_2x_5 - 21.681 \quad (4)$$

$$y_3 = -(2.598 \times 10^{-4})x_4^2x_1 - (6.829 \times 10^{-3})x_5^2x_2 + (3.615 \times 10^{-4})x_1x_2x_4 + (3.834 \times 10^{-4})x_1x_4x_5 - 0.698 \quad (5)$$

The regression statistics and ANOVA for the expression above are presented in Table 2. From this table, it is depicted that for Cu, Zn, and Cd, the significance F, and the P-value reported for intercept and all independent variables are less than 0.05; showing that the results are quite reliable and the variable is statistically significant [46-47]. The adjusted R^2 obtained for Zn and Cd were 0.9676 and 0.9283, respectively, indicating that the data were very well fitted. Meanwhile, for Cu, the obtained adjusted R^2 was 0.6884, which shows that the data were acceptably fit, although it was slightly lower than the adjusted R^2 of Zn and Cd.

It is evident from Eq. (3), (4), and (5) that all independent variables or parameters depend on each other significantly except for the initial concentration of Cd (x_3). The x_3 is also insignificant to the final concentration of Cu (y_1), Zn (y_2), and Cd (y_3). The concentration of Cd used in this study is considered very low; hence Cd does not influence the competitive hydroxide precipitation of multi-metals.

Fig. 4 shows the comparison between the experimental and predicted value of the final concentration of Cu (y_1), Zn (y_2), and Cd (y_3). It is clearly shown that the scatter plots of Zn and Cd are denser at around the 45-degree lines which indicates that the experimental data were close to the predicted value calculated from the mathematical expression. Meanwhile, several Cu scatter plots are distant from the

Table 2. Regression statistics and ANOVA for the percentage of the final concentration of Cu, Zn, and Cd

Regression statistics and ANOVA			
	Cu	Zn	Cd
Multiple R	0.9037	0.9895	0.9722
R Square	0.8167	0.9790	0.9452
Adjusted R Square	0.6884	0.9676	0.9283
Standard Error	0.0896	0.2889	0.1337
Observations	18	18	18
Significance F	0.0048	1.383×10^{-8}	4.5271×10^{-8}
P-value for intercept	0.0275	0.0376	0.039
P-value for x_5^3	-	0.0190	-
P-value for x_4^3	0.0213	-	-
P-value for x_4^2	0.0234	-	-
P-value for x_5^2	0.0052	-	-
P-value for $x_2^2x_5$	0.0470	-	-
P-value for $x_4^2x_5$	0.0233	-	-
P-value for $x_4^2x_1$	-	0.0092	2.9590×10^{-8}
P-value for $x_4^2x_2$	-	0.0459	-
P-value for $x_5^2x_2$	-	0.0005	0.0061
P-value for $x_1x_2x_4$	0.0254	0.02179	1.0774×10^{-6}
P-value for $x_1x_2x_5$	-	0.0076	-
P-value for $x_1x_4x_5$	0.0371	-	0.0117

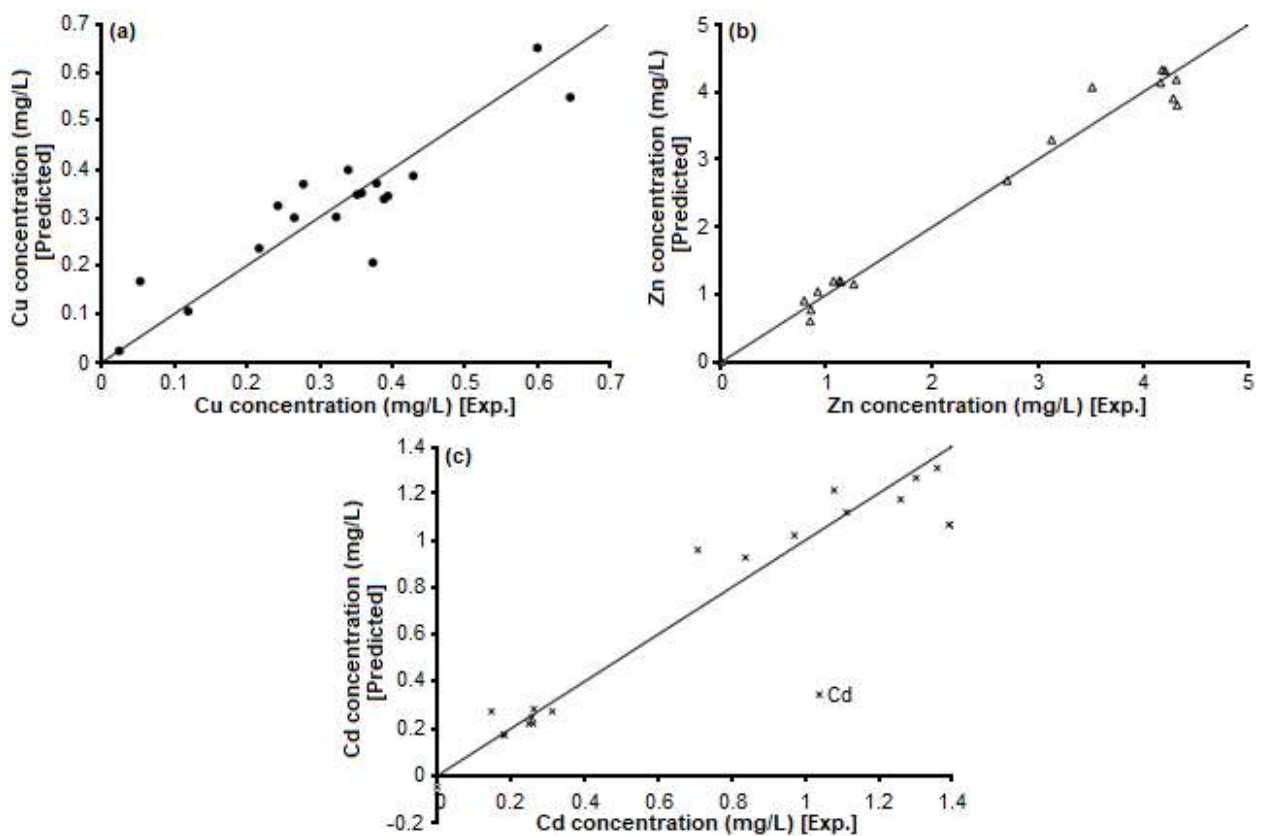
**Fig 4.** Comparison between the experimental and predicted value of the final concentration of (a) Cu, (b) Zn, and (c) Cd

Table 3. Results of the heavy metal mixture before and after treatment for actual wastewater

pH of hydroxide precipitation	Volume of FeCl ₃ (mL)	Initial metal concentration (mg/L)			Final metal concentration (mg/L)		
		Cu	Zn	Cd	Cu	Zn	Cd
9.50	0.07	78.89	10.23	0.89	1.06	1.85	0.28
10.00	0.07	78.89	10.23	0.89	1.17	1.36	0.18
10.50	0.16	78.89	10.23	0.89	0.96	1.13	0.18
11.00	0.67	78.89	10.23	0.89	0.87	1.15	0
11.50	1.29	78.89	10.23	0.89	0.61	1.26	0
12.00	3.43	78.89	10.23	0.89	0.49	1.23	0

45-degree line, which is in agreement with the results of adjusted R² obtained in Table 2.

Treatment of Actual Wastewater from the Electroplating Industry

The treatment of actual wastewater from the electroplating industry was experimentally conducted via coagulation/flocculation method, while Eq. (3), (4), and (5) were used to predict the final concentration of Cu, Zn, and Cd for this treatment. Results for the final concentration of multi-metals obtained after treatment (Table 3) were compared with the predicted value and presented in Fig. 5. It is noticeable from this figure that the final concentration of multi-metals decreased with the increase of pH for hydroxide precipitation. The lowest final concentration of Cu, Zn, and Cd after treatment was 0.487, 1.232, and 0 mg/L respectively at hydroxide precipitation pH of 12, which complied with Standard B, of IER 2009. This finding is in good agreement with results obtained for coagulation/flocculation of synthetic wastewater. It is also evident from this finding that the presence of organic and other constituents in the actual wastewater does not influence the efficiency of the coagulation/flocculation process in multi metals removal. It is also observed from Fig. 5 that most of the final concentrations of Zn and Cd obtained from the predicted value were almost similar with error distribution between 2% to 19%, except for Cd at pH 11 to 12, whereby Cd was completely removed at this condition. Most of the final concentrations of the multi-metals obtained from the experiments were found to be lower than the predicted value, especially for Cu. Therefore, it can be concluded that the mathematical expression of Eq. (3), (4), and (5) are

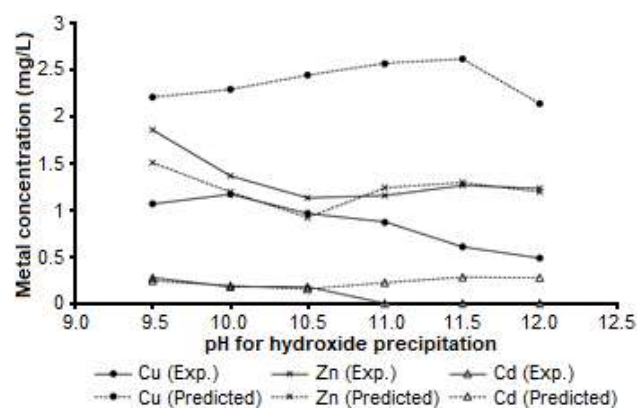


Fig 5. Final concentration of Cu, Zn, and Cd obtained from experiments and the predicted value for coagulation/flocculation treatment of actual wastewater

useful in predicting the final concentration of multi-metals for the coagulation/flocculation process.

CONCLUSION

The removal of synthetic multi-metals that consisted of Cu, Zn, and Cd was investigated in this study via coagulation/flocculation method using NaOH as the source of (OH⁻) ions and FeCl₃ as the coagulant or co-precipitator. This method was found to be significantly capable of removing up to 100% of the multi-metals concentration in aqueous solution to meet the requirement as stipulated in the Environmental Quality (Industrial Effluent) Regulation (IER) 2009 under Environmental Quality Act (EQA) 1974. The highest removal achieved for S1 was 99.75% of Cu, 99.91% of Zn, and 99.98% of Cd, while 99.71% of Cu, 86.45% of Zn, and 58.11% of Cd removal were obtained for S2 at hydroxide precipitation pH of 12. The final concentration of Cu, Zn, and Cd after coagulation/flocculation treatment

were verified in this study by using polynomial regression (PR) via Excel software. It was proven from the ANOVA analysis that the data were acceptably fitted for Cu and very well fitted for Zn and Cd. The significance F and probability value obtained for all variables were less than 0.05, which proved that the mathematical expression obtained from polynomial regression could be used to predict the final concentration of Cu, Zn, and Cd obtained after coagulation/flocculation treatment. The actual wastewater was successfully treated via the coagulation/flocculation method. The lowest final concentration of Cu, Zn, and Cd was 0.487, 1.232, and 0 mg/L respectively, at hydroxide precipitation pH of 12, which complied with Standard B, of IER 2009. The mathematical expression obtained from PR was proven to be useful in predicting the final concentration of multi-metals for the coagulation/flocculation process. Future works may focus on the optimization of hydroxide precipitation on the operating cost of the treatment process, including the disposal of sludge produced from treatment.

■ ACKNOWLEDGMENTS

The authors gratefully acknowledge the support received from the Ministry of Higher Education Malaysia (MOHE) for the FRGS research funding 600-IRMI/FRGS 5/3 (103/2017), the Institute of Research Management & Innovation (IRMI), and the Faculty of Chemical Engineering, Universiti Teknologi MARA, Shah Alam, Selangor, Malaysia that have made this important research viable and effective. The authors also wish to thank Mr. Shamsul Ahmad Aini for providing a technical consultant for this research study.

■ REFERENCES

- [1] Calzadilla, A., Rehdanz, K., and Tol, R.S.J., 2011, Water scarcity and the impact of improved irrigation management: A computable general equilibrium analysis, *Agric. Econ.*, 42 (3), 305–323.
- [2] Fu, F., and Wang, Q., 2011, Removal of heavy metal ions from wastewaters: A review, *J. Environ. Manage.*, 92 (3), 407–418.
- [3] Kim, C., Lee, C.R., Song, Y.E., Heo, J., Choi, S.M., Lim, D.H., Cho, J., Park, C., Jang, M., and Kim, J.R., 2017, Hexavalent chromium as a cathodic electron acceptor in a bipolar membrane microbial fuel cell with the simultaneous treatment of electroplating wastewater, *Chem. Eng. J.*, 328, 703–707.
- [4] Chen, R., Liao, X., and Ge, Q., 2021, A novel multinuclear zinc complex Zn-Bet-Tf₂N for electroplating wastewater treatment using forward osmosis technique, *Chem. Eng. J.*, 404, 126569.
- [5] Yan, F.L., Wang, Y., Wang, W.H., Zhao, J.X., Feng, L.L., Li, J.J., and Zhao, J.C., 2020, Application of biochars obtained through the pyrolysis of *Lemna minor* in the treatment of Ni-electroplating wastewater, *J. Water Process Eng.*, 37, 101464.
- [6] Bankole, M.T., Abdulkareem, A.S., Mohammed, I.A., Ochigbo, S.S., Tijani, J.O., Abubakre, O.K., and Roos, W.R., 2019, Selected heavy metals removal from electroplating wastewater by purified and polyhydroxybutyrate functionalized carbon nanotubes adsorbents, *Sci. Rep.*, 9 (1), 4475.
- [7] Martín-Lara, M.A., Blázquez, G., Trujillo, M.C., Pérez, A., and Calero, M., 2014, New treatment of real electroplating wastewater containing heavy metal ions by adsorption onto olive stone, *J. Cleaner Prod.*, 81, 120–129.
- [8] Martínez-Quiroz, M., López-Maldonado, E.A., Ochoa-Terán, A., Pina-Luis, G.E., and Oropeza-Guzman, M.T., 2018, Modification of chitosan with carbamoyl benzoic acids for testing its coagulant-flocculant and binding capacities in removal of metallic ions typically contained in plating wastewater, *Chem. Eng. J.*, 332, 749–756.
- [9] Mehdipour, S., Vatanpour, V., and Kariminia, H.R., 2015, Influence of ion interaction on lead removal by a polyamide nanofiltration membrane, *Desalination*, 362, 84–92.
- [10] Wang, G., Chang, Q., Han, X., and Zhang, M., 2013, Removal of Cr(VI) from aqueous solution by flocculant with the capacity of reduction and chelation, *J. Hazard. Mater.*, 248-249, 115–121.
- [11] Sudarsan, J.S., Deeptha, V.T., Maurya, D., Goel, M., Kumar, K.R., and Das, A., 2015, Study on treatment of electroplating wastewater using constructed

- wetland, *Nat. Environ. Pollut. Technol.*, 14 (1), 95–100.
- [12] Zhao, S., Chen, Z., Shen, J., Kang, J., Qu, Y., Wang, B., Wang, X., and Yuan, L., 2017, Response surface methodology investigation into optimization of the removal condition and mechanism of Cr(VI) by Na₂SO₃/CaO, 2017, *J. Environ. Manage.*, 202 (Part 1), 38–45.
- [13] Carolin, C.F., Kumar, P.S., Saravanan, A., Joshiba, G.J., and Naushad, M., 2017, Efficient techniques for the removal of toxic heavy metals from aquatic environment: A review, *J. Environ. Chem. Eng.*, 5 (3), 2782–2799.
- [14] Xiong, Z., Cao, J., Yang, D., Lai, B., and Yang, P., 2017, Coagulation-flocculation as pre-treatment for micro-scale Fe/Cu/O₃ process (CF-mFe/Cu/O₃) treatment of the coating wastewater from automobile manufacturing, *Chemosphere*, 166, 343–351.
- [15] Rekha, T.M., Vinod, B., and Murthy, K.V.R., 2014, Removal of heavy metals from electroplating industry by electrocoagulation, *JCHPS*, 3, 111–118.
- [16] Hargreaves, A.J., Vale, P., Whelan, J., Alibardi, L., Constantino, C., Dotro, G., Cartmell, E., and Campo, P., 2018, Impacts of coagulation-flocculation treatment on the size distribution and bioavailability of trace metals (Cu, Pb, Ni, Zn) in municipal wastewater, *Water Res.*, 128, 120–128.
- [17] Siziba, N., Mwedzi, T., and Muisa, N., 2020, Assessment of nutrient enrichment and heavy metal pollution of headwater streams of Bulawayo, Zimbabwe, *Phys. Chem. Earth.*, In Press, Corrected Proof.
- [18] L.R. Board, 2017, *Environmental Quality Act 1974 (Act 127)*, International Law Book Services, Malaysia.
- [19] Jumina, Priastomo, Setiawan, H.R., Mutmainah, Kurniawan, Y.S., and Ohto, K., 2020, Simultaneous removal of lead(II), chromium(III), and copper(II) heavy metal ions through an adsorption process using C-phenylcalix[4]pyrogallolarene material, *J. Environ. Chem. Eng.*, 8 (4), 103971.
- [20] Sadeghi, M.H., Tofighy, M.A., and Mohammadi, T., 2020, One-dimensional graphene for efficient aqueous heavy metal adsorption: Rapid removal of arsenic and mercury ions by graphene oxide nanoribbons (GONRs), *Chemosphere*, 253, 126647.
- [21] Aloulou, W., Aloulou, H., Khemakhem, M., Duplay, J., Daramola, M.O., and Amar, R.B., 2020, Synthesis and characterization of clay-based ultrafiltration membranes supported on natural zeolite for removal of heavy metals from wastewater, *Environ. Technol. Innovation*, 18, 100794.
- [22] Hosseini, S.M., Alibakhshi, H., Jashni, E., Parvizian, F., Shen, J.N., Taheri, M., Ebrahimi, M., and Rafiei, N., 2020, A novel layer-by-layer heterogeneous cation exchange membrane for heavy metal ions removal from water, *J. Hazard. Mater.*, 381, 120884.
- [23] Tavakoli, O., Goodarzi, V., Saeb, M.R., Mahmoodi, N.M., and Borja, R., 2017, Competitive removal of heavy metal ions from squid oil under isothermal condition by CR11 chelate ion exchanger, *J. Hazard. Mater.*, 334, 256–266.
- [24] Sun, Y., Zhou, S., Pan, S.Y., Zhu, S., Yu, Y., and Zheng, H., 2020, Performance evaluation and optimization of flocculation process for removing heavy metal, *Chem. Eng. J.*, 385, 123911.
- [25] de la Varga, D.D.L., Díaz, M.A., Ruiz, I., and Soto, M., 2013, Heavy metal removal in an UASB-CW system treating municipal wastewater, *Chemosphere*, 93 (7), 1317–1323.
- [26] Ya, V., Martin, N., Chou, Y.H., Chen, Y.M., Choo, K.H., Chen, S.S., and Li, C.W., 2018, Electrochemical treatment for simultaneous removal of heavy metals and organics from surface finishing wastewater using sacrificial iron anode, *J. Taiwan Inst. Chem. Eng.*, 83, 107–144.
- [27] Sun, J., Liu, L., and Yang, F., 2020, A WO₃/PPy/ACF modified electrode in electrochemical system for simultaneous removal of heavy metal ion Cu²⁺ and organic acid, *J. Hazard. Mater.*, 394, 122534.
- [28] Tran, T.K., Chiu, K.F., Lin, C.Y., and Leu, H.J., 2017, Electrochemical treatment of wastewater: Selectivity of the heavy metals removal process, *Int. J. Hydrogen Energy*, 42 (45), 27741–27748.
- [29] US EPA, 1983, *Methods for Chemical Analysis of Water and Wastes*, EPA/600/4-79/020, U.S.

- Environmental Protection Agency, Washington, D.C.
- [30] Abdullah, S.R.S., Rahman, R.A., Mohamad, A.B., Mustafa, M.M., and Khadum, A.A.H., 1999, Removal of mixed heavy metals by hydroxide precipitation, *Jurnal Kejuruteraan*, 11 (2), 85–101.
- [31] Pascual, D., and McPhee, M., 2015, Fulfilment of EPA Discharge Requirements for ARD Using Co-Precipitation Iron Process at Neutral pH, *10th International Conference on Acid Rock Drainage & IMWA Annual Conference*, 21-24 April 2015, Santiago, Chile.
- [32] APHA, 2014, *Standard Methods for the Examination of Water and Wastewater*, American Public Health Association, Washington, D.C.
- [33] Hashim, M.A., Mukhopadhyay, S., Sahu, J.N., and Sengupta, B., 2011, Remediation technologies for heavy metal contaminated groundwater, *J. Environ. Manage.*, 92 (10), 2355–2388.
- [34] Daud, N.M., Abdullah, S.R.S., and Hasan, H.A., 2018, Response surface methodological analysis for the optimization of acid-catalyzed transesterification biodiesel wastewater pre-treatment using coagulation-flocculation process, *Process Saf. Environ. Prot.*, 113, 184–192.
- [35] AlMubaddal, F., AlRumaihi, K., and Ajbar, A., 2009, Performance optimization of coagulation/flocculation in the treatment of wastewater from a polyvinyl chloride plant, *J. Hazard. Mater.*, 161 (1), 431–438.
- [36] Bratskaya, S.Y., Pestov, A.V., Yatluk, Y.G., and Avramenko, V.A., 2009, Heavy metals removal by flocculation/precipitation using N-(2-carboxyethyl)chitosans, *Colloids Surf., A*, 339 (1-3), 140–144.
- [37] Ghorpade, A., and Ahammed, M.M., 2018, Water treatment sludge for removal of heavy metals from electroplating wastewater, *Environ. Eng. Res.*, 23 (1), 92–98.
- [38] US EPA, 1984, *Development Document for Effluent Limitations Guidelines and Standards for the Copper Forming Point Source Category*, U.S. Environmental Protection Agency, Washington, D.C.
- [39] Ngatenah, S.N.I., Kutty, S.R.M., and Isa, M.H., 2010, Optimization of heavy metal removal from aqueous solution using groundwater treatment plant sludge (GWTPS), *International Conference on Environment 2010 (ICENV 2010)*, 15 December 2010, Penang, Malaysia.
- [40] Kobielska, P.A., Howarth, A.J., Farha, O.K., and Nayak, S., 2018, Metal-organic frameworks for heavy metal removal from water, *Coord. Chem. Rev.*, 358, 92–107.
- [41] Ebrahimi, M., Gerber, E.L., and Rockaway, T.D., 2017, Temporal performance assessment of wastewater treatment plants by using multivariate statistical analysis, *J. Environ. Manage.*, 193, 234–246.
- [42] Santos, B., Galinha, C.F., Crespo, J.G., Santos, M.A., and Velizarov, S., 2013, Prediction of polar oil and grease contamination levels in refinery wastewater through multivariate statistical modeling, *Sep. Purif. Technol.*, 119, 51–57.
- [43] Ebbing, D.D., and Gammon, S.D., 2016, *General Chemistry*, 10th Ed., Cengage Learning, Boston, US.
- [44] Liu, D.H.F., and Liptak, B.G., 1997, *Environmental Engineers' Handbook*, 2nd Ed., CRC Press, Boca Raton, Florida, US.
- [45] Johnson, P.D., Girinathannair, P., Ohlinger, K.N., Ritchie, S., Teuber, L., and Kirby, J., 2008, Enhanced removal of heavy metals in primary treatment using coagulation and flocculation, *Water Environ. Res.*, 80 (5), 472–479.
- [46] Brown, A.M., 2001, A step-by-step guide to non-linear regression analysis of experimental data using a Microsoft Excel spreadsheet, *Comput. Methods Programs Biomed.*, 65 (3), 191–200.
- [47] Hu, G., Li, J., and Hou, H., 2015, A combination of solvent extraction and freeze thaw for oil recovery from petroleum refinery wastewater treatment pond sludge, *J. Hazard. Mater.*, 283, 832–840.

Preparation of Green-Emissive Zinc Oxide Composites Using Natural Betacyanin Pigment Isolated from Red Dragon Fruit

Yehezkiel Steven Kurniawan¹, Hendrik Oktendy Lintang^{1,2}, and Leny Yuliati^{1,2,*}

¹Ma Chung Research Center for Photosynthetic Pigments, Universitas Ma Chung, Villa Puncak Tidar N-01, Malang 65151, East Java, Indonesia

²Department of Chemistry, Faculty of Science and Technology, Universitas Ma Chung, Villa Puncak Tidar N-01, Malang 65151, East Java, Indonesia

* **Corresponding author:**

tel: +62-341-550171

email: leny.yuliati@machung.ac.id

Received: December 9, 2019

Accepted: August 25, 2020

DOI: 10.22146/ijc.52351

Abstract: In this work, we reported the synthesis of green-emissive composite materials of zinc oxide (ZnO) and isolated betacyanin pigment from red dragon fruit (RDF) extract utilizing organic linkers, i.e. (3-chloropropyl)trimethoxysilane (CPTMS) and (3-aminopropyl)trimethoxysilane (APTMS). Betacyanin was extracted using a maceration technique, while CPTMS-ZnO and APTMS-ZnO were prepared by mixing ZnO and the respective organic linker in ethanol. The obtained ZnO/CPTMS and APTMS-ZnO composites were separately added into the RDF extract, followed by stirring at room temperature for 24 h. As high as 80 and 90% of betacyanin was successfully impregnated onto CPTMS-ZnO and APTMS-ZnO, respectively. A comparison study was made by preparing RDF-CPTMS and RDF-APTMS first and then introducing them onto ZnO. In this case, as high as 81 and 100% of betacyanin in RDF-CPTMS and RDF-APTMS, respectively, were impregnated onto ZnO. These results revealed that APTMS was a better organic linker than CPTMS and the order of the steps to introduce APTMS was important. The presence of betacyanin on the composite materials was confirmed by FTIR and fluorescence spectroscopy. All the composite materials had an excitation signal at 426–428 nm and emission signals at 459 and 517–518 nm, demonstrating their promising application as green-emissive materials.

Keywords: betacyanin; composite; green-emissive; red dragon fruit; ZnO

■ INTRODUCTION

In recent years, there has been a high demand for research related to photonic materials due to its wide application for human appliances [1-5]. Regarding this topic, many researches are still focused on enhancing and optimizing the efficiency of the materials. Zinc oxide (ZnO), a material with a direct bandgap of 3.3 eV, has been used over the past several years as photocatalysts, semiconductors, electronic material, etc. [6-7]. With such a large bandgap, pure ZnO can only be applied in the UV region [8]. Therefore, enhancing the efficiency of ZnO material in the visible region leaves a challenge for material scientists. Sensitizing ZnO material with either synthetic dye or natural pigment is a well-known procedure to enhance the light absorption region of this

material [9-10]. However, synthetic dye generates serious environmental problems in their application to produce dye-sensitized materials [11].

Red dragon fruit (RDF) is an abundantly available tropical fruit in Indonesia, which contains several unique secondary metabolites, such as betacyanin, flavonoid, and carotenoid [12-14]. It has been reported that betacyanin pigment could be isolated from the flesh of RDF using a maceration method for 24 h [15]. Incorporation of natural pigments may overcome the limitation of the ZnO material as a photocatalyst to be utilized in the visible region, especially in the red color region as the main part of the visible region in the solar spectrum. Betacyanin is recognized as one of the major red natural pigments, and therefore, very potential to be

used to widen the light absorption of ZnO. Owing to the alcohol and carboxylic acid functional groups, it is possible to immobilize the betacyanin pigment onto the surface of ZnO materials using a suitable linker agent. Even though the visible light emissive material is promising, the method to prepare the ZnO composites consisting of the betacyanin pigment from RDF has not been developed yet. We demonstrated that the use of a suitable organic linker would be a great method to prepare the composite. This research opens the possibility to utilize natural pigments to improve the properties of the photonic materials such as ZnO.

In the present work, we also reported that the prepared betacyanin-modified ZnO exhibited strong green emission, which would be very interesting for photonic material application. We prepared green emissive ZnO based composite materials utilizing isolated betacyanin pigment from RDF and either (3-chloropropyl)trimethoxysilane (CPTMS) or (3-aminopropyl)trimethoxysilane (APTMS) as the organic linker agent. By a stirring method for 24 h, four (4) types of ZnO based materials, named as RDF/CPTMS-ZnO, RDF/APTMS-ZnO, RDF-CPTMS/ZnO and RDF-APTMS/ZnO have been successfully obtained based on the use of different linkers and the order to introduce the betacyanin pigment on the ZnO. These materials were thoroughly characterized by spectroscopy instruments to investigate the physicochemical properties as green emissive composite materials.

■ EXPERIMENTAL SECTION

Materials

Fresh RDFs were obtained commercially from a supermarket in Malang, East Java. Meanwhile, the ZnO materials were prepared in a similar manner to the procedure which has been reported previously [16]. The organic linkers (3-chloropropyl)trimethoxysilane (CPTMS) and (3-aminopropyl)trimethoxysilane (APTMS) were purchased from Sigma Aldrich. Ethanol was purchased from E-Merck in pro analysis grade and used without any further purifications.

The optical properties of the composite materials were measured by diffuse reflectance ultraviolet-visible

(DR UV-Vis) spectrophotometer (JASCO V-760), while the bandgap energy of the composite materials was calculated from Tauc plot using the data. The infrared and fluorescence spectra of the composite materials were recorded by Fourier transform infrared spectrophotometer (JASCO FTIR-6800) and spectrofluorometer (JASCO FP-8500), respectively.

Procedure

Isolation of betacyanin pigment from the RDF

The isolation of betacyanin pigment from RDF was carried out according to the previously described method [15,17]. In short, the flesh of RDF (5.0 g) was dried at room temperature overnight and macerated with distilled water (50 mL) for 24 h. Afterward, the mixture was filtered. The clear filtrate was finally characterized by FTIR spectrophotometer and spectrofluorometer.

Preparation of composite materials

In this work, there were two types of composite materials, namely RDF/linker-ZnO and RDF-linker/ZnO materials. The term RDF/linker-ZnO material showed that the organic linker was reacted first with ZnO and then further reacted with RDF extract, while the term RDF-linker/ZnO material indicated that the organic linker was first reacted with RDF extract and then further reacted with ZnO.

The RDF/linker-ZnO materials, i.e., RDF/CPTMS-ZnO and RDF/APTMS-ZnO, were prepared through a simple stirring method. First, the organic linker (0.25 mL) and ZnO (0.25 g) were added stepwise into ethanol (12.5 mL), and then the mixture was stirred at 500 rpm at room temperature for 24 h. After that, the residue was filtered and added to 5% v/v RDF extract in ethanol (12.5 mL). The mixture was stirred for another 24 h. The mixture was then filtered and the residue was dried to obtain the RDF/linker-ZnO composite materials.

The RDF-linker/ZnO materials, i.e. RDF-CPTMS/ZnO and RDF-APTMS/ZnO were also simply obtained by a stirring method. First, the organic linker (0.25 mL) was added dropwise to 5% v/v RDF extract in ethanol (12.5 mL) and the mixture was stirred at 500 rpm for 24 h. Afterward, ZnO (0.25 g) was added

and the mixture was stirred for 24 h. The mixture was filtered and the residue was dried to obtain the RDF-linker/ZnO composite materials.

■ RESULTS AND DISCUSSION

Preparation of Composite Materials

In this work, ZnO-based composite materials were prepared and evaluated for their potential application as emissive materials. At first, the betacyanin pigment was isolated from RDF extract through a maceration method with distilled water. As has been reported, betacyanin pigment was confirmed to be successfully isolated from RDF extract using the maceration method [15,18-19]. On the other hand, the prepared ZnO has been reported to give a bandgap energy value of 3.29 eV [16].

The isolated betacyanin pigment was used to prepare the composites in two different procedures. In the first procedure, the organic linker was attached first on the surface of the ZnO material and then the isolated betacyanin pigment was immobilized onto it. Meanwhile, the other way involved the reaction between the isolated betacyanin pigment and organic linker, followed by its immobilization onto the surface of the ZnO material.

The color appearances of the prepared ZnO based materials can be seen in their photographs as shown in Fig. 1. From Fig. 1(a), it can clearly be observed that ZnO has a white color. In contrast, both RDF/CPTMS-ZnO and RDF-CPTMS/ZnO were obtained as bright purplish

solids as shown in Fig. 1(b) and (c), respectively. On the other hand, Fig. 1(d) and (e) showed that RDF/APTMS-ZnO appeared as a pale yellow solid while RDF-APTMS/ZnO appeared as a bright yellow solid. The difference of the color appearance showed the different forms of immobilized betacyanin on the composite material. It was previously reported by Strack et al. (2003) that the color of betacyanin would depend on the pH of the solution [20]. Below pH 10, the color of betacyanin solution is red, while its color turns to yellow when the pH is higher than 10. Since the CPTMS organic linker is acidic, the pH of the filtrate during the reaction was 4.53. Therefore, the color of RDF/CPTMS-ZnO and RDF-CPTMS/ZnO was purplish. On the other hand, the use of APTMS caused the mixture to be alkaline (pH = 10.8), hence the color of betacyanin pigment changed from red to bright yellow. Therefore, it is reasonable for both RDF/APTMS-ZnO and RDF-APTMS/ZnO to be obtained as yellow solids. The formation of such color in the composites showed that the light absorption of ZnO had been expanded successfully to the visible light region.

Characterization of Composite Materials

DR UV-vis spectra of ZnO and the composite materials are shown in Fig. 2. As expected, the white ZnO sample only showed absorption in the UV region up to 380 nm. On the other hand, the composite materials gave extra absorption at the background level in

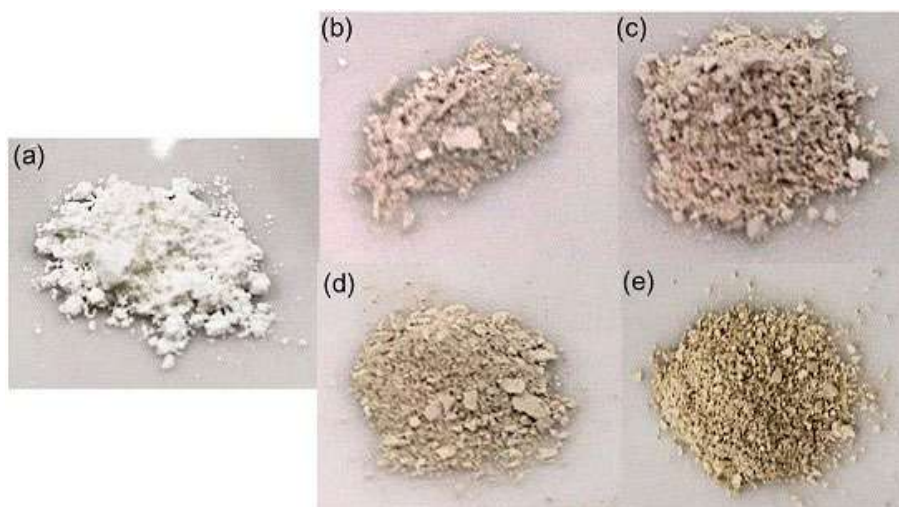


Fig 1. Photographs of (a) ZnO and ZnO based composite materials, including (b) RDF/CPTMS-ZnO, (c) RDF-CPTMS/ZnO, (d) RDF/APTMS-ZnO, and (e) RDF-APTMS/ZnO

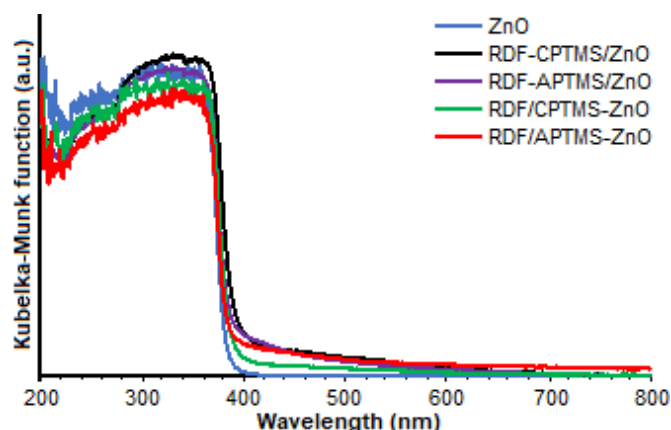


Fig 2. DR UV-vis spectra of ZnO and ZnO based composite materials

the visible region due to the presence of betacyanin from the RDF extract, which is in good agreement to the color appearances of the composites. From the DR UV-vis spectra of the composite materials, the bandgap energy of the composite materials was calculated accordingly and shown in Table 1. The bandgap energy of unmodified ZnO, RDF-CPTMS/ZnO, RDF-APTMS/ZnO, RDF/CPTMS-ZnO and RDF/APTMS-ZnO composite materials were 3.29, 3.22, 3.23, 3.26 and 3.26 eV, respectively. The bandgap energy of the composite materials was not significantly different from the unmodified ZnO because the betacyanin pigment was only immobilized on the surface of the ZnO materials. In this case, the betacyanin pigment would act as the sensitizer. The values of the bandgap energy in this work were close to other reported ZnO dye-sensitized solar cells

[21] and natural pigment-modified ZnO materials prepared from laali [22].

The bandgap energy of the composite materials seemed to be independent on the organic linker, but dependent on the order of betacyanin introduction. For example, when the organic linker was immobilized first onto the ZnO surface, the bandgap energy was 3.26 eV for both CPTMS and APTMS. However, when the organic linker-betacyanin was immobilized onto the ZnO surface, the bandgap energy was slightly lower, which were 3.22 and 3.23 eV for CPTMS and APTMS, respectively. When betacyanin was reacted first with the organic linker, the betacyanin-linker might have created new energy states that were more positive than the conduction band of ZnO and the linker or betacyanin itself, which in turn gave a slightly lower bandgap energy than ZnO and RDF/linker-ZnO.

The FTIR spectra of ZnO, RDF extract, and composite materials are shown in Fig. 3. The FTIR spectrum of unmodified ZnO showed two main absorption peaks at 3394 and 434 cm^{-1} , corresponding to Zn-O-H and Zn-O-Zn moieties, respectively [23].

Table 1. Bandgap energy of the composite materials

Materials	Bandgap (eV)
ZnO	3.29
RDF-CPTMS/ZnO	3.22
RDF-APTMS/ZnO	3.23
RDF/CPTMS-ZnO	3.26
RDF/APTMS-ZnO	3.26

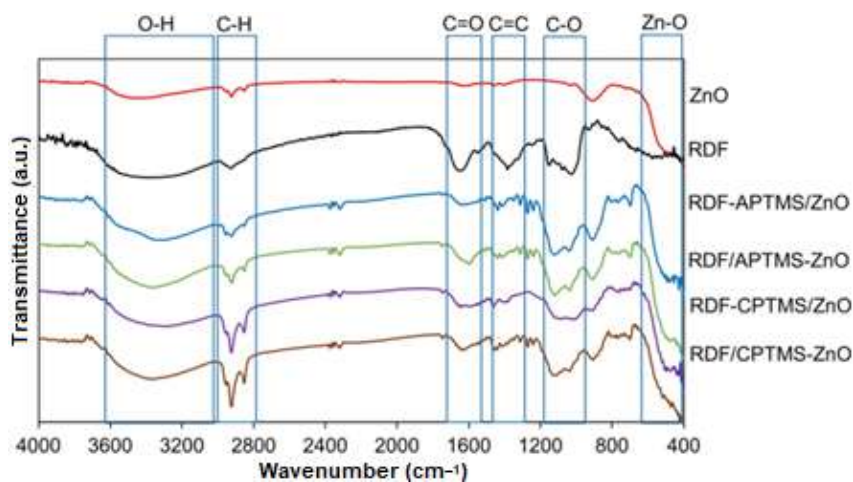


Fig 3. FTIR spectra of ZnO, RDF, and ZnO based composite materials

The FTIR spectrum of isolated betacyanin from the RDF extract showed O–H, C–H sp^3 , C=O, C=C, and C–O functional groups at 3340, 2902–2891, 1628, 1512–1314, and 1024 cm^{-1} , respectively [19]. As depicted in the FTIR spectra of the composite materials, in addition to the ZnO absorption peaks, the peaks of betacyanin functional group also existed, strongly indicating that the

immobilization of betacyanin pigment on the surface of the ZnO material has been successfully carried out.

Further characterization of composite materials was investigated by fluorescence spectroscopy. The three-dimensional fluorescence spectra of unmodified ZnO, RDF extract, and the composite materials are shown in Fig. 4. The unmodified ZnO gave a strong excitation

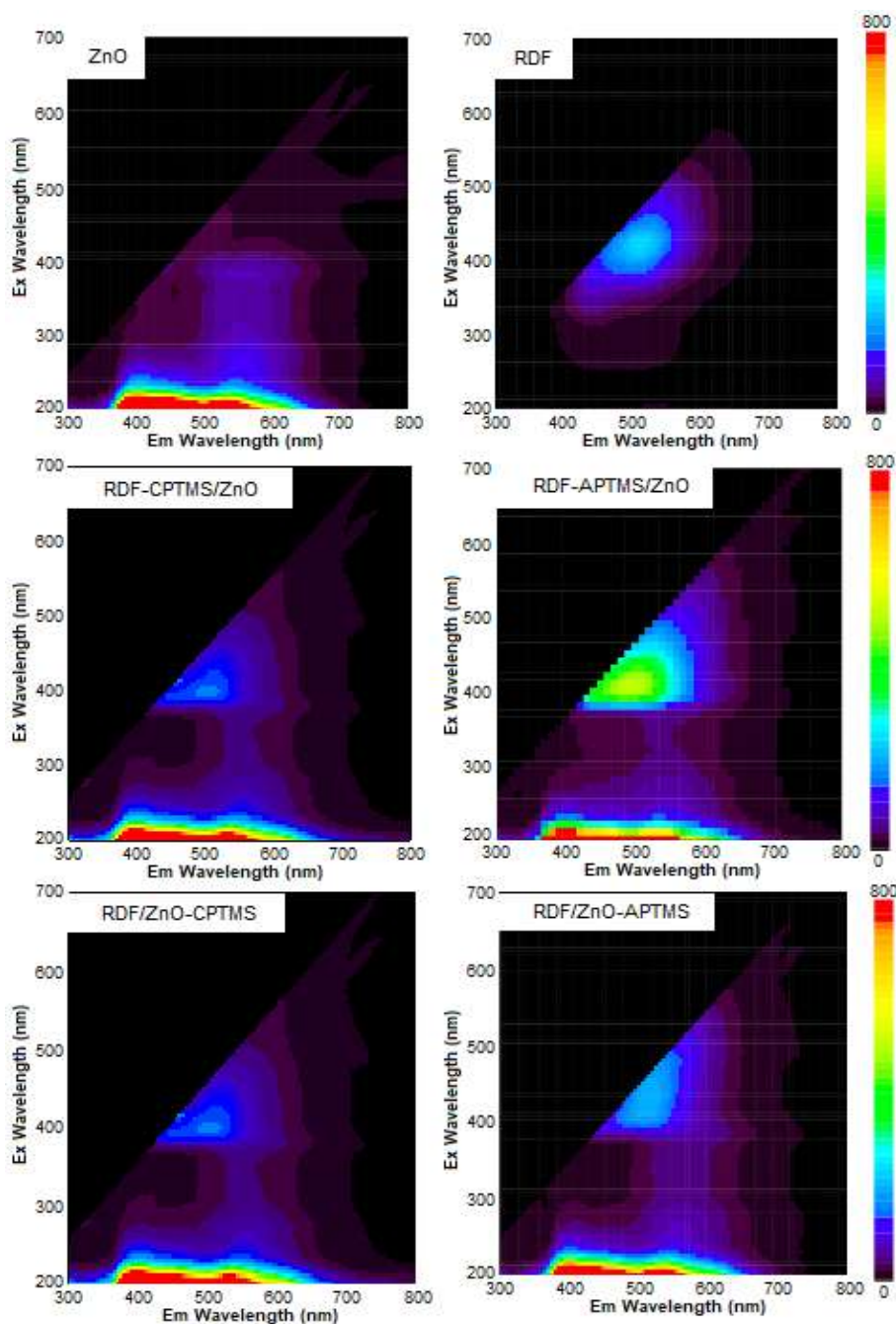


Fig 4. Three-dimensional fluorescence spectra of ZnO, RDF, and ZnO based composite materials

peak around 200 nm in good agreement with the strong light absorption of ZnO in the UV region and the weak excitation peak could be observed around 428 nm. The emission region of ZnO was wide and in the range of 350–650 nm. On the other hand, the RDF extract gave a weak excitation peak around 405 nm and the emission region was in the range of 430–680 nm. It was obvious that the three-dimensional fluorescence spectrum of composite materials was indeed a combination of the

three-dimensional fluorescence spectrum of ZnO and RDF extract. This result again clearly indicated the successful immobilization of the RDF extract onto ZnO.

From the fluorescence spectrum in the visible region of ZnO (Fig. 5), it was confirmed that the wavelengths of the excitation and emission were at 428 and 459 nm, respectively. These wavelengths were different from those of the RDF extract, where the maximum wavelengths of the excitation and emission

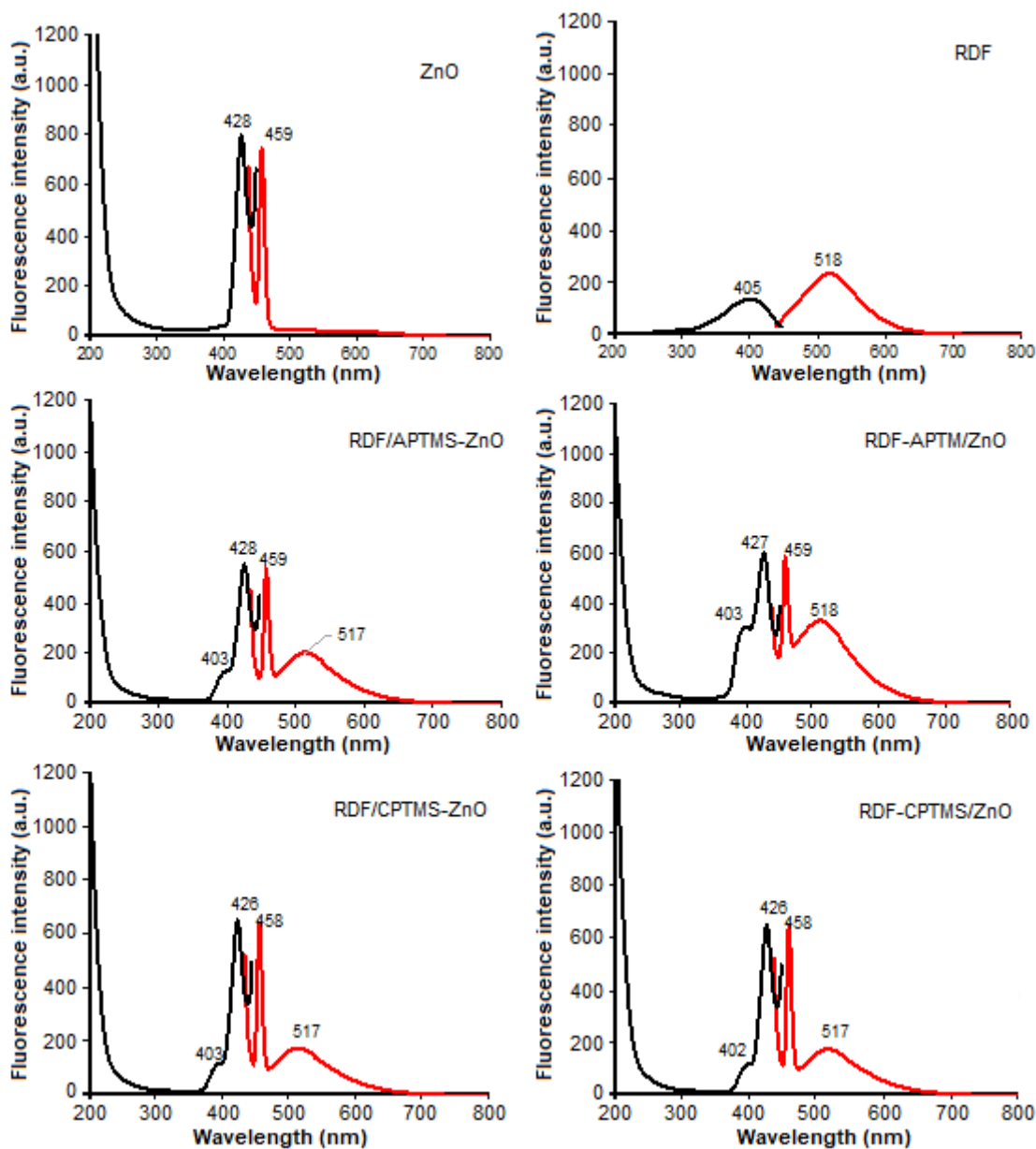


Fig 5. Fluorescence spectra of ZnO, RDF, and ZnO based composite materials. Black and red lines represent excitation and emission spectrum, respectively

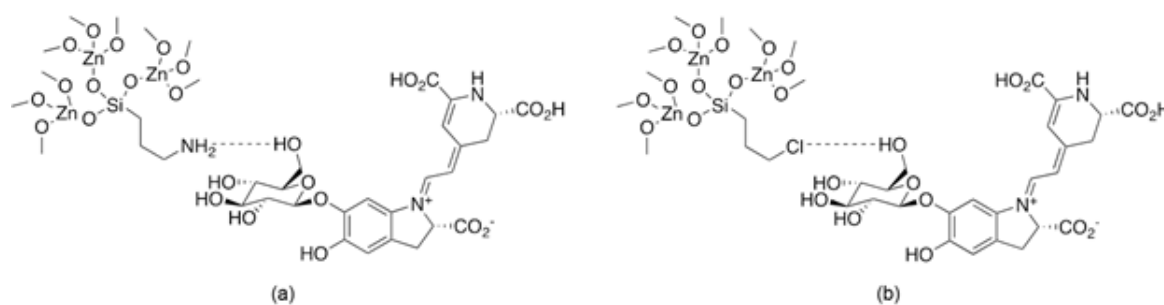


Fig 6. Proposed interactions between betacyanin pigment with (a) APTMS and (b) CPTMS on the ZnO surface

spectrum were found at 405 and 518 nm, respectively. As shown in Fig. 4, all the excitation and emission peaks of ZnO and RDF extract also existed on the composite materials. This work demonstrated that the immobilization of betacyanin pigment onto the ZnO surface has successfully enhanced the absorption region of the composite materials. Since the emission signals were found in 458–518 nm region, the prepared composite materials are promising to be used as green-emissive materials.

From the fluorescence intensity of the emission peak at 518 nm, the immobilization percentage of betacyanin pigment on the composite materials was calculated and shown in Table 2. The immobilized betacyanin amounts on the RDF-CPTMS/ZnO and the RDF-APTMS/ZnO were found to be 81% and 100%, respectively. This result showed that APTMS was a better organic linker than CPTMS in obtaining the ZnO composite. As betacyanin pigment has alcohol and carboxylic acid groups, betacyanin pigment would interact well with the amino substituent of APTMS through the hydrogen bondings rather than with the chloro substituent of CPTMS. This would be the reason why the immobilization percentages of betacyanin pigment were higher on the APTMS-based composite than the CPTMS-based one. The proposed interactions between the betacyanin pigment and the organic linker on the ZnO surface are shown in Fig. 6. Similar to our previous work [24], the interactions would mainly happen between either amino or chloro substituent of the organic linker and the primary alcohol substituent on the tetrahydropyran ring of the betacyanin due to less steric hindrance. Therefore, it was reasonable that flavonoid and carotenoid pigments were not immobilized

Table 2. Immobilized betacyanin percentages on the ZnO based composite materials

Materials	Immobilized betacyanin (%)
ZnO	0
RDF-CPTMS/ZnO	81
RDF-APTMS/ZnO	100
RDF/CPTMS-ZnO	80
RDF/APTMS-ZnO	90

on the ZnO materials because these pigments are non-polar [25], and thus, could not interact through hydrogen bondings with the linker agents.

On the other hand, only 80% and 90% of betacyanin was impregnated onto CPTMS-ZnO and APTMS-ZnO, respectively. While this result also showed that APTMS was better than CPTMS to impregnate the betacyanin onto ZnO, the order to introduce APTMS was found to be critical to obtaining larger amounts of immobilized betacyanin. When the betacyanin pigment was reacted with APTMS-ZnO material, it is possible for the betacyanin pigment to interact weakly with the Zn-OH group. Because of that, after filtration the immobilization percentage of betacyanin pigment on the RDF/APTMS-ZnO was lower than that of the RDF-APTMS/ZnO material.

■ CONCLUSION

In the present work, we successfully prepared four types of ZnO based composite materials through immobilization of betacyanin pigment on the surface of ZnO material using either CPTMS or APTMS as the organic linker. Both the RDF/CPTMS-ZnO and RDF-CPTMS/ZnO were obtained as purplish solids, while the RDF/APTMS-ZnO and RDF-APTMS/ZnO materials

appeared as pale yellow and bright yellow solid, respectively. The bandgap energy of the composite materials was not significantly different from the unmodified ZnO because the betacyanin pigment was immobilized on the surface of the ZnO. The FTIR spectra of the composite materials showed the presence of O–H, C–H sp^3 , C=O, C=C, and C–O functional groups. As high as 100% immobilized betacyanin could be achieved when the betacyanin was reacted first with APTMS, followed by impregnation onto ZnO. This result showed the importance of using APTMS and the order to introduce the betacyanin pigment onto ZnO. From the fluorescence spectrum of the composite materials, the emission signals were found at 458–518 nm region, demonstrating that the prepared composite materials are promising to be used as green-emissive materials.

■ ACKNOWLEDGMENTS

Support from the Directorate General of Research Strengthening and Development, Ministry of Research, Technology and Higher Education of the Republic of Indonesia via the Higher Education Excellent Applied Research scheme (PTUPT 2019 and PTUPT 2020, No. 041/SP2H/LT/MULTI/L7/2019 as revised in 041/SP2H/AMD/LT/MULTI/L7/2020, No. 005/MACHUNG/LPPM/SP2H-LIT-MULTI/III/2019, and No. 002/MACHUNG/LPPM/SP2H-LIT-MULTI/AMD/VI/2020) is greatly acknowledged.

■ REFERENCES

- [1] Ramkumar, V., and Kannan, P., 2015, Novel heterocyclic based blue and green emissive materials for opto-electronics, *Opt. Mater.*, 46, 314–323.
- [2] Zhu, C., Liu, X., Ni, Y., Fang, J., Fang, L., Lu, C., and Xu, Z., 2017, Novel fluorescence adjustable photonic crystal materials, *Opt. Mater.*, 73, 415–422.
- [3] Böttner, S., Jorgensen, M.R., and Schmidt, O.G., 2016, Rolled-up nanotechnology: 3D photonic materials by design, *Scr. Mater.*, 122, 119–124.
- [4] Freitag, M., Teuscher, J., Saygili, Y., Zhang, X., Giordano, F., Liska, P., Hua, J., Zakeeruddin, S.M., Moser, J.E., Grätzel, M., and Hagfeldt, A., 2017, Dye-sensitized solar cells for efficient power generation under ambient lighting, *Nat. Photonics*, 11 (6), 372–378.
- [5] Zheng, X., Li, D., Li, X., Chen, J., Cao, C., Fang, J., Wang, J., He, Y., and Zheng, Y., 2015, Construction of ZnO/TiO₂ photonic crystal heterostructures for enhanced photocatalytic properties, *Appl. Catal., B*, 168–169, 408–415.
- [6] Chen, Y., Bagnall, D., and Yao, T., 2000, ZnO as a novel photonic material for the UV region, *Mater. Sci. Eng., B*, 75 (2-3), 190–198.
- [7] Lee, K.M., Lai, C.W., Ngai, K.S., and Juan, J.C., 2016, Recent developments of zinc oxide based photocatalyst in water treatment technology: A review, *Water Res.*, 88, 428–448.
- [8] Xu, L., Zhou, Y., Wu, Z., Zheng, G., He, J., and Zhou, Y., 2017, Improved photocatalytic activity of nanocrystalline ZnO by coupling with CuO, *J. Phys. Chem. Solids*, 106, 29–36.
- [9] Dhafina, W.A., Salleh, H., Daud, M.Z., and Ghazali, M.S.M., 2018, Low cost dye-sensitized solar cells based on zinc oxide and natural anthocyanin dye from *Ardisia elliptica* fruits, *Optik*, 172, 28–34.
- [10] Vittal, R., and Ho, K.C., 2017, Zinc oxide based dye-sensitized solar cells: A review, *Renewable Sustainable Energy Rev.*, 70, 920–935.
- [11] Hassaan, M.A., and Nemr, A.E., 2017, Health and environmental impacts of dyes: Mini review, *Am. J. Environ. Sci. Eng.*, 1 (3), 64–67.
- [12] Liaotrakoon, W., De Clercq, N., Van Hoed, V., Van de Walle, D., Lewille, B., and Dewettinck, K., 2013, Impact of thermal treatment on physicochemical, antioxidative and rheological properties of white-flesh and red-flesh dragon fruit (*Hylocereus* spp.) purees, *Food Bioprocess Technol.*, 6 (2), 416–430.
- [13] Lee, K.H., Wu, T.Y., and Siow, L.F., 2013, Spray drying of red (*Hylocereus polyrhizus*) and white (*Hylocereus undatus*) dragon fruit juices: Physicochemical and antioxidant properties of the powder, *Int. J. Food Sci. Technol.*, 48 (11), 2391–2399.
- [14] Kim, H., Choi, H.K., Moon, J.Y., Kim, Y.S., Mosaddik, A., and Cho, S.K., 2011, Comparative antioxidant and antiproliferative activities of red and white pitayas and their correlation with

- flavonoid and polyphenol content, *J. Food Sci.*, 76 (1), C38–45.
- [15] Priatni, S., and Pradita, A., 2015, Stability study of betacyanin extract from red dragon fruit (*Hylocereus polyrhizus*) peels, *Procedia Chem.*, 16, 438–444.
- [16] Nimpoeno, W.A., Lintang, H.O., and Yuliati, L., 2020, Methyl red dye-sensitized zinc oxide as photocatalyst for phenol degradation under visible light, *AIP Conf. Proc.*, 2237, 020048.
- [17] Kurniawan, Y.S., Adhiwibawa, M.A.S., Setiyono, E., Fahmi, M.R.G., and Lintang, H.O., 2019, Statistical analysis for evaluating natural yellow coloring agents from peel of local fruits in Malang: Mangosteen, honey pineapple and red dragon fruits, *Indones. J. Nat. Pigm.*, 1 (2), 49–52.
- [18] Stintzing, F.C., Schieber, A., and Carle, R., 2002, Betacyanins in fruits from red-purple pitaya, *Hylocereus polyrhizus* (Weber) Britton & Rose, *Food Chem.*, 77 (1), 101–106.
- [19] Calogero, G., Yum, J.H., Sinopoli, A., Marco, G.D., Grätzel, M., and Nazeeruddin, M.K., 2012, Anthocyanins and betalains as light-harvesting pigments for dye-sensitized solar cells, *Sol. Energy*, 86 (5), 1536–1575.
- [20] Strack, D., Vogt, T., and Schliemman, W., 2003, Recent advances in betalain research, *Phytochemistry*, 62 (3), 247–269.
- [21] Ayinde, W.B., Dare, E.O., Bada, D.A., Alayande, S.O., Oladoyindo, F.O., Idowu, M.A., Bolaji, B.O., Ezeh, M.I., and Osuji, R.U., 2017, Dye-modified ZnO nanohybrids: Optical properties of the potential solar cell nanocomposites, *Int. Nano Lett.*, 7 (3), 171–179.
- [22] Nunes, V.F., Souza, A.P.S., Lima, F., Oliveira, G., Freire, F.N., and Almeida, A.F., 2018, Effects of potential deposition on the parameters of ZnO dye-sensitized solar cells, *Mat. Res.*, 21 (4), e20170990.
- [23] Zhang, Q., Xu, M., You, B., Zhang, Q., Yuan, H., and Ostrikov, K., 2018, Oxygen vacancy-mediated ZnO nanoparticle photocatalyst for degradation of methylene blue, *Appl. Sci.*, 8 (3), 353.
- [24] Kurniawan, Y.S., Anggraeni, K., Indrawati, R., and Yuliati, L., 2019, Selective betalain impregnation from red amaranth extract onto titanium dioxide nanoparticles, *AIP Conf. Proc.*, 2175, 020049.
- [25] Purnomo, T.A.B., Kurniawan, Y.S., Kesuma, R.F., and Yuliati, L., 2020, Selection of maceration solvent for natural pigment extraction from red fruit (*Pandanus conoideus* Lam), *Indones. J. Nat. Pigm.*, 2 (1), 8–12.

CoMFA, Molecular Docking and Molecular Dynamics Studies on Cycloguanil Analogues as Potent Antimalarial Agents

Isman Kurniawan^{1,*}, Muhamad Salman Fareza², and Ponco Iswanto³

¹School of Computing, Telkom University, Jl. Telekomunikasi, Terusan Buah Batu, Bandung 40257, Indonesia

²Department of Pharmacy, Universitas Jenderal Soedirman, Jl. Dr. Soeparno, Karangwangkal, Purwokerto 53123, Indonesia

³Department of Chemistry, Universitas Jenderal Soedirman, Jl. Dr. Soeparno, Karangwangkal, Purwokerto 53123, Indonesia

* **Corresponding author:**

email: ismankrn@telkomuniversity.ac.id

Received: December 10, 2019

Accepted: April 3, 2020

DOI: 10.22146/ijc.52388

Abstract: Malaria is a disease that commonly infects humans in many tropical areas. This disease becomes a serious problem because of the high resistance of *Plasmodium* parasite against the well-established antimalarial agents, such as Artemisinin. Hence, new potent compounds are urgently needed to resolve this resistance problem. In the present study, we investigated cycloguanil analogues as a potent antimalarial agent by utilizing several studies, i.e., comparative of molecular field analysis (CoMFA), molecular docking and molecular dynamics (MD) simulation. A CoMFA model with five partial least square regressions (PLSR) was developed to predict the pIC₅₀ value of the compound by utilizing a data set of 42 cycloguanil analogues. From statistical analysis, we obtained the r^2 values of the training and test sets that were 0.85 and 0.70, respectively, while q^2 of the leave-one-out cross-validation was 0.77. The contour maps of the CoMFA model were also interpreted to analyze the structural requirement regarding electrostatic and steric factors. The most active compound (c33) and least active compound (c8) were picked for molecular docking and MD analysis. From the docking analysis, we found that the attached substituent on the backbone structure of cycloguanil gives a significant contribution to antimalarial activity. The results of the MD simulation confirm the stability of the binding pose obtained from the docking simulations.

Keywords: malaria; cycloguanil; CoMFA; molecular docking; molecular dynamics

■ INTRODUCTION

Malaria is a life-threatening disease that causes public health problems in many regions of Africa and Asia. In 2016, malaria had infected 216 million people across the world and had caused 445,000 deaths, as reported by the World Health Organization [1]. Furthermore, this disease leads to the increase of economic and social burden on infected patients [2]. This disease is mostly caused by the *Plasmodium falciparum* parasite which is a major factor of malaria-related deaths in the world. Several antimalarial drugs, such as chloroquine, pyrimethamine, and cycloguanil, have been used to treat the infection of malaria. These drugs act as antimalarial agents by inhibiting the activity of dihydrofolate reductase of *P. falciparum* enzyme, i.e., dihydrofolate reductase-

thymidylate synthase (PfDHFR-TS) [3].

However, the resistance of the parasite against well-established antimalarial agents has been found in many countries. The widespread occurrences of malaria could be the main factor of this resistance [4]. Therefore, new antimalarial drugs are urgently required to overcome the resistance problem. Regarding this issue, a series of cycloguanil analogues which are known to have an ability to effectively bind to wild type and mutant type PfDHFR, an antimalarial drug target, have been employed in this study [5-6]. The cycloguanil analogues backbone contains 1,3,5-dihydrotriazine in which *p*-chlorophenyl is attached at N1 position, as shown in Fig. 1.

In silico approach is commonly used to design the new drug candidate by investigating the type of attached

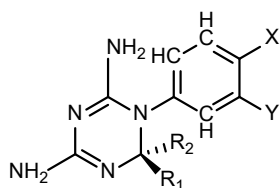


Fig 1. Chemical structure of cycloguanil analogues

substituent in cycloguanil analogues. Several studies have been reported concerning the utilization of *in silico* approaches, such as quantitative structure-activity relationship (QSAR) [7-8], pharmacophore [9], homology modelling [10], molecular docking [9], and molecular dynamics [11], in designing new drug candidates. Relating to *in silico* studies on cycloguanil analogues as an antimalarial agent, Kuhmar Ojha and co-workers have performed QSAR, pharmacophore mapping and docking studies to obtain cycloguanil derivatives with high binding affinity against PfDHFR-TS target [12]. A prediction model of cycloguanil analogues has also been developed by Nattee and co-workers. They used an extremely randomized tree to develop the model and obtained a satisfying result [13]. In addition, Inthajak and co-workers developed a QSAR model to predict the activity of cycloguanil analogues by using PSO-SVR method [14]. However, to the best of our knowledge, there is no report on the investigation of the dynamics of cycloguanil analogues and the DHFR receptor.

In this study, we utilized a series of *in silico* approach, i.e., comparative of molecular field analysis (CoMFA), molecular docking, and molecular dynamics, to explore the structural contribution of cycloguanil analogues on antimalarial activity. The observed pIC_{50} values were considered as target values in developing the CoMFA model. The contribution of a steric and electrostatic factor was revealed by carrying out contour maps analysis. We also investigated the binding pose of the complex of cycloguanil analogues and the receptor target by using molecular docking. Finally, the binding pose was confirmed by carrying out molecular dynamic simulation.

■ COMPUTATIONAL METHODS

Molecular Data Set

A series of 42 cycloguanil analogues, used in this

study, were obtained from references [6,15]. The experimental IC_{50} values of the compounds at nano-molar (nM) units were converted to molar (M) units. To obtain target values in a smaller range, we converted the IC_{50} to pIC_{50} by using the formula $pIC_{50} = -\log IC_{50}$. Then, pIC_{50} values were used as target values for the development of the CoMFA model. From the data set, training and test sets which contain 32 and 10 compounds, respectively, were randomly selected. The chemical structure and experimental pIC_{50} values of cycloguanil analogues are provided in Table 1. The 2D structures of the compounds were constructed by using the MarvinSketch program [16] and were converted to a 3D structure by using Open Babel package [17]. The structures were optimized by using AM1 method in MOPAC package [18] and were converted to SDF file format containing all compound structures. This SDF file was used for performing molecular alignment of CoMFA analysis.

CoMFA Modelling

The CoMFA model was developed by utilizing the optimized compound structure with pIC_{50} as the target values. The development of the CoMFA model was begun by performing molecular alignment analysis by using Open3DALIGN package [19]. In this stage, molecular alignment processes were performed by using each compound as a template, so 42 alignments were generated. The alignment with compound 42 (c42) as a template, as shown in Fig. 2, has the maximum alignment score and thus was considered for developing the CoMFA model.

CoMFA model was built in Open3DQSAR package [20] by inserting the alignment with c42 as a template into a grid box with 1 Å grid spacing and was expanded to 5 Å in all directions from the alignment as the center. Molecular interaction fields (MIF) were generated in terms of the steric field and electrostatic field. For the steric field, MIF was calculated by using a carbon atom probe, while for the electrostatic field, MIF was calculated by using a volume-less probe with +1 charge. Before building the model, pre-treatment processes were performed to obtain an acceptable

model. The pre-treatment processes consisted of the following steps: (a) determination of the cut-off of maximum and minimum energy values at ± 30 kcal/mol, (b) interaction fields with the values of absolute energy lower than 0.05 were adjusted to zero, (c) independent variables with the value of standard deviation lower than 0.1 were removed, (d) independent variables matrices were scaled with the block unscaled weighting (BUW) technique [20-21].

To increase the interpretability, a variable selection procedure was carried out to discard fewer influent variables. This procedure was performed by using the combination of smart region definition (SRD) and factorial design (FFD) [20,22]. Ten cycloguanil analogues

data were randomly selected for a test set, while the rest of the data was set as a training set. Finally, a prediction model was built with partial least square regression (PLSR) by utilizing the pIC_{50} values as the dependent

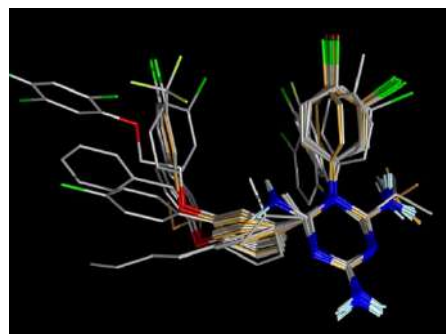
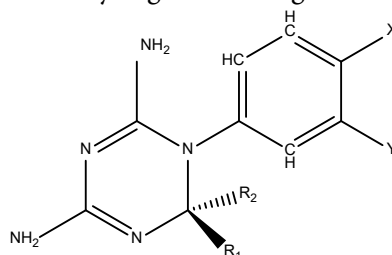


Fig 2. The best alignment with c42 as a template

Table 1. Data set of cycloguanil analogues used in this study



Comp.	R1	R2	X	Y	pIC_{50}	Comp.	R1	R2	X	Y	pIC_{50}
1	CH ₃	CH ₃	Cl	H	5.61	22	CH ₃	CH ₃	H	H	6.35
2	H	H	Cl	H	6.50	23 ^a	CH ₃	CH ₃	F	H	6.00
3	CH ₃	H	Cl	H	6.46	24	H	H	H	H	6.45
4 ^a	CH ₂ CH ₃	H	Cl	H	6.31	25	H	H	F	H	6.51
5	(CH ₂) ₂ CH ₃	H	Cl	H	6.64	26	CH ₃	CH ₃	H	Cl	6.53
6	(CH ₂) ₃ CH ₃	H	Cl	H	6.60	27	CH ₃	CH ₃	Cl	Cl	6.51
7 ^a	CH(CH ₃) ₂	H	Cl	H	5.55	28 ^a	CH ₃	H	H	Cl	7.55
8	C(CH ₃) ₃	H	Cl	H	4.18	29	CH ₃	H	Cl	Cl	7.72
9	C ₆ H ₅	CH ₃	Cl	H	7.36	30 ^a	C ₆ H ₅	H	H	Cl	7.62
10	CH ₃	CH ₃	Br	H	5.56	31	C ₆ H ₅	H	Cl	Cl	7.54
11	CH ₃	H	Br	H	6.56	32	C ₆ H ₄ -p-OC ₆ H ₅	H	Cl	H	7.40
12 ^a	CH ₂ CH ₃	H	Br	H	6.66	33	C ₆ H ₄ -p-OC ₆ H ₅	H	H	Cl	8.40
13	(CH ₂) ₂ CH ₃	H	Br	H	6.60	34 ^a	C ₆ H ₄ -m-OC ₆ H ₅	H	H	Cl	7.22
14	CH(CH ₃) ₂	H	Br	H	6.14	35	C ₆ H ₄ -m-OCH ₂ C ₆ H ₅	H	H	Cl	6.72
15 ^a	C ₆ H ₅	H	Br	H	6.74	36	C ₆ H ₄ -m-(OC ₆ H ₄ -4-Cl)	H	Cl	H	6.38
16	CH ₃	CH ₃	CH ₃	H	5.44	37	C ₆ H ₄ -m-(4-ClC ₆ H ₄)	H	H	Cl	6.41
17	CH ₃	H	CH ₃	H	6.33	38	n-C ₇ H ₁₅	H	H	Cl	8.40
18 ^a	CH ₂ CH ₃	H	CH ₃	H	6.29	39 ^a	C ₆ H ₄ -p-OC ₃ H ₇	H	H	Cl	8.40
19	(CH ₂) ₂ CH ₃	H	CH ₃	H	6.82	40	C ₆ H ₄ -m-(OC ₆ H ₃ -3,5-Cl ₂)	H	H	Cl	7.30
20	CH(CH ₃) ₂	H	CH ₃	H	5.46	41	C ₆ H ₄ -m-O(CH ₂) ₂ -O(2,4,5-Cl ₃ -C ₆ H ₂)	H	H	Cl	6.43
21	C ₆ H ₅	H	CH ₃	H	7.41	42	C ₆ H ₄ -m-(3-CF ₃ -OC ₆ H ₄)	H	H	Cl	6.74

^a refers test set compound

variables and selected CoMFA variables as independent variables.

Model Validation

To validate the CoMFA model, we performed both internal and external validation tests and compared the value with the threshold. The internal validation was performed by calculating the coefficient of determination (R_{train}^2) and leave-one-out (LOO) cross-validation (Q_{loo}^2) using the training set. Meanwhile, the external validation was conducted by calculating the coefficient of determination (R_{test}^2) using the test set. The model was acceptable if the value of R^2 and Q^2 were more than 0.6 and 0.5, respectively. Furthermore, several validation parameters were calculated to confirm the acceptability of the model. The calculation of the validation parameters is summarized as follows

$$R_{\text{train}}^2 = 1 - \frac{\sum(y_{\text{train}} - \hat{y}_{\text{train}})^2}{\sum(y_{\text{train}} - \bar{y}_{\text{train}})^2} \quad (1)$$

$$Q_{\text{loo}}^2 = 1 - \frac{\sum(y_{\text{train}} - \hat{y}_{\text{loo}})^2}{\sum(y_{\text{train}} - \bar{y}_{\text{train}})^2} \quad (2)$$

$$R_{\text{test}}^2 = 1 - \frac{\sum(y_{\text{test}} - \hat{y}_{\text{test}})^2}{\sum(y_{\text{test}} - \bar{y}_{\text{train}})^2} \quad (3)$$

$$k = \frac{\sum(y \times \hat{y})}{\sum(\hat{y})^2} \quad (4)$$

$$k' = \frac{\sum(y \times \hat{y})}{\sum(y)^2} \quad (5)$$

$$r^2 = \frac{[\sum(y - \bar{y})(\hat{y} - \bar{\hat{y}})]^2}{\sum(y - \bar{y})^2 \times \sum(\hat{y} - \bar{\hat{y}})^2} \quad (6)$$

$$r_0^2 = 1 - \frac{\sum(y - k \times \hat{y})^2}{\sum(y - \bar{y})^2} \quad (7)$$

$$r_0'^2 = 1 - \frac{\sum(\hat{y} - k' \times y)^2}{\sum(\hat{y} - \bar{\hat{y}})^2} \quad (8)$$

$$r_m^2 = r^2 \times \left(1 - \sqrt{r^2 - r_0^2}\right) \quad (9)$$

$$r_m'^2 = r^2 \times \left(1 - \sqrt{r^2 - r_0'^2}\right) \quad (10)$$

$$\bar{r}_m^2 = \frac{(r_m^2 + r_m'^2)}{2} \quad (11)$$

$$\Delta r_m^2 = |r_m^2 - r_m'^2| \quad (12)$$

$${}^c R_p^2 = R \times \sqrt{R^2 - R_r^2} \quad (13)$$

where y and \hat{y} represent the experimental and predicted value of pIC_{50} , respectively, while \bar{y} and $\bar{\hat{y}}$ represent the average of the experimental and predicted value, respectively. The value of ${}^c R_p^2$ represents the correlation coefficient which is calculated by considering randomized and non-randomized models. This parameter can be used to verify that the model is not overfitting. The acceptability of the model was considered according to the following criteria [23-25]

$$R^2 > 0.6$$

$$Q^2 > 0.5$$

$$0.85 \leq k \leq 1.15 \text{ or } 0.85 \leq k' \leq 1.15$$

$$\frac{(r^2 - r_0^2)}{r^2} < 0.1 \text{ or } \frac{(r^2 - r_0'^2)}{r^2} < 0.1$$

$$|r_0^2 - r_0'^2| < 0.3$$

$$\bar{r}_m^2 > 0.5$$

$$\Delta r_m^2 < 0.2$$

$${}^c R_p^2 > 0.5$$

Applicability domain (AD) of the model was also determined to confirm that the data set lies in the domain of the model. The determination of AD was performed by using leverage method that is formulated as $H = X(X^T X)^{-1} X^T$ (14) where X represents the score matrix obtained from the PLSR procedure. The critical leverage (h^*) value was defined as $3p/n$, where p and n are the numbers of attributes and data set, respectively, that are involved in the training process. The predicted value of a data set was acceptable if the calculated leverage value was smaller than the critical leverage. The AD of the CoMFA model was figured out by using the William plot [26]. Finally, we interpreted the CoMFA contour map of the steric and electrostatic factors by using MacPymol package [27].

Molecular Docking

According to the pIC_{50} values, the most active (c33) and least active compound (c8) were selected for further

analysis of molecular docking and molecular dynamics simulation. Regarding the docking scenario, we implemented a flexible ligand-rigid receptor scheme to represent lock and key theory of ligand-receptor interaction. The receptor molecule was prepared by downloading the X-ray crystal structure of wild-type *Plasmodium falciparum* DHFR-TS complexed with cycloguanil and NADPH at 2.6 Å resolution (PDB ID: 3UM8, <https://www.rcsb.org/structure/3um8>) from RCSB protein data bank [28]. The binding site of the receptor was identified from the position of native cycloguanil found in the X-ray structure. However, we removed the original cycloguanil from the structure as part of the preparation process.

To construct pdbqt file of the receptor, we used Open Babel package [17] to add polar hydrogens and assign Gasteier charge to the ligand. The grid box, which defines the docking area, was constructed by using the native ligand position as the center and expanded the box with a size of 8 Å. The docking simulation was performed by using Smina docking package [29] and the binding pose obtained from the docking simulation was plotted by using LigPlot package [30].

The docking procedure was validated by extracting native cycloguanil ligand from wild-type *Plasmodium falciparum* DHFR-TS complex and re-docking the ligand to the receptor. The validity of the method was determined by aligning the ligand obtained from docking simulation and original X-ray crystal structure, and calculating the deviation between both structures. In this case, the deviation was represented as the root mean square displacement (RMSD) parameter.

Molecular Dynamics

The binding poses of the docked ligand into the receptor were obtained instantaneously from docking simulation. Consequently, the interaction may be unstable due to the rigid receptor approximation. Therefore, we confirmed the stability and validity of the interaction by carrying out molecular dynamics simulation for the complex system. The molecular dynamics simulation of ligand-protein complexes was performed by using Gromacs 2018 package [31].

The preparation of the structure of the complex was carried out by using MacPymol package [27]. The topology of protein was prepared by using CHARMM36 force field. Meanwhile, the topology of ligand was estimated by using CHARMM General Force Field (CGenFF) server (<https://cgenff.umaryland.edu/>). Then, the complex was solvated into dodecahedron box of SPC water with 1.00 nm from the molecule to the edge of the box. The solvated complex system was neutralized by replacing the solvent molecule with Cl⁻ ions.

After completing the preparation step, the system was minimized by using the steepest descent algorithm, followed by consecutive NVT (1 ns) and NPT (1 ns) equilibrations. During the equilibrations, the temperature was fixed at 300 K by utilizing V-rescale thermostat algorithm [32], and the pressure was fixed at 1.0 bar by utilizing Berendsen barostat algorithm [33]. Finally, MD simulation was performed for 20 ns with a time step of 2 fs. Neighbor searching was carried out by using Verlet algorithm with a cut-off radius of Van der Waals (VdW) short interaction that was set at 1.2 nm. Long-range electrostatic interaction was carried out by using Particle Mesh Ewald scheme-38 with a cut-off radius set at 1.2 nm. The results of the simulation were investigated by using Gromacs analysis tools [31].

■ RESULTS AND DISCUSSION

CoMFA Modelling

To develop the CoMFA model, we used the best alignment of molecules by considering the c42 molecule as a template. The model was developed by using the partial least square regressions (PLSR) method with five PLS components. The comparison of predicted and experimental values of pIC₅₀ is shown in Fig. 3(a), while the Williams plot that represents the applicability domain (AD) of the model is shown in Fig. 3(b). Those analyses confirm that all of the data lie inside the AD region, indicating that no outlier data existed in the data set. Furthermore, the predictive model is confirmed to be acceptable for all compounds. To validate the CoMFA model, several statistical parameters were calculated and compared to threshold values [23-25]. We found that the calculated values of the validation parameters, as provided

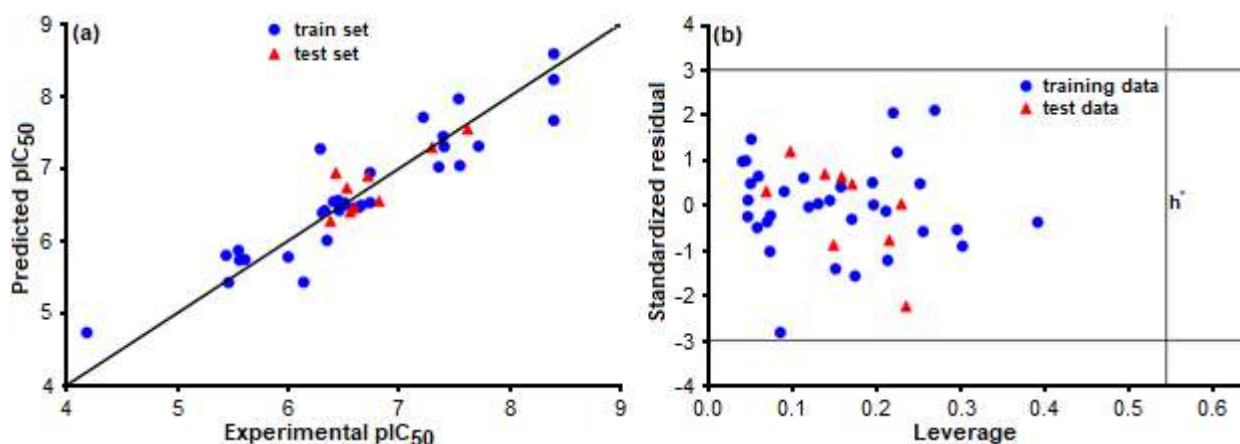


Fig 3. (a) Scatter plot of predicted pIC_{50} vs. experimental pIC_{50} ; (b) Williams plot of applicability domain

in Table 2, met the criteria. These results indicate that the CoMFA model was valid and acceptable. In addition, we found that the value of ${}^cR_p^2$ is larger than 0.5, which indicates that the model is not overfitting.

The contour maps of the CoMFA model that represent the steric and electrostatic field of favorable substituents are presented in Fig. 4. In the steric field, the green and yellow contours depict the favorable and unfavorable position, respectively, for bulky group substituents. Meanwhile, in the electrostatic field, the red and blue contours depict the favorable position for negatively and positively charged substituents, respectively. In the steric contour map, we found a large green contour around R_1 position. This indicates that bulky

Table 2. Calculated statistical parameter of CoMFA model

Parameter	Training set	Test set	Threshold [23-25]
R^2	0.85	0.70	> 0.6
Q^2	0.77	-	> 0.5
k'	0.86	1.05	$0.85 \leq k' \leq 1.15$
$\frac{(r^2 - r_0^2)}{r^2}$	0.07	0.00	< 0.1
$\left \frac{r_0^2 - r_0'^2}{r_0^2} \right $	0.05	0.09	< 0.3
$\overline{r_m^2}$	0.72	0.57	> 0.5
Δr_m^2	0.14	0.18	< 0.2
${}^cR_p^2$	0.76	-	> 0.5

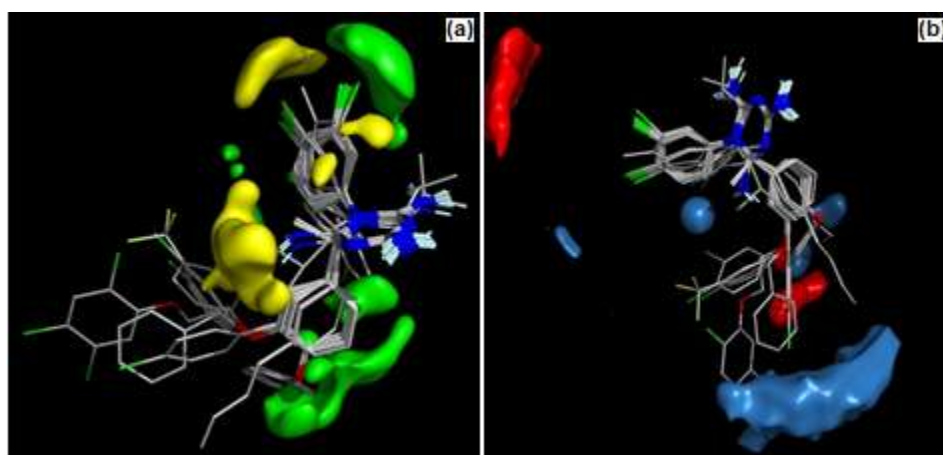


Fig 4. (a) Steric CoMFA contour map, green and yellow contour indicate a region where bulky substituent is favorable and unfavorable, respectively; (b) Electrostatic CoMFA contour map, red and blue contour indicate a favorable region for a substituent with positively and negatively charged, respectively

group substituents are favorable to attach at this position. Among the data set, several compounds contained a bulky group attached at R_1 position, namely c9, c15, c21, c32–c42. The greater activity of c9 compared to c1 corresponds to the substitution of the methyl group of c1 by the phenyl group of c9. Therefore, the attachment of a phenyl group at R_1 position increased the steric effect and thus increased the activity of the compounds.

Besides that, the green contour was also found around the X position that indicates a favorable position for the more steric group at this position. The greater activity of c12 compared to c4 was also related to the increase of the steric effect of the substituent at this position, namely Br^- and Cl^- for c12 and c4, respectively. Meanwhile, the yellow contours were found around the R_2 position that indicates the unfavorable position for a bulky group in this position. We found that most of the compounds in the data set had a low steric substituent. The attachment of more steric substituents at this position decreased the activity of the compound. This finding was confirmed by the comparison of the pIC_{50} of c1 (5.61) with a methyl substituent that was greater than c3 (6.46) with a hydrogen substituent. In addition, yellow contours were found around the Y position that indicates the unfavorable position for a bulky group in this position.

In the electrostatic contours, we found two dominant contours that consists of one blue contour around the R_1 position and one red contour around the X and Y positions. This indicates that positively charged substituents are favorable to attach at R_1 position, while negatively charged substituents are favorable to attach to both X and Y position. The activity of c4 was higher than that of c5 due to the existence of a more positive (ethyl group) substituent. Generally, the increase in the activity of a molecule was related to the increase in the negative charge of the substituent at X and Y positions. For example, the attachment of Cl^- substituent at c26 contributed to the higher activity of the molecule compared to that of c22.

Molecular Docking

Molecular docking analysis was carried out on the most active compound (c33) and the least active

compound (c8). We found that the calculated binding score for c33 and c8 compound were -10.7 kcal/mol and -7.9 kcal/mol, respectively. The lower value of the binding score indicated that c33 binds to the receptor better than c8, which is in agreement with the experimental results. The binding poses of both compounds that were docked into 3UM8 receptor, obtained from the docking simulation, are provided in Fig. 5(a) and 5(b). From the binding poses, we found that both compounds were docked in a similar binding site of the receptor.

The 2D plots of ligand-receptor interaction between c33 and c8 compounds with 3UM8 receptor are presented in Fig. 5(c) and 5(d). The number of hydrogen bonds found in the interaction of the receptor with c33 and c8 were four and one, respectively. For c33 ligands, the hydrogen bonds were found in the interaction of the ligands with ALA16, LEU40 and SER111. Meanwhile for c8 ligands, a hydrogen bond was found in the interaction of the ligands with ALA16. From the docking results, we found that the higher number of hydrogen bonds found in c33-receptor interaction contributed to the high activity of the ligand.

The acceptability of our docking simulations was confirmed by validating the docking procedure. The validity of the procedure was represented by the value of RMSD of the alignment between the ligand configuration obtained from docking simulation and the original X-ray crystal structure, in which the alignment is shown in Fig. 6. According to the validation analysis, we found that the RMSD value is 1.09 Å, which is low enough to confirm that the docking procedure is valid [34].

Molecular Dynamics

To confirm the stability of the solvated complex system, we analyzed the fluctuation of RMSD and the radius of gyration for 20 ns simulation of both complexes, as shown in Fig. 7(a). RMSD analysis shows that both c33 and c8 complexes reached the equilibrium state after 10 ns. We also found that the RMSD value of the c33 complex was slightly lower than that of the c8 complex, indicating the better stability of the c33 complex. The fluctuation of the radius of gyration, which

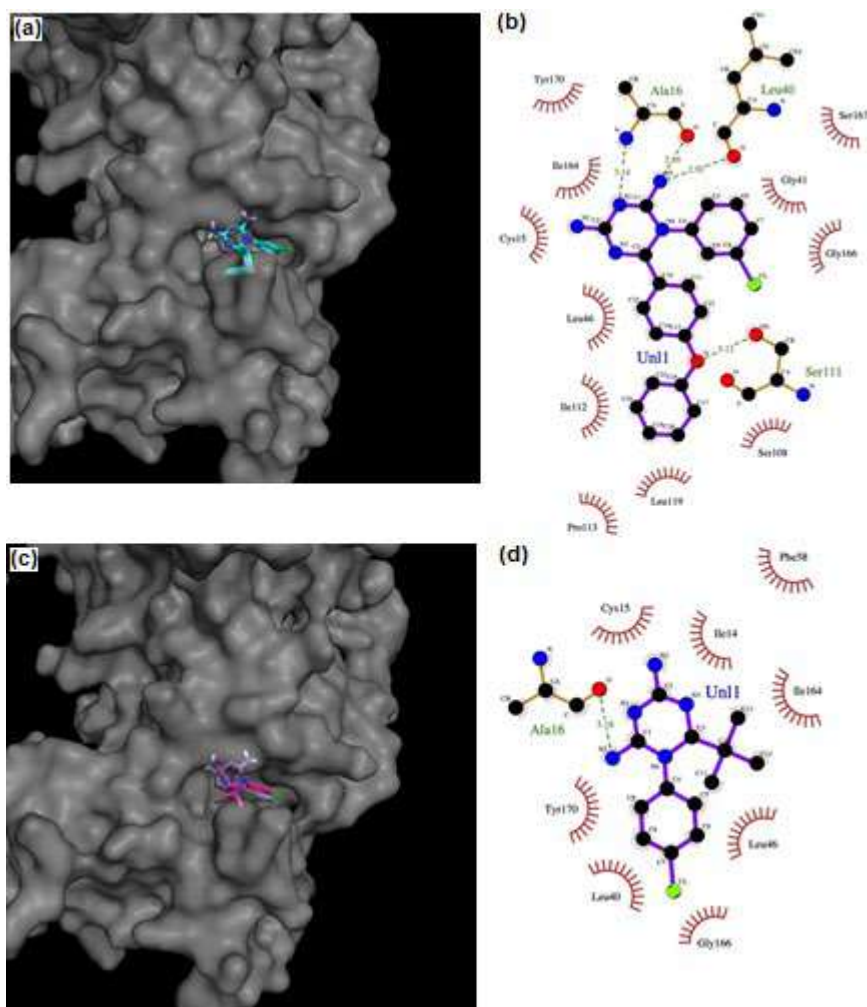


Fig 5. The binding poses of (a) c33 and (c) c8 that are docked into 3UM8 binding site, and the plot of ligand-receptor interaction of (b) c33 and (d) c8 ligands

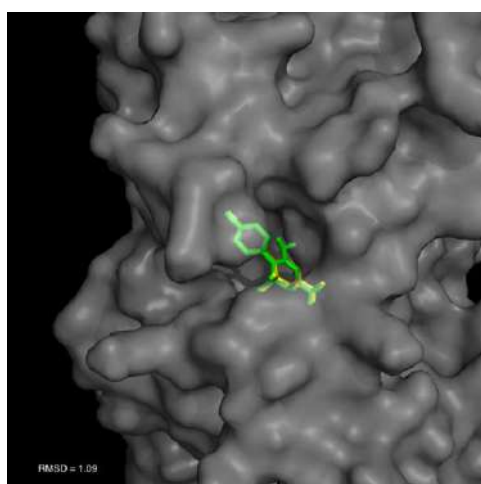


Fig 6. The alignment of the ligand configuration obtained from docking simulation (green) and original X-ray crystal structure (yellow)

indicates the compactness of the complex system, is provided in Fig. 7(b). We found that the compactness of the c33 complex was lower than that of the c8 complex.

We also analyzed the fluctuation of the hydrogen bond formed during the simulation, as shown in Fig. 7(c). We found that the hydrogen bond formed during the simulation of the c33 complex was more than that of the c8 complex. In the case of the c33 complex, the maximum number and the average number of hydrogen bonds were 4 and 0.78, respectively. Meanwhile, in the case of the c8 complex, the maximum number and the average number of hydrogen bonds were 3 and 0.82, respectively. According to the results, it seems that the number of hydrogen bonds formed during the simulation was quite similar between both complexes.

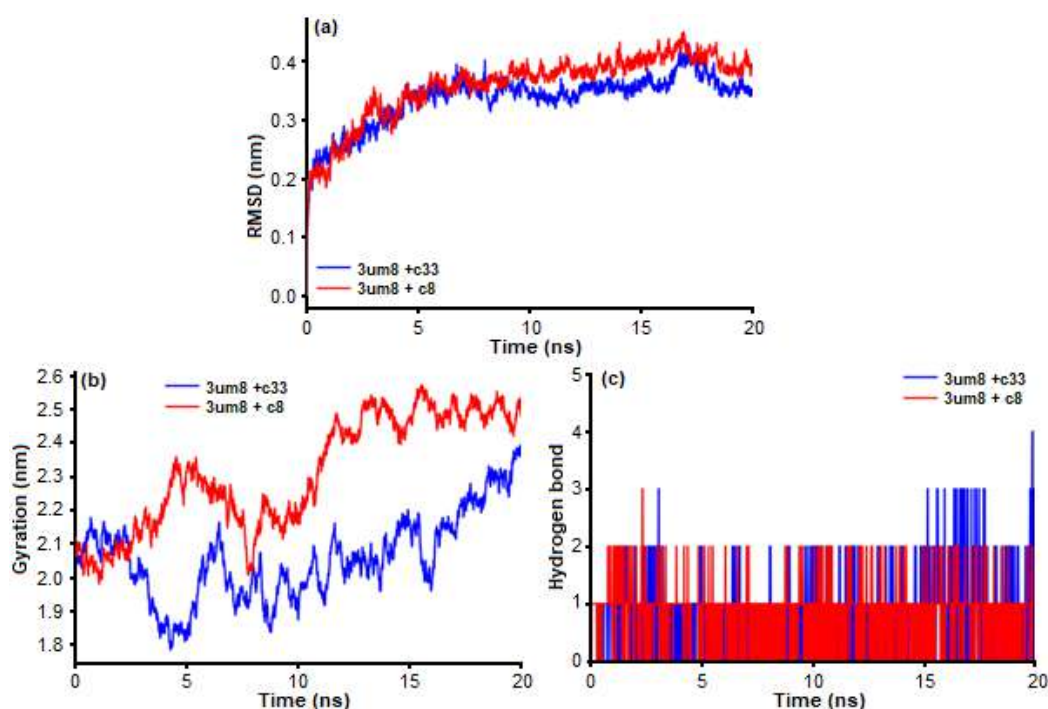


Fig 7. Plots of (a) RMSD, (b) radius of gyration and (c) hydrogen bonds number from MD simulation of c33 and c8 complex

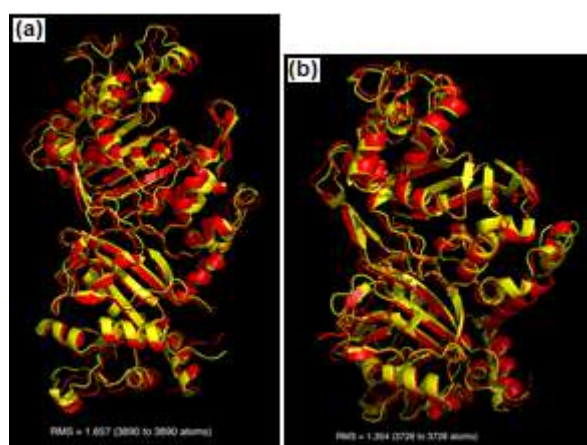


Fig 8. The alignment of the initial (yellow) and final (red) structure obtained from MD simulation of 3UM8 complex with (a) c33 and (b) c8 ligand

Finally, we aligned the final structure of the complex obtained from MD simulation with the initial structure to verify that the structure did not change significantly during the simulation. The results of the alignment for both complexes are presented in Fig. 8. We found that the final structure for both complexes resembles the initial structure with a small deviation. This is indicated by the low RMSD that is evaluated from the alignment processes, which

were 1.657 Å and 1.354 Å for the complex with c33 and c8, respectively. This points out that the structure did not change significantly during the simulation.

■ CONCLUSION

This study aims to explore the structural contribution of cycloguanil analogues on antimalarial activity. The CoMFA model was developed and validated by using several statistical parameters. Based on contour maps analysis, the bulky group with a positively charged atom was favorable to attach at the R1 position, while the bulky group with a negatively charged atom was favorable to attach at the Y position. From the docking analysis, we found that the existing hydrogen bonds in the binding pose of c33 was more than that of c8. This finding points out the importance of the hydrogen bond in supporting inhibition activity. The results of the MD simulation confirmed the stability of the binding pose obtained from the docking simulation.

■ ACKNOWLEDGMENTS

This work was supported in part through High Performance Computing (HPC) resources provided by

the School of Computing, Telkom University.

■ REFERENCES

- [1] World Health Organization, 2018, *Ready to beat malaria*, World Malaria Day 2018, 26 March 2018, 1–3.
- [2] Alonso, S., Chaccour, C.J., Elobolobo, E., Nacima, A., Candrinho, B., Saifodine, A., Saute, F., Robertson, M., and Zulliger, R., 2019, The economic burden of malaria on households and the health system in a high transmission district of Mozambique, *Malar. J.*, 18 (1), 360.
- [3] Mharakurwa, S., Kumwenda, T., Mkulama, M.A.P., Musapa, M., Chishimba, S., Shiff, C.J., Sullivan, D.J., Thuma, P.E., Liu, K., and Agre, P., 2011, Malaria antifolate resistance with contrasting *Plasmodium falciparum* dihydrofolate reductase (DHFR) polymorphisms in humans and *Anopheles* mosquitoes, *Proc. Natl. Acad. Sci. U.S.A.*, 108 (46), 18796–18801.
- [4] Blasco, B., Leroy, D., and Fidock, D.A., 2017, Antimalarial drug resistance: Linking *Plasmodium falciparum* parasite biology to the clinic, *Nat. Med.*, 23 (8), 917–928.
- [5] Yuthavong, Y., Tarnchompoo, B., Vilaivan, T., Chitnumsub, P., Kamchonwongpaisan, S., Charman, S.A., McLennan, D.N., White, K.L., Vivas, L., Bongard, E., Thongphanchang, C., Tawechai, S., Vanichtanankul, J., Rattanajak, R., Arwon, U., Fantauzzi, P., Yuvaniyama, J., Charman, W.N., and Matthews, D., 2012, Malarial dihydrofolate reductase as a paradigm for drug development against a resistance-compromised target, *Proc. Natl. Acad. Sci. U.S.A.*, 109 (42), 16823–16828.
- [6] Kulatee, S., Toochinda, P., Suksangpanomrung, A., and Lawtrakul, L., 2017, Theoretical investigation of the enantioselective complexations between *pf*DHFR and cycloguanil derivatives, *Sci. Pharm.*, 85 (4), 37.
- [7] Kurniawan, I., Rosalinda, M., and Ikhsan, N., 2020, Implementation of ensemble methods on QSAR Study of NS3 inhibitor activity as anti-dengue agent, *SAR QSAR Environ. Res.*, 31 (6), 477–492.
- [8] Kurniawan, I., Tarwidi, D., and Jondri, 2019, QSAR modeling of PTP1B inhibitor by using Genetic algorithm-Neural network methods, *J. Phys. Conf. Ser.*, 1192, 012059.
- [9] Sattarov, B., Baskin, I.I., Horvath, D., Marcou, G., Bjerrum, E.J., and Varnek, A., 2019, De novo molecular design by combining deep autoencoder recurrent neural networks with generative topographic mapping, *J. Chem. Inf. Model.*, 59 (3), 1182–1196.
- [10] Hu, X., Xie, J., Hu, S., Zhang, L., and Dong, Y., 2017, Exploration of the binding affinities between ecdysone agonists and EcR/USP by docking and MM-PB/GBSA approaches, *J. Mol. Model.*, 23 (5), 166.
- [11] Dehury, B., Behera, S.K., and Mahapatra, N., 2017, Structural dynamics of Casein Kinase I (CKI) from malarial parasite *Plasmodium falciparum* (Isolate 3D7): Insights from theoretical modelling and molecular simulations, *J. Mol. Graphics Modell.*, 71, 154–166.
- [12] Ojha, P.K., and Roy, K., 2011, Exploring QSAR, pharmacophore mapping and docking studies and virtual library generation for cycloguanil derivatives as PfDHFR-TS inhibitors, *Med. Chem.*, 7 (3), 173–199.
- [13] Nattee, C., Khamsemanan, N., Lawtrakul, L., Toochinda, P., and Hannongbua, S., 2017, A novel prediction approach for antimalarial activities of Trimethoprim, Pyrimethamine, and Cycloguanil analogues using extremely randomized trees, *J. Mol. Graphics Modell.*, 71, 13–27.
- [14] Inthajak, K., Toochinda, P., and Lawtrakul, L., 2018, Application of molecular docking and PSO–SVR intelligent approaches in antimalarial activity prediction of enantiomeric cycloguanil analogues, *SAR QSAR Environ. Res.*, 29 (12), 957–974.
- [15] Yuthavong, Y., Vilaivan, T., Chareonsethakul, N., Kamchonwongpaisan, S., Sirawaraporn, W., Quarrell, R., and Lowe, G., 2000, Development of a lead inhibitor for the A16V+S108T mutant of dihydrofolate reductase from the cycloguanil-

- resistant strain (T9/94) of *Plasmodium falciparum*, *J. Med. Chem.*, 43 (14), 2738–2744.
- [16] ChemAxon, 2015, Marvin was used for drawing, displaying and characterizing chemical structures, substructures and reactions, Marvin 5.12.3, ChemAxon.
- [17] O'Boyle, N.M., Banck, M., James, C.A., Morley, C., Vandermeersch, T., and Hutchison, G.R., 2011, Open Babel: An Open chemical toolbox, *J. Cheminf.*, 3 (1), 33.
- [18] Stewart, J.J.P., 2016, *MOPAC2016*, Stewart Computational Chemistry, Colorado Spring, USA.
- [19] Tosco, P., Balle, T., and Shiri, F., 2011, Open3DALIGN: An open-source software aimed at unsupervised ligand alignment, *J. Comput.-Aided Mol. Des.*, 25 (8), 777–783.
- [20] Tosco, P., and Balle, T., 2011, Open3DQSAR: A new open-source software aimed at high-throughput chemometric analysis of molecular interaction fields, *J. Mol. Model.*, 17 (1), 201–208.
- [21] Goodford, P., 2006, "The basic principles of GRID" in *Molecular Interaction Fields: Applications in Drug Discovery and ADME Prediction*, Eds. Cruciani, G., Manhold, R., Kubinyi, H., and Folkers, G., John Wiley & Sons, Inc., Hoboken, New Jersey, United States.
- [22] Pastor, M., Cruciani, G., and Clementi, S., 1997, Smart region definition: A new way to improve the predictive ability and interpretability of three-dimensional quantitative structure-activity relationships, *J. Med. Chem.*, 40 (10), 1455–1464.
- [23] Golbraikh, A., and Tropsha, A., 2002, Beware of q^2 !, *J. Mol. Graphics Modell.*, 20 (4), 269–276.
- [24] Ojha, P.K., Mitra, I., Das, R.N., and Roy, K., 2011, Further exploring r_m^2 metrics for validation of QSPR models, *Chemom. Intell. Lab. Syst.*, 107 (1), 194–205.
- [25] Chtita, S., Aouidate, A., Belhassan, A., Ousaa, A., Taourati, A.I., Elidrissi, B., Ghamali, M., Bouachrine, M., and Lakhlifi, T., 2020, QSAR study of N-substituted oseltamivir derivatives as potent avian influenza virus H5N1 inhibitors using quantum chemical descriptors and statistical methods, *New J. Chem.*, 44 (5), 1747–1760.
- [26] Sahigara, F., Mansouri, K., Ballabio, D., Mauri, A., Consonni, V., and Todeschini, R., 2012, Comparison of different approaches to define the applicability domain of QSAR models, *Molecules*, 17 (5), 4791–4810.
- [27] DeLano, W.L., 2015, *The PyMOL Molecular Graphics System*, Version 1.8, Schrödinger, LLC.
- [28] Vanichtanankul, J., Taweechai, S., Uttamapinant, C., Chitnumsub, P., Vilaivan, T., Yuthavong, Y., and Kamchonwongpaisan, S., 2012, Combined spatial limitation around residues 16 and 108 of *Plasmodium falciparum* dihydrofolate reductase explains resistance to cycloguanil, *Antimicrob. Agents Chemother.*, 56 (7), 3928–3935.
- [29] Koes, D.R., Baumgartner, M.P., and Camacho, C.J., 2013, Lessons learned in empirical scoring with smina from the CSAR 2011 benchmarking exercise, *J. Chem. Inf. Model.*, 53 (8), 1893–1904.
- [30] Laskowski, R.A., and Swindells, M.B., 2011, {LigPlot}+: Multiple ligand-protein interaction diagrams for drug discovery, *J. Chem. Inf. Model.*, 51 (10), 2778–2786.
- [31] Abraham, M.J., Murtola, T., Schulz, R., Páll, S., Smith, J.C., Hess, B., and Lindah, E., 2015, GROMACS: High performance molecular simulations through multi-level parallelism from laptops to supercomputers, *SoftwareX*, 1-2, 19–25.
- [32] Bussi, G., Donadio, D., and Parrinello, M., 2007, Canonical sampling through velocity rescaling, *J. Chem. Phys.*, 126 (1), 014101.
- [33] Berendsen, H.J.C., Postma, J.P.M., van Gunsteren, W.F., DiNola, A., and Haak, J.R., 1984, Molecular dynamics with coupling to an external bath, *J. Chem. Phys.*, 81 (8), 3684–3690.
- [34] Agrawal, P., Singh, H., Srivastava, H.K., Singh, S., Kishore, G., and Raghava, G.P.S., 2019, Benchmarking of different molecular docking methods for protein-peptide docking, *BMC Bioinf.*, 19 (13), 426.

Synthesis and Characterization of Copper Impregnated Mesoporous Carbon as Heterogeneous Catalyst for Phenylacetylene Carboxylation with Carbon Dioxide

Putri Nurul Amalia, Iman Abdullah*, Dyah Utami Cahyaning Rahayu, and Yuni Krisyuningsih Krisnandi

Department of Chemistry, Faculty of Mathematics and Natural Sciences, Universitas Indonesia, Depok 1642, Indonesia

* **Corresponding author:**

email: iman.abdullah@sci.ui.ac.id

Received: December 21, 2019

Accepted: July 20, 2020

DOI: 10.22146/ijc.52778

Abstract: Carbon dioxide (CO₂) is a compound that can potentially be used as a carbon source in the synthesis of fine chemicals. However, the utilization of CO₂ is still constrained due to its inert and stable nature. Therefore, the presence of a catalyst is needed in CO₂ conversion. This study aims to synthesize copper impregnated mesoporous carbon (Cu/MC) as a catalyst for phenylacetylene carboxylation reaction with CO₂ to produce phenylpropionic acid. The synthesis of mesoporous carbon was performed via the soft template method. The as-synthesized Cu/MC material was characterized by FTIR, SAA, XRD, and SEM-EDX. BET surface area analysis of mesoporous carbon showed that the material has a high surface area of 405.8 m²/g with an average pore diameter of 7.2 nm. XRD pattern of Cu/MC indicates that Cu has been successfully impregnated in the form of Cu(0) and Cu(I). Phenylacetylene carboxylation reaction with CO₂ was carried out by varying reaction temperatures (25, 50, and 75 °C), amount of catalyst (28.6, 57.2, and 85.8 mg), type of base (Cs₂CO₃, K₂CO₃, and Na₂CO₃), and variation of support. The reaction mixtures were analyzed by HPLC and showed that the highest phenylacetylene conversion of 41% was obtained for the reaction at 75 °C using Cs₂CO₃ as a base.

Keywords: carbon dioxide; mesoporous carbon; copper; catalyst; phenylacetylene; carboxylation reaction

■ INTRODUCTION

Carbon dioxide (CO₂) is a compound that can potentially be used as a carbon source and an attractive C1 building block in organic synthesis due to its intriguing features, such as being non-toxic, renewable, inexpensive, and readily available [1]. But in reality, utilization and large-scale CO₂ conversion are still limited due to thermodynamic stability and inert nature, making CO₂ difficult to react with other compounds. Thus, a low-valence metal is needed as a catalyst to activate CO₂ [2].

Various types of transition metals have been extensively studied in their capacity as catalysts for CO₂ utilization in fine chemical synthesis. Nickel is one of the most studied in the carboxylation reaction using CO₂ as a carbon source. Various types of substrates have been investigated in carboxylation reactions using nickel catalysts such as alkynes [3], ynamides [4-5], alkenes [6], and alkyl halides [7], and the results show that the nickel

works well in catalyzing the reaction. However, the instability of Ni(0) becomes an obstacle in the use of Ni as a catalyst. In nickel as a catalyst, reducing agents such as reactive metals or pyrogenic organozinc are often added in large quantities to keep the Ni(0) species in existence during the reaction [3-4,6]. Other transition metals from noble metals such as Au, Pt, Ag, and Pd are also known to have good activity as catalysts in carboxylation reactions [8-11]. However, the use of these metals in industrial-scale applications is constrained by high production costs. Another transition metal that is quite promising as a carboxylation reaction catalyst is copper. It is known that catalysts containing Cu or Ag are suitable for activating the C–C triple bond generally for carboxylation with CO₂, and Cu is also the only element that can make C–C bonds directly from CO₂RR with good selectivity [2,12-15]. In this context, the direct

carboxylation of terminal alkynes with CO₂ is the simplest and most straightforward way to access alkynyl carboxylic acids [1]. Recently, Wang et al. [16] reported that CuCl is an efficient catalyst for carboxylation of terminal alkynes in the presence of quaternary ammonium salts as a CO₂ activator. The reaction proceeded well under ligand-free conditions to give high to excellent yields of various propionic acids. However, the catalytic system is still homogeneous, which is relatively less preferred for industrial applications than the heterogeneous one.

Meanwhile, in terms of catalyst support, mesoporous carbon is a material known to have several advantages, such as a large pore diameter (2–50 nm), regularly arranged pores, and high thermal stability [17–18]. These advantages make mesoporous carbon good catalyst support. It can assist the loading process of active catalyst species, facilitate good reactant transport, and expand the temperature range in reaction applications. It is known that mesoporous carbon can be impregnated well with various types of metals for multiple applications such as Ag [19–20], Pd [20], Ni [21–22], Co [23], Ru [24], and Cu [25]. In addition, mesoporous carbon is also a potential material to be used as a CO₂ adsorbent [26–27]. Based on previous studies, it can be seen that mesoporous carbon is good solid catalyst support as well as a potential CO₂ adsorbent. Thus, the present work was aimed to synthesize Cu impregnated on mesoporous carbon prepared by the soft-template method. Structural changes that occur in mesoporous carbon after the impregnation process was studied through several characterizations such as SEM-EDX, XRD, and SAA and are compared with the phenomenon that occurs in activated carbon as a comparison. Furthermore, we also tested the catalytic activity of the impregnated Cu on mesoporous carbon (Cu/MC) in the carboxylation of phenylacetylene with CO₂ to produce carboxylic acid under mild conditions.

■ EXPERIMENTAL SECTION

Materials

Pluronic F-127, phloroglucinol (>99.0%), HCl (37%), formaldehyde (37%), Cu(NO₃)₂·3H₂O, phenylacetylene (98%), DMF (99.8%), Cs₂CO₃, K₂CO₃, and Na₂CO₃ were obtained from Sigma Aldrich, while ethanol, methanol,

and acetic acid were from Merck. All materials were used directly without any further purification. All ultra-high purity gases (CO₂, H₂, and N₂) were purchased from CV Retno Gas, Jakarta.

Procedure

Preparation of mesoporous carbon (MC)

The synthesis of mesoporous carbon as catalyst support was done through the soft-template method using Pluronic F-127 as a pore-forming, formaldehyde and phloroglucinol as carbon sources, and HCl as an acid catalyst [28]. Approximately 1.25 g of phloroglucinol and 1.25 g of Pluronic F127 were dissolved in a mixture of ethanol: water (10:9 wt.%). Then, 0.08 mL of 37% HCl was added, and the mixture was stirred for 30 min, followed by adding 1.25 mL of 37% formaldehyde still under stirring. After 30 min, the solution's color became cloudy, and after 1–2 h, the mixture was separated into two phases. The lower phase was taken and stirred for 12 h to form a monolith, which then was heated at 100 °C for 24 h. Furthermore, the material was carbonized in tubular furnaces under N₂ gas flow with heating profile as follow: from 100 to 400 °C with a flow rate of 1 °C/min; from 400 to 850 °C with a flow rate of 5 °C/min; and finally with a temperature of 850 °C for 2 h.

Preparation of Cu/MC catalysts

The as-synthesized mesoporous carbon was then impregnated with copper metal (Cu/MC) according to a previously reported method [13]. The procedure was carried out by dissolving 0.592 g of Cu(NO₃)₂·3H₂O in 24.5 mL of water, and then 1.4 g of mesoporous carbon was added to the solution. The mixture was stirred for 1 h while heated at 80 °C. The mixture was further dried in an oven at 110 °C for 24 h, followed by reduction with H₂ gas with a flow rate of 15–20 mL/min at 300 °C for 3 h in a tubular furnace. In addition to mesoporous carbon as catalyst support, commercial activated carbon (AC) was also tested as a comparison. Prior to use, the activated carbon was modified using HNO₃ acid according to the previously reported method [29]. The impregnation of Cu on AC was conducted using the same method as that of Cu/MC. The prepared catalysts (Cu/MC and Cu/AC), as well as the supports (MC and

AC), were characterized using X-ray diffraction (XRD PANalytical X'Pert PRO, K- α Cu of 1.54 Å), SEM-EDX (JEOL JED-2300 Analysis Station), and SAA (Quantachrome Quadrasorb-Evo Surface Area and Pore Size Analyzer). The average crystallite size of Cu on Cu/MC was calculated using the Scherer equation as follows,

$$D = \frac{0.9\lambda}{\beta \cos \theta} \quad (1)$$

where D is the average crystallite size (nm), λ is the wavelength of the X-rays (0.154 nm), β is the broadening of the diffraction peak measured at full-width half-maximum in rad.

Application of Cu/MC as catalyst for carboxylation reaction with CO₂. Into a 30 mL batch reactor, phenylacetylene (98.8 μ L; 0.9 mmol), Cu/MC (28.6 mg; 0.045 mmol), Cs₂CO₃ (58.6 mg; 1.8 mmol) and DMF (9 mL) were added. Then a CO₂ gas balloon was attached to the reactor. Prior to the attachment of the CO₂ balloon, CO₂ gas was flowed into the reactor to remove the air in the reactor. The mixture was then stirred for 4 h under CO₂ pressure of 1 atm. The carboxylation reactions were conducted by varying the reaction temperature (25, 50, 75 °C), the amount of catalyst (28.6; 57.2; and 85.8 mg), the type of base (Cs₂CO₃, Na₂CO₃, and K₂CO₃), and the type of support (mesoporous carbon and activated carbon). The reaction mixtures were then acidified with HCl and analyzed using HPLC (Shimadzu Prominence 10) with the following measurement conditions: methanol and 1% acetic acid as solvent (volume ratio of 55:45, respectively), column C18 Diamonsil, the flow rate of 1.5 mL/min, and detected with UV-Vis detector at a wavelength of 254 nm. Prior to HPLC analysis of reaction mixture, some phenylacetylene, phenylpropionic acid, and cinnamic acid standard solutions have been injected into the HPLC column to provide a calibration curve for determination of phenylacetylene conversion and the yield of the product. The carboxylation products were also characterized using FTIR (Shimadzu IR Prestige 21) to obtain functional group information of the samples.

Study of phenylacetylene adsorption on Cu/MC

The adsorption isotherm model was determined by conducting adsorption of phenylacetylene at various

concentrations on Cu/MC. The phenylacetylene concentrations used were 500, 750, 1500, and 2000 ppm in DMF solvent. A total of 50 mg of Cu/MC catalyst was added to each 5 mL of phenylacetylene solution, and the mixture was stirred for 4 h. The mixture was filtered, and the filtrate was analyzed by HPLC. The obtained data were then fitted to Langmuir, Freundlich, and Temkin isotherm adsorption model to find the most appropriate model for adsorption of phenylacetylene on Cu/MC. The isotherm equations are described as follows:

$$\text{Langmuir } q_e = \frac{q_{\max} K_L C_e}{1 + K_L C_e} \text{ or } \frac{1}{q_e} = \frac{1}{q_{\max} K_L C_e} + \frac{1}{q_{\max}} \quad (2)$$

$$\text{Freundlich } q_e = K_F C_e^{1/n} \text{ or } \log q_e = \log K_F + \frac{1}{n} \log C_e \quad (3)$$

$$\text{Temkin } q_e = \frac{RT}{b_T} \ln(K_T C_e) \text{ or } q_e = \ln K_T + \frac{RT}{b_T} \ln C_e \quad (4)$$

where C_e (mg/L) is the equilibrium concentration of phenylacetylene in DMF solvent, q_e is the amount (mg) of phenylacetylene adsorbed per gram Cu/MC, q_{\max} (mg/g) is the maximum adsorption capacity, K_L , K_F , and $1/n$, K_T and b_T are the constant values related to each isotherm models.

■ RESULTS AND DISCUSSION

Characterization of Cu/MC Catalyst

The Cu/MC catalyst was characterized using SEM-EDX, XRD, and SAA. Scanning Electron Microscopy (SEM) analysis was used to determine the morphology of the as-synthesized mesoporous carbon. Fig. 1(a) shows that the morphology of mesoporous carbon is quite smooth, and there are uniform pores on the surface. Meanwhile, Fig. 1(b) shows the impregnated Cu attached to the surface of mesoporous carbon. The figure also shows a change in the morphology of mesoporous carbon after the impregnation process, which indicates the partial closure of the MC pores by copper. Fig. 1(c) shows the impregnated Cu on activated carbon. The morphology of Cu/AC is rougher than that of Cu/MC. Based on the characterization with Energy Dispersed X-Ray (EDX) spectroscopy, it is known that MC has a composition of 94.87% carbon and 5.13% oxygen, while Cu/MC consists of 58.97% carbon, 4.84% oxygen, and 36.19% copper by mass (Fig. 2). The low

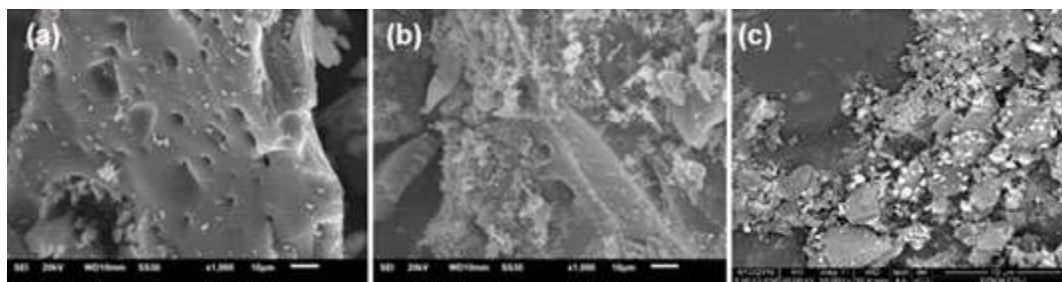


Fig 1. SEM micrograph of (a) MC, (b) Cu/MC in $\times 1000$ magnification, and (c) Cu/AC in $\times 5000$ magnification

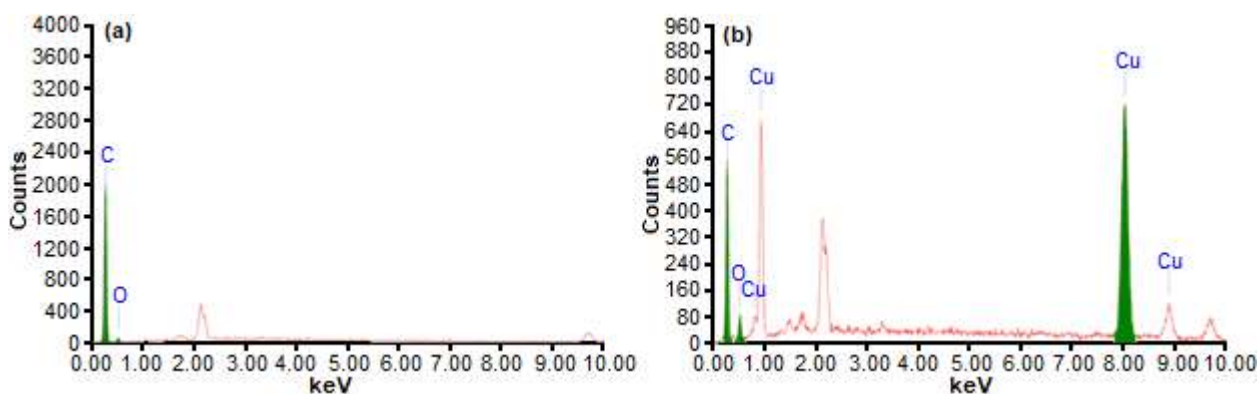


Fig 2. EDX spectrum of (a) MC and (b) Cu/MC

oxygen content of Cu/MC indicates that copper has been successfully deposited on mesoporous carbon as Cu(0) metal as the dominant species.

The XRD patterns of the Cu/MC sample in Fig. 3 exhibit characteristic diffractogram peaks of the metallic phase of Cu(0), which corresponds to 2θ values of 43.47° , 50.63° , and 74.19° and of Cu(I), which corresponds to 2θ value of 36.62° [13,25,29-30]. This result indicates that two Cu species existed in Cu/MC due to the reduction of copper(II) salt with hydrogen gas during calcination. The result is similar to that observed by Bondarenko et al. [13] for copper nanoparticles supported on Al_2O_3 prepared through the reduction of copper salt with hydrogen gas. Meanwhile, peaks of the mesoporous carbon support show 2θ values of 24.56° and 43.94° , which is typical for carbon-based material according to JCPDS File Index No. 75-1621. Calculation using the Scherer equation from the diffraction peak at 43.47° gives an average crystallite size of copper on Cu/MC of 36.54 nm.

Characterization using Surface Area Analyzer (SAA) was conducted to determine the surface character of mesoporous carbon, such as surface area, pore distribution, and pore diameter. In determining the surface

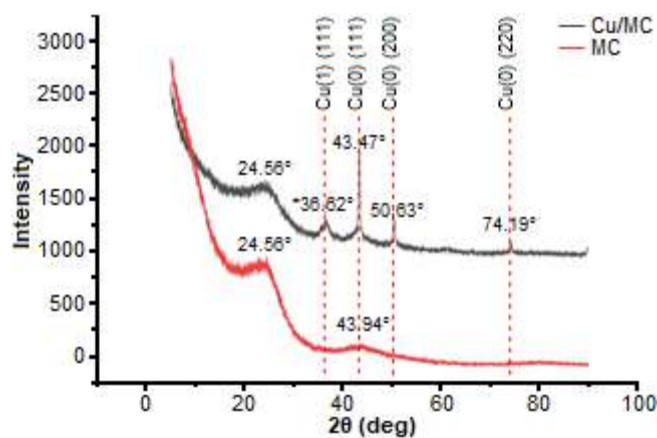


Fig 3. XRD patterns of mesoporous carbon (MC) and Cu/MC

area of a porous material, the method used is the Brunauer-Emmett-Teller (BET) method. The principle of measuring surface area with the BET method is based on the adsorption and desorption of N_2 gas. Fig. 4(a) and (b) show that the synthesized mesoporous carbon and impregnated Cu on mesoporous carbon has an IV type of adsorption isotherm curve, where there is a hysteresis loop, which indicates that the pore is meso size [31]. Fig. 4(c) and (d) show the type of isotherm adsorption of AC

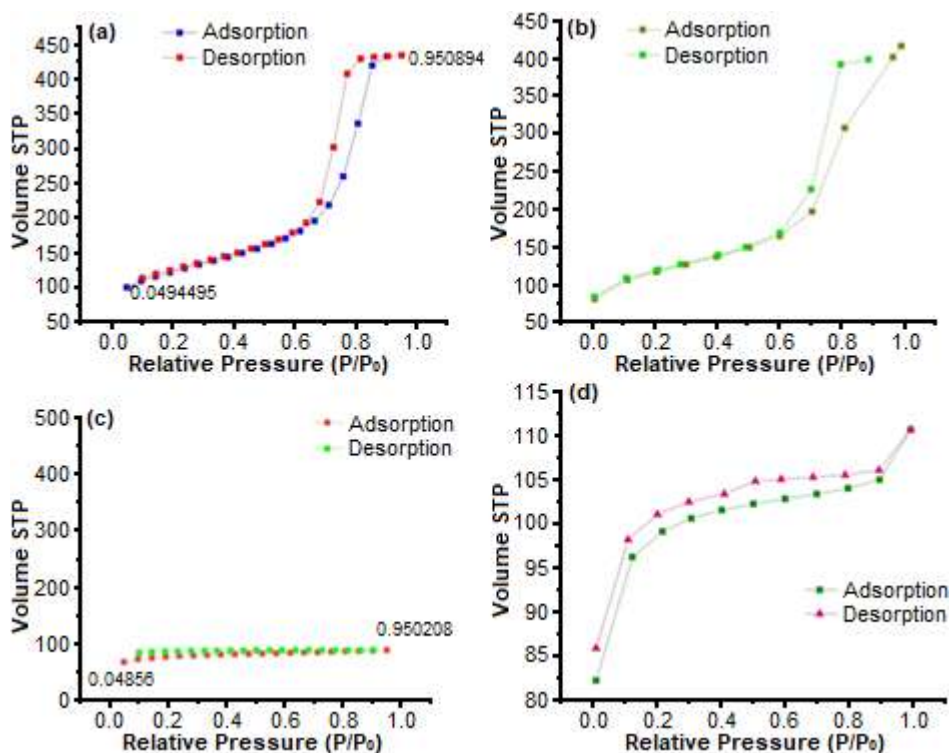


Fig 4. N₂ adsorption/desorption of (a) MC, (b) Cu/MC, (c) AC, and (d) Cu/AC

and Cu/AC satisfies the type I isotherm, which indicated the porosity is micro. Based on the BET calculation, it is found that the surface area of the synthesized mesoporous carbon is 405.78 m²/g, which is almost double than that of activated carbon (242.77 m²/g). The impregnation of copper on MC slightly lowered the surface area, mesopore volume, and the average of pore diameter. This result indicates that the copper species is possibly impregnated not only on the surface of MC but also inside its mesopore structure. Thus, the pore size distribution shifts slightly to a narrower size range (Fig. 5(a)). The contrary phenomenon is observed on Cu/AC. Copper impregnation

increased the surface area from 242.77 to 307.06 m²/g, which indicates that the presence of copper contributes to the rough surface of the material as shown by the SEM image, thus increasing its surface area. However, there were no significant changes in the pore size distribution, as shown in Fig. 5(b). This supports the previous explanation that copper is impregnated on the activated carbon's outer surface, and the micropore character remains unchanged. The complete data of the textural properties of MC, Cu/MC, AC, and Cu/AC obtained from SAA are summarized in Table 1.

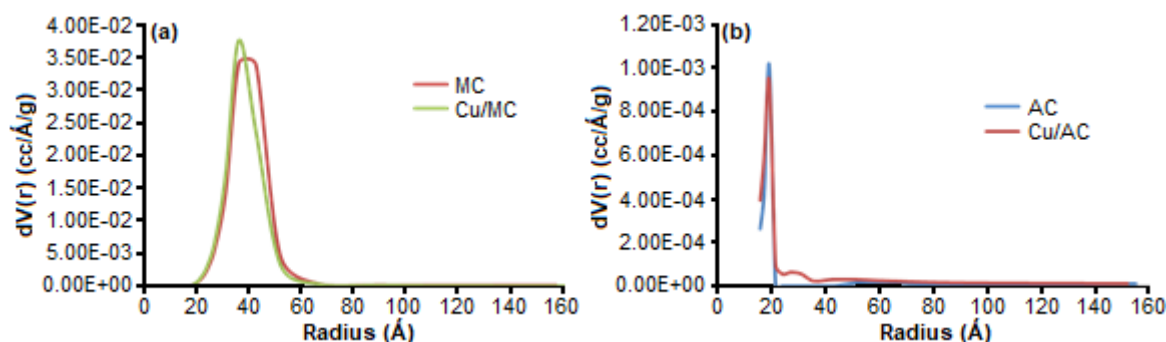


Fig 5. The pore size distribution of (a) MC and Cu/MC and (b) AC and Cu/AC calculated by BJH Desorption Method

Table 1. Textural properties of MC, Cu/MC, AC, and Cu/AC

Sample	$S_{\text{BET}}^{\text{a}}$ (m^2/g)	$S_{\text{ext}}^{\text{b}}$ (m^2/g)	$S_{\text{micro}}^{\text{b}}$ (m^2/g)	$V_{\text{tot}}^{\text{c}}$ (cc/g)	$V_{\text{meso}}^{\text{d}}$ (cc/g)	$V_{\text{micro}}^{\text{d}}$ (cc/g)	Pore Diameter ^c (Å)
MC	405.78	287.44	118.34	0.67	0.60	0.06	72.32
Cu/MC	388.68	262.23	126.44	0.64	0.58	0.06	66.24
AC	242.77	20.38	222.38	0.13	0.02	0.11	19.35
Cu/AC	307.06	71.11	235.95	0.17	0.05	0.12	19.53

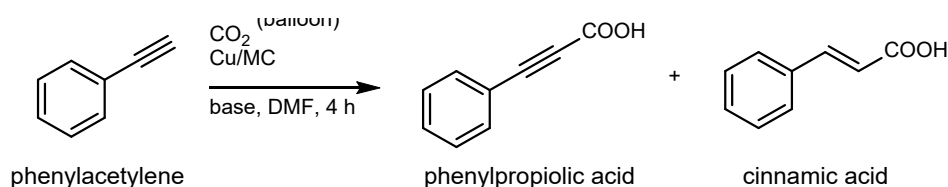
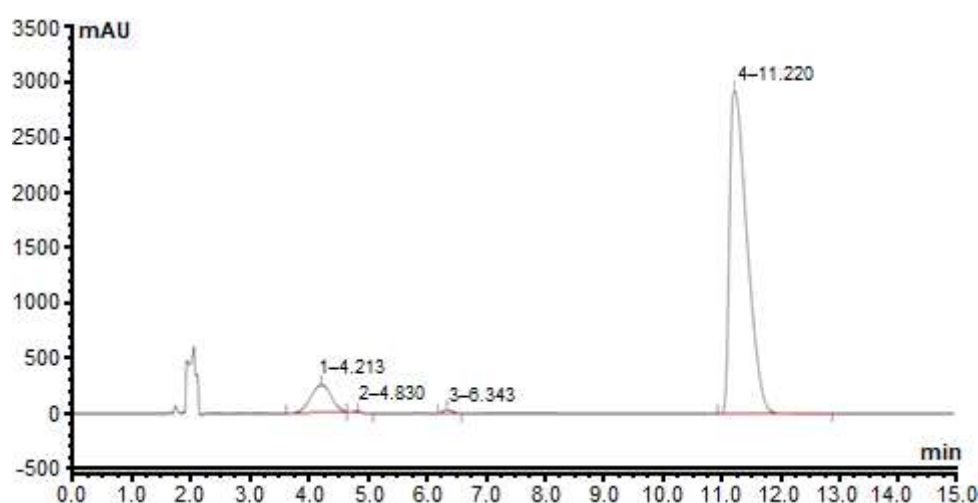
Note: ^a is determined by the BET method; ^b is determined by the t-plot method; ^c is determined by the highest point of P-P₀ (adsorption-desorption); ^d is determined by means of $V_{\text{meso}} = V_{\text{tot}} - V_{\text{micro}}$

Application of Cu/MC as Catalyst for Carboxylation Reaction with CO₂

The phenylacetylene carboxylation reaction with CO₂ was performed in the presence of Cu/MC catalyst by varying reaction temperature (25, 50, and 75 °C), the amount of catalysts (28.6, 57.2, and 85.8 mg), the types of bases (Cs₂CO₃, K₂CO₃, and Na₂CO₃), and the types of support (mesoporous carbon and activated carbon), in DMF as solvent under CO₂ pressure of 1 atm for 4 h. The reaction is provided in Scheme 1, which shows that it could give two products: 3-phenylpropionic acid as the main product and cinnamic acid as the side product [13]. The typical HPLC chromatogram of the reaction mixture

is shown in Fig. 6. Three peaks appear in the chromatogram, which belongs to the unreacted phenylacetylene (retention time of 11 min), cinnamic acid as the minor product (retention time of 6 min), and phenylpropionic acid as the main-product (retention time of 4 min).

The carboxylation results are summarized in Fig. 7, in terms of percentage (%) of phenylacetylene conversion. As shown in the graph, reaction temperature plays a significant role in the reaction. When the temperature is increased, the rate of phenylacetylene conversion also increases, with the highest conversion percentage obtained at 75 °C (41%).

**Scheme 1.** Carboxylation reaction of phenylacetylene with CO₂**Fig 6.** The typical HPLC chromatogram of the reaction mixture (reaction conditions: Cs₂CO₃ as the base at 75 °C)

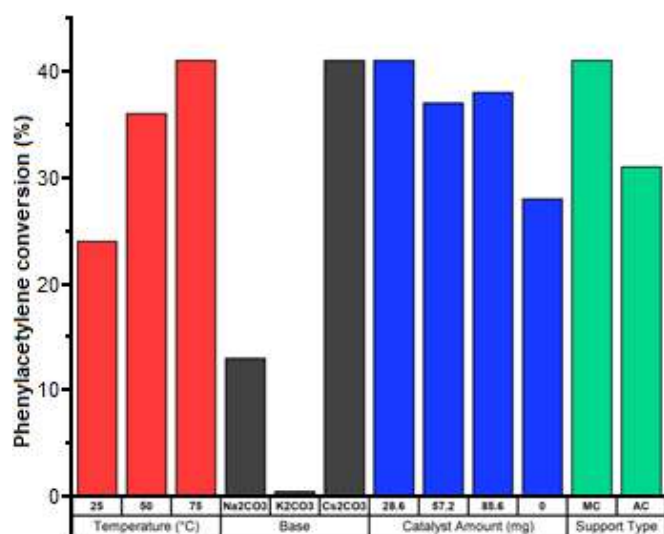


Fig 7. The effect of reaction temperature, type of bases, catalyst amount, and support type to phenylacetylene conversion in carboxylation reaction with CO₂

This result indicates that phenylacetylene conversion is a thermal-dependent reaction. Compared to the Ag catalyst for the same reaction, copper exhibits similar catalytic activity. However, since the reaction time used in this study was quite short (4 h), the amount of phenylacetylene converted is lower than that of Ag catalyst for the reaction time of 16–36 h [1,10,15].

The type of base also influences the reaction, in which cesium carbonate provides superior results compared to the other two bases used (Na₂CO₃ and K₂CO₃). This occurred because cesium carbonate is a stronger base than Na₂CO₃ and K₂CO₃; therefore, it is stronger in abstracting a proton from the terminal alkyne group in phenylacetylene, thus more feasible in facilitating the reaction. In addition to that, Cs₂CO₃ also has the highest solubility in DMF among the carbonate salts used [32]. Surprisingly, increasing the amount of the catalyst up to three times the original (85.6 mg) did not increase the amount of phenylacetylene converted. However, in the absence of catalysts, the amount of phenylacetylene turned decreased to 28%, indicating the catalyst's importance in the reaction.

We also compared mesoporous carbon to activated carbon as catalyst support. Activated carbon used is a commercial activated carbon that was modified using acid. The purpose of an acid modification is to add some

oxygen groups, which are expected to increase adsorption ability [29]. As predicted, the reaction catalyzed by Cu/MC has higher phenylacetylene conversion than that catalyzed by Cu/AC. The result is in line with the textural properties of the two materials. Cu/MC poses a higher surface area, larger mesopore volume, and wider pore diameter that provides better reactant transport and facilitates the reaction better.

We also analyzed the reaction conditions on the formation of the products, and the results are presented in Fig. 8. Similar results were obtained for the effect of temperature, especially in the formation of the major products. When the reaction is carried out at a higher temperature, the major product (retention time of 4 min) increases significantly. However, unlike phenylacetylene conversion, base type did not give any different results on the products' formation. In the absence of any base, the products are hardly observed. Meanwhile, the amount of catalyst also did not have a different effect on the formation of major and minor products.

Interestingly, even without the presence of Cu/MC catalyst (but in the presence of Cs₂CO₃ base), the product was still formed, though with a smaller percentage of converted reactants. A previous study by Dingyi and Yugen [33] reported using a stoichiometric amount of Cs₂CO₃ in direct carboxylation of terminal alkynes in the absence of a metal catalyst. Although the reaction proceeded well, it requires harsh reaction conditions such as high reaction temperature (120 °C) and higher CO₂ pressure. This indicates that the catalyst plays a role in the adsorption and activation of the reactants, while the base plays a role in the further reaction process (related to hydrogen abstraction). Thus, the Cu/MC catalyst plays a role in facilitating the reaction to take place under milder conditions. However, further studies regarding the reaction mechanism and each component's role need to be studied further. Finally, as in the case of phenylacetylene conversion, the type of support determines the amount of the products as well as its selectivity. In this case, Cu/MC provides a higher amount of the products with selectivity leading to the formation of the major product.

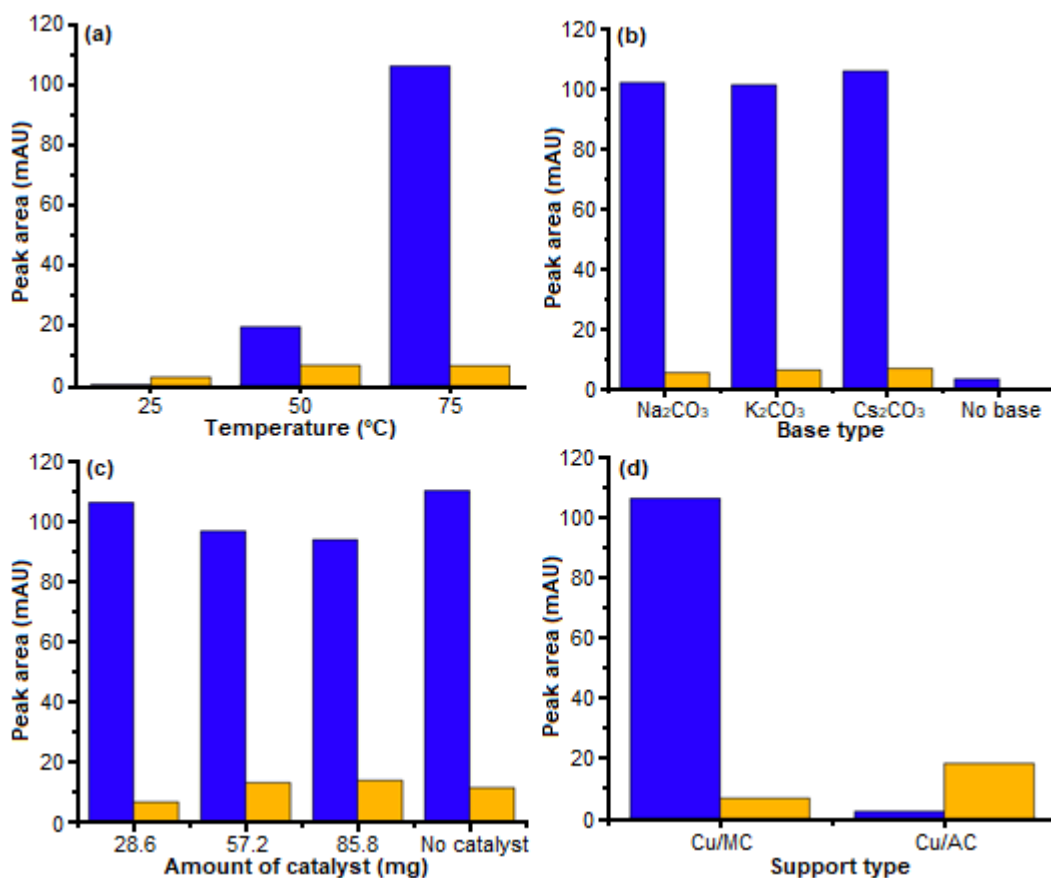


Fig 8. The effect of (a) reaction temperature, (b) the type of bases, (c) the amount of catalyst, and (d) the type of support to the peak area of the major product (blue chart) and minor product (yellow chart) in HPLC chromatography. R_t of major product = 4 min, R_t of minor product = 6 min

Fig. 9 shows the FTIR spectra of the product obtained at various reaction conditions. Based on this figure, it is known that there are peaks at 3200–3400 cm^{-1} derived from O–H stretching, at 1720–1750 cm^{-1} from C=O stretching of a carboxylic group, and at 1450–1620 cm^{-1} that possibly comes from the C=C stretching. The presence of peak C=O stretching of a carboxylic group indicates that the phenylacetylene carboxylation reaction with CO_2 has taken place.

In this work, we also conducted the study of phenylacetylene adsorption on Cu/MC catalysts in DMF solvent to get some additional information on how the reactant interacts with the surface of the catalyst. The adsorption data were plotted using Langmuir, Freundlich, and Temkin Adsorption Isotherm Models. The Temkin Isotherm Models gave the most suitable result to describe the adsorption process with an R^2 of 0.993. Calculations

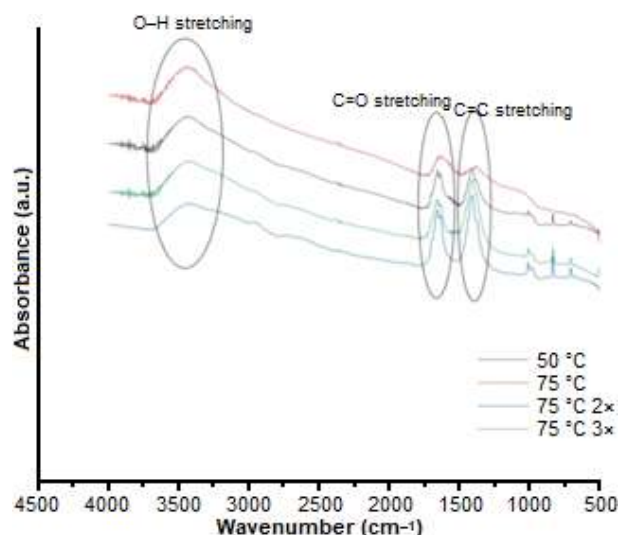


Fig 9. FTIR spectra of phenylacetylene carboxylation product obtained at various reaction conditions (at 50, 75 °C, and in the presence of the double and triple amount of the catalyst)

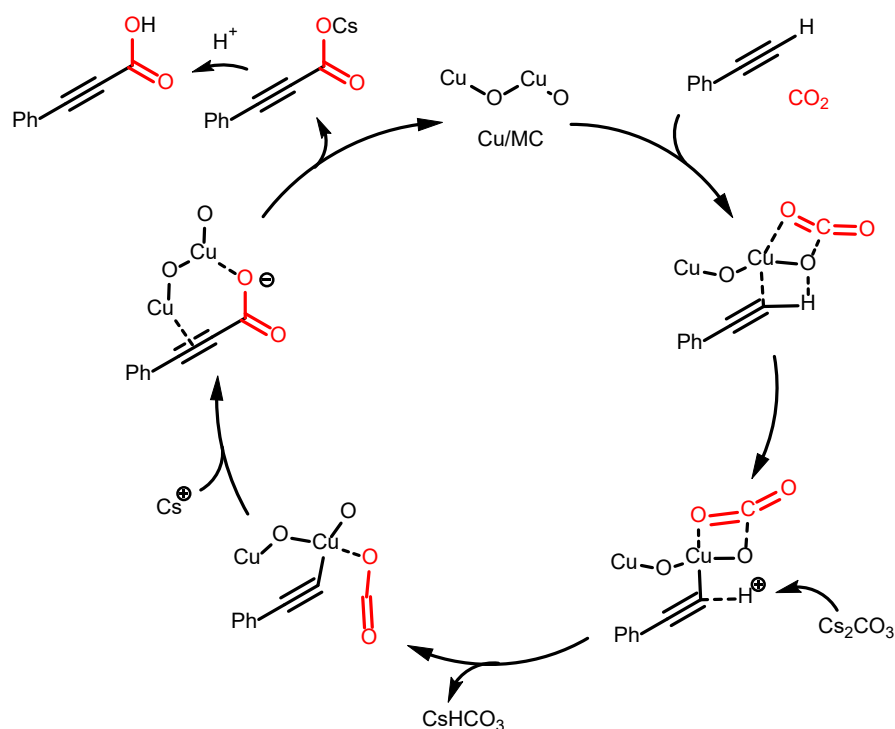


Fig 10. The proposed mechanism for phenylacetylene carboxylation on the surface of copper covered by copper oxides rewrites from Bondarenko et al. with some modifications [13]

from the linear regression equation provides the values of binding constant (K_T) and adsorption energy (b_T) at 298 K of 448 L/g and -2.696×10^7 J g mol⁻², respectively. As Temkin Models fit best the data, the result indicates that the catalyst surface has a uniform distribution of binding energies, and the heat of adsorption of adsorbates decreases linearly with the increase of surface coverage [34-35].

Based on the results of the carboxylation reactions, the adsorption study, and the literature study, herein we proposed a mechanism for the catalytic carboxylation on the surface of copper covered by copper oxides. As shown in Fig. 10, the reaction starts with interactions between phenylacetylene, CO₂, and Cu/MC catalyst through weak hydrogen bonding and some dipole-dipole interactions. The presence of base is important for abstracting protons in the terminal alkyne of phenylacetylene, facilitating the insertion of CO₂ to the alkyne part [13,36]. Another cesium cation would take part in a transmetallation reaction to produce cesium salt of the product as well as regenerate the catalyst. Finally, acidification of the salt

would produce phenylpropionic acid as the desired product.

CONCLUSION

Copper impregnated on mesoporous carbon was successfully prepared and further tested as a catalyst for the carboxylation reaction of phenylacetylene with CO₂ in the presence of a base. The impregnation changes the structure of mesoporous carbon, which including the surface area, pore-volume, and average pore size, which are found to be reduced. The carboxylation reaction of phenylacetylene took place at an optimum temperature of 75 °C and using Cs₂CO₃ as a base to produce 3-phenylpropionic acid as a major product and cinnamic acid as a minor product.

ACKNOWLEDGMENTS

The authors gratefully acknowledge Universitas Indonesia for funding this research through the PITTA B research grant with contract number NKB-0635/UN2.R3.1/HKP.05.00/2019.

■ REFERENCES

- [1] Wu, Z., Sun, L., Liu, Q., Yang, X., Ye, X., Hu, Y., and Huang, Y., 2017, A Schiff base-modified silver catalyst for efficient fixation of CO₂ as carboxylic acid at ambient pressure, *Green Chem.*, 19 (17), 2080–2085.
- [2] Yu, B., Xie, J.N., Zhong, C.L., Li, W., and He, L.N., 2015, Copper(I)-carbon-catalyzed carboxylation of terminal alkynes with CO₂ at atmospheric pressure, *ACS Catal.*, 5 (7), 3940–3944.
- [3] Wang, X., Nakajima, M., and Martin, R., 2015, Ni-catalyzed regioselective hydrocarboxylation of alkynes with CO₂ by using simple alcohols as proton sources, *J. Am. Chem. Soc.*, 137 (28), 8924–8927.
- [4] Doi, R., Abdullah, I., Taniguchi, T., Saito, N., and Sato, Y., 2017, Nickel-catalyzed hydrocarboxylation of ynamides with CO₂ and H₂O: Observation of unexpected regioselectivity, *Chem. Commun.*, 53 (55), 7720–7723.
- [5] Doi, R., Okano, T., Abdullah, I., and Sato, Y., 2019, Nickel-catalyzed β-carboxylation of ynamides with carbon dioxide, *Synlett*, 30 (9), 1048–1052.
- [6] Williams, C.M., Johnson, J.B., and Rovis, T., 2008, Nickel-catalyzed reductive carboxylation of styrenes using CO₂, *J. Am. Chem. Soc.*, 130 (45), 14936–14937.
- [7] Börjesson, M., Moragas, T., and Martin, R., 2016, Ni-catalyzed carboxylation of unactivated alkyl chlorides with CO₂, *J. Am. Chem. Soc.*, 138 (24), 7504–7507.
- [8] Boogaerts, I.I.F., Nolan, S.P., 2010, Carboxylation of C–H bonds using N-heterocyclic carbene gold(I) complexes, *J. Am. Chem. Soc.*, 132 (26), 8858–8859.
- [9] Steinmann, S.N., Michel, C., Schwiedernoch, R., Wu, M., and Sautet, P., 2016, Electro-carboxylation of butadiene and ethene over Pt and Ni catalysts, *J. Catal.*, 343, 240–247.
- [10] Shah, D.J., Sharma, A.S., Shah, A.P., Sharma, V.S., Athar, M., and Soni, J.Y., 2019, Fixation of CO₂ as a carboxylic acid precursor by microcrystalline cellulose (MCC) supported AgNPs: A more efficient, sustainable, biodegradable and eco-friendly catalyst, *New J. Chem.*, 43 (22), 8669–8676.
- [11] Song, J., Liu, Q., Liu, H., and Jiang, X., 2018, Recent Advances in palladium-catalyzed carboxylation with CO₂, *Eur. J. Org. Chem.*, 2018 (6), 696–713.
- [12] Whang, H.S., Lim, J., Choi, M.S., Lee, J., and Lee, H., 2019, Heterogeneous catalysts for catalytic CO₂ conversion into value-added chemicals, *BMC Chem. Eng.*, 1 (1), 9.
- [13] Bondarenko, G.N., Dvurechenskaya, E.G., Magomedov, E.S., and Beletskaya, I.P., 2017, Copper(0) nanoparticles supported on Al₂O₃ as catalyst for carboxylation of terminal alkynes, *Catal. Lett.*, 147 (10), 2570–2580.
- [14] Zhang, X., Zhang, W.Z., Ren, X., Zhang, L.L., and Lu, X.B., 2011, Ligand-free Ag(I)-catalyzed carboxylation of terminal alkynes with CO₂, *Org. Lett.*, 13 (9), 2402–2405.
- [15] Yu, D., Tan, M.X., and Zhang, Y., 2012, Carboxylation of terminal alkynes with carbon dioxide catalyzed by poly(N-heterocyclic carbene)-supported silver nanoparticles, *Adv. Synth. Catal.*, 354 (6), 969–974.
- [16] Wang, W.H., Jia, L., Feng, X., Fang, D., Guo, H., and Bao, M., 2019, Efficient carboxylation of terminal alkynes with carbon dioxide catalyzed by ligand-free copper catalyst under ambient conditions, *Asian J. Org. Chem.*, 8 (8), 1501–1505.
- [17] Liang, C., and Dai, S., 2006, Synthesis of mesoporous carbon materials via enhanced hydrogen-bonding interaction, *J. Am. Chem. Soc.*, 128 (16), 5316–5317.
- [18] Wang, X., Liang, C., and Dai, S., 2008, Facile synthesis of ordered mesoporous carbons with high thermal stability by self assembly of resorcinol-formaldehyde and block copolymers under highly acidic conditions, *Langmuir*, 24 (14), 7500–7505.
- [19] Cao, J.M., Cao, Y.L., Chang, X., Zheng, M.B., Liu, J.S., and Ji, H.M., 2005, Synthesis of silver nanoparticles within ordered CMK-3 mesoporous carbon, *Stud. Surf. Sci. Catal.*, 156, 423–426.
- [20] Li, J.G., Tsai, C.Y., and Kuo, S.W., 2014, Fabrication and characterization of inorganic silver and palladium nanostructures within hexagonal

- cylindrical channels of mesoporous carbon, *Polymers*, 6 (6), 1794–1809.
- [21] Prasiwi, A.D., Trisunaryanti, W., Triyono, Falah, I.I., Santi, D., and Marsuki, M.F., 2019, Synthesis of mesoporous carbon from Merbau wood (*Intsia spp.*) by microwave method as Ni catalyst support for α -cellulose hydrocracking, *Indones. J. Chem.*, 19 (3), 575–582.
- [22] Pamungkas, A.Z., Abdullah, I., and Krisnandi, Y.K., 2019, Synthesis and characterization of Ni nanoparticles supported on nitrogen-doped mesoporous carbon, *IOP Conf. Ser.: Mater. Sci. Eng.*, 496, 012003.
- [23] Liu, J., Wang, Z., Yan, X., and Jian, P., 2017, Metallic cobalt nanoparticles imbedded into ordered mesoporous carbon: A non-precious metal catalyst with excellent hydrogenation performance, *J. Colloid Interface Sci.*, 505, 789–795.
- [24] Liu, X., Lan, G., Su, P., Qian, L., Reina, T.R., Wang, L., Li, Y., and Liu, J., 2020, Highly stable Ru nanoparticles incorporated in mesoporous carbon catalysts for production of γ -valerolactone, *Catal. Today*, 351, 75–82.
- [25] Şahin, N.E., Comminges, C., Valant, A.L., Kiener, J., Parmentier, J., Napporn, T.W., Melinte, G., Ersen, O., and Kokoh, K.B., 2018, One-pot soft-template synthesis of nanostructured copper-supported mesoporous carbon FDU-15 electrocatalysts for efficient CO₂ reduction, *ChemPhysChem*, 19 (11), 1371–1381.
- [26] Liu, L., Zhang, H., Wang, G., Du, J., Zhang, Y., Fu, X., and Chen, A., 2017, Synthesis of mesoporous carbon nanospheres via “pyrolysis-deposition” strategy for CO₂ capture, *J. Mater. Sci.*, 52 (16), 9640–9647.
- [27] Ardhyarini, N., and Krisnandi, Y.K., 2017, Carbon dioxide capture by activated methyl diethanol amine impregnated mesoporous carbon, *AIP Conf. Proc.*, 1862 (1), 030090.
- [28] Pal, N., and Bhaumik, A., 2013, Soft templating strategies for the synthesis of mesoporous materials: Inorganic, organic–inorganic hybrid and purely organic solids, *Adv. Colloid Interface Sci.*, 189–190, 21–41.
- [29] Hosseini, S., Bayesti, I., Marahel, E., Babadi, F.E., Abdullah, L.C., and Choong, T.S.Y., 2015, Adsorption of carbon dioxide using activated carbon impregnated with Cu promoted by zinc, *J. Taiwan Inst. Chem. Eng.*, 52, 109–117.
- [30] Kooti, M., and Matouri, L., 2010, Fabrication of nanosized cuprous oxide using Fehling’s solution, *Sci. Iran., Trans. F*, 17 (1), 73–78.
- [31] Górká, J., Zawislak, A., Choma, J., and Jaroniec, M., 2008, KOH activation of mesoporous carbons obtained by soft-templating, *Carbon*, 46 (8), 1159–1161.
- [32] Yuan, Z., 2014, Applications of bases in transition metal catalyzed reactions, *Postdoc J.*, 2 (3), 17–28.
- [33] Dingyi, Y., and Yugen, Z., 2011, The direct carboxylation of terminal alkynes with carbon dioxide, *Green Chem.*, 13 (5), 1275–1279.
- [34] Piccin, J.S., Dotto, G.L., and Pinto, L.A.A., 2011, Adsorption isotherms and thermochemical data of FD&C Red n° 40 binding by chitosan, *Braz. J. Chem. Eng.*, 28 (2), 295–304.
- [35] Ayawei, N., Ebelegi, A.N., and Wankasi, D., 2017, Modelling and interpretation of adsorption isotherms, *J. Chem.*, 2017, 3039817.
- [36] Wu, Z., Liu, Q., Yang, X., Ye, X., Duan, H., Zhang, J., Zhao, B., and Huang, Y., 2017, Knitting aryl network polymers-incorporated Ag nanoparticles: A mild and efficient catalyst for the fixation of CO₂ as carboxylic acid, *ACS Sustainable Chem. Eng.*, 5 (11), 9634–9639.

Synthesis and Characterization of Sodium Silicate Produced from Corncobs as a Heterogeneous Catalyst in Biodiesel Production

Alwi Gery Agustan Siregar, Renita Manurung*, and Taslim Taslim

Department of Chemical Engineering, Faculty of Engineering, Universitas Sumatera Utara,
Jl. Almamater, Padang Bulan, Medan 20155, Indonesia

* **Corresponding author:**

tel: +62-8126080681

email: renita.manurung@usu.ac.id

Received: December 31, 2019

Accepted: June 23, 2020

DOI: 10.22146/ijc.53057

Abstract: In this study, silica derived from corncobs impregnated with sodium hydroxide to obtain sodium silicate was calcined, prepared, and employed as a solid base catalyst for the conversion of oils to biodiesel. The catalyst was characterized by X-Ray Diffraction (XRD), Fourier-Transform Infrared Spectroscopy (FTIR), Scanning Electron Microscope Energy Dispersive X-Ray Spectroscopy (SEM-EDS), and Brunauer-Emmet-Teller (BET) and Barrett-Joyner-Halenda (BJH) methods. Gas Chromatography-Mass Spectrometry (GC-MS) was used to characterize the biodiesel products. The optimum catalyst conditions were calcination temperature of 400 °C for 2 h, catalyst loading of 2%, and methanol: oil molar ratio of 12:1 at 60 °C for 60 min, that resulted in a yield of 79.49%. The final product conforms to the selected biodiesel fuel properties of European standard (EN14214) specifications. Calcined corncob-derived sodium silicate showed high potential for use as a low-cost, high-performance, simple-to-prepare solid catalyst for biodiesel synthesis.

Keywords: biodiesel; corncobs; silica; heterogeneous catalyst

■ INTRODUCTION

Currently, alternative fuels for diesel engines are particularly crucial because of diminishing petroleum reserves and the environmental consequences of exhaust gases from petroleum-fueled engines. Biodiesel is a good candidate for replacing petrol-diesel fuel because it is clean, renewable, biodegradable, non-toxic, and environmentally friendly [1-2]. Biodiesel can be produced via a direct transesterification reaction between renewable vegetable oils or animal fats source and alcohol in the presence of a catalyst [3]. In the transesterification reaction, a triglyceride reacts with an alcohol in the presence of a catalyst, producing a mixture of fatty acid methyl esters (FAME) and glycerol [4]. Usually, KOH and NaOH are used as homogeneous base catalysts because of their high catalytic activity, which enables the reaction to complete in 1 h at 40–60 °C [5]. However, the use of these catalysts involves some drawbacks, such as its removal and inability to be reused or regenerated, difficult catalyst separation, soap formation, and reactor corrosion. Also, a large amount of water is required to wash the biodiesel product to eliminate

the catalyst, leading to an increase in the overall production costs and environmental problems [6].

The use of heterogeneous catalysts could be an attractive solution to these problems. Heterogeneous catalysts can be easily separated through filtration, reused and recycled several times, and requires no neutralization or washing process. In addition, they can also produce high-purity glycerol as a side product. Hence, heterogeneous catalysts are effective and efficient materials for biodiesel production [7-9]. Sodium silicate with the formula $\text{Na}_2\text{O}\cdot n\text{SiO}_2$ (commonly known as water glass or liquid glass) can be easily prepared from silica and sodium hydroxide [10-11]. It is an effective solid base catalyst for the transesterification process at operating conditions of 60 °C and 60 min. Furthermore, it can be reused at least five times without loss of activity [12-13]. Silica is widely used in various industries as catalysts [14], catalyst support materials [15-16], and used in ceramics [17]. Silica is highly stable, chemically flexible, biocompatible [18], and can be obtained from minerals and vegetable ingredients.

Corncoobs are a form of agricultural waste obtained from corn plants. Corncob ash contains > 60% silica, together with a small amount of metal elements [19] and is an economical raw material for the production of silicates, silica, and silica nanoparticles. It is obtained as a fine powder after combustion and further grinding.

The focus of this research is the synthesis and characterization of calcined sodium silicate solid catalysts derived from waste corncoobs via impregnation with the alkali metal sodium. The obtained material is used as a heterogeneous catalyst in biodiesel production from palm oil and methanol. The European standard method (EN 14214) for biofuels is used to evaluate the fuel properties of the obtained biodiesel after purification and treatment.

■ EXPERIMENTAL SECTION

Materials

Refined, bleached, and deodorized palm olein (RBDPO) containing 0.15% FFA and 0.06% moisture purchased from Deli Serdang, Indonesia, was used as the raw material. Other materials used were methanol from Merck, with a purity of > 99.5%; HCl 37% from Sigma-Aldrich, NaOH from Sigma-Aldrich with a purity of > 97%, and corncoobs collected from Deli Serdang, washed with deionized water and dried at 110 °C overnight.

Instrumentation

Crystallinity of materials both before and after calcination was analyzed by XRD using a Bruker with Cu voltage of 40 kV and a current of 30 mA. The morphological structure and composition of the catalyst were characterized using SEM-EDS EVO-10 Zeiss and GSA Quantachrome to investigate the surface area, pore diameter, and pore volume of the catalyst. The functional groups of the catalyst were analyzed by FTIR Shimadzu IR-21 with a range of 450–4000 cm^{-1} , while GC-MS Shimadzu-2010 was used to investigate the obtained biodiesel products.

Procedure

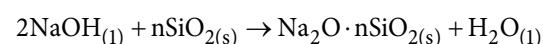
Preparation of corncob ash (CCA)

Dry corncoobs, which had been sifted with 100 mesh filters, were calcined at 700 °C for 3 h to remove organic

compounds [16]. Then, 10 g of corncob ash was washed with 60 mL HCl 1 M to eliminate organic compounds and increase the silica content. The sample was then dried again in an oven at 105 °C for 2 h and cooled to room temperature to obtain the corncob ash for further experiments [15-16].

Catalyst preparation

The sodium silicate was prepared using the wet impregnation method. As an initial step, corncob ash was dissolved in water, and the NaOH solution was then slowly added to the suspension. The mixture of NaOH:CCA with a mole ratio of 1:2 was then stirred at 300 rpm and heated at 80 °C for 2 h [20]. After the impregnation process was completed, the slurry was dried at 150 °C for 1 h and calcined at 400, 500, and 600 °C for 2 h [15,21]. The reaction for sodium silicate formation from corncob ash is as follows:



Transesterification process

The transesterification process was conducted in a three-neck flask-batch reactor system with condenser reflux equipment with a magnetic stirrer rate of 300 rpm equipped with a thermometer. The catalyst was mixed with methanol for 1 h at room temperature and added to 25 g of RBDPO. The biodiesel obtained was then filtered to separate the catalyst. The washing process was then carried out using 500 mL water, followed by heating at 105 °C to remove the water content and the remaining methanol.

Product analysis

Biodiesel products were analyzed to determine the levels of methyl ester using GC-MS Shimadzu-2010. A digital density hydrometer (ZEAL) was used to measure the density of biodiesel. Meanwhile, the viscosity of the biodiesel was measured using a Cole-Parmer rotational viscometer with stainless steel spindles and viscosity measurements ranging from 20 to 2×10^6 mPa. The biodiesel was tested according to the European standard method (EN14214) for fuels derived from vegetable oils. The yield of biodiesel is determined as follows:

$$\text{The yield of biodiesel (\%)} = \frac{\text{Weight of biodiesel}}{\text{Weight of oil}} \times 100$$

■ RESULTS AND DISCUSSION

FTIR Analysis

FTIR provides information on catalyst surface characteristics in terms of the structure of metal oxides, with the position of the bands or peaks showing metal-oxygen bonding. Fig. 1 presents the results of the FTIR analysis of corncob ash and the sodium silicate catalyst. In all samples, there is a Si-OH function group that appears at a wavenumber of 3151–3383 cm^{-1} . The hydroxyl group found in this sample is water vapor bound to the Si element as a good adsorbent [16]. No absorptions were found at 2800–3000 cm^{-1} in any samples, suggesting the absence of remaining organic compounds as a result of the silica purification process [15]. Furthermore, a Si-OH group with flexible vibrational mode was found in corncob ash at 1631.78 cm^{-1} . The presence of bending vibration of water molecules bound to the silica in the catalyst is observed at the wavenumber of 1662.64–1666.50 cm^{-1} [15]. The same phenomenon was reported by Attol and Mihsen in which a broadband appeared at 3200 and 3600 cm^{-1} due to the O-H stretching vibrations of the Si-OH group and water absorbed onto the silica

surface of rice husk ash [22]. In addition, O-H stretching vibrations of the silanol group (Si-OH) appears at the wavenumber of 3426 cm^{-1} for silica gel from rice husk ash, as reported by Sakti et al. in 2013 [23].

In corncob ash, there is a functional group Si-O-Si (siloxane group), which can be seen at wavenumber of 1080.14 cm^{-1} and on the catalyst at 1454.33 cm^{-1} , where this siloxane group will transform into Si-O-Na group. This group can be observed between the wavenumbers of 871–983 cm^{-1} [13,15-16]. The presence of this Si-O-Na group was obtained from the wet impregnation process using alkali metal in the form of NaOH in the corncob ash, indicating a successful synthesis of sodium silicate solid catalyst. The results of the sodium silicate synthesis are compared with commercial sodium silicate, where the stretches located at the wavenumbers of ~1005, 941, and ~1400 cm^{-1} correspond to Si-O-Na and Si-O-Si stretches [24]. The results of the FTIR show that the synthesis of sodium silicate from corncob ash does not differ significantly from commercial sodium silicate, except for the -OH group absorption at the wavenumber of 3600 cm^{-1} .

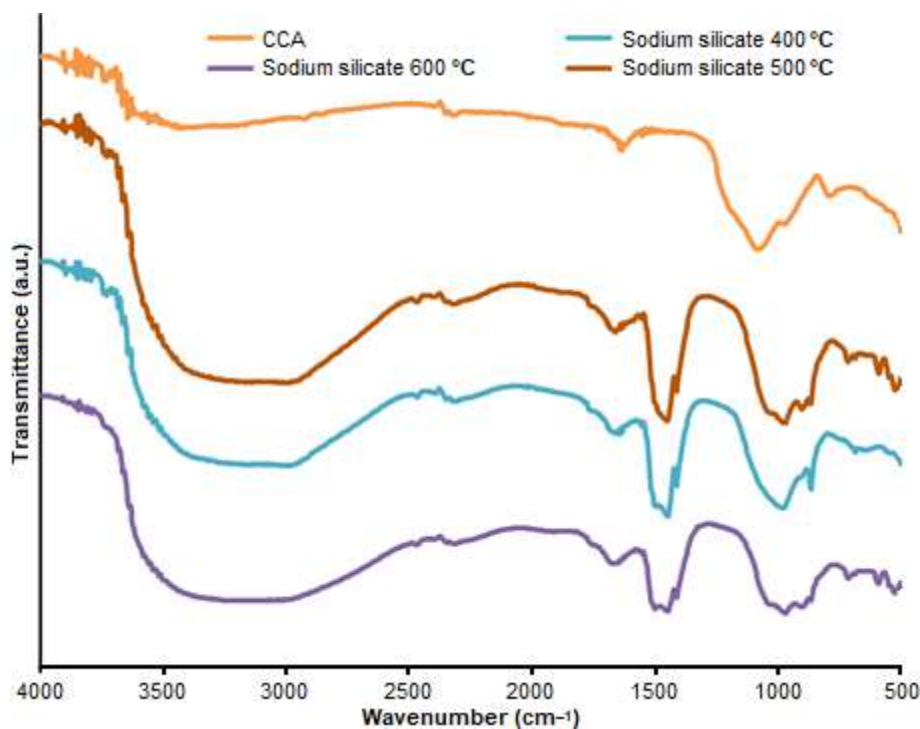


Fig 1. FTIR spectra of CCA and sodium silicate

XRD Analysis

Characterization by XRD is intended to identify catalyst bulk phase and to determine the crystallinity of the catalyst. Amorphous analysis of corncob ash and the crystalline structure of the catalyst using XRD were obtained. Fig. 2 shows the XRD results of corncob ash in the range of $2\theta = 16\text{--}40^\circ$ with sharp peaks at $2\theta = 21.8557$, 26.6516 , and 28.0366° , suggesting that the silica particles are amorphous structures [15-17]. The results indicate that corncob ash is amorphous and can be used as a catalyst buffer with alkali metals since it has a random and irregular pattern of atoms and molecules so that in various conditions, amorphous silica is more reactive in the presence of hydroxyl groups.

The effect of calcination temperature can be seen in the crystalline phase of the sodium silicate catalyst. In Fig. 2, the catalyst obtained a range of $2\theta = 17.17\text{--}67.10^\circ$, with the strongest peak at 29.50° , indicating the formation of the crystalline phase by calcination [13,15-16]. Thus, the process of impregnation of NaOH onto calcined silica corncob ash was successfully carried out to form a crystalline phase of the sodium silicate catalyst.

BET and BJH Analysis

Generally, textures of pore structures of particles are characterized as surface area, pore size distribution, and

pore shape. Configuration of the heterogeneous catalyst surface area (m^2/g) is a crucial criterion for solid catalysts because it determines the number of active sites for catalyst activity. Surface area, pore volume, and pore size distribution are also important parameters since they can control displacement phenomena and selectivity in catalytic reactions.

The BET method is used in determining the surface area of solids. This method is based on the kinetic model of the Langmuir adsorption process.

All samples were measured for the specific surface area using BET for nitrogen gas sorption at a liquid nitrogen temperature of 77.35 K. Upon impregnation and calcination of alkali metals, the BET surface area decreased as a result of the sintering effect (Table 1). The relative pressure in the range of 0.1–0.4 corresponds to the formation of the monolayer nitrogen molecule on the surface of the material, as shown by the initial linear curve in Fig. 3. The study of pore uniformity is particularly important in the synthesis of mesoporous solids because pore uniformity determines the quality of the solid as a catalyst. The level of uniformity is ascertained by looking at the distribution patterns obtained from BJH nitrogen isotherm adsorption data. Fig. 4 shows the uniformity of pores with a radius of $17\text{--}20^\circ$ (Table 1). From Fig. 4, it can be seen that the pore

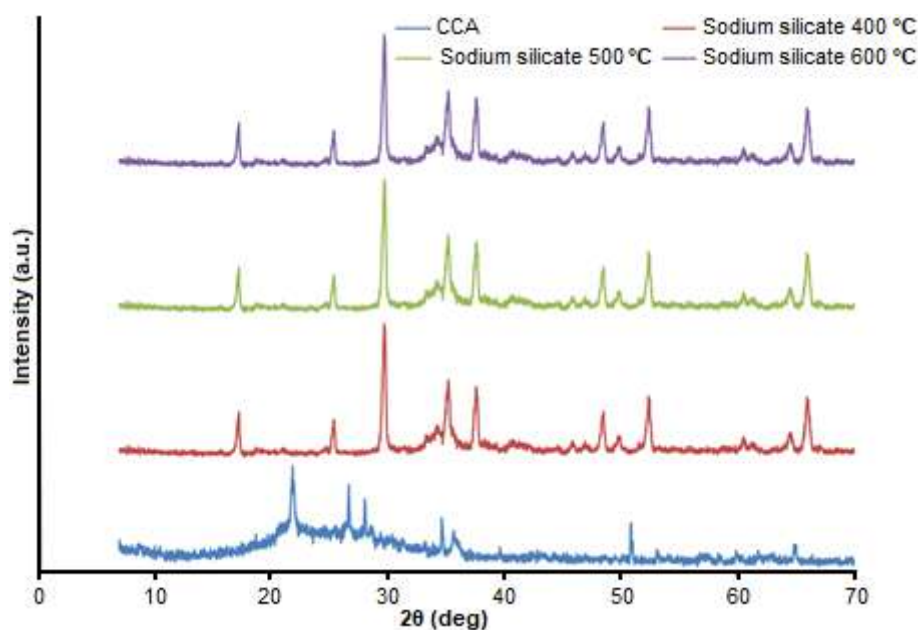


Fig 2. XRD patterns of corncob ash and sodium silicate

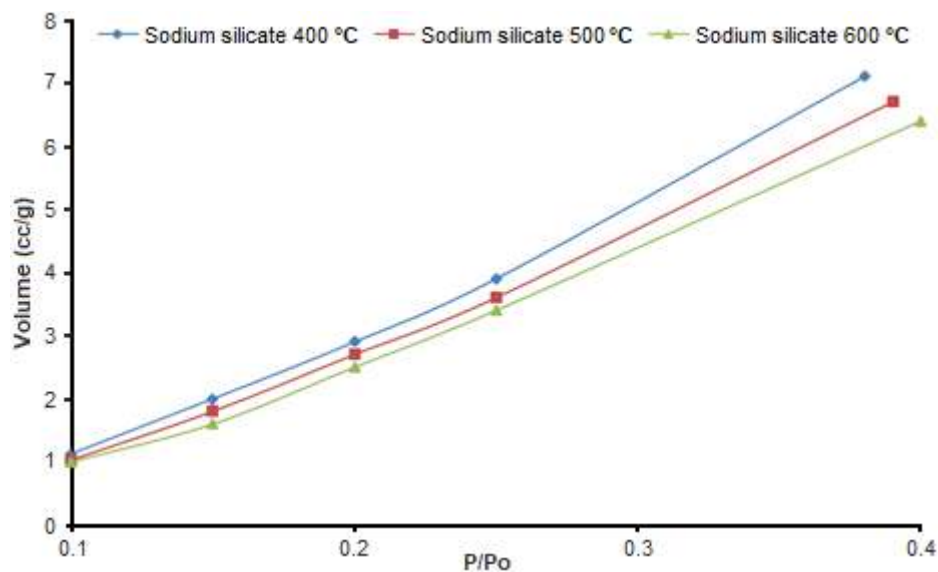


Fig 3. Multipoint sodium silicate curve

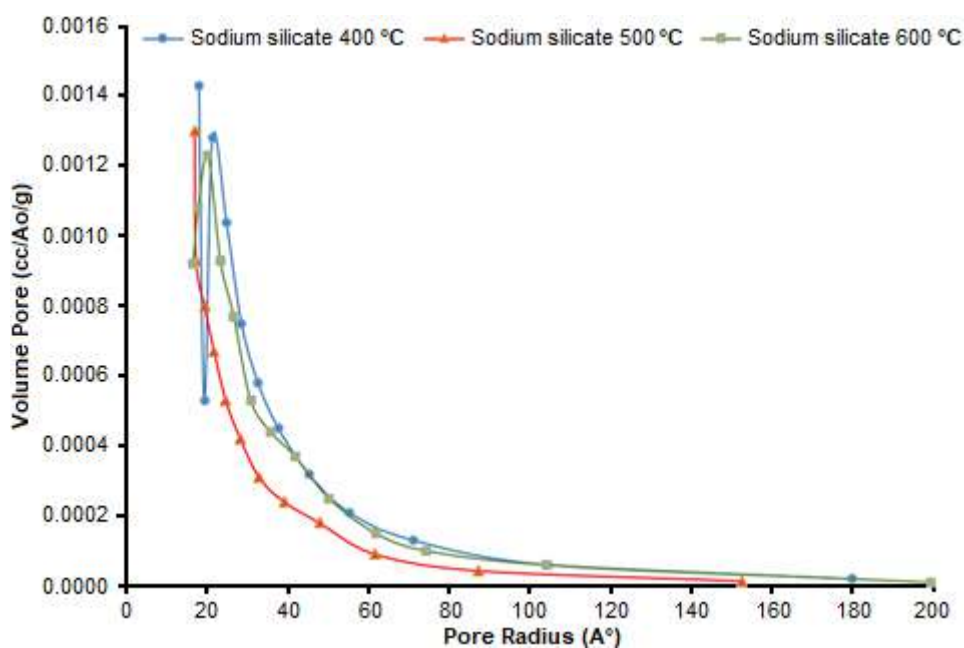


Fig 4. Sodium silicate pore distribution curve

Table 1. Surface analysis and pore structure of sodium silicate

Sample	S (BET) (m ² /g)	V (BJH)(cm ³ /g)	D (nm) (BJH)
Sodium silicate 400 °C	72.824	0.034	30.42
Sodium silicate 500 °C	67.846	0.033	34.22
Sodium silicate 600 °C	22.868	0.021	40.16

uniformity level of sodium silicate is quite high, as indicated by the pore distribution pattern not having widened [25].

The average pore diameter of sodium silicate with different calcination temperatures is summarized in Table 1. Even though the value of the porous diameter is

almost the same, sodium silicate at 600 °C with a ratio of 1:2 has a more homogeneous pore distribution [15].

Based on Table 1, it can be seen that the sample has a surface area that shrinks with increasing calcination temperature, possibly due to the sintering process [16]. Furthermore, the pore volume decreases with increasing calcination temperature. Note that the sintering process at higher temperature resulted in a smaller surface area and pore volume, inversely proportional to the pore radius.

SEM-EDS Analysis

SEM analysis was carried out to determine the morphology of the sodium silicate catalyst. Fig. 5 shows a significant agglomeration of particles on the surface of the amorphous silica. The pores within the agglomerates were found to be smaller as silica content increased. The EDS profile of sodium silicate contains predominantly the elements listed in Table 2, which are Na, O, and Si. Both Si and O peaks correspond to the silica, and the signal of carbon is originated from carbon coating in the SEM-EDS analysis.

This indicates that the sodium content of corncobs raw material is higher than rice husk; however, the higher sodium content shows that the alkaline impregnation has been successful.

The Effect of the Calcination Temperature of the Catalyst on the Yield of the Biodiesel

Sodium silicate was applied as a catalyst in the palm oil transesterification process. The amount of catalyst was 2% (w/w oil), while the molar ratio of the methanol to oil was 12:1. The reaction was kept at 65 °C for 1 h. The raw material used was RBDPO obtained from crude palm oil purification with an FFA of 0.15% and moisture of 0.06%.

Table 2. Elemental composition sodium silicate catalysts

Sample	Na (%)	O (%)	Si (%)
Sodium silicate from corncob ash	43.29	36.48	20.23
Sodium silicate from rice husk [26]	22.63	71.98	5.39

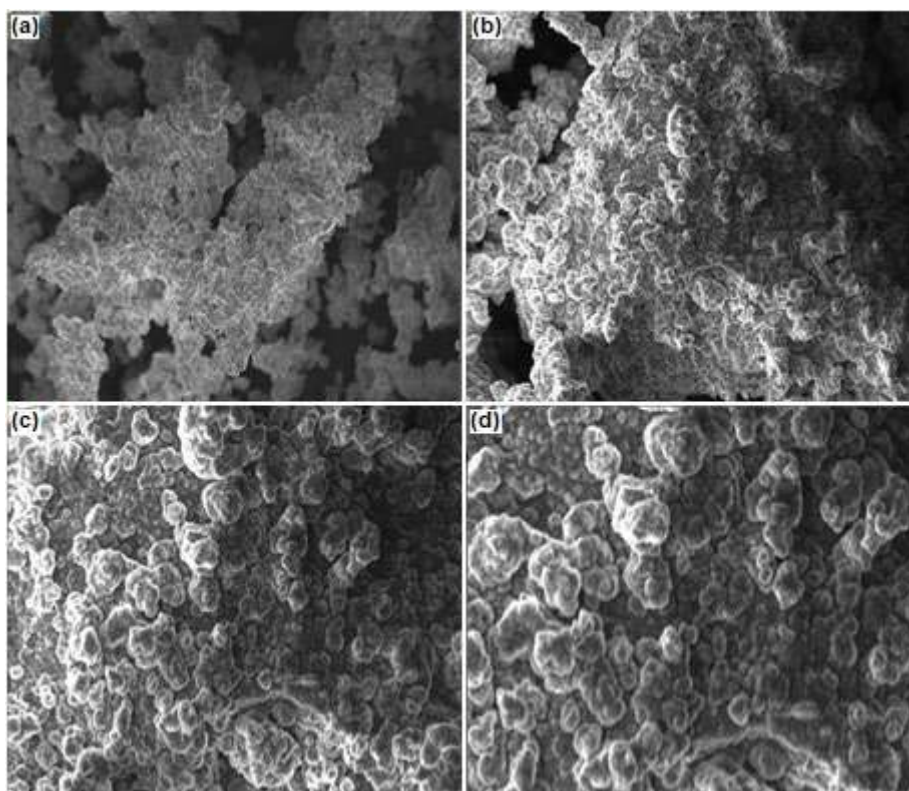


Fig 5. Surface morphology: (a) corncob ash; (b) sodium silicate 400 °C; (c) sodium silicate 500 °C; (d) sodium silicate 600 °C

Biodiesel is composed of fatty acid methyl esters, and their composition is commonly determined by GC analysis. Analysis result of the current study is presented in Table 3 which shows that seven types of methyl ester compounds were found in the biodiesel produced from RBDPO. Unsaturated and saturated fractions were obtained at 98.04 and 1.3285%, respectively, while the overall level of FAMES was 99.3685%. It can be stated that the oil was successfully transesterified to biodiesel using the sodium silicate catalyst. The performance of calcined sodium silicate for transesterification of RBDPO was compared with other reported solid catalysts using palm oil (waste cooking oil/WCO), a low grade oil, as raw material. The use of commercial sodium silicate in the production of biodiesel with waste cooking palm oil (WCO) raw material was able to provide a yield of 57.9% despite the poor quality raw material, as shown in Table 4 [23]. WCO is palm oil that has been used for cooking thus it can be ascertained that the hydrolysis reaction occurred during the cooking process due to the contact with water at high temperatures. This causes an increase in FFA and water content. With relatively high FFA and water content, the sodium silicate catalyst was able to catalyze reactions without WCO pretreatment, thus exhibiting a good catalytic performance.

Fig. 6 shows the impact of calcination temperature on the yield of biodiesel. The higher the calcination temperature, the lower the yield of biodiesel. The sintering effect caused this reduction of yield during calculations, which resulted in the lowering of surface area (Table 1). The optimum condition that resulted in a yield of 79.49% was observed at temperature of 400 °C.

Properties of Palm Oil Biodiesel

The physicochemical properties of the biodiesel was

Table 4. Sodium silicate in the biodiesel production using different quality of raw material

Catalyst	Type of oil	Catalyst dosage (%)	Alcohol	Ratio	Reaction temp. (°C)	Reaction time (min)	Yield (%)
Commercial sodium silicate [23]	WCO	2.5	Methanol	6:1	64	240	57.9
Synthesis sodium silicate [this study]	RBDPO	2	Methanol	9:1	65	60	79.49

studied after going through a purification process, in order to remove impurities, and a heating process to remove residual [15]. The biodiesel was measured according to EN14214 standard.

The results shown in Table 5 indicate that the biodiesel produced in this study that was measured against six physicochemical parameters, has values that comply with EN14214 standards. Although there are still many other parameters to be looked at in analyzing biodiesel products as fuel, the above six parameters can serve as an indicator for the initial stage of such production.

Table 3. Methyl ester composition of the synthesized biodiesel

Peak	Identified Compound	Composition (%)
1	Methyl palmitate (C16:0)	0.3803
2	Methyl stearate (C18:0)	0.9482
3	Methyl oleate (C18:1)	36.9969
4	Methyl oleate (C18:1)	59.7634
5	Methyl linoleate (C18:2)	0.0670
6	Methyl linolenate (C18:3)	0.6517
7	Methyl arachidate (C20:0)	0.5610

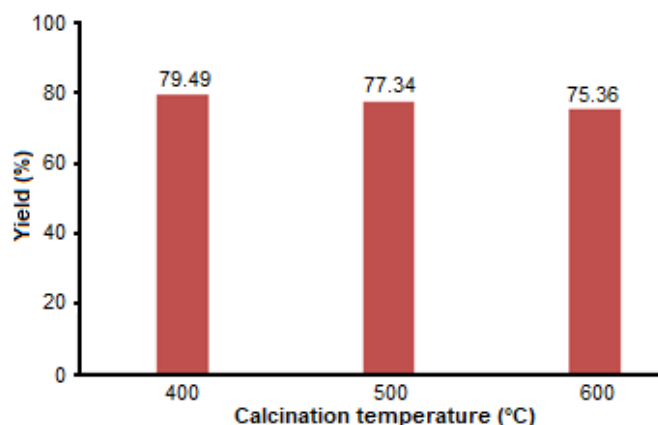


Fig 6. Effect of the temperature of calcination on biodiesel yield

Table 5. Physicochemical properties of biodiesel from palm oil

Fuel Properties	Unit	This Work	EN14214/03
Methyl ester content	%w/w	99.3685	≥ 96.5
Density	kg/m ³	868	860–900
Viscosity kinematic	mm ² /s	4.57	3.5–5.0
Monoglyceride	%	0.24	Max 0.8
Diglyceride	%	-	Max 0.2
Triglyceride	%	-	Max 0.2

■ CONCLUSION

In summary, an efficient sodium silicate solid base catalyst was synthesized using corncobs and NaOH solution. The prepared catalyst was used in the transesterification conversion of palm oil to biodiesel. Under optimized reaction conditions, the yield reached 79.50% after only 60 min at 65 °C, at catalyst content of 2% and a molar ratio of 1:12. The obtained biodiesel product after purification and treatment processes had high-quality fuel properties according to EN14214 standards, showing that low-cost sodium-silicate-derived corncob catalysts have high catalytic performance and could be used for biodiesel production at industrial scales.

■ ACKNOWLEDGMENTS

The authors gratefully acknowledge that their research was facilitated by the Department of Chemical Engineering, Faculty of Engineering, Universitas Sumatera Utara, Medan, North Sumatera, Indonesia.

■ REFERENCES

- [1] Huang, R., Cheng, J., Qiu, Y., Li, T., Zhou, J., and Chen, K., 2015, Using renewable ethanol and isopropanol for lipid transesterification in wet microalgae cells to produce biodiesel with low crystallization temperature, *Energy Convers. Manage.*, 105, 791–797.
- [2] Chen, S.Y., Lao-ubol, S., Mochizuki, T., Abe, Y., Toba, M., and Yoshimura, Y., 2014, Transformation of non-edible vegetable oils into biodiesel fuels catalyzed by unconventional sulfonic acid-functionalized SBA-15, *Appl. Catal., A*, 485, 28–39.
- [3] Yee, K.F., Kansendo, J., and Lee, K.T., 2010, Biodiesel production from palm oil via heterogeneous transesterification: Optimization study, *Chem. Eng. Commun.*, 197 (12), 1597–1611.
- [4] Lani, N.S., Ngadi, N., Yahya, N.Y., and Rahman, R.A., 2017, Synthesis, characterization and performance of silica impregnated calcium oxide as heterogeneous catalyst in biodiesel production, *J. Cleaner Prod.*, 146, 116–124.
- [5] Tubino, M., Junior, J.G.R., and Bauerfeldt, G.F., 2016, Biodiesel synthesis: A study of the triglyceride methanolysis reaction with alkaline catalysts, *Catal. Commun.*, 75, 6–12.
- [6] Lee, S.L., Wong, Y.C., Tan, Y.P., and Yew, S.Y., 2015, Transesterification of palm oil to biodiesel by using waste obtuse horn shell-derived CaO catalyst, *Energy Convers. Manage.*, 93, 282–288.
- [7] Xie, W., and Zhao, L., 2014, Heterogeneous CaO–MoO₃–SBA-15 catalysts for biodiesel production from soybean oil, *Energy Convers. Manage.*, 79, 34–42.
- [8] Taufiq-Yap, Y.H., Teo, S.H., Rashid, U., Islam, A., Hussien, M.Z., and Lee, K.T., 2014, Transesterification of *Jatropha curcas* crude oil to biodiesel on calcium lanthanum mixed oxide catalyst: Effect of stoichiometric composition, *Energy Convers. Manage.*, 88, 1290–1296.
- [9] Sánchez, M., Marchetti, J.M., Boulifi, N.E., Aracil, J., and Martínez, M., 2015, Kinetics of jojoba oil methanolysis using a waste from the fish industry as a catalyst, *Chem. Eng. J.*, 262, 640–647.
- [10] Li, B., Li, H., Zhang, X., Fan, P., Liu, L., Li, B., Dong, W., and Zhao, B., 2019, Calcined sodium silicate as an efficient and benign heterogeneous catalyst for the transesterification of natural lecithin to L- α -glycerophosphocholine, *Green Process. Synth.*, 8 (1), 78–84.
- [11] Arantes, R.S., and Lima, R.M.F., 2013, Influence of sodium silicate modulus on iron ore flotation with sodium oleate, *Int. J. Miner. Process.*, 125, 157–160.
- [12] He, F., Wang, X., and Wu, D., 2015, Phase-change characteristics and thermal performance of form-stable *n*-alkanes/silica composite phase change materials fabricated by sodium silicate precursor, *Renewable Energy*, 74, 689–698.

- [13] Guo, F., Wei, N.N., Xiu, Z.L., and Fang, Z., 2012, Transesterification mechanism of soybean oil to biodiesel catalyzed by calcined sodium silicate, *Fuel*, 93, 468–472.
- [14] Long, Y.D., Guo, F., Fang, Z., Tian, X.F., Jiang, L.Q., and Zhang, F., 2011, Production of biodiesel and lactic acid from rapeseed oil using sodium silicate as the catalyst, *Bioresour. Technol.*, 102 (13), 6884–6886.
- [15] Hindryawati, N., Maniam, G.A., Karim, M.R., and Chong, K.F., 2014, Transesterification of used cooking oil over alkali metal (Li, Na, K) supported rice husk silica as the potential solid base catalyst, *Eng. Sci. Technol. Int. J.*, 17 (2), 95–103.
- [16] Roschat, W., Siritanon, T., Yoosuk, B., and Promarak, V., 2016, Rice husk-derived sodium silicate as a highly efficient and low-cost basic heterogeneous catalyst for biodiesel production, *Energy Convers. Manage.*, 119, 453–462.
- [17] Mutalib, A.A.A., Ibrahim, M.A., Matmin, J., Kassim, M.F., Mastuli, M.S., Taufiq-Yap, Y.H., Shohaimi, N.A.M., Islam, A., Tan, Y.H., and Kaus, N.H.M., 2020, SiO₂-Rich sugar cane bagasse ash catalyst for transesterification of palm oil, *Bioenergy Res.*, 2020, 1–12.
- [18] Nandiyanto, A.B.D., Suhendi, A., Ogi, T., Umemoto, R., and Okuyama, K., 2014, Size- and charge-controllable polystyrene spheres for templates in the preparation of porous silica particles with tunable internal hole configurations, *Chem. Eng. J.*, 256, 421–430.
- [19] Olafusi, O.S., Kupolati, W.K., Sadiku, R., Snyman, J., and Ndambuki, J.M., 2018, Characterization of corncob ash (CCA) as a pozzolanic material, *IJCET*, 9 (12), 1016–1024.
- [20] Manurung, R., Siregar, H., and Zuhri, R.R.S., 2019, Synthesis and characterization of K-Silica catalyst based bamboo-leaves for transesterification reaction, *AIP Conf. Proc.*, 2085, 020069.
- [21] Zhao, C., Lv, P., Yang, L., Xing, S., Luo, W., and Wang, Z., 2018, Biodiesel synthesis over biochar-based catalyst from biomass waste pomelo peel, *Energy Convers. Manage.*, 160, 477–485.
- [22] Attol, D.H., and Mihsen, H.H., 2020, Synthesis of silica-salen derivative from rice husk ash and its use for extraction of divalent metal ions Co(II), Ni(II) and Cu(II), *Indones. J. Chem.*, 20 (1), 16–28.
- [23] Sakti, S.C.W., Siswanta, D., and Nuryono, 2013, Adsorption of gold(III) on ionic imprinted amino-silica hybrid prepared from rice hull ash, *Pure Appl. Chem.*, 85 (1), 211–223.
- [24] Daramola, M.O., Mtshali, K., Senokoane, L., and Fayemiwo, O.M., 2016, Influence of operating variables on the transesterification of waste cooking oil to biodiesel over sodium silicate catalyst: A statistical approach, *J. Taibah Univ. Sci.*, 10 (5), 675–684.
- [25] Sutarno, Arryanto, Y., and Wigati, S., 2003, The influence of Si/Al mole ratio of precursor solution on the structural properties of MCM-41 from fly ash, *Indones. J. Chem.*, 3 (2), 126–134.
- [26] Trivana, L., Sugiarti, S., and Rohaeti, E., 2015, Sintesis dan karakterisasi natrium silikat (Na₂SiO₃) dari sekam padi, *JSTL*, 7 (2), 66–75.

Degradation of Methylene Blue Using Cadmium Sulfide Photoanode in Photofuel Cell System with Variation of Electrolytes

Gunawan^{1*}, Abdul Haris¹, Didik Setiyo Widodo¹, Linda Suyati¹, and Wilman Septina²

¹Department of Chemistry, Faculty of Science and Mathematics, Diponegoro University, Jl. Prof. H. Soedarto, S.H., Tembalang Semarang 50275, Indonesia

²Hawaii Natural Energy Institute, University of Hawai'i at Mānoa (UHM), 1680 East West Road, POST 109 Honolulu, HI 96822, United States

* **Corresponding author:**

tel: +62-24-7474754

email: gunawan@live.undip.ac.id

Received: January 4, 2020

Accepted: February 19, 2020

DOI: 10.22146/ijc.53131

Abstract: Methylene blue degradation carried out using cadmium sulfide (CdS) photoanode in photofuel cell (PFC) had been done. CdS synthesized by chemical bath deposition (CBD) on the FTO substrate was used as anode and platinum as a cathode in photoelectrochemical studies. Characterization of CdS thin film was done using EDX, XRD, SEM, Raman, UV-Vis absorption spectrophotometer as well as photocurrent test of the CdS thin film under illumination using potentiostat with the three-electrode system. The EDX result indicated the presence of CdS with an elemental composition of Cd rich. XRD showed the appearance of CdS crystals in cubic and hexagonal formations. SEM image of CdS gave results in the form of crystals of less than 1 μm . Raman spectrum showed the appearance of CdS peaks. The bandgap of CdS was estimated to be 2.38 eV, and the photocurrent test confirmed that the film had a property of n-type semiconductor. Application of CdS thin film as a photoanode in the PFC system using 100 mg/L methylene blue solution showed degradation up to 48% for 2.5 h using a 4 cm^2 photoanode, and the maximum potential of 0.8 V was obtained with a photoanode area of 1 cm^2 .

Keywords: cadmium sulphide; photoanode; photofuel cell; methylene blue

■ INTRODUCTION

Recently, a photofuel cell (PFC) has attracted the attention of the scientific community as a potential wastewater treatment technology that can generate electricity from chemical energy conversion from organic pollutants [1-9]. Generally, PFC consists of a photoanode in the form of a semiconductor photocatalyst and a cathode, usually of platinum (Fig. 1). The photocatalyst undergoes photoexcitation upon light illumination and generates electron-hole pairs. The electrons will be excited from the valence band (VB) to the conduction band (CB) of the photoanode and flow to the cathode through the outer circuit to produce electricity. Meanwhile, the holes will oxidize and destroy organic pollutants, or react with OH^- or H_2O to form hydroxyl radical (OH^*) through H_2O oxidation. The resulting OH^* has a very strong oxidation potential (2.80 V), which is

capable of oxidizing organic pollutants to produce CO_2 , H_2O , and other byproducts [10].

PFC using a series of TiO_2 nanotubes (TNA) photoanode has been studied recently [2-3,11-13]. The properties of photoanode structures, such as specific surface area and thickness of photoanodes, can affect the ability to utilize light and inhibit transport of electrons produced under illumination [2-3,11,14]. Other researchers used ZnO/Zn as photoanodes [15] with open and closed-circuit systems without supporting electrolytes. The presence of supporting electrolytes, however, can improve the PFC performance [1] by increasing the conductivity of the solution and reducing the internal resistance. Decreasing internal barriers results in greater potential differences in both electrodes and enhances the electrons flow at the cathode, leaving holes in the photoanode that have a strong oxidation property.

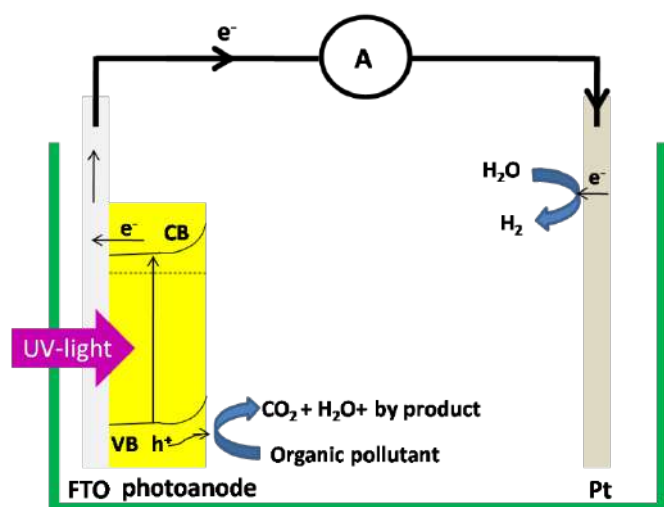


Fig 1. Illustration of organic pollutant degradation process using photofuel cell with photoanode under UV-light illumination. CB, VB, h^+ , and e^- represent conduction band, valence band, hole, electron, respectively. Under the UV-light illumination, electrons are excited to the CB of n-CdS, leaving holes at VB. The photogenerated electrons are then driven to FTO as back contact to an external circuit (the current flow is measured by Ampere meter) and return to a platinum electrode where they may reduce protons to molecular hydrogen. Meanwhile, the photogenerated holes will oxidize organic pollutants to produce CO_2 , H_2O , and byproducts

Therefore, most researchers use supporting electrolytes in PFC to improve the efficiency of degradation and generation of electricity from PFCs [16-18].

So far, there are limited studies of bare CdS thin film prepared by chemical bath deposition (CBD) in the PFC system, although it has potency as a photoanode due to its high absorption coefficient (10^4 cm^{-1}) and wide-bandgap. The previous researchers used CdS sandwiched with other photoanodes such as ZnS and TiO_2 for PFC [19]. The CdS thin film is widely used as a buffer layer in solar cells [20-21] and photoelectrochemical water splitting [20,22-26]. The CdS thin film can be prepared by electrochemical deposition [27] and chemical bath deposition [28-31]. In this study, CdS thin film was prepared by the CBD method and characterized by SEM-EDX, XRD, Raman, UV-Vis absorption spectrophotometer as well as photocurrent test under

illumination using potentiostat with the three-electrode system. Then, the CdS thin film was applied as a photoanode in the PFC system with electrolytes and an organic compound of methylene blue. The effects of other parameters such as open and closed-circuits, initial concentration, and pH from methylene blue degradation were also studied.

EXPERIMENTAL SECTION

Materials

Aquadest was supplied from Batraco (Indonesia), nitrogen gas was supplied from Samator (Indonesia). Acetone, hydrochloric acid, cadmium sulfate, thiourea, ammonia, methylene blue, Na_2SO_4 , Na_2SO_3 , NaOH were pro-analytical grade and were purchased from Merck (Darmstadt, Germany).

Procedure

Preparation of CdS thin film

Preparation of working electrode. Fluorine-doped tin oxide (FTO)-coated glass ($1 \text{ cm} \times 2 \text{ cm}$) was used as a substrate for CdS thin film deposition. Before the deposition, the FTO glass substrates were cleaned with sequential sonication in acetone and distilled water for 10 min, then dried using N_2 gas.

Deposition of CdS by chemical bath deposition (CBD). The deposition of CdS was similar to our previous work [22]. Typical FTO glass substrates were covered with sticky tape at half of the area (it was used as the contact of photoanode). Then, the uncovered areas were immersed in an aqueous solution containing 12.5 mM $CdSO_4$, 0.22 M thiourea (H_2NCSNH_2), and 11 M ammonia at $60 \text{ }^\circ\text{C}$ for 7 min. The film was then washed with demineralized water and dried using N_2 gas. The area of single FTO covered with CdS as the working area of photoanode was $1 \text{ cm} \times 1 \text{ cm}$.

Characterization

Crystalline structures of the CdS film was analyzed by X-ray diffraction (XRD) using a PANalytical X Pert³ Powder X-ray diffractometer (Cu $K\alpha$, Ni filter). Raman spectrum was analyzed by a Jasco NRC 3100 Laser Raman Spectrophotometer with an excitation laser of the wavelength of 532 nm. Morphologies of the films

were examined using a JSM-6510LA Analytical SEM (scanning electron microscope) at an acceleration voltage of 20 kV. Atomic percentages were analyzed by SEM-EDX (Phenom Pro-X desktop SEM with EDX). Bandgap determination was done by the UV-Vis absorption spectrophotometer (Shimadzu series prestige 21). Photocurrent (J-V) test was conducted in 1 M Na₂SO₃ as hole scavenging using potentiostat-galvanostat (Electrochemical Workstation CorrTest CS Studio 150) under 1.5 AM solar simulation with a three-electrode system (CdS thin film, Ag/AgCl electrode and Pt electrode as working, reference, and counter electrodes, respectively). The measurements were done from the potential of 1.0 to -0.2 V (vs. Ag/AgCl) with a scan rate of 10 mV/s.

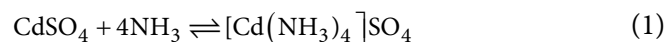
Application of CdS photoanode for degradation of methylene blue in photofuel cell (PFC)

Methylene blue degradation was conducted using the equipment shown in Fig. 1. It consists of a photoanode and a platinum sheet (2 cm × 1 cm) that is arranged and inserted into a reactor containing methylene blue as artificial waste. Next, irradiation was carried out using a 25 Watt UV lamp (365 nm) at a distance of 20 cm apart. The initial concentration of dyes (100 mg/L), the time of treatment, and the use of 0.1 M electrolytes of Na₂SO₄, HCl, and NaOH were evaluated. Concentrations of the dyes after treatment were carried out using a UV-Vis spectrophotometer by plotting the measured absorbance to the calibration curve (absorbance vs. concentration of methylene blue) at 662 nm as the maximum absorbance peak of methylene blue at the acidic and neutral condition. For alkaline condition maximum wavelength of methylene blue was c.a 620 nm. Potential generated from the PFC was measured using a multimeter (SANWA).

RESULTS AND DISCUSSION

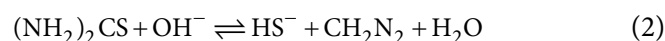
The films obtained by this method were yellow, very compact, continuous, and adhere very well, as shown in Fig. 2. The classical mechanism of CdS growth using CBD can be summarized by the following chemical reactions [32]:

Complex formation of cadmium salt with ammonia:



The formation of [Cd(NH₃)₄]SO₄ prevents the precipitation of Cd(OH)₂. The complex ions [Cd(NH₃)₄]²⁺, SO₄²⁻, OH⁻, and thiourea diffuse to the catalytic surface of the substrate

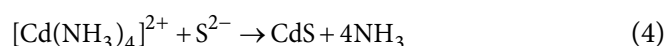
Hydrolysis of thiourea in an alkaline medium:



where HS⁻ ions are in equilibrium with water and give S²⁻ ions according to this equation:



Cadmium sulfide formation:



EDX Analysis of CdS Thin Film

The atomic percentage of CdS on the FTO glass was shown in Table 1. It shows that there are six elements from EDX results, namely tin, calcium, cadmium, sulfur, oxygen, and silicon. The dominant elements are tin, cadmium, and oxygen. The tin comes from the FTO constituent, namely fluorinated tin oxide, while the calcium and silicon were derived from the glass materials. From these observations, it can be seen that the CdS composition is not 1:1, but Cd rich. This deviation



Fig 2. The thin film of CdS deposited by CBD

Table 1. Atomic percentages of CdS on FTO

Element symbol	Element name	Percentage (%)
Sn	Tin	60.8
Ca	Calcium	0.4
Cd	Cadmium	17.9
S	Sulfur	3.3
O	Oxygen	17.0
Si	Silicon	0.6

could be due to the presence of oxygen that comes from the atmosphere or the solution used for the chemical bath deposition of CdS. Here, the ammonia that is used as the alkaline condition can affect the OH⁻ ions and the possibility of inclusion of oxygen in the deposition process. As a result, it will cause a higher percentage of oxygen in the thin film [33].

XRD Analysis

The XRD peaks of CdS thin film are depicted in Fig. 3. The peaks at $2\theta = 34.29^\circ$, 38.32° , and 62.15° are the peaks of SnO₂ coming from the substrate used (FTO). Other diffractions in the XRD pattern are observed at $2\theta = 27.05^\circ$, 52° , 66° , and 78.88° , attributable to the reflection of CdS at (0 0 2), (1 1 2), (2 0 3), and (2 0 4) which have hexagonal crystal structure, with lattice parameters $a = 4.157 \text{ \AA}$ and $c = 6.580 \text{ \AA}$ (JCPDS card no. 41-1049) [34]. Some small peaks are observed at $2\theta = 29.84^\circ$ and 44.80° , corresponds to the reflection of CdS (2 0 0) and (2 0 0) from the CdS cube (JCPDS card no. 80-0019) [35]. The average crystallite size (nm) measured using Scherrer's formula [33] was found to be 30.13 nm. The Scherrer's formula is written as:

$$D = k\lambda / (\beta \cdot \cos\theta) \quad (5)$$

where k is a constant of 0.94, λ is the wavelength of X-ray source (in this case, Cu-K α is 0.15406 nm), β is the full width at half the peak maximum (radians), and θ is Bragg's angle.

From the XRD study, it can be seen that the CdS is a mixture of cube and hexagonal phase that is a characteristic of the film prepared by the CBD method and also in a good agreement with the previous report for CdS thin layer [33].

SEM Analysis

Fig. 4 shows the SEM image of CdS on FTO at 20,000 magnifications. It can be seen that the FTO substrate was covered well without a small crack or hole. This SEM proves that the film is uniform and homogeneous. The thin film sample has a morphology of platelets-like nanocrystalline CdS with a size of less than 1 μm .

Raman Analysis

Raman spectroscopy can be used to characterize the

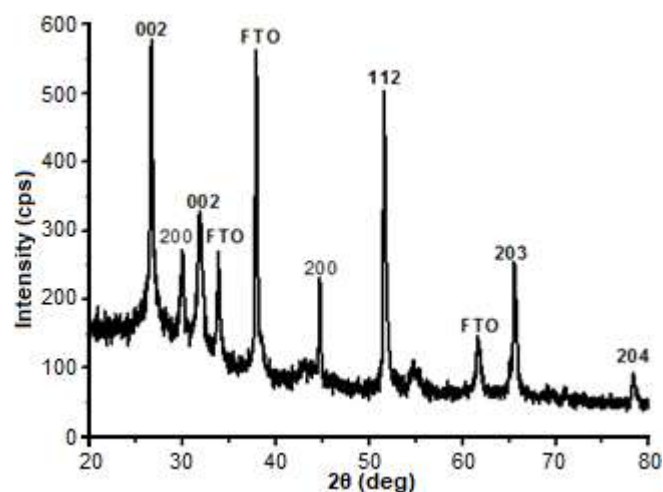


Fig 3. XRD of CdS thin film on FTO

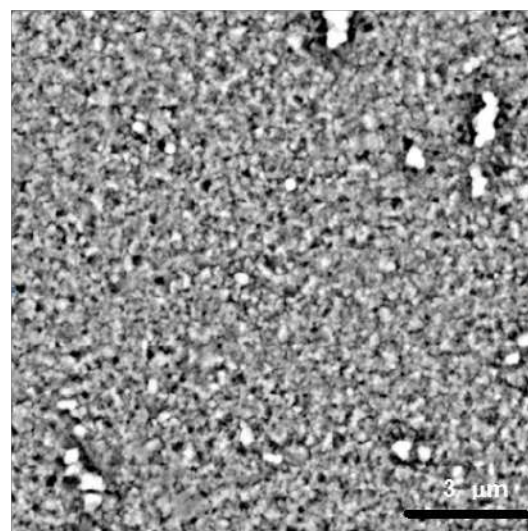


Fig 4. SEM image of CdS on FTO with 20,000 magnification

crystalline behavior of the material quality, including the surface condition and homogeneity with fast and non-destructive work, with a sharp peak for the crystalline sample and very broad peaks for amorphous or polycrystalline ones [36]. Hence, Raman spectroscopy was used for the structural characterization of CdS thin film. Fig. 5 shows the typical Raman spectrum of CdS thin film prepared by chemical bath deposition. The spectrum shows the presence of peaks at 295 and 595 cm^{-1} , which are typical wavenumber regions for CdS crystals of hexagonal wurtzite. This result is in good agreement with the previous work [36] that reported the sharp peaks at 295 and 592 cm^{-1} with a different route of

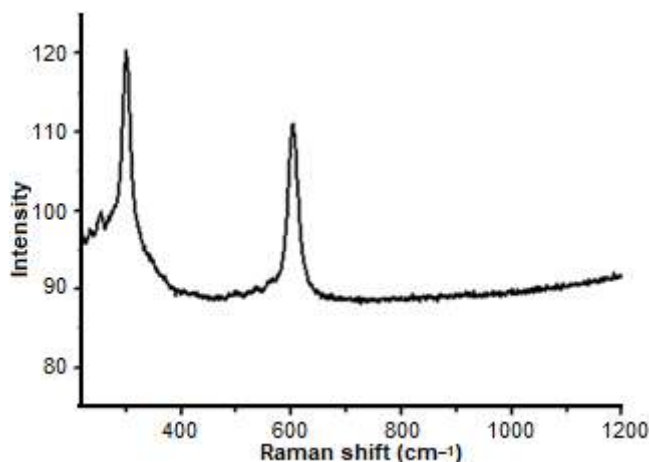


Fig 5. Raman spectrum of CdS on FTO

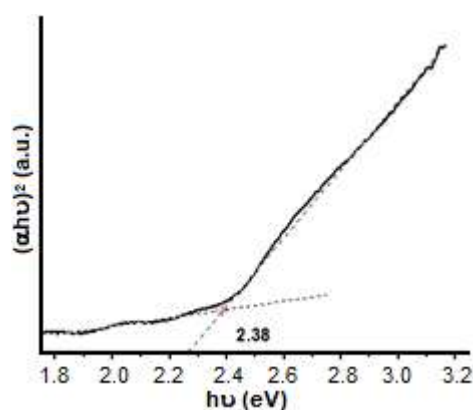


Fig 6. Graph of $(\alpha h\nu)^2$ correlation with $h\nu$ for direct optical transition of CdS

CdS growth. A slight shift to 303.5 and 593.0 cm^{-1} that corresponds to the values with the first and second harmonic modes in the Raman spectrum was observed from the CdS sample prepared by the solvothermal process [37].

Bandgap

Determination of the bandgap (E_g) of a synthesized semiconductor is important on behalf of sunlight irradiation harvesting at an appropriate wavelength region (ultraviolet, visible, or infrared). From the previous study, CdS as an n -type semiconductor has a wider bandgap (close to UV region) than a p -type semiconductor. Therefore, CdS is usually used as a buffer layer in a solar cell or photoelectrochemical water splitting [20-26].

The bandgap value of CdS is determined by the Tauc graph expressed in the following equation:

$$(\alpha h\nu)^n = A(h\nu - E_g) \quad (6)$$

The magnitude α is the absorption coefficient, $h\nu$ is the energy of the incoming photon, A is a constant, and n varies from 0.5 to 2.0 depending on the optical transition properties. For the CdS thin layer, a straight line for the plot $(\alpha h\nu)^2$ (that is, $n = 2$) is obtained, suggesting the direct band character of the film. Fig. 6 shows the Tauc plot for the determination of the bandgap of the CdS thin layer. The bandgap is obtained to be 2.38 eV for CdS prepared by the CBD method, deposited for 7 min. The wavelength of 520.6 nm was obtained by converting the bandgap using equation $\lambda = 1240/E_g$. It indicates that the CdS thin film semiconductor will work effectively below 520.6 nm.

Photocurrent Measurement

The photo-voltammetry technique offers a powerful method to evaluate the photoactivity of semiconductors. The measurement is conducted by sweeping the electrode potential under chopped light. White light or LED light with the wavelengths where the semiconductor absorbs strongly is commonly used as the light source. The fraction of photogenerated minority carriers contributing to the photocurrent is shown by the magnitude of the photocurrent. Hence, it shows the existence of surface or bulk traps, and also indicates the external quantum efficiency (EQE). Information of the pinholes in the film or any impurities in the film is indicated by scanning in the dark (light off), which can be deduced from the high dark currents and the appearance of transient current spikes associated with oxidation and reduction of redox couple in contact with the metal substrate or impurities [38].

Fig. 7 shows the voltammogram of CdS thin film measured using Na_2SO_3 solution as hole scavenging measured under chopped illumination of sunlight simulation irradiation at 1.5 AM. It shows that the CdS film has an n -type semiconductor property, as observed by the positive photocurrent. The photocurrent at 1.0 V (vs. Ag/AgCl) is c.a. 0.04 mA/cm^2 . This value is higher

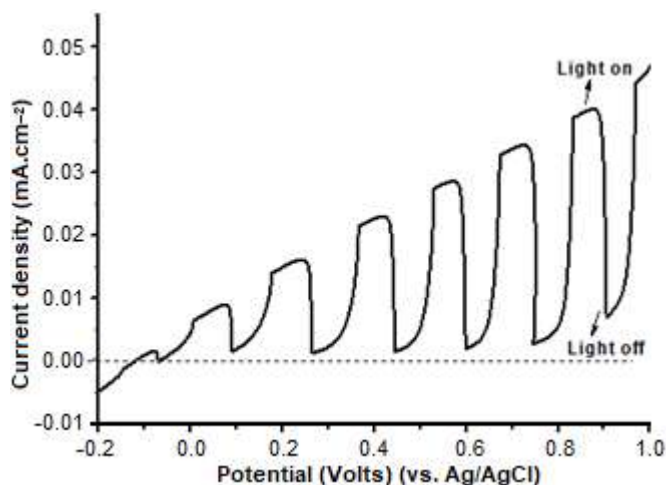


Fig 7. Potential and photocurrent curve of CdS thin film (2 cm × 2 cm) measured in 0.1 M Na₂SO₃ in three-electrode systems with chopped irradiation of 1.5 AM solar simulator

than the previous work [39]. The photocurrent response shows the quality of the thin-film semiconductor. The higher the photocurrent, the higher the impact to produce hole and electron when the semiconductor is illuminated. Consequently, it will produce more effective dye degradation.

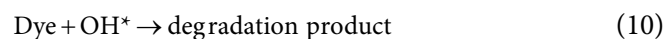
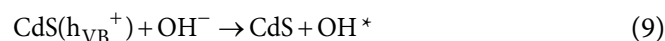
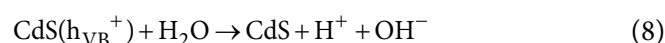
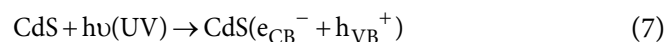
Application of CdS Thin Film Photoanode for Degradation of Methylene Blue in Photofuel Cell (PFC)

Fig. 8 shows the percentage of methylene blue (MB) decrease at various times of light exposure. It shows that there is a significant decrease in MB degradation until the time of 90 min of UV light exposure. However, there is a minor decrease of MB after 90 min, possibly due to the photocathode coverage by MB that hinders the passage of light for the commences of the photoelectrochemical process. The degradation of MB at 150 min is around 1.06 mg (50 mL MB 100 mg/L). Concerning our previous work [22], the thickness of CdS is c.a. 100 nm, and the density of CdS is 4.82 g/cm³ so that the mass of CdS thin film is 48.2 ug. Finally, the effectiveness of CdS thin film as a photoanode to degrade MB is around 1: 51,000 (or 1 mg of CdS thin film can convert 51,000 mg or 51 g of MB).

The effect of electrolytes on the destruction process of MB using PFC with photoanode was also investigated. MB degradation with various additional electrolytes after CdS treatment, either with or without bias, for CdS

photoanodes with the areas of both 1 × 1 cm² and 2 × 2 cm² is given in Fig. 9.

The addition of electrolytes increased the methylene blue degradation process. This phenomenon is due to the increase in the conductivity of the solution. However, the lowest degradation was obtained from the use of sodium sulfate, followed by HCl and NaOH. Since sodium sulfate functions merely as an electrolyte that improves conductivity, there is no reaction occurs at anode and cathode. Meanwhile, for HCl and NaOH, their anions will enhance the degradation of MB. Chloride ions will be oxidized at the anode to form chlorine that is a strong oxidant to degrade MB. The effect will be even more significant when NaOH is used as the electrolyte due to the formation of *OH radical (from hydroxide ions) and hole of CdS semiconductor when illuminated. The radical is a powerful oxidant for the destruction of MB. The mechanisms occur during CdS irradiation with UV light as follows [40]:



OH* radical will increase with the increase of pH (alkaline solution). Therefore, it has more effect on dye degradation at high pH solution.

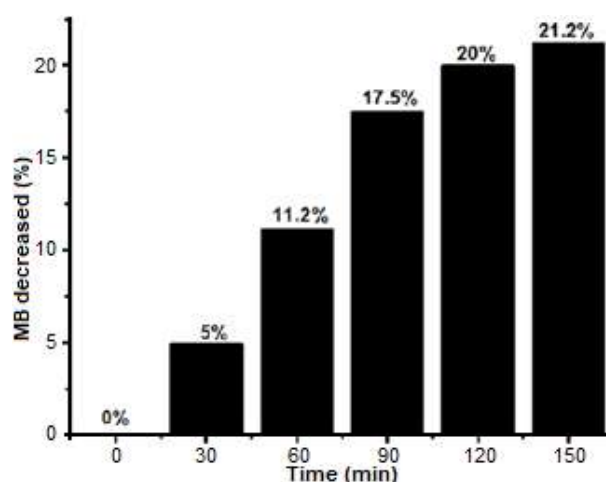


Fig 8. MB decrease calculated at the maximum wavelength (662 nm) when treated by CdS photoanode in PFC with Na₂SO₄ electrolyte at various times of light exposure with the bias of 0.5 V

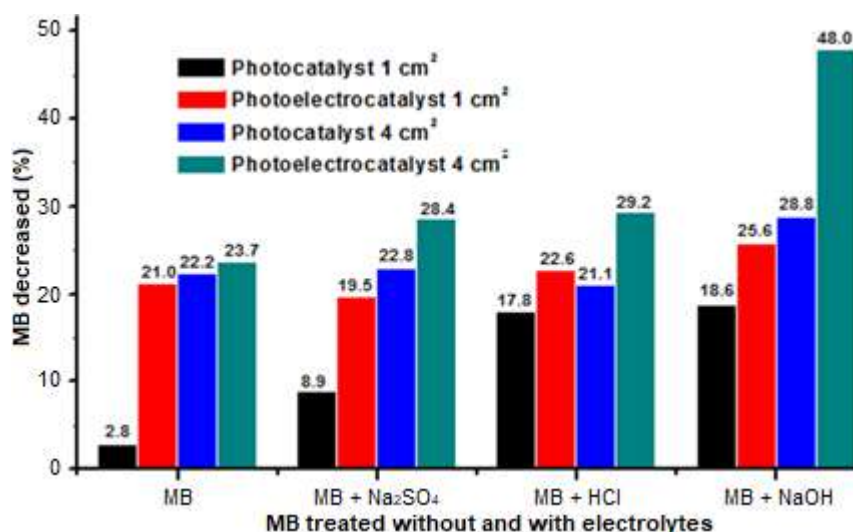


Fig 9. Graph of methylene blue (MB) degradation with and without electrolytes using photoanode areas of 1 cm × 1 cm and 2 cm × 2 cm, both for PFC with and without bias

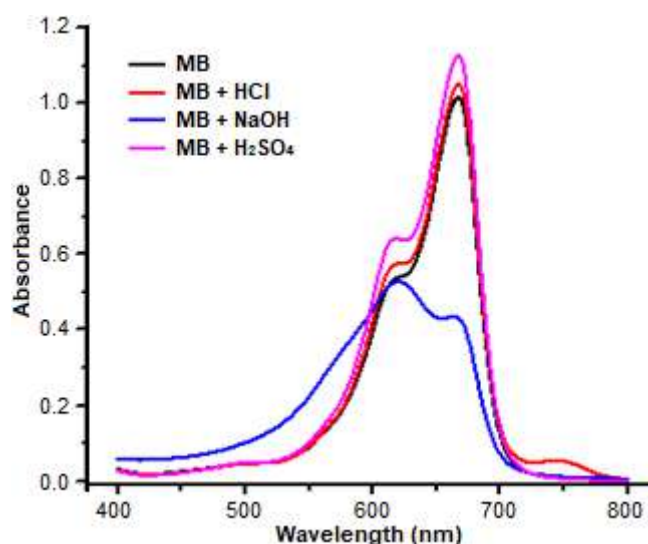


Fig 10. The absorption spectra of methylene blue solution Cl⁻ with and without electrolytes

Meanwhile, bias potential from the external source enhanced the photodegradation process because of the increase in the generated electron and hole by external potential. The larger area of the photoanode also increases MB degradation. An increase in the CdS working area from 1 to 4 cm² on the sample with NaOH electrolytes resulted in the improvement of the MB degradation up to twice larger. Since the current produced at the photoanode was enhanced with the use of a wider area, the degradation of MB will also increase.

The possibility of MB degradation at different pH was also evaluated. The use of HCl and NaOH at the concentration of 0.1 M was found not to degrade the MB (data not shown). However, they only change the visible light absorption spectra of the methylene blue with and without the addition of the electrolyte (Fig. 10). The maximum peak is different for methylene blue in alkaline solution compare to the other electrolytes. The changes in pH do not degrade the dye (data not shown) but might shift the maximum peak. Therefore, for alkaline conditions, the maximum peak near 600 nm was used to determine the concentration of photodegradation MB.

The intermediates resulted from the degradation process were investigated by using GC-MS and LC-MS, identified by the commercially standard comparison and mass spectra for interpretation of their fragment ions. Fig. 11 shows the methylene blue degradation pathways in detail. The final products of the CdS photoanode of PFC are the almost completed mineralization of carbon, nitrogen, and sulfur heteroatoms into CO₂, NH₄⁺, NO₃⁻, and SO₄²⁻, respectively [41].

The open-circuit potential (V_{oc}) of the PFC system is a potential measured using voltmeter without load from the photoelectrochemical cell consists of photoanode, MB either with and without electrolytes, and

- photoelectrochemical cell functioning in the presence of organic wastes, *Sol. Energy Mater. Sol. Cells*, 94 (3), 592–597.
- [2] Li, J., Li, J., Chen, Q., Bai, J., and Zhou, B., 2013, Converting hazardous organics into clean energy using a solar responsive dual photoelectrode photocatalytic fuel cell, *J. Hazard. Mater.*, 262, 304–310.
- [3] Li, K., Xu, Y., He, Y., Yang, C., Wang, Y., and Jia, J., 2013, Photocatalytic fuel cell (PFC) and dye self-photosensitization photocatalytic fuel cell (DSPFC) with BiOCl/Ti photoanode under UV and visible light irradiation, *Environ. Sci. Technol.*, 47 (7), 3490–3497.
- [4] Xia, L., Bai, J., Li, J., Zeng, Q., Li, X., and Zhou, B., 2016, A highly efficient BiVO₄/WO₃/W heterojunction photoanode for visible-light responsive dual photoelectrode photocatalytic fuel cell, *Appl. Catal., B*, 183, 224–230.
- [5] Ogura, Y., Okamoto, S., Itoi, T., Fujishima, Y., Yoshida, Y., and Izumi, Y., 2014, A photofuel cell comprising titanium oxide and silver (I/0) photocatalysts for use of acidic water as a fuel, *Chem. Commun.*, 50 (23), 3067–3070.
- [6] Iyatani, K., Horiuchi, Y., Fukumoto, S., Takeuchi, M., Anpo, M., and Matsuoka, M., 2013, Separate-type Pt-free photofuel cell based on a visible light-responsive TiO₂ photoanode: Effect of hydrofluoric acid treatment of the photoanode, *Appl. Catal., A*, 458, 162–168.
- [7] Fujiwara, K., Akita, A., Kawano, S., Fujishima, M., and Tada, H., 2017, Hydrogen peroxide-photofuel cell using TiO₂ photoanode, *Electrochem. Commun.*, 84, 71–74.
- [8] Seger, B., Lu, G.Q., and Wang, L., 2012, Electrical power and hydrogen production from a photo-fuel cell using formic acid and other single-carbon organics, *J. Mater. Chem.*, 22 (21), 10709–10715.
- [9] Fujishima, Y., Okamoto, S., Yoshida, M., Itoi, T., Kawamura, S., Yoshida, Y., Ogura, Y., and Izumi, Y., 2015, Photofuel cell comprising titanium oxide and bismuth oxychloride (BiO_{1-x}Cl_{1-y}) photocatalysts that uses acidic water as a fuel, *J. Mater. Chem. A*, 3 (16), 8389–8404.
- [10] Konstantinou, I.K., and Albanis, T.A., 2004, TiO₂-assisted photocatalytic degradation of azo dyes in aqueous solution: kinetic and mechanistic investigations: A review, *Appl. Catal., B*, 49 (1), 1–14.
- [11] Liu, Y., Zhou, B., Li, J., Gan, X., Bai, J., and Cai, W., 2009, Preparation of short, robust and highly ordered TiO₂ nanotube arrays and their applications as electrode, *Appl. Catal., B*, 92 (3-4), 326–332.
- [12] Liu, Y., Li, J., Zhou, B., Chen, H., Wang, Z., and Cai, W., 2011, A TiO₂-nanotube-array-based photocatalytic fuel cell using refractory organic compounds as substrates for electricity generation, *Chem. Commun.*, 47 (37), 10314–10316.
- [13] Liu, Y., Li, J., Zhou, B., Li, X., Chen, H., Chen, Q., Wang, Z., Li, L., Wang, J., and Cai, W., 2011, Efficient electricity production and simultaneously wastewater treatment via a high-performance photocatalytic fuel cell, *Water Res.*, 45 (13), 3991–3998.
- [14] Liu, Y., Zhou, B., Bai, J., Li, J., Zhang, J., Zheng, Q., Zhu, X., and Cai, W., 2009, Efficient photochemical water splitting and organic pollutant degradation by highly ordered TiO₂ nanopore arrays, *Appl. Catal., B*, 89 (1-2), 142–148.
- [15] Lee, S.L., Ho, I.N., Ong, S.A., Wong, Y.S., Voon, C.H., Khalik, W.F., Yusoff, N.A., and Nordin, N., 2017, A highly efficient immobilized ZnO/Zn photoanode for degradation of azo dye Reactive Green 19 in a photocatalytic fuel cell, *Chemosphere*, 166, 118–125.
- [16] Wang, B., Zhang, H., Lu, X.Y., Xuan, J., and Leung, M.K.H., 2014, Solar photocatalytic fuel cell using CdS–TiO₂ photoanode and air-breathing cathode for wastewater treatment and simultaneous electricity production, *Chem. Eng. J.*, 253, 174–182.
- [17] Yang, J., Liao, W., Liu, Y., Muruganathan, M., and Zhang, Y., 2014, Degradation of rhodamine B using a visible-light driven photocatalytic fuel cell, *Electrochim. Acta*, 144, 7–15.

- [18] Li, L., Xue, S., Chen, R., Liao, Q., Zhu, X., Wang, Z., He, X., Feng, H., and Cheng, X., 2015, Performance characteristics of a membraneless solar responsive photocatalytic fuel cell with an air-breathing cathode under different fuels and electrolytes and air conditions, *Electrochim. Acta*, 182, 280–288.
- [19] Antoniadou, M., Daskalaki, V.M., Balis, N., Kondarides, D.I., Kordulis, C., and Lianos, P., 2011, Photocatalysis and photoelectrocatalysis using (CdS-ZnS)/TiO₂ combined photocatalysts, *Appl. Catal., B*, 107 (1-2), 188–196.
- [20] Ikeda, S., Nonogaki, M., Septina, W., Gunawan, G., Harada, T., and Matsumura, M., 2013, Fabrication of CuInS₂ and Cu(In,Ga)S₂ thin films by a facile spray pyrolysis and their photovoltaic and photoelectrochemical properties, *Catal. Sci. Technol.*, 3 (7), 1849–1854.
- [21] Jiang, F., Ozaki, C., Gunawan, Harada, T., Tang, Z., Minemoto, T., Nose, Y., and Ikeda, S., 2016, Effect of indium doping on surface optoelectrical properties of Cu₂ZnSnS₄ photoabsorber and interfacial/photovoltaic performance of cadmium free In₂S₃/Cu₂ZnSnS₄ heterojunction thin film solar cell, *Chem. Matter.*, 28 (10), 3283–3291.
- [22] Gunawan, G., Septina, W., Ikeda, S., Harada, T., Minegishi, T., Domen, K., and Matsumura, M., 2014, Platinum and indium sulfide-modified CuInS₂ as efficient photocathodes for photoelectrochemical water splitting, *Chem. Commun.*, 50 (64), 8941–8943.
- [23] Zhao, J., Minegishi, T., Zhang, L., Zhong, M., Gunawan, Nakabayashi, M., Ma, G., Hisatomi, T., Kayatama, M., Ikeda, S., Shibata, N., Yamada, T., and Domen, K., 2014, Enhancement of solar hydrogen evolution from water by surface modification with CdS and TiO₂ on porous CuInS₂ photocathodes prepared by an electrodeposition-sulfurization method, *Angew. Chem. Int. Ed.*, 53 (44), 11808–11812.
- [24] Gunawan, Septina, W., Harada, T., Nose, Y., and Ikeda, S., 2015, Investigation of the electric structures of heterointerfaces in Pt- and In₂S₃-modified CuInS₂ photocathodes used for sunlight-induced hydrogen evolution, *ACS Appl. Mater. Interfaces*, 7 (29), 16086–16092.
- [25] Septina, W., Gunawan, Ikeda, S., Harada, T., Higashi, M., Abe, R., and Matsumura, M., 2015, Photosplitting of water from wide-gap Cu(In,Ga)S₂ thin films modified with a CdS layer and Pt nanoparticles for a high-onset-potential photocathode, *J. Phys. Chem. C*, 119 (16), 8576–8583.
- [26] Jiang, F., Gunawan, Harada, T., Kuang, Y., Minegishi, T., Domen, K., and Ikeda, S., 2015, Pt/In₂S₃/CdS/Cu₂ZnSnS₄ thin film as an efficient and stable photocathode for water reduction under sunlight radiation, *J. Am. Chem. Soc.*, 137 (42), 13691–13697.
- [27] Zarębska, K., and Skompska, M., 2011, Electrodeposition of CdS from acidic aqueous thiosulfate solution—Investigation of the mechanism by electrochemical quartz microbalance technique, *Electrochim. Acta*, 56 (16), 5731–5739.
- [28] Patil, B.N., Naik, D.B., and Shrivastava, V.S., 2011, Synthesis and characterization of Al doped CdS thin films grown by chemical bath deposition method and its application to remove dye by photocatalytic treatment, *Chalcogenide Lett.*, 8 (2), 117–121.
- [29] Zyoud, A., Saa'deddin, I., Khudruj, S., Hawash, Z.M., Park, D., Campet, G., and Hilal, H.S., 2013, CdS/FTO thin film electrodes deposited by chemical bath deposition and by electrochemical deposition: a comparative assessment of photoelectrochemical characteristics, *Solid State Sci.*, 18, 83–90.
- [30] Mir, F.A., Chattarjee, I., Dar, A.A., Asokan, K., and Bhat, G.M., 2015, Preparation and characterizations of cadmium sulfide nanoparticles, *Optik*, 126 (11-12), 1240–1244.
- [31] Dumbrava, A., Badea, C., Prodan, G., and Ciupina, V., 2010, Synthesis and characterization of cadmium sulphide obtained at room temperature, *Chalcogenide Lett.*, 7 (2), 111–118.

- [32] Rami, M., Benamar, E., Fahoume, M., Chraibi, F., and Ennaoui, A., 1999, Effect of the cadmium ion source on the structural and optical properties of chemical bath deposited CdS thin films, *Solid State Sci.*, 1 (4), 179–188.
- [33] Barote, M.A., Yadav, A.A., and Masumdar, E.U., 2011, Synthesis, characterization and photoelectrochemical properties of n-CdS thin films, *Physica B*, 406 (10), 1865–1871.
- [34] Yang, F., Tian, X., Zhang, K., Zhang, X., and Liu, L., 2018, The morphology–property effect and synergetic catalytic effect of CdS as electrocatalysts for dye-sensitized solar cells, *ECS J. Solid State Sci. Technol.*, 7 (6), P311–P316.
- [35] Yeh, C.Y., Lu, Z.W., Froyen, S., and Zunger, A., 1992, Zinc-blende–wurtzite polytypism in semiconductors, *Phys. Rev. B*, 46 (16), 10086–10097.
- [36] Ganesh, R.S., Sharma, S.K., Durgadevi, E., Navaneethan, M., Binitha, H.S., Ponnusamy, S., Muthamizhchelvan, C., Hayakawa, Y., and Kim, D.Y., 2017, Surfactant free synthesis of CdS nanospheres, microstructural analysis, chemical bonding, optical properties and photocatalytic activities, *Superlattices Microstruct.*, 104, 247–257.
- [37] Phuruangrat, A., Thongtem, T., and Thongtem, S., 2009, Characterization of cadmium sulfide nanorods prepared by the solvothermal process, *Mater. Lett.*, 63 (17), 1562–1565.
- [38] Alkire, R.C., Kolb, D.M., Lipkowsky, J., and Ross, P.N., 2010, *Photoelectrochemical Materials, and Energy Conversion Processes*, Wiley-VCH, Hoboken, New Jersey, USA.
- [39] Jiang, J.B., Huo, P., Wang, P., Wu, Y.Y., Bian, G.Q., Zhu, Q.Y., and Dai, J., 2014, Synthesis and photocurrent responsive properties of CdS/Se clusters integrated with methylviologen, *J. Mater. Chem. C*, 2 (14), 2528–2533.
- [40] Akpan, U.G., and Hameed, B.H., 2009, Parameters affecting the photocatalytic degradation of dyes using TiO₂-based photocatalysts: A review, *J. Hazard. Mater.*, 170 (2-3), 520–529.
- [41] Houas, A., Lachheb, H., Ksibi, M., Elaloui, E., Guillard, C., and Herrmann, J.M., 2001, Photocatalytic degradation pathway of methylene blue in water, *Appl. Catal., B*, 31 (2), 145–157.
- [42] Chen, Q., Bai, J., Li, J., Huang, K., Li, X., Zhou, B., and Cai, W., 2014, Aerated visible-light responsive photocatalytic fuel cell for wastewater treatment with producing sustainable electricity in neutral solution, *Chem. Eng. J.*, 252, 89–94.
- [43] Zhang, B., Fan, W., Yao, T., Liao, S., Li, A., Li, D., Liu, M., Shi, J., Liao, S., and Li, C., 2016, Design and fabrication of a dual-photoelectrode fuel cell towards cost-effective electricity production from biomass, *ChemSusChem*, 10 (1), 99–105.

Bismuth Oxide Prepared by Sol-Gel Method: Variation of Physicochemical Characteristics and Photocatalytic Activity Due to Difference in Calcination Temperature

Yayuk Astuti*, Brigita Maria Listyani, Linda Suyati, and Adi Darmawan

Department of Chemistry, Faculty of Science and Mathematics, Diponegoro University,
Jl. Prof. Soedharto SH, Tembalang, Semarang 50275, Indonesia

* **Corresponding author:**

email: yayuk.astuti@live.undip.ac.id

Received: January 4, 2020

Accepted: June 9, 2020

DOI: 10.22146/ijc.53144

Abstract: Research on synthesis of bismuth oxide (Bi_2O_3) using sol-gel method with varying calcination temperatures at 500, 600, and 700 °C has been done. This study aims to determine the effect of calcination temperature on the characteristics of the obtained products which encompasses crystal structure, surface morphology, band-gap energy, and photocatalytic activity for the decolorization of methyl orange dyes through its kinetic study. Bismuth oxide prepared by sol-gel method was undertaken by dissolving $\text{Bi}(\text{NO}_3)_3 \cdot 5\text{H}_2\text{O}$ and citric acid in HNO_3 . The mixture was stirred then heated at 100 °C. The gel formed was dried in the oven and then calcined at 500, 600, and 700 °C for 5 h. The obtained products were a pale yellow powder, indicating the formation of bismuth oxide. This is confirmed by the existence of Bi–O and Bi–O–Bi functional groups through FTIR analysis. All three products possess the same mixed crystal structures of $\alpha\text{-Bi}_2\text{O}_3$ (monoclinic) and $\gamma\text{-Bi}_2\text{O}_3$ (body center cubic), but their morphologies and band gap values are different. The higher the calcination temperature, the larger the particle size and the smaller the band gap value. The accumulative differences in characteristics appoint SG700 to have the highest photocatalytic activity compared to SG600 and SG500 as indicated by its percent degradation value and decolorization rate constant.

Keywords: bismuth oxide; sol-gel; calcination temperature; photocatalytic activity; photocatalyst

■ INTRODUCTION

Bismuth oxide (Bi_2O_3) is a semiconductor metal in the form of a yellow solid that has a melting point of around 825 °C [1]. Bismuth oxide has potential as a solid oxide fuel cell [2] and photocatalyst [3-5] since it has a wide band gap energy of 2–3.96 eV [6]. In general, bismuth oxide has six types polymorphs comprising of $\alpha\text{-Bi}_2\text{O}_3$ (monoclinic), $\beta\text{-Bi}_2\text{O}_3$ (tetragonal), $\gamma\text{-Bi}_2\text{O}_3$ (body-centered cubic), $\epsilon\text{-Bi}_2\text{O}_3$ (orthorhombic), $\delta\text{-Bi}_2\text{O}_3$ (face-centered cubic), and $\omega\text{-Bi}_2\text{O}_3$ (triclinic). The formation of $\alpha\text{-Bi}_2\text{O}_3$ is stable at low temperatures whereas $\delta\text{-Bi}_2\text{O}_3$ is stable at high temperatures; others have metastable crystal structures [7].

Bismuth oxide (Bi_2O_3) can be synthesized by several methods, including precipitation [8] or deposition [9], solution combustion [10-12], hydrothermal [13], and sol-gel methods [1]. In this study the sol-gel (SG) method was

applied with variations in calcination temperatures of 500, 600, and 700 °C. Among these methods, the sol-gel method has several advantages, including high purity, high degree of homogeneity because the reagents are mixed at the molecular level, synthesis at low temperatures because certain materials can be carried out at room temperature [14], no reaction with residual compounds and loss of material because evaporation can be reduced [15]. The sol-gel method is one of the “wet methods”, where changes occur from liquid precursors to sols and finally to a network of structure called 'gel' that will form a solid during calcination [16]. Calcination temperature has a significant effect on the crystallinity, structure and surface properties of the synthesized product because at the sol-gel method stage, heating plays an important role in the formation of

solids in which heat applied to some substances lead to chemical reactions or chemical changes which further lead to formation of one or more substances with different properties [17-18].

Xiaohong et al. [19] has synthesized bismuth oxide in the form of films using different variations of annealing temperature composed of monoclinic and tetragonal crystalline phases. The result showed that the photocatalytic activity of bismuth oxide on Rhodamine B dye degradation was the highest at 550 °C since it contained high tetragonal crystalline phase. Mallahi et al. [1] have synthesized bismuth oxide in the form of nanoparticles through the sol-gel method with calcination temperature variations of 200, 500, 800 °C and studied changes in the surface morphology of the synthesized surface. At these temperature variations, the crystals have an irregular pseudospheric surface shape and when the calcination temperature was raised to 800 °C, the particles acquired a lumpy shape. Exploration of the potential of bismuth oxide as a photocatalyst was not carried out in this study. In contrast to previous studies, this study was conducted to synthesize bismuth oxide through the sol-gel (SG) method with calcination temperature variations of 500, 600, and 700 °C and a 1:2 ratio of bismuth nitrate pentahydrate to citric acid. Citric acid is a weak triprotic acid with three carboxylic acid functional groups, capable of forming various complexes with metal ions. It is an effective chelating agent. When aqueous metal salts (e.g. nitrates) are added with citric acid and then heated, a viscous solution or gel is formed [16]. This study also determined the product's physico-chemical characteristics such as the crystal structure, morphology, band gap values, and investigated their photocatalytic properties in degrading organic dyes. The findings of this research are expected to contribute to the science of the effect of calcination temperature within the sol-gel method on the physicochemical characteristics and performance of bismuth oxide as a photocatalyst in the degradation of organic dyes.

■ EXPERIMENTAL SECTION

Materials

The materials used in this study were $\text{Bi}(\text{NO}_3)_3 \cdot 5\text{H}_2\text{O}$ from Sigma-Aldrich (white color powder

and soluble in dilute nitric acid solution), nitric acid (HNO_3) 65% from Merck (clear colorless liquid, strong acid), citric acid monohydrate from Merck (weak acid, colorless and odorless crystals with an acid taste), Polyethylene Glycol (PEG) 6000 from Merck (white color powder and odorless crystals), methyl orange (MO) from Merck (orange-yellow powder or crystalline scales), distilled water (purified water, applied as solvent, colorless and odorless liquid).

Procedure

Bismuth oxide synthesis

The synthesis of Bismuth oxide through the sol-gel method followed the method recommended by Mallahi et al. [1] with a slight modification. Synthesis of bismuth oxide by the sol-gel method was proceeded by preparing 4 g of $\text{Bi}(\text{NO}_3)_3 \cdot 5\text{H}_2\text{O}$ which was dissolved in a 50 mL nitric acid solution and mixed with citric acid solution with a molar ratio of 1:2. Subsequently, 1 g of PEG 6000 was added and the solution was heated to 90 °C for 20 h whilst being stirred at a moderate speed of 667 rpm. The solution was allowed to stand in an aging process (ripening) for 12 h to form a gel. The formed gel was then dried in an oven at 100 °C for 12 h. The calcination process was later carried out for 5 h with variations in temperature at 500, 600, and 700 °C (SG500, SG600, and SG700).

Characterization of synthesized bismuth oxide

Product characterizations were carried out using FTIR, XRD, SEM, and DRS-UV. Characterization using infrared spectroscopy was carried out using an ALPHA type FTIR BRUKER spectrometer with wavenumber in the range of 400–4000 cm^{-1} to determine the functional groups contained in the synthesized product. Meanwhile, characterization using XRD (XRD Bruker) was carried out by firing the sample with X-rays of a $\text{CuK}\alpha$ source that has a wavelength of 1.54178 Å and a voltage of 30.0 kV. The XRD patterns were collected at the diffraction angle range of $2\theta = 10\text{--}80^\circ$ with an angle step of 0.02°. The XRD patterns were then compared with the Joint Commission on Powder Diffraction Standards (JCPDS) data.

Morphological characterization of the samples was carried out using SEM (JEOL-JSM-6510LV) with an

energy range of 0–20 keV, a voltage of 20.0 kV, and a calculating speed of 2729 cps. The UV-Vis spectra was collected using the UV 1700 Pharmaspec DRS-UV instrument with wavelength of 200–800 nm to obtain the R values. The R values were then processed by using the Kubelka Munk method to determine the band gap value.

Photocatalytic activity test

A total of 0.1 g of bismuth oxide sample (SG500) was put into 50 mL of 5 ppm methyl orange solution and the solution was stirred at a medium speed of 667 rpm. The stirring process was carried out for 2 h for photocatalyst test without light, while photocatalyst test with light was carried out using UV-A (352 nm) with 15 watts of power and time variations of 60, 90, 120, 150, and 180 min. After photocatalysis, the solution was filtered and the filtrate was then analyzed using UV-Vis spectroscopy at a wavelength of 463 nm. This procedure was applied to products SG600 and SG700. A schematic of the photocatalysis reactor is shown in Fig. 1.

RESULTS AND DISCUSSION

Bismuth Oxide Synthesis

The synthesis of bismuth oxide involved the use of sol-gel method with bismuth nitrate pentahydrate ($\text{Bi}(\text{NO}_3)_3 \cdot 5\text{H}_2\text{O}$) as a precursor, citric acid as a complexing agent and HNO_3 as a solvent. In addition, polyethylene glycol (PEG 6000) was also added as a dispersing agent that prevents agglomeration or clumping of products [20]. The sol-gel reaction initially occurred with the formation of a citrate-metal complex that reacted to form chelates with the addition polyethylene glycol

assisted by stirring and heating at a temperature of around 90 °C. This would enable cross-linking to occur and form a gel through an esterification process [21]. The formed gel was dried in an oven at 100 °C for 12 h to remove remaining solvent in the synthesized product. The obtained result was a swollen yellowish brown xerogel. The xerogel was then calcined in a furnace to obtain yellow powder with different masses of 1.635, 1.683, and 1.587 g for SG500, SG600 and SG700, respectively (see Fig. 2). The weight difference among the products is insignificant even though the degradation of elements derived from PEG 6000, citric acid and nitric acid indeed occurred due to the high calcination temperature. This can be identified by the absence of functional groups of those compounds observed in FTIR spectra as presented in Fig. 3. Moreover, the yellow color possessed by the three samples signified that bismuth oxide had formed [22].

The three products (SG500, SG600, SG700) were further analyzed using FTIR to identify the presence of vibration group of Bi–O or Bi–O–Bi functional groups.

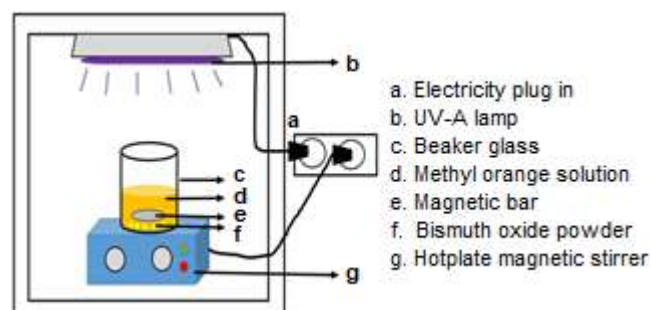


Fig 1. Scheme of a photocatalysis reactor used in the photocatalysis process

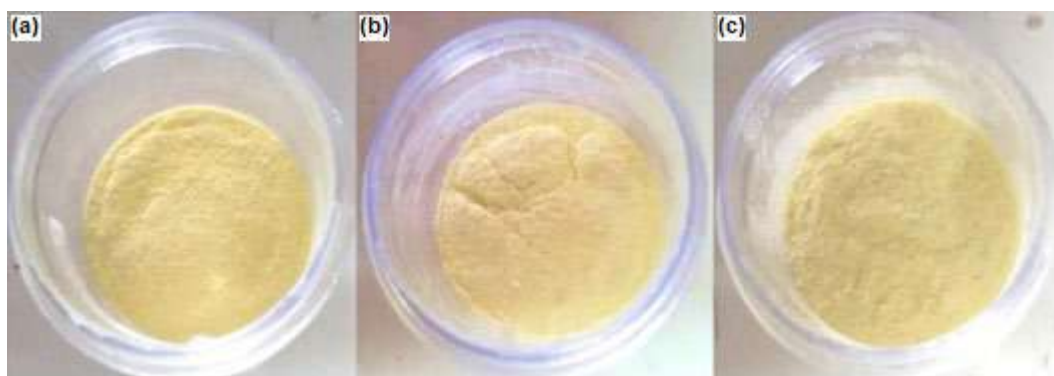


Fig 2. Powders of synthesized bismuth oxide: (a) SG500; (b) SG600; (c) SG700

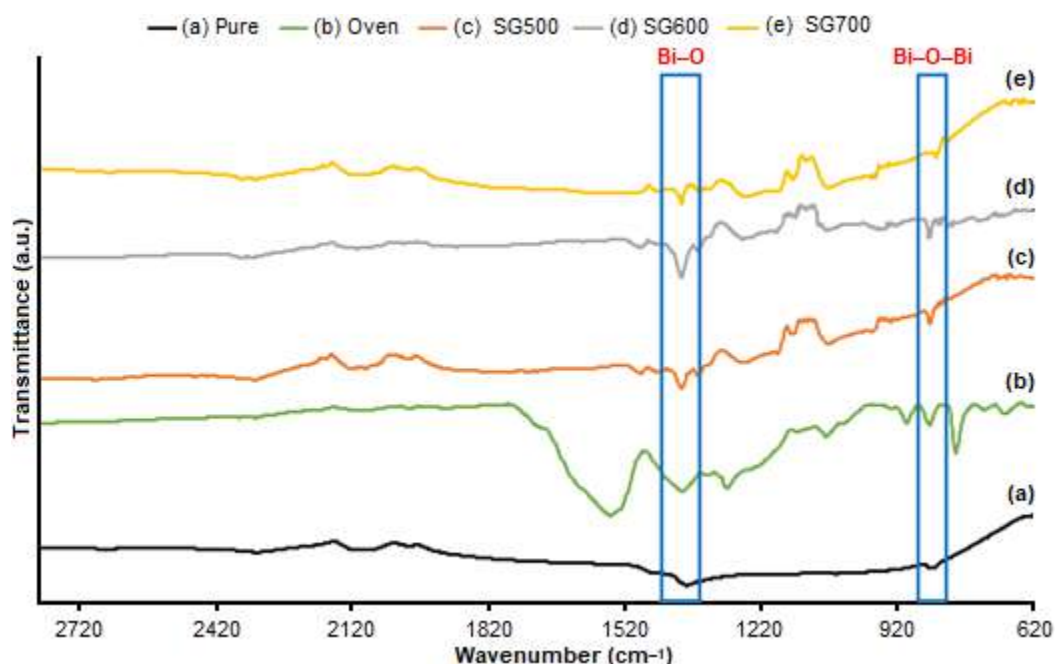


Fig 3. FTIR spectra of bismuth oxide: (a) pure [12]; (b) oven, (c) SG500; (d) SG600; (e) SG700

Fig. 3(c), (d), and (e) show the respective bismuth oxide FTIR spectra of SG500, SG600 and SG700. FTIR spectra show absorbances at around 848, 850, and 834 cm^{-1} indicating the symmetrical stretching of Bi–O–Bi bonds [23–25]. In addition, the wavenumber 1394 cm^{-1} points to the stretching vibration of the Bi–O bond [25]. These spectra indicate that bismuth oxide has formed. These results are also confirmed by the pure bismuth FTIR spectrum in Fig. 3(a) showing similar absorption patterns at wavenumbers around 840 and 1384 cm^{-1} [12].

In addition, the content of the Bi–O–Bi functional groups in each product can be predicted through a comparison approach between the peak absorbance of 840 cm^{-1} attributed to vibration mode of Bi–O–Bi and 2100 cm^{-1} as control (constant wavenumber). Peak at 2100 cm^{-1} was applied as control since it was observed at every sample. Table 1 shows that bismuth oxide SG700 has the highest absorbance ratio value for the Bi–O–Bi group.

The high ratio of Bi–O–Bi on the SG700 is due to the high calcination temperature applied followed by SG600 and SG500. Calcination temperature influences the formation of Bi_2O_3 . As shown in Fig. 4, the SG500 shows rough X-ray diffraction patterns indicating an imperfect crystal growth and as the temperature rises, the X-ray diffraction pattern becomes smoother as seen in the SG600 and SG700. Therefore, increasing the calcination temperature improved the crystallinity of the product. This also occurred in the synthesis of bismuth oxides doped with Europium [26] and Co_3O_4 [27].

Characteristics of Synthesized Bismuth Oxides

Crystal structure

The crystal structure of the synthesized bismuth oxide was identified using XRD. The XRD patterns were obtained and identified by comparing some of the highest peaks of the samples with peaks from the JCPDS

Table 1. Comparison of Bi–O–Bi bond and control absorbance ratios of the three products

	Bi–O–Bi Group (840 cm^{-1})	Control Group (2100 cm^{-1})	Bi–O–Bi/Control Ratio
Pure	0.0828	0.0611	1.3554
SG500	0.0535	0.1064	0.5032
SG600	0.0314	0.0439	0.7162
SG700	0.0653	0.0850	0.7684

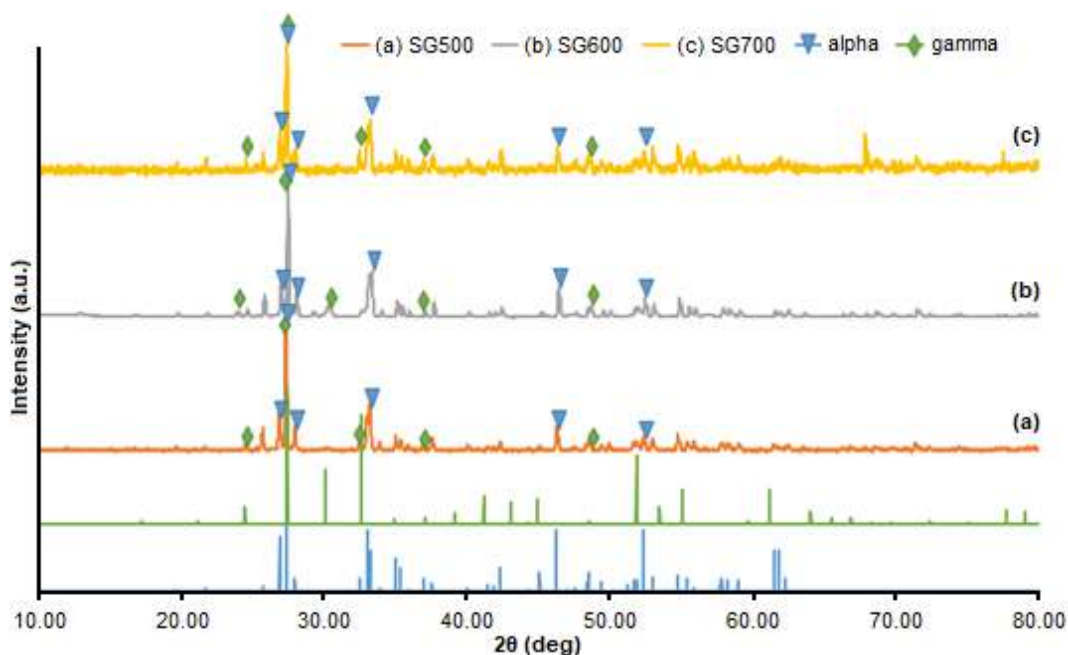


Fig 4. The XRD patterns of (a) SG500, (b) SG600, and (c) SG700 along with JCPDS database No. 41-1449 and 45-1344

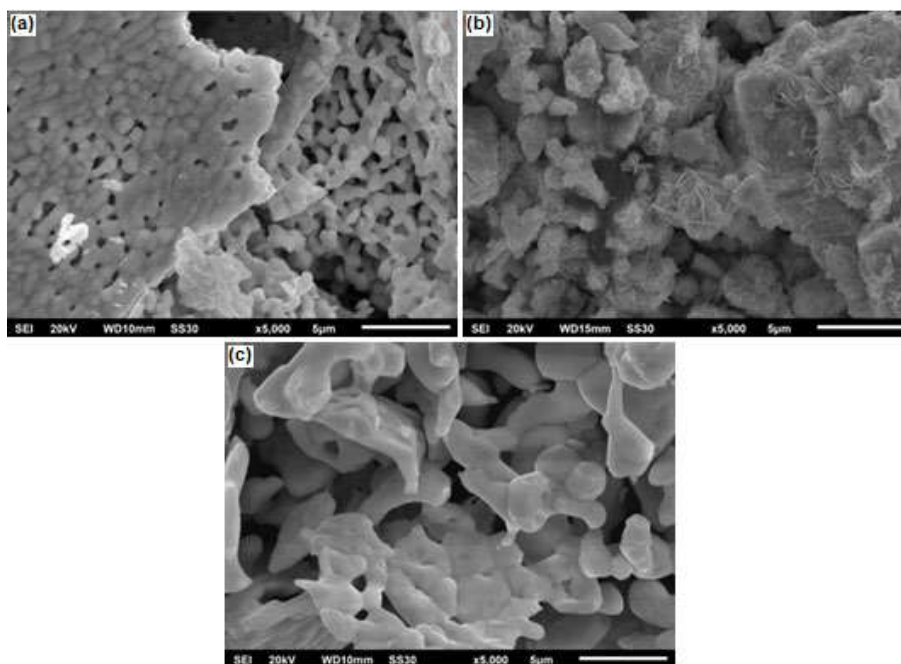


Fig 5. SEM images of bismuth oxide with 5000× magnification (a) SG500; (b) SG600; (c) SG700

database under the numbers 41-1449 for α - Bi_2O_3 and 45-1344 for γ - Bi_2O_3 . Fig. 4 shows that bismuth oxide SG500 has α - Bi_2O_3 (monoclinic) crystal structure while SG600 and SG700 have the same mixed crystal structure of α - Bi_2O_3 (monoclinic) and γ - Bi_2O_3 (body-centered cubic).

Morphology

Fig. 5(a) shows the crystal morphology of the SG500 bismuth oxide which has an irregular shape with a size of about 0.49–2.92 μm . Fig. 5(b) shows irregular shape with whiskers-like form on the surface of the

bismuth oxide SG600 crystal with uneven distribution of sizes, which are around 1.54–4.61 μm . Fig. 5(c) shows the morphology of the SG700 bismuth oxide crystal surface which resembles a coral reef with an irregular shape and larger particle surface of about 0.71–6.30 μm in which the surface of the particle is smoother than bismuth oxide SG600.

Band-gap energy value

Fig. 6 shows that the bismuth oxides of SG500, SG600 and SG700 have band gap energy values of 2.85, 2.80, and 2.77 eV, respectively. Based on the band-gap energy value, it can be explained that a higher calcination temperature would result in the decrease of the band-gap energy. According to Cheng et al. [28], $\alpha\text{-Bi}_2\text{O}_3$ has a band-gap energy value of 2.81 eV. This is consistent with the XRD patterns in Fig. 4 that depict the presence of a mixture of $\alpha\text{-Bi}_2\text{O}_3$ and $\gamma\text{-Bi}_2\text{O}_3$ crystals. However, the DRS-UV analysis results show that the $\alpha\text{-Bi}_2\text{O}_3$ content was more dominant than $\gamma\text{-Bi}_2\text{O}_3$. All products contain $\alpha\text{-Bi}_2\text{O}_3$ since this polymorph is the most stable at room temperature. The band gap difference among the products

is due to the presence of other polymorphs. As reported by Hou et al. [29], the combined polymorph affects the band gap. The small band gap in the SG600 is possibly due to more $\gamma\text{-Bi}_2\text{O}_3$ content than other products which can be seen in the XRD patterns in Fig. 4(b) at the peak 2θ 30.124. While, $\alpha\text{-Bi}_2\text{O}_3$ in the SG500 is dominant since the calcination temperature is temperature at which $\alpha\text{-Bi}_2\text{O}_3$ is formed.

Photocatalytic Test

The photocatalytic activity of the bismuth oxide SG500, SG600 and SG700 is shown in Fig. 7. Fig. 7(a) shows the UV-Vis spectra of methyl orange that has been decolorized by the three products over a 180 minute time span; whereas Fig. 7(b) shows the percentage of decolorization of MO dyes by bismuth oxides SG500, SG600, and SG700. In Fig. 7(a) and 7(b), SG700 displays better photocatalytic activity compared to the other two products because it is able to reduce the highest concentration of methyl orange. This is because bismuth oxide SG700 has a higher Bismuth oxide content (see Fig. 3) and has the lowest band gap energy

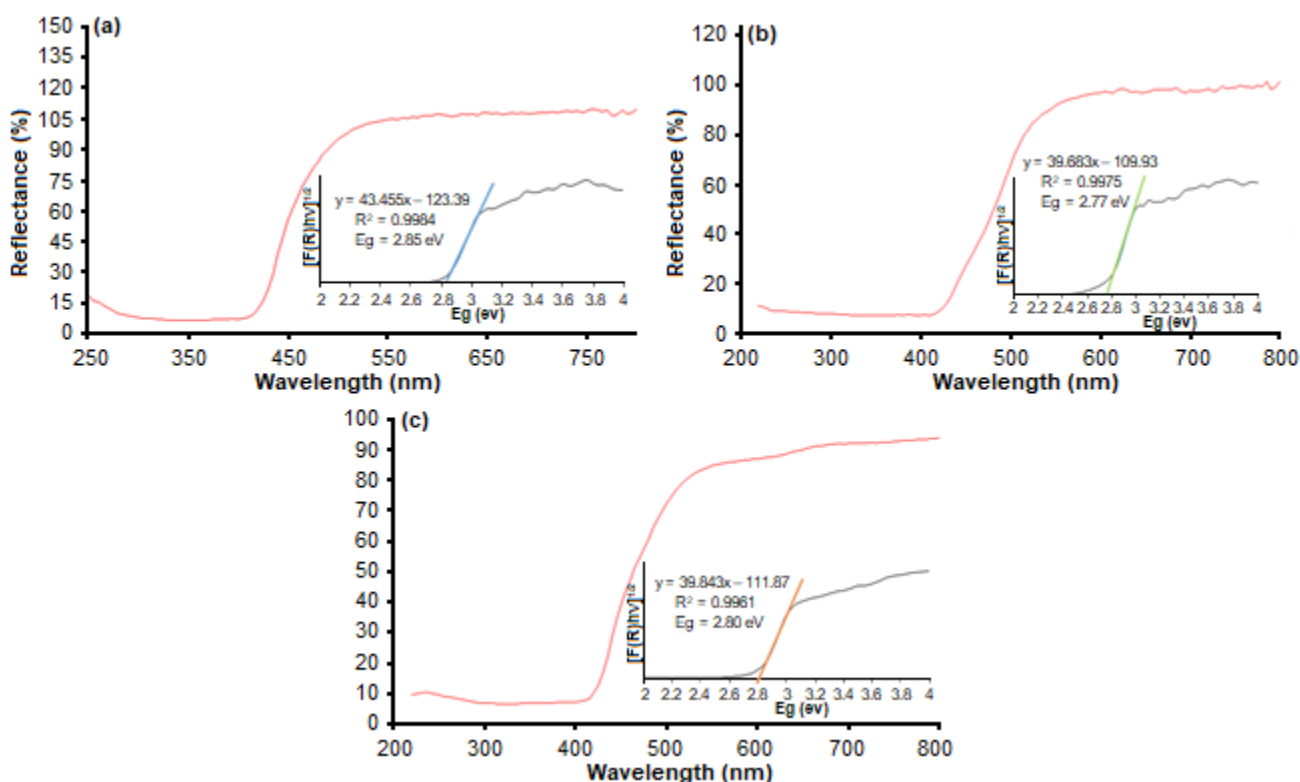


Fig 6. DR Spectra of (a) SG500, (b) SG600, (c) SG700

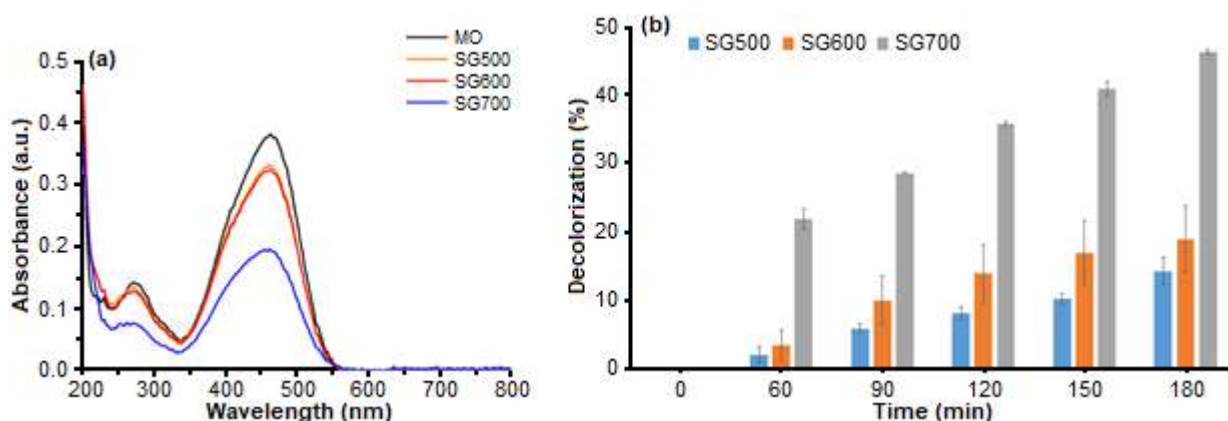


Fig 7. (a) UV-Vis Spectra of MO photocatalyzed for 180 min; (b) Decolorization percentages of MO dye

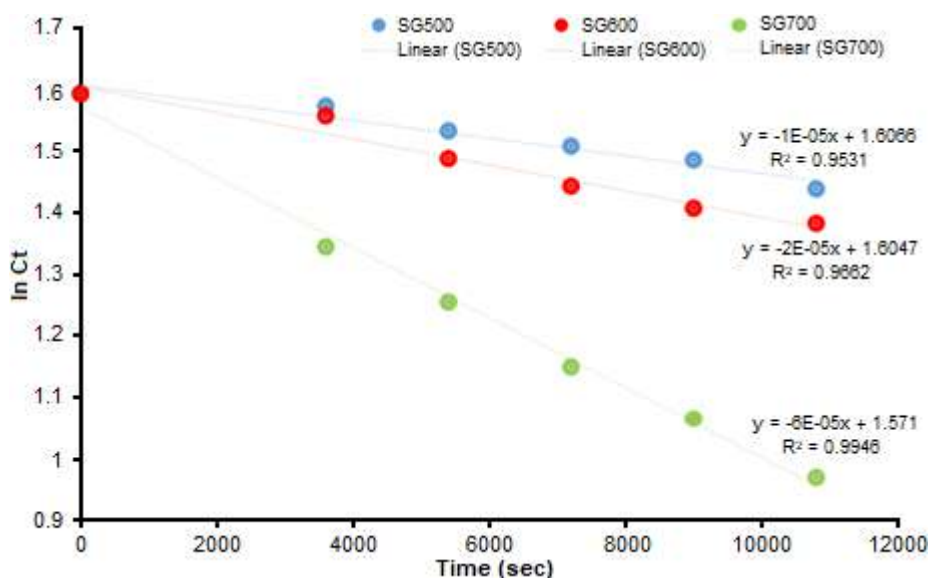


Fig 8. The first-order kinetic decolorization rate of methyl orange

value compared to the others as shown in Fig. 6. The smaller the band gap energy value of a compound or element, the easier the electrons are able to be excited resulting in a more impactful photocatalyst effect. In addition to band gap energy, bismuth oxide SG700 contains a mixture of α - Bi_2O_3 and γ - Bi_2O_3 polymorphs (see Fig. 4). It has been mentioned previously that the combination of the two crystalline phase structures could increase the photocatalytic activity of bismuth oxide in the degradation of dyes [29].

To identify bismuth oxide is inactive as photocatalyst when the light is off, a photocatalytic test was also performed without the exposure of light for 2 h. The test was also intended to discern the amount of methyl orange adsorbed by bismuth oxide. The

percentage of methyl orange decolorization after 2 h without light in the presence of bismuth oxides SG500, SG600 and SG700 were 1.229, 0.983, and 0.368%, respectively. These results indicate that MO dyes are not easily decolorized in a state without irradiation of light. The difference in adsorption activity for each sample is due to the morphological difference especially particle size as depicted by SEM images in Fig. 5. The SG500 has the highest adsorption activity since having the smallest particle size range followed by SG600 and SG 700. The smaller the particle size the higher the surface area consequently the higher the adsorption activity.

The photocatalytic activity of synthesized bismuth oxide on MO dyes can be determined using decolorization rate calculations through chemical

kinetics studies. Generally, the decolorization activity of dyes follows the kinetics of first-order reactions [8,12,30-32] expressed by the formula:

$$\ln C_t = \ln C_0 - kt$$

with k = the reaction rate constant in the first order (s^{-1}), C_0 = initial concentration of methyl orange solution (ppm), and C_t = concentration of methyl orange solution (ppm) at time t . This approach is substantiated by comparing the value of the correlation coefficient (R^2) between the methyl orange decolorization rate graphs and applying the integral equation of first and second order decolorization rates.

The values of the decolorization rates of methyl orange by bismuth oxides SG500, SG600, and SG700 (see Fig. 8) are $1.43 \times 10^{-5} s^{-1}$; $2.11 \times 10^{-5} s^{-1}$; and $5.69 \times 10^{-5} s^{-1}$, respectively. Based on the value of the decolorization rate constant, bismuth oxide SG700 has the highest reaction rate constant.

■ CONCLUSION

The variation of calcination temperature in bismuth oxide synthesis affects the characteristics of the product obtained. In this study, the effects of calcination temperatures of 500, 600 and 700 °C on bismuth oxide synthesis were investigated. Bismuth oxide calcined at 700 °C contained the highest Bi-O-Bi functional groups and a mixture of α - Bi_2O_3 (monoclinic) and γ - Bi_2O_3 (body-centered cubic) with a low band gap energy value. This characteristics led to bismuth oxide SG700 to have the highest photocatalytic activity even though the particle size is greater than others.

■ ACKNOWLEDGMENTS

The authors would like to thank the Faculty of Natural Sciences and Mathematics and Diponegoro University for the financial support with grant number No. 1644a/UN7.5.8/PP/2017 and 831.1-05/UN7.P4.3/PP/2019 (scheme of *Riset Publikasi Internasional (RPI)*), respectively.

■ REFERENCES

- [1] Mallahi, M., Shokuhfar, A., Vaezi, M.R., Esmaeilrad, A., and Mazinani, V., 2014, Synthesis and characterization of bismuth oxide nanoparticles via sol-gel method, *Am. J. Eng. Res.*, 3 (4), 162–165.
- [2] Sammes, N.M., Tompsett, G.A., Näfe, H., and Aldinger, F., 1999, Bismuth based oxide electrolytes—Structure and ionic conductivity, *J. Eur. Ceram. Soc.*, 19 (10), 1801–1826.
- [3] Weidong, H., Wei, Q., Xiaohong, W., Xianbo, D., Long, C., and Zhaohua, J., 2007, The photocatalytic properties of bismuth oxide films prepared through the sol-gel method, *Thin Solid Films*, 515 (13), 5362–5365.
- [4] Zhang, L., Ghimire, P., Phuriragpitikhon, J., Jiang, B., Gonçalves, A.A.S, and Jaroniec, M., 2018, Facile formation of metallic bismuth/bismuth oxide heterojunction on porous carbon with enhanced photocatalytic activity, *J. Colloid Interface Sci.*, 513, 82–91.
- [5] Reverberi, A.P., Varbanov, P.S., Vocciante, M., and Fabiano, B., 2018, Bismuth oxide-related photocatalysts in green nanotechnology: A critical analysis, *Front. Chem. Sci. Eng.*, 12 (4), 878–892.
- [6] Jiang, H.Y., Li, P., Liu, G., Ye, J., and Lin, J., 2015, Synthesis and photocatalytic properties of metastable β - Bi_2O_3 stabilized by surface-coordination effects, *J. Mater. Chem. A*, 3 (9), 5119–5125.
- [7] Yilmaz, S., Turkoglu, O., Ari, M., and Belenli, I., 2011, Electrical conductivity of the ionic conductor tetragonal $(Bi_2O_3)_{1-x}(Eu_2O_3)_x$, *Cerâmica*, 57 (342), 185–192.
- [8] Astuti, Y., Andianingrum, R., Arnelli, A., Haris, A., and Darmawan, A., 2020, The role of $H_2C_2O_4$ and Na_2CO_3 as precipitating agents on the physicochemical properties and photocatalytic activity of bismuth oxide, *Open Chem.*, 18 (1), 129–137.
- [9] Hernandez-Delgadillo, R., Velasco-Arias, D., Martinez-Sanmiguel, J.J., Diaz, D., Zumeta-Dube, I., Arevalo-Niño, K., and Cabral-Romero, C., 2013, Bismuth oxide aqueous colloidal nanoparticles inhibit *Candida albicans* growth and biofilm formation, *Int. J. Nanomed.*, 8, 1645–1652.

- [10] La, J., Huang, Y., Luo, G., Lai, J., Liu, C., and Chu, G., 2013, Synthesis of bismuth oxide nanoparticles by solution combustion method, *Part. Sci. Technol.*, 31 (3), 287–290.
- [11] Astuti, Y., Fauziyah, A., Widiyandari, H., and Widodo, D.S., 2019, Studying impact of citric acid-bismuth nitrate pentahydrate ratio on photocatalytic activity of bismuth oxide prepared by solution combustion method, *Rasayan J. Chem.*, 12 (4), 2210–2217.
- [12] Astuti, Y., Elesta, P.P., Widodo, D.S., Widiyandari, H., and Balgis, R., 2020, Hydrazine and urea fueled-solution combustion method for Bi₂O₃ synthesis: Characterization of physicochemical properties and photocatalytic activity, *Bull. Chem. React. Eng. Catal.*, 15 (1), 104–111.
- [13] Wu, C., Shen, L., Huang, Q., and Zhang, Y.C., 2011, Hydrothermal synthesis and characterization of Bi₂O₃ nanowires, *Mater. Lett.*, 65 (7), 1134–1136.
- [14] Amiri, A., 2016, Solid-phase microextraction-based sol-gel technique, *TrAC, Trends Anal. Chem.*, 75, 57–74.
- [15] Pinjari, D.V., Prasad, K., Gogate, P.R., Mhaske, S.T., and Pandit, A.B., 2015, Synthesis of titanium dioxide by ultrasound assisted sol-gel technique: effect of calcination and sonication time, *Ultrason. Sonochem.*, 23, 185–191.
- [16] Danks, A.E., Hall, S.R., and Schnepf, Z., 2016, The evolution of ‘sol-gel’ chemistry as a technique for materials synthesis, *Mater. Horiz.*, 3 (2), 91–112.
- [17] Messel, H., 2014, *Abridged Science for High School Students: The Nuclear Research Foundation School Certificate Integrated*, Vol. II, Elsevier, London, UK.
- [18] Miedema, A.R., Boom, R., and De Boer, F.R., 1975, On the heat of formation of solid alloys, *J. Less Common. Met.*, 41 (2), 283–298.
- [19] Xiaohong, W., Wei, Q., and Weidong, H., 2007, Thin bismuth oxide films prepared through the sol-gel method as photocatalyst, *J. Mol. Catal. A: Chem.*, 261 (2), 167–171.
- [20] Jiang, Z., and Wang, Y., 2015, Preparation of porous bismuth oxide by sol-gel method using citric acid, *Material Science and Environmental Engineering: Proceedings of the 3rd Annual 2015 International Conference on Material Science and Environmental Engineering (ICMSEE2015)*, Wuhan, Hubei, China, 5-6 June 2015.
- [21] Dimesso, L., 2016, “Pechini processes: An alternate approach of the sol-gel method, preparation, properties, and applications” in *Handbook of Sol-Gel Science and Technology*, Springer, Cham, Switzerland, 1–22.
- [22] Eastaugh, N., Walsh, V., Chaplin, T., and Siddall, R., 2008, *Pigment Compendium: A Dictionary and Optical Microscopy of Historical Pigments*, Routledge, London, UK.
- [23] Selvapandiyani, M., and Sathiyaraj, K., 2019, Synthesis, preparation, structural, optical, morphological and elemental analysis of bismuth oxides nanoparticles, *Silicon*, 1–7.
- [24] Bartonicikova, E., Cihlar, J., and Castkova, K., 2007, Microwave-assisted synthesis of bismuth oxide, *Process. Appl. Ceram.*, 1 (1-2), 29–33.
- [25] Bandyopadhyay, S., and Dutta, A., 2017, Thermal, optical and dielectric properties of phase stabilized δ -Dy-Bi₂O₃ ionic conductors, *J. Phys. Chem. Solids*, 102, 12–20.
- [26] Zhong, S., Zou, S., Peng, X., Ma, J., and Zhang, F., 2015, Effects of calcination temperature on preparation and properties of europium-doped bismuth oxide as visible light catalyst, *J. Sol-Gel Sci. Technol.*, 74 (1), 220–226.
- [27] Zhang, G., Hu, L., Wang, P., and Yuan, Y., 2017, The effect of calcination temperature on the performance of Co₃O₄-Bi₂O₃ as a heterogeneous catalyst of peroxy monosulfate, *IOP Conf. Ser.: Earth Environ. Sci.*, 94, 012029.
- [28] Cheng, H., Huang, B., Lu, J., Wang, Z., Xu, B., Qin, X., Zhang, X., and Dai, Y., 2010, Synergistic effect of crystal and electronic structures on the visible-light-driven photocatalytic performances of Bi₂O₃ polymorphs, *Phys. Chem. Chem. Phys.*, 12 (47), 15468–15475.
- [29] Hou, J., Yang, C., Wang, Z., Zhou, W., Jiao, S., and Zhu, H., 2013, In situ synthesis of α - β phase heterojunction on Bi₂O₃ nanowires with

- exceptional visible-light photocatalytic performance, *Appl. Catal., B*, 142-143, 504–511.
- [30] Liu, X., Deng, H., Yao, W., Jiang, Q., and Shen, J., 2015, Preparation and photocatalytic activity of Y-doped Bi₂O₃, *J. Alloys Compd.*, 651, 135–142.
- [31] Wang, Q., Hui, J., Yang, L., Huang, H., Cai, Y., Yin, S., and Ding, Y., 2014, Enhanced photocatalytic performance of Bi₂O₃/H-ZSM-5 composite for rhodamine B degradation under UV light irradiation, *Appl. Surf. Sci.*, 289, 224–229.
- [32] Astuti, Y., Amri, D., Widodo, D.S., Widiyandari, H., Balgis, R., and Ogi, T., 2020, Effect of fuels on the physicochemical properties and photocatalytic activity of bismuth oxide, synthesized using solution combustion method, *Int. J. Technol.*, 11 (1), 26–36.

Assessing the Effect of Weak and Strong Acids as Electrolytes in the Removal of Cesium by Soil Electrokinetic Remediation

Rudy Syah Putra^{1,2,*}, Alfi Ihda Amalia¹, and Naila Zahrotul Jannah¹

¹Department of Chemistry, Faculty of Mathematics and Natural Sciences, Universitas Islam Indonesia, Jl. Kaliurang km. 14, Yogyakarta 55584, Indonesia

²Environmental Remediation Research Group, Department of Chemistry, Faculty of Mathematics and Natural Sciences, Universitas Islam Indonesia, Jl. Kaliurang km. 14, Yogyakarta 55584, Indonesia

* **Corresponding author:**

tel: +62-81327709104

email: rudy.syahputra@uii.ac.id

Received: January 8, 2020

Accepted: May 28, 2020

DOI: 10.22146/ijc.53283

Abstract: The removal of cesium from artificially contaminated soil using electrokinetic remediation with nitric and acetic acid as electrolytes had been evaluated. In this study, uncontaminated soil was taken from four different sampling points (i.e., A, B, C, and D) in Kotagede, Yogyakarta, Indonesia. All samples were prepared as cesium contaminated soil (100 mg CsCl/kg soil), which have similar physicochemical characteristics with Fukushima soil, Japan. The electrokinetic remediation (EKR) was conducted using a graphite electrode in a constant voltage of 1.0 Vcm⁻¹ for 7 days without electrolyte pH control, with 1.0 M nitric and acetic acid as electrolytes. The current profile during the EKR was recorded by a data logger for every 10 min. The remaining cesium in the soil was measured by a flame atomic absorption spectrophotometer at a wavelength of 852.1 nm. The results showed that the type of acid used in the experiments affected the removal of cesium. The highest cesium removal was achieved when nitric acid was used in the experiment and then followed by acetic acid. For all acids, the removal ability of cesium from soil was in the following order: soil C > soil A > soil D > soil B.

Keywords: cesium; electrokinetic remediation; Fukushima; soil

■ INTRODUCTION

The rapid growth of the economic sector has caused Indonesia to experience a serious power shortage. Power consumption grows as the industry grows, which means that there must be more electricity to be produced. By an industrial production growth rate of 10.5%, the electricity demand is estimated to reach 450 billion kWh in 2026 [1]. Under these circumstances, it is hardly a surprise that nuclear plants would not be left out of the government plan for the electrification of the country. On November 30th, 2011, the Minister of State-Owned Enterprises of the Republic of Indonesia had adopted a long-term plan for the development of nuclear energy in Indonesia [2]. Fear of accidents in nuclear power plants is a major factor that led many to oppose the construction of nuclear power plants in Indonesia. The fear comes from the history of several cases involving nuclear energy, including the

Chernobyl and Fukushima accidents [3-4], which led to adsorption of Cs-137 into the soil that persisted for many years resulting in the restriction of the land to be reused as agricultural land. In addition, the development of a nuclear power plant has a possibility to release radionuclide to the environment that imposes a strict requirement on the development of a cost-effective method to remove radionuclides from contaminated soils [5]. Several technologies have been developed for remediation of contaminated soil, which includes bioremediation [6], thermal desorption [7], soil leaching [8], and electrokinetic remediation [9].

Electrokinetic remediation is one of the promising technologies that can be used to separate and extract heavy metals, radionuclides, and organic contaminants from saturated or unsaturated soils, sludges and sediments, and groundwater. When an electric field is applied to the soil, the water electrolysis induce H⁺ and

OH^- ions at the anode and cathode electrode. In addition, the electrokinetic transport phenomena include the movement of water (electroosmosis), ions and polar molecules (electromigration), and charged solid particles (electrophoresis) formed between two electrodes [5,9]. These processes, together, are referred to as electrokinetics and can be used to remediate contaminated soil in place without excavation.

The advantages of electrokinetic remediation have been reported in numerous studies [3,9] as follows (1) applicability to specific low permeability contaminated soils that have high adsorption of pollutants (e.g., clays, silts, and layers) and groundwater. These soils are resistant to clean using common in-situ remedial techniques, such as pump-and-treat method which require a hydraulic gradient to be efficient in the process; (2) flow direction of the fluid in the soil is highly controlled, unlike in the soil flushing process; (3) can be used in a wide range removal of contaminants such as heavy metals, radionuclides, and organic compounds; and (4) the treatment has a low electric power consumption.

The objective of this study is to evaluate the feasibility of the electrokinetic remediation on the removal of cesium from artificially contaminated soils from Kotagede, Yogyakarta, Indonesia. These soil samples have similar physicochemical characteristics with Fukushima soil. In addition, the investigation of acids effect (e.g., nitric acid and acetic acid) as enhancing agents, and the optimum condition for the efficient removal were also evaluated. Therefore, a safer experiment was carried out for feasibility application in a real radionuclide contaminated soil in the future. Obtained results from this study can be used to predict the possible application of the technology for soil remediation at actual conditions in Fukushima.

■ EXPERIMENTAL SECTION

Materials

Cesium chloride was purchased from Wako Chemical, Japan, while nitric and acetic acid were purchased from Merck, Germany, without further purification.

Instrumentation

Minerals characteristic in the soil were measured by X-ray benchtop diffractometer (Bruker D2 Phaser, Germany) using $\text{CuK}\alpha$ radiation over a 2θ range from 5 to 80° with a step size of 0.02° at a scanning speed of $0.4^\circ/\text{sec}$. Reference patterns from the ICDD PDF database were used for qualitative phase identification of minerals in each soil. The remaining concentration of cesium in the soil was extracted using concentrated nitric acid, and then cesium concentration in the solution was determined by flame atomic absorption spectrophotometry (Perkin-Elmer, PinAAcle 900T, USA) at wavelength of 852.1 nm.

Procedure

Collection and preparation of soil

Clean soil samples were collected from four different locations at Kotagede district in Yogyakarta, Indonesia (i.e., GPS for soil A: $\text{S}07^\circ49,291'$ $\text{E}110^\circ23,996'$, soil B: $\text{S}07^\circ49,627'$ $\text{E}110^\circ23,895'$, soil C: $\text{S}07^\circ49,578'$ $\text{E}110^\circ23,878'$, soil D: $\text{S}07^\circ49,589'$ $\text{E}110^\circ23,713'$). Measurement of the soil properties was described in a reported paper elsewhere [10]. All soils from Kotagede were artificially contaminated by 100 mg/kg cesium (i.e., CsCl salts) and treated by five cycles (1 cycle for 2 weeks) of saturation process and air-dried before being aged for five months.

For Fukushima soil, Japan, the samples were collected from two different locations, which were Sarukubo soil, Kawamata ($\text{N} 37.67127$ $\text{E} 140.64745$), and Haramaci soil, Minamisoma ($\text{N} 37.63820$ $\text{E} 141.00637$). At the time of sampling in October 2011, the soil had been contaminated with radiocesium of about $0.3 \mu\text{S}/\text{h}$ for the Sarukubo soil and $0.1 \mu\text{S}/\text{h}$ for the Haramaci soil.

Electrokinetic remediation (EKR) treatment

A series of bench-scale EKR experiments were conducted according to a previous paper [10]. The electrokinetic remediation setup is shown in Fig. 1. The testing box consists of three major parts, a soil chamber and two electrode compartments. The EKR reactor contained 200 g of soil and was well connected to the electrode in both ends. Graphite electrodes were used

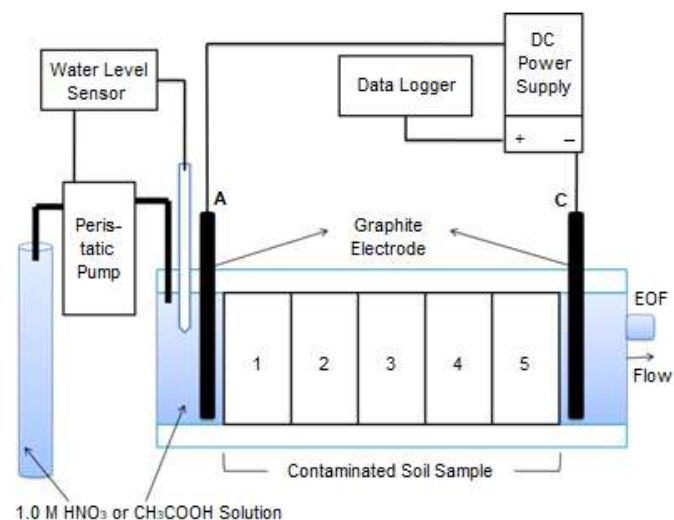


Fig 1. Electrokinetic remediation set up reactor used in this study

for the cathode (C) and anode (A). In this study, nitric acid and acetic acid were used as an electrolyte. A 1.0 V cm^{-1} of potential gradient was applied for 7 days of experiment [10]. The electric currents were monitored by a data logger (GL200A, Graphtec USA) for every 10 min. After the experiment, the soil was sectioned into five parts, and the soil pH was measured by mixing 0.5 g soil with 10 mL of distilled water and stirring for 30 min. The remaining cesium was extracted from soil by mixing about 0.5 g soil with 10 mL of 65% HNO_3 and then shaking it for 24 h.

■ RESULTS AND DISCUSSION

Soil Characterization

The similarity of Kotagede and Fukushima soils were in terms of soil texture, soil properties, and mineral content. All soil samples from Kotagede have the same texture with Fukushima soil and was characterized as sandy loam, and they all have high CEC values and organic matter content. In addition, soils A and C were relatively easy to acidify compared to soils B and D [10]. Qualitatively, the mineralogy of soil from Kotagede was identified by comparing 2θ diffractograms of reported studies [11]. The major mineral characteristic of soils A, B, C, and D based on the diffractogram were silica (quartz), dolomite, kaolinite, lawsonite, and muscovite. Meanwhile, the major mineral composition in the Fukushima soils were silica (quartz), kaolinite, lawsonite,

and muscovite. Kaolinite was one of the minerals that would bond strongly with cesium [12]. Therefore, in this regard, the soil from Kotagede was quite like Fukushima soil. The soil properties of Kotagede and Fukushima were summarized, as shown in Table 1.

Distribution of pH after EKR Treatment

The application of direct current via electrodes resulted in oxidation at the anode, generating the acid front, while reduction at the cathode produced a base front as shown by Eq. (1) and Eq. (2). Therefore, oxidation and reduction in the electrode resulted in the pH profiles during the EKR treatment. The initial pH of soil A, B, C, and D were 7.7, 7.8, 6.9, 7.4, respectively. Fig. 2 shows the distribution of soil pH when HNO_3 and

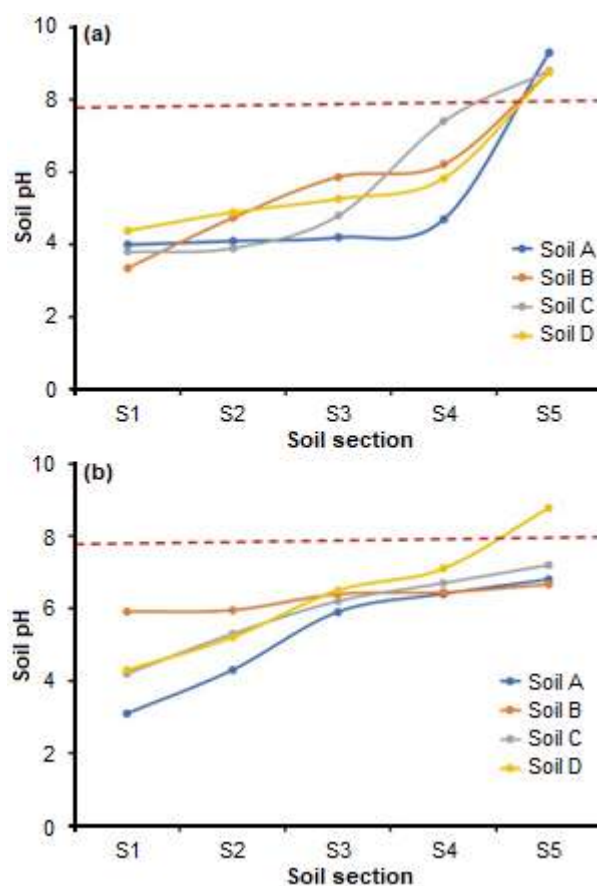


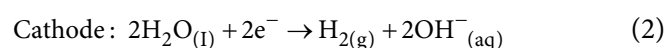
Fig 2. Soil pH profiles in after EKR used 1.0 M HNO_3 (a) and CH_3COOH (b) as electrolyte. S1 was compartment near the anode and S5 was compartment near the cathode. The red line indicated the initial pH in the soil before EKR treatment

Table 1. Soil Characterization of Kotagede and Fukushima

Parameters	Kotagede soils				Fukushima soil ^a		
	Soil A	Soil B	Soil C	Soil D	(Kawamata)		
Particle size distribution (%):							
Sand	66.43	64.35	51.84	68.16	83.4		
Silt	23.09	24.35	36.05	23.68	8.8		
Clay	10.48	11.31	12.11	8.16	7.8		
Soil texture	Sandy loam	Sandy loam	Sandy loam	Sandy loam	Sandy loam		
Organic C (%)	0.83	1.64	1.47	4.27	0.74		
Organic matter (%)	1.43	2.83	2.54	4.27	3.91 (g/kg)		
Total N (%)	0.09	0.05	0.11	0.14	0.8 (g/kg)		
CEC (meq/100g)	12.35	16.83	18.06	16.95	9 (cmol/kg)		
pH (1:20, w/v)	7.7	7.8	6.9	7.4	6.32 (1:5)		
Surface area, m ² /g	25.67	35.10	40.69	28.46	-		
Pore volume, m ³ /g	52.37	64.02	64.11	50.17	-		
Mineral composition:	2θ				Fukushima soil ^b		
					K	M	
Silica (quartz)	21,800–21,900						
	27,700–27,750	Minor	Major	Minor	Minor	Major	
	49,600–49,850	(3.0%)	(12.9%)	(2.3%)	(3.4%)	(49.6%)	
	67,500–67,900					(25.5%)	
Dolomite	31,500						
	42,150	Minor	Major	Minor	Major	Minor	
	52,270	(4.4%)	(7.1%)	(2.4%)	(5.5%)	(4.1%)	
Ilmenite	35,540–35,680						
	48,350–48,420	Minor	Major	Minor	Minor	Minor	
	62,240–62,320	(4.2%)	(6.3%)	(5.0%)	(3.9%)	(1.9%)	
Franklinite	30,320–30,330	Minor	Minor	Minor	Minor	Minor	
		(2.3%)	(3.3%)	(1.4%)	(3.5%)	(1.3%)	
Kaolinite	23,640–23,690	Major	Major	Major	Major	Major	
		(16.2%)	(23.5%)	(8.8%)	(10.9%)	(20.3%)	
Lawsonite	42,360–42,960	Major	Major	Major	Major	Major	
		(14.1%)	(16.5%)	(7.5%)	(9.2%)	(10.7%)	
Goethite	34,960	Minor	Minor	Minor	Minor	Minor	
	53,370	(1.6%)	(3.7%)	(1.1%)	(2.3%)	(2.5%)	
Pyrolusite	57,360	Minor	Major	Minor	Minor	Trace	
	29,790	(5.0%)	(8.9%)	(3.1%)	(4.7%)	(0.4%)	
Muscovite	28,450	Major	Major	Major	Major	Major	
		(48.0%)	(11.3%)	(67.8%)	(55.4%)	(6.0%)	
Anatase	27,730	Minor	Trace	Trace	Minor	Minor	
		(1.2%)	(0.9%)	(0.7%)	(1.1%)	(2.5%)	

^aTran Q.T. et al., 2017 [34]; ^bThis work (K: Kawamata soil; M: Minamisoma soil)

CH₃COOH were used as an electrolyte. It shows that each pH soil increased by the distance from anode to cathode (e.g., from S1 to S5) in the range from 3 to 7. These results are in accordance with the findings reported in various studies [13-14].



Generally, the acid front can enhance the desorption of cesium from soil and dissolve the cesium ions, causing the ions to freely move through the soil and ideally to the cathode reservoir where they can be removed. Meanwhile, alkaline front significantly

declined the mobility of the cesium ions because of the metal hydroxide precipitation, thereby immobilizing the metals before they reach the cathode. The soil pH increased from anode to the cathode at more than 6.8. This is a typical soil pH profile for EKR treatment [15-16]. The soil pH near to the cathode sharply increased to above the initial soil pH when using HNO_3 as the electrolyte. However, there was no significant pH increase in the soil when CH_3COOH was used as the electrolyte.

High acidification of the remaining soil after the EKR treatment caused the loss of base cations, non-reversible clay mineral dissolution, and a reduction in cation exchange capacity, accompanied by structural deterioration [17]. In agriculture, simple treatment of soil acidity is ameliorated by applying lime or other unconventional acid-neutralizing materials such as rice husk ash [18], wood ash [19], and steel slag [20]. In addition, to neutralize the acid, sometimes ecologically sound remediation of acidic soil using bicarbonate-rich swine wastewater [21] and marble wastes are also used [22].

Cesium Concentration after EKR Treatment

Generally, the remaining cesium concentration in all soils was lower than the initial concentration (100 mg/kg) with a varied concentration. Fig. 3 shows that the remaining cesium concentration was much lower in soil A (from 49.14 to 89.34 mg/kg) and soil C (from 35.05 to 85.41 mg/kg) than that in soil B (from 55.18 to 101.89 mg/kg) and soil D (from 25.30 to 87.25 mg/kg) when HNO_3 was used as the electrolyte. Meanwhile, when CH_3COOH was used as the electrolyte, the remaining cesium concentration in the soil was as much as 32.34 to 105.41 mg/kg, 45.41 to 69.92 mg/kg, 55.64 to 96.65 mg/kg and 78.35 to 95.63 mg/kg for soil A, C, B and D respectively. The removal of cesium in soil A and C was much higher than the removal of cesium in soil B and D, even though a strong acid like HNO_3 was used as an electrolyte. This can occur because the soils have a low buffering capacity against acid. Previously reported results showed that soils B and D have a low buffering capacity against base [10]. Therefore, soils B and D are relatively easy to alkalinize compared to soils A and C. In addition, during the EKR treatment, the low pH (i.e., acid)

near the anode can promote more Cs^+ ions from the soil into the pore fluid, enabling the ions to be transported by electromigration. Thus, high removal of cesium from soil was observed near the anode. On the contrary, the high pH in the soil near the cathode (e.g., alkaline) was associated with metal hydroxide (MeOH) in the pore fluid that hindered the removal of cesium from soil. High amounts of heavy metals are retained in the soil when the buffer capacity is high enough to resist a change under the alkaline condition [23].

Most of the Cs have remained on the surface of the soil because the Cs ions were strongly adsorbed in the interlayer spaces of the clay soil, aluminosilicate sheet structures, particularly the vermiculite [24-25]. The treatment on the removal of cesium from contaminated soil depends on the penetration depth of the cesium in the soil, which is influenced by the soil characteristics such as clay content, particle size, and organic carbon content [26]. If the soil had vermiculite content, the migration efficiency of Cs ions in the EKR treatment decreased as the vermiculite content increased because the Cs ions can easily enter the interlayer of the basal spacing [27]. The observation of the changed structure of the vermiculite in aqueous suspension was measured by small-angle X-ray and it showed that the abruptness of the clay sheets was induced by the localization of Cs ions at the interlayer clay structure [28]. In addition, the removal efficiency of cesium using EKR in the radioactive soil decreased somewhat due to the aging effect [29].

Electric Current Profiles

Fig. 4(a) and 4(b) show the current profiles across the soil in the EKR experiments with HNO_3 and CH_3COOH as the electrolyte. How much the metal ions moved by electromigration in the pore fluid during the EKR process can be shown by the current profiles [30]. As seen in Fig. 4, the current increased in the first few days and then declined, finally remaining stable. Stable currents in all experiments was obtained depending on the migration rates of ions from the pore fluid in the soil [31]. Generally, the current reached a peak near or at the start of the experiment when the number of ions in the

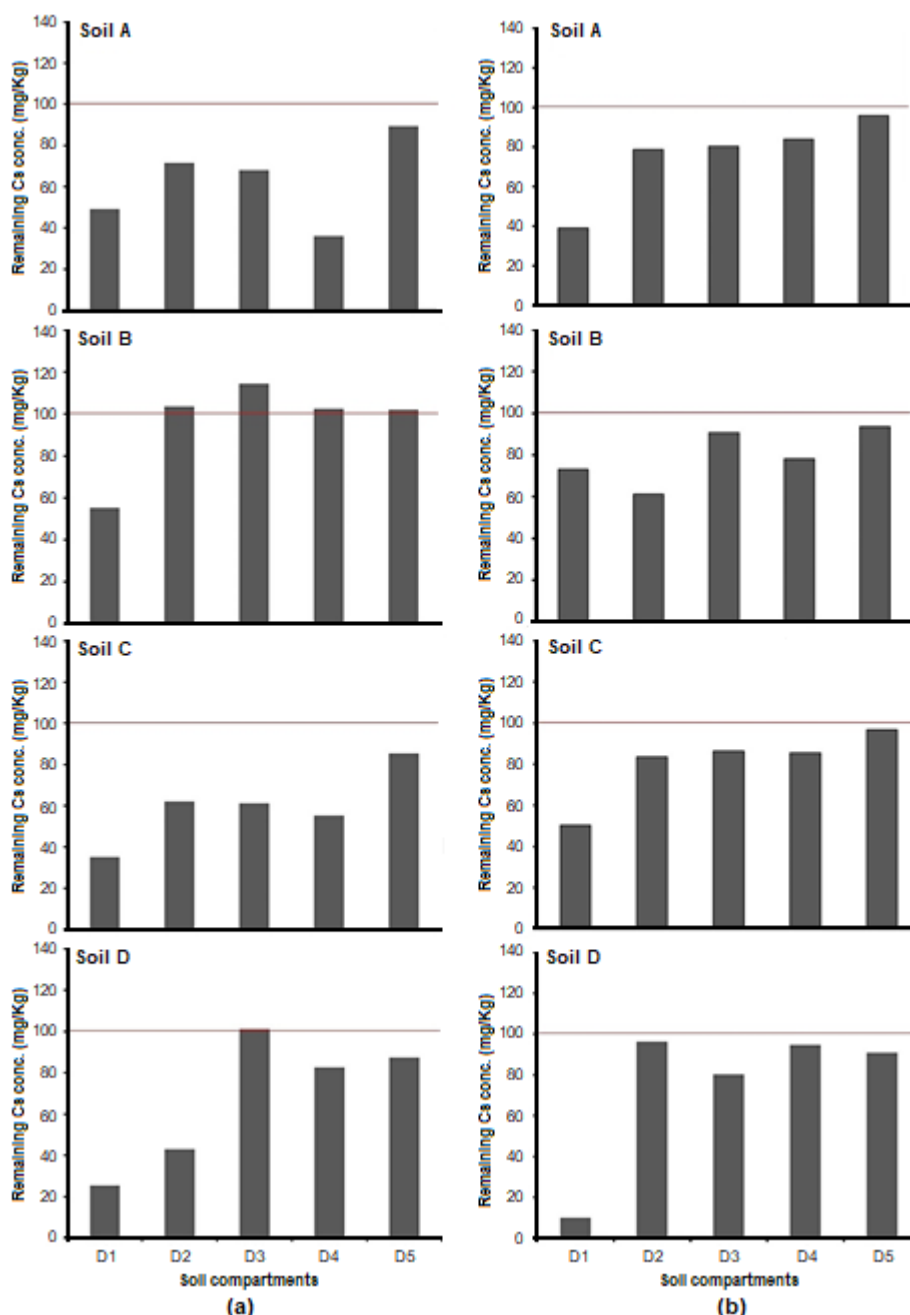


Fig 3. Remaining Cs concentration in the soil A, B, C and D after EKR process when used 1.0 M HNO₃ (a) and CH₃COOH (b) as electrolyte. The component near to the anode is D1 and the component near to the cathode is D5. The red line indicated the initial concentration of Cs in the soil before EKR treatment

pore fluid was high due to dissolved ions associated with dry soil particles. As the ions electromigrated towards the electrodes, the current gradually declined as similarly reported in several publications [30-32].

Fig. 4(a) shows the current profile when HNO₃ was used as the electrolyte. Nitric acid in the solution

produced high amounts of H⁺ ions, which moved toward the cathode. Consequently, the soil was acidified, which in turn promoted the desorption of cesium ions into the pore fluid. As a result, the current crossing in the soil increased rapidly, then declined and reached a stable current (see Fig. 4(a)). The phenomenon can be

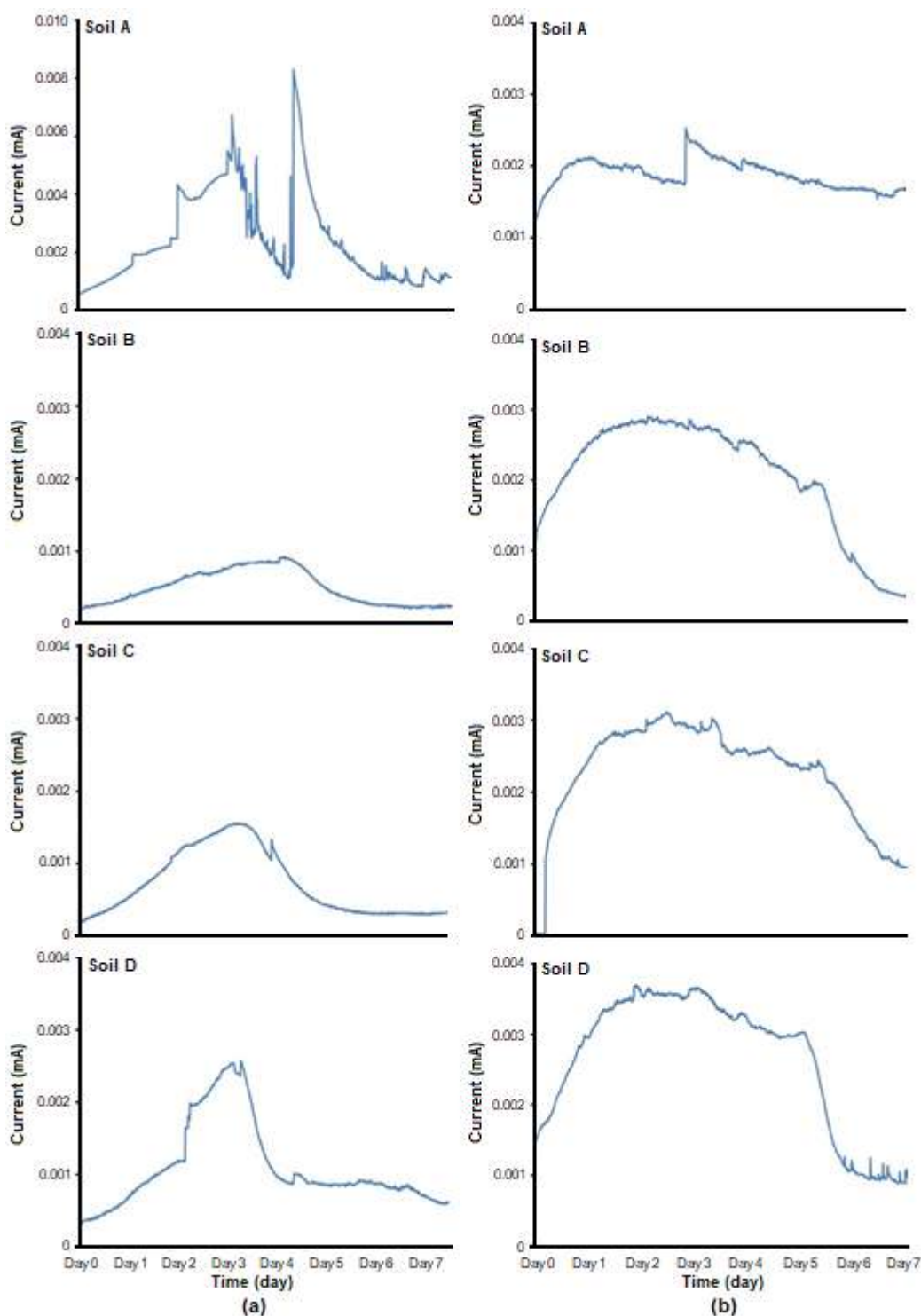
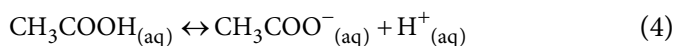
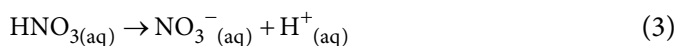


Fig 4. Current profiles during the EK remediation using 0.1 M HNO_3 (A) and CH_3COOH (B) as the electrolyte

explained by two reasons; (i) resistance at the interface between the electrodes and the electrolyte might have increased because of the concentration polarization and water dissociation in the electrolysis and (ii) ions with

positive or negative charges moved to the two ends of the electric cell (e.g., anode and cathode), which resulted in the drop of the ionic strength in the soils and the current as well [33]. This phenomenon occurs when a strong

acid like HNO_3 undergoes complete dissociation to NO_3^- and H^+ ions, as shown in Eq. (3). However, reversible dissociation occurs when weak organic acids like CH_3COOH is applied as an electrolyte, as shown in Eq. (4). Therefore, the current profile was high-broad, which indicates that the soil resistance was high (see Fig. 4(b)).



The acidic solution enhanced the desorption of ions from the soil into the pore fluid so that the high concentration of ions in the pore fluid increased the electric current under a constant voltage condition. However, a higher current led to high power consumption.

■ CONCLUSION

According to the results of the experiments, the following conclusion can be stated briefly. The soil samples from Kotagede, Yogyakarta, Indonesia have a similar physico-chemical properties with the contaminated soils from Fukushima, Japan, in terms of soil texture, soil properties, and mineral content. In this regard, the major mineral content was silica (quartz) and kaolinite, and the soil texture was sandy loam. The soil pH near the cathode sharply increased to above the initial soil pH when using HNO_3 as the electrolyte. However, there was no significant pH increase in the soil when CH_3COOH was used as the electrolyte. High soil pH occurred near the cathode, indicating the precipitation of cesium ions in the cathode area. The removal of cesium from soils were highly effective when HNO_3 was used as the electrolyte. However, the order of the highest to lowest cesium removal in the soil for all acids (e.g., HNO_3 and CH_3COOH) were as follows: soils $C > A > D > B$. The current profiles in the EKR treatment showed that HNO_3 as an electrolyte was undergoing complete dissociation, which caused a low resistance in the soil showed by a low current plateau. Meanwhile, CH_3COOH as a weak acid undergoes partial dissociation, which caused a high resistance in the soil during EKR treatment, producing a high current plateau.

■ ACKNOWLEDGMENTS

The authors would like to thank the Ministry of Education and Culture and the Ministry of Research and Technology of the Republic of Indonesia for their financial support through the Excellence Higher Education Basic Research (PDUPT) 2019-2020 (Research contract: B/1436.1/L5/DRA.00/2019; LLDIKTI and UII contract: 1627.1/LL5/PG/2020). Financial support from the Directorate of Talent Development and Student Welfare of Universitas Islam Indonesia to N.Z.J. and A.I.A. are also gratefully acknowledged.

■ REFERENCES

- [1] Ariyanto, S., and Widodo, W.L., 2014, *Status of Nuclear Power Plant Development in Indonesia*, Center for Nuclear Energy Development (BATAN), Jakarta.
- [2] Sriyana, 2012, *Current Status of Indonesia's Nuclear Power Program*, IAEA Technical Meeting/Workshop on Topical Issues on Infrastructure Development: Managing the Development of National Infrastructure for NPPP, Vienna, Austria, 24–27 January 2012.
- [3] Mao, X., Han, F.X., Shao, X., Guo, K., McComb, J., Arslan, Z., and Zhang, Z., 2016, Electro-kinetic remediation coupled with phytoremediation to remove lead, arsenic and cesium from contaminated paddy soil, *Ecotoxicol. Environ. Saf.*, 125, 16–24.
- [4] Ding, D., Zhang, Z., Lei, Z., Yang, Y., and Cai, T., 2016, Remediation of radiocesium-contaminated liquid waste, soil, and ash: A mini review since the Fukushima Daiichi Nuclear Power Plant accident, *Environ. Sci. Pollut. Res.*, 23 (3), 2249–2263.
- [5] Evrard, O., Laceby, J.P., and Nakao, A., 2019, Effectiveness of landscape decontamination following the Fukushima nuclear accident: A review, *Soil*, 5, 333–350.
- [6] Shukla, A., Parmar, P., and Saraf, M., 2017, Radiation, radionuclides and bacteria: An in-perspective review, *J. Environ. Radioact.*, 180, 27–35.

- [7] Zhao, C., Dong, Y., Feng, Y., Lia, Y., and Dong, Y., 2019, Thermal desorption for remediation of contaminated soil: A review, *Chemosphere*, 221, 841–855.
- [8] Chu, C.Y., and Ko, T.H., 2018, Evaluation of acid leaching on the removal of heavy metals and soil fertility in contaminated soil, *J. Chem.*, 2018, 5036581.
- [9] Acar, Y.B., and Alshawabkeh, A.N., 1993, Principles of electrokinetic remediation, *Environ. Sci. Technol.*, 27 (13), 2638–2647.
- [10] Putra, R.S., Budiarmo, S., and Yendi, N., 2016, Removal characteristics of silver with electrokinetic by adsorption on soil mineral from Kotagede Yogyakarta, *Proceeding of 3rd International Conference on Research, Implementation and Education of Mathematics and Science*, Universitas Negeri Yogyakarta, Yogyakarta, Indonesia, 16–17 May 2016.
- [11] Pratama, K., 2016, Karakterisasi tanah kotagede terhadap adsorpsi logam perak (Ag): Remediasi logam perak (Ag) dengan metode elektrokinetik menggunakan elektrolit asam asetat, *Undergraduate Thesis*, Department of Chemistry, Faculty of Mathematics and Natural Sciences, Universitas Islam Indonesia, Yogyakarta, Indonesia.
- [12] Durrant, C.B., Begg, J.D., Kersting, A.B., and Zavarin, M., 2018, Cesium sorption reversibility and kinetics on illite, montmorillonite, and kaolinite, *Sci. Total Environ.*, 610-611, 511–520.
- [13] Bahemmat, M., and Farahbakhsh, M., 2015, Catholyte-conditioning enhanced electrokinetic remediation of Co- and Pb polluted soil, *Environ. Eng. Manage. J.*, 14 (1), 89–96.
- [14] Kim, G.N., Yang, B.I., Choi, W.K., Lee, K.W., and Hyeon, J.H., 2009, Washing-electrokinetic decontamination for concrete contaminated with cobalt and cesium, *Nucl. Eng. Technol.*, 41 (8), 1079–1086.
- [15] Huang, T., Li, D., Kexiang, L., and Zhang, Y., 2015, Heavy metal removal from MSWI fly ash by electrokinetic remediation coupled with a permeable activated charcoal reactive barrier, *Sci. Rep.*, 5 (1), 15412.
- [16] Arbai, S., Mohamed, Z., Mohamed, K., and Bakar, A.A., 2014, “Electrokinetic remediation to remove heavy metal from contaminated soils using purging solution” in *InCIEC 2013*, Eds. Hassan, R., Yussof, M., Ismail, Z., Amin, N., and Fadzil, M., Springer, Singapore, 531–538.
- [17] Goulding, K.W.T., 2016, Soil acidification and the importance of liming agricultural soils with particular reference to the United Kingdom, *Soil Use Manage.*, 32 (3), 390–399.
- [18] Islabão, G.O., Vahl, L.C., Timm, L.C., Paul, D.L., and Kath, A.H., 2014, Rice husk ash as corrective of soil acidity, *Rev. Bras. Ciênc. Solo*, 38 (3), 934–941.
- [19] Ohno, T., 1992, Neutralization of soil acidity and release of phosphorus and potassium by wood ash, *J. Environ. Qual.*, 21 (3), 433–438.
- [20] Plopeanu, G., Gamenț, E., Marinescu, M., Vrînceanu, N., and Carabulea, V., 2017, Steel slag - Unconventional amendment for acid soils, *AgroLife Sci. J.*, 6 (1), 195–200.
- [21] Qilu, C., Xuelling, W., Igen X, Hui, L., Yuhua, Z., and Qifa, Z., 2017, High-quality, ecologically sound remediation of acidic soil using bicarbonate-rich swine wastewater, *Sci. Rep.*, 7 (1), 11911.
- [22] Tozsin, G., Arol, A.I., Oztas, T., and Kalkan, E., 2014, Using marble wastes as a soil amendment for acidic soil neutralization, *J. Environ. Manage.*, 133, 374–377.
- [23] Villen-Guzman, M., Paz-Garcia, J.M., Amaya-Santos, G., Rodriguez-Maroto, J.M., Vereda-Alonso, C., and Gomez-Lahoz, C., 2015, Effects of the buffering capacity of the soil on the mobilization of heavy metals. Equilibrium and kinetics, *Chemosphere*, 131, 78–84.
- [24] Kato, H., Onda, Y., and Teramage, M., 2012, Depth distribution of ¹³⁷Cs, ¹³⁴Cs, and ¹³¹I in soil profile after Fukushima Dai-ichi Nuclear Power Plant accident, *J. Environ. Radioactiv.*, 111, 59–64.
- [25] Kaneko, M., Iwata, H., Shiotsu, H., Masaki, S., Kawamoto, Y., Yamasaki, S., Nakamatsu, Y., Imoto,

- J., Furuki, G., Ochiai, A., Nanba, K., Ohnuki, T., Ewing, R.C., and Utsunomiya, S., 2015, Radioactive Cs in the severely contaminated soils near the Fukushima Daiichi Nuclear Power Plant, *Front. Energy Res.*, 3, 37.
- [26] Ochi, K., Sasaki, M., Ishida, M., Hamamoto, S., Nishimura, T., and Sanada, Y., 2017, Estimation of the vertical distribution of radiocesium in soil on the basis of the characteristics of gamma-ray spectra obtained via aerial radiation monitoring using an unmanned helicopter, *Int. J. Environ. Res. Public Health*, 14 (8), 926.
- [27] Akemoto, Y., Kan, M., and Tanaka, S., 2019, Static adsorption of cesium ions on kaolin/vermiculite and dynamic adsorption/desorption using electrokinetic process, *J. Chem. Eng. Jpn.*, 52 (7), 662–669.
- [28] Motokawa, R., Endo, H., Yokoyama, S., Nishitsuji, S., Kobayashi, T., Suzuki, S., and Yaita, T., 2015, Collective structural changes in vermiculite clay suspensions induced by cesium ions, *Sci. Rep.*, 4 (1), 6585.
- [29] Kim, G.N., Oh, W.Z., Won, H.Z., and Jung, C.H., 2004, An analysis of the aging effect on the removal of cesium and cobalt from radioactive soil by the electrokinetic method, *J. Korean Nucl. Soc.*, 36 (4), 304–315.
- [30] Putra, R.S., and Tanaka, S., 2011, Aluminum drinking water treatment residuals (Al-WTRs) as an entrapping zone for lead in soil by electrokinetic remediation, *Sep. Purif. Technol.*, 79 (2), 208–215.
- [31] Zhang, T., Zou, H., Ji, M., Li, X., Li, L., and Tang, T., 2014, Enhanced electrokinetic remediation of lead-contaminated soil by complexing agents and approaching anodes, *Environ. Sci. Pollut. Res.*, 21 (4), 3126–3133.
- [32] Ng, Y.S., Gupta, B.S., and Hashim, M.A., 2016, Remediation of Pb/Cr co-contaminated soil using electrokinetic process and approaching electrode techniques, *Environ. Sci. Pollut. Res.*, 23 (1), 546–555.
- [33] Acar, Y.B., and Alshawabkeh, A.N., 1996, Electrokinetic remediation. I: Pilot-scale tests with lead-spiked kaolinite, *J. Geotech. Eng.*, 122 (3), 173–185.
- [34] Tran, Q.T., Maeda, M., Oshita, K., and Takaoka, M., 2017, Phosphorus release from cattle manure ash as soil amendment in laboratory-scale tests, *Soil Sci. Plant Nutr.*, 63 (4), 369–376.

FTIR-based Fingerprinting and Chemometrics for Rapid Investigation of Antioxidant Activity from *Syzygium polyanthum* Extracts

Eti Rohaeti^{1,2,*}, Fadila Karunina¹, and Mohamad Rafi^{1,2}

¹Department of Chemistry, Faculty of Mathematics and Natural Sciences, IPB University, Jl. Tanjung Kampus IPB Dramaga, Bogor 16680, Indonesia

²Tropical Biopharmaca Research Center – Institute of Research and Community Empowerment, IPB University, Jl. Taman Kencana No. 3 Kampus IPB Taman Kencana, Bogor 16128, Indonesia

* **Corresponding author:**

email: etirohaeti@apps.ipb.ac.id

Received: March 6, 2020

Accepted: May 28, 2020

DOI: 10.22146/ijc.54577

Abstract: *Syzygium polyanthum*, known as salam in Indonesia, which is rich in phenolics compounds with high antioxidant activity. In this study, we performed the determination of total phenolics and characterization of the antioxidant activity of *S. polyanthum* leaves extracts using the FTIR-based fingerprinting technique. The extracts of *S. polyanthum* in water, ethanol, and ethanol-water (30, 50, and 70%) were measured for their antioxidant activity, total phenolics, and FTIR spectra. The antioxidant activity of *S. polyanthum* extract with different solvent extraction showed the highest antioxidant activity and total phenolic content is 70% and 50% ethanolic extract, respectively. The FTIR spectrum of each extract showed identical FTIR spectra patterns. According to their different solvent extraction, *S. polyanthum* extract could be grouped based on FTIR spectra using principal component analysis. Correlation between the functional group in the FTIR spectra with IC_{50} from *S. polyanthum* extract was analyzed using partial least square (PLS). The PLS analysis results showed that O-H, C-H sp^3 , C=O, C=C, C-O, and C-H aromatic are the main functional groups contributed to the antioxidant activity of *S. polyanthum* extract. FTIR-based fingerprinting combined with chemometrics could be used to classify different extracts of *S. polyanthum* and predicted functional groups having a significant contribution to antioxidant activity.

Keywords: antioxidant; chemometrics; fingerprinting; FTIR; *S. polyanthum*

■ INTRODUCTION

Syzygium polyanthum (*S. polyanthum*), or locally known in Indonesia as *salam*, belongs to the Myrtaceae family. Traditionally, *S. polyanthum* leaves were used as a food flavoring and medicinal uses. *S. polyanthum* extract known to have some biological activities such as antioxidant [1], antidiarrheal [2], antihypertensive [3], antihyperglycemic [4], antibacterial [5], cytotoxic and antiproliferative effect [6]. In addition, *S. polyanthum* extract could be used as a preservative for chicken meat [7]. Darusman et al. [1] reported that *S. polyanthum* extract showed inhibition of acetylcholinesterase, which is used for the treatment of Alzheimer's disease. Those biological activities came from *S. polyanthum* is related to the bioactive compounds found in this plant.

Chemical compounds present in *S. polyanthum*, such as flavonoids, alkaloids, steroids, triterpenoids, and tannins with the major class was from the flavonoids group [6]. Flavonoids are widely distributed in plants and are known to have various biological activities, and one of them is antioxidant activity [8]. The content of its bioactive compounds determines the characteristics of biological activity in plants. The method and extracting solvent type have a significant role in the extraction of metabolites because the content of various compounds in plants has different chemical characteristics and polarity [9]. Polar solvents such as water, ethanol, and a mixture of water and ethanol are widely used to extract phenolic compounds like flavonoids. Water and ethanol solvents have been reported to be effective in extracting

plant metabolites with intense biological activity [9-10]. Therefore, in this research, we used maceration with ethanol, water, and their mixture to analyze the effect of extracting solvent on extracted metabolites. In addition, the correlation of extracted metabolites showed in FTIR spectra with antioxidant activity in *S. polyanthum* leaves was determined.

The correlation between the composition of metabolites and its bioactivity of the plant extracts could be performed by the metabolomics approach. Metabolomics is the process of analyzing the metabolites present in organism comprehensively both quantitatively and qualitatively using multivariate analysis [11]. Metabolomics approach could display the profile of detected metabolites and evaluate the changes in the metabolite profile under various circumstances [12]. Finding the correlation of biological activity with their respective signal output of metabolites from spectrum or chromatogram is one example of the used metabolomics [13-14].

There are several papers reported in the study of metabolite profile changes and their correlation with bioactivity in plants by a combination of Fourier transform infrared (FTIR) spectra and chemometrics. This approach has been used for the correlation of metabolites and bioactivity to identify the functional group, which is correlated with antioxidant activity and inhibition of α -glucosidase of the crude extracts and fractions of *Phaleria macrocarpa*, *Momordica charantia*, and *Smalanthus sonchifolius* [15-17]. However, there is no reported study for the classification of *S. polyanthum* extracts using FTIR and its correlation with its antioxidant activity.

FTIR spectroscopy was chosen because it is a low-cost, quick, easy, and reproducible analysis. Hence, FTIR could be used as a method in classifying samples based on their biological properties. The FTIR spectrum produces complex data and difficult for interpreting the data, thus chemometrics assistance is needed to process the data. Chemometrics analysis used in this study were principal component analysis (PCA) and partial least square regression (PLS). PCA was used for classifying the samples according to its solvent extraction, while PLS was used for determining functional groups that give a

significant contribution to the antioxidant activity of *S. polyanthum*. In this work, we would like to classify *S. polyanthum* extracts with different solvent extraction and determined the functional group of compounds gives a significant contribution to the antioxidant activity of *S. polyanthum* extracts based on FTIR spectra.

■ EXPERIMENTAL SECTION

Materials

S. polyanthum leaves were obtained from Tropical Biopharmaca Research Center (TropBRC) medicinal plant garden, IPB University, Bogor, Indonesia. Sample identification was made by Mr. Taopik Ridwan (TropBRC), and a voucher specimen was stored in TropBRC, IPB University, Bogor, Indonesia. Ethanol absolute was purchased from Merck (Darmstadt, Germany). Ascorbic acid, Folin-Ciocalteu reagent, 2,2-diphenyl-1-picrylhydrazyl (DPPH), gallic acid, potassium bromide for IR spectra, and sodium carbonate were obtained from Sigma Aldrich (Steinheim, Germany).

Instrumentation

Rotary evaporator-114 (Buchi, Flawil, Switzerland) was used for the evaporation of solvent extraction. Measurement of total phenolic and antioxidant activity was performed in Epoch microplate reader (BioTek Instruments Inc. Winooski, USA). FTIR spectra were measured in Bruker Tensor 37 FTIR spectrophotometer (Bruker Optik GmbH, Karlsruhe, Germany).

Procedure

Sample preparation and extraction

Fresh *S. polyanthum* leaves were cleaned with water and dried in the oven at 45 °C. After that, the samples were pulverized to obtain 40 mesh powder samples. The extraction of the samples was carried out by maceration according to the method developed by BPOM [18] with slight modification. Different solvent extraction, i.e., ethanol, 30% ethanol, 50% ethanol, 70% ethanol, and water, were used for extraction of the sample. A total of 10 g of *S. polyanthum* leaves powder and 100 mL of solvent were put into the Erlenmeyer and soaked for 6 h while stirring occasionally. The sample

was immersed for 3×24 h in a dark room. Furthermore, the filtrate was collected by filtering the mixture using filter paper. Each sample extract was concentrated using a rotary evaporator. The sample extract is then ready to be used for further analysis.

Determination of total phenolic

Total phenolic content was determined using the Folin-Ciocalteu method using the procedure of Prekumara et al. [19] in 96 well microplates. Sample extracts were weighed about 10 mg and dissolved in 1 mL of ethanol, obtaining an extract solution with a concentration of 10,000 $\mu\text{g/mL}$. The extract solution was diluted to 250 $\mu\text{g/mL}$. About 20 μL of extract solution was mixed with 110 μL of Folin-Ciocalteu reagent and 70 μL of sodium carbonate and incubated at $25 (\pm 2) ^\circ\text{C}$ for 30 min. After that, the absorbance of the solution was measured at 765 nm. Total phenolic content was expressed as gallic acid equivalent (GAE) in grams of dried powder sample (mg GAE/g dried powder).

Determination of antioxidant activity

The determination of antioxidant activity was performed by the DPPH method using the procedure developed by Salazar et al. [20]. A total of 100 μL of *S. polyanthum* extract and 100 μL of DPPH 125 μM were mixed in the 96 well microplates, then incubated at room temperature for 30 min. The absorbance of the solution was measured at 517 nm against ethanol as a blank. The concentration range used was between 1.56 to 25.00 $\mu\text{g/mL}$ for *S. polyanthum* extract solution. Ascorbic acid was used as a positive control, and the antioxidant activity was reported as IC_{50} that can be calculated by the correlation of each concentration with the inhibition value of DPPH.

FTIR spectra

FTIR spectra were measured in the FTIR spectrophotometer Tensor 37 (Bruker, Ettlingen, Germany) equipped with a deuterated triglycine sulfate detector. The sample was prepared by mixing 2 mg of extract and 180 mg of KBr until homogeneous, and then the pellet was formed with a pressure of 8 tons for 15 min using a manual compression. The pellet was placed in the sample compartment. Measurement of the FTIR spectra was performed in the region of $4000\text{--}400 \text{ cm}^{-1}$ with a

resolution of 4 cm^{-1} and 32 scans/min controlled by OPUS 4.2 software (Bruker, Ettlingen, Germany). FTIR spectra were stored as a data point table.

Chemometrics analysis

Analysis of variance (ANOVA) and Duncan test were used to determine the significant difference between the results of extraction yield, total phenolics content, and antioxidant activity. A significant difference was defined at the 95% confidence level ($p < 0.05$). Classification of *S. polyanthum* extracts according to the solvent extraction was performed using PCA. The identification of functional groups in antioxidant compounds was determined using PLS analysis by a correlation between the FTIR spectra and IC_{50} from antioxidant activity. The Unscrambler X version 10.1 (CAMO, Oslo, Norway) was used for running the PCA and PLS analysis.

■ RESULTS AND DISCUSSION

Extraction Yield and Total Phenolic Content

S. polyanthum leaves were extracted by maceration using ethanol, water, and their mixture as solvent extraction. Solvent replacement after 24 h for three times aims to extract more effectively and gave an increase in the yield. Extraction with 30% ethanol gave the highest yield followed by 50% ethanol, 70% ethanol, ethanol, and water (Table 1), indicating the different polarity of the solvent extraction give a different level of extracted metabolites.

The determination of phenolic content in *S. polyanthum* leaves extract was performed using the Folin-Ciocalteu method. In this method, the oxidation reaction of phenolic compounds in an alkaline condition by the Folin-Ciocalteu reagent will produce a blue molybdenum-tungsten complex that provides strong absorption at a wavelength of 750 nm. Total phenolic content is reported as the gallic acid equivalent. The results of total phenolic content in *S. polyanthum* extract are shown in Table 1.

Total phenolic levels in *S. polyanthum* extracts in the order from the highest to the lowest are 50% ethanol > 30% ethanol > 70% ethanol > ethanol > water. The

Table 1. Extraction yield, total phenolic content, and antioxidant activity of *S. polyanthum* extracts

Solvent extraction	Extraction yield (%)	Total Phenolic content (mg GAE/g dried powder)	Antioxidant activity (IC ₅₀ , µg/mL)
Ethanol	12.46 ± 0.95 ^a	2.21 ± 0.24 ^a	6.75 ± 0.35 ^a
30% ethanol	27.42 ± 4.54 ^b	6.87 ± 0.83 ^c	8.92 ± 0.51 ^a
50% ethanol	25.94 ± 0.98 ^b	6.88 ± 0.80 ^c	7.59 ± 0.16 ^a
70% ethanol	22.46 ± 0.42 ^b	4.66 ± 0.58 ^b	6.19 ± 0.78 ^a
Water	11.42 ± 3.93 ^a	1.90 ± 0.68 ^a	21.13 ± 4.38 ^b

The reported values are mean ± SD of the triplicate assay for each sample. The mean ± SD within each extract in the same column followed with different superscript letters represent significant differences at $p < 0.05$

results of total phenolic content showed that phenolic could be extracted higher in mixed ethanol-water solvents compared to the pure solvents. The most efficient extracting solvent is 30%, and 50% ethanol for extracting phenolic compounds in *S. polyanthum* leaves with total phenolic content about 6.87 and 6.88 mg GAE/g dried powder, respectively. The two extracts gave higher results compared to other extracts and not significantly different in total phenolic content as a result of ANOVA.

Antioxidant Activity of *S. polyanthum* Extracts

The antioxidant activity of the sample was determined by the DPPH method. The DPPH method has the advantages, such as easy to perform, quick analysis, and provide the information on the reactivity of compounds tested using a stable radical. DPPH solution when mixed with a substance that can donate hydrogen atoms with a change in color from purple to yellow [21]. The higher the antioxidant activity of a sample, the lower the intensity of the remaining purple color will be, so that its absorption at a wavelength of 517 nm will be smaller. Increasing the concentration of the sample would give a higher percentage of DPPH inhibition, meaning the higher antioxidant activity that can inhibit more free radicals. Based on the measurement results obtained, the value of absorbance decreased with increasing concentrations of *S. polyanthum* leaves extract.

The antioxidant activity of each extract was expressed with IC₅₀ value. The IC₅₀ values were obtained from the equation in the correlation curve of *S. polyanthum* extract concentration and the percentage of DPPH inhibition. According to Molyneux [21], a sample with IC₅₀ < 50 µg/mL, between 50–100 µg/mL, and > 200 µg/mL

is classified as strong, weak, and very weak antioxidant activity, respectively. The antioxidant activity of the five *S. polyanthum* leaves extracts is classified as strong because it has an IC₅₀ value below 50 µg/mL.

From the result obtained, 70% ethanol extract has the smallest IC₅₀ followed by ethanol, 50% ethanol, 30% ethanol, and water (Table 1). So, 70% ethanol extract showed the highest antioxidant activity. As can be seen, when the water ratio decreases, the antioxidant activity significantly increases. However, when ethanol only was used, the antioxidant activity did not give higher results compared to 70% ethanol extract. Mediani et al. [22] also found that extraction with ethanol only gave lower antioxidant activity compared to the 70% ethanol extract in *Cosmos caudatus*.

Classification of *S. polyanthum* Leaves Extracts Based on IR Spectra and Chemometrics

Fig. 1 shows the IR spectra of each *S. polyanthum* leaves extract. From the IR spectra, no differences are obtained in the peak position, or each extract has a similar pattern and only differ in their intensities. Water extracts showed a lower peak absorption intensity compared to the other extracts. Meanwhile, very similar patterns and intensities are found in 30% and 50% ethanol extracts. These similar patterns in each extract mean that there is a similar composition in the metabolite extracted from *S. polyanthum* leaves using each solvent extraction. Therefore, the classification of *S. polyanthum* leaves extracts by using only IR spectra will not be easy, so that aid from chemometrics analysis is needed to discriminate each extract.

The identification of the functional groups found in

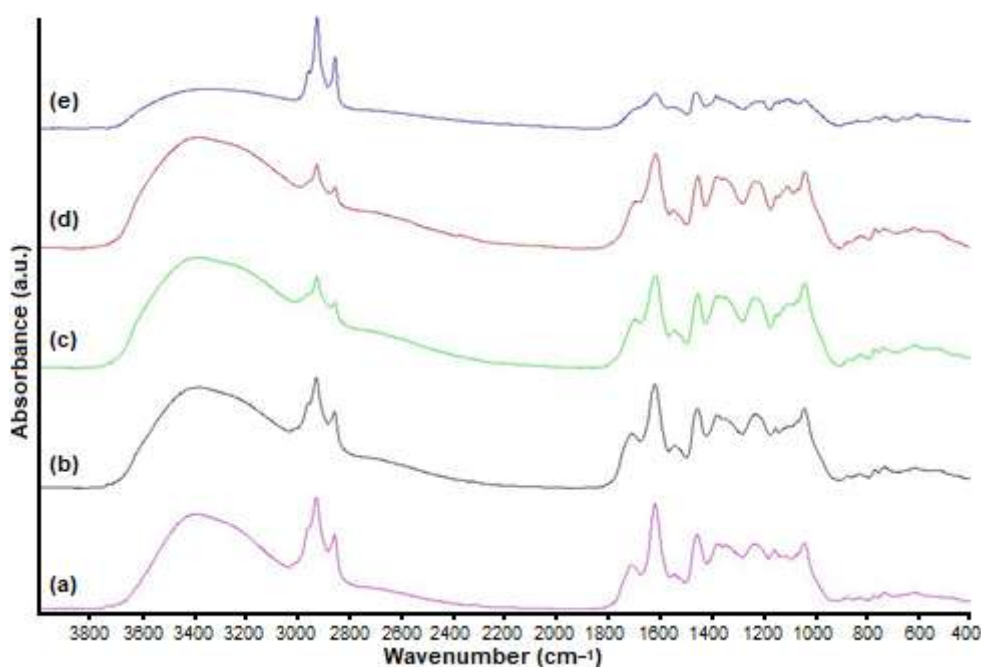


Fig 1. FTIR spectrum of *S. polyanthum* (a) EtOH, (b) 70% EtOH, (c) 50% EtOH, (d) 30% EtOH, and (e) water extract

the *S. polyanthum* leaves extracts is shown in Table 2. There is a difference in the intensity of the absorbance value at a wavenumber of 1680–1600 cm^{-1} with the highest value found in 70% ethanol and the lowest value found in the water extract. At the wavenumber of 900–690 cm^{-1} , the water extraction absorption has a lower value than other extracts. The differences in the absorbance values at some peaks in each extract indicates differences in the amount of metabolite.

In this study, PCA was used for the classification of *S. polyanthum* extracts according to different solvent extraction. Before subjected to PCA, each spectrum was pre-processed to reduce variations in the data but did not have any effect on the analytical information. PCA worked to simplify the observed variables by reducing their dimensions, and with the score plot obtained from the principal component, a grouping sample was obtained. Fig. 2 shows the PCA score plot of the *S. polyanthum* leaves extracts.

In the PCA score plot, all of the extracts were classified into their group (five classes). The first two PC's were used with 88% total variance with PC-1 explained 59%, and PC-2 explained 29% of the variance. In Fig. 2, the 30% ethanol and 50% ethanol extract were adjacent for

their position in the PCA plot. This closeness shows that the composition and level of metabolite extracted with those solvents are almost similar.

Correlation between *S. polyanthum* Leaves Extract FTIR Spectra with Antioxidant Activity

Identification of functional group, which has a major contribution to the level of antioxidant activity of *S. polyanthum* leaves extracts, was determined using the partial least square (PLS) regression method. In the PLS modeling, it should have a variable data and response variables. Antioxidant activity, expressed as IC_{50} obtained by the DPPH method, was used as the response variable (y), while the absorbance from FTIR spectra was used as the estimating variable (x). Before subjected to the

Table 2. Functional group present in *S. polyanthum* extracts

Wavenumber (cm^{-1})	Assign functional group
3400–3300	O–H
3000–2840	C–H sp^3
1740–1720	C=O
1680–1600	C=C
1300–1000	C–O
900–690	C–H aromatic

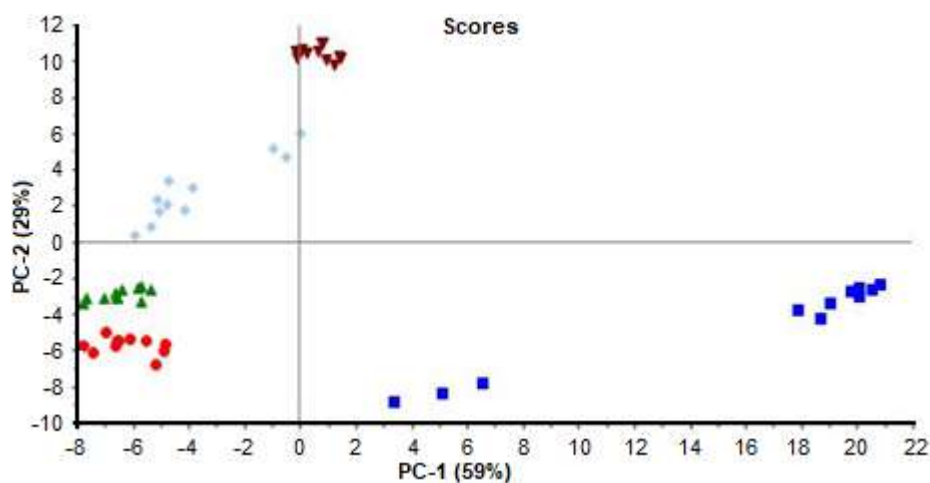


Fig 2. PCA plot of *S. polyanthum* leaves (▼) EtOH, (◆) 70% EtOH, (▲) 50% EtOH, (●) 30% EtOH, and (■) water extract

PLS, the FTIR spectra were given the same pre-processing treatment as in the PCA.

The X-Y relation score and regression coefficient plot will be obtained in the PLS regression. The X-Y relation score plot was shown in Fig. 3. This plot explains the relationship between the absorbance data related to the functional groups as variable X and antioxidant activity as variable Y. Also, the plot shows that a grouping of extracts exhibit active and not active as antioxidant sources. An active extract with high antioxidant activity is grouped in the negative area. In contrast, the less active extracts are in the positive area of the plot because the low IC_{50} value indicates a high antioxidant activity. As can be seen in Fig. 3, 30% ethanol, 50% ethanol, 70% ethanol, and

ethanol extracts were the active extract because the four extracts had lower IC_{50} values compared to water extracts.

In this study, the identification of a functional group from a metabolite that gives a major contribution to the antioxidant activity could be identified from the plot of the regression coefficient in the PLS analysis. The plot of regression coefficients (Fig. 4) is used to summarize the relationship between all predictors and responses given to PLS; the regression coefficient can take into account several components or factors. For example, in Fig. 4, the model is obtained from factor 5. It has information that the regression coefficient can summarize the relationship between the predictor and

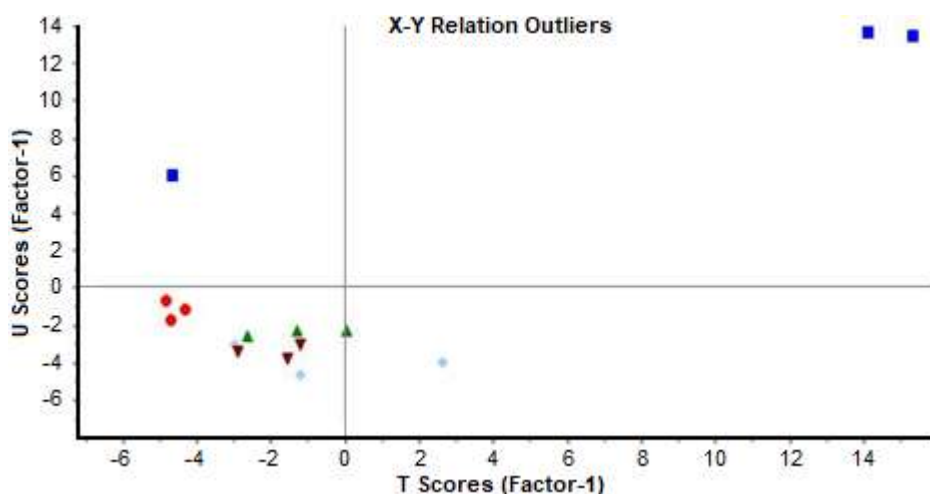


Fig 3. PLS plot as a relationship between absorbance from the functional groups and antioxidant activity of *S. polyanthum* leaves (▼) EtOH, (◆) 70% EtOH, (▲) 50% EtOH, (●) 30% EtOH, and (■) water extract

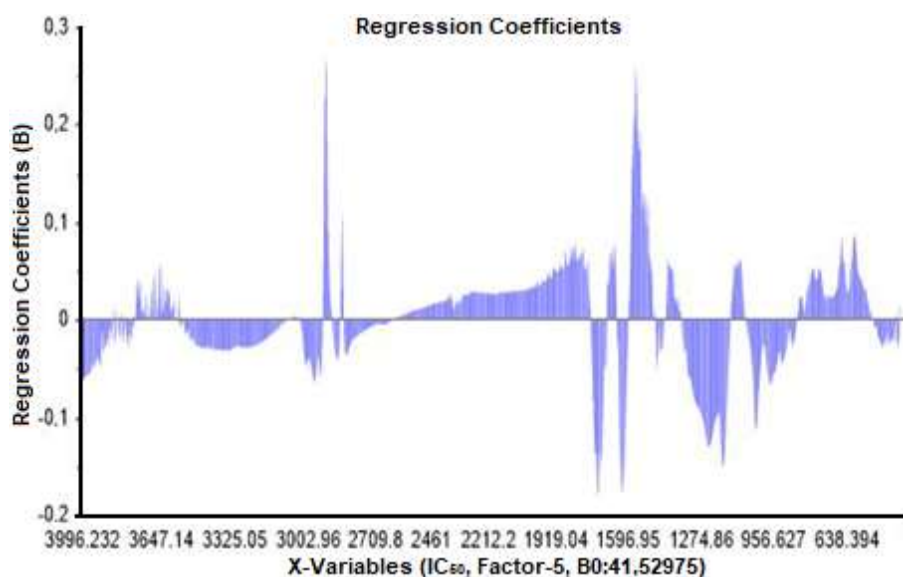


Fig 4. Regression coefficient plot of *S. polyanthum* extracts

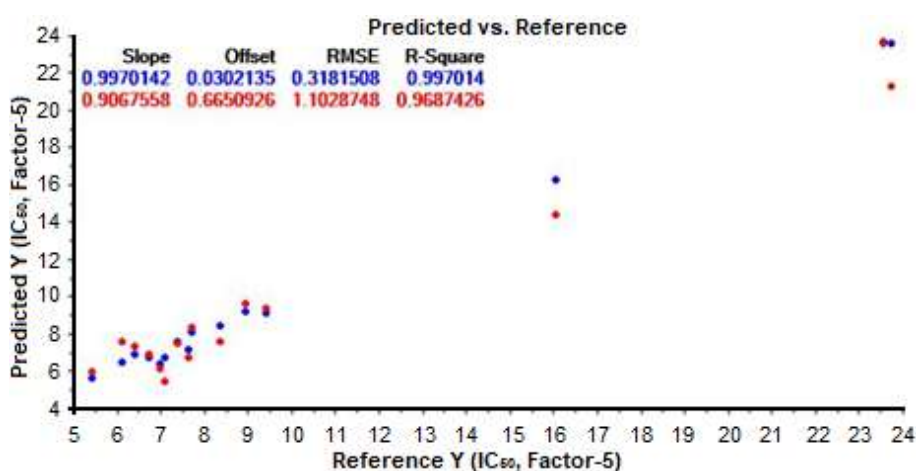


Fig 5. Predicted vs. reference plot for calibration and validation *S. polyanthum* extracts

response by using factor 5 as the best model predicted. Plot regression coefficients provide information about how important the variable X to variable Y. Variable X, which has a large regression coefficient, is a variable that has an important role in the regression model. The absorption of functional groups that play an active role in antioxidant activity expressed by IC_{50} values has a negative regression coefficient [14]. Fig. 4 shows that there are several functional groups have a negative regression coefficient, such as O–H ($3400\text{--}3080\text{ cm}^{-1}$), C–H sp^3 ($3012\text{--}2831\text{ cm}^{-1}$), C=O ($1740\text{--}1720\text{ cm}^{-1}$), C=C (around 1600 cm^{-1}), C–O ($1300\text{--}1000\text{ cm}^{-1}$), and C–H aromatics ($900\text{--}690\text{ cm}^{-1}$). Thus, the antioxidant

compound in the *S. polyanthum* would have those functional groups with C=O has the lowest regression coefficient value. From the result obtained, it could be predicted that the antioxidant compound from *S. polyanthum* leaves extract is mainly from phenolics class such as phenolic acid, flavonoids, etc.

Validation of the predictive model is very important to avoid overfitting in the model. The cross-validation method was used, and the result is showed as predicted vs. reference plot for calibration and validation (Fig. 5). In this plot, a good predictive model will obtain linearity (R^2) between the predicted value and the measured value is close to 1, and the root mean

square error (RMSE) for calibration and validation is close to 0. As can be seen from the plot, the R^2 for calibration and validation were 0.977 and 0.969, while the RMSE for calibration and validation were 0.32 and 1.10, respectively. Hence, in this study, the PLS model was categorized as a good model because the R^2 and RMSE value is close to 1 and 0, respectively.

■ CONCLUSION

Antioxidant activity and FTIR spectrum of *S. polyanthum* leave extract are affected by variations in solvent concentration. The highest antioxidant activity and total phenolic content were shown in 30% and 50% ethanol extract, respectively. FTIR spectra of each extract have a similar pattern but could be grouped by PCA with a total variance of PC-1 and PC-2 about 88%. Based on PLS analysis, it was found that O–H, C–H sp^3 , C=O, C=C, C–O, and C–H aromatic give a contribution to the antioxidant activity of *S. polyanthum* leave extract.

■ REFERENCES

- [1] Darusman, L.K., Wahyuni, W.T., and Alwi, F., 2013, Acetylcholinesterase inhibition and antioxidant activity of *Syzygium cumini*, *S. Aromaticum* and *S. Polyanthum* from Indonesia, *J. Biol. Sci.*, 13 (5), 412–416.
- [2] Malik, A., and Ahmad, A.R., 2013, Antidiarrheal activity of ethanolic extract of bay leaves (*Syzygium polyanthum* (Wight) Walp.), *Int. Res. J. Pharm.*, 4 (4), 106–108.
- [3] Muthia, R., Suganda, A.G., and Sukandar, E.Y., 2017, Angiotensin-1 converting enzyme (ACE) inhibitory activity of several Indonesian medicinal plants, *Res. J. Pharm. Biol. Chem. Sci.*, 8 (Suppl. 1), 192–199.
- [4] Widyawati, T., Yusoff, N.A., Asmawi, M.Z., and Ahmad, M., 2015, Antihyperglycemic effect of methanol extract of *Syzygium polyanthum* (Wight.) leaf in streptozotocin-induced diabetic rats, *Nutrients*, 7 (9), 7764–7780.
- [5] Kusuma, I.W., Kuspradini, H., Arung, E.T., Aryani, F., Min, Y.H., Kim, J.S., and Kim, Y.U., 2011, Biological activity and phytochemical analysis of three Indonesian medicinal plants, *Murraya koenigii*, *Syzygium polyanthum* and *Zingiber purpurea*, *J. Acupunct. Meridian Stud.*, 4 (1), 75–79.
- [6] Sulistiyani, Falah, S., Wahyuni, W.T., Sugahara, T., Tachibana, S., and Syaefudin, 2014, Cellular mechanism of the cytotoxic effect of extracts from *Syzygium polyanthum* leaves, *Am. J. Drug Discovery Dev.*, 4 (2), 90–101.
- [7] Hartanti, D., Djalil, A.D., Yulianingsih, N., and Hamad, A., 2019, The effect of infusion of *Syzygium polyanthum* (Wight) Walp. leaves as natural preservative chicken meats, *JKI*, 9 (1), 19–27.
- [8] Lin, S., Zhang, G., Liao, Y., Pan, J., and Gong, D., 2015, Dietary flavonoids as xanthine oxidase inhibitors: Structure affinity and structure activity relationships, *J. Agric. Food Chem.*, 63 (35), 7784–7794.
- [9] Sultana, B., Anwar, F., and Ashraf, M., 2009, Effect of extraction solvent/technique on the antioxidant activity of selected medicinal plant extracts, *Molecules*, 14 (6), 2167–2180.
- [10] Trabelsi, N., Megdiche, W., Ksouri, R., Falleh, H., Oueslati, S., Soumaya, B., Hajlaoui, H., and Abdelly, C., 2010, Solvent effects on phenolic contents and biological activities of the halophyte *Limoniastrum monopetalum* leaves, *LWT Food Sci. Technol.*, 43 (4), 632–639.
- [11] Cambiaghi, A., Ferrario, M., and Masseroli, M., 2017, Analysis of metabolomic data: tools, current strategies and future challenges for omics data integration, *Briefings Bioinf.*, 18 (3), 498–510.
- [12] Lohr, E.K., Khattri, R.B., Guingab-Cagmat, J., Camp, E.F., Merritt, M.E., Garrett, T.J., and Patterson, J.T., 2019, Metabolomic profiles differ among unique genotypes of a threatened Caribbean coral, *Sci. Rep.*, 9, 6067.
- [13] Sajak, A.A.B., Abas, F., Ismail, A., and Khatib, A., 2016, Effect of different drying treatments and solvent ratios on phytochemical constituents of *Ipomoea aquatica* and correlation with α -glucosidase inhibitory activity, *Int. J. Food Prop.*, 19 (12), 2817–2831.
- [14] Guo, S., Yu, S., Qian, Y., Hu, M., Shan, M., Chen, P., Chen, Y., Zhang, L., Ding, A., Wu, Q., and Li, S.,

- 2017, Correlation of antioxidant activity and volatile oil chemical components from *Schizonepeta tenuifolia* herbs by chemometric method, *Int. J. Food Prop.*, 51 (20), 1082–1092.
- [15] Easmin, S., Sarker, M.Z.I., Ghafoor, K., Ferdosh, S., Jaffri, J., Ali, M.E., Mirhosseini, Al-Juhaimi, F.Y., Perumal, V., and Khatib, A., 2017, Rapid investigation of α -glucosidase inhibitory activity of *Phaleria macrocarpa* extracts using FTIR-ATR based fingerprinting, *J. Food Drug Anal.*, 25 (2), 306–315.
- [16] Khatib, A., Perumal, V., Ahmed, Q.U., Uzir, B.F., Abas, F., and Murugesu, S., 2017, Characterization of antioxidant activity of *Momordica charantia* fruit by infrared based fingerprinting, *Anal. Lett.*, 50 (12), 1977–1991.
- [17] Aziz, Z., Yuliana, N.D., Simanjuntak, P., Rafi, M., and Abdillah, S., 2020, FTIR and HPLC-based metabolomics of yacon leaves extracts (*Smallanthus sonchifolius* [Poepp & Endl.] H. Robinson) from two locations in Indonesia, *Indones. J. Chem.*, 20 (3), 567–578.
- [18] Badan Pengawas Obat dan Makanan, 2004, *Monografi Ekstrak Tumbuhan Obat Indonesia*, Volume 1, Badan Pemeriksa Obat dan Makanan RI, Jakarta.
- [19] Premakumara, G.A.S., Abeysekera, W.K.S.M., Ratnasooriya, W.D., Chandrasekharan, N.V., and Bentota, A.P., 2013, Antioxidant, anti-amylase and anti-glycation potential of brans of some Sri Lankan traditional and improved rice (*Oryza sativa* L.) varieties, *J. Cereal Sci.*, 58 (3), 451–456.
- [20] Salazar-Arandra, R., Perez-Lopez, L.A., Lopez-Arroyo, J., Alanis-Garza, B.A., Torres, N.W., 2011, Antimicrobial and antioxidant activities of plants from Northeast of Mexico, *Evid. Based Compl. Altern. Med.*, 2011, 536139.
- [21] Molyneux, P., 2004, The use of the stable free radical diphenylpicrylhydrazyl (DPPH) for estimating antioxidant activity, *Songklanakarinn J. Sci. Technol.*, 26 (2), 211–219.
- [22] Mediani, A., Abas, F., Khatib, A., Maulidiani, H., Shaari, K., Choi, Y.H., and Lajis, N.H., 2012, ¹H-NMR-based metabolomics approach to understanding the drying effects on the phytochemicals in *Cosmos caudatus*, *Food Res. Int.*, 49 (2), 763–770.

Supplementary Data

This supplementary data is a part of paper entitled “Ligand Based Pharmacophore Modeling, Virtual Screening, and Molecular Docking Studies of Asymmetrical Hexahydro-2H-Indazole Analogs of Curcumin (AIACs) to Discover Novel Estrogen Receptors Alpha (ER α) Inhibitor”.

Table S1.a. The intermediate of designed compound structures

No	Compound code	Structure	R ₁	R ₂
1	1A		H	H
2	1B		H	CH ₃
3	1C		H	Cl
4	1D		H	F
5	1E		H	OCH ₃
6	1F		OCH ₃	OCH ₃

Table S1.b. The AMACs compound structures

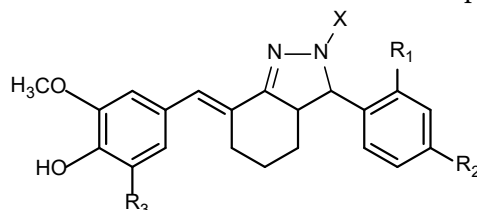
No	Compound code	Structure	R ₁	R ₂	R ₃
7	2A		H	H	H
8	2B		H	CH ₃	H
9	2C		H	Cl	H
10	2D		H	F	H
11	2E		H	OCH ₃	H
12	2F		OCH ₃	OCH ₃	H

Table S1.c. The AIACs compound structures I

No	Compound code	Structure	R ₁	R ₂	R ₃	X
13	3A1		H	H	H	H
14	3A2		H	CH ₃	H	H
15	3A3		H	Cl	H	H
16	3A4		H	F	H	H
17	3A5		H	OCH ₃	H	H
18	3A6		OCH ₃	OCH ₃	H	H
19	3A7		H	H	H	phenyl
20	3A8		H	CH ₃	H	phenyl
21	3A9		H	Cl	H	phenyl
22	3A10		H	F	H	phenyl
23	3A11		H	OCH ₃	H	phenyl
24	3A12		OCH ₃	OCH ₃	H	phenyl

Table S1.d. The AIACs compound structures II

No	Compound code	Structure	R ₁	R ₂	R ₃	X
25	3B1		H	H	H	H
26	3B2		H	CH ₃	H	H
27	3B3		H	Cl	H	H
28	3B4		H	F	H	H
29	3B5		H	OCH ₃	H	H
30	3B6		OCH ₃	OCH ₃	H	H
31	3B7		H	H	H	phenyl
32	3B8		H	CH ₃	H	phenyl
33	3B9		H	Cl	H	phenyl
34	3B10		H	F	H	phenyl
35	3B11		H	OCH ₃	H	phenyl
36	3B12		OCH ₃	OCH ₃	H	phenyl

Table S1.e. The Mannich base derivative of AIACs compound structures I

No	Compound code	R ₁	R ₂	R ₃ ')	X
37	4A1A	H	H	CH ₂ -(A)	H
38	4A1B	H	H	CH ₂ -(B)	H
39	4A1C	H	H	CH ₂ -(C)	H
40	4A1D	H	H	CH ₂ -(D)	H
41	4A1E	H	H	CH ₂ -(E)	H
42	4A2A	H	CH ₃	CH ₂ -(A)	H
43	4A2B	H	CH ₃	CH ₂ -(B)	H
44	4A2C	H	CH ₃	CH ₂ -(C)	H
45	4A2D	H	CH ₃	CH ₂ -(D)	H
46	4A2E	H	CH ₃	CH ₂ -(E)	H
47	4A3A	H	Cl	CH ₂ -(A)	H
48	4A3B	H	Cl	CH ₂ -(B)	H
49	4A3C	H	Cl	CH ₂ -(C)	H
50	4A3D	H	Cl	CH ₂ -(D)	H
51	4A3E	H	Cl	CH ₂ -(E)	H
52	4A4A	H	F	CH ₂ -(A)	H
53	4A4B	H	F	CH ₂ -(B)	H
54	4A4C	H	F	CH ₂ -(C)	H
55	4A4D	H	F	CH ₂ -(D)	H
56	4A4E	H	F	CH ₂ -(E)	H
57	4A5A	H	OCH ₃	CH ₂ -(A)	H

Table S1.e. The Mannich base derivative of AIACs compound structures I (*Continued*)

No	Compound code	R ₁	R ₂	R ₃ ^{*)}	X
58	4A5B	H	OCH ₃	CH ₂ -(B)	H
59	4A5C	H	OCH ₃	CH ₂ -(C)	H
60	4A5D	H	OCH ₃	CH ₂ -(D)	H
61	4A5E	H	OCH ₃	CH ₂ -(E)	H
62	4A6A	OCH ₃	OCH ₃	CH ₂ -(A)	H
63	4A6B	OCH ₃	OCH ₃	CH ₂ -(B)	H
64	4A6C	OCH ₃	OCH ₃	CH ₂ -(C)	H
65	4A6D	OCH ₃	OCH ₃	CH ₂ -(D)	H
66	4A6E	OCH ₃	OCH ₃	CH ₂ -(E)	H
67	4A7A	H	H	CH ₂ -(A)	phenyl
68	4A7B	H	H	CH ₂ -(B)	phenyl
69	4A7C	H	H	CH ₂ -(C)	phenyl
70	4A7D	H	H	CH ₂ -(D)	phenyl
71	4A7E	H	H	CH ₂ -(E)	phenyl
72	4A8A	H	CH ₃	CH ₂ -(A)	phenyl
73	4A8B	H	CH ₃	CH ₂ -(B)	phenyl
74	4A8C	H	CH ₃	CH ₂ -(C)	phenyl
75	4A8D	H	CH ₃	CH ₂ -(D)	phenyl
76	4A8E	H	CH ₃	CH ₂ -(E)	phenyl
77	4A9A	H	Cl	CH ₂ -(A)	phenyl
78	4A9B	H	Cl	CH ₂ -(B)	phenyl
79	4A9C	H	Cl	CH ₂ -(C)	phenyl
80	4A9D	H	Cl	CH ₂ -(D)	phenyl
81	4A9E	H	Cl	CH ₂ -(E)	phenyl
82	4A10A	H	F	CH ₂ -(A)	phenyl
83	4A10B	H	F	CH ₂ -(B)	phenyl
84	4A10C	H	F	CH ₂ -(C)	phenyl
85	4A10D	H	F	CH ₂ -(D)	phenyl
86	4A10E	H	F	CH ₂ -(E)	phenyl
87	4A11A	H	OCH ₃	CH ₂ -(A)	phenyl
88	4A11B	H	OCH ₃	CH ₂ -(B)	phenyl
89	4A11C	H	OCH ₃	CH ₂ -(C)	phenyl
90	4A11D	H	OCH ₃	CH ₂ -(D)	phenyl
91	4A11E	H	OCH ₃	CH ₂ -(E)	phenyl
92	4A12A	OCH ₃	OCH ₃	CH ₂ -(A)	phenyl
93	4A12B	OCH ₃	OCH ₃	CH ₂ -(B)	phenyl
94	4A12C	OCH ₃	OCH ₃	CH ₂ -(C)	phenyl
95	4A12D	OCH ₃	OCH ₃	CH ₂ -(D)	phenyl
96	4A12E	OCH ₃	OCH ₃	CH ₂ -(E)	phenyl

*) R₃ = CH₂-(..) = Mannich bases group

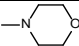
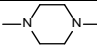
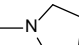
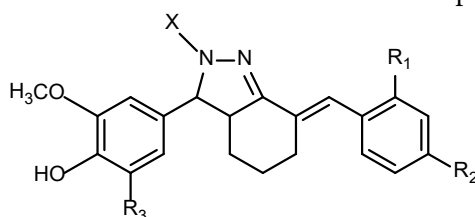
(..)	Structure	(..)	Structure	(..)	Structure
A	-N(CH ₃) ₂	C		E	
B	-N(C ₂ H ₅) ₂	D			

Table S1.f. The Mannich base derivative of AIACs compound structures II

No	Compound code	R ₁	R ₂	R ₃ ^{a)}	X
97	4B1A	H	H	CH ₂ -(A)	H
98	4B1B	H	H	CH ₂ -(B)	H
99	4B1C	H	H	CH ₂ -(C)	H
100	4B1D	H	H	CH ₂ -(D)	H
101	4B1E	H	H	CH ₂ -(E)	H
102	4B2A	H	CH ₃	CH ₂ -(A)	H
103	4B2B	H	CH ₃	CH ₂ -(B)	H
104	4B2C	H	CH ₃	CH ₂ -(C)	H
105	4B2D	H	CH ₃	CH ₂ -(D)	H
106	4B2E	H	CH ₃	CH ₂ -(E)	H
107	4B3A	H	Cl	CH ₂ -(A)	H
108	4B3B	H	Cl	CH ₂ -(B)	H
109	4B3C	H	Cl	CH ₂ -(C)	H
110	4B3D	H	Cl	CH ₂ -(D)	H
111	4B3E	H	Cl	CH ₂ -(E)	H
112	4B4A	H	F	CH ₂ -(A)	H
113	4B4B	H	F	CH ₂ -(B)	H
114	4B4C	H	F	CH ₂ -(C)	H
115	4B4D	H	F	CH ₂ -(D)	H
116	4B4E	H	F	CH ₂ -(E)	H
117	4B5A	H	OCH ₃	CH ₂ -(A)	H
118	4B5B	H	OCH ₃	CH ₂ -(B)	H
119	4B5C	H	OCH ₃	CH ₂ -(C)	H
120	4B5D	H	OCH ₃	CH ₂ -(D)	H
121	4B5E	H	OCH ₃	CH ₂ -(E)	H
122	4B6A	OCH ₃	OCH ₃	CH ₂ -(A)	H
123	4B6B	OCH ₃	OCH ₃	CH ₂ -(B)	H
124	4B6C	OCH ₃	OCH ₃	CH ₂ -(C)	H
125	4B6D	OCH ₃	OCH ₃	CH ₂ -(D)	H
126	4B6E	OCH ₃	OCH ₃	CH ₂ -(E)	H
127	4B7A	H	H	CH ₂ -(A)	phenyl
128	4B7B	H	H	CH ₂ -(B)	phenyl
129	4B7C	H	H	CH ₂ -(C)	phenyl
130	4B7D	H	H	CH ₂ -(D)	phenyl
131	4B7E	H	H	CH ₂ -(E)	phenyl
132	4B8A	H	CH ₃	CH ₂ -(A)	phenyl
133	4B8B	H	CH ₃	CH ₂ -(B)	phenyl

Table S1.f. The Mannich base derivative of AIACs compound structures II (*Continued*)

No	Compound code	R ₁	R ₂	R ₃ ^{*)}	X
134	4B8C	H	CH ₃	CH ₂ -(C)	phenyl
135	4B8D	H	CH ₃	CH ₂ -(D)	phenyl
136	4B8E	H	CH ₃	CH ₂ -(E)	phenyl
137	4B9A	H	Cl	CH ₂ -(A)	phenyl
138	4B9B	H	Cl	CH ₂ -(B)	phenyl
139	4B9C	H	Cl	CH ₂ -(C)	phenyl
140	4B9D	H	Cl	CH ₂ -(D)	phenyl
141	4B9E	H	Cl	CH ₂ -(E)	phenyl
142	4B10A	H	F	CH ₂ -(A)	phenyl
143	4B10B	H	F	CH ₂ -(B)	phenyl
144	4B10C	H	F	CH ₂ -(C)	phenyl
145	4B10D	H	F	CH ₂ -(D)	phenyl
146	4B10E	H	F	CH ₂ -(E)	phenyl
147	4B11A	H	OCH ₃	CH ₂ -(A)	phenyl
148	4B11B	H	OCH ₃	CH ₂ -(B)	phenyl
149	4B11C	H	OCH ₃	CH ₂ -(C)	phenyl
150	4B11D	H	OCH ₃	CH ₂ -(D)	phenyl
151	4B11E	H	OCH ₃	CH ₂ -(E)	phenyl
152	4B12A	OCH ₃	OCH ₃	CH ₂ -(A)	phenyl
153	4B12B	OCH ₃	OCH ₃	CH ₂ -(B)	phenyl
154	4B12C	OCH ₃	OCH ₃	CH ₂ -(C)	phenyl
155	4B12D	OCH ₃	OCH ₃	CH ₂ -(D)	phenyl
156	4B12E	OCH ₃	OCH ₃	CH ₂ -(E)	phenyl

*) R₃ = CH₂-(..) = Mannich bases group

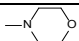
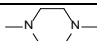
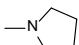
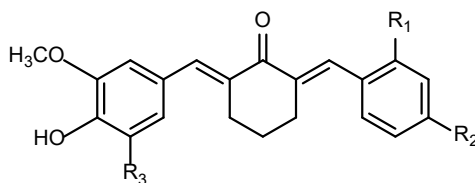
(..)	Structure	(..)	Structure	(..)	Structure
A	-N(CH ₃) ₂	C		E	
B	-N(C ₂ H ₅) ₂	D			

Table S1.g. The Mannich base derivative of AMACs compound structures

No	Compound code	R ₁	R ₂	R ₃
157	2AA	H	H	CH ₂ -(A)
158	2AB	H	H	CH ₂ -(B)
159	2AC	H	H	CH ₂ -(C)
160	2AD	H	H	CH ₂ -(D)
161	2AE	H	H	CH ₂ -(E)
162	2BA	H	CH ₃	CH ₂ -(A)
163	2BB	H	CH ₃	CH ₂ -(B)
164	2BC	H	CH ₃	CH ₂ -(C)
165	2BD	H	CH ₃	CH ₂ -(D)
166	2BE	H	CH ₃	CH ₂ -(E)
167	2CA	H	Cl	CH ₂ -(A)
168	2CB	H	Cl	CH ₂ -(B)
169	2CC	H	Cl	CH ₂ -(C)
170	2CD	H	Cl	CH ₂ -(D)
171	2CE	H	Cl	CH ₂ -(E)
172	2CA	H	F	CH ₂ -(A)
173	2DB	H	F	CH ₂ -(B)
174	2DC	H	F	CH ₂ -(C)
175	2DD	H	F	CH ₂ -(D)
176	2DE	H	F	CH ₂ -(E)
177	2EA	H	OCH ₃	CH ₂ -(A)
178	2EB	H	OCH ₃	CH ₂ -(B)
179	2EC	H	OCH ₃	CH ₂ -(C)
180	2ED	H	OCH ₃	CH ₂ -(D)
181	2EE	H	OCH ₃	CH ₂ -(E)
182	2FA	OCH ₃	OCH ₃	CH ₂ -(A)
183	2FB	OCH ₃	OCH ₃	CH ₂ -(B)
184	2FC	OCH ₃	OCH ₃	CH ₂ -(C)
185	2FD	OCH ₃	OCH ₃	CH ₂ -(D)
186	2FE	OCH ₃	OCH ₃	CH ₂ -(E)

^{*)} R₃ = CH₂-(..) = Mannich bases group

(..)	Structure	(..)	Structure	(..)	Structure
A	-N(CH ₃) ₂	C		E	
B	-N(C ₂ H ₅) ₂	D			

Table S2.a. Four native ligands of ER α receptor

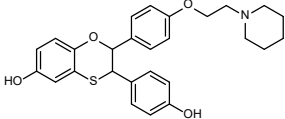
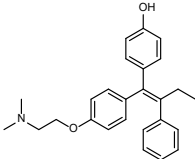
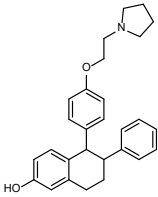
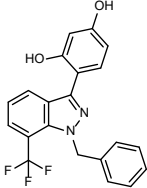
No	Native Ligand Name	PDB ID	Molecular Formula	Molecular Weight
1	E4D600	1SJ0	C ₂₇ H ₂₉ N ₁ O ₄ S ₁	463.60
				
2	OHT201	2OUZ	C ₂₆ H ₃₀ N ₁ O ₂	388.53
				
3	C3D999	2P7Z	C ₂₈ H ₃₁ N ₁ O ₂	413.56
				
4	KN01	3OS8	C ₂₁ H ₁₅ N ₂ O ₂ F ₃	384.36
				

Table S2.b. Data of 30 ER α inhibitor compounds

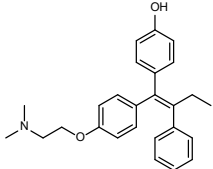
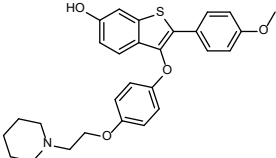
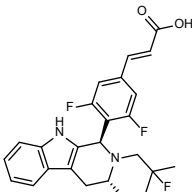
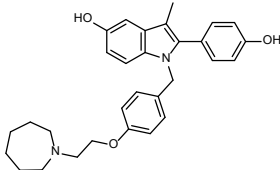
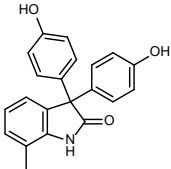
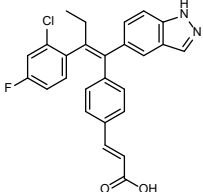
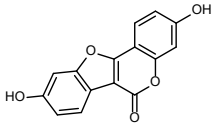
No	ER α inhibitor compounds	Pubchem CID	Molecular Formula	Molecular Weight	pIC ₅₀ (M)
1	4-OH-Tamoxifene/Afimoxifene 	449459	C ₂₆ H ₂₉ NO ₂	387.5	9.30
2	Arzoxifene 	179337	C ₂₈ H ₂₉ NO ₄ S	475.6	7.67
3	AZD9496 	86287635	C ₂₅ H ₂₅ F ₃ N ₂ O ₂	442.5	9.86
4	Bazedoxifene 	154257	C ₃₀ H ₃₄ N ₂ O ₃	470.6	9.22
5	BHPI 	3860640	C ₂₁ H ₁₇ NO ₃	331.4	7.57
6	Brilanestrant/GDC-0810 	56941241	C ₂₆ H ₂₀ ClFN ₂ O ₂	446.9	8.21
7	Coumestrol 	5281707	C ₁₅ H ₈ O ₅	268.22	7.96

Table S2.b. Data of 30 ER α inhibitor compounds (*Continued*)

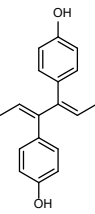
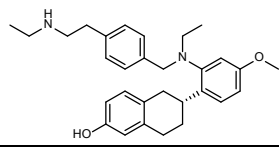
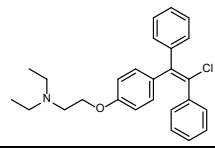
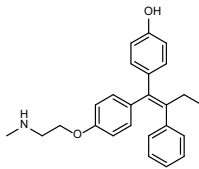
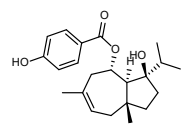
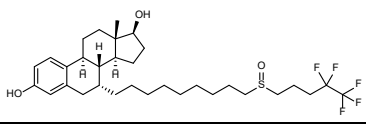
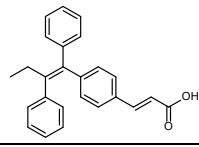
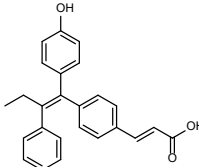
No	ER α inhibitor compounds	Pubchem CID	Molecular Formula	Molecular Weight	pIC ₅₀ (M)
8	Dienestrol 	667476	C ₁₈ H ₁₈ O ₂	266.3	7.82
9	Elacestrant 	23642301	C ₃₀ H ₃₈ N ₂ O ₂	458.6	7.32
10	Enclomiphene 	1548953	C ₂₆ H ₂₈ ClNO	406	7.11
11	Endoxifen 	10090750	C ₂₅ H ₂₇ NO ₂	373.5	7.82
12	Ferutinin 	354654	C ₂₂ H ₃₀ O ₄	358.5	7.48
13	Fulvestran = Faslodex 	104741	C ₃₂ H ₄₇ F ₅ O ₃ S	606.8	9.09
14	GW 5638 	5288494	C ₂₅ H ₂₂ O ₂	354.4	8.49
15	GW 7604 	9799518	C ₂₅ H ₂₂ O ₃	370.4	6.89

Table S2.b. Data of 30 ER α inhibitor compounds (*Continued*)

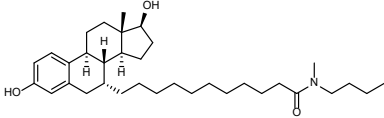
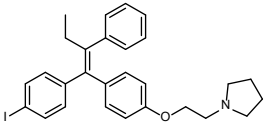
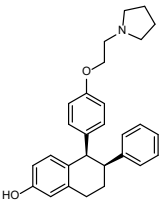
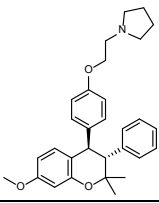
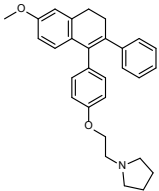
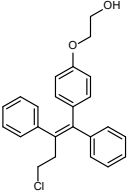
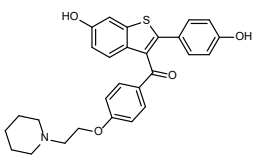
No	ER α inhibitor compounds	Pubchem CID	Molecular Formula	Molecular Weight	pIC ₅₀ (M)
16	ICI-164384 	104772	C ₃₄ H ₅₅ NO ₃	525.8	8.52
17	Idoxifene 	3034011	C ₂₈ H ₃₀ INO	523.4	6.47
18	Lasofoxifene 	3081919	C ₃₂ H ₃₇ NO ₈	563.6	8.82
19	Levormeloxifene 	35805	C ₃₀ H ₃₅ NO ₃	457.6	8.14
20	Nafoxidine 	4416	C ₂₉ H ₃₁ NO ₂	425.6	5.13
21	Ospemiphene 	3036505	C ₂₄ H ₂₃ ClO ₂	378.9	6.10
22	Raloxifene 	5035	C ₂₈ H ₂₇ NO ₄ S	473.6	8.40

Table S2.b. Data of 30 ER α inhibitor compounds (*Continued*)

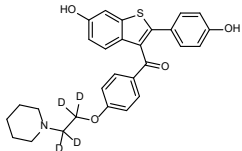
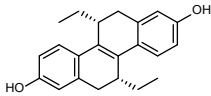
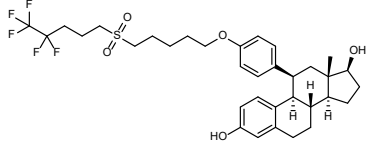
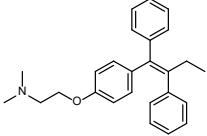
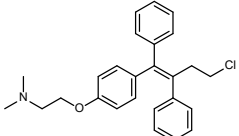
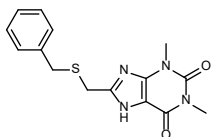
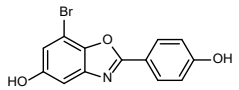
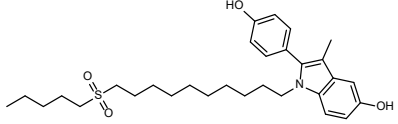
No	ER α inhibitor compounds	Pubchem CID	Molecular Formula	Molecular Weight	pIC ₅₀ (M)
23	Raloxifene d4 	25217190	C ₂₈ H ₂₇ NO ₄ S	477.6	9.43
24	(R,R)-THC 	446849	C ₂₂ H ₂₄ O ₂	320.4	4.98
25	RU58668 	6918261	C ₃₄ H ₄₃ F ₅ O ₅ S	658.8	4.40
26	Tamoxifene 	2733526	C ₂₆ H ₂₉ NO	371.5	6.76
27	Toremifene 	3005573	C ₂₆ H ₂₈ ClNO	406	6.00
28	TPBM 	262425	C ₁₅ H ₁₆ N ₄ O ₂ S	316.4	5.30
29	WAY 200070 	135418373	C ₁₃ H ₈ BrNO ₃	306.11	7.20
30	ZK 164015 	9806489	C ₃₀ H ₄₃ NO ₄ S	513.7	4.60

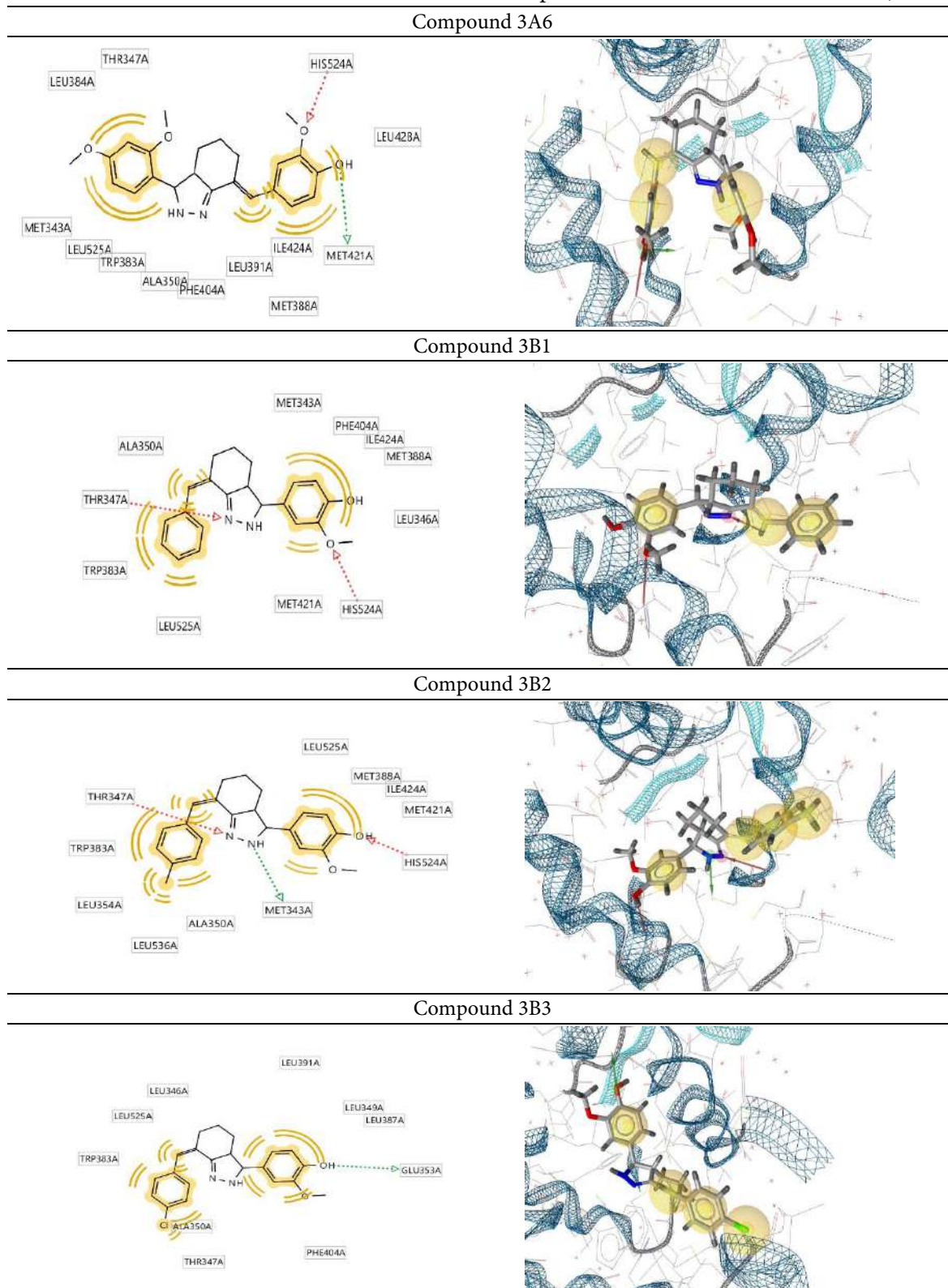
Table S3. 2D and 3D visualization results of 10 selected compounds and Tamoxifen docked at 1SJ0 receptors

Table S3. 2D and 3D visualization results of 10 selected compounds and Tamoxifen docked at 1SJ0 receptors (Continued)

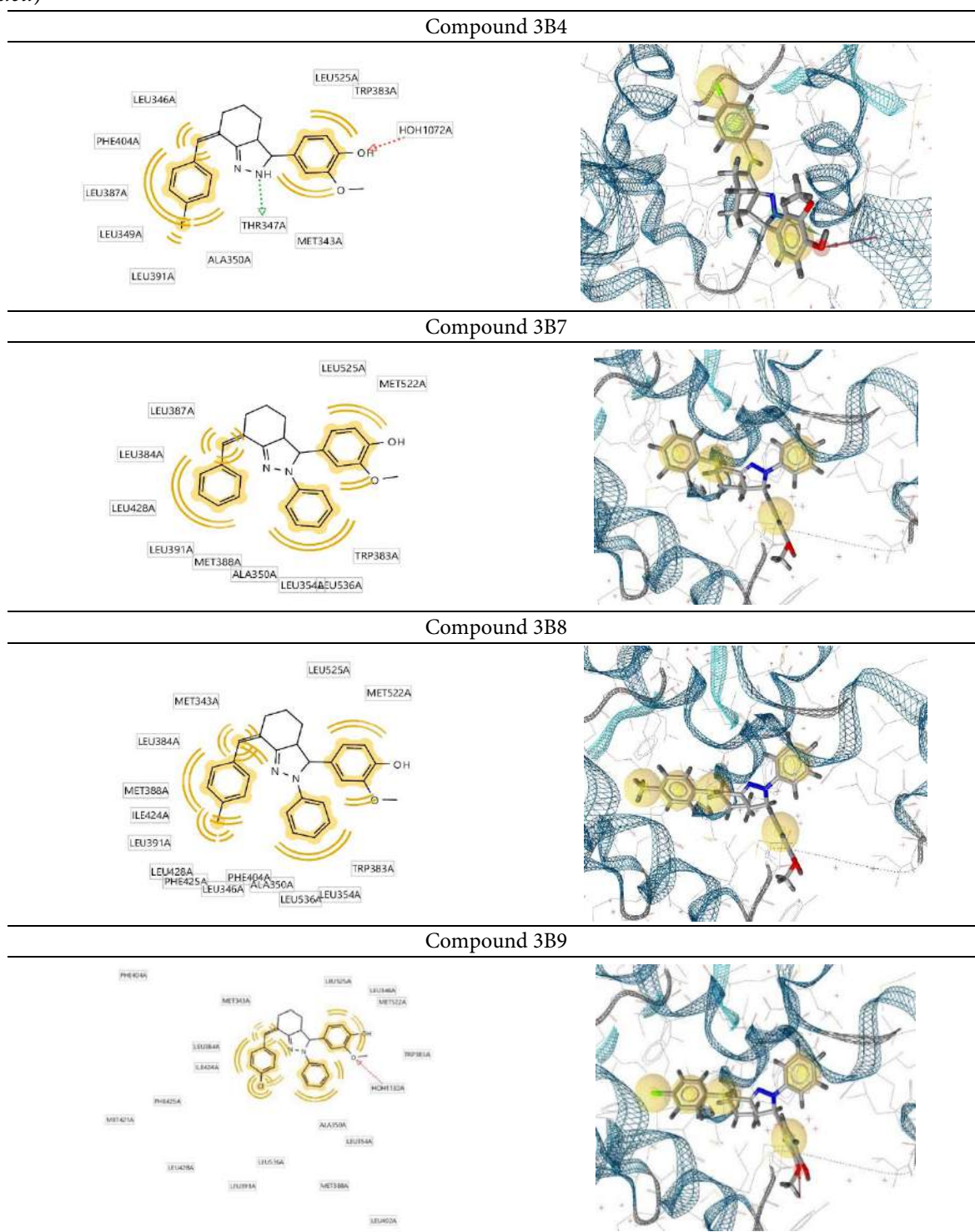


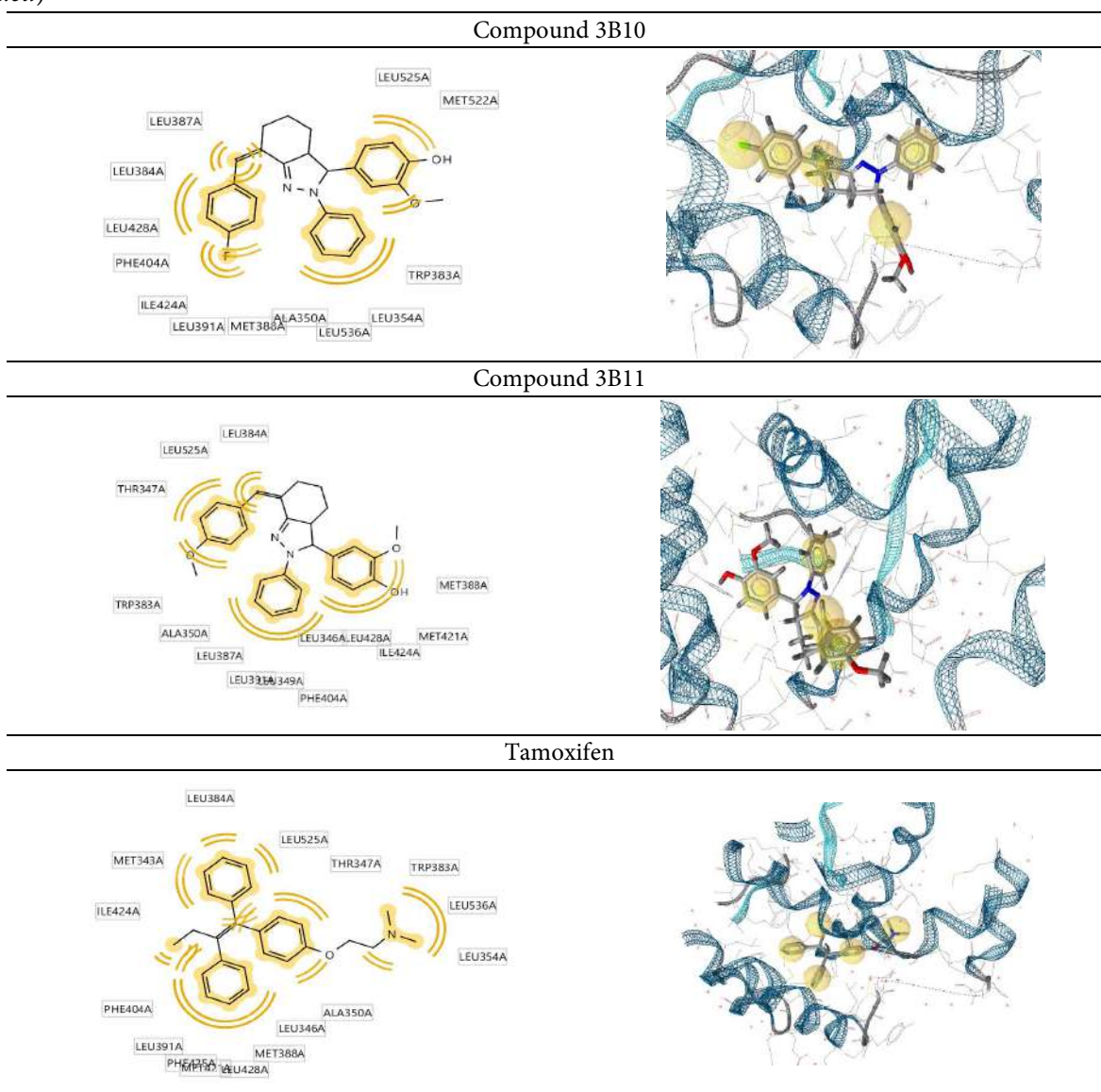

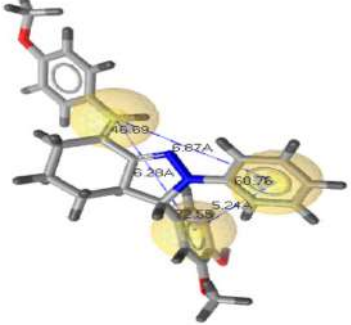
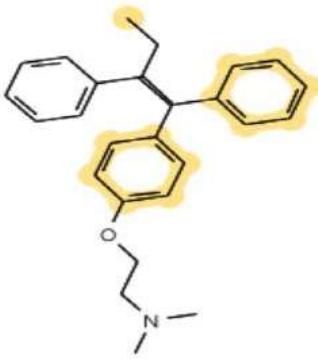
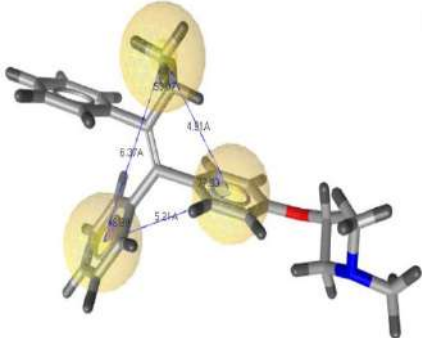
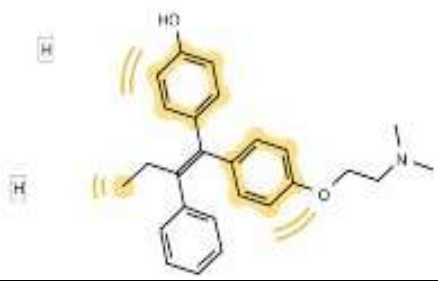
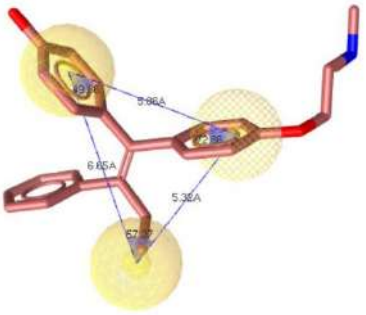
Table S3. 2D and 3D visualization results of 10 selected compounds and Tamoxifen docked at 1SJO receptors (Continued)

Table S4. 2D and 3D visualization of chemical features with triangular patterns (*Continued*)

Ligands	2D feature image	3D feature image
3B11		
Tamoxifen		
Feature Model 2		

Ligand Based Pharmacophore Modeling, Virtual Screening, and Molecular Docking Studies of Asymmetrical Hexahydro-2H-Indazole Analogs of Curcumin (AIACs) to Discover Novel Estrogen Receptors Alpha (ER α) Inhibitor

Hariyanti¹, Kusmardi², Arry Yanuar³, and Hayun^{3,*}

¹Faculty of Pharmacy and Science, Universitas Muhammadiyah Prof. DR. HAMKA, Jl. Delima II/IV, Duren Sawit, East Jakarta 13460, Indonesia

²Faculty of Medicine, Universitas Indonesia, UI Salemba Campus, Jl. Salemba Raya No. 6, Central Jakarta 10430, Indonesia

³Faculty of Pharmacy, Universitas Indonesia, Depok 16424, West Java, Indonesia

* **Corresponding author:**

email: hayun@farmasi.ui.ac.id

Received: March 8, 2020

Accepted: September 17, 2020

DOI: 10.22146/ijc.54745

Abstract: The estrogen receptor alpha (ER α) plays an important role in breast development and pro-proliferation signal activation in the normal and cancerous breast. The ER α inhibitors were potentially active as cytotoxic agents against breast cancer. This study was conducted in order to find Asymmetrical Hexahydro-2H-Indazole Analogs of Curcumin (AIACs) as hits of ER α inhibitor. A training set of 17 selected ER α inhibitors was used to create 10 pharmacophore models using LigandScout 4.2. The pharmacophore models were validated using 383 active compounds as positive data and 20674 decoys as negative data obtained from DUD.E. Model 2 was found as the best pharmacophore model and consisted of three types of pharmacophore features, viz. one hydrophobic, one hydrogen bond acceptor, and aromatic interactions. Model 2 was utilized for ligand-based virtual screening 186 of AIACs, AMACs, intermediates, and Mannich base derivative compounds. The hits obtained were further screened using molecular docking, analyzed using drug scan, and tested for its synthesis accessibility. Fourteen compounds were fulfilled as hits in pharmacophore modeling, in which 10 hits were selected by molecular docking, but only seven hits met Lipinski's rule of five and had medium synthesis accessibility. In conclusion, seven compounds were suggested to be potentially active as ER α inhibitors and deserve to be synthesized and further investigated.

Keywords: asymmetric hexahydro-2H-indazole analogs of curcumin; AIACs; estrogen receptor alpha inhibitor; ER α inhibitor; pharmacophore modeling; molecular docking; breast cancer

■ INTRODUCTION

Breast cancer is a disease that occurs almost entirely in women. It is the second leading cause of death by a disease [1]. In 2018, 2.1 million new cases of breast cancer were found. In most countries, this disease was the most commonly diagnosed cancer (154 out of 185) [2]. The estrogen receptor alpha (ER α) plays a role in breast development and the activation of the pro-proliferation signal in normal and cancerous breasts [3]. The growth of breast cancer cells is characterized by the high expression

of the receptors [4]. Nowadays, ER α has been developed and tested as molecular targets for the treatment and prevention of breast cancer [5].

Monocarbonyl Analogs of Curcumin (MACs) and Asymmetrical Monocarbonyl Analogs of Curcumin (AMACs) were reported to show better inhibition against cancer cell proliferation of SMMC-7221, MCF-7, and PC-3 compared to curcumin [6]. Diethylamine Mannich base substitution of the phenyl ring of MACs showed increased activity and selectivity of its anticancer properties [7]. Mannich base substitution of AMACs

also showed cytotoxicity potential against HeLa, MCF-7, and WiDr cells [8-9]. The Mannich base acted as an important pharmacophore group in high-potential drugs [10].

Several studies reported that structural modification of symmetrical MACs into symmetrical Hexahydro-2H-Indazole Analog (IAC) exhibited good antioxidant and antitumor activity against Hep G2, WI38, VERO, and MCF-7 cells [11-12]. Some studies also reported that modified compounds with indazole group formation show better anticancer activity [13-14]. However, to the best of our knowledge, there were no reports about the development of AMACs into AIACs and its derivatives. In the present study, we designed 186 structures of AIACs, their derivatives, and intermediate compounds that have different substituents in one of the benzene rings.

In this study, the initial virtual screening of 186 ligand designs was carried out using the Ligand-based virtual screening (LBVS) method. The LBVS methods compare a library of compounds with a known active ligand. Two notable advantages of LBVS methods are that they do not require structural information of a target receptor and that they are faster than structure-based methods [15]. The objective of the study was to discover a new molecular entity of AIACs compounds as hits for ER α inhibitor. The 186 AIACs, AMACs, intermediates, and the Mannich base derivative compounds were screened virtually through ligand-based pharmacophore modeling, structure-based molecular docking, analysis by drug scan, and tested for its synthesis accessibility.

■ COMPUTATIONAL METHODS

Equipment

The hardware used for the calculations, pharmacophore modeling, and molecular docking was a laptop with the following specification: Desktop-AF57S8U, Processor Intel(R) Core(TM) i5-5200 CPU@ 2.20 GHz 2.20 GHz, RAM 16 GB, Operating System Windows 10, 64 bit, Graphic Card AMD Radeon R9-M275 4GB. The software used includes MarvinSketch, LigandScout 4.2, and AutoDockTools (v 4.2) integrated LigandScout software 4.2.

Procedure

Data preparation

The 186 compounds of Asymmetrical Hexahydro-2H-Indazole Analogs of Curcumin (AIACs), AMACs, its intermediate, and Mannich base derivatives were drawn using MarvinSketch (www.chemaxon.com). The structures are shown in Table S1.a-g. A set of data of 34 ER α inhibitor compounds (Table S2.a-b) that consists of four native ligands of ER PDB and 30 other compounds with pIC₅₀ values in the range of 4.40 to 9.86, were obtained from www.pubchem.com. The three-dimensional (3D) Estrogen Homo sapiens receptor alpha (ER α) in the complex with E4D600 ligands (PDB code: 1SJ0) was obtained online from a database: NCBI, Research Collaboratory for Structural Bioinformatics Protein Data Bank <http://www.pdb.org/pdb/home/> [9,16].

Pharmacophore models preparation and validation

The pharmacophore models were created using LigandScout4.2 [17]. A set of data of 34 ER α inhibitor compounds were grouped according to their cluster of chemical structure similarity. Every cluster of the compounds found was divided in the same proportion randomly to obtain two groups that consist of 17 molecules of ER α inhibitors. Seventeen selected molecules were used as a training set to create ten pharmacophore models. The 383 active compounds and 20674 decoys were used as positive and negative data to validate the pharmacophore models and determine the best pharmacophore model. The validation parameter of the receiver operating characteristic (ROC) that consisted of areas under the curves (AUC 100%) and enrichment factors (EF 1%) was calculated to determine the sensitivity, specificity, and accuracy values. The pharmacophore model with sensitivity > 0.5, specificity > 0.5, AUC value > 0.7, and a hit score > 0.7 was used as a virtual screening model [18].

Ligand-based virtual screening

The virtual screening was used to find AIACs compounds as hits of ER α inhibitors. A database of 186 AIACs and AMACs compounds in .mol file format was put in a screening database of a selected and validated pharmacophore model, then the screening process was

performed until completed. Tamoxifen was used as a positive control. The hit compounds obtained were further sorted based on the best pharmacophore fit values.

Molecular docking study

Docking simulations were carried out to visualize molecular-level interactions between the hits obtained from ligand-based pharmacophore modeling with the active site of ER α (PDB code: 1SJ0) using tamoxifen as a positive control. The docking was done using AutoDock (v4.2) (autodock.scripps.edu/resources/autodock-force-field) integrated with LigandScout. The method was validated by extracting the co-crystalline ligand (E4D600) from the ER α crystallographic structure and re-docking the copy of the ligand into its active site. The root-mean-square deviation (RMSD) value of the copy ligand conformation docked at the receptor as compared to the co-crystalline ligand conformation at the same receptor was calculated. The molecular docking was performed by running the Genetic Algorithm parameters 100 times, with algorithm generation number of 27,000, 2,500,000 energy evaluation numbers, and 150 population.

Drug scan and synthesis accessibility analysis

The drug scan and synthesis accessibility were analyzed online on a website (<http://swissadme.ch>). The analysis involved uploading the ligand file in .smile format. Then, the results were downloaded in excel format.

RESULTS AND DISCUSSION

The asymmetrical hexahydro-2H-indazole curcumins (AIACs) were designed as the development of AMACs that refers to the modification of MACs into a symmetrical hexahydro-2H-indazole analog of curcumins (IACs) that provided good results for activity in several cancer cells including breast cancer cells [12]. The AMACs and derivatives exhibited cytotoxicity potential against HeLa, MCF-7, and WiDr cell lines [8-9], thus AIACs were also predicted to have cytotoxic activities as well. The structure of the designed AIACs (Table S1.c-f) had different substituents in one of the benzene rings (-H, -CH₃, -F, -Cl, -OCH₃, -dimethoxy) by considering their different characteristics of electronegativity, electronic charge, and induction effect of the substituents resulting in different geometric shapes for each analog compound. Therefore,

the structures had variations in the bonding interactions with the receptors. In the present study, the AIACs were first screened virtually by ligand-based pharmacophore modeling. The hits obtained were then screened by structure-based modeling using molecular docking and further screened again by drug scan and synthesis accessibility analysis to obtain the new bioactive compounds as hits of ER α inhibitor.

Virtual screening (VS) has emerged as a crucial device in identifying bioactive compounds via computational means by employing knowledge on the protein target or known bioactive ligands [19]. Several VS with ER α as a protein target using the structure-based virtual screening (SBVS) protocol had been reported. The protocol screened compounds based on the interactions of the 3D structure of the compounds with the target protein [20-21]. In this study, before the compounds were screened with the SBVS protocol, the compounds were first screened using the LBVS protocol. The compounds were selected based on the similarity of the molecular structure (in terms of shape, pharmacophoric features, molecular fields, etc.), which was believed to show similar behavior. LBVS techniques that consist of substructure mining and fingerprint searches are faster than SBVS techniques (e.g., molecular docking) [22-24]. The benefit of combining docking primarily based digital screening with pharmacophore-primarily based digital screening is that the database of ligands can be pre-filtered by using a pharmacophore query, before assessment using docking simulations. The docking simulations can be published and filtered with the use of a pharmacophore question to dispose of any compounds that fail to bind consistently with the pharmacophore query. The pharmacophore version can in this case be used for the position of the ligand, in addition to the precision of a molecule towards the pharmacophore question; or to guide the placement via a constraint while scoring the extraordinary docking poses [25].

Pharmacophore Model Preparation and Validation

The 3D pharmacophore of the various training sets produced 10 pharmacophore models. The validation of the models by a data set of 383 active compounds as

positive data and 20674 decoys as negative data produced hit scores in the range of 0.7679–0.7718 and three pharmacophore features marked by red, yellow, and purple for HBA, hydrophobic, and AR interaction, respectively. The HBA interaction was formed by the hydroxyl groups in the AR and the ether group; the hydrophobic interaction was formed by the AR, which also showed AR interactions. Fig. 1 presents the 3D pharmacophore model 2 with the type of features and distance between features. The 3D and 2D pharmacophores model of training set E4D600, is shown in Fig. 2, and the types of pharmacophore features marked by color differences in the training set compound are shown in Table 1. The ROC curve of model 2 is shown in Fig. 3. The screening of the ER α inhibitors using model 2 pharmacophore produced the best result in sensitivity = 0.687; specificity = 0.845; AUC 100% = 0.80; accuracy = 0.843; EF_{1%} = 26.7 and hit score = 0.7712. The set of five hypotheses with sensitivity > 0.5, specificity > 0.5, AUC value > 0.7, and hit score > 0.7 can be used as a virtual screening model [26]. The EF and AUC values showed that the virtual screening method using pharmacophore model 2 was an excellent screening model. The EF and AUC values were worse than the SBVS protocol reported by Yuniarti et al. [27], but it was still better than the results reported by Setiawati et al. [28], and also the EF and AUC values of the SBVS protocol used to identify ligands for ER α in DUD-E (EF = 15.4, AUC = 0.675) [29]. Therefore, the virtual screening of 186 AIACs and AMACs compounds was performed using model 2.

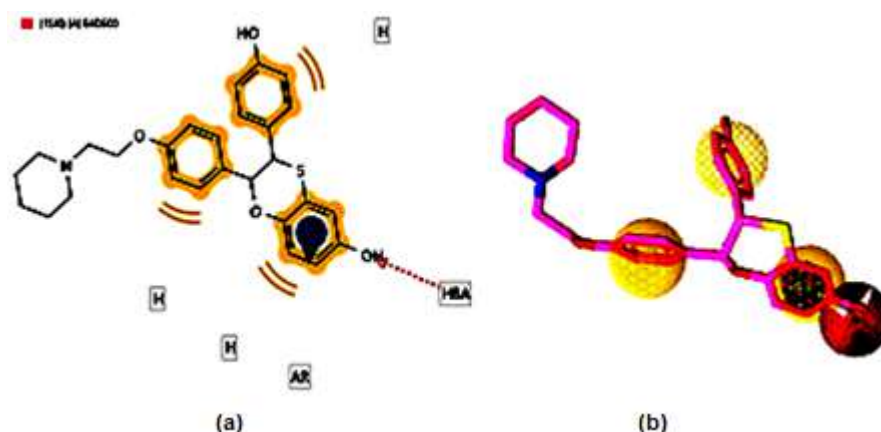


Fig 2. Pharmacophore (a) 2D and (b) 3D models of E4D600 obtained by the LigandScout 4.2 software

Ligand-Based Virtual Screening

The key features of the pharmacophore interactions of tamoxifen on ER α were hydrophobic interactions, HBAs, and AR interactions (Fig. 1). The virtual screening of 186 AIACs and AMACs compounds resulted in 14 hit compounds that are shown in Table 2. The pharmacophore fit values measured geometric features of molecules for 3D structure-based pharmacophore models. The higher the pharmacophore fit values indicated the higher possibility of the hit to match with the pharmacophore model and show higher activity as ER α inhibitors. The pharmacophore fit values of 14 hits ranged from 45.32 to 53.43. Compounds 3B8,

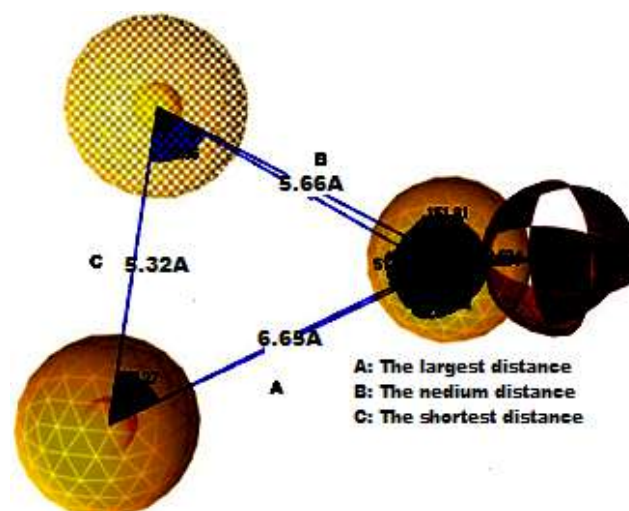


Fig 1. The pharmacophore model 2 features and the distance between features obtained by the LigandScout 4.2 software

Table 1. Types of pharmacophoric features and pharmacophore fit values of 17 training set compounds obtained by the LigandScout 4.2 software. Red, yellow, and purple indicate HBA, hydrophobic, and AR interaction, respectively

No	Active compound name	Type	Matching features ^{*)}				Pharmacophore fit
1	4-Hydroxytamoxifen	Training	AR	Hydrophobic	Hydrophobic	HBA	44.59
2	Arzoxifene	Training	AR	Hydrophobic	Hydrophobic	HBA	55.22
3	AZD9496	Training	Hydrophobic	Hydrophobic	Hydrophobic	HBA	33.87
4	BHPI	Training	Hydrophobic	Hydrophobic	Hydrophobic	HBA	43.95
5	Brilanestrant	Training	AR	Hydrophobic	Hydrophobic	HBA	43.60
6	C3D999	Training	AR	Hydrophobic	Hydrophobic	HBA	53.99
7	E4D600	Training	AR	Hydrophobic	Hydrophobic	HBA	54.13
8	Elacestrant	Training	AR	Hydrophobic	Hydrophobic	HBA	54.11
9	Ferutinin	Training	AR	Hydrophobic	Hydrophobic	HBA	45.44
10	GW_5638	Training	AR	Hydrophobic	Hydrophobic	HBA	43.42
11	GW_7604	Training	AR	Hydrophobic	Hydrophobic	HBA	44.23
12	ICI_164384	Training	AR	Hydrophobic	Hydrophobic	HBA	44.83
13	Nafoxidine	Training	AR	Hydrophobic	Hydrophobic	HBA	46.52
14	Raloxifene	Training	AR	Hydrophobic	Hydrophobic	HBA	55.10
15	Raloxifene_D4	Training	AR	Hydrophobic	Hydrophobic	HBA	55.14

Table 2. Screening results of 186 AIACS, its intermediate, and derivative compounds with pharmacophore model 2

No	Compound code	Pharmacophore features ^{*)}				Pharmacophore fit
1	3B8	AR	Hydrophobic	Hydrophobic	HBA	53.43
2	3B10	AR	Hydrophobic	Hydrophobic	HBA	53.39
3	3B7	AR	Hydrophobic	Hydrophobic	HBA	53.39
4	3A4	Hydrophobic	Hydrophobic	Hydrophobic	HBA	46.27
5	3B5	AR	Hydrophobic	Hydrophobic	HBA	46.22
6	3B2	AR	Hydrophobic	Hydrophobic	HBA	46.20
7	3B4	AR	Hydrophobic	Hydrophobic	HBA	45.96
8	3B3	AR	Hydrophobic	Hydrophobic	HBA	45.95
9	3B1	AR	Hydrophobic	Hydrophobic	HBA	45.92
10	3A11	AR	Hydrophobic	Hydrophobic	HBA	45.89
11	3B9	AR	Hydrophobic	Hydrophobic	HBA	45.79
12	3A12	AR	Hydrophobic	Hydrophobic	HBA	45.58
13	3B11	AR	Hydrophobic	Hydrophobic	HBA	45.53
14	3A6	AR	Hydrophobic	Hydrophobic	HBA	45.32

^{*)} Red, yellow, and purple indicated HBA, hydrophobic, and AR interaction, respectively

3B10, and 3B7 had the best pharmacophore fit values as indicated by their chemical features that are in harmony with the features of the tamoxifen pharmacophore model. None of the hits were Mannich base derivatives. The result was different from the result of *in vitro* evaluation against MCF-7 cell lines of the Mannich base of AMACs reported previously (active but nonselective) [8-9].

Molecular Docking

The structure of ER α in the complex with E4D600 ligands (PDB code: 1SJ0) was selected for *in silico* study because the parameters were suitable for experimental studies, with a resolution of 1.9 Å, free R-values of 0.272, and working R-values of 0.218. The R-value illustrates a measure of how well the enhanced structure predicts the

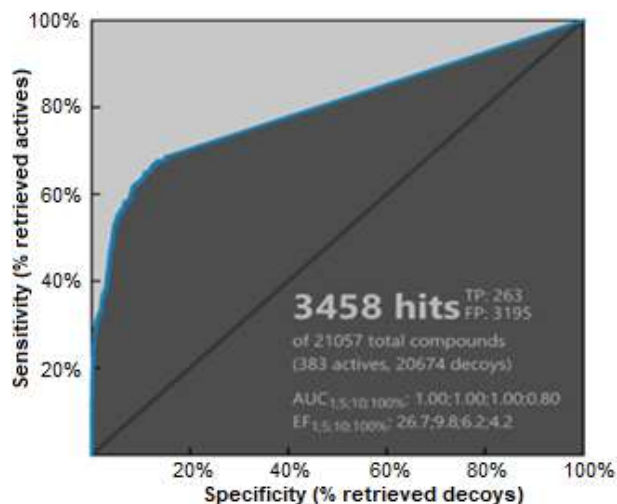


Fig 3. ROC curve model 2

observed data [30]. Interactions between co-crystalline ligand E4D600 with the active site of ER α were dominated by hydrophobic interactions with ARs, and hydrogen bonds with phenoxy and hydroxyl oxygen (Fig. 4 and 5). The best ligand-docking conformation is shown in Fig. 6. The RMSD value of the copy ligand-docking conformation in the active site of ER α compared to the co-crystalline ligand-docking conformation at the same receptor was 0.940 Å (< 2.0 Å), indicating the validity of the protocol.

The results of molecular docking of 14 hit compounds obtained from the ligand-based pharmacophore model are shown in Table 3. The free energy values, ΔG , of the 10 best hits (3A6, 3B1, 3B2, 3B3, 3B4, 3B7, 3B8, 3B9, 3B10, and 3B11) did not differ significantly with that of tamoxifen. The interaction of amino acid residues with compounds 3B8 and 3B9 was 14 and 15. It was comparable with the interaction of amino acid with tamoxifen having 17 residues (Table S3 and Table 4). The hydrophobic interaction patterns of compounds 3B7, 3B8, 3B9, 3B10, and 3B11 showed similar triangular patterns and two little differences in the distance (Table S4 and Table 5).

Drug Scan and Synthesis Accessibility Analysis

The drug scan and synthesis accessibility analysis of 10 hit compounds were performed using molecular docking study by running them in www.swissadme.ch. The results showed that seven compounds (3A6, 3B1, 3B2, 3B3, 3B4, 3B7, and 3B11) fulfilled Lipinski's Rule of

Five (Table 6) and three compounds (3B8, 3B9, and 3B10) had log P values higher than other ligands (log P > 5), while the synthesis accessibility (SA) values ranged from 4.24 to 4.67. The molecular weights of the ligands were in the range of 334.41–444.95 g/mol which is higher than tamoxifen but still met Lipinski's Rule of Five (MW < 500 g/mol). The rule was a set of in silico guidelines applied to drug discovery to prioritize compounds with a



Fig 4. Pharmacophoric features between the native ligand E4D600 with ER α derived from X-ray derivative structures (PDB code: 1SJO)

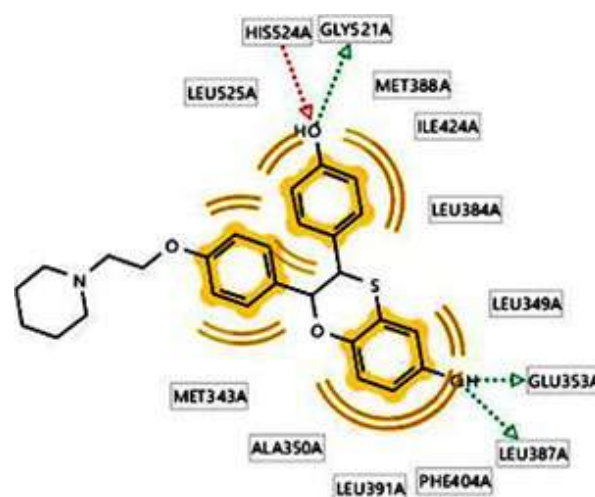


Fig 5. 2D structure visualization describes a hydrophobic bag in the form of a hydrophobic interaction of the native ligand E4D600 with a residue at the receptor. Hydrophobic interactions, donor and acceptor hydrogen bonds are described as yellow balls, green, and red arrows, respectively

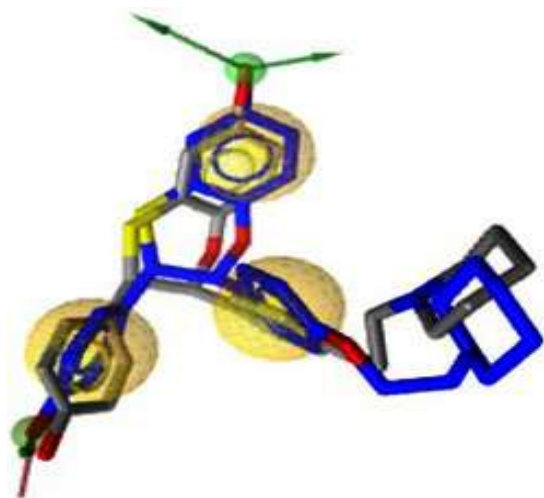


Fig 6. Superpose visualization of co-crystalline ligand (blue) with copy ligand using Autodock 4.2 integrated with Ligandscout 4.2

Table 3. Docking results of design compound molecules with estrogen receptors α (PDB code: 1SJ0)

No	Compound code	ΔG (kcal/mol)
1	3A4	-18.04
2	3A6	-18.11
3	3A11	-14.26
4	3A12	-16.34
5	3B1	-18.36
6	3B2	-18.57
7	3B3	-18.92
8	3B4	-18.37
9	3B5	-16.87
10	3B7	-20.97
11	3B8	-20.88
12	3B9	-20.90
13	3B10	-20.57
14	3B11	-20.47
15	Tamoxifen	-19.87

Table 4. Contact residues of 10 selected compounds and Tamoxifen

Contact residue	Compounds code										
	3A6	3B1	3B2	3B3	3B4	3B7	3B8	3B9	3B10	3B11	Tam*
Leu 525A	√	√	√	√	√	√	√	√	√	√	√
Thr 347A	√	√	√	√	√					√	√
Trp 383A	√	√	√	√	√	√	√	√	√	√	√
Leu 536A			√			√	√	√	√		√
Leu 354A			√			√	√	√	√		√
Ala 350A	√	√	√	√	√	√	√	√	√	√	√
Met 388A	√	√	√			√	√	√	√	√	√
Leu 391A	√			√	√	√	√	√	√	√	√
Phe 404A				√	√		√	√	√	√	√
Leu 428A	√					√	√	√	√	√	√
Leu 384A	√					√	√	√	√	√	√
Ile 424A	√	√	√				√	√	√	√	√
Met 343A	√		√		√		√	√			√
Phe 425A							√	√			√
His 524A	√	√	√								√
Met 421A	√	√	√					√		√	√
Leu 346A		√		√	√		√	√		√	√
Glu 353A				√							
Leu 349A				√	√					√	
Leu 387A				√	√	√			√	√	
Met 522A						√	√	√	√		
Leu 402A							√				

*Tam = Tamoxifen

high probability of absorption [31]. In general, Lipinski's rules describe the solubility of certain compounds that

affect the penetration of these compounds across cell membranes through passive diffusion [32]. This rule can

Table 5. The distance between the pharmacophore features of the selected compounds. Distance A, B, and C refer to Fig. 1

No	Compounds code	Distance (Å)		
		A	B	C
1	3B7	6.87	6.26	5.24
2	3B8	6.96	6.21	5.26
3	3B9	6.98	6.86	5.11
4	3B10	6.91	6.22	5.15
5	3B11	6.87	6.28	5.24
Average Distance (Å) ± SD		6.92 ± 0.051	6.37 ± 0.28	5.20 ± 0.066
6	Pharmacophores Features of Model 2	6.65	5.86	5.32
7	Tamoxifen	6.37	5.21	4.91
Difference in average distance of compounds to Model 2		0.27	0.81	0.12
Difference in average distance of compounds to Tamoxifen		0.55	1.16	0.29

Table 6. The prediction results based on Lipinski's rule of five and synthesis accessibility

Compounds code	Prediction using Lipinski's Rule of Five					Synthesis Accessibility
	MW (g/mol)	Log P (Consensus)	Hydrogen Bond Acceptor	Hydrogen bond Donor	TPSA (Å)	
3A6	394.46	3.56	5	2	72.31	4.60
3B1	334.41	3.59	3	2	53.85	4.26
3B2	348.44	3.88	3	2	53.85	4.37
3B3	368.86	4.13	3	2	53.85	4.24
3B4	352.40	3.85	4	2	53.85	4.23
3B7	410.15	4.64	3	1	45.06	4.52
3B8	424.53	5.20	3	1	45.06	4.64
3B9	444.95	5.41	3	1	45.06	4.51
3B10	428.50	5.19	4	1	45.06	4.53
3B11	440.53	4.95	4	1	54.29	4.67
Tamoxifen	371.51	5.77	2	0	12.47	3.01

also be used to predict the pharmacokinetics of a compound as a drug candidate [33].

The SA values of the 10 hits ranged from 4.23 to 4.67, which indicated that the synthesis difficulty was medium and there were no differences among the compounds. However, compounds 3B1, 3B2, 3B3, and 3B4 with SA values in the range of 4.23–4.37 were easier to synthesize than the others. The SA values were based on the analysis of structural fragments of more than 13 million compounds, assuming that the more numerous the molecular fragments, the more difficult the molecules are to prepare. Descriptors correct this fragmental

contribution method for molecular size and complexity and the SA values range from 1 (easily synthesized) to 10 (difficult to be synthesized) [34].

■ CONCLUSION

One hundred and eighty-six AIACs, AMACs, intermediates, and their Mannich base derivative compounds were successfully screened using ligand-based pharmacophore modeling, and the hits obtained were further screened using structure-based molecular docking in the active site of ER α , and were analyzed using drug scan and synthesis accessibility. Seven

compounds namely 3A6, 3B1, 3B2, 3B3, 3B4, 3B7, and 3B11 were suggested to be potentially active as ER α inhibitors and deserve to be synthesized and further investigated.

■ SUPPORTING INFORMATION

Table S1.a-g: Structures of the 186 Asymmetrical Hexahydro-2H-Indazole Analogs of Curcumin (AIACs), AMACs, its intermediate, and Mannich base derivative compounds; **Table S2.a:** Four native ligands of ER α receptor; **Table S2.b.:** Data of 30 ER α inhibitor compounds **Table S3:** 2D and 3D visualization results of 10 selected compounds and Tamoxifen docked at 1SJ0 receptors; **Table S4:** 2D and 3D visualization of chemical features with triangular patterns.

■ ACKNOWLEDGMENTS

This work was supported by the Doctoral Program Dissertation Grant Universitas Indonesia, No.: NKB-0092/UN2.R3.1/HKP.05.00/2019, which was gratefully appreciated.

■ AUTHOR CONTRIBUTIONS

HYT conducted the experiment; HY, AY and KMD supervised the experiment; HYT, HY, and AY wrote and revised the manuscript. All authors agreed to the final version of this manuscript.

■ REFERENCES

- [1] Mellatyar, H., Talaei, S., Nejati-Koshki, K., and Akbarzadeh, A., 2016, Targeting HSP90 gene expression with 17-DMAG nanoparticles in breast cancer cells, *Asian Pac. J. Cancer Prev.*, 17 (5), 2453–2457.
- [2] Bray, F., Ferlay, J., Soerjomataram, I., Siegel, R.L., Torre, L.A., and Jemal, A., 2018, Global cancer statistics 2018: GLOBOCAN estimates of incidence and mortality worldwide for 36 cancers in 185 countries, *CA Cancer J. Clin.*, 68 (6), 394–424.
- [3] Caldon, C.E., 2014, Estrogen signaling and the DNA damage response in hormone dependent breast cancer, *Front. Oncol.*, 4, 1–9.
- [4] Hayashi, S.I., Eguchi, H., Tanimoto, K., Yoshida, T., Omoto, Y., Inoue, A., Yoshida, N., and Yamaguchi, Y., 2003, The expression and function of estrogen receptor alpha and beta in human breast cancer and its clinical application, *Endocr. Relat. Cancer*, 10 (2), 193–202.
- [5] den Hollander, P., Savage, M.I., and Brown, P.H., 2013, Targeted therapy for breast cancer prevention. *Front. Oncol.*, 3, 250.
- [6] Revalde, J.L., Li, Y., Hawkins, B.C., Rosengren, R.J., and Paxton, J.W., 2015, Heterocyclic cyclohexanone monocarbonyl analogs of curcumin can inhibit the activity of ATP-binding cassette transporters in cancer multidrug resistance, *Biochem. Pharmacol.*, 93 (3), 305–317.
- [7] Yerdelen, K.O., Gul, H.I., Sakagami, H., and Umemura, N., 2015, Synthesis and biological evaluation of 1, 5-bis (4-hydroxy-3-methoxyphenyl) Penta-1, 4-dien-3-one and its aminomethyl derivatives, *J. Enzyme Inhib. Med. Chem.*, 30 (3), 383–388.
- [8] Kurnia, A., Saputri, F.C., and Hayun, H., 2019, Synthesis and anticancer potential of aminomethyl derivatives of methyl-substituted asymmetrical curcumin mono-carbonyl, *J. Appl. Pharm. Sci.*, 9 (8), 18–24.
- [9] Prasetyaningrum, P.W., Bahtiar, A., and Hayun, H., 2018, Synthesis and cytotoxicity evaluation of novel asymmetrical mono-carbonyl analogs of curcumin (AMACs) against Vero, HeLa, and MCF7 cell lines, *Sci. Pharm.*, 86, 25.
- [10] Bala, S., Sharma, N., Kajal, A., Kamboj, S., and Saini, V., 2014, Mannich bases: An important pharmacophore in present scenario, *Int. J. Med. Chem.*, 2014, 191072.
- [11] Bayomi, S.M., El-Kashef, H.A., El-Ashmawy, M.B., Nasr, M.N.A., El-Sherbeny, M.A., Badria, A., Abouzeid, L.A., Ghaly, M.A., Abdel-Aziz, N.I., 2013, Synthesis and biological evaluation of new curcumin derivatives as antioxidant and antitumor agents, *Med. Chem. Res.*, 22 (3), 1147–1162.
- [12] Bayomi, S.M., El-Kashef, H.A., El-Ashmawy, M.B., Nasr, M.N.A., El-Sherbeny, M.A., Abdel-Aziz, N.I., El-Sayed, M.A.A., Suddek, G.M., El-Messery, S.M., and Ghaly, M.A., 2015, Synthesis and biological

- evaluation of new curcumin analogues as antioxidant and antitumor agents: Molecular modeling study, *Eur. J. Med. Chem.*, 101, 584–594.
- [13] Reddy, M.T., Rddy, V.H., Reddy R.C.K., Reddy, V.K., and Reddy, Y.V.R., 2010, Synthesis and molecular docking studies of new substituted indazole derivatives for anti-breast cancer activity, *Der Pharma Chem.*, 6 (6), 411–417.
- [14] Plescia, S., Raffa, D., Plescia, F., Casula, G., Maggio, B., Daidone, G., Raimondi, M.V., Cusimano, M.G., Bombieri, G., and Meneghetti, F., 2010, Synthesis and biological evaluation of new indazole derivatives, *ARKIVOC*, 10, 163–177
- [15] Shin, W.H., Zhu, X., Bures, M.G., and Kihara, D., 2015, Three-dimensional compound comparison methods and their application in drug discovery, *Molecules*, 20 (7), 12841–12862.
- [16] Li, Q., Chen, J., Luo, S., Xu, J., Huang, Q., and Liu, T., 2015, Synthesis and assessment of the antioxidant and antitumor properties of asymmetric curcumin analogues, *Eur. J. Med. Chem.*, 93, 461–469.
- [17] Wolber, G., and Langer, T., 2005, LigandScout: 3-D pharmacophores derived from protein-bound ligands and their use as virtual screening filters, *J. Chem. Inf. Model.*, 45 (1), 160–169.
- [18] Seidel, T., Ibis, G., Bendix, F., and Wolber, G., 2010, Strategies for 3D pharmacophore-based virtual screening, *Drug Discovery Today Technol.*, 7 (4), e221–e228.
- [19] Kar, S., and Roy, K., 2013, How far can virtual screening take us in drug discovery?, *Expert Opin. Drug Discovery*, 8 (3), 245–261.
- [20] Maruthanila, V.L., Elancheran, R., Roy, N.K., Bhattacharya, A., Kunnumakkara, A.B., Kabilan, S., and Kotoky, J., 2019, In silico molecular modelling of selected natural ligands and their binding features with estrogen receptor alpha, *Curr. Comput. Aided Drug Des.*, 15 (1), 89–96.
- [21] Afreen, S., Uddin, N., Mehjabin, K.Z., Niketa, T.K., Nesa, F., Akther, S., Akther, S., Chakraborty, S., Chowdhury D., and Akther, N., 2018, In silico molecular docking approach of some selected isolated phytochemicals from *Phyllanthus emblic* against breast cancer, *BJSTR*, 10 (2), 7661–7665.
- [22] Banegas Luna, A.J., Cerón-Carrasco, J.P., and Pérez-Sánchez, H., 2018, A review of ligand-based virtual screening web tools and screening algorithms in large molecular databases in the age of big data, *Future Med. Chem.*, 10 (22), 2641–2648
- [23] Sun, Y., Zhou, H., Zhu, H., and Leung, S.W., 2016, Ligand-based virtual screening and inductive learning for identification of SIRT1 inhibitors in natural products, *Sci. Rep.*, 6 (1), 19312.
- [24] Liu, C., Yin, J., Yao, J., Xu, Z., Tao, Y., and Zhang, H., 2020, Pharmacophore-based virtual screening toward the discovery of novel anti-echinococcal compounds, *Front. Cell. Infect. Microbiol.*, 10, 118.
- [25] Qing, X., Lee, X.Y., De Raeymaecker, J., Tame, J., Zhang, K., De Maeyer, M., and Voet, A., 2014, Pharmacophore modeling: Advances, limitations, and current utility in drug discovery, *J. Recept. Ligand Channel Res.*, 7, 81–92.
- [26] Lone, M.Y., Manhas, A., Athar, M., and Jha, P.C., 2018, Identification of InhA inhibitors: A combination of virtual screening, molecular dynamics simulations, and quantum chemical studies, *J. Biomol. Struct. Dyn.*, 36 (11), 2951–2965.
- [27] Yuniarti, N., Mungkasi, S., Yuliani, S.H., and Istyastono, E.P., 2019, Development of a graphical user interface application to identify marginal and potent ligands for estrogen receptor alpha, *Indones. J. Chem.*, 19 (2), 531–537.
- [28] Setiawati, A., Riswanto, F.D.O., Yuliani, S.H., and Istyastono, E.P., 2014, Retrospective validation of a structure-based virtual screening protocol to identify ligands for estrogen receptor alpha and its application to identify the alpha-mangostin binding pose, *Indones. J. Chem.*, 14 (2), 103–108.
- [29] Mysinger, M.M., Carchia, M., Irwin, J.J., and Shoichet, B.K., 2012, Directory of useful decoys, enhanced (DUD-E): Better ligands and decoys for better benchmarking, *J. Med. Chem.*, 55 (14), 6582–6594.
- [30] Kim, S., Wu, J.Y., Birzin, E.T., Frisch, K., Chan, W., Pai, L.Y., Yang, Y.T., Mosley, R.T., Fitzgerald, P.M.D., Sharma, N., Dahllund, J., Thorsell, A.G.,

- DiNinno, F., Rohrer, S.P., Schaeffer, J.M., and Hammond, M.L., 2004, Estrogen receptor ligands. II. Discovery of benzoxathiins as potent, selective estrogen receptor alpha modulators, *J. Med. Chem.*, 47 (9), 2171–2175.
- [31] Doak, B.C., Over, B., Giordanetto, F., and Kihlberg, J., 2014, Oral druggable space beyond the rule of 5: Insights from drugs and clinical candidates, *Chem. Biol.*, 21 (9), 1115–1142.
- [32] Lipinski, C.A., Lombardo, F., Dominy, B.W., and Feeney, P.J., 1997, Experimental and computational approaches to estimate solubility and permeability in drug discovery and development settings, *Adv. Drug Delivery Rev.*, 23 (1-3), 3–25.
- [33] Benet, L.Z., Hosey, C.M., Ursu, O., and Oprea, T.I., 2016, BDDCS, the rule of 5 and drugability, *Adv. Drug Delivery Rev.*, 101, 89–98.
- [34] Daina, A., Michielin, O., and Zoete, V., 2017, SwissADME: A free web tool to evaluate pharmacokinetics, drug-likeness and medicinal chemistry friendliness of small molecules, *Sci. Rep.*, 7, 42717.

Analysis of Dissolution of Salicylamide from Carrageenan Based Hard-Shell Capsules: A Study of the Drug-Matrix Interaction

Muhammad Al Rizqi Dharma Fauzi¹, Esti Hendradi^{2*}, Pratiwi Pudjiastuti¹, and Riyanto Teguh Widodo³

¹Department of Chemistry, Faculty of Science, Universitas Airlangga, Campus C Mulyorejo, Surabaya 60115, Indonesia

²Department of Pharmaceutics, Faculty of Pharmacy, Universitas Airlangga, Campus C Mulyorejo, Surabaya 60115, Indonesia

³Department of Pharmaceutical Technology, Faculty of Pharmacy, University of Malaya, Kuala Lumpur 50603, Malaysia

* **Corresponding author:**

email: esti-h@ff.unair.ac.id

Received: March 25, 2020

Accepted: September 22, 2020

DOI: 10.22146/ijc.55047

Abstract: In drug release kinetics, the drug-matrix interaction is one of the important mechanisms to be dictated. Unfortunately, there is still minimum information discussing the effect of interaction between a drug and its matrix to the release profile of the drug. Therefore, there is an urgent need to conduct research related to the study of drug-matrix interaction. This paper reports the preparation of a drug delivery system (DDS) in the form of hard-shell capsules containing salicylamide (SCA) and analyses its drug-matrix interaction via dissolution test at different pH media and various release kinetics models. The matrix of hard-shell capsules was prepared from κ -carrageenan (CRG), crosslinked with maltodextrin (MD), and plasticized by sorbitol (SOR). The chemical properties of SCA were compared with paracetamol (PCT) using computational analysis to help to depict its drug-matrix interaction. The statistical analyses showed that SCA and PCT at pH 1.2, 4.5, and 6.8 had all different release profiles. Based on the goodness of fit evaluation, the diffusion mechanism of SCA at pH 1.2 and 4.5 could be best described by the Peppas-Sahlin model while the zeroth-order model fitted the dissolution profile at pH 6.8. In summary, it was proven that a different drug-matrix interaction produced a different dissolution profile.

Keywords: polymer; carrageenan; drug release; release kinetic; dissolution

■ INTRODUCTION

Drug-matrix interaction is one of the most important mechanisms dictating the drug release profiles [1]. Unfortunately, there is minimum information discussing the effect of interaction between a drug and its matrix to its release profile, specifically for the matrix in the form of a hard-shell capsule. Press et al. [2] reported that polyether-based triblock tricopolymer micelles act as an agent to give the effect to the physicochemical properties of the matrix as well as the actual conditions during encapsulation interfere during the formulation of nanoparticulate drug-matrix systems. On the other hand, drug molecules may directly interact with matrix molecules, lowering their solubility and/or retarding their release from the matrixes [1,3]. In addition, Srinarong et

al. [3] stated that a fast drug dissolution with a high drug load such as diazepam could be obtained with the matrix such as polyvinylpyrrolidone that showed interaction with the drug. Therefore, there is an urgent need to study and conduct more research on drug-matrix interaction.

A matrix for a drug, which is also known as a drug delivery system (DDS), could be produced in different forms from different sources [4-5] where one of the common matrixes used in capsules [6]. Capsules used to be prepared from gelatin in the form of soft- or hard-shell capsules [7]. As an inert material, capsules are a great DDS providing many advantages as compared to other DDS such as tablets and syrups [8]. Moreover, capsules can deliver both solid and liquid forms of drugs [9].

Fauzi et al. [6] prepared hard-shell capsules from CRG that were crosslinked with MD and plasticized by SOR. One pivotal advantage of this hard-shell capsule was that it had a longer disintegration time so that the dissolution process was easier to be observed as compared to hard gelatin capsules. It was found that PCT was more quickly dissolved at pH 4.5 than that at pH 1.2 and 6.8 due to the intermolecular interaction between PCT and citrate buffer in pH 4.5 medium. However, this paper did not take into account the possibility of drug-matrix interactions that might contribute to this phenomenon.

Taking the aforementioned background into account, this paper reports the dissolution analysis of SCA released from CRG-MD/SOR capsules. In order to support the explanations about drug-matrix interaction, computational analysis was conducted to analyze the quantitative structure-activity relationship (QSAR) properties of SCA. Statistical study was evaluated using the DDSolver and Origin Pro 9 software to determine the significance of dissolution profiles of SCA and to determine the best model that could describe the release profiles. The goodness of fit data was used to describe the release mechanism of SCA from CRG-MD/SOR capsules at each acidity.

■ EXPERIMENTAL SECTION

Materials

Food grade CRG powder was purchased from Kappa Carrageenan Nusantara, Inc., Pasuruan, Indonesia. Food grade MD powder was purchased from Yishui Dadi Corn Developing, Inc., Shandong, China. Pro analysis SOR was purchased from Sigma-Aldrich. Food grade lecithin was purchased from Tianjin Hexiyuan Lecithin Technology Inc., Pro analysis (purity: 99.0%) while SCA was purchased from Sigma-Aldrich. Technical grade HCl, citrate buffer, and phosphate buffer were all purchased from Sigma-Aldrich.

Instrumentation

Standard laboratory apparatuses such as beaker glass, volume pipette, hot plate, and others were used. Special apparatus for capsule preparation that was used is the size 0 dipping pens consisting of the body and head

parts of hard-shell capsules. Several instruments were used such as Mettler Toledo NewClassic MS Balance to measure the mass of each material, Mettler Toledo SevenEasy to measure the pH value, Veego Dissolution Tester Type Dis 8000 to analyze the disintegration time of the capsules, and UV-Vis Spectrophotometer Shimadzu Type UV-1601 to obtain the absorbation of drug dissolved in the medium of dissolution analysis.

Procedure

Capsules preparation

CRG and MD were mixed in a ratio of mass (6:1 w/w). The mixture was diluted with 100 mL of deionized water, and then added with 1.5% v/v of SOR. This heterogeneous mixture was heated for 5 h until it formed a homogeneous mixture. Dipping pens used to print the capsules were dipped into this mixture and dried for 3 h at room temperature. Dried capsules were collected from dipping pens and cut neatly to produce a good shape of hard-shell capsules [6].

Computational analysis for SCA and PCT

The chemical properties of SCA and PCT were computed using HyperChem 8.0. Both geometries of molecules were optimized with the magnetic field of the Molecular Mechanics (MM+) field and with the conjugate gradient algorithm of Polak-Ribiere. After optimization, chemical properties were computed using the QSAR analysis method. The data analyzed was saved in hardware with the specifications of DELL type P24T with the processor of AMD A9-9420e RADEON R5 and with the core processor of 5 compute 2C+3G 1.80 GHz.

In vitro dissolution medium preparation

Three different media were prepared in this research to follow USP-711 (United States Pharmacopeia). A medium with standard pH of 1.2 to represent gastric acid fluid was obtained by diluting 52 mL of HCl (36.5%) in 10 L of deionized water, while a Standard pH of 4.5 to represent body fluid was obtained by dissolving 1.212 g of citric acid and 29.41 g of trisodium citrate dihydrate in 10 L of deionized water. Finally, a standard pH of 6.8 to represent intestine fluid was obtained by dissolving 2.844 mg of KH_2PO_4 and 17.42 g of K_2HPO_4 in 10 L of deionized water.

In vitro dissolution test and drug-matrix interaction analysis

At first, a standard curve was prepared for determining the concentration of SCA in each result. A primary standard solution of each medium was prepared by diluting 10.0 mg of SCA in 100 mL of medium to produce a 100 ppm solution. Afterward, 100 ppm of SCA was diluted again to obtain 1, 10, 20, 40, and 50 ppm of solutions. Standard curves of SCA in pH 1.2, 4.5, and 6.8 medium were made by plotting the absorbance of SCA solutions at 236.6 nm vs the concentrations.

Dissolution testing was conducted as per the USP-711 recommendation. Six CRG-MD/SOR capsules containing SCA were placed in 900 mL of dissolution medium at 37 ± 0.5 °C. A sample of 10 mL solution from each of the vessels was taken out at a pre-determined time interval and replaced it by 10 mL of the fresh dissolution medium to maintain sink condition. The concentration of SCA in all samples collected was measured using UV-Vis Spectrophotometer at 236.6 nm [10]. Profile dissolutions were then built-up by plotting between accumulated concentrations against interval times.

Release kinetic analysis

Five candidates of release kinetics models were identified to fit the dissolution of SCA from CRG-MD/SOR, namely zero order, first order, Higuchi, Ritger-Peppas, and the Peppas-Sahlin model [4]. They can be expressed by Eq. (1) to (5), respectively.

$$Q_f = k_0 t + Q_0 \quad (1)$$

where Q is the accumulated concentration, k_0 is the zeroth-order release kinetics constant, and t is time.

$$\ln Q_f = k_1 t + \ln Q_0 \quad (2)$$

where k_1 is the first-order release kinetics constant.

$$Q = k_H \sqrt{t} \quad (3)$$

where k_H is the Higuchi constant.

$$Q = k_p t^n \quad (4)$$

where k_p is the Ritger-Peppas constant and n is diffusion exponential. Ritger-Peppas equation is also known as the Power Law. The value of n will give specific information about the diffusion mechanism experienced by the drug released from the matrix. For the cylinder-like matrix [11], if $n = 0.45$, the mechanism will be the Fickian

Diffusion. If the value of n is $0.45 < n < 0.89$, the mechanism will be the Anomalous (Non-Fickian) Transport. The Case-II Transport mechanism does not occur for $n = 0.89$ due to geometric factors involved in the related mathematical analysis [12]. Therefore, $n = 0.89$ only indicates a non-Fickian transport. If $n > 0.89$, the mechanism will be the Super-Case-II Transport.

$$Q = k_D t^n + k_R t^{2n} \quad (5)$$

where k_D is the diffusion constant and k_R is the relaxational constant. Uliniuc et al. [13] explained that the interaction mechanism between drugs and matrixes will be changed if the swelling process happens. In addition, material that is able to be swollen tends to have a non-Fickian diffusion mechanism [4]. In order to determine the best model that fits the release profile, statistical analysis was used.

Statistical analysis

Statistical analysis using Origin Pro 9 and DDSolver software was employed to compare and evaluate the different concentrations of SCA dissolved/released at each point of the three dissolution profiles obtained. The best model that fits the drug release profile was determined by their goodness of fit. The parameters used for the goodness of fit were R^2 , mean squared error (MSE), sums of squares (SS), and Akaike Information Criterion (AIC) [4,14]. AIC was used as a primary determination since most studies tend to use this method as a diagnostic criterion for model selection [14]. Eq. (6) shows the expression for AIC evaluation [15].

$$AIC = N(\ln RSS) + 2p \quad (6)$$

where N is the number of experimental data points, p is the number of parameters in an estimated model, and RSS is the residual sum of squares.

RESULTS AND DISCUSSION

Computational Analysis of SCA and its Comparison with PCT

To collect deeper information about the drug-matrix interaction, we compared SCA and PCT using computational analysis. This helped us to depict the result of the SCA interaction with the CRG-MD/SOR

capsules. Both SCA and PCT contained phenol and amide groups. The difference is the hydroxyl groups of PCT and SCA on the *para* and *meta* to the amide groups respectively. It makes SCA narrower in surface area and smaller in volume than PCT. Table 1 shows the results of the computational analysis using HyperChem 8.0.

PCT and SCA as shown in Fig. 1 have a close polarizability value since they consist of the same groups. However, the difference between the amides that bond the benzene rings might be the ones that are affecting the polarizability. In PCT, the benzene ring directly binds with the atom N of the amide group that makes it act as an electron-donating group. On the contrary, the benzene ring in SCA binds the carbonyl of the amide to act as an electron-withdrawing group. Thus, electrons in SCA distributed more equal than that of PCT, making PCT a more polar compound than SCA.

It is known that the pKa of PCT is 9.38 [16] and the pKa of SCA is 8.20 [17]. One possible explanation is that

the hydroxyl group of SCA that is close to the amide group might create an intramolecular hydrogen bond and thus reducing the ability of the amide group to donate its electron-pair. This circumstance might not be found in PCT and make it a better Lewis-base compound.

Dissolution Profiles of SCA Released from CRG-MD/SOR Capsules

SCA (Fig. 2) was dissolved well at pH 1.2 and 4.5 but was poorly dissolved at pH 6.8. In this almost-basic medium, even in 90 min, the SCA was dissolved for only

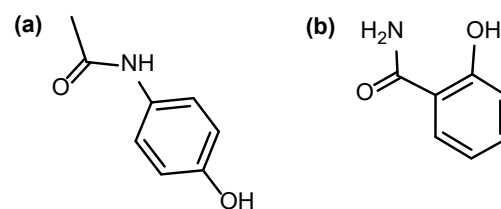


Fig 1. Optimized chemical structure of (a) paracetamol (PCT) and (b) salicylamide (SCA) using HyperChem 8.0

Table 1. Computational analysis results of paracetamol (PCT) and salicylamide (SCA) using HyperChem 8.0

No	QSAR Properties	Compound	
		PCT C ₈ H ₉ NO ₂	SCA C ₇ H ₇ NO ₂
1	Net charge	0.00 e	0.00 e
2	Surface area (approx.)	299.39 Å ²	216.45 Å ²
3	Volume	488.76 Å ³	422.73 Å ³
4	Log P	-1.32	-0.91
5	Refractivity	45.55 Å ³	40.38 Å ³
6	Polarizability	16.18 Å ³	14.34 Å ³
7	Molecular Mass (amu)	151.16	137.14

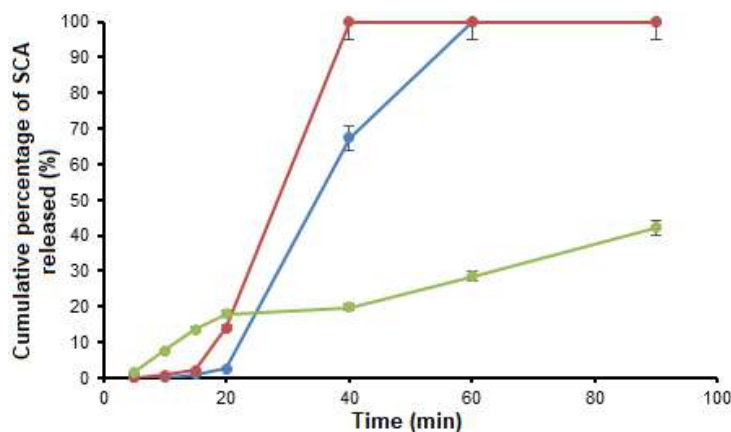


Fig 2. The dissolution profile of salicylamide (SCA) from carrageenan-maltodextrin plasticized by sorbitol (CRG-MD/SOR) capsules at pH 1.2 (blue), 4.5 (red), and 6.8 (green)

42.19 ± 7.22%. One possible explanation is that SCA is a weak-basic drug. The consequence of this fact supports the mentioned results that the drugs were dissolved poorly at pH 6.8. In addition, CRG-MD/SOR capsules were not recommended for drugs targeted at the intestinal parts [6].

Using the similarity factor (f_2) method on DDSolver, the difference between SCA and PCT [6] could be determined. This method is used because the dissolution plateau has been reached (> 85%) [14]. The value of f_2 at pH 1.2 was 39.40 which indicated no similarity between the two profiles. The same condition also happened to the profiles at pH 4.5 where the value of f_2 was 35.83. The profiles at pH 6.8 were analyzed using the multivariate confidence region method since both dissolution profiles did not reach 85%. The advantage of the multivariate method is that it takes the variability and correlation structure of the data into account in measuring the difference between the means of two sets of dissolution data [14]. The maximum difference means fraction used was 10.0% and the maximum multivariate statistical distance of the profiles was 28.32. This indicates that there was no similarity between SCA and PCT [6] at pH 6.8.

This difference might be caused by the acidity that affects the activity of the amide and phenol groups on SCA. At pH 1.2, the amide groups might be protonated more than that of pH 4.5. This protonated state increased the radius of the amide group so that the molecules might not interact well on the network of CRG-MD/SOR capsules due to the Van der Waals interaction that is

affected by the size of the molecules [18]. On the other side, SCA would interact better with each other. When the medium penetrated the matrix, the less interaction between SCA and CRG-MD/SOR resulted in a slow dissolution process of SCA compared to that of pH 4.5 because the medium would take a longer time to interact with SCA that interacted better with each other.

***In Vitro* Release Kinetics Analysis of SCA**

All release kinetics models are valid at 60% of initial drug release from the capsules [19]. Hence, all of the calculations to determine each coefficient and R^2 were obtained from the 60% data of drug released. This validity was pivotal, especially in the determination of the AIC values for each release kinetics model. The values depended on the number of data involved in the calculation. Based on the lowest AIC value, as shown in Table 2, the Peppas-Sahlin model was the best model to describe the release kinetics mechanism of SCA at pH 1.2. This suggestion was supported by high R^2 and low MSE and SS, where the lowest value indicated the data had low deviancy [4].

The zeroth-order model could not be applied to the release kinetics of SCA, because an ideal carrier for zeroth-order release should have a constant release rate over the entire release duration [20]. First-order model also could not be applied because the carrier must be a non-swelling porous matrix [21]. The Higuchi model in this report had the highest AIC value, meaning it really could not describe the release process. It is because the

Table 2. Statistical results of salicylamide (SCA) released from carrageenan-maltodextrin plasticized by sorbitol (CRG-MD/SOR) capsules at pH 1.2. DDSolver was used to analyze zeroth-order, first-order, Higuchi model, and Peppas-Sahlin model. Since the software could not be able to analyze the Peppas-Ritger model, Origin Pro 9 was used instead

Model	Constants	R^2	MSE	SS	AIC
Zeroth-Order	1.17	0.63	321.29	1285.15	37.76
First-Order	0.01	0.55	395.63	1582.52	38.79
Higuchi	4.89	0.33	589.09	2356.36	40.79
Peppas-Ritger					
n	4.43	0.99	0.51	1622.42	40.96
k_p	5.18×10^{-6}				
Peppas-Sahlin					
k_D	5.00×10^{-6}	0.99	0.42	0.83	3.84
k_R	4.00×10^{-13}				

Higuchi model is expected to happen in a drug that is dispersed in a uniform matrix [22]. Based on the Peppas-Ritger model, the exponential constant (n) was 4.43. According to Paarakh et al. [23], if n is higher than 0.85, the diffusion mechanism will be the Super-Case-II transport. This might be caused by the capsules that were swollen for more than 15 min before finally disintegrated and dissolved. The swelling of the capsule might be the primary reason for non-Fickian diffusion that happened to CRG-MD/SOR. The Peppas-Sahlin model fitted the release profiles at pH 1.2 and 4.5 (Table 3) according to AIC evaluation. Small diffusion and relaxation constants at both acidities also showed that the diffusion took a longer time.

The predicted equations formed by the parameters that were calculated by DDSolver in the Peppas-Sahlin model were processed by the program to form the predicted graphs (Fig. 3). When all observed points were

fitted to the graphs, they demonstrated good performances. Fig. 3 showed that the Peppas-Sahlin model could describe the release kinetics of SCA from CRG-MD/SOR capsules at pH 1.2 and 4.5.

Eq. (5) can be rewritten as:

$$Q = k_D t^n + \left(1 + \frac{k_R}{k_D} t^n \right) \quad (7)$$

Based on Eq. (7), the percentage of drug release due to the Fickian mechanism (F) is clearly calculated as [11]:

$$\frac{1}{F} = \frac{k_2}{k_1} t^n + 1 \quad (8)$$

By plotting $1/F$ as x-axis and t^n as y-axis, Fig. 4 was produced.

Fig. 3 shows the diffusion of SCA more rapidly transforms from Fickian to non-Fickian diffusion at pH 4.5 than that of pH 1.2. This was possibly due to the different relaxation constant of CRG-MD/SOR at pH 4.5

Table 3. Statistical results of salicylamide (SCA) released from carrageenan-maltodextrin plasticized by sorbitol (CRG-MD/SOR) capsules at pH 4.5. DDSolver was used to analyze zeroth-order, first-order, Higuchi model, and Peppas-Sahlin model. Since the software could not be able to analyze the Peppas-Ritger model, Origin Pro 9 was used instead

Model	Constants	R ²	MSE	SS	AIC
Zeroth-Order	1.84	0.68	610.90	2443.60	40.91
First-Order	0.02	0.54	875.46	3501.84	42.77
Higuchi	7.84	0.47	1210.53	4842.11	44.41
Peppas-Ritger					
n	4.25	0.94	1.83	1487.21	33.22
k_p	3.25×10^{-5}				
Peppas-Sahlin					
k_D	4.00×10^{-5}	0.99	39.65	79.31	19.50
k_R	1.00×10^{-10}				

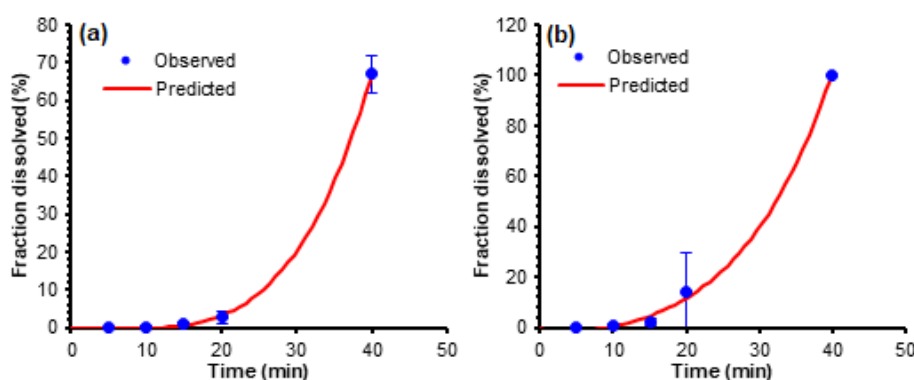


Fig 3. Predicted graphs of the Peppas-Sahlin model of salicylamide (SCA) release kinetics at (a) pH 1.2 and (b) pH 4.5. DDSolver was used to analyze the performance of the model

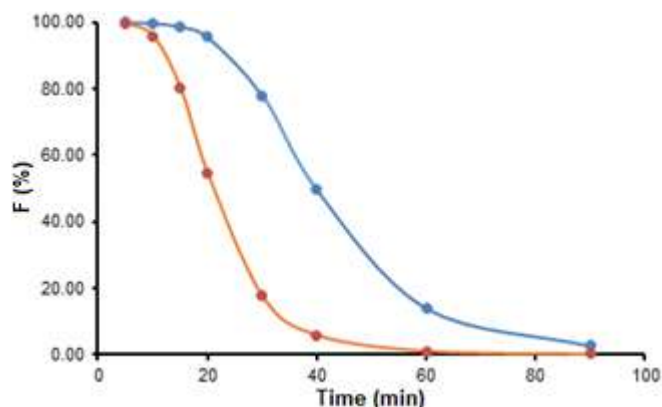


Fig 4. Fickian diffusion percentage (F) of salicylamide (SCA) vs time at pH 1.2 (blue) and 4.5 (red)

and 1.2 where the former showed 200 higher than the latter. As a consequence, CRG-MD/SOR at pH 4.5 exhibited faster swelling and transition from glassy to rubbery state [24]. Hence, faster swelling would cause faster disintegration and dissolution.

Based on our analysis, DDSolver could not be used accurately for a dissolution profile that did not reach 60%. Based on AIC value where it was 33.06 for the Peppas-Sahlin model and 32.69 for the first-order model, the release mechanism of SCA from CRG-MD/SOR capsules was best described by the first-order model. Interestingly, the MSE and SS of the first-order model were 13.07 and 65.34. These parameters were higher than those of the Peppas-Sahlin model, which the MSE and SS of it were 12.82 and 51.28, respectively. These results indicate that the first-order model had high deviancy compared to that of the Peppas-Sahlin model. The results were

contradictory. Therefore, we chose the results from Origin Pro 9 calculation to analyze the release mechanism of SCA from CRG-MD/SOR capsules at pH 6.8.

Based on Table 4, the best model to describe the release kinetic process at pH 6.8 was the zeroth-order model. The diffusion follows the zeroth-order, indicating that the capsule acted as a nonswelling porous matrix [21]. This also indicated that Fickian diffusion was the dominant mechanism occurring in that condition. This conclusion was supported by the fact that the release process at pH 6.8 was slow where only $42.19 \pm 7.22\%$ of SCA was released in 90 min. The analysis was supported by Fig. 5 where the observed data fitted well on the zeroth-order model.

Diffusion and relaxation constant could also be interpreted as a competition between Fickian and non-Fickian diffusion [4]. By modifying Eq. (7), the ratio of relaxational over Fickian contribution can be expressed by Eq. (9) as follows:

$$\frac{R}{F} = \frac{k_2}{k_1} t^n \quad (9)$$

The increase in R/F indicated the increase of relaxation contribution and thus increasing the non-Fickian diffusion percentage [4]. Fig. 6 indicated that the non-Fickian diffusion was dominant at pH 1.2 and 4.5 while the Fickian diffusion was dominant at pH 6.8. Therefore, the dissolution of SCA from CRG-MD/SOR capsules depended on the acidity of the medium. The determination of the diffusion mechanism was helpful to understand the dissolution process.

Table 4. Statistical results of salicylamide (SCA) released from carrageenan-maltodextrin plasticized by sorbitol (CRG-MD/SOR) capsules at pH 6.8. The analyze was done using Origin Pro 9

Model	Constant	R ²	RSS	AIC
Zeroth-Order	0.42	0.94	63.50	33.06
First-Order	0.03	0.61	2738.17	59.40
Higuchi	5.02	0.96	1954.54	57.04
Peppas-Ritger				
n	1.09	0.82	106.42	38.67
k _p	0.41			
Peppas-Sahlin				
k _D	0.27	0.85	5717.10	68.56
k _R	0.0018			

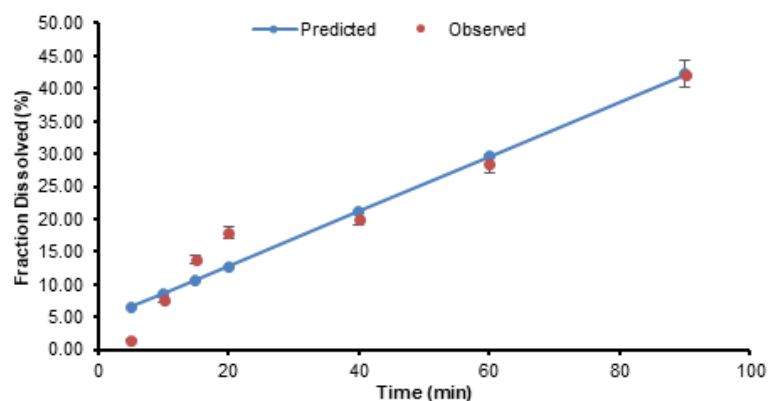


Fig 5. Predicted graphs of the zeroth-order model of salicylamide (SCA) release kinetics at pH 6.8

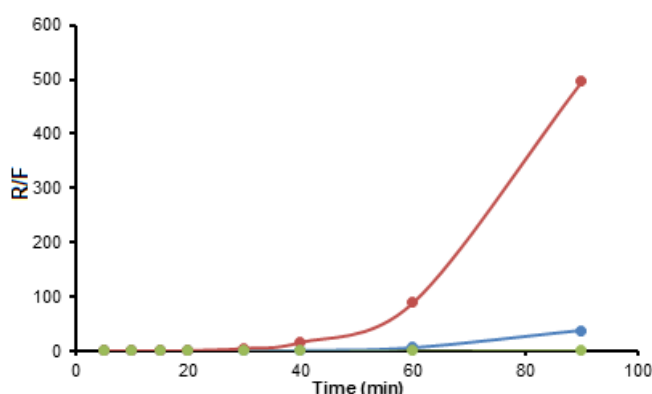


Fig 6. Relaxation process and its Fickian contribution ratio of salicylamide (SCA) dissolution at pH 1.2 (blue), pH 4.5 (red), and pH 6.8 (green)

CONCLUSION

Based on the computational analyses, SCA and PCT have significantly different drug-matrix interactions due to their different functional groups' position where the significance was clearly seen at pH 1.2 and 4.5. The benzene ring in SCA binds the carbonyl of the amide that makes it act as an electron withdrawing group, making SCA easier to be protonated compared to PCT. This fact supports the fact that SCA and PCT have different results in their interaction with the CRG-MD/SOR capsules, especially at pH 1.2 and 4.5 where SCA was released faster at pH 4.5 than at pH 1.2. In other words, the drug-matrix interaction affected the ability of the medium to dissolve the SCA. Finally, the diffusion mechanism of SCA at pH 1.2 and 4.5 could be best described by the Peppas-Sahlin model while the first-order model fitted the dissolution profile at pH 6.8.

ACKNOWLEDGMENTS

The authors would like to thank the Ministry of Education of Indonesia for the research fund granted to us through the PMDSU (*Program Menuju Doktor untuk Sarjana Unggul*) scholarship program.

AUTHOR CONTRIBUTIONS

Muhammad Al Rizqi Dharma Fauzi conducted the research and analyses, Esti Hendradi supervised the research conducted, Pratiwi Pudjiastuti and Riyanto Teguh Widodo reviewed the manuscript written. All authors agreed to the final version of this manuscript.

REFERENCES

- [1] Zeng, L., An, L., and Wu, X., 2011, Modelling drug-carrier interaction in the drug release from nanocarriers, *J. Drug Delivery*, 2011, 370308.
- [2] Press, A.T., Ramoji, A., von der Lühe, M., Rinkenauer, A.C., Hoff, J., Butans, M., Rössel, C., Pietsch, C., Neugebauer, U., Schacher, F.H., and Bauer, M., 2017, Cargo-carrier interactions significantly contribute to micellar conformation and biodistribution, *NPG Asia Mater.*, 9, e444.
- [3] Srinarong, P., Kouwen, S., Visser, M.R., Hinrichs, W.L.J., and Frijlink, H.W., 2010, Effect of drug-carrier interaction on the dissolution behavior of solid dispersion tablets, *Pharm. Dev. Technol.*, 15 (5), 460–468.
- [4] Unagolla, J.M., and Jayasuriya, A.C., 2018, Drug transport mechanisms, and *in vitro* release kinetics of vancomycin encapsulated chitosan-alginate

- polyelectrolyte microparticles as a controlled drug delivery system, *Eur. J. Pharm. Sci.*, 114, 199–209.
- [5] Hariyadi, D.M., Hendradi, E., and Sharon, N., 2019, Development of carrageenan polymer for encapsulation of ciprofloxacin HCL: In vitro characterization, *Int. J. Drug Delivery Technol.*, 9 (1), 89–93.
- [6] Fauzi, M.A.R.D., Pudjiastuti, P., Hendradi, E., Widodo, R.T., and Amin, M.C.I.M., 2020, Characterization, disintegration, and dissolution analyses of carrageenan based hard-shell capsules cross-linked with maltodextrin as a potential alternative drug delivery system, *Int. J. Polym. Sci.*, 2020, 3565931.
- [7] The United States Pharmacopoeial Convention, 2014, *United States Pharmacopoeia (USP)*, Rockville, Maryland.
- [8] Srividya, B., Sowmya, C., and Chappidi, S.R., 2014, Capsules and its technology: An overview, *Int. J. Pharm. Drug Anal.*, 2 (9), 727–733
- [9] Gullapalli, R.P., and Mazzitelli, C.L., 2017, Gelatin and non-gelatin capsule dosage forms, *J. Pharm. Sci.*, 106 (6), 1453–1465.
- [10] Ali, N.W., Zaazaa, H.E., and Abdelrahman, M.M., 2014, Novel spectrophotometric methods for determination of salicylamide and ascorbic acid in their binary mixture, *J. Chem. Soc. Pak.*, 36 (6), 988–995.
- [11] Peppas, N.A., and Sahlin, J.J., 1989, A simple equation for the description of solute release. III. Coupling of diffusion and relaxation, *Int. J. Pharm.*, 57 (2), 169–172.
- [12] Peppas, N.A., 1985, Analysis of Fickian and non-Fickian drug release from polymers, *Pharm. Acta Helv.*, 60 (4), 110–111
- [13] Uliniuc, A., Hamaide, T., Popa, M., and Băcăiță, S., 2014, Modified starch-based hydrogels cross-linked with citric acid and their use as drug delivery systems for levofloxacin, *Soft Mater.*, 11 (4), 483–493.
- [14] Zhang, Y., Huo, M., Zhou, J., Zou, A., Li, W., Yao, C., and Xie, S., 2010, DDSolver: An add-in program for modeling and comparison of drug dissolution profiles, *AAPS J.*, 12 (3), 263–271.
- [15] Kulpreechanan, N., and Sorasitthyanukarn, F.N., 2020, Evaluation of in vitro release kinetics of Capsaicin-loaded chitosan nanoparticles using DDSolver, *Int. J. Res. Pharm. Sci.*, 11 (3), 4555–4559.
- [16] Bernal, V., Erto, A., Giraldo, L., and Piraján, J.C.M., 2017, Effect of solution pH on the adsorption of paracetamol on chemistry modified activated carbons, *Molecules*, 22 (7), 1032.
- [17] Lemke, T.L., Williams, D.A., Roche, V.F., and Zito, S.W., 2017, *Foye's Principles of Medicinal Chemistry*, 7th Ed., Lippincott Williams & Wilkins, Philadelphia, USA, 965–970.
- [18] Hermann, J., DiStasio, R.A., and Tkachenko, A., 2017, First-principles models for van der Waals interactions in molecules and materials: Concepts, theory, and applications, *Chem. Rev.*, 117 (6), 4714–4758.
- [19] Fu, T., and Kao, W.J., 2010, Drug release kinetics and transport mechanisms of non-degradable and degradable polymeric delivery systems, *Expert Opin. Drug Delivery*, 7 (4), 429–444.
- [20] Zhao, Y.N., Xu, X., Wen, N., Song, R., Meng, Q., Guan, Y., Cheng, S., Cao, D., Dong, Y., Qie, J., Liu, K., and Zhang, K., 2017, A drug carrier for sustained zero order release of peptide therapeutics, *Sci. Rep.*, 7, 5524.
- [21] Varelas, C.G., Dixon, D.G., and Steiner, C.A., 1995, Zero-order release from biphasic polymer hydrogels, *J. Controlled Release*, 34 (3), 185–192.
- [22] Paul, D.R., 2011, Elaborations on the Higuchi model for drug delivery, *Int. J. Pharm.*, 418 (1), 13–17.
- [23] Paarakh, M.P., Jose, P.A., Setty, C.M., and Christopher, G.V.P., 2018, Release kinetics – Concepts and applications, *IJPRT.*, 8, 12–20.
- [24] Diksha, S., Dhruv, D., Prasad D.N., and Mansi, H., 2019, Sustained release drug delivery system with the role of natural polymers: A review, *J. Drug Delivery Ther.*, 9 (3-s), 913–923.

Supplementary Data

This supplementary data is a part of paper entitled “Conformational Analysis of Diterpene Lactone Andrographolide towards Reestablishment of Its Absolute Configuration via Theoretical and Experimental ECD and VCD Methods”.

The major constituent was isolated as a pale yellowish powder (mp 231–233 °C) from *Andrographis paniculata* (whole plant) and was identified as andrographolide **1** (Fig. 1) [1-2]. The IR spectrum of **1** shows a strong peak at 1724.46 cm⁻¹, representing a lactone-type carbonyl stretch, while a weak sharp peak at 3391.91 cm⁻¹ indicates the presence of the free hydroxyl group. Another characteristic peak of medium intensity observed at 1675.46 cm⁻¹ shows the presence of alkenyl C=C stretch. The ¹³C NMR spectrum of **1** (Table 1) displayed 20 carbons, attributed to a carbonyl (δ 172.6), two quaternary olefins (δ 129.8 and 148.8), olefinic methylene (δ 109.2), an olefinic methine (δ 149.3), two oxymethines (δ 66.8 and 80.9), two oxymethylene (δ 65.0 and 76.1), two quaternary aliphatics (δ 40.0 and 43.7), an aliphatic methine (δ 56.4), five aliphatic methylenes (δ 25.2, 25.7, 29.0, 38.1 and 39.0), and two methyl carbons (δ 15.5 and 23.2). Its ¹H NMR spectrum (Table 1) showed signals typical of olefinic methine and methylene protons at δ 6.85 (td, *J* = 6.8, 1.7 Hz, H-12) and 4.89/4.67 (s, H-17) respectively. Furthermore, the characteristic signals for two oxymethine protons were seen at δ 3.41 (dd, *J* = 9.6, 6.0 Hz, H-3) and 5.01 (d, *J* = 6.1 Hz, H-13), while signals typical for two oxymethylene protons were seen at δ 4.46 (dd, *J* = 10.2, 6.1 Hz, H-15a)/4.16 (dd, *J* = 10.2, 2.0 Hz, H-15b) and 4.12 (d, *J* = 11.1 Hz, H-19a)/3.37 (d, *J* = 10.8 Hz, H-19b). These ¹H and ¹³C NMR spectroscopic data were consistent with those of the known andrographolide.

The relative configurations at the six stereogenic centers of **1** were determined based on its NOE spectral data. The strong NOE correlation (Fig. 2) between olefinic proton H-12 and protons H-9/H-11b/H-17b established the *cis*-orientation of H-12/H-9, and *trans*-orientation of H-12/H-11b and H-12/H-17, while the correlation of protons H-11a and H-14 showed the *trans*-orientation of H-12/H-14 and *cis*-orientation of H-12/carbonyl at the lactone ring. Furthermore, the spatial correlation between proton H-5 and protons H-1b/H-3/H-7a/H-9 results in ring strain and confirmed the protons arrangement in the bicyclic ring of **1** skeleton *cis*-orientation. Next, the correlation between hydroxyl protons H-3b and H-19b established the *cis*-orientation of 19-CH₂ and 3-OH group. However, the configuration of 14-OH and 19-OH is supported only by a single NOE correlation. The ambiguity in the configuration warrants further experiments. Based on the NOE correlations, the relative configuration of the six stereogenic centers in **1** could be deduced as 3*R*, 4*R*, 5*S*, 9*R*, 10*R*, and 14*S*, as shown in Fig. 3.

The chromophoric derivatization of **1** at room temperature using 2-naphthoyl chloride or benzoyl chloride as chromophore proceeded *via* S_N2 nucleophilic substitution reaction (Scheme 1). The three hydroxyl groups in andrographolide act as active sites in this reaction. Based on its position, the allylic hydroxyl group at carbon C-14 (secondary alcohol) is more acidic compared to those at carbons C-3/C-19, consequently, it can be easily deprotonated. Trimethylamine as base at room temperature, derivatization of **1** with both benzoyl and 2-naphthoyl chlorides was only achieved at C-14 instead at C-3 or C-19 at the end of the reaction. However, by increasing the reaction temperature to 40 °C (increasing the kinetic energy), the activation energy of the reaction system has decreased and successfully introduced chromophore at both C-14 and C-19 of **1**. This fact indicated that steric hindrance around the hydroxyl group at C-3 and C-19 of **1** caused the nucleophilic attack to be less susceptible to both the chromophores. Structural characterization of all derivatives was carried out by NMR analysis in acetone-*d*₆. Table 1 shows the chemical structures of andrographolide derivatives (2–5), while Table 2 shows the ¹H and ¹³C NMR spectral details of the compounds. Derivatives **2**, **3** and derivatives **4**, **5** were obtained from a single reaction of different chromophores used for derivatization.

References

- [1] Hossain, M.S., Urbi, Z., Sule, A., and Rahman, K.M.H., 2014, *Andrographis paniculata* (Burm. f.) Wall. ex Nees: A review of ethnobotany, phytochemistry, and pharmacology, *Sci. World J.*, 2014, 1–28.
- [2] Chen, L., Zhu, H., Wang, R., Zhou, K., Jing, Y., and Qiu, F., 2008, *ent*-Labdane diterpenoid lactone stereoisomers from *Andrographis paniculata*, *J. Nat. Prod.*, 71 (5), 852–855.

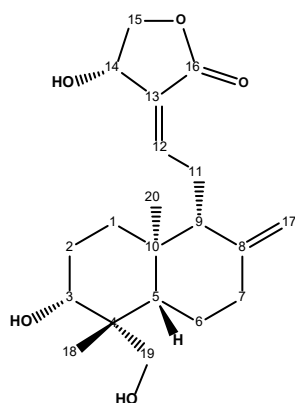


Fig 1S. Chemical structure of andrographolide with carbon numbering. The configuration was determined using single-crystal technique from the previous studies

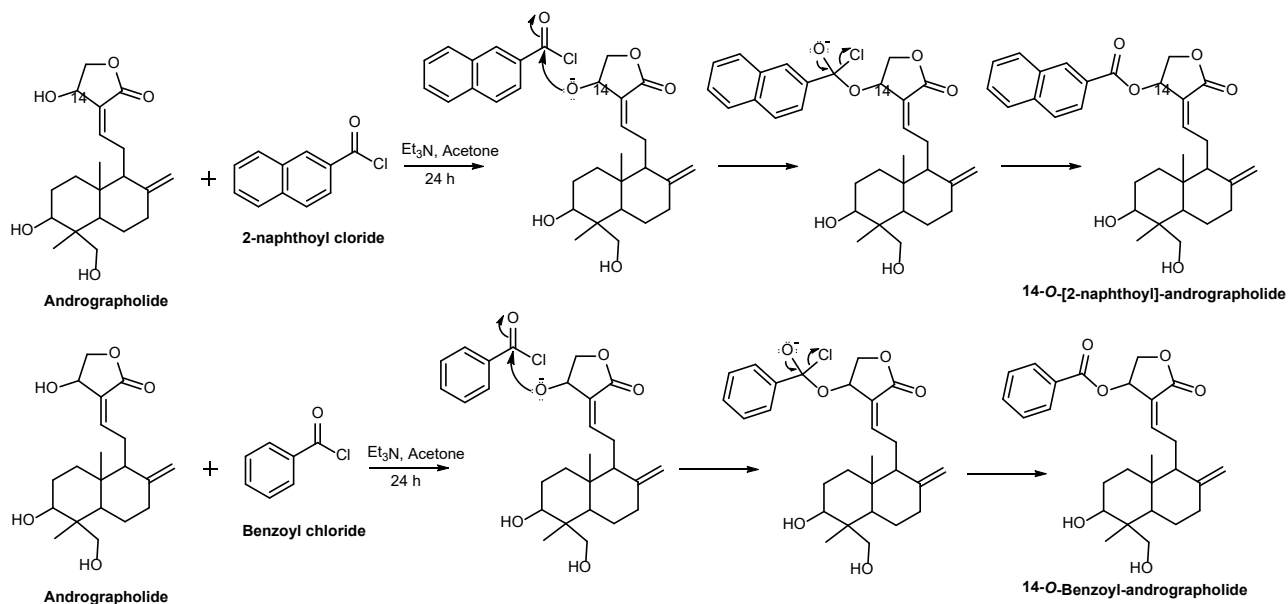
Total mass isolated: 396mg

Physical properties: pale-yellowish, powder.

Molecular mass: 350.45

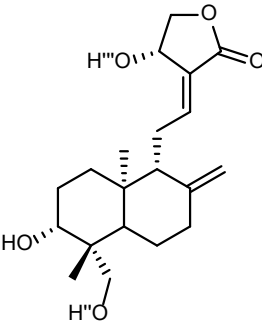
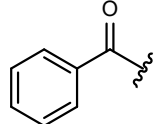
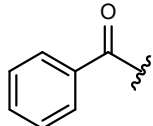
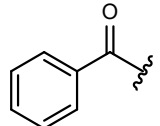
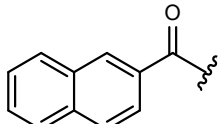
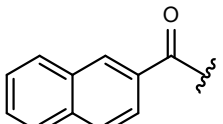
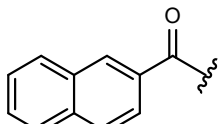
CHN Analysis:

	Theoretical	Experimental
Carbon	240.20	238.66
Hydrogen	30.30	29.35
Nitrogen	0	



Scheme 1. Reaction mechanism of chromophoric derivatization of andrographolide

Table 1S. Chemical structures of andrographolide derivatives (2–5). Derivatives 2, 3 and derivatives 4, 5 were obtained from single reaction of different chromophores used for derivatization

Derivative	Yield (mg)	Molecular mass (g/mol)	Substitution		
			H''	H'''	
	2	5.10	454.4565	-	
	3	3.12	558.6691		
	4	4.68	504.6321	-	
	5	7.48	658.8091		

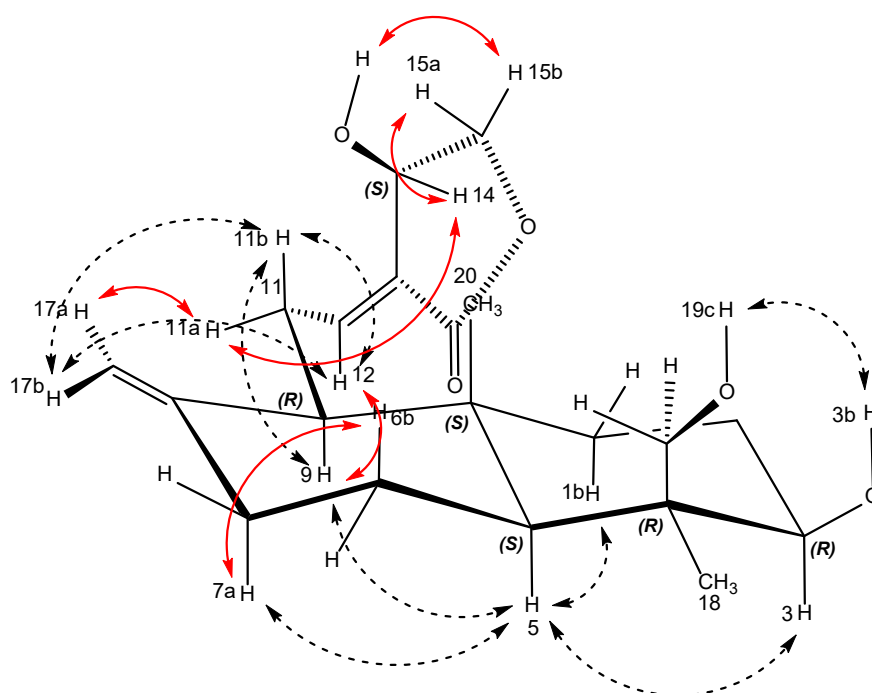
**Fig 2S.** Key NOESY correlations of **1**

Table 2S. The NMR spectral data of **1** and its derivatives

No	Andrographolide 1		14- <i>O</i> -benzoyl andrographolide 2		14,19- <i>O</i> -dibenzoyl andrographolide 3	
	δ_{H} (mult., J =Hz)	δ_{C}	δ_{H} (mult., J =Hz)	δ_{C}	δ_{H} (mult., J =Hz)	δ_{C}
1	2.43 (ddd, J =12.9, 3.7, 2.5) 2.04 (td, J =12.6, 4.7)	39.0	2.37 (br dd, J =11.7, 3.3) 2.01 (m)	37.6	2.42 (br dd, J =11.5, 3.3) 2.07 (m)	37.8
2	1.78 (m)	29.0	1.72 (m)	28.1	1.72 (m)	27.8
3	3.41 (dd, J =9.6, 6.0)	80.9	3.39 (dd, J =9.7, 5.9)	79.6	3.42 (m)	77.6
4	-	43.7	-	42.6	-	42.5
5	1.32 (m)	56.4	1.31 (m)	55.0	1.41 (m)	54.8
6	1.38 (qd, J = 12.7, 4.1) 1.78 (m)	25.2	1.31 (m) 1.81 (m)	23.8	1.41 (m) 1.82 (m)	22.4
7	1.29 (m) 1.80 (m)	38.1	1.75 (m) 1.26 (m)	36.8	1.65 (m) 1.27 (m)	37.1
8	-	148.8	-	147.9	-	148.0
9	1.92 (dd, J =10.8, 2.4)	57.4	2.02 (m)	55.7	2.01 (m)	55.9
10	-	40.0	-	38.7	-	39.1
11	2.63 (ddd, J =16.8, 7.1, 3.8) 2.58 (ddd, J =17.1, 10.8, 6.8)	25.7	2.68 (ddd, J =16.7, 6.6, 3.7) 2.54 (ddd, J =17.2, 10.6, 7.1)	25.1	2.74 (dq, J =16.8, 3.3) 2.60 (m)	25.2
12	6.85 (td, J =6.8, 1.7)	149.3	6.99 (td, J =6.8, 1.7)-	149.6	7.02 (td, J =6.9, 1.6)	149.5
13	-	129.8	-	134.6	-	133.5
14	5.01 (d, J = 6.1)	66.8	6.32 (br d, J =6.1)	68.8	6.35 (br d, J =6.0)	68.9
15	4.46 (dd, J =10.2, 6.1) 4.16 (dd, J =10.2, 2.0)	76.1	4.72 (dd, J =11.1, 6.1) 4.45 (dd, J =11.1, 1.9)	71.3	4.53 (m) 4.47 (m)	71.3
16	-	172.6	-	173.8	-	168.6
17	4.89 (s) 4.67 (s)	109.2	4.83 (d, J =1.3) 4.58 (d, J =1.3).	107.8	4.85 (s) 4.61 (s)	107.7
18	0.75 (s)	15.5	0.63 (s)	14.4	0.73 (s)	13.8
19	4.12 (d, J =11.1) 3.37 (d, J = 10.8)	65.0	4.06 (d, J =10.9) 3.25 (br d, J =10.7)	63.4	3.94 (d, J =4.7) 4.74 (m)	65.7
20	1.22 (s)	23.2	1.19 (s)	22.6	1.26 (s)	22.4
1' ^[1^{''}]	-	-	-	124.6	-	124.7
2' ^[2^{''}]	-	-	8.05 (dd, J =8.4, 1.4)	129.4	8.01 (dd, J =8.3, 1.3)	129.3 [129.5]
3' ^[3^{''}]	-	-	7.54 (tt, J =7.5, 1.5)	128.7	7.57 (m)	128.5 [128.7]
4' ^[4^{''}]	-	-	7.68 (tt, J =7.5, 1.5)	133.6	7.64 (m)	132.8 [133.5]
5' ^[5^{''}]	-	-	7.54 (tt, J =7.5, 1.5)	128.7	7.50 (dq, J =7.3, 1.5)	130.8
6' ^[6^{''}]	-	-	8.05 (dd, J =8.4, 1.4)	129.4	8.02 (dd, J =8.3, 1.3)	148.0 [149.5]
7' ^[7^{''}]	-	-	-	-	-	-
8' ^[8^{''}]	-	-	-	-	-	-
9' ^[9^{''}]	-	-	-	-	-	-
10' ^[10^{''}]	-	-	-	-	-	-
C=O	-	-	-	165.5	-	165.6 [166.0]

Table 2S. The NMR spectral data of **1** and its derivatives (*Continued*)

No	14- <i>O</i> -(2-naphthoyl) andrographolide 4		14,19- <i>O</i> -di(2-naphthoyl) andrographolide 5	
	δ_{H} (mult., J =Hz)	δ_{C}	δ_{H} (mult., J =Hz)	δ_{C}
1	2.39 (br dd, J =11.4, 4.2) 2.07 (m)	38.5	2.44 (m) 2.09 (m)	38.8
2	1.73 (m)	29.0	1.74 (m)	28.8
3	3.41 (m)	80.9	3.44 (m)	78.5
4	-	42.3	-	43.5
5	1.32 (m)	55.9	1.44 (m)	56.9
6	1.32 (m) 1.82 (m)	25.2	2.10 (m) 1.68 (m)	26.0
7	1.77 (m) 1.29 (m)	37.7	1.87 (m) 1.45 (m)	38.0
8	-	148.9	-	149.0
9	2.08 (m)	56.7	2.13 (m)	55.7
10	-	39.7	-	40.0
11	2.73 (ddd, J =16.8, 6.3, 3.4) 2.61 (m)	26.1	2.76 (m) 2.67 (m)	26.2
12	7.04 (td, J =7.2, 1.8)	150.6	7.06 (td, J =7.0, 1.5)	150.6
13	-	127.7	-	127.2
14	6.41 (br d, J =6.1)	69.8	6.43 (br d, J =6.0)	69.9
15	4.78 (dd, J =11.2, 6.2) 4.53 (dd, J =11.2, 1.9)	72.3	4.79 (dd, J =11.0, 6.0) 4.54 (dd, J =11.0, 2.0)	72.3
16	-	183.3	-	169.6
17	4.87 (d, J =1.2) 4.66 (br s)	108.7	4.87 (br s) 4.68 (br s)	108.7
18	0.64 (s)	15.4	0.78 (s)	23.4
19	4.06 (dd, J =10.5, 1.6) 3.25 (t, J =10.8)	64.3	4.59 (d, J =11.5) 4.50 (d, J =12.0)	66.8
20	1.20 (s)	23.5	1.33 (s)	14.8
1' ^[1^{''}]	8.71 (s)	132.1	8.70 (s) [8.62 (s)]	132.1 [131.5]
2' ^[2^{''}]	-	125.6	-	125.6 [125.6]
3' ^[3^{''}]	8.13 (d, J =7.8)	125.8	8.12-7.97 (m)	125.8 [126.0]
4' ^[4^{''}]	8.06-8.03 (m)	129.4	8.12-7.97 (m)	129.2 [129.1]
5' ^[5^{''}]	-	136.7	-	136.7 [136.4]
6' ^[6^{''}]	7.71 (td, J =7.5, 1.1)	128.7	7.67 (t, J =8.0) [7.68 (t, J =8.0)]	128.7 [128.6]
7' ^[7^{''}]	7.66 (td, J =7.5, 1.1)	129.6	7.61 (t, J =7.0) [7.61 (t, J =7.0)]	129.6 [129.4]
8' ^[8^{''}]	8.06-8.03 (m)	128.0	8.12-7.97 (m)	127.9 [127.7]
9' ^[9^{''}]	8.06-8.03 (m)	130.2	8.12-7.97 (m)	130.3 [130.2]
10' ^[10^{''}]	-	133.5	-	133.5 [133.4]
C=O	-	169.6	-	167.0 [166.7]

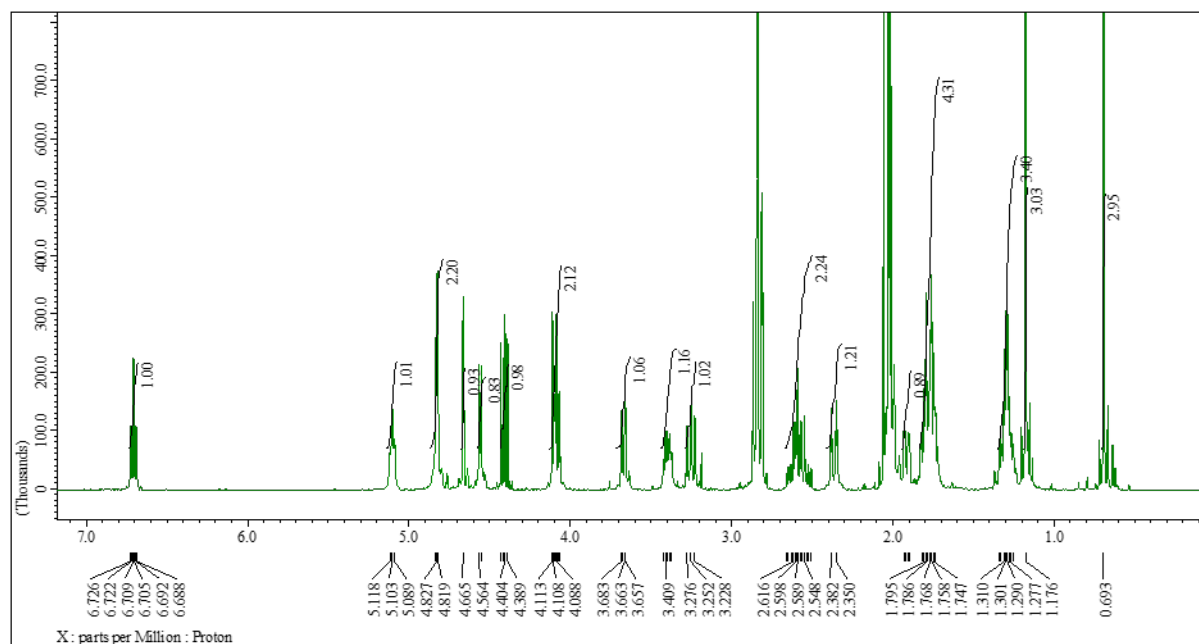


Fig 3S. ¹H NMR spectrum for andrographolide (1)

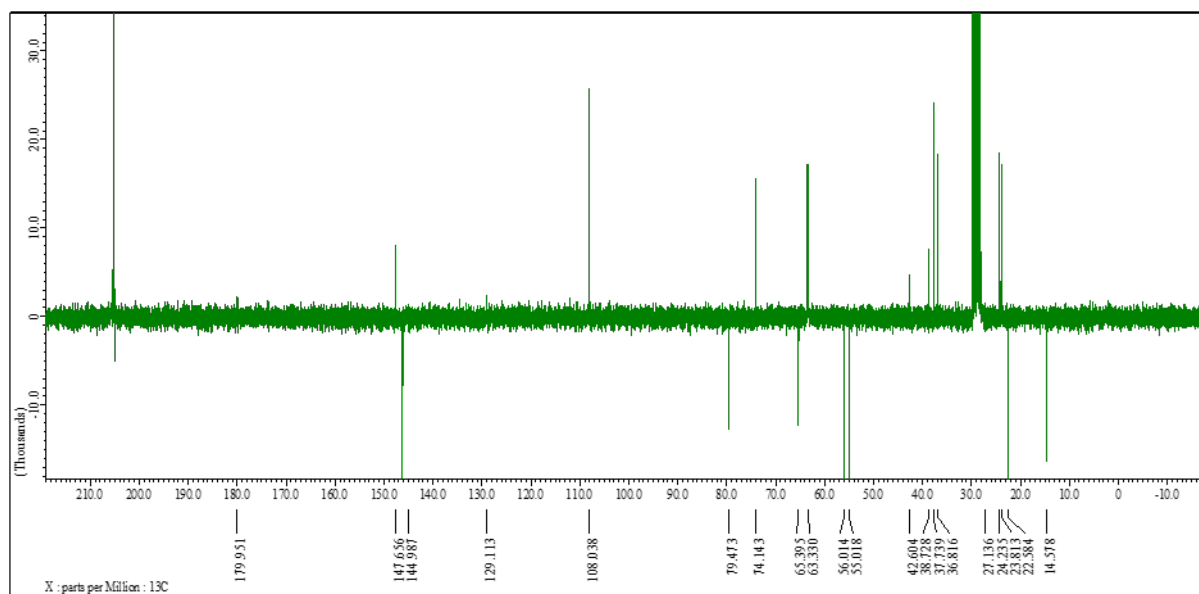


Fig 4S. DEPT ¹³C NMR spectrum for andrographolide (1)

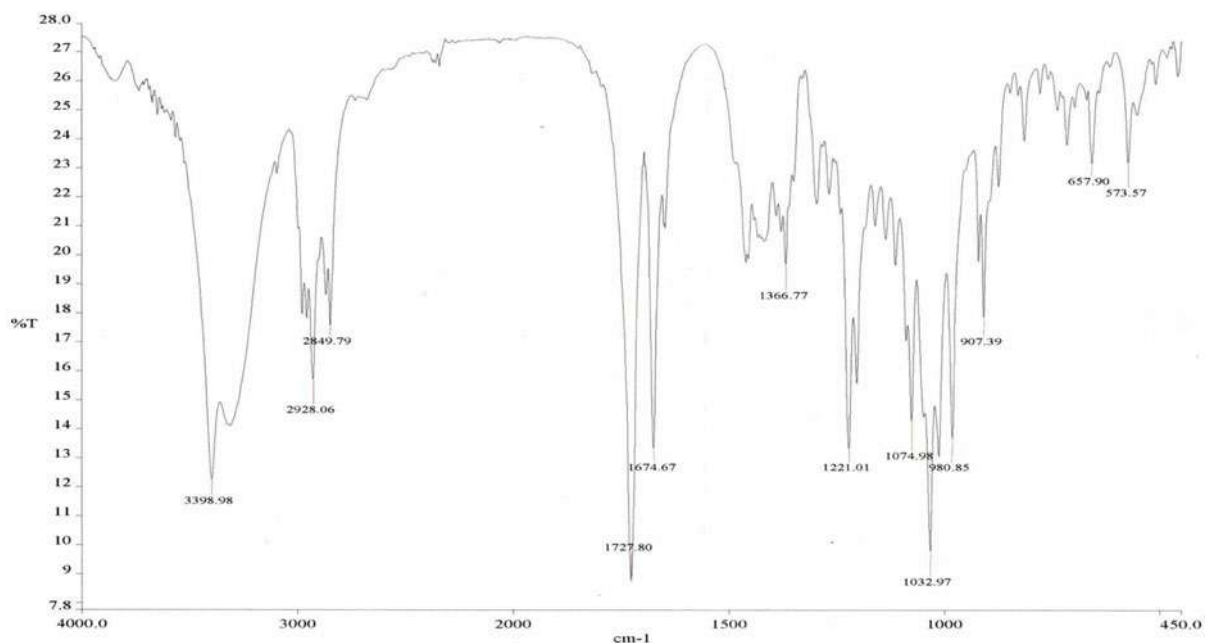


Fig 5S. IR spectrum for spectrum for andrographolide (1)

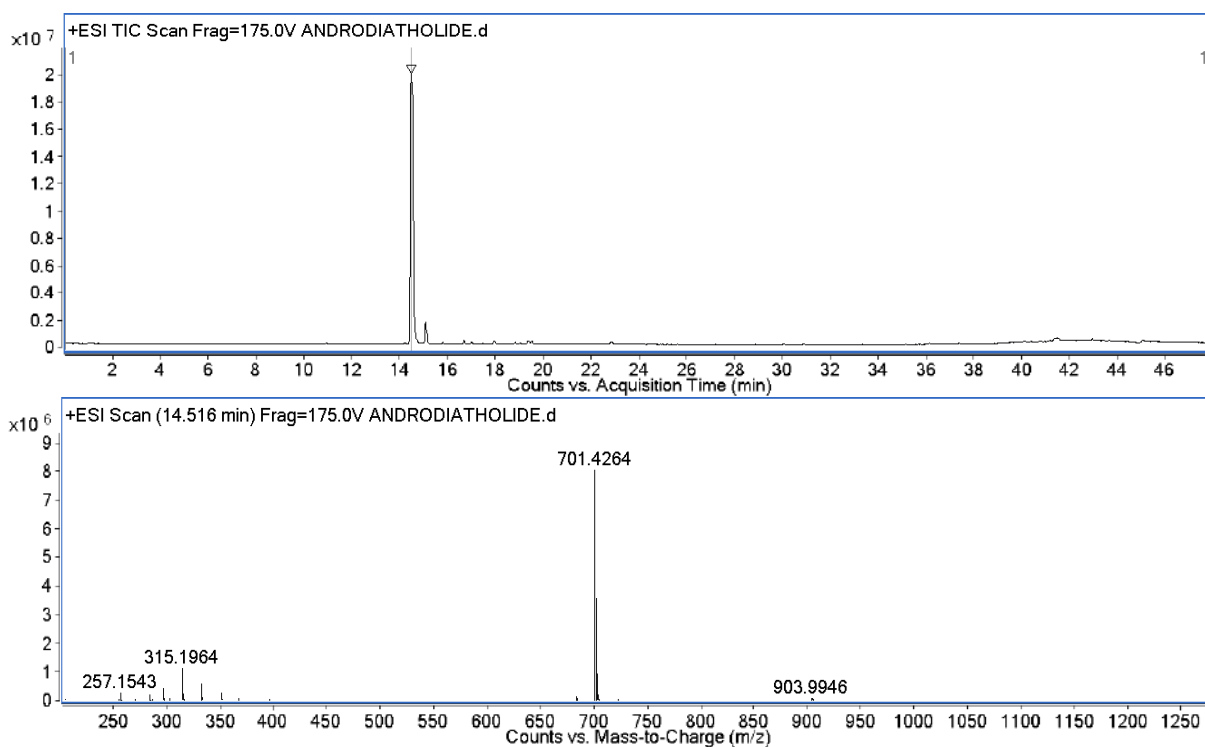


Fig 6S. MS spectra for for andrographolide (1)

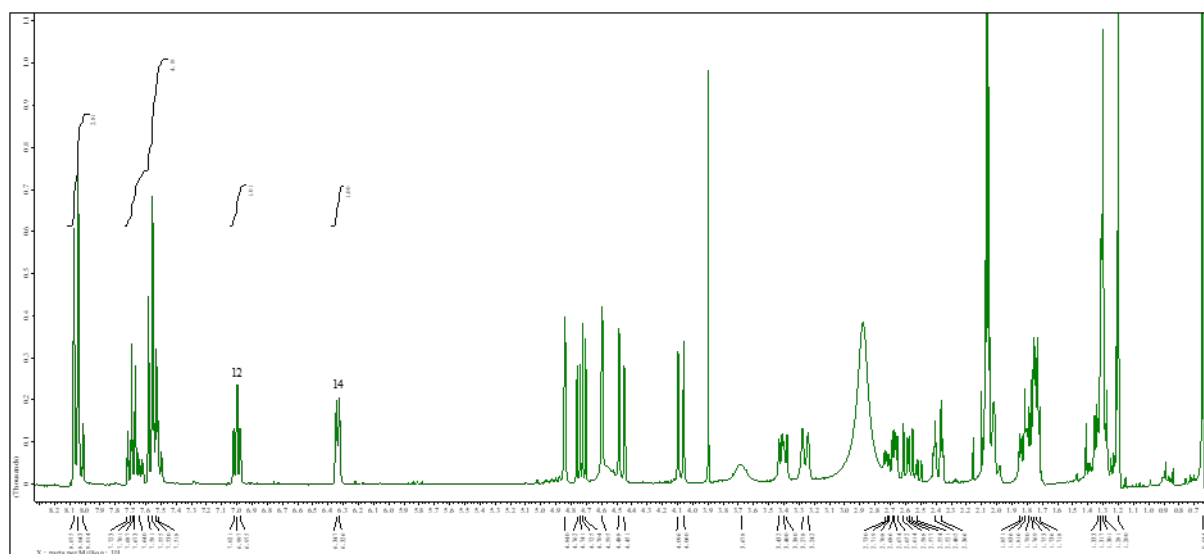


Fig 7S. ¹H NMR spectrum for 14-O-benzoyl adrographolide (2)

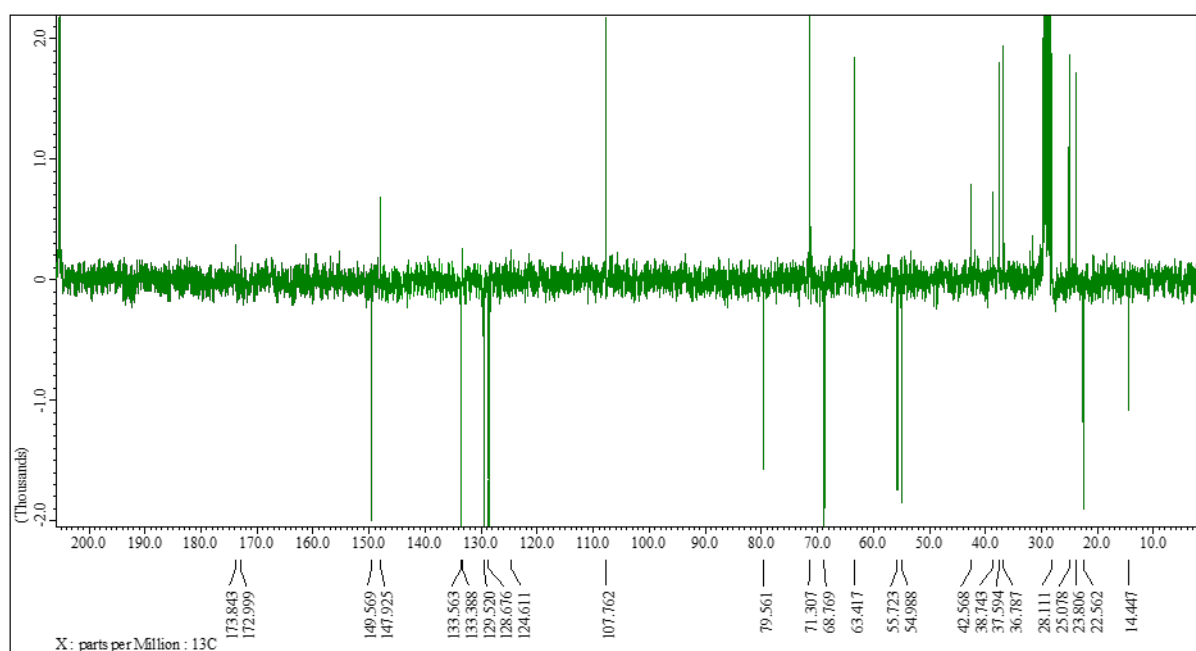


Fig 8S. DEPT ¹³C NMR spectrum for 14-O-benzoyl adrographolide (2)

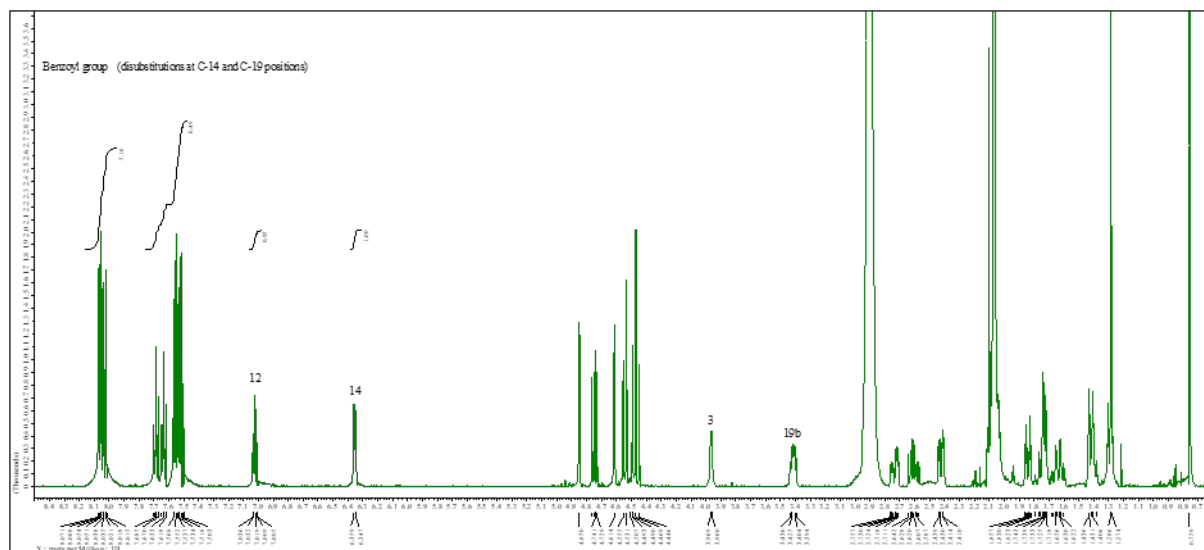


Fig 9S. ^1H NMR spectrum for 14,19-O-dibenzoyl andrographolide (3)

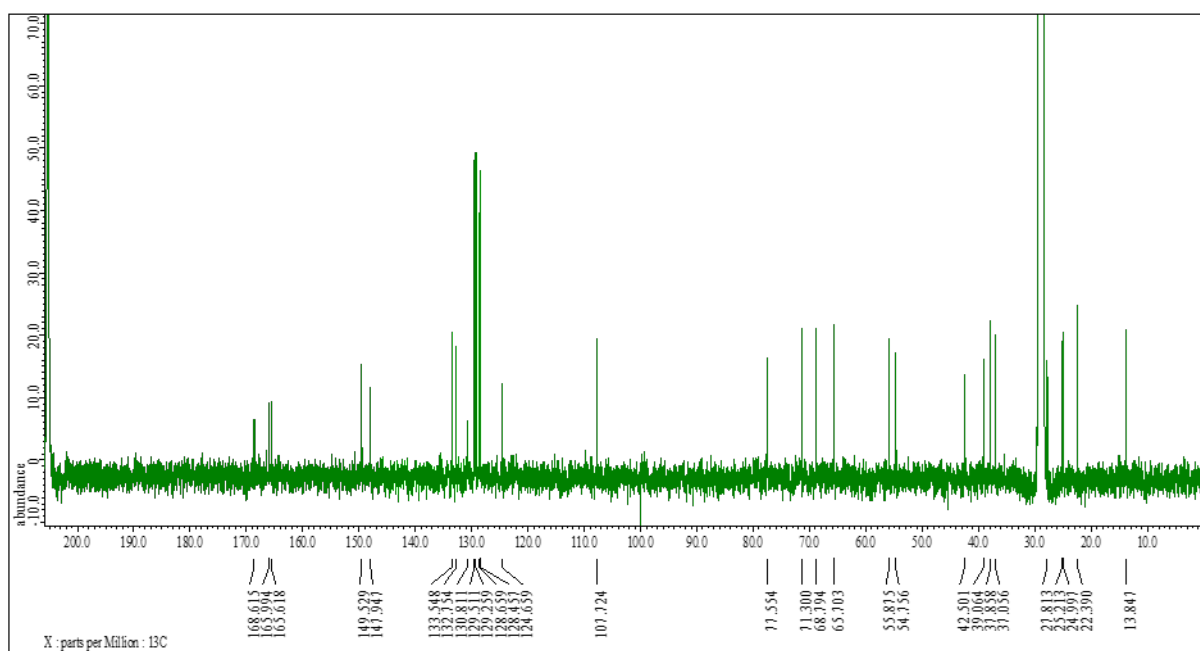


Fig 10S. ^{13}C NMR spectrum for 14,19-O-dibenzoyl andrographolide (3)

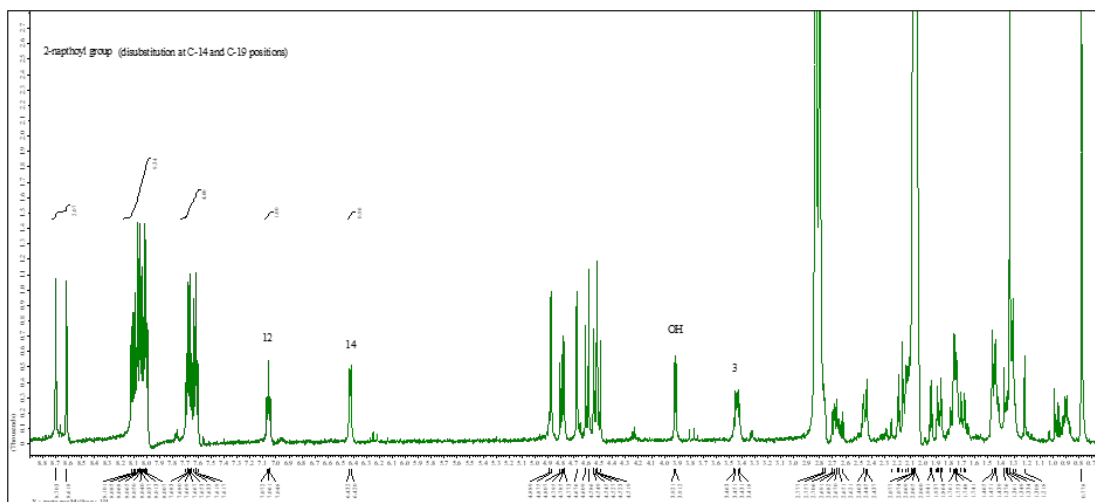


Fig 13S: ^1H NMR spectrum for 14,19-O-di(2-naphthoyl) andrographolide (5)

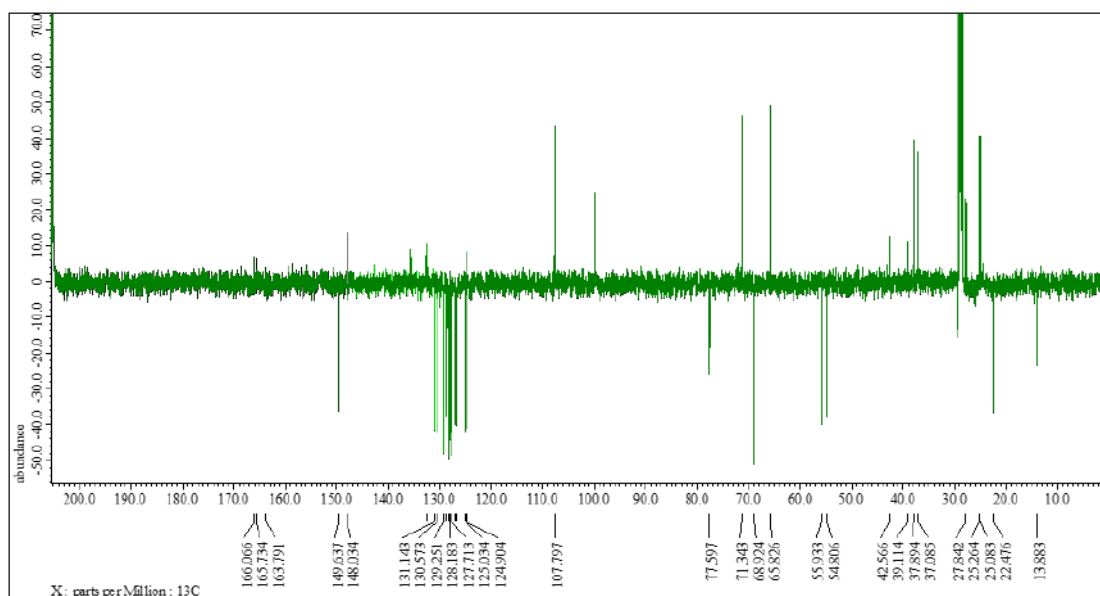


Fig 14S. DEPT ^{13}C NMR spectrum for 14,19-O-di(2-naphthoyl) andrographolide (5)

Table 3S. Key peaks for the experimental and calculated VA and VCD spectra of andrographolide (1)

Peak	VA		VCD	
	Experimental	Calculated	Experimental	Calculated
1850	X	X		
1820			X	X
1720	X	X		
1700			X	X
1570		X		
1470			X	X
1420			X	X
1270			X	X
1220			X	X
1200	X	X		

Conformational Analysis of Diterpene Lactone Andrographolide towards Reestablishment of Its Absolute Configuration via Theoretical and Experimental ECD and VCD Methods

Muhamad Faid A Kadir¹, Agustono Wibowo², Fatimah Salim^{3,4}, El Hassane Anouar⁵, Khalijah Awang⁶, Moses Kiprotich Langat⁷, and Rohaya Ahmad^{1,*}

¹Faculty of Applied Sciences, Universiti Teknologi MARA, 40450 Shah Alam, Selangor Darul Ehsan, Malaysia

²Faculty of Applied Sciences, Universiti Teknologi MARA, Pahang Branch, Jengka Campus, 26400 Bandar Tun Abdul Razak Jengka, Pahang Darul Makmur, Malaysia

³Atta-ur-Rahman Institute for Natural Products Discovery (AuRIns), Universiti Teknologi MARA, 42300 Bandar Puncak Alam, Selangor Darul Ehsan, Malaysia

⁴Centre of Foundation Studies, Universiti Teknologi MARA, Selangor Branch, Dengkil Campus 42800 Dengkil, Selangor, Malaysia

⁵Department of Chemistry, College of Sciences and Humanities Studies in Al-Kharj, Prince Sattam bin Abdulaziz University, Al Kharj 11942, Saudi Arabia

⁶Department of Chemistry, Faculty of Science, University of Malaya, 50603 Kuala Lumpur, Malaysia

⁷Jodrell Laboratory, Natural Capital and Plant Health Department, Royal Botanic Gardens, Kew, Richmond, TW9 3DS, UK

* Corresponding author:

tel: +60-355435592

email: rohayaahmad@uitm.edu.my

Received: April 2, 2020

Accepted: August 25, 2020

DOI: 10.22146/ijc.55206

Abstract: Andrographolide, the major constituent from the terrestrial plant *Andrographis paniculata* is a much-studied bioactive ent-labdane diterpene lactone and has become an important medicinal intermediate. As determined by X-ray crystallography, its structure has been applied in molecular docking studies to explain biological activities. Nevertheless, recently, several conflicting reports concerning the stereochemistry at the C-14 and C-10 positions affect the absolute configuration (AC) of the compound. Since a lack of information on the molecular flexibility of the molecule can lead to misleading conclusions on biological activity, a conformational analysis of the molecule in the solution state is necessary. The conformational analysis was performed by the Spartan14 package using the Merck Molecular Force Field (MMFF). The exciton chirality method in electronic circular dichroism spectroscopy (ECM-ECD) and vibrational circular dichroism (VCD) techniques were then jointly employed to re-establish the AC of andrographolide. Theoretical calculations were performed using TD-DFT methods employing the hybrid functionals B3LYP and CAM-B3LYP combined with 6-31G(d,p) basis set. Long-range exciton coupling of 2-naphthoyl chromophores at C-14 and C-19 led to the establishment of the AC to be 3R, 4R, 5S, 9R, 10R, and 14S. Comparison between the theoretical VCD data of **14-S** and **14-R** stereoisomer confirmed a configuration of S at C-14 position instead of R.

Keywords: andrographolide; conformational analysis; exciton coupling; vibrational circular dichroism; absolute configuration

■ INTRODUCTION

Natural products are known as medicinal intermediates, and the determination of their absolute

stereochemistry presents a considerable challenge due to their flexibility in solution state [1-2]. There is an urgency to study the conformational analysis of

bioactive chiral molecules in the solution state in which the bio-activity is observed since it will affect their absolute configuration. The correct stereochemistry is crucial for the understanding of the bioactivity of chiral compounds via molecular docking studies.

ECD and VCD are highly sensitive techniques in investigating the molecular conformation, configuration, solvation, and aggregation of chiral molecules [3]. Both ECD and VCD spectra allow the assignment of absolute stereochemistry determination feasible and conformational analysis in a solution for a compound alongside NMR (1D & 2D) experiments leading to relative stereostructure determination [4]. In addition, ECD provides a powerful tool for the AC assignment to chiral molecules in solution form as the chemical properties of chiral compounds are more clearly interpreted without the crystallization or the use of chiral auxiliaries for which single crystal X-ray methods are not applicable. The limitation of ECD is the requirement of a strong UV-Vis chromophore. However, this can be overcome by attaching chromophores to the molecule, as applied in the exciton chirality method (ECM-ECD method).

While the VCD technique offers the same benefits as ECD, it is not as sensitive as ECD, but it is applicable to most organic compounds capable of IR absorption. Furthermore, VCD also provides more spectral peaks with high signal resolution and good conformational sensitivity for chiral molecules compared to ECD, which helps reduce the efforts to determine the AC [5]. For both techniques, the interpretation of resulting spectra is nevertheless compromised by the number of overlapping transitions. Therefore, ECD and VCD spectra are most often compared to theoretical spectra calculated by applying first-principles theory *ab initio* methods by quantum mechanics (QM) [6-7].

Diterpenes are bicyclic compounds widely recognized as bioactive natural products. For these chromophore-lacking compounds, the application of ECM-ECD technique for its AC determination via long-range coupling of attached chromophores seemed feasible. Due to its important role as a medicinal intermediate and the absence of reports for its conformational analysis in the solution form,

andrographolide was chosen to be studied. The AC of the molecule was first determined by X-ray crystallography more than three decades ago [8-9]. While the early study reported by Fujita et al. [9] suggested an *R* configuration at the C-14 position, a 3D structure indicates the opposing *S* configuration. Similarly, a recent report [10] assigned the stereochemistry at the C-10 position as *S* via X-ray crystallography, which is inconsistent with a regular *ent*-labdane structure.

In this study, 2-benzoyl and 2-naphthoyl chromophores were employed with moderate electric dipole moments (2.24D & 5.07D) for the derivatization of the lactone to yield four derivatives via the ECM-ECD technique. The conformational analysis of each derivative was then carried out, and the experimental and theoretical ECD data were compared. As a complementary method, the experimental and theoretical VCD spectra of andrographolide **1** were also obtained to deduce the AC of the labdane diterpene lactone. In addition, the theoretical VCD data for its C-14 stereoisomer **Iis-14** was also calculated to confirm the stereochemistry at C-14.

■ EXPERIMENTAL SECTION

Material

All the chemicals used in this work were of analytical grade. The plant material (aerial parts of *Andrographis paniculata*) was obtained from Sungai Petani, Kedah, Malaysia. This specimen was supplied to the Herbarium Unit, Department of Botany, University of Malaya, with herbarium series number KL4930. The plant was dried for four days and ground into a fine powder.

Instrumentation

ECD data were collected on a JASCO J-815 CD spectropolarimeter with λ_{\max} ($\Delta\epsilon$) in the range of 190–400 nm. VCD measurements were done on a JASCO FVS-6000 (JASCO Inc, Mary's Court Easton, MD, USA). NMR spectra were recorded on a JEOL ECZS400 400 MHz spectrometer operating at 400 (^1H) and 100 (^{13}C) MHz equipped with shims gradient selective ^2H and ^1H

series and autosampler. 2D NMR experiments were performed using standard JEOL programs. All measurements were carried out at 291.15 K. Chemical shifts were reported as δ values (ppm) with the residual solvent signal and tetramethylsilane (TMS) as internal reference. *J*-coupling in Hz, and standard pulse sequences from the Delta NMR processing and control (v5.0.4.4, windows) software package were used (JEOL Inc., Peabody, MA, USA).

Procedures

Isolation of andrographolide

Two kilograms (2 kg) of dried *A. paniculata* powder was soaked in methanol (100%) for 3 days. The liquid extract was then filtered, and the solvent was removed at reduced pressure. This first procedure was repeated five times until a clear solution was obtained. Next, an aqueous solution of the dried methanol extract was subjected to liquid-liquid partitioning with hexane, dichloromethane (DCM), and ethyl acetate (EA) to yield the hexane, DCM, and EA extracts, respectively, upon evaporation of the solvent. The EA fraction (15 g) was then subjected to column chromatography with solvent system CHCl_3 :Acetone:MeOH, 7:3:1, which produced the best separation on TLC. Fifty fractions were collected, and each fraction was left to dry. Next, the combined fraction of 10–20 was subjected to centrifugal preparative TLC (CHCl_3 :MeOH, 9.5:0.5) followed by recrystallization (using EA as solvent) to yield andrographolide **1** (396 mg). The relative structure of the known andrographolide was confirmed by 1D and 2D NMR spectroscopy.

Chromophoric derivatization of andrographolide

Andrographolide (15 mg, 42.8 μmol) dissolved in 5 mL of anhydrous acetonitrile together with triethylamine (29.82, 5 eq) were added in a 25 mL round bottom flask. After 5 min of stirring, benzoyl chloride (29.83 μL , 6 eq) was added. The mixture was stirred at room temperature for 24 h in a nitrogen environment, and the reaction was monitored by TLC (silica gel, UV detection, and CrSO_4 as spraying reagent). Products **2** and **3** were purified using radial chromatography with solvent system CHCl_3 :MeOH, 9.5:0.5. Structure elucidation of the products was carried out using 1D and 2D NMR spectroscopy. The

same method was applied to the chromophore 2-naphthoyl chloride to yield derivatives **4** and **5**.

Computational analysis

The initial conformational analysis was performed by the Spartan '14 package using the MMFF molecular mechanics force field of *Monte Carlo* protocol. After collecting and selecting the conformational distribution calculated, the conformers within 2 kcal/mol range from the global minimum window were chosen and subjected to energy minimization using DFT calculations as implemented in the Gaussian 09W package.

Theoretical calculations of ECD and VCD spectra were performed by Gaussian 09W at the TDDFT level of theory using either the B3LYP (gaseous phase) or CAM-B3LYP (solvent phase) functionals, and suitable selection of basis set; 6-31+(d,p). The use of the long-range corrected CAM-B3LYP (solvent phase) functional was predicted to provide better ECD spectra simulation results than the more common B3LYP functional. For each optimized conformer, the excitation energy (in nm) and rotatory strength *R* (unit: 10–40 cgs) in the dipole velocity (*R_{vel}*) and dipole length (*R_{len}*) forms were calculated in acetonitrile (CH_3CN) by TDDFT/B3LYP/6-31G**, using the SCRF method, with the CPCM model. The theoretical CD spectra were obtained as weighted averages of Boltzmann populations. The final results of the calculated spectra were compared with experimental CD spectra to establish the AC of the selected compound [1,5].

RESULTS AND DISCUSSION

ECM-ECD Analysis of 1-5

Andrographolide **1** (Fig. 1) is a labdane-type diterpene and is widely recognized as a bioactive natural product [11-12]. The experimental ECD spectrum of **1** did not give much valuable information for AC determination. Furthermore, the spectrum results from the $\pi \rightarrow \pi^*$ electronic transitions of 'ene' lactone moiety at the furanone ring, which does not significantly represent the absolute configuration of the global molecule structure. The sensitivity of **1** towards ECD analysis is expected to increase by replacement of hydrogen atoms of hydroxyl groups at C-14 and C-19

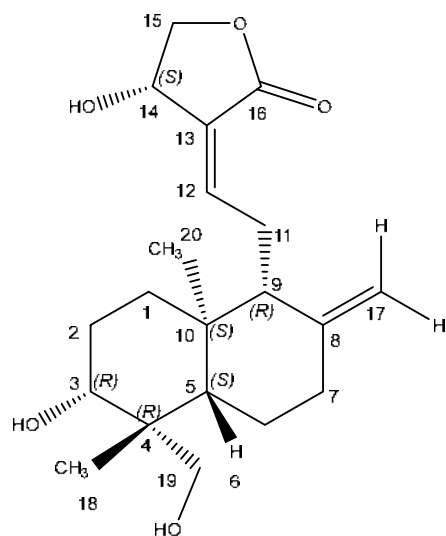
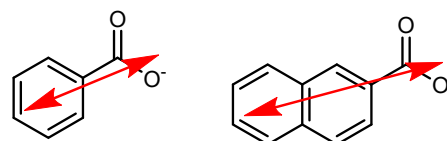


Fig 1. Chemical structure of andrographolide (1) with carbon numbering. The configuration was determined using single-crystal X-ray crystallographic technique from previous studies

carbon atoms (bond distance $\sim 8 \text{ \AA}$) by the selected chromophores (Fig. 2) as the steric hindrance for both deprotonated hydroxyl groups is relatively low. Thus, they can exist as stable nucleophiles. For anticipating this, 4 andrographolide derivatives (2–5) were successfully synthesized (Fig. 3) according to standard methodologies yielding products with a yield of 50–70%. The structures of 2–5 were confirmed by 1D and 2D NMR data (See Supplementary Materials).

Upon confirmation of their structures, the derivatives were subjected to ECD analysis. All four derivatives (2–5) showed a good CE split (bisignate curve)

at maximum absorbance between 210–240 nm with a higher intensity as compared to 1 at the same concentration of 0.03 mM (Fig. 4). Having additional chromophores has thoroughly increased the sensitivity of selected compounds at the minimum concentration (UV absorption intensity = 0.6–1.4). In contrast, the strength of electric dipole moments, interchromophoric distance, and chiral dihedral angle are the key factors that affect the total exciton coupling between the two chromophores, although their position in space is relatively near/far to each other [13–14]. Nevertheless, all the CE observed (Fig. 4) for all four derivatives showed negative first maxima at λ_{max} 236 nm ($\Delta\epsilon$ -20.9), λ_{max} 235 nm ($\Delta\epsilon$ -47.3), λ_{max} 243 nm ($\Delta\epsilon$ -30.3) and λ_{max} 240 nm ($\Delta\epsilon$ -70.7), respectively. This data indicates that the dihedral twist between the chromophores is arranged in space in a counter-clockwise manner. Interestingly, it is observed that the ECD signals for 2, 3, and 4 did not show a very distinguishable bisignate CE



Name	Benzoyl ester	Naphthoyl ester
λ_{max}	230 nm	239 nm
Dipole moment	2.24 D	5.07 D

Fig 2. Selected chromophores chosen for exciton-coupled circular dichroism method. Red arrows show the electric transition dipole (dipole moment was calculated by semi-empirical method using Spartan '14)

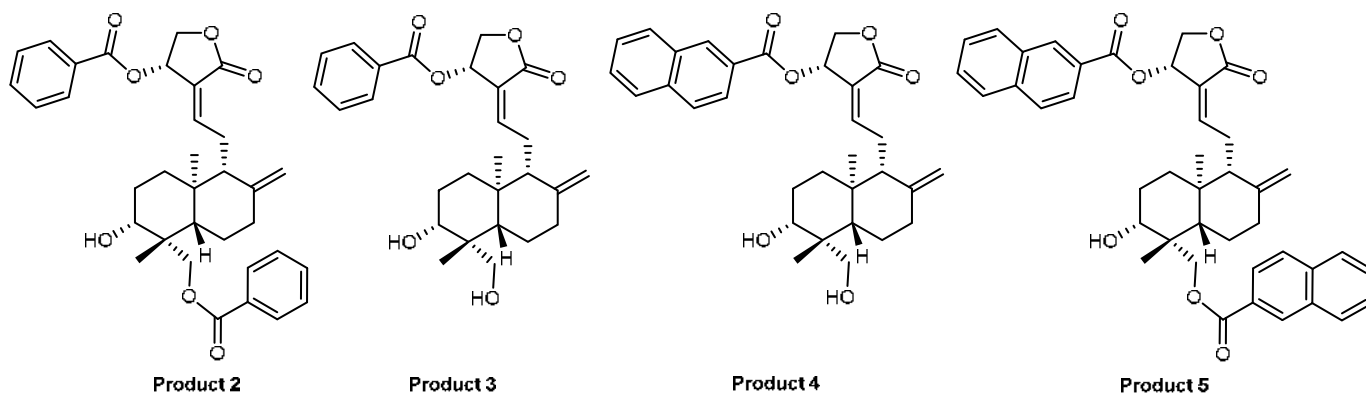


Fig 3. Chemical structures of andrographolide derivatives (2–5). Derivatives 2 and 3 and derivatives 4 and 5 were obtained from single reaction of different chromophores used for derivatization

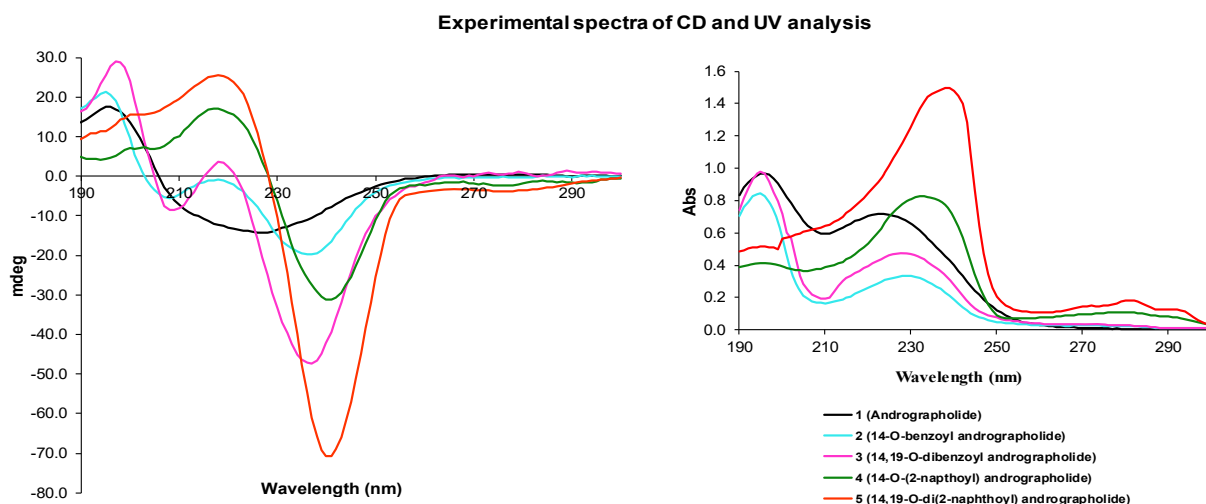


Fig 4. Experimental CD (left) and UV (right) spectra of compounds **1–5**. CD analysis were done in acetonitrile as solvent and the concentration was constant at 0.03 ppm. The wavelength was collected between 190–400 nm and only significant absorption up to 300 nm was considered

to allow the elucidation of the AC of the whole molecular structure while the spectrum observed for **5** is conclusively intense and distinguishable.

The exciton couplet from the interaction between two 2-naphthoyl ester chromophores in the skeleton of **5** showed an intense and good distinct negative CE (243 nm $\Delta\epsilon$ -70.7 and 218 nm $\Delta\epsilon$ +25.5) around the UV maximum (λ_{max} of 240 nm), suggesting the *S*-absolute and *R*-absolute configuration of chiral centers C-14 and C-4, respectively (Fig. 5). These assignments are in accordance with previous studies in terms of 3D structures [8-9]. However, Fujita et al. [8] described the stereochemistry at C-14 as *R*. Furthermore, the results suggest how 2-naphthoyl ester structures introduced to **1** restrict the space rotation flexibility and rationalize the absolute configuration within a distance of 8 Å [13,15].

The experimental data agreed well with predicted ECD spectra using time-dependent density functional theory (TD-DFT) calculation. A conformational analysis study was first carried out in order to reduce the uncertainty and determine the conformer distribution in the solution state at room temperature. Geometry optimization was carried out to reduce the calculation period for the conformer distribution population. Thereafter, the calculation was calculated in the protocol

of *Monte Carlo* to reduce the computational effort in the conformational analysis [5,16-18].

Structure **5** was defined as a tweezer-like structure based on the negative chirality data obtained and 3D structure drawn from the conformational analysis. Prediction on the minimal energy optimization of **5** showed that the Boltzmann distribution for conformers was predominated by the tweezer-like structure in a negative chirality manner within the minimum energy

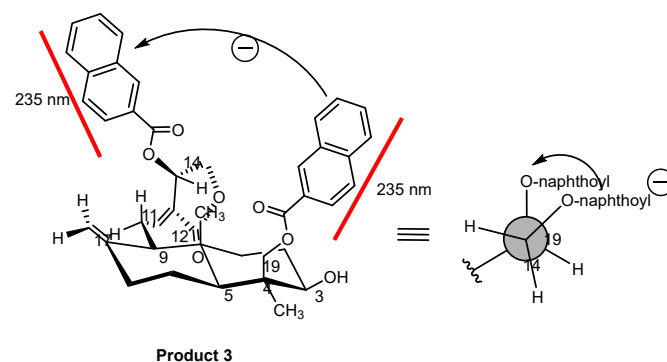


Fig 5. Negative chirality of **5** resulting from exciton coupling of two chromophores with interchromophoric distance 8 Å. Anticlockwise coupling from the front view of chromophoric couple indicates the negative chirality. The structure and interchromophoric distance were determined using ChemDraw software

of 2 kcal/mol. The postulated structure of **5** suggests that the dihedral angle of the coupling electric-dipole transition moment contributed to the perturbation of the negative ECD spectrum. In addition, specific properties of the steric arrangement for both 2-naphthoyl ester rings in **5** that are not parallel to each other (energy minimization) likely reduce the flexible rotation of the whole molecule and ease the calculation of theoretical ECD spectra [19-20]. There was no change in the number of conformers for Structures **4** and **5**.

Table 1 shows the conformer distribution of **1** and its derivatives. As shown in this table, the monosubstituted andrographolide derivatives **2** and **4** possess six and four conformers, respectively. Meanwhile, the disubstituted andrographolide derivatives **3** and **5** have five and four conformers, respectively. The different number of stable conformers within the energy of 2 kcal/mol was governed by the geometric flexibility of the calculated molecules. For derivative **5**, its large structure with a higher dipole moment of chromophore introduced has significantly hindered the conformer flexibility as the couple and interact spatially through space. Besides that, the first conformer of **5** (CF1), possessing the least energy, shows high Boltzmann distribution (> 0.5) which indicates geometry dominance in nature [17,21-22].

The ECD spectra were predicted at the B3LYP/6-311+G(d,p) level of theory in the gas phase initially followed by calculations within the PCM solvation model of acetonitrile for each compound. Based on the experimental ECD spectra of **1-5**, which were used as

diagnostic chirality markers, the simulated spectra were expected to produce negative CE. Additionally, **5** is expected to exhibit a good bisignate CE in the context of the exciton coupling method [1-2]. Upon comparison, the overall pattern of simulated ECD spectra was in excellent agreement with the experimental spectra of **1-5** (Fig. 6). The predicted spectra for **4** and **5** showed a bisignate CE similar to that observed in the experimental data. Furthermore, CF1 of **5** exhibited the highest percentage agreement, and the Boltzmann distribution resulted in more than 50% population where it is considered more reliable for AC determination in nature.

Experimental VA and VCD Analysis of **1**

The vibrational absorbance (VA) and vibrational circular dichroism (VCD) spectra of **1** were recorded in solution (DMSO-*d*₆) to replicate the properties of the tested compound in a non-rigid chemical environment at a controlled temperature (25.0 °C) with a band resolution of 4.0 cm⁻¹. The sample concentration was tested initially at 1.0 M at 50 µL to identify the weak signal throughout the full range of the spectrum (800–2000 cm⁻¹). Then, the concentration was gradually reduced down to 0.1 M to measure the specific region with strong vibrational absorbance in order to obtain reliable data of strong VCD signal.

The initial VA analysis measured using the KBr plate method showed a good absorption in the mid-IR region (800–2000 cm⁻¹). From the VA spectra of **1**, five

Table 1. The energy conformations of andrographolide derivatives **2-5** with Boltzmann distribution to indicate the conformer stability after geometry optimization at minimum energy configuration where Rel. E represents the relative energy

Conformer No.	2			3			4			5		
	Energy (kcal/mol)		Boltz. Dist	Energy (kcal/mol)		Boltz. Dist	Energy (kcal/mol)		Boltz. Dist	Energy (kcal/mol)		Boltz. Dist
	E	Rel. E		E	Rel. E		E	Rel. E		E	Rel. E	
CF1	107.20	0.00	0.429	137.37	0.00	0.387	157.92	0.00	0.537	157.92	0.00	0.537
CF2	107.33	0.13	0.343	137.45	0.09	0.335	158.26	0.34	0.301	158.26	0.34	0.301
CF3	108.09	0.89	0.096	138.01	0.64	0.132	159.15	1.23	0.067	159.15	1.23	0.067
CF4	108.43	1.24	0.053	138.07	0.47	0.119	159.44	1.53	0.041	159.44	1.53	0.041
CF5	108.45	1.25	0.052	139.20	1.83	0.018	-	-	-	-	-	-
CF6	109.10	1.91	0.017	-	-	-	-	-	-	-	-	-

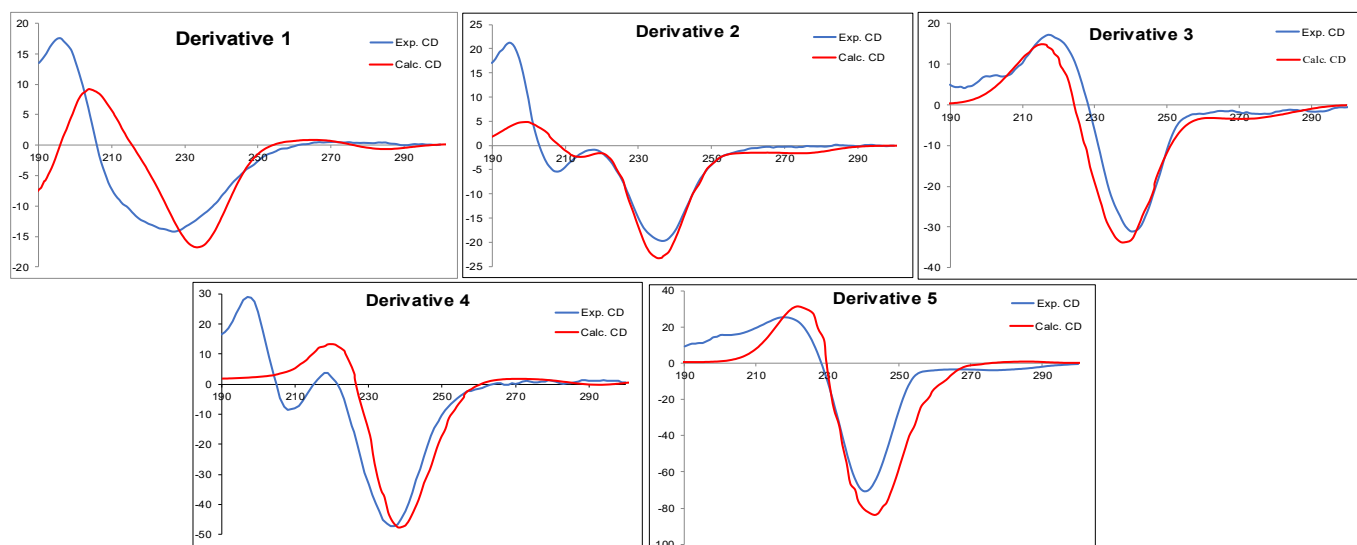


Fig 6. Experimental (blue) and Boltzmann weighted calculated (black) ECD spectra for **5**. Experimental in acetonitrile, simulated calculated with TDDFT/B3LYP//6-311+G(d,p)

strong and medium peaks were selected as a reference before the analysis was carried out in the solution state. A strong peak was observed at 1727.80 cm^{-1} , which represent stretching energy from the conjugation of ester carbonyl functional group at C-16. Other characteristic peaks are seen as sharp peaks at 3398.98 and 2928.06 cm^{-1} represent -OH and C-H stretching. In addition, the pattern of peaks in the near IR region stipulates that **1** is involved in a number of intramolecular hydrogen bonding specifically for hydroxyl group for C-3 and C-19 that are naturally positioned near each other in space. Although there are a few strong and sharp absorption peaks that can be observed from $2800\text{--}3400\text{ cm}^{-1}$, it is relatively uncommon to analyze VCD absorption at this region due to unstable and broad vibrational absorption. This region is also routinely neglected or only considered for certain and complicated cases. This is mainly caused

by the fact that this region does not fully represent the vibration energy on total chemical structure and sensitive towards the hydrogen bonding vibration specifically for molecules that contain hydroxyl groups like **1**. Other important considerations are the type of bonding directly attached to chiral centers, i.e., C-O, C-C, C-H bending energy. Table 2 gives comprehensive data of characteristic peaks identified by their type of bonding vibration energy and their contribution to chirality, indicating direct attachment or involvement of functional structure in chiral rotation and configuration.

VCD analysis of **1** was recorded at 48000 scan number, which is equivalent to 8 h. As reported by García-Sánchez et al., 2014 [23], other labdane diterpenes may take 6 to 11 h of VCD analysis period depending on the flexibility of the compound tested. This phenomenon due to the fact that the vibrational transition of chemical

Table 2. VA Peak characterization of **1** using KBr plate method

Band number	Experimental frequency	Vibrational origin	Contribution to chirality
1	3398.98	O-H stretching	Positive
2	2928.06	C-H stretching, sp^3	Positive
3	1727.80	C=O stretching of carbonyl ester	Positive
4	1674.67	C=C stretching, sp^2	Negative
5	1221.01	=C-O stretching	Positive
6	1032.98	C-O alkoxy stretching	Positive
7	980.85	CH out of plane bending for trans alkene	Negative

bonding is a weak quantized energy produced by electron wavefunction [24]. Rationally, as the number of scans increases, more data can be collected, repeated to improve the signal-to-noise (S/N) ratio and produce VCD at a higher intensity. However, due to solvent effects, the vibrational absorbance at region $800\text{--}1000\text{ cm}^{-1}$ could not be obtained clearly, and this minimal complication usually has no negative upshot of total VCD spectra.

Furthermore, the natural existence of C=O group in **1** can significantly improve the VCD assignment since the signal produced is alienated from the fingerprint region. A good band-to-band comparison of calculated and experimental VCD spectra is very important for configuration assignment since calculated frequencies are derived from a harmonic force field. In contrast, calculated IR and VCD frequencies are derived from a non-harmonic force field from the bending or stretching. Thus, the uncertainty of VCD experimental analysis can be justified by the calculated spectra and thereby establishing absolute configuration [23].

Theoretical VCD Calculation of **1** and Its C-14 Stereoisomer

The calculated VA and VCD spectra were done at a similar functional theory level as the previous ECD calculation, CAM-B3LYP/6-311+G(d,p). The vibrational response resulted in five clear VA bands and corresponding VCD peak from which a peak for the carbonyl band gave rise to an isolated VCD peak. However, the peaks in the fingerprint region were more congested, and the VCD response for both experimental and simulated could not be seen clearly. Some broad and yet weak peak fairly envelope in the region $\sim 1300\text{ cm}^{-1}$. Their appearance may be attributed to the presence of closely spaced vibration bands between the conformers. The total populated calculation led to the conclusion that

the latter rationale is more applicable to the study of other stereoisomers [25], thus reconfirming the reliability of calculated VCD spectra of **1**.

Table 3 shows the conformer distribution of **1** and its theoretical stereoisomers. The most prominent peaks were observed in the carbonyl region, giving rise to a VCD response. The theoretical vibrational energy was calculated for a stereoisomer of **1** with an *R* configuration for C-14. The analysis of **1** with the theoretical isomers was prominent as a tool for observing the vibrational energy region involved in changing the pattern of calculated VCD data obtained. However, observation in the region $2800\text{--}3500\text{ cm}^{-1}$ was also taken into account to pinpoint whether its contribution in VCD analysis was relevant for the AC assignment. From the structure modification, only calculated VCD data were affected, while no apparent changes can be observed from calculated VA data.

The method of primary VCD calculation was used for this section to ensure the results obtained did not contradict with andrographolide VCD calculation. Furthermore, calculation with a similar method was more reliable for the different signals of simulated VCD comparison. After geometry optimization and conformational search, the two proposed stereoisomers were subjected to VCD analysis. Comparing the two stereoisomers helps improve the data confidence level and deduce the correct stereochemistry at C-14.

Fig. 7 shows the spectral agreement of VA and corresponding VCD of **1** at the region $1600\text{--}1700\text{ cm}^{-1}$ and the difference between the theoretical calculation for **1** and **Iis-14**. The key peaks from the spectra are shown in Table 3S (Supplementary Materials). The spectra in black represent the experimental, while the spectra in blue represent the calculated spectra of both

Table 3. Conformer distribution of **1** and its theoretical stereoisomers

Stereoisomers	1	Iis-14	Stereoisomers	1	Iis-14
CF1	0.281	0.750	CF6	0.047	-
CF2	0.200	0.241	CF7	0.043	-
CF3	0.139	0.003	CF8	0.034	-
CF4	0.054	0.002	CF9	0.032	-
CF5	0.047	0.002	CF10	0.017	-

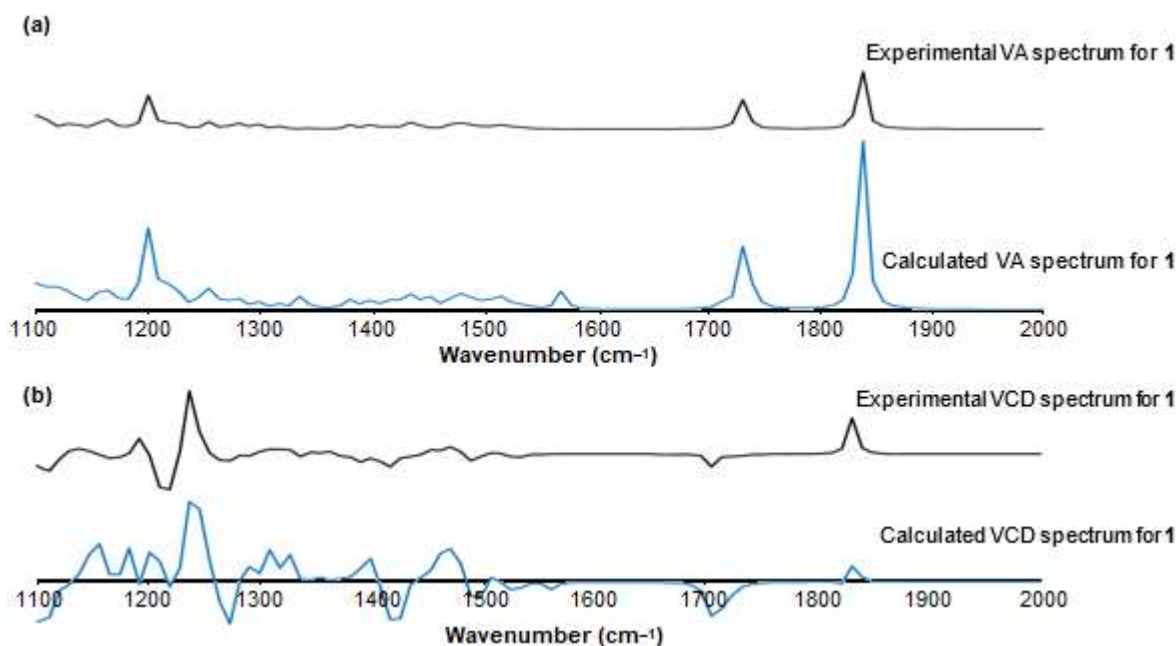


Fig 7. Experimental (black) and calculated (blue) VA (a) and VCD (b) spectra of andrographolide (**1**)

VA and calculated VCD spectra of **1** and **1is-14** weighted from the ten and six conformers from the global window, respectively. Clear correlations can be seen at the region 1700–1900 cm^{-1} . In the fingerprint region, only one peak was prominent. Experimental analysis of VA and VCD was done for 1 min at 32 and 8 h at 48000 scan numbers, respectively, using BaF₂ glass cuvette with a pathlength of 50 μm . The absorption intensity of the experimental spectra was slightly weaker than the calculated data. These results were consistent with literature that focused on the VCD of labdane-type diterpene compound for AC determination [23,25]. The chemical environment, such as the solvent employed, is one reason why infrared energy was not absorbed for the vibrational transition within the molecule. Nonetheless, VA and VCD spectra have a similar pattern from 1100–2000 cm^{-1} , which clearly justifies the liability of the experimental analysis.

The two stereoisomers produced a variable pattern of VCD spectra. Two pivotal peaks at $\sim 1700 \text{ cm}^{-1}$ were used as the primary reference for the VCD response of all stereoisomers. VA signals above 2800 cm^{-1} did not seem to have a significant contribution towards VCD analysis. Likewise, the unique pattern of coupled VCD response at $\sim 1700 \text{ cm}^{-1}$ provided important information for the differentiation between andrographolide and its C-14

isomer **1is-14**. However, the intensity of VCD response for **1is-14** was comparatively higher than **1**.

Some observations can be made from the region 1600–1900 cm^{-1} (C=O stretching), where the VCD response was seen as two distinct peaks. Each stereoisomer has different peak order (+/-, +/+, -/+, -/-) and is easily compared as they were excluded from the fingerprint region. Nevertheless, the order of VCD peak in the carbonyl region for both **1** and **1is-14** is identical (-/+). Thus, the signal which lay within the fingerprint region was used to differentiate between the two stereoisomers, although the VCD response for **1** was slightly weaker than **1is-14**. We have shown that comparing theoretical data between stereoisomers is critical to avoid a mismatched assignment in determining absolute configuration.

CONCLUSION

The conformational analysis of andrographolide derivatives and re-establish its AC were carried out in the solution state via the joint ECM-ECD and VCD techniques. The attachment of 2-naphthoyl group at C-14 and C-19 in derivative **5** was found to reduce its molecular flexibility and the number of conformers resulting in four conformers with relative energy less

than 2 kcal. Conformer 1 (CF1) was found to possess the least energy and had the highest Boltzmann distribution (> 0.5), which indicates geometry dominance in nature. Due to its higher electric transition dipole moment, exciton coupling observed between the 2-naphthoyl moieties produced a more significant bisignate CE than between the benzoyl groups. Long-range exciton coupling of 2-naphthoyl chromophores at C-14 and C-19 in derivative **5**, using the ECM-ECD technique, led to the establishment of the AC to be 3*R*, 4*R*, 5*S*, 9*R*, 10*R*, and 14*S*. In the VCD method, a relatively good match was found between the experimental spectra and the theoretical spectra of **1** performed at the TDDFT level of theory using the long range corrected CAM-B3LYP (solvent phase) functionals and basis set; 6-311+G(d,p). Comparison between the theoretical VCD spectra for **1** and **Iis-14** further minimizes the possibility of a 14*R* configuration for andrographolide.

■ ACKNOWLEDGMENTS

This work was fully supported by the Ministry of Higher Education, Malaysia (MOHE) under FRGS and BESTARI Grant, Ref: 600-RMI/FRGS5/3(49/2013) and 600-IRMI/DANA5/3/BESTARI(0028/2016), respectively.

AUTHOR CONTRIBUTIONS

MFAK conducted the experiment and drafted the manuscript, AW carried out chromophoric derivitization and assisted with NMR interpretation, FS assisted with the CD experiments, E-HA conducted conformational analysis and the DFT calculations, KA assisted in the project design, ML assisted with the interpretation of ECD spectra, RA designed the project and revised the manuscript. All authors agreed to the final version of this manuscript.

■ REFERENCES

- [1] Anouar, E.H., and Weber J.-F.F., 2013, Time-dependent density functional theory study of UV/vis spectra of natural styrylpyrones, *Spectrochim. Acta, Part A*, 115, 675–682.
- [2] Pescitelli, G., Di Bari, L., and Berova, N., 2011, Conformational aspects in the studies of organic compounds by electronic circular dichroism, *Chem. Soc. Rev.*, 40 (9), 4603–4625.
- [3] Bultinck, P., Cherblanc, F.L., Fuchter, M.J., Herrebout, W.A., Lo, Y.P., Rzepa, H.S., Siligardi, G., and Weimar, M., 2015, Chiroptical studies on brevianamide B: Vibrational and electronic circular dichroism confronted, *J. Org. Chem.*, 80 (7), 3359–3367.
- [4] Mishra, S.K., and Suryaprakash, N., 2017, Some new protocols for the assignment of absolute configuration by NMR spectroscopy using chiral solvating agents and CDAs, *Tetrahedron: Asymmetry*, 28 (10), 1220–1232.
- [5] Petrovic G.A., Navarro-Vazquez, A., and Alonso-Gomez J.L., 2010, From relative to absolute configuration of complex natural products: Interplay between NMR, ECD, VCD, and ORD assisted by ab initio calculations, *Curr. Org. Chem.*, 14 (15), 1612–1628.
- [6] Batista, J.M., and da Silva Bolzani, V., 2014, Chapter 13. Determination of the absolute configuration of natural product molecules using vibrational circular dichroism, *Stud. Nat. Prod. Chem.*, 41, 383–417.
- [7] Salim, F., Yunus, Y.M., Anouar, E.H., Awang, K., Langat, M., Cordell, G.A., and Ahmad, R., 2019, Absolute configuration of alkaloids from *Uncaria longiflora* through experimental and theoretical approaches, *J. Nat. Prod.*, 82 (11), 2933–2940.
- [8] Smith, A.B., Toder, B.H., Carroll, P.J., and Donohue, J., 1982, Andrographolide: An X-ray crystallographic analysis, *J. Crystallogr. Spectrosc. Res.*, 12 (4), 309–319.
- [9] Fujita, T., Fujitani, R., Takeda, Y., Takaishi, Y., Yamada, T., Kido, M., Miura, I., 1984, On the diterpenoids of *Andrographis paniculata*: X-ray crystallographic analysis of andrographolide and structure determination of new minor diterpenoids, *Chem. Pharm. Bull.*, 32 (6), 2117–2125.
- [10] Chantrapromma, S., Boonnak, N., Pitakpornprecha, T., Yordthong, T., Kumar, C.S.C., and Fun, H.K., 2018, Absolute configuration of andrographolide and its proliferation of

- osteoblast cell lines, *Crystallogr. Rep.*, 63 (3), 416–421.
- [11] Jayakumar, T., Hsieh, C.Y., Lee, J.J., and Sheu, J.R., 2013, Experimental and clinical pharmacology of *Andrographis paniculata* and its major bioactive phytoconstituent andrographolide, *Evid. Based Complement. Altern. Med.*, 2013, 846740.
- [12] Hossain, M.S., Urbi, Z., Sule, A., and Rahman, K.M.H., 2014, *Andrographis paniculata* (Burm. f.) Wall. ex Nees: A review of ethnobotany, phytochemistry, and pharmacology, *Sci. World J.*, 2014, 1–28.
- [13] Berova, N., Ellestad, G.A., and Harada, N., 2010, “Characterization by circular dichroism spectroscopy” in *Comprehensive Natural Products II: Chemistry and Biology*, Eds. Mander, L., and Liu, H.W., Elsevier Science, United Kingdom, 91–146.
- [14] Berova, N., Polavarapu, P.L., Nakanishi, K., and Woody, R.W., 2012, *Comprehensive Chiroptical Spectroscopy: Applications in Stereochemical Analysis of Synthetic Compounds, Natural Products, and Biomolecules*, John Wiley & Sons, Inc., Hoboken, New Jersey, United States.
- [15] Li, X., Burrell, C.E., Staples, R.J., and Borhan, B., 2012, Absolute configuration for 1, *n*-Glycols: A nonempirical approach to long-range stereochemical determination, *J. Am. Chem. Soc.*, 134 (22), 9026–9029.
- [16] Tanaka, H., Inoue, Y., Nakano, T., and Mori, T., 2017, Absolute configuration determination through the unique intramolecular excitonic coupling in the circular dichroisms of *o,p'*-DDT and *o,p'*-DDD. A combined experimental and theoretical study, *Photochem. Photobiol. Sci.*, 16 (4), 606–610.
- [17] Autschbach, J., 2009, Computing chiroptical properties with first-principles theoretical methods: Background and illustrative examples, *Chirality*, 21 (1E), E116–E152.
- [18] Taniguchi, T., 2017, Analysis of molecular configuration and conformation by (electronic and) vibrational circular dichroism: Theoretical calculation and exciton chirality method, *Bull. Chem. Soc. Jpn.*, 90 (9), 1005–1016.
- [19] Pescitelli, G., Di Bari, L., and Barova, N., 2014, Application of electronic circular dichroism in the study of supramolecular systems, *Chem. Soc. Rev.*, 43 (15), 5211–5233.
- [20] Nicu, V.P., and Jan Baerends, E., 2011, On the origin dependence of the angle made by the electric and magnetic vibrational transition dipole moment vectors, *Phys. Chem. Chem. Phys.*, 13 (36), 16126.
- [21] Person, R.V., Monde, K., Humpf, H., Berova, N., and Nakanishi, K., 1995, A new approach in exciton-coupled circular dichroism (ECCD)-Insertion of an auxiliary stereogenic center, *Chirality*, 7 (3), 128–135.
- [22] Berova, N., Nakanishi, K., and Woody, R.W., 2000, *Circular Dichroism. Principles and Applications*, 2nd Ed., John Wiley & Sons, Inc., New York, US.
- [23] García-Sánchez, E., Ramírez-López, C.B., Talavera-Alemán, A., León-Hernández, A., Martínez-Muñoz, R.E., Martínez-Pacheco, M.M., Gómez-Hurtado, M.A., Cerda-García-Rojas, C.M., Joseph-Nathan, P., and del Río, R.E., 2014, Absolute configuration of (13*R*)- and (13*S*)-labdane diterpenes coexisting in *Ageratina jocospecana*, *J. Nat. Prod.*, 77 (4), 1005–1012.
- [24] Hoffmann, S.V., Fano, M., and Van de Weert, M., 2016, “Circular dichroism spectroscopy for structural characterization of proteins” in *Analytical Techniques in the Pharmaceutical Sciences. Advances in Delivery Science and Technology*, Eds. Müllertz, A., Perrie, Y., and Rades, T., Springer, New York, NY, 223–251.
- [25] Joseph-Nathan, P., Gordillo-Román, B., 2015, Vibrational circular dichroism absolute configuration determination of natural products, *Prog. Chem. Org. Nat. Prod.*, 100, 311–452.

Synthesis, Characterization, and Study of Proton Exchange Polymer Membrane Properties of Sulfonated Copolymer Eugenol-diallyl Phthalate

Ngadiwiyana^{1,*}, Nor Basid Adiwibawa Prasetya¹, Gunawan¹, Tutuk Djoko Kusworo², and Heru Susanto²

¹Department of Chemistry, Faculty of Science and Mathematics, Universitas Diponegoro, Jl. Prof. Soedharto SH, Tembalang, Semarang 50275, Indonesia

²Department of Chemical Engineering, Faculty of Engineering, Universitas Diponegoro, Jl. Prof. Soedharto SH, Tembalang, Semarang 50275, Indonesia

* **Corresponding author:**

tel: +62-82135243883

email: ngadiwiyana@live.undip.ac.id

Received: March 17, 2020

Accepted: August 31, 2020

DOI: 10.22146/ijc.55353

Abstract: Synthesis biopolymer of sulfonated copolymer eugenol-diallyl phthalate (PEGDAF), its characterization, and study of proton exchange polymer membrane properties had been done. This synthesis was conducted by eugenol and diallyl phthalate reaction to form PEGDAF, which is sulfonated using sulfuric acid. In addition, the functional groups of the PEGDAF and its sulfonated form were analyzed using FT-IR. Furthermore, the polymer properties were determined by measuring values of sulfonation degree, cation exchange capacity, proton conductivity, and water uptake. FT-IR spectra showed that the vinyl group had been added to the process of PEGDAF formation, while spectra deconvolution was used to confirm the occurrence of sulfonation reaction. The sulfonation of PEGDAF in 2 h optimum reaction time produces a black solid with a melting point of 133 °C in 16.55% yield. The highest proton conductivity, cation exchange capacity (CEC), and water uptake were $8.334 \times 10^{-6} \text{ S cm}^{-1}$, 0.44 meq/g, and 73.0%, respectively.

Keywords: eugenol; diallyl phthalate; membrane; proton exchange; polymer

■ INTRODUCTION

In recent years, the development of polymer materials from renewable bioresources has become an interesting study due to the decrease in fossil oil resources and increased environmental problems such as CO₂ emission and the greenhouse effect [1]. A study conducted in the United States of America predicts 90% of organic chemical products from renewable natural resources in 2090 [2]. Therefore, it is important to determine and propose renewable natural resources as an alternative to fossil oil, especially for polymer industries [1].

One of the renewable natural resources used for polymer synthesis is eugenol, which acts as the major constituent of clove oil (*Eugenia caryophyllata*), with 70–90% contents [3]. Eugenol has several functional groups of allyl, methoxy, and hydroxy, so it can be transformed into other useful compounds [4]. Moreover, the presence of an allyl group ($-\text{CH}_2\text{CH}=\text{CH}_2$) enables the occurrence of polymerization through an addition reaction. Several

studies have been carried out on the synthesis of polymers from eugenol and the products were used as antibacterial and antioxidant agents, as well as biorenewable thermosetting materials [4-5].

Eugenol based polymers have structures that are similar to polystyrene with the aromatic rings in the phenolic ($-\text{OH}$) groups used to release protons, therefore they have the potential to be used as polymer membrane fuel cells. This is in line with the advanced research on non-fluorinated polymers for fuel cell membranes such as sulfonated polystyrenes (PS), polyimides, poly(arylene ether ketone) [6], high-impact polystyrene (HIPS), HIPS doped with poly(styrene-ethylene-butylene) (SEBS) [7], and styrofoam waste [8].

The eugenol polymer structure could be modified to improve its ability as a polymer membrane fuel cell. Cross-linked on Eugenol polymer could limit the swelling degree values [9] and diallyl phthalate could be used as a linker [10]. In this case, two allyl groups on diallyl phthalate will bind to the allyl group from eugenol

to form a crosslinked polymer. This copolymerization process could be performed via cationic polymerization using a Lewis acid catalyst, $\text{BF}_3\text{O}(\text{C}_2\text{H}_5)_2$ [11].

Eugenol-diallyl phthalate copolymer (PEGDAF) is expected to have a low swelling degree, making it possible to be a stable polymer for the polymer electrolyte membrane [12]. Therefore, the modification of PEGDAF could be conducted with the addition of sulfonate groups using sulfuric acid as a sulfonation agent [13]. Sulfonate group is defined as a superacid functional group which easily transfer protons [14], thus opening up the opportunities for PEGDAF to be used as a basic ingredient for polymer electrolyte membrane (PEM). In addition, the ideal electrolytic polymer membrane needs to have a large proton conductivity and cation-exchange capacity to assure high current density [15-16]. Moreover, water uptake also plays an essential role in proton conduction through the dissociation of sulfonic acid groups and the facilitation of transported protons [17]. Therefore, this research aims to synthesize PEGDAF and sulfonated PEG-DAF, and determine the PEM properties such as the degree of sulfonation, proton conductivity, cation exchange capacity, and water uptake.

■ EXPERIMENTAL SECTION

Materials

The materials used were eugenol, boron trifluoride etherate, methanol, diethyl ether, chloroform, sodium sulfate anhydrous, sodium hydroxide, and sodium chloride obtained from Merck. In addition, the diallyl phthalate and sulfuric acid (98%) were obtained from Sigma Aldrich and Mallinckrodt, respectively.

Instrumentation

The instruments used were a set of reflux apparatus, an oven, FTIR (Perkin Elmer Spotlight 200S/N96766-96681), porcelain cups, Ubbelohde viscometer, and LCR Meter (HOKI 3522-50 LCR HITESTER). The thermal analysis was carried out under a nitrogen atmosphere using Thermogravimetric Analyzer (TG7300) at a temperature range of 50–700 °C with a 5 °C heating rate per minute and platinum as the reference material.

Procedure

Copolymerization of eugenol-diallyl phthalate (PEGDAF)

Eugenol (65 mmol), diallyl phthalate (6.5 mmol), and chloroform (9 mL) were added into a three-neck flask and stirred at room temperature under a nitrogen atmosphere. This was followed by a dropwise addition of boron trifluoride etherate catalyst (1 mL) then the reaction allowed to curdle and the copolymerization stopped by adding 2 mL of methanol. The copolymerization product was dissolved in diethyl ether and washed with distilled water to obtain a neutral pH. The organic phase was added with anhydrous Na_2SO_4 to absorb the remaining distilled water, the solvent was evaporated in a water bath at 50 °C and finally, the residue was stored in a desiccator. The copolymerization product (PEGDAF) was analyzed for its functional groups using the FTIR spectrophotometer [18] and the physical properties were performed by measuring its melting point, solubility, and swelling degree, while the molecular weight was determined using the viscometry method.

Sulfonation of PEGDAF with H_2SO_4

PEGDAF (4 g) was added to 60 mL of chloroform in the beaker and stirred until homogeneous. The PEGDAF solution was then put into a three-neck flask and refluxed at 60 °C with the addition of concentrated sulfuric acid (1.6 mL, 0.03 mol) and stirred. The sulfonation reactions were carried out during time variations of 1.5, 2.0, and 2.5 h. Each solution was added with cold distilled water to form two layers and separated using a separating funnel. The organic layers were washed with distilled water to a neutral pH, evaporated until dry, and kept in a desiccator. The various sulfonated PEGDAF obtained was then analyzed to determine its functional groups using an FTIR spectrophotometer [19].

Determination of the degree of sulfonation (DS) of sulfonated PEGDAF

The degree of sulfonation (DS) was determined using the acid-base titration method. This was carried out by immersing sulfonated PEGDAF (0.1 g) into 10 mL of NaCl 0.1 M solution for 48 h. After separation, the filtrate was obtained and titrated with NaOH (0.02 M)

using PP indicator [20]. The degree of sulfonation is obtained from Eq. (1) [20].

$$DS = \frac{\text{Volume}_{\text{NaOH}} \times \text{Molecular weight}_{\text{monomer}}}{\text{sample weight}} \quad (1)$$

Determination of cation exchange capacity (CEC)

The sulfonated PEGDAF (0.1 g) was immersed in 10 mL of NaCl 0.1 M solution for 48 h. Furthermore, it was filtered to obtain residues and filtrates, which were titrated with 0.02 M of NaOH using phenolphthalein (PP) indicator. The CEC values can be obtained from Eq. (2).

$$CEC = \frac{\text{Volume}_{\text{NaOH}} \times \text{Concentration}_{\text{NaOH}}}{\text{sample weight}} \quad (2)$$

Determination of proton conductivity

The sulfonated PEGDAF was prepared into a pellet with a thickness and diameter of 5 and 10 mm, respectively, using a 300 psi pressurized Enerpac machine. The frequency used in this study was 1–100 kHz with a voltage of 20 mV. Subsequently, the sulfonated PEGDAF was clamped between 2 electrodes connected to the positive and negative poles of the LCR meter to measure its impedance. Proton conductivity can be calculated using Eq. (3).

$$\rho = \frac{R \times A}{i}; \sigma = \frac{1}{\rho} \quad (3)$$

Determination of water uptake

Water uptake was determined by the ratio of dry and wet masses of each polymer sample. The sulfonated PEGDAF was dried in an oven at 60 °C for 3 h and weighed to obtain a dry weight (W_{dry}). Furthermore, the sulfonated PEGDAF was immersed in 2 mL of distilled water for 24 h with the residue separated and drained to obtain the wet weight (W_{wet}). The water uptake value is obtained from Eq. (4) [20].

$$WU (\%) = \frac{W_{\text{wet}} - W_{\text{dry}}}{W_{\text{dry}}} \times 100\% \quad (4)$$

RESULTS AND DISCUSSION

Copolymerization of Eugenol-diallyl Phthalate (PEGDAF)

The copolymerization of eugenol and diallyl phthalate was carried out based on the method conducted by Kiswandono et al. [18] and modified using the cross-linking agent. In this research, diallyl phthalate acts as a

cross-linking agent in the copolymerization of eugenol, which takes place through the cationic addition polymerization reaction. This reaction is conducted in three stages, namely initiation, propagation, and termination. The initiation stage is marked by a change in color from clear to blackish brown and this is followed by the propagation stage that takes place during the stirring process. At the termination stage, copolymerization is quenched by the addition of methanol, with the reaction characterized by the formation of a purple gel. The final product is a brown solid with a melting point of 84 °C, a molecular weight of 6329.913 Dalton, and a yield of 85.96%.

The FTIR spectra of PEGDAF compared to eugenol, which acts as the monomer, is shown in Fig. 1. Eugenol has absorption at a wavenumber of 1637 cm^{-1} , which is responsible for C=C alkene of the allyl group. Meanwhile, the spectrum of PEDGAF does not show this wavenumber, indicating that the copolymer product has been formed with the loss of the vinyl group. In addition, the wavenumber of the PEDGAF spectrum at the peaks of 1724 and 1271 cm^{-1} are responsible for C=O and C-O ester groups of diallyl phthalate structures, respectively. The detail of both spectra's important peaks is shown in Table 1. While comparing the spectra of eugenol and PEGDAF, there is a decrease in all peaks into lower wavenumber. This is probably due to the presence of the DAF in the copolymer which has ester groups to introduce more intramolecular hydrogen bonding through the C=O from the ester and OH groups from the eugenol, thereby leading to a shift in peak value towards the lower wavenumber.

The solubility test was carried out on PEGDAF using various solvents, as shown in Table 2. It shows that the PEGDAF completely dissolves in chloroform and diethyl ether and this result will be used for determining the appropriate solvent for the sulfonation reaction.

PEGDAF has a low swelling degree of 26.6% due to a cross-linked chain structure of PEGDAF capable of reducing the inflow of water into the polymer chain, therefore avoiding expanding. Based on this result, PEGDAF has potential as a base material for electrolyte polymer membranes.

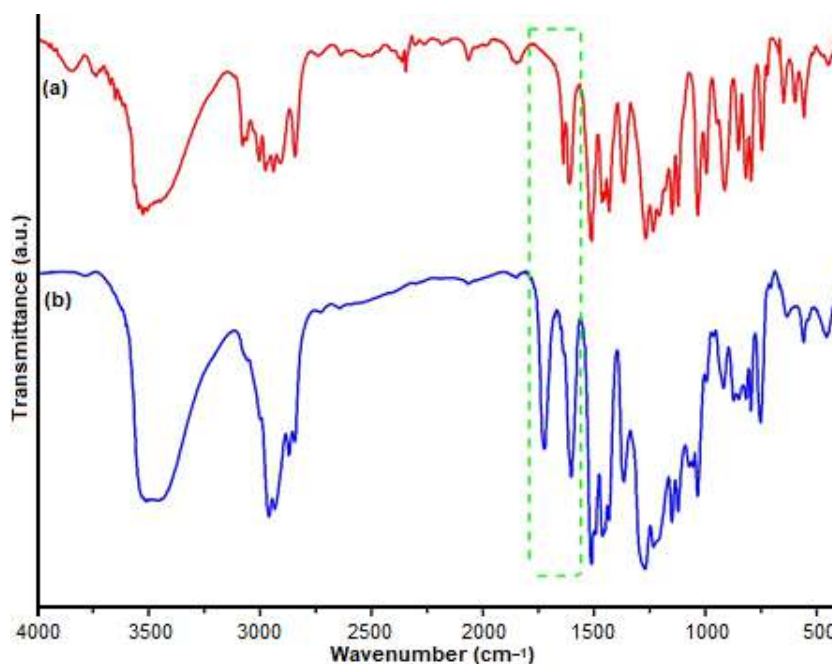


Fig 1. FTIR spectra of (a) eugenol and (b) PEGDAF

Table 1. Functional groups and wavenumbers of eugenol and PEDGAF

Functional groups	Wavenumber (cm ⁻¹)	
	Eugenol	PEGDAF
OH	3525	3513
C-H sp ³ (stretching)	2976	2959
C=C aromatic (stretching)	1610	1602
C-H sp ³ (bending)	1464	1460
C-O ether	1233	1232
C=C alkene	1637	-
C=O ester	-	1724
C-O ester	-	1271

Table 2. Solubility test results of PEGDAF

Solvent	PEGDAF
Distilled water	xxx
Methanol	xxx
Ethanol	+
Chloroform	+++
Diethyl ether	+++
Ethyl acetate	++

Note: x = insoluble, + = soluble

Sulfonation of PEGDAF

Sulfonation of PEGDAF was carried out using concentrated H₂SO₄ as the sulfonation agents (98%) with time variations of 1.5; 2; and 2.5 h [19]. The sulfonated PEGDAF undergoes color changes from brown to black

before and after sulfonation, respectively. In addition, the sulfonation increases the melting point properties of the polymer, i.e., PEGDAF has a melting point of 84 °C, while the sulfonated state increases to 133 °C.

Sulfonation reactions mechanism with sulfuric acid is proposed in Fig. 2. The sulfur trioxide obtained from the dissociation of concentrated sulfuric acid acts as an electrophile that attracts the ring of electrons, followed by a transfer of hydrogen from the ring to the negative oxygen to obtain a sulfonated product.

It was known that both eugenol and diallyl phthalate have benzene rings as sulfonation sites. However, the benzene ring in eugenol is more activated due to the presence of electron-donating groups, such as hydroxyl, methoxy, and alkyl. Whereas diallyl phthalate has two electron-withdrawing groups, which are esters, therefore, they deactivate the benzene ring to undergo an electrophilic substitution reaction.

Analysis of sulfonated PEGDAF was carried out using an FTIR spectrophotometer to prove the occurrence of sulfonation reaction. The result of the FTIR analysis of sulfonated PEGDAF was shown in Fig. 3 and the complete absorption data before and after sulfonation was shown in Table 3. Sulfonated PEGDAF spectra show the presence of sulfonic acid group (-SO₃H), which has

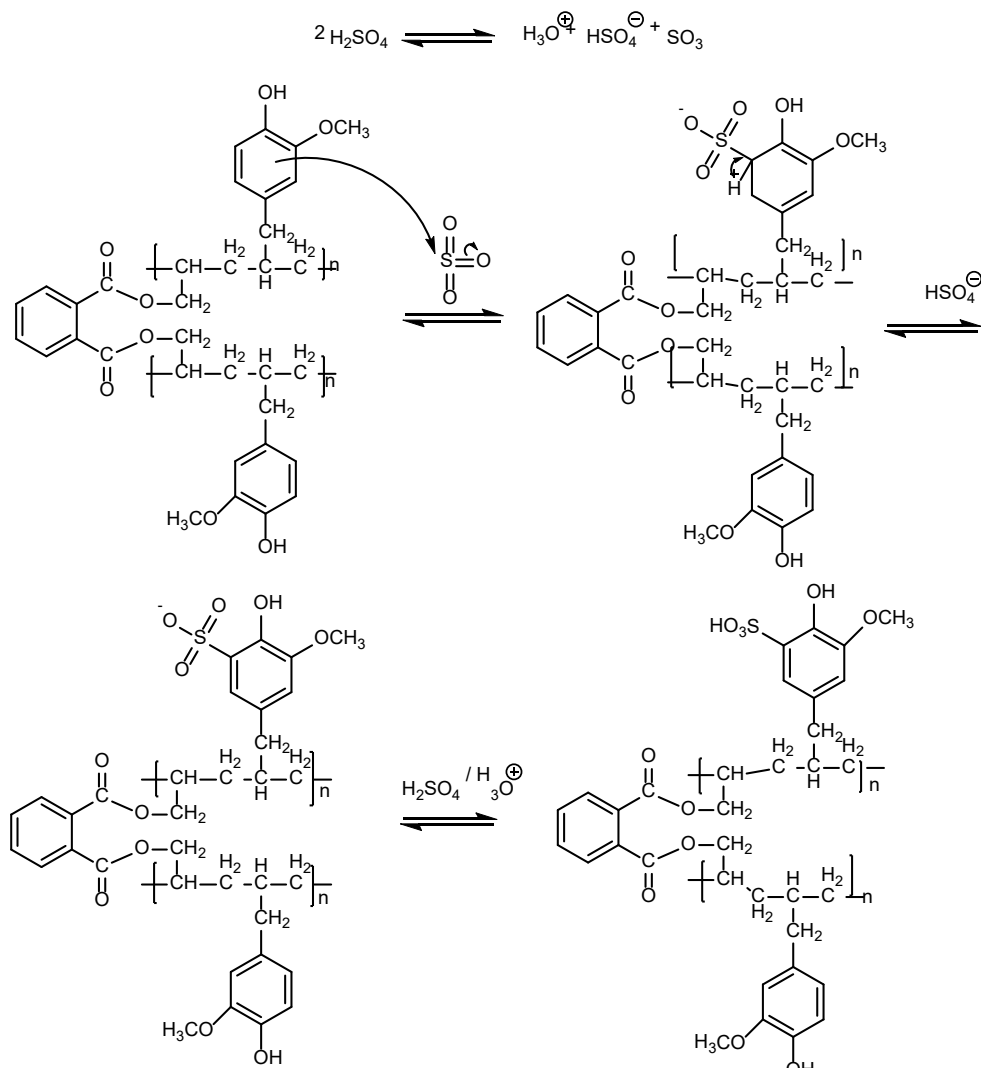


Fig 2. Mechanisms of the copolymer sulfonation reaction (PEGDAF)

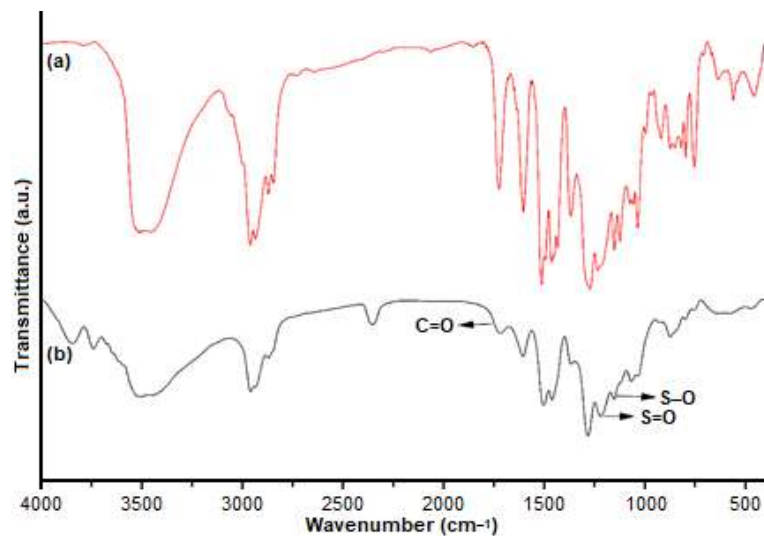


Fig 3. FTIR spectra of (a) PEGDAF, (b) sulfonated PEGDAF

Table 3. Functional groups of PEGDAF and sulfonated PEGDAF

Functional groups	PEGDAF (cm ⁻¹)	Sulfonated PEGDAF (cm ⁻¹)
O-H	3513	3503
C-H sp ³	2960	2958
C=C aromatic	1603	1605
C-O ether	1233	1219
C-H aromatic (bending)	1460	1459
C=O ester	1725	1717
S=O	-	1219
S-O	-	1065
C-S	-	578

three absorption peaks, i.e., 1219 cm⁻¹ (S=O), 1065 cm⁻¹ (S-O), and 578 cm⁻¹ (C-S). Thus, it proves that the sulfonated product has been yielded.

The success of the sulfonation reaction is determined by calculating the % transmittance ratio of C-O ether before and after sulfonation with absorption of C=C benzene used as an internal standard. The C=C benzene group was chosen as a comparison because its amounts before and after sulfonation remained the same. The % transmittance ratio of C-O ether before and after sulfonation is 0.97 and 0.88, respectively. This difference shows that the concentration of the group in the spectra increased after sulfonation. This is in accordance with Lambert beer law, which stated that concentration is inversely proportional to transmittance. An increase in concentration after sulfonation is due to the contribution of the S=O of the sulfonate bound to PEGDAF.

The FTIR peaks obtained for C-O groups after sulfonation and S=O are not clearly seen due to overlapping. Therefore, to confirm the occurrence of sulfonation, FTIR spectra deconvolution was carried out in the wavenumber area of 1180–1240 cm⁻¹ as shown in Fig. 4. Furthermore, the deconvolution results show that when the absorption is at 1198 cm⁻¹ (blue line), it belongs to S=O while at 1221 cm⁻¹ (red line) it is C-O ether of the PEGDAF. Based on the results, it was concluded that sulfonation was successfully conducted.

Determination of Sulfonation Degrees (DS)

The degree of sulfonation was determined using the acid-base titration method [20]. The sulfonation results with time variations, which shows an increase in the degree

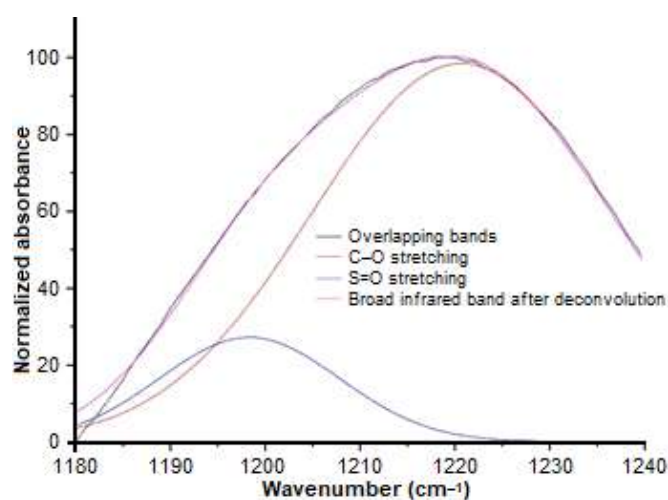


Fig 4. FTIR spectra deconvolution of sulfonated PEGDAF at absorption range of 1180–1240 cm⁻¹

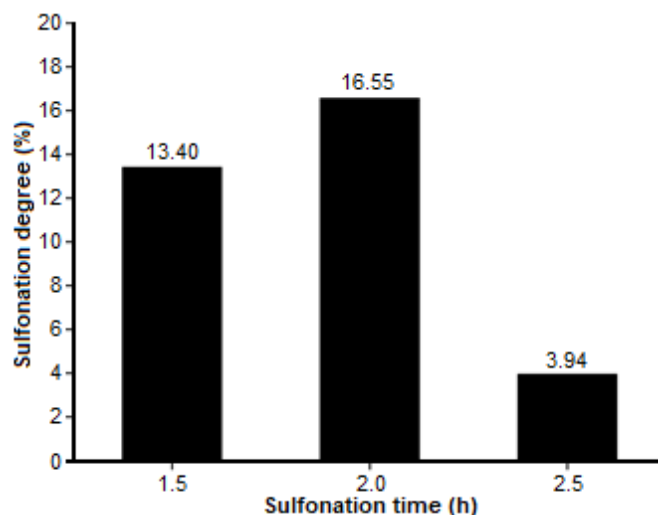


Fig 5. Sulfonation degree of sulfonated PEGDAF

of sulfonation value within 2 h is illustrated in Fig. 5. However, an additional 30 min of sulfonation results in

a decrease in the degree of sulfonation. This is probably due to the reversibility of the sulfonation process, in which the reaction runs until an optimized number of sulfonate groups is attached. The additional time makes de-attachment of the sulfonate group to obtain a lower sulfonation degree. In general, this reaction shows a typical trend of the sulfonation reaction where the rate at the initial stage goes fast and tends to slow down due to the influence of the steric hindrance, which increases because it is in the form of a polymer.

Another factor likely to affect the low sulfonation degree is the presence of water and acid in the sulfonation reaction, and this is capable of causing side reactions in PEGDAF in an ester group, which is easily hydrolyzed in the presence of sulfuric acid, as shown in Fig. 6. The longer

the reaction time, the greater the chance of breaking the ester group's polymer chain, making the shorter polymer chain more soluble in water. Therefore, the sulfonation product obtained remains with a small degree of sulfonation, supported by the smaller reaction yield. The sulfonation interval time of 1.5, 2.0, and 2.5 h yielded 96, 92, and 71%, respectively. It can be concluded that the optimum time for sulfonation of PEGDAF is 2 h.

Determination of Thermal Properties

The thermal properties of PEGDAF and sulfonated PEGDAF were investigated by TGA and DTG techniques. Fig. 7 shows that the TGA and DTG curves obtained thermally stable copolymers, while the polymers exhibited two steps of degradation patterns

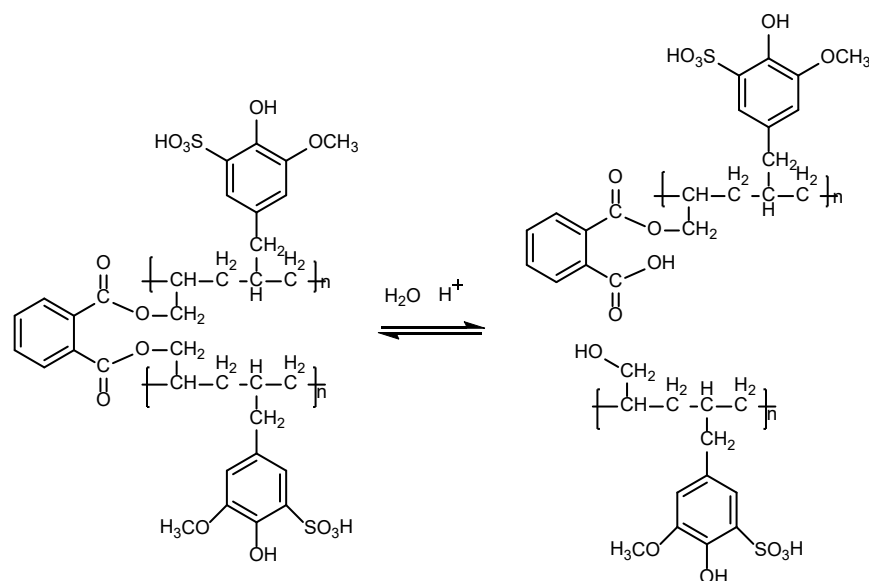


Fig 6. Hydrolysis of PEGDAF in the presence of water and acid

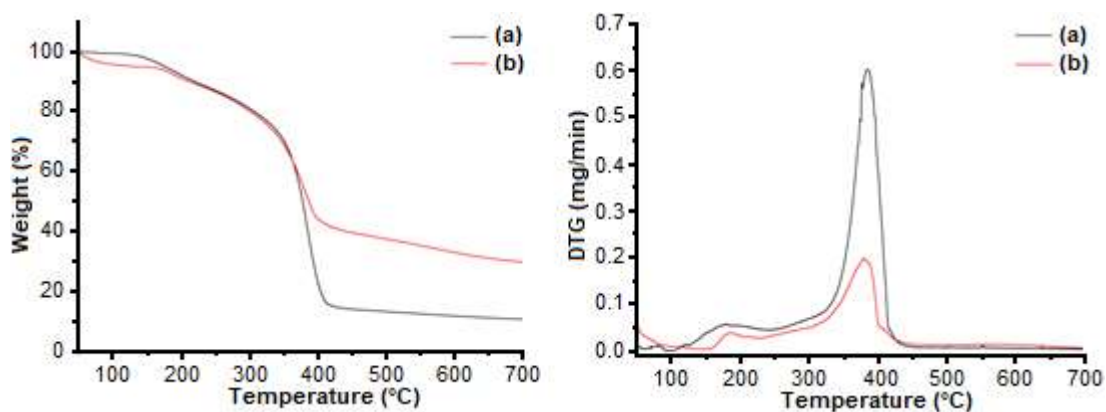


Fig 7. TGA (left) and DTG (right) graphs of (a) PEGDAF and (b) sulfonated PEGDAF

under a nitrogen atmosphere. The initial degradation step was observed at room temperature of 200 °C, which is attributed to the loss of water molecules absorbed. Subsequently, the loss of water molecule from sulfonated PEGDAF is higher due to more water is absorbed by the SO₃H groups. The second main weight loss step that started above 350 °C was assigned to the polymer chain decomposition. The 10% weight loss temperatures of PEGDAF and sulfonated PEGDAF were 218 and 211 °C, respectively. In addition, the thermal stability of the polymer is slightly decreased with the sulfonation due to the degradation of sulfonic acid groups.

Determination of Cation Exchange Capacity (CEC)

The cation exchange capacity is an important parameter of the electrolyte polymer membrane in a fuel cell. This means that the material used as an electrolyte polymer membrane in a fuel cell needs to have an excellent ability to exchange cations [14]. This analysis aims to determine the ability of polymers to exchange cations that are bound to their functional groups with those given in the system. In this case, the cation bound to the functional group is the H⁺ ion, while the cation in the system is the Na⁺ ion. The graph representing the effect of sulfonation time on the value of cation exchange capacity is shown in Fig. 8.

Fig. 8 shows that the cation exchange capacity value is directly proportional to the degree of sulfonation, which

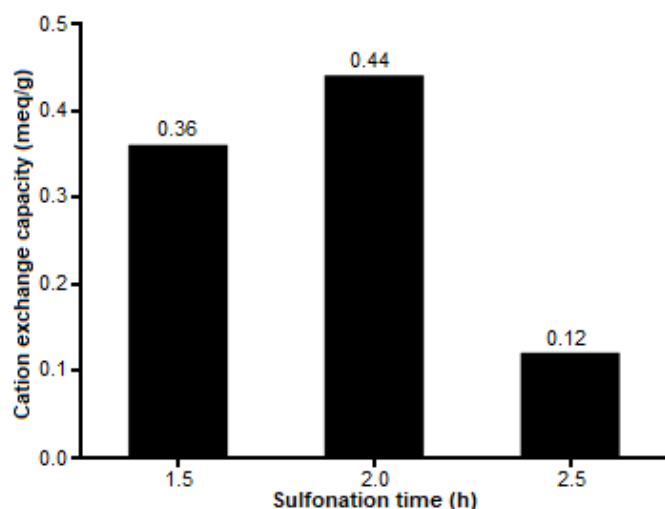


Fig 8. Relationship of sulfonation time to CEC of sulfonated PEGDAF

provides advantages due to its strong acid property. Therefore, it increases the value of CEC with a rise in sulfonation time. Furthermore, the longer the sulfonation time, the more sulfonate (–SO₃H) the groups substituted in the benzene ring, thereby leading to significant and more H⁺ ions that can be exchanged. The easier a polymer to release H⁺ ions, the greater the tendency to increase its cation exchange capacity. In its application as an electrolyte polymer membrane in a fuel cell, the polymer needs to have a large cation exchange capacity. This is because an increase in the value of cation exchange capacity leads to a rise in the ionic capacity, therefore increasing the polymer's ability to conduct electricity.

The cation exchange capacity analysis graph shows that the largest CEC value is the sulfonate PEGDAF with 2 h sulfonation time, i.e., 0.44 meq/g. The CEC value decreased after 2 h because the sulfonate group was detached from the benzene ring and the optimum time for copolymer sulfonation (EG-DAF) is 2 h.

Determination of Proton Conductivity

Proton conductivity is a polymer's ability to deliver protons and become an essential parameter of an electrolyte membrane. The determination of the proton conductivity value of sulfonated PEGDAF is presented in Fig. 9. The result showed that proton conductivity increased with a rise in the degrees of sulfonation. For proton exchange membranes, the number of sulfonate groups (–SO₃H) found in sulfonated copolymers had a significant effect on the proton conductivity value. Substituted sulfonate groups increase hydrophilicity and then it can absorb more water molecules through hydrogen bonds. The water molecule will facilitate proton exchange; therefore, sulfonation has the ability to increase the proton conductivity of the polymer. Before sulfonation (PEGDAF), the polymer has a very small proton conductivity value, which is $0.031 \times 10^{-6} \Omega^{-1}\text{cm}^{-1}$. After sulfonation, the proton conductivity value was increased and the 2 h sulfonated PEGDAF owns the highest conductivity value of $8.343 \times 10^{-6} \Omega^{-1}\text{cm}^{-1}$. Based on the proton conductivity value, the sulfonated PEGDAF is categorized as a semiconductor material because its conductivity value is in the range of 10^{-8} – $10^3 \Omega^{-1}\text{cm}^{-1}$.

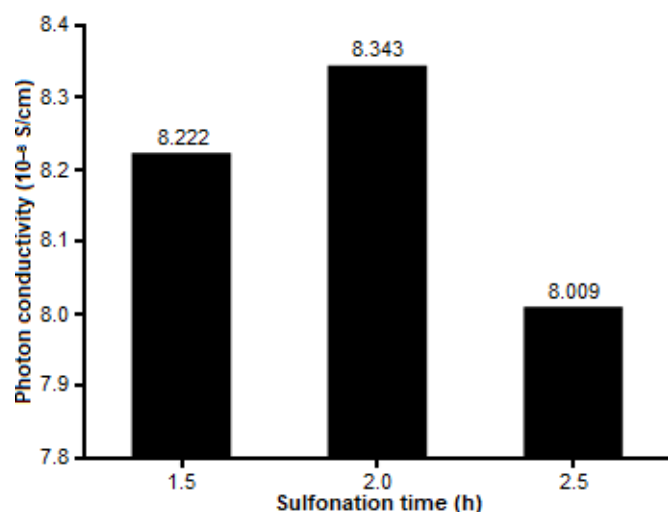


Fig 9. Proton conductivity value of PEGDAF sulfonate

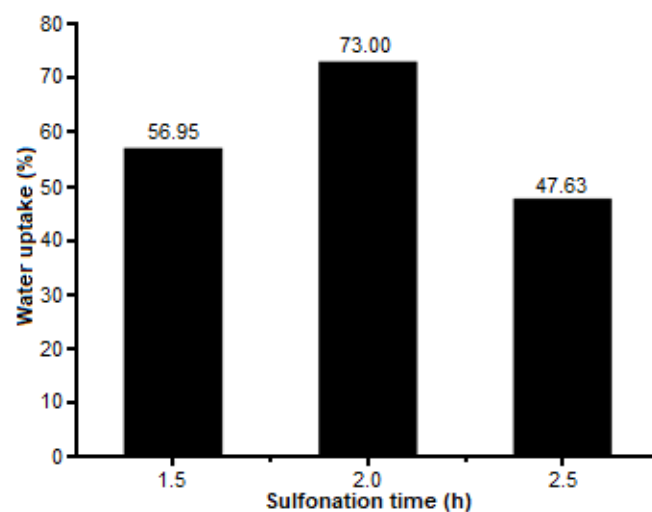


Fig 10. Water uptake value of PEGDAF sulfonated

Table 4. Comparison of the polymer properties with previous work by Muller et al. [7]

Sample	Sulfonation degree (%)	CEC (meq/g)	Proton conductivity ($S \cdot cm^{-1}$)	Water uptake (%)
This work	16.55	0.44	8.343×10^{-6}	73.0
Muller et al. [7]	9–13	0.3–1.24	4.2×10^{-10} – 1.5×10^{-7}	8–36

Determination of Water Uptake

The ability of a polymer to absorb water is an important parameter in its application as an electrolyte membrane; this is because the water absorbed by the polymer facilitates proton transfer. The result of water uptake determination on sulfonated PEGDAF is shown in Fig. 10. The sulfonated PEGDAF in 2 h reaction time gives the highest value of water uptake (73%), and this value decreased for the 2.5 h of sulfonated PEGDAF. A high degree of sulfonation shows that the higher the number of $-SO_3H$ groups in the copolymer, the higher the copolymer ability to absorb water. Nonetheless, very high water absorption induces membrane swelling, thereby reducing mechanical stability in the membrane (brittle).

Table 4 summarizes this work with the research carried out by Muller et al. [7] on polymer properties. The sulfonation degree has a higher value and impact on the CEC and water uptake values. Consequently, it tends to improve the proton conductivity value with the eugenol based biopolymer used as a renewable source. This result shows that sulfonated PEGDAF is promising as a proton exchange membrane compared to the sulfonated and SEBS polymers reported by Muller.

CONCLUSION

The copolymerization of eugenol-diallyl phthalate produces a solid brown copolymer with a melting point, molecular weight, and yield of 84 °C, 6,329 Daltons, and 85.96%. In addition, the sulfonation of PEGDAF produces a black solid with a melting point of 133 °C and the greatest degree of sulfonation is 16.55%, at an optimum reaction time of 2 h. The highest proton conductivity, cation exchange capacity (CEC), and water uptake during 2 h of sulfonation were $8.343 \times 10^{-6} S \cdot cm^{-1}$, 0.44 meq/g, and 73.0%, respectively.

ACKNOWLEDGMENTS

The authors are grateful to the Directorate of Research and Community Service of the Ministry of Research and Technology and Higher Education of Indonesia for funding the 2019 PDUPT research grant with contract number 257-58/UN7.P4.3/PP/2019.

REFERENCES

- [1] Modjinou, T., Versace, D.L., Abbad-Andallousi, S., Bousserrhine, N., Dubot, P., Langlois, V., and Renard, E., 2016, Antibacterial and antioxidant

- bio-based networks derived from eugenol using photo-activated thiol-ene reaction, *React. Funct. Polym.*, 101, 47–53.
- [2] Eissen, M., Metzger, J.O., Schmidt, E., and Schneidewind, U., 2002, 10 Years after Rio—Concepts on the contribution of chemistry to a sustainable development, *Angew. Chem. Int. Ed.*, 41 (3), 414–436.
- [3] Khalil, A.A., Ur Rahman, U., Khan, R.M., Sahar, A., Mehmood, T., and Khan, M., 2017, Essential oil eugenol: Sources, extraction techniques and nutraceutical perspectives, *RSC Adv.*, 7, 32669–32681.
- [4] Neda, M., Okinaga, K., and Shibata, M., 2014, High-performance bio-based thermosetting resins based on bismaleimide and allyl-etherified eugenol derivatives, *Mater. Chem. Phys.*, 148 (1-2), 319–327.
- [5] Li, Q., Ma, Z., Yue, Q., Gao, B., Li, W., and Xu, X., 2012, Synthesis, characterization and swelling behavior of superabsorbent wheat straw graft copolymers, *Bioresour. Technol.*, 118, 204–209.
- [6] Munavalli, B.B., and Kariduraganavar, Y.M., 2018, Enhancement of fuel cell performance of sulfonated poly(arylene ether ketone) membrane using different crosslinkers, *J. Membr. Sci.*, 566, 383–395.
- [7] Müller, F., Ferreira, C.A., Franco, L., Puiggali, J., Alemán, C., and Armelin, E., 2012, New sulfonated polystyrene and styrene–ethylene/butylene–styrene block copolymers for applications in electro dialysis, *J. Phys. Chem. B*, 116 (38), 11767–11779.
- [8] Ngadiwiyana, Ismiyarto, Gunawan, Purbowatiningrum, R.S., Prasetya, N.B.A., Kusworo, T.D., and Susanto, H., 2018, Sulfonated polystyrene and its characterization as a material of electrolyte polymer, *J. Phys. Conf. Ser.*, 1025, 012133.
- [9] Liu, S., Wang, L., Ding, Y., Liu, B., Han, X., and Song, Y., 2014, Novel sulfonated poly(ether ether ketone)/polyetherimide acid-base blend membranes for vanadium redox flow battery applications, *Electrochim. Acta*, 130, 90–96.
- [10] Zhu, Y., Liang, C., Bo, Y., and Xu, S., 2015, Compatibilization of polypropylene/recycled polyethylene terephthalate blends with maleic anhydride grafted polypropylene in the presence of diallyl phthalate, *J. Polym. Res.*, 22 (3), 35.
- [11] Prasetya, N.B.A., Ngadiwiyana, Ismiyarto, and Purbowatiningrum, R.S., 2019, Synthesis of copolymer eugenol crosslinked with divinyl benzene and preliminary study on its antibacterial activity, *IOP Conf. Ser.: Mater. Sci. Eng.*, 509, 012102.
- [12] An, D., Wu, B., Zhang, G., Zhang, W., and Wang, Y., 2016, Gradiently crosslinked polymer electrolyte membranes in fuel cells, *J. Power Sources*, 301, 204–209.
- [13] Zhai, S., Dai, W., Lin, J., He, S., Zhang, B., and Chen, L., 2019, Enhanced proton conductivity in sulfonated poly(ether ether ketone) membranes by incorporating sodium dodecyl benzene sulfonate, *Polymers*, 11 (2), 203.
- [14] Wang, Q., Lu, Y., and Li, N., 2016, Preparation, characterization and performance of sulfonated poly(styrene-ethylene/butylene-styrene) block copolymer membranes for water desalination by pervaporation, *Desalination*, 390, 33–46.
- [15] Guimet, A., Chikh, L., Morin, A., and Fichet, O., 2016, Strengthening of perfluorosulfonic acid ionomer with sulfonated hydrocarbon polyelectrolyte for application in medium-temperature fuel cell, *J. Membr. Sci.*, 514, 358–365.
- [16] Larminie, J., and Dicks, A., 2013, *Fuel Cell Systems Explained*, 2nd Ed., John Wiley & Son, Chichester, England.
- [17] Fang, J.H., 2018, “Polyimide proton exchange membranes” in *Advanced Polyimide Materials, Synthesis, Characterization and Applications*, Eds. Yang, S.Y., Elsevier Science, Amsterdam, 323–383.
- [18] Kiswandono, A.A., Hadi, S., Mudasir, Sinjia, F., Sari, M.Y., and Irfan, M., 2019, Copoly eugenol crosslinked diallylphthalate 8% as a carrier in phenol and Pb(II) metal transport, *J. Phys. Conf. Ser.*, 1338, 012004.
- [19] Parnian, M.J., Rowshanzamir, S., and Gashoul, F., 2017, Comprehensive investigation of physicochemical and electrochemical properties of sulfonated poly(ether ether ketone) membranes with different degrees of sulfonation for proton

- exchange membrane fuel cell applications, *Energy*, 125, 614–628.
- [20] Tang, Y., Xue, Z., Zhou, X., Xie, X., and Tang, C., 2014, Novel sulfonated polysulfone ion exchange membranes for ionic polymer-metal composite actuators, *Sens. Actuators, B*, 202, 1164–1174.

Supplementary Data

This supplementary data is a part of paper entitled “*Nicotiana tabacum* Mediated Green Synthesis of Silver Nanoparticles and Ag-Ni Nanohybrid: Optical and Antimicrobial Efficiency”.

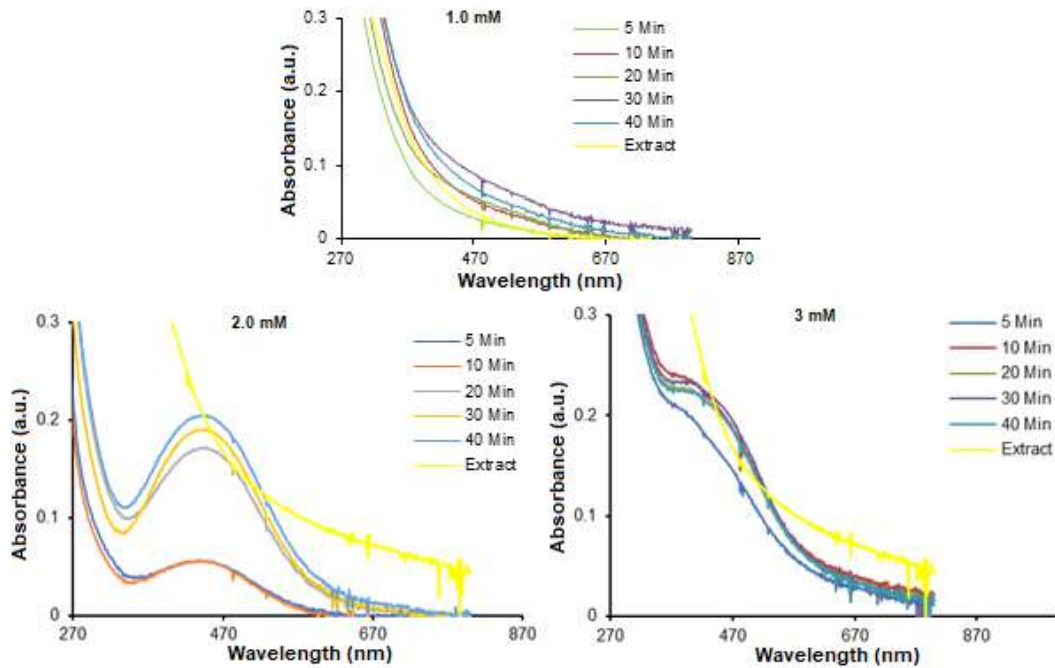


Fig S1. SPR of Ag NPs prepared from 1.0–3.0 mM precursor concentrations

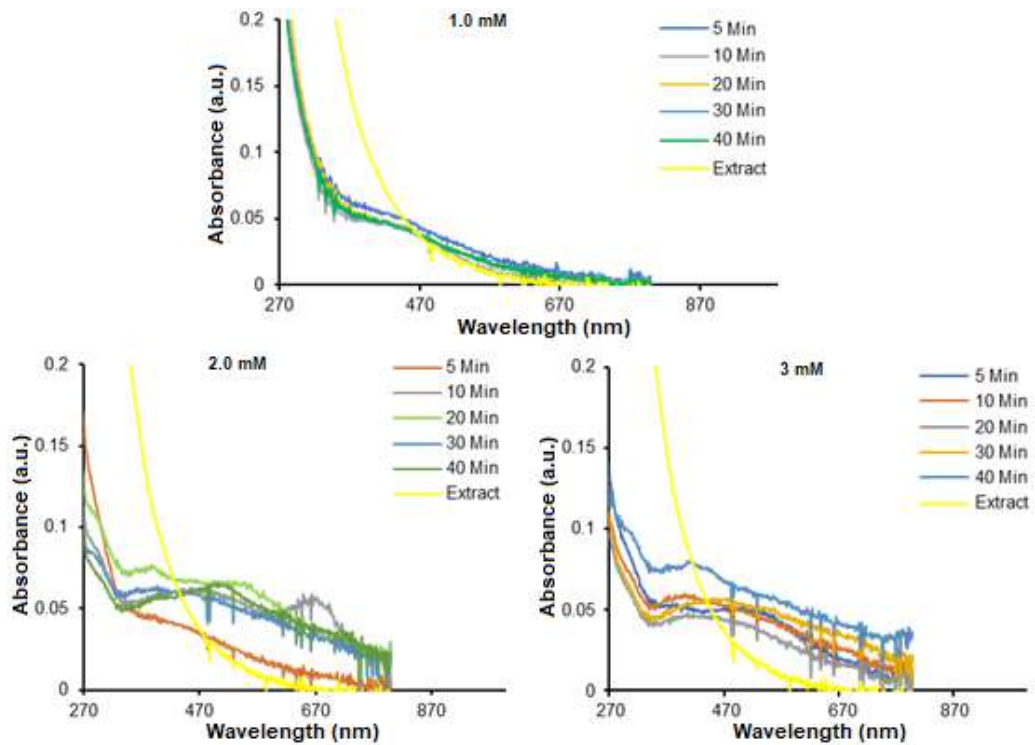


Fig S2. Absorption spectra of Ag-Ni NPs prepared from 1.0, 2.0 and 3.0 mM precursor concentrations at 80 °C

Table S3. The EDX Ag NPs prepared from the extract of *N. tabacum* leaves

Element	series	[wt.%]	[norm. wt.%]	[norm. at.%]	Error in %
Silver	L-series	71.22	89.11	85.52	0.77
Oxygen	K-series	5.28	3.99	9.87	1.11
Carbon	K-series	6.66	4.78	3.38	0.36
Nickel	K-series	0.83	0.99	0.62	0.09
Cobalt	K-series	0.03	1.11	0.60	0.09
Phosphorus	K-series	0.01	0.02	0.01	0.00
Sulphur	K-series	0.00	0.00	0.00	0.00
	Sum:	84.03	100.00	100.00	

Table S4. EDX of Ag-Ni bimetallic nanoparticles prepared with the extract of *N. tabacum* leaves

Element	series	[wt.%]	[norm. wt.%]	[norm. at.%]	Error in %
Silver	L-series	39.75	63.76	69.70	0.77
Oxygen	K-series	7.77	18.51	5.95	5.77
Carbon	K-series	13.03	14.85	13.70	0.21
Nickel	K-series	10.70	11.13	10.43	0.06
Cobalt	K-series	0.79	1.26	0.48	0.06
Phosphorus	K-series	0.27	0.44	0.32	0.04
Sulphur	K-series	0.03	0.06	0.04	0.00
	Sum:	62.35	100.00	100.00	

Nicotiana tabacum Mediated Green Synthesis of Silver Nanoparticles and Ag-Ni Nanohybrid: Optical and Antimicrobial Efficiency

Anuoluwa Abimbola Akinsiku^{1*}, Joseph Adeyemi Adekoya¹, and Enock Olugbenga Dare^{2,**}

¹Department of Chemistry, College of Science and Technology, Covenant University, Canaanland, Km 10 Idiroko Road, P.M.B. 1023, Ota, Ogun State, Nigeria

²Department of Chemistry, Federal University of Agriculture Abeokuta, Alabata Road, P.M.B. 2240, Abeokuta, Ogun State, Nigeria

*** Corresponding author:**

email:

anu.akinsiku@covenantuniversity.edu.ng*;
dare3160@hotmail.com**

Received: May 13, 2020

Accepted: June 18, 2020

DOI: 10.22146/ijc.56072

Abstract: A sustainable method was considered for the preparation of nanosilver and its allied nanoparticles. *Nicotiana tabacum*, an abused plant, has found an application as a bio-chemical instead of lethal chemical in the synthesis of nanoparticles. As part of green chemistry implementation, double distilled water was the solvent used for extraction. The phytochemicals present were analyzed using standard procedures. Nanoparticle synthesis was carried out at varying precursor concentrations, and the reaction was monitored with a UV-visible spectrophotometer. Another optical characterization was also achieved with photoluminescence. Other characterization involved: X-ray diffraction (XRD), transmission electron microscopy (TEM), energy dispersive X-ray (EDS), and Fourier transform infrared spectroscopy techniques (FTIR). A matched phase identification of nanosilver resembled a face-centered cubic of Ag with a mean size of 11.68 nm, and a lattice constant of 4.0862 Å. The Ag NPs displayed activity against clinical isolates of fungi, Gram-positive, and Gram-negative bacteria as the growth inhibition was significant at $P < 0.05$. Ag NPs obtained from the *Nicotiana tabacum* proved to be an antibacterial and antifungal candidate, unlike the Ag NPs derived using chemical and physical methods, which were harmful for this purpose. Both the Ag NPs and Ag-Ni NPs displayed optical activity, which qualifies them for application in visual materials.

Keywords: green synthesis; optical properties; antimicrobial; *Nicotiana tabacum*

■ INTRODUCTION

Great use of nanoparticles (NPs) and nanomaterials (NMs) in the last decade is on the rise across the fields of science and technology. Materials with sizes of less than 100 nm have been proven to possess enhanced structural features that equip them with excellent properties such as enhanced optical, surface activity, magnetic and electrical properties. These materials are further developed for applications in cancer diagnosis (medicine), pharmaceuticals, battery electrodes, communication technology (use of carbon nanotubes), textile, food industries, etc. [1]. It is of note that physical and chemical methods of producing nanoparticles and nanomaterials involve the use of toxic chemicals, and these protocols pose a threat to the environment and human health.

Moreover, the procedures are costly, while the products are hardly appropriated for medicine [2-3]. Hence, the application of green chemistry in nanotechnology is considered an alternative to overcome earlier mentioned problems.

Microorganisms, plants, and plant extracts are often utilized in place of chemicals for the biosynthesis of nanoparticles and nanomaterials. Furthermore, plant-mediated synthesis is of many advantages, like sustainability and renewability of plant materials, which are the sources of secondary metabolites – the reducer. The protocol is also nature-friendly, cost-effective, rapid, etc. Metal ion reduction is possible by plant extracts due to the presence of chemicals and bioactive compounds (phytochemicals) naturally present in them,

most notably the medicinal plants. *N. tabacum* has been identified to contain phenolic compounds, terpenoids, essential oils, and alkaloids, which includes an *N*-methyl group [4]. These active functional groups in *N. tabacum* qualifies it as a metal ion reducer for the formation of nanoparticles.

Nicotiana tabacum (Tobacco) is an annual herb, and it belongs to the Solanaceae family. It is known as 'ewe taba' by the Yoruba tribe in Nigeria, and it can grow to a maximum height of 3 meters. *N. tabacum* possesses green leaves that are commercially processed into tobacco [5]. The plant is ornamental and also secretes nicotine. Its ethnobotanical use includes treatment of ringworm, cold, ulcers, nausea, anthelmintic, hemorrhoids (pile), dysmenorrhea, hair fertilizer, etc. [6-7]. The large amount of toxins in tobacco makes it useful in the manufacture of insecticides. It also finds an application in medicine. Unfortunately, it is abused for chronic smoking, and this addictive effect is dangerous to health [8].

Many studies have reported silver-based nanoparticles using green synthesis. Recent publications exploited the use of bio-reducing agents like ulvan from green algae [9], *Withania coagulans* [10], *Annona reticulata* leaves [11], *Origanum vulgare* plant [12], *Canna indica* plant [13], etc. for various applications. Synthesis of Ag-Ni nanoparticles involving physical and chemical methods like flame synthesis [14], chemical-wet approach [15], solvothermal [16], etc., were also documented. However, to the best of our knowledge, not much work regarding the plant-mediated green synthesis of Ag NPs and Ag-Ni NPs using tobacco as a renewable reducing agent has been published. Furthermore, since the mechanism of the reaction of nanoparticles as an antimicrobial agent does not require penetrating the cell walls of bacteria, the problem of drug resistance in bacteria due to large applications could be tackled via this synthetic route. In addition, silver-based nanoparticles have been proven to be able to overcome biofilm formation, one of the antibiotics resistance mechanisms [17]. This study focused on the exploitation of *N. tabacum* for silver and its hybrid nanoparticles with potential optical and antimicrobial applications. The antimicrobial properties

of the synthesized nanoparticles were tested on Gram-negative bacteria, Gram-positive bacteria, and fungi.

■ EXPERIMENTAL SECTION

Materials

The *N. tabacum* used in this study was obtained from the university campus. The plant was bio-authenticated, and a voucher FHI. No.109929 was deposited at the herbarium. Analytical grade of all inorganic salts and reagents, which include AgNO₃, and Ni(NO₃)₂·6H₂O (Sigma-Aldrich, UK), were used. Double distilled water was used throughout the preparations, and for the rinsing of leaves for the removal of sand.

Instrumentation

Sample characterization

For the optical study, the absorption spectra were obtained from a double beam (Thermos Scientific Genesys 10S) spectrophotometer. Perkin-Elmer 55 luminescence spectrophotometer was used for the photoluminescence of the particles. Double distilled water was used as blank, and samples were prepared by diluting each aliquot to one fifth, then placed in the quartz cuvette at 25 °C. The absorption was measured at 200–800 nm. For the morphological characterization of the biosynthesized nanoparticles, the transmission electron microscopy technique was engaged. Measurements were achieved with a Technai G2 microscope attached with an energy dispersive x-ray spectrometer, ran at a current of 20 μA and accelerated voltage of 200 keV. A drip of each nanoparticle solution was positioned on copper TEM grids covered with carbon. The solution was allowed to dry by evaporation, after which snapshots were taken. For structural analysis and purity of the as-prepared nanoparticles, XRD (Bruker AXS D8 model) equipped with nickel Cu Kα radiation source at room temperature from 20° to 80° at 40 kV, 40 mA, $k = 1.5418 \text{ \AA}$ and scanning rate of 0.050 min⁻¹ was used. The moieties present in the nanoparticles were determined with FTIR (Perkin Elmer 100). Centrifugation was carried out with Thermo Fisher scientific centrifuge (Thermo Electron LED).

Procedure

Extraction was achieved by modifying the method described in our previous works [12,18]. The leaves were cut, ground with a clean blender, and then subjected to extraction at the weight (20 g) to volume (200 mL) ratio. The slurry formed was separated with Whatman filter paper (no. 1) at ambient temperature. The filtrate was reserved in the refrigerator for analysis and use. A qualitative study to determine secondary metabolites in the aqueous extract of *N. tabacum* was carried out using a standard method [19].

Preparation of silver and silver-nickel nanoparticles by *N. tabacum*

For the synthesis of silver nanoparticles (Ag NPs), an aqueous solution of *N. tabacum* leaf extract (40 mL) was introduced into 0.5 mM aqueous solution of AgNO_3 (400 mL) in a beaker, heated up to 80 °C on a magnetic stirrer for 40 min. This procedure was used again for different ratios of metal ion concentrations (1.0, 2.0, and 3.0 mM) and extract at a 1:10 v/v ratio. The reaction mixture was monitored for color change (notification of nanoparticle formation), confirmed by UV-visible spectroscopy measurement of the samples taken at various time intervals. To separate and purify the as-prepared nanoparticles, centrifugation was performed at 5000 revolutions/min for 45 min. The samples were later thoroughly washed in double distilled water, evaporated, then collected for characterization and antimicrobial study. In the case of nanohybrid synthesis, an aqueous extract of *N. tabacum* was poured to the mixture of equal molar concentrations of AgNO_3 and $\text{Ni}(\text{NO}_3)_2 \cdot 6\text{H}_2\text{O}$ in 1:10 v/v ratio. Then, the procedure mentioned above was repeated using 1.0 and 2.0 mM precursor mixture solutions.

Antimicrobial assay

Fresh isolates of fungi *Trichophyton rubrum* and *Candida albicans*, Gram-positive *Streptococcus pyogenes* and *Staphylococcus aureus* and Gram-negative *Pseudomonas aeruginosa* and *Escherichia coli* bacteria were used as the test organisms. The experiment was conducted at the Department of Medical Microbiology and Parasitology of Sacred Heart Hospital, Abeokuta, Nigeria.

0.5 McFarland turbidity standard. In preparing turbidity for inocula, the British Society for Antimicrobial Chemotherapy (BSAC) procedure was followed. For the standardization of the organisms, 0.5 McFarland standard was developed using laboratory guidance- (0.5 mL of 0.048 M BaCl_2 (1.175% w/v BaCl_2 in $2\text{H}_2\text{O}$) was added to 99.5 mL of 0.18 M H_2SO_4 with constant stirring to maintain a suspension). An acceptable standard is between 0.08–0.13 for 0.5 McFarland standard (1.5×10^8 bacterial cell per mL). Afterwards, the density of the turbidity was confirmed with a UV-vis spectrophotometer (T90+ model) operated at wavelength of 625 nm. The prepared standard was then evenly distributed into screw cap test tubes, firmly closed, and then kept in the dark at 25 °C [20].

Mueller Hinton broth (5 mL) containing strains of the isolates (inocula) was dispensed into each screw-capped test tube and sterilized in an autoclave for 15 min at 121 °C. After cooling, the test tubes were kept inside an incubator for 24 h at 37 °C to ensure sterility. The pathogenic isolates were then inoculated into the sterilized test tubes containing medium and incubated overnight at 3 °C. The apparent turbidity in the broth culture was adjusted to 0.5 McFarland (standard) by adding sterile normal saline. Hence, the 0.5 McFarland standard produced turbidity equivalent to a bacterial suspension containing 1.5×10^8 cfu/mL. The suspension was used within 5 min to avoid population increase [21].

The sensitivity of test organisms. The sensitivity of the test organisms on the prepared nanoparticles was investigated using a modified procedure by Aida, as recommended by the National Committee for Clinical Laboratory Standards (NCCLS). Sterile agar slant was used to collect the test organisms, incubated at 37 °C for 24 h. Afterwards, the following biochemical analyses - gram staining, sugar fermentation, gelatin liquefaction, capsule staining, citrate utilization, motility, oxidase reaction, indole test, urease test, and hydrogen test were carried out on the isolated bacteria. Sugar fermentation, gram staining, and germ test tube were used to identify *Candida albicans*. In contrast, macroscopic and microscopic techniques using lactophenol cotton blue

stains were used to distinguish *Trichophyton rubrum* fungus. The stock culture was then stored and agar well diffusion procedure was used to check the antibacterial activity of the Ag and Ag-Ni nanoparticles at 4 °C as described by Portillo et al. [22].

The as-prepared microbial cultures were inoculated on a 9 cm diameter Mueller Hinton agar plate and then flooded with 1 mL of each standardized test organism. Wells of 6 mm diameter were dug into the agar plate with a sterile cork borer. Afterwards, 0.1 mL of 100 mg/mL nanoparticles (constituted in 50% DMSO) was introduced to each of them. Ciprofloxacin and fluconazole were the positive controls for bacteria and fungi, respectively. Test control (0.1 mL of 5 µg/mL) was also initiated on the agar plate in duplicates. The plates were incubated at 37 °C for 24 h for bacteria and yeast, while *T. rubrum* was incubated at 28 °C for 72 h. Antibacterial activity of the nanoparticles was determined by measuring the zones of inhibition around each well on the agar plate in millimeters (excluding the diameter of the well). This procedure was done in duplicates.

Furthermore, Minimum Inhibitory Concentration (MIC) was determined using a tube dilution method. Ten (10) sterilized test tubes were organized in a rack, then sterile nutrient broth (1 mL each) was introduced into the test tubes 2 to 8. Then, a serial doubling dilution was made to tubes 2 to 8, disposing of the last mL of the broth. Ciprofloxacin (1 mL) was added to tube 9, and double-distilled water to tube 10 as a negative control. A mix of 1 mL of McFarland and 1 mL broth culture were added to each test tube; covered, left overnight, and incubated at 37 °C. The experiment was monitored for the highest dilution with no turbidity. The zone of inhibition and MIC was determined using the Clinical and Laboratory Standards Institute guidelines [23].

Minimum Bactericidal Concentration (MBC) and the Minimum Fungicidal Concentration (MFC) were also determined using a revised method by Doughari [24]. For the determination of MBC, 0.5 mL of the sample from the MIC test, which showed no visible sign of growth, was taken and inoculated on sterile Mueller Hinton agar by streaking. In the case of MFC, 0.5 mL of the sample with no noticeable growth from the MIC test was taken and

inoculated on sterile potato dextrose agar by streaking. Both plates were incubated at 37 °C for 24 h. The concentration at which no visible growth was observed was recorded as the MBC and MFC after each inoculation.

RESULTS AND DISCUSSION

From the UV-visible spectroscopy analysis, Fig. 1–2 reveal the combined surface plasmon resonance (SPR) bands and collective oscillations of conduction band electrons of the Ag NPs and Ag-Ni NPs [25]. The transitions, $\pi \rightarrow \pi^*$ (C=C in the alkaloids), and $n \rightarrow \pi^*$ (O–H, C–O in carbohydrate and glycosides), as supported by the FTIR spectra (Fig. 5), confirmed the moieties present in the green synthesized nanoparticles. These functional groups were considered to be responsible for capping and stabilizing the newly formed nanocluster.

Evidence of nanoparticle formation was a change in color from light green to dark brown. However, there was no indication of nanoparticle formation in the reaction between the 1.0 mM AgNO₃ solution and the

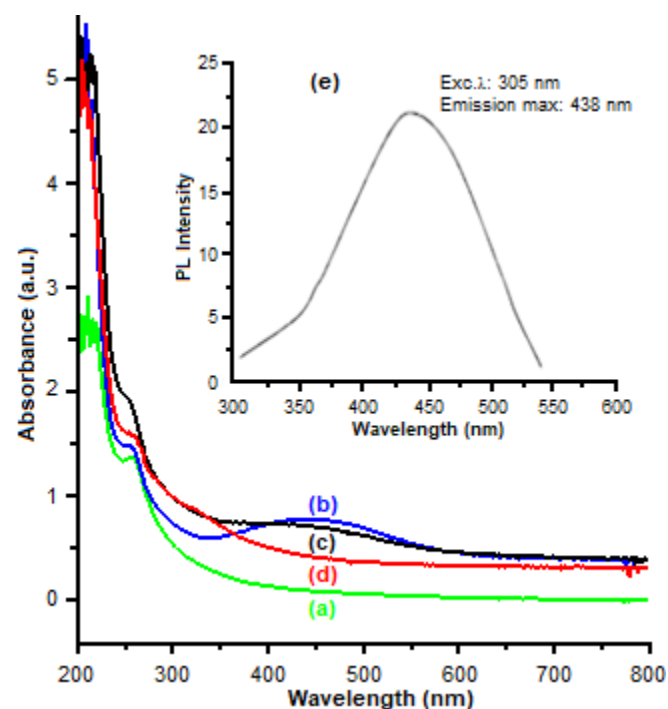


Fig 1. Absorption spectra (a) 1.0 mM (b) 2.0 mM (c) 3.0 mM (d) extract (e) inset Photoluminescence emission spectrum of Ag NPs at 40 min, 80 °C

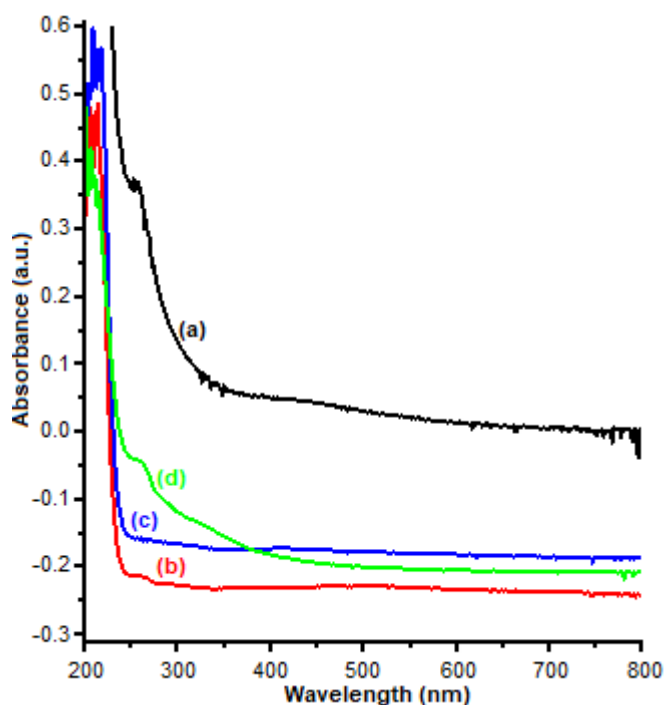


Fig 2. Absorbance spectra of Ag-Ni NPs (a) 1.0 mM (b) 2.0 mM (c) 3.0 mM (d) extract at 40 min, 80 °C

extract due to the absence of SPR. This occurrence could be due to the low concentration of precursors for the extract to reduce and nucleate the Ag ion. This finding is similar to the results of Fernando and Zhou [26]. Nucleation and onset growth occurred rapidly, as early as 5 min into the reaction involving 2.0 and 3.0 mM metal solutions, which is one of the advantages of 'green' synthesis of nanoparticles (See supplementary Fig. S1). Fig. 1 shows that the reaction mixture of silver nitrate solution (2.0 mM) and the metabolites were considered to be the optimum condition for Ag NPs using *N. tabacum* as reducing agent, as the SPR increased in peak intensity at 450 nm, which is the characteristic band for Ag NPs. The shape of the spectrum also connotes proximity to unity in the aspect ratio of as-synthesized NPs.

In the case of silver hybrid nanoparticles, the reduction of silver ions by *N. tabacum* commenced as early as 5 min at all the precursor solution concentrations. There is no doubt that the nucleation and growth occurred rapidly, as indicated by the early appearance of SPR, suggesting that the bio-reducing agent used was adequate for the reduction process (See supplementary Fig. S2). However, the SPR bands formed were of low extinction

coefficient intensity: 0.05, 0.06 and 0.07 a.u. for 1.0, 2.0 and 3.0 mM concentrations, respectively. A peak width-broadening was observed in the nanohybrid prepared from 2.0 mM precursor solution (Fig. 2), compared to the corresponding Ag NPs in Fig. 1. The redshift and reduction in the SPR peak intensity might be due to the presence of nickel, and the effect of aggregation between nanoclusters, which led to the particle size increase, corroborated by the previous model [27] (See supplementary Fig. S2). Moreover, the characteristic absorbance of the nanohybrid suggests $\text{Ag}_{\text{core}}\text{Ni}_{\text{shell}}$ formation. The observed absorption spectra also indicated that Ag NPs with a characteristic peak between 400–450 nm are not the shell, but the core of the nanohybrid, while Ni formed the shell as further corroborated by the EDX (See supplementary Fig. S4) and XRD patterns. The intensity of absorbance was higher in monosilver nanoparticles compared to its allied nanoparticles. Absorption spectra comparing growth of Ag NPs and Ag-Ni NPs are shown in Fig. 1 and 2, respectively. Photoluminescence study carried out on the as-prepared Ag NPs displayed quantum yield during vibrational relaxation at triple excited state as shown in Fig. 1 (Inset e). Excitation took place at 305 nm, and this resulted in the low intensity of emission with a single peak at 438 nm.

The phase analysis and crystalline nature of the Ag-Ni NPs, that was prepared using *N. tabacum* leaf extract as a reducing agent, were studied with X-ray diffraction (XRD). XRD pattern of the as-prepared nanohybrid is depicted in Fig. 3(a). The diffraction peak patterns indicate the formation of alloy Ag-Ni bimetallic nanoparticles. Match phase identification is presented in Fig. 3(b). Composition of the nanoalloy resembles a face-centered cubic phase of Ag with reflection peaks at 2θ values of 37.96° [111], 44.10° [200], 62.44° [220] and 77.56° [311]. However, there is a small deviation from the actual 2θ angles as a result of lattice insertion of Ni in the Ag crystal lattice, and this suggests alloying of the nanohybrid, which agrees with previous studies [28-29]. A characteristic peak of Ni at $2\theta = 46.24^\circ$ is shown. There is an overlapping peak for the (111) plane of Ni with that of Ag plane at $2\theta = 46.24^\circ$, but no crystalline phase of Ni (52.1°) was detected

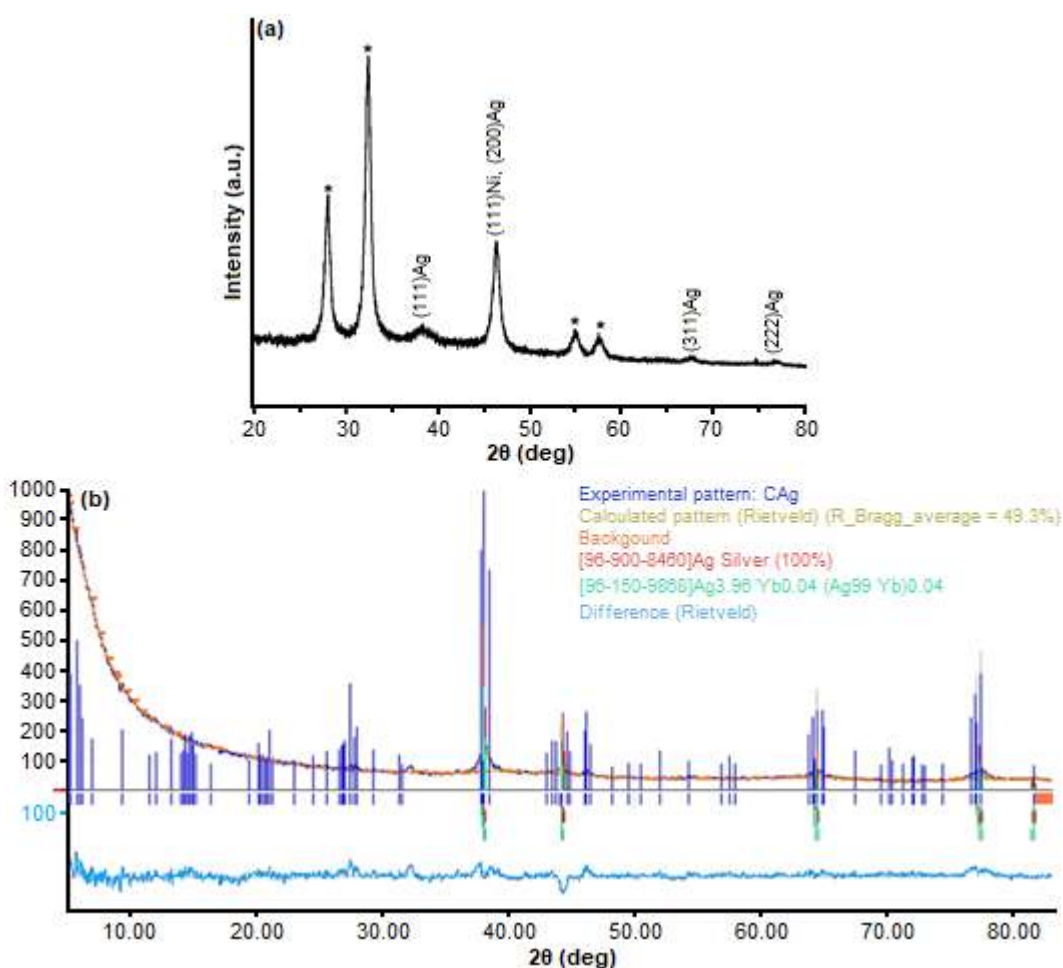


Fig 3. (a) XRD pattern of Ag-Ni NPs synthesized using *N. tabacum* (b) Phase matching

Table 1. Structural parameters of Ag-Ni nanohybrid

Miller indices (hkl)	2θ ($^{\circ}$)	Interplane distance, d (\AA)	Lattice constant, a (\AA)	Volume of cell, (\AA) ³	Crystallite size, D (nm)	FWHM
(111)	37.96	2.3705	4.1058	67.330	11.68	0.7098
(200)	44.10	2.0535	4.1070	68.63		0.6625
(220)	62.44	1.4524	4.1081	68.398		0.5205
(311)	77.50	1.3696	4.1088	68.172		0.2839

in the diffractogram. This phenomenon suggests core-shell formation. The additional peaks in the diffractogram could plausibly mean a presence of phase impurities in the sample or oxidation of nickel to NiO or Ni₂O₃ or Ni(OH)₂. The average crystallite size of 11.68 nm for d_{111} , with an experimental lattice constant 4.0862 \AA of Ag fcc, agrees with the unit cell value, $a = 4.086 \text{\AA}$ obtained from Rietveld calculation for Ag fcc phase using FullProf software, where $a_1 = a_2 = a_3$, $\alpha, \beta, \gamma = 90^{\circ}$, with space group Fm $\bar{3}$ m

(ICDD#96-900-8460). From the matched phase identification (Fig. 3(b)), Rietveld refinement convergence was also confirmed by FullProf software for the as-synthesized Ag NPs. As XRD is unable to differentiate two boundaries, the crystallite size is smaller in size compared with the particle size. The observation is in agreement with a previous study [30]. Table 1 gives detailed structural parameters using the following formulas; the lattice constant, $a, = d \cdot \sqrt{h^2 + k^2 + l^2}$, where

d = interplane distance obtained from FullProf software. The volume of unit cell $V = a^3$ and $D = k\lambda/\beta\cos\theta$, where D is the crystallite size in nm, k = Scherrer's constant (0.94), λ is wavelength of incident X-ray = 1.5417 Å, β = Full width half maximum (FWHM) in radians and θ = Bragg angle in radian. 2θ correction = 0.07516°, the phase match displays specimen displacement correction (Bragg Brentano geometry) $T = (s/R) = 0.0026336$, wavelength = 1.541874 Å.

A representation of the TEM image and histogram showing the particle size distribution of the Ag NPs prepared using *N. tabacum* as a reductant is presented in Fig. 4. The TEM micrograph shows irregular shapes and different orientations with discontinuity in the grain boundary of Ag nanoparticles. The TEM micrograph of Ag NPs reveals a quasi-cube shaped nanoparticle with an average size of 19.14 ± 6.43 nm (using Image J software). Quantified elemental composition analysis also supports the formation of Ag NPs, as shown in the EDX analysis. The as-prepared Ag NPs are dominated by silver (89.11 wt.%), oxygen (3.99 wt.%) and carbon (4.78 wt.%) originated from the plant extract (See supplementary Table, S3).

TEM micrograph of the as-prepared Ag-Ni NPs also shows the formation of cubes with truncated edges due to the reducing power of the plant extract (Fig. 4(d)). Morphology of the nanohybrid could be controlled by adjusting the concentration of the bio reducing agent. Furthermore, the reaction method is also a factor that determines the shape of the nanohybrid, as indicated in the study by Tsuji et al. [31], where $\text{Ag}_{\text{core}}\text{Ni}_{\text{shell}}$ was obtained using a microwave-polyol method. In Fig. 4(a), it is shown that the particle size ranges from 15.71 to 52.81 nm with a mean particle size of 30.45 ± 8.40 nm. The EDX analysis also supported the formation of Ag-Ni hybrid nanoparticles (See supplementary Table, S4). Ag and Ni were in the approximate ratio of 4:1 composition in cps. The weight composition of silver was 63.76%, and Ni was 11.13%. Carbon (14.85 wt.%) and oxygen (3.99 wt.%) were from the plant that was used. The aggregation of particles was also observed in the TEM image, which could be controlled by monitoring the quantity of bio-reducing agent that was used.

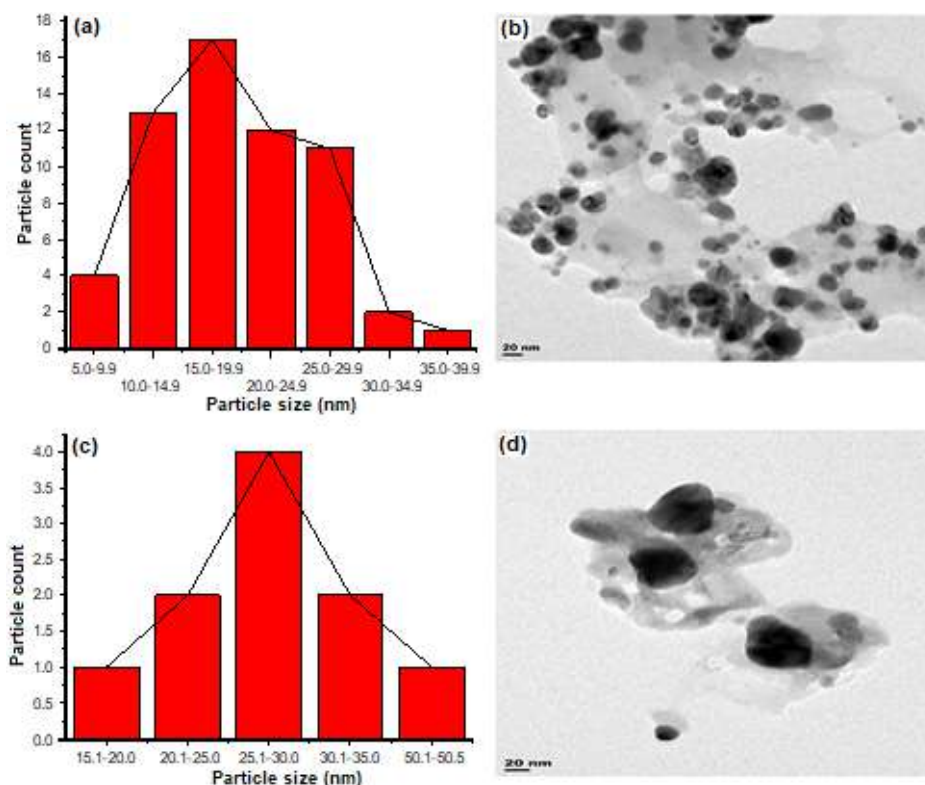


Fig 4. Particle size distribution histograms of (a) Ag NPs (c) Ag-Ni nanoparticles, and representative TEM images of (b) Ag NPs (d) Ag-Ni NPs

Phytochemical screening of the aqueous extract of the *Nicotiana tabacum* indicated the presence of alkaloids, carbohydrates, and glycosides (Table 2). Water was chosen as the solvent medium following the principle of green chemistry. A qualitative study using FTIR spectroscopy revealed the moieties adsorbed on the surface of the as-prepared nanoparticles (Fig. 5), which were also responsible for the capping and stability of the nanomaterials [32]. Some characteristic peaks with frequency at 3274 cm^{-1} assigned to N–H stretching of amine group were present in the alkaloid, which acted as the bio-reducing agent. Other prominent peaks include the peaks at 2935 cm^{-1} (C–H stretching from SP^3 hybridization), 1641 cm^{-1} (C=C stretching), 1534 cm^{-1} (C=N stretching), 1228 cm^{-1} (C–N of amine or C–O stretching) that were detected from the phytochemical analysis (Table 4).

The proposed biosynthesis reaction took place through the active sites created by nitrogen present in the alkaloids of *N. tabacum*, resulting in the attachment of methylene groups to nitrogen on the surface of the Ag nanoparticles as proposed in our earlier study [33]. There appears to be no peak in the carbonyl (C=O) region characteristic of carbohydrates and glycosides (Scheme

1). This observation is different from the phytoconstituents present in the *Senna occidentalis* plant as reported in a previous work [34]. The observed C–O stretch is weak, which indicates more alkaloids in the tobacco plant. Hence, the proposed mechanism of reaction suggests the reduction of Ag^+ ions to Ag^0 and Ni^{2+} to Ni^0 could be due to abundant alkaloids in the plant extract. This observation is similar to the findings by Shekins et al. [35].

Table 2. Phytochemical constituents of *Nicotiana tabacum* leaf extract

Biochemical	Water extract
Proteins	-
Alkaloids	+
Saponins	-
Carbohydrates	+
Phenols	-
Tannins	-
Glycosides	+
Flavonoids	-
Terpenoids	-
Steroids	-

+ Present - Absent

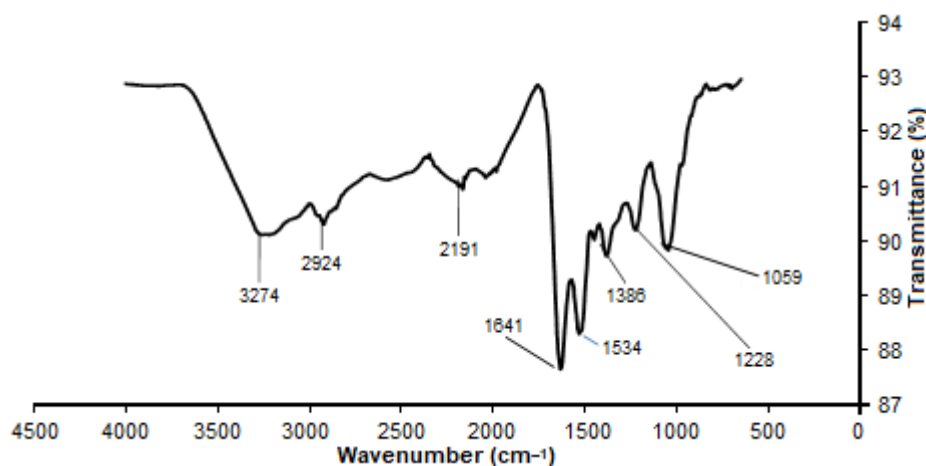
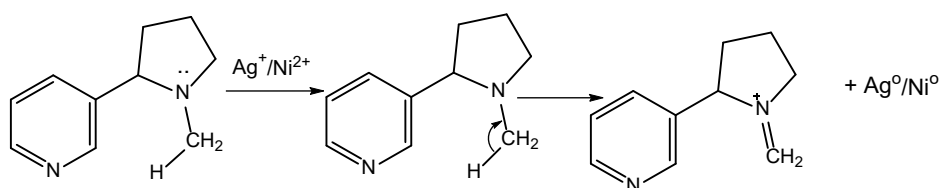


Fig 5. FTIR spectrum of Ag-NPs using the extract of *Nicotiana tabacum*



Scheme 1. Proposed reduction reaction mechanism by alkaloids [36]

Antimicrobial Assay

From the measured zones of inhibition displayed by the Ag NPs prepared by using *N. tabacum*, the activity of Ag NPs was revealed. Preliminary screening of Ag NPs (agar diffusion test) showed that the nanocluster exhibited moderate activities on all organisms except *P. aeruginosa*, where comparatively low activity was recorded (Table 3). However, the result of statistical analysis (ANOVA and SPSS) indicated there was no significant difference at the two precursor concentrations when $P > 0.05$. When compared with the standard, the activity of Ag NPs on the organisms was similar at concentrations of 2.0 and 3.0 mM. These observations led to the susceptible antimicrobial testing MIC, MFC, and MBC.

From Table 3, it is shown that higher activity was observed in Ag NPs prepared with 3.0 mM precursor concentration. *Streptococcus pyogenes* (Gram-positive bacterium), a human pathogen responsible for acute infections like pharyngitis, was the most susceptible species to the nanoparticles [37]. This sensitivity could be a result of the large volume of surface area possessed by nanoparticles, as this fostered more contact and interaction with cells [38]. Our result is different from the findings by Sarwar et al. [39] and Domínguez et al. [40], in which Gram-negative bacteria were more susceptible to nanoparticles compared to Gram-positive bacteria. This could be attributed to the nature of the cell wall found in Gram-negative bacteria, which is composed of phospholipids, lipoprotein, and thin lipopolysaccharides. However, *S. pyogenes* had the highest susceptibility to the as-prepared Ag NPs, that could be attributed to the component structure on the bacteria cell. A lot of pores

and teichoic acid have been reported to be present in Gram-positive bacteria, which allow the infiltration of foreign molecules, thereby causing damage to the cell membrane or even killing it. It could also be possible that the Ag NPs could not adhere to the negatively-charged peptidoglycan layer organized on the organism, thereby permitting the penetration of the nanoparticles [16]. The same MIC and MBC (least concentration) of 12.5 mg/mL observed was an indication that the nanoparticles were bactericidal. In order of sensitivity, *Streptococcus pyogenes* was followed by *Staphylococcus aureus* (Gram-positive bacterium) and a fungus - *Candida albicans*, with the same MIC and MFC concentrations of 12.5 mg/mL and 25 mg/mL, respectively. *S. aureus* is usually found on the skin and upper respiratory tract of individuals [41].

Other organisms were less sensitive to the Ag NPs compared to *Streptococcus pyogenes*. The observed activity of Ag NPs against *E. coli* was at MIC concentration of 25 mg/mL, which is the same value for MBC as well. In the case of *Trichophyton rubrum*, the nanocluster was active at 25 mg/mL MIC and 50 mg/mL MFC concentrations. Least activity was detected in the Gram-negative bacterium - *Pseudomonas aeruginosa*. This pathogen that causes chronic infections in the urinary tract, surgical wounds, and the respiratory tract was sensitive to the Ag NPs at the same MIC and MBC concentration of 50 mg/mL.

In contrast, no activity was found on *P. aeruginosa* by Ag NPs prepared with 2.0 mM metal precursor (Table 4). This experimental insensitivity could be due to the high negatively-charged lipopolysaccharides on the cell wall of *P. aeruginosa*, protecting the cell membrane [42].

Table 3. Sensitivity testing of organisms with standard deviation in zones of inhibition (Agar Diffusion Test)

Nanoparticles	Organisms/Mean zone diameter (mm) \pm SD					
	<i>Staphylococcus aureus</i>	<i>Streptococcus pyogenes</i>	<i>Escherichia coli</i>	<i>Pseudomonas aeruginosa</i>	<i>Candida albicans</i>	<i>Trichophyton rubrum</i>
Ag 2.0	10 \pm 0.5	11 \pm 0.5	9 \pm 0.2	7 \pm 0.1	10 \pm 0.2	9 \pm 0.3
Ag 3.0	12 \pm 0.3	13 \pm 0.5	10 \pm 0.5	9 \pm 0.1	12 \pm 0.1	10 \pm 0.5
Control	21 \pm 0.8	18 \pm 0.3	21 \pm 0.2	20 \pm 0.4	19 \pm 0.6	18 \pm 0.3
STAT	$P > 0.05$	$P > 0.05$	$P > 0.05$	$P > 0.05$	$P > 0.05$	$P > 0.05$

Standard/Control = Ciprofloxacin (Bacteria) and Fluconazole (Fungi). Ag 2.0 = Silver nanoparticles prepared from 2.0 mM precursor concentration using *N. tabacum* leaf extract. Ag 3.0 = Silver nanoparticles prepared from 3.0 mM precursor concentration using *N. tabacum* leaf extract

Table 4. Minimum inhibitory concentration (MIC), minimum bactericidal concentration (MBC) and minimum fungicidal concentration (MFC)

Nanoparticles	Organisms/MIC, MBC & MFC (mg/mL)					
	<i>Staphylococcus aureus</i>	<i>Streptococcus pyogenes</i>	<i>Escherichia coli</i>	<i>Pseudomonas aeruginosa</i>	<i>Candida albicans</i>	<i>Trichophyton rubrum</i>
	MIC, MBC	MIC, MBC	MIC, MBC	MIC, MBC	MIC, MFC	MIC, MFC
Ag 2.0	50, 50	25, 25	50, 100	100, 100	25, 50	50, 100
Ag 3.0	12.5, 25	12.5, 12.5	25, 25	50, 50	12.5, 25	25, 50
STATISTICS	<i>P</i> < 0.05	<i>P</i> < 0.05	<i>P</i> < 0.05	<i>P</i> < 0.05	<i>P</i> < 0.05	<i>P</i> < 0.05
Control	3.13	6.25	6.25	6.25	6.25	6.25
STATISTICS	Control vs Aa, Ba, Ca, Da, Ea, A, B, C, E, F-value 34.06, <i>P</i> < 0.05					

Control- Ciprofloxacin (Bacteria) and Fluconazole (Fungi)

The activity of Ag NPs was lower compared to ciprofloxacin and fluconazole (standards). However, a one-way analysis of variance using SPSS tool proved that the growth inhibition by Ag NPs was significant at $P < 0.05$.

■ CONCLUSION

This work has explored the possibilities and better utilization of *N. tabacum*. The known addictive plant used for smoking was converted into monometallic and bimetallic nanoparticles. From UV-visible spectroscopy, it was shown that the nanoparticles possess optical properties with the appearance of surface plasmon resonance at 438 nm for Ag NPs, and broad peak-broadening in the Ag_{core}Ni_{shell} nanohybrid that was formed. SPR bands formed in the Ag-Ni nanohybrid had lower extinction coefficient intensity with peak width-broadening, compared to the corresponding Ag NPs. Photoluminescence study revealed low emission potential in Ag NPs. TEM, EDX, XRD, and FTIR characterizations supported the formation of Ag and Ag-Ni hybrid nanoparticles. Ag NPs prepared from 3.0 mM metal nanoparticles have proven to overcome the challenge of biofilm formation in drug resistance. Ag NPs displayed the highest activity against the clinically isolated *Streptococcus pyogenes*, Gram-positive bacterium, with 12.5 mg/mL MIC and MBC value, followed by *Staphylococcus aureus* (Gram-positive bacterium) and a fungus - *Candida albicans*, with the same MIC and MFC concentrations of 12.5 mg/mL, 25mg/mL, respectively. The lower sensitivity of Ag NPs was observed against *E. coli* and *Trichophyton rubrum* with the same MIC and MBC concentration of

25 mg/mL and. The Ag nanoparticle was active at 25 mg/mL MIC concentration, and 50 mg/mL MFC concentration. No activity was noticed against *P. aeruginosa* by Ag NPs prepared with 2.0 mM metal precursor. Finally, ANOVA statistical tool that was used to validate the growth inhibition of Ag NPs showed that it was significant at $P < 0.05$. From this study, Ag NPs prepared from *Nicotiana tabacum* was proven to be a possible candidate for developing antibacterial and antifungal drugs.

■ ACKNOWLEDGMENTS

The authors acknowledge Oluwaseun Ejilude of Sacred Heart Hospital, Nigeria, for the antimicrobial assay. We would also like to thank Mr. Shitole Joseph of iThemba Labs, South Africa, for the morphology characterization. Covenant University is appreciated for supporting this publication.

■ SUPPORTING INFORMATION

Additional figures, tables, and data are available in the supplementary material.

■ AUTHOR CONTRIBUTIONS

EO Dare designed the research, A.A. Akinsiku conducted the experiment and wrote the manuscript. J.A. Adekoya revised the manuscript.

■ REFERENCES

- [1] Nasrollahzadeh, M., Sajjadi, M., Sajadi, S.M., and Issaabadi, Z., 2019, "Green nanotechnology" in *An*

- Introduction to Green Nanotechnology*, Volume 28, Academic Press, London, 145–198.
- [2] Sathishkumar, P., Vennila, K., Jayakumar, R., Yusoff, A.R.M., Hadibarata, T., and Palvannan, T., 2016, Phyto-synthesis of silver nanoparticles using *Alternanthera tenella* leaf extract: An effective inhibitor for the migration of human breast adenocarcinoma (MCF-7) cells, *Bioprocess Biosyst. Eng.*, 39 (4), 651–659.
- [3] Michna, A., Morga, M.M., Adamczyk, Z., and Kubiak, K., 2019, Monolayers of silver nanoparticles obtained by green synthesis on macrocation modified substrates, *Mater. Chem. Phys.*, 227, 224–235.
- [4] Oyekunle, I.P., Nwogu, U.S., Orababa, O.Q., Nsude, C.C., Ikpa, J.O., and Azuka, D.C., 2019, Phytochemical, antimicrobial, and proximate composition of *Nicotiana tabacum* leaves extract, *IJISRT*, 4 (5), 406–410.
- [5] Adeniyi, P.A.O., Ghazal, O.K., Musa, A.A., and Caxton-Martins, E.A., 2010, The neurobehavioural effects of smoke and ethanolic extract of *Nicotiana tabacum* leaves exposure in mice, *Res. J. Anim. Sci.*, 4 (4), 99–102.
- [6] Ningthoujam, S.S., Talukdar, A.D., Potsangbam, K.S., and Choudhury, M.D., 2013, Traditional uses of herbal vapour therapy in Manipur, North-East India: An ethnobotanical survey, *J. Ethnopharmacol.*, 147 (1), 136–147.
- [7] Fongnzossie, E.F., Tize, Z., Nde, P.J.F., Biyegue, C.F.N., Ntsama, I.S.B., Dibong, S.D., and Nkongmeneck, B.A., 2017, Ethnobotany and pharmacognostic perspective of plant species used as traditional cosmetics and cosmeceuticals among the Gbaya ethnic group in Eastern Cameroon, *S. Afr. J. Bot.*, 112, 29–39.
- [8] Smith, R.A., Andrews, K.S., Brooks, D., Fedewa, S.A., Manassaram-Baptiste, D., Saslow, D., Brawley, O.W., and Wender, R.C., 2018, Cancer screening in the United States, 2018: A review of current American Cancer Society guidelines and current issues in cancer screening, *CA Cancer J. Clin.*, 68 (4), 297–316.
- [9] Massironi, A., Morelli, A., Grassi, L., Puppi, D., Braccini, S., Maisetta, G., Esin, S., Batoni, G., Pina, C.P., and Chiellini, F., 2019, Ulvan as novel reducing and stabilizing agent from renewable algal biomass: Application to the green synthesis of silver nanoparticles, *Carbohydr. Polym.*, 203, 310–321.
- [10] Tripathi, D., Modi, A., Narayan, G., and Rai, S.P., 2019, Green and cost effective synthesis of silver nanoparticles from endangered medicinal plant *Withania coagulans* and their potential biomedical properties, *Mater. Sci. Eng., C*, 100, 152–164.
- [11] Parthiban, E., Manivannan, N., Ramanibai, R., and Mathivanan, N., 2019, Green synthesis of silver nanoparticles from *Annona reticulata* leaves aqueous extract and its mosquito larvicidal and anti-microbial activity on human pathogens, *Biotechnol. Rep.*, 21, e00297.
- [12] Baláž, M., Daneu, N., Balážová, L., Dutková, E., Tkáčiková, L., Briančin, J., Vargová, M., Balážová, M., Zorkovská, A., and Baláž, P., 2017, Bio-mechanochemical synthesis of silver nanoparticles with antibacterial activity, *Adv. Powder Technol.*, 28 (12), 3307–3312.
- [13] Akinsiku, A.A., Dare, E.O., Ajani, O.O., Ayo-Ajayi, J., Ademosun, O.T., and Ajayi, S.O., 2018, Room temperature phytosynthesis of Ag/Co bimetallic nanoparticles using aqueous leaf extract of *Canna indica*, *IOP Conf. Ser.: Earth Environ. Sci.*, 173, 012019.
- [14] Mohammadi, M.M., Gunturi, S.S., Shao, S., Konda, S., Buchner, R.D., and Swihart, M.T., 2019, Flame-synthesized nickel-silver nanoparticle inks provide high conductivity without sintering, *Chem. Eng. J.*, 372, 648–655.
- [15] Pinkas, J., Sopoušek, J., Brož, P., Vykoukal, V., Buršík, J., and Vřešťal, J., 2019, Synthesis, structure, stability and phase diagrams of selected bimetallic silver- and nickel-based nanoparticles, *Calphad*, 64, 139–148.
- [16] Vykoukal, V., Bursík, J., Roupčova, P., Cullen, D.A., and Pinkas, J., 2019, Solvothermal hot injection synthesis of core-shell AgNi nanoparticles, *J. Alloys Compd.*, 770, 377–385.
- [17] Wang, L., Hu, C., and Shao, L., 2017, The antimicrobial activity of nanoparticles: Present

- situation and prospects for the future, *Int. J. Nanomed.*, 12, 1227–1249.
- [18] Akinsiku, A.A., Ajanaku, K.O., Adekoya, J.A., and Dare, E.O., 2015, Green synthesis, characterization of silver nanoparticles using *Canna indica* and *Senna occidentalis* leaf extracts, *Proceedings of 2nd Covenant University – International Conference on African Development Issues 2015 (CU-ICADI 2015)*, 154–157.
- [19] Gul, R., Jan, S.U., Faridullah, S., Sherani, S., and Jahan, N., 2017, Preliminary phytochemical screening, quantitative analysis of alkaloids, and antioxidant activity of crude plant extracts from *Ephedra intermedia* indigenous to Balochistan, *Sci. World J.*, 2017, 5873648.
- [20] White, A.R., 2008, The British Society for Antimicrobial Chemotherapy Resistance Surveillance Project: A successful collaborative model, *J. Antimicrob. Chemother.*, 62 (Suppl. 2), ii3–ii14.
- [21] Kiehlbauch, J.A., Hannett, G.E., Salfinger, M., Archinal, W., Monserrat, C., and Carlyn, C., 2000, Use of the National Committee for Clinical Laboratory Standards guidelines for disk diffusion susceptibility testing in New York State Laboratories, *J. Clin. Microbiol.*, 38 (9), 3341–3348.
- [22] Portillo, A., Vila, R., Freixa, B., Adzet, T., and Cañigüeral, S., 2001, Antifungal activity of Paraguayan plants used in traditional medicine, *J. Ethnopharmacol.*, 76 (1), 93–98.
- [23] Clinical and Laboratory Standards Institute, 2020, *Performance standards for antimicrobial susceptibility testing*, 30th Ed., CLSI supplement M100, Clinical and Laboratory Standards Institute, Wayne, PA.
- [24] Mostafa, A.A., Al-Askar, A.A., Almaary, K.S., Dawoud, T.M., Sholkarny, E.N., and Bakri, M.M., 2018, Antimicrobial activity of some plant extracts against bacterial strains causing food poisoning diseases, *Saudi J. Biol. Sci.*, 25 (2), 361–366.
- [25] Nasrollahzadeh, M., Sajadi, S.M., Babaei, F., and Maham, M., 2015, *Euphorbia helioscopia* Linn as a green source for the synthesis of silver nanoparticles and their optical and catalytic properties, *J. Colloid Interface Sci.*, 450, 374–380.
- [26] Fernando, I., and Zhou, Y., 2019, Impact of pH on the stability, dissolution and aggregation kinetics of silver nanoparticles, *Chemosphere*, 216, 297–305.
- [27] Panariello, L., Mazzei, L., and Gavriilidis, A., 2018, Modelling the synthesis of nanoparticles in continuous microreactors: The role of diffusion and residence time distribution on nanoparticle characteristics, *Chem. Eng. J.*, 350, 1144–1154.
- [28] Kumar, M., and Deka, S., 2014, Multiply twinned AgNi alloy nanoparticles as a highly active catalyst for multiple reductions and degradation reactions, *ACS Appl. Mater. Interfaces*, 6 (18), 16071–16081.
- [29] Adekoya, J.A., Dare, E.O., Mesubi, M.A., and Revaprasadu, N., 2014, Synthesis and characterization of optically active fractal seed-mediated silver nickel bimetallic nanoparticles, *J. Mater.*, 2014, 184216.
- [30] Mourdikoudis, S., Pallares, R.M., and Thanh, N.T.K., 2018, Characterization techniques for nanoparticles: Comparison and complementarity upon studying nanoparticle properties, *Nanoscale*, 10 (27), 12871–12934.
- [31] Tsuji, M., Hikino, S., Matsunaga, M., Sano, Y., Hashizume, T., and Kawazumi, H., 2010, Rapid synthesis of Ag@Ni core-shell nanoparticles using a microwave-polyol method, *Mater. Lett.*, 64 (16), 1793–1797.
- [32] Hashemi, S.F., Tasharrofi, N., and Saber, M.M., 2020, Green synthesis of silver nanoparticles using *Teucrium polium* leaf extract and assessment of their antitumor effects against MNK45 human gastric cancer cell line, *J. Mol. Struct.*, 1208, 127889.
- [33] Akinsiku, A.A., Ajanaku, K.O., Adebisi, A.A., Edobor-Osoh, A., Aladesuyi, O., Taiwo, O.S., and Dare, E.O., 2019, *Momordica charantia* stem extract mediated biogenic synthesis of silver nanoparticles: Optical and antimicrobial efficacy, *IOP Conf. Ser.: Mater. Sci. Eng.*, 509, 012018.
- [34] Akinsiku, A.A., Ajanaku, K.O., and Dare, E.O., 2019, Green synthesis of pseudo-cubic Ag/Ni

- bimetallic nanoparticles using *Senna occidentalis* leaf extract, *J. Phys. Conf. Ser.*, 1299, 012133.
- [35] Shekins, O.O., Dorathy, E.U., Labaran, M.L., and Joel, P., 2016, Phytochemical screening of tobacco (*Nicotiana tabacum*) and its effects on some haematological parameters and histopathology of liver and brain in male rats, *Int. J. Biochem. Res. Rev.*, 14 (4), 1–9.
- [36] Akinsiku, A.A., Dare, E.O., Ajanaku, K.O., Ajani, O.O., Olugbuyiro, J.A.O., Siyanbola, T.O., Ejilude, O., and Emeteri, M.E., 2018, Modeling and synthesis of Ag and Ag/Ni allied bimetallic nanoparticles by the green method: Optical and biological properties, *Int. J. Biomater.*, 2018, 9658080.
- [37] Bryant, A.E., and Stevens, D.L., 2015, “*Streptococcus pyogenes*” in *Mandell, Douglas, and Bennett's Principles and Practice of Infectious Diseases*, 8th Ed., Eds. Bennet, J.E., Dolin, R., and Blaser, M.J., Elsevier Saunders, Philadelphia, PA, 2285–2299.
- [38] Huh, A.J., and Kwon, Y.J., 2011, “Nanoantibiotics”: A new paradigm for treating infectious diseases using nanomaterials in the antibiotics resistant era, *J. Controlled Release*, 156 (2), 128–145.
- [39] Sarwar, A., Katas, H., Samsudin, S.N., and Zin, N.M., 2015, Regioselective sequential modification of chitosan via azide-alkyne click reaction: Synthesis, characterization, and antimicrobial activity of chitosan derivatives and nanoparticles, *PLoS One*, 10, (4), e0123084.
- [40] Domínguez, A.V., Algaba, R.A., Canturri, A.M., Villodres, A.R., and Smani, Y.Y., 2020, Antibacterial activity of colloidal silver against Gram-negative and Gram-positive bacteria, *Antibiotics*, 9 (1), 36.
- [41] Zhang, L., Hou, L., Zhang, S., Kou, X., Li, R., and Wang, S., 2020, Mechanism of *S. aureus* ATCC 25923 in response to heat stress under different water activity and heating rates, *Food Control*, 108, 106837.
- [42] Dakal, T.C., Kumar, A., Majumdar, R.S., and Yadav, V., 2016, Mechanistic basis of antimicrobial actions of silver nanoparticles, *Front. Microbiol.*, 7, 1831.

Supplementary Data

This supplementary data is a part of the paper entitled “Determination of Eugenol in Personal-Care Products by Dispersive Liquid-Liquid Microextraction Followed by Spectrophotometry Using *p*-Amino-*N,N*-dimethylaniline as a Derivatizing Agent”.

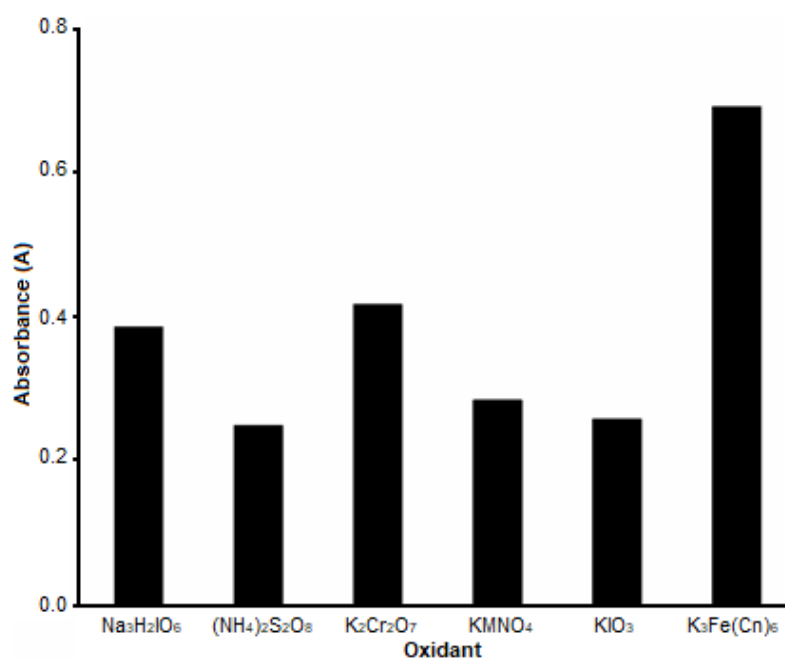


Fig A. Oxidant optimization for oxidative coupling of eugenol. Conditions: oxidant 0.4 mM, eugenol and PADA 0.2 mM; ammonium hydroxide 2 mM

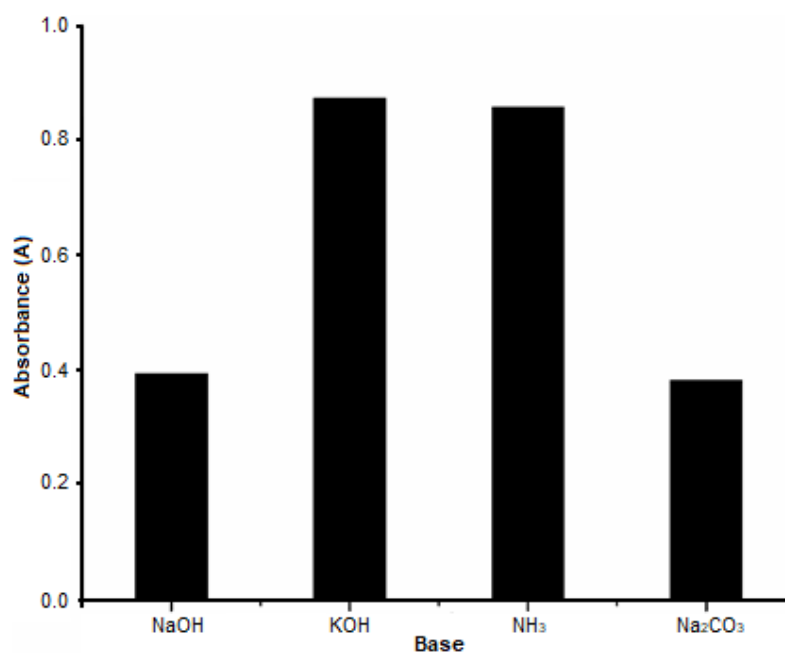
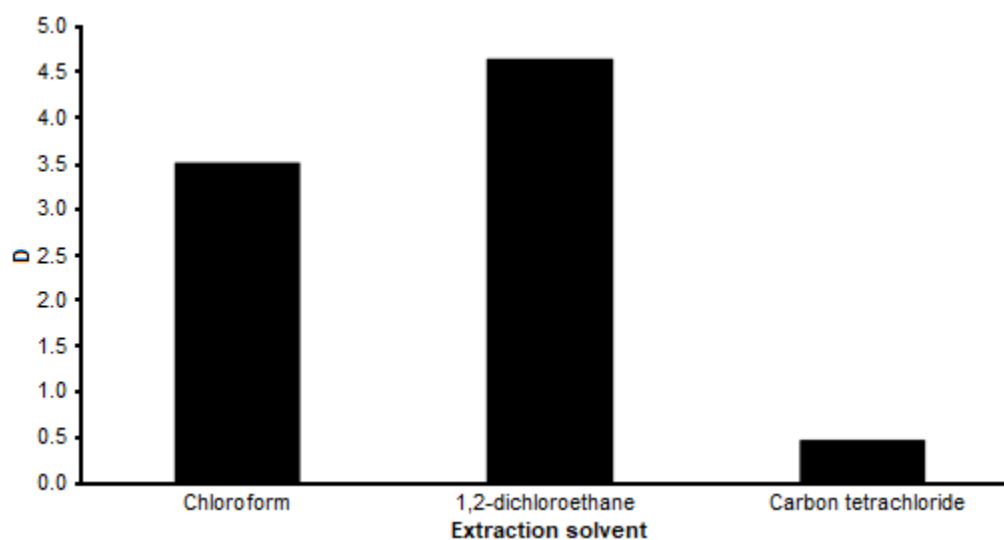
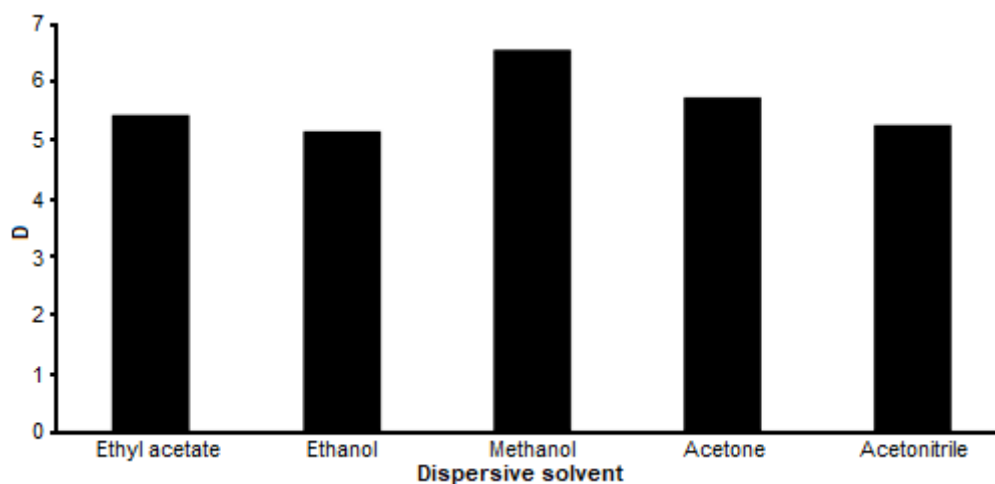


Fig B. Base optimization for oxidative coupling of eugenol. Conditions: base 2 mM, eugenol and PADA 0.2 mM, hexacyanoferrate 0.6 mM

Table A. Order of addition. Eugenol 0.2 mM, hexacyanoferrate 0.6 mM, potassium hydroxide 3 mM, PADA. 0.3 mM

	Order of addition				A
1	D	R	O	B	0.982
2	D	O	R	B	0.341
3	D	B	R	O	0.557
4	D	B	O	R	0.089
5	R	O	D	B	0.223
6	R	O	B	D	0.149
7	R	B	D	O	0.403
8	O	B	D	R	0.085
9	O	B	R	D	0.171
10	B	R	O	D	0.162

*(D = eugenol, R=PADA, O = hexacyanoferrate B = potassium hydroxide), A = Absorbance

**Fig C.** DLLME extraction solvent study. conditions: eugenol 0.2 mM, t dispersive solvent (acetone) 25 μ L, the volume of aqueous phase (dye) 14 mL, KCl 20 mM, centrifugation 5 min at 1100 rpm**Fig D.** DLLME dispersive solvent study conditions: dispersive solvent 25 μ L, eugenol 0.2 mM, (extraction solvent) 550 μ L, aqueous phase (dye) 14 mL, KCl 20 mM, centrifugation 5 min at 1100 rpm

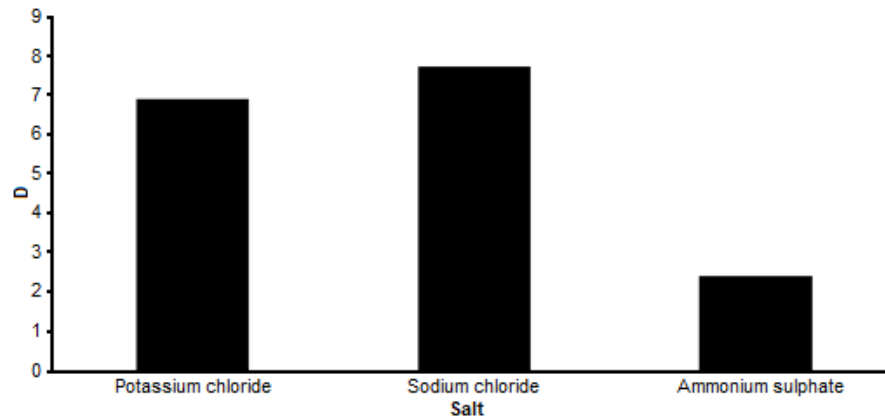


Fig E. DLLME salt selection: eugenol 0.2 mM, (extraction solvent) 550 μ L, (dispersive solvent) 100 μ L, aqueous phase (dye) 14 mL, centrifugation 5 min at 1100 rpm

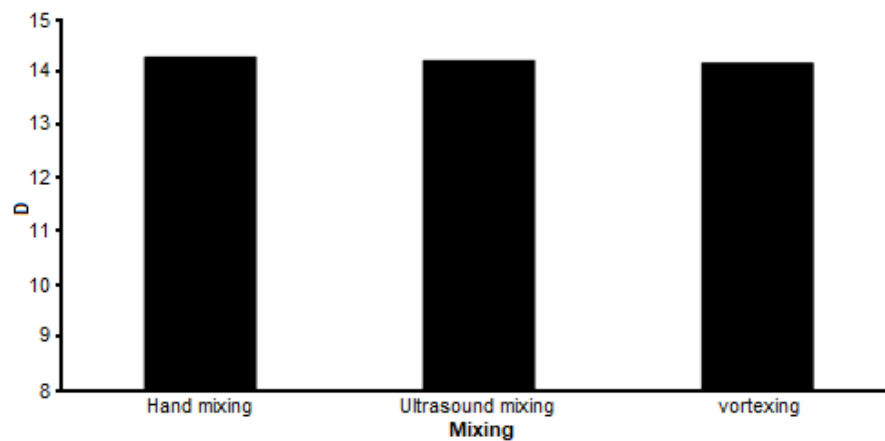


Fig F. DLLME reagent mixing effect. Conditions: eugenol 0.2 mM, sodium chloride 28 mM, (extraction solvent) 550 μ L, (dispersive solvent) 100 μ L, aqueous phase (dye) 14 mL, centrifugation 5 min at 1100 rpm

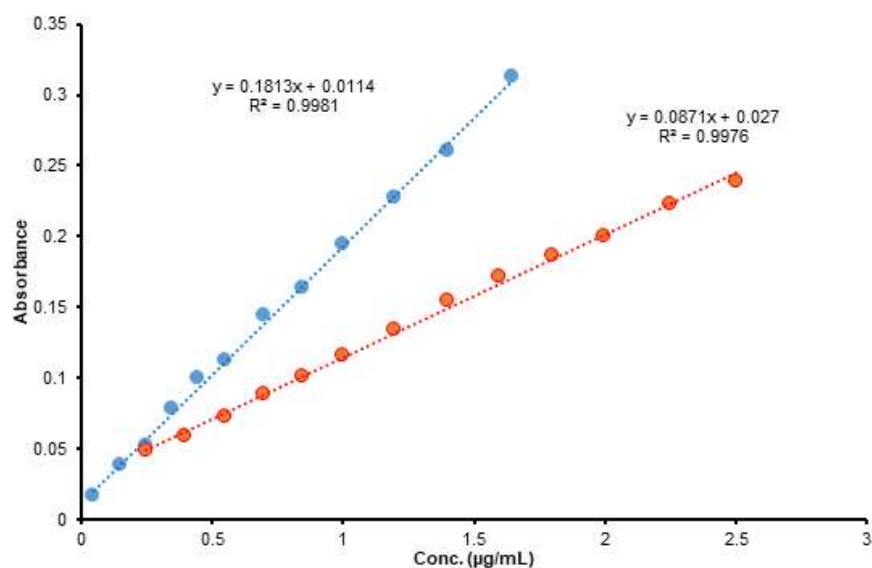


Fig G. Calibration curves for eugenol A. the Derivatization reaction mixture (red symbols) B. DLLME method (blue symbols), both under optimal conditions

Determination of Eugenol in Personal-Care Products by Dispersive Liquid-Liquid Microextraction Followed by Spectrophotometry Using *p*-Amino-*N,N*-dimethylaniline as a Derivatizing Agent

Bahaa Malik Altahir^{1,*}, Omar Abdulazeez¹, Sarmad Bahjat Dikran^{2‡}, and Keith Edward Taylor³

¹Department of Biology, College of Science, University of Baghdad, Baghdad 10071, Iraq

²Department of Chemistry, College of Education for Pure Science – Ibn Al-Haitham, University of Baghdad, Baghdad 10071, Iraq

³Department of Chemistry and Biochemistry, University of Windsor, 401 Sunset Avenue, Windsor, Ontario N9B 3P4, Canada

* **Corresponding author:**

tel: +964-7901567986

email: baha782004@gmail.com

Received: June 23, 2020

Accepted: September 11, 2020

DOI: 10.22146/ijc.56198

[‡]This paper is dedicated to the memory of the late Sarmad Bahjat Dikran.

Deceased July 6, 2020

Abstract: Two simple methods for the determination of eugenol were developed. The first depends on the oxidative coupling of eugenol with *p*-amino-*N,N*-dimethylaniline (PADA) in the presence of $K_3[Fe(CN)_6]$. A linear regression calibration plot for eugenol was constructed at 600 nm, within a concentration range of 0.25–2.50 $\mu\text{g}\cdot\text{mL}^{-1}$ and a correlation coefficient (*r*) value of 0.9988. The limits of detection (LOD) and quantitation (LOQ) were 0.086 and 0.284 $\mu\text{g}\cdot\text{mL}^{-1}$, respectively. The second method is based on the dispersive liquid-liquid microextraction of the derivatized oxidative coupling product of eugenol with PADA. Under the optimized extraction procedure, the extracted colored product was determined spectrophotometrically at 618 nm. A linear plot within a concentration range of 0.05–1.65 $\mu\text{g}\cdot\text{mL}^{-1}$ (*r* = 0.9997) was constructed. The LOD and LOQ were 0.053 and 0.177 $\mu\text{g}\cdot\text{mL}^{-1}$, respectively. Both methods were tested for the analysis of eugenol in commercial personal-care products, and the results confirmed that the procedures are accurate, precise, and reproducible (RSD < 1%).

Keywords: dispersive liquid-liquid microextraction; derivatizing agent; eugenol; *p*-amino-*N,N*-dimethylaniline

■ INTRODUCTION

Eugenol (E) ($\text{C}_{10}\text{H}_{12}\text{O}_2$; 4-allyl-2-methoxy phenol) is a phenylpropene or allylbenzene [1]. It is a component of aromatic plants, such as wormwood, clove, celery, cinnamon, and ginger [2]. Due to its potent antimicrobial and antioxidant properties, eugenol has been widely used in cosmetics and pharmaceuticals [3]. It is useful in dentistry to increase the protection against oxidative injury, periodontal ligament fibroblasts, and prosthodontic uses [4]. This compound has recognized acaricidal activity, including activity on *R. microplus* [5]. Despite these benefits of eugenol, there are also caveats about its use, including allergenicity, cause of some skin diseases, toxicity, generation of reactive oxygen species, enzyme inhibition, carcinogenicity, and geno-, immuno-, cyto- toxicity [6].

Analytical techniques, such as spectrophotometry, currently provide the ability to measure many pharmaceutical compounds down to low levels in conjunction with modern extraction techniques, i.e., derivatization and clean-up methods [7]. Sample preparation is one of the most critical aspects of such organic analytical procedures [8]. The extraction of pharmaceuticals from prepared samples into a limited solvent amount is the first and most critical step [9]. Analysis requires careful standardization and pre-analytical handling of the samples [10]. However, matrix effects, such as the presence of macromolecules, small molecules, additives and/or salts, interfere with analysis [11]. Careful sample preparation is needed for the low analyte concentration and to overcome the biological matrix effect, which is incompatible with the instrumental

technique chosen. Thus, careful sample preparation should be used to overcome matrix effects, starting with enhancing the selectivity and sensitivity of the study to improve analytical criteria and/or protect the analytical instrument from potential harm [12]. Several techniques may be used to do this, the most common being liquid-liquid extraction, solid-phase microextraction (SPME), solid-phase extraction (SPE), and soxhlet extraction processes [9].

Dispersive liquid-liquid microextraction techniques (DLLME) have been used recently for the preconcentration of organic analytes from aqueous matrices [13]. The process has the benefits of low consumption of organic solvents, a high extraction efficiency, short extraction time, and high enrichment factors [14]. The main objective of microextraction is to obtain a reproducible, representative amount of the analyte from the sample rather than to retrieve all of the analyte [15].

Eugenol has also been determined using liquid chromatography [16] provided with electrochemical [17-18] or UV detection [19], voltammetric [20], photodiode array (PDA) [21] and oscillating methods [22]. These methods are accurate and efficient, but they have some drawbacks such as complexity, expense, and time-consuming. The proposed methods are simple, low cost, and quick.

Chemical derivatization is used to transform a molecule into a derivative that has better properties for the intended study and enhances the sensitivity through an easy, rapid reaction that forms a highly stable and reproducible derivative [23].

The aim of this study was to propose and optimize an accurate and time-effective method for the quantitative estimation of eugenol in personal-care products with a combination of spectrophotometry and pre-extraction using the DLLME technique. The pre-treatment method was enhanced by a derivatization step using a new derivatizing agent, *para*-amino-*N,N*-dimethylaniline (PADA), where derivatization was accomplished by oxidative coupling. A current literature survey found that no previous study focused on the existence of eugenol in personal-care products. In addition, no study presented a reagent for eugenol derivatization and simple

spectrophotometric detection in the visible region.

■ EXPERIMENTAL SECTION

Materials

The primary reference standard was (eugenol 4-(H₂C=CHCH₂)C₆H₃-2-(OCH₃)OH). *Para*-amino-*N,N*-dimethylaniline 4-dimethylamino aniline 97%, potassium hexacyanoferrate(III) (K₃Fe(CN)₆) 99%, potassium hydroxide pellets (KOH) ≥ 85%, ammonia solution 25% (NH₄OH), potassium chloride (KCl) 99.0%, methanol (CH₃OH) ≥ 99.9%, chloroform (CHCl₃) ≥ 99.8%, analytical grade of ethanol (CH₃CH₂OH) ≥ 99.8%, acetone (CH₃COCH₃) ≥ 99.5%, and acetonitrile (CH₃CN) ≥ 99.9% were used as dispersive solvents and were purchased from Sigma Aldrich (Baghdad, Iraq). Dichloromethane (CH₂Cl₂) ≥ 99.5%, chloroform (CHCl₃) ≥ 99.8%, and carbon tetrachloride (CCl₄) 99.5% were used as extraction solvents and were obtained from VWR (Leicestershire, England). Solutions were prepared in double-distilled water. Other required salts were of > 98% purity.

Instrumentation

A Cary 100 double-beam UV-Vis spectrophotometer (Mulgrave, Victoria, Australia) with 1 cm matched quartz cells was used for all spectrophotometric measurements. pH measurements were carried out with an EA940 pH meter supplied with a stainless steel micro pH probe from Orion (Beverly, MA, USA); calibration buffers of pH 4.0, 7.0, and 10.0 were purchased from VWR (Batavia, USA). A DT-2234A+ ONPhoto, Shenzhen Liweihui (Guangdong, China) digital tachometer was used to regulate the rpm speed of centrifugation. A Genie 2 vortex mixer (Scientific Industries, Inc., Bohemia, NY6), an Elmasonic S 300 bath sonicator, Elma (Singen, Germany), and a Corning (Tewksbury, MA, USA) LSE TM Compact centrifuge holding 6 × 15 mL centrifuge tubes and having a maximum speed of 6000 rpm, were used to enhance phase separation. Eugenol was weighed by the Sartorius Analytic MC1 balance (Sartorius, Göttingen, Germany).

Procedure

General derivatization procedure

Aliquots of a sample containing 0.25–2.5 mg of eugenol were transferred into a series of 50 mL standard flasks. A volume of 1.5 mL of 10 mM PADA solution, 1.5 mL of 20 mM potassium hexacyanoferrate(III) and 1.5 mL of 100 mM potassium hydroxide solution were added in that order. The contents of the flasks were brought to volume with distilled water, mixed well, and left to stand for 5 min. The absorbance was measured at 600 nm (at room temperature 25 °C) against a reagent blank containing all materials except eugenol. A calibration curve was plotted, and the regression analysis data were obtained (Table 1).

General DLLME procedure

In a 16 mL plastic sealed centrifuge tube, 14 mL of the formed, colored derivative solution was transferred. Then, 550 μ L of chloroform as the extracting solvent was added to this solution, followed by the addition of 100 μ L of methanol as a dispersive solvent and 132 μ L of 3 M sodium chloride as a salt. After shaking by hand, a cloudy dispersion of the solvent mixture was formed, which was centrifuged for 20 min at 2500 rpm. Finally, 450 μ L of the organic phase was transferred by syringe into a micro-cuvette for spectrophotometric determination of eugenol at 618 nm. A calibration curve was plotted, and the regression analysis data were obtained (Table 1).

Analysis of commercial personal-care products

Eugenol was determined in different samples of mouthwashes, hand washes, and cosmetics. The samples were analyzed according to the proposed method, and sample dilution was applied for samples with eugenol concentration above the linearity range. The samples were determined by the general derivatization and extracted by the DLLME procedure. Spiked samples were prepared for recovery determination by adding 0.5 mL of 10 μ g.mL⁻¹ of eugenol [24].

■ RESULTS AND DISCUSSION

Eugenol was determined by two consecutive methods: the first was the direct spectrophotometric measurement based on derivatization via an oxidative

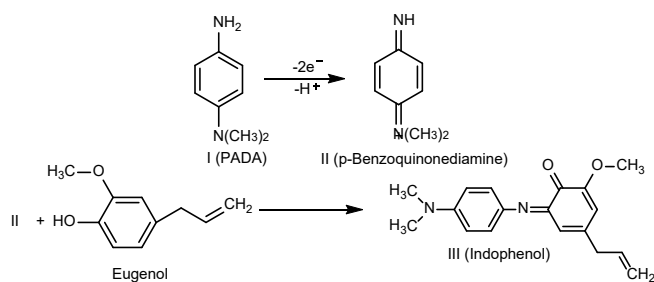
coupling reaction. The second utilized the DLLME procedure for the extraction of the derivative into a small volume of organic solvent. The optimum parameters of both methods were achieved. For the direct oxidative coupling method, optimization included the type and concentration of the oxidant and base in addition to the concentration of the coupling reagent and the order of additions. On the other hand, optimization of the DLLME involved the type and volume of the extraction solvent and dispersive solvent, the type and concentration of the salt solution, and the speed and time of centrifugation.

The results confirmed the success of both methods as inexpensive and highly accurate, sensitive methods for the determination of eugenol in different pharmaceutical and medical preparations. The combination of DLLME with the known advantage of the direct oxidative coupling method gave an additional advantage in decreasing both the sample volume and the reagent consumption, increasing the sensitivity and selectivity by using a selective derivatization reagent, i.e., *para*-amino-*N,N*-dimethylaniline.

Optimization Study of Derivatization Reaction

The oxidative coupling reaction mechanism was proposed by Faust and Anderson [25], in which a colored dye containing a quinone imine structure is produced. The oxidized form of the amino group of PADA produced by K₃Fe(CN)₆, i.e., the imino cation, couples with the eugenol phenolic ring via an electrophilic attack at the *para*-position [26]. The λ_{max} of *p*-quinoid chromophore formed was shifted into the visible region as a blue-colored solution was formed [27] (Scheme 1).

The optimization of the experimental parameters affecting the formation of the colored product was carried out when an aliquot of eugenol standard solution containing 1.642 mg was mixed with 0.2 mM coupling reagent in a final volume of 50 mL. The type and concentration of the oxidant used were studied, including hexacyanoferrate, potassium iodate, potassium permanganate, potassium dichromate, ammonium thiosulfate, and sodium paraperiodate (data shown for the latter five oxidants in Supplementary Material Fig. A).



Scheme 1. The proposed mechanism of eugenol coupling [26]

The study shows 0.6 mM hexacyanoferrate was optimal for 0.2 mM eugenol (Fig. 1) when the reaction medium was rendered alkaline with a 2 mM solution of ammonium hydroxide.

The absorbance decreased at low and high concentrations of hexacyanoferrate. The decrease at low concentration may be due to the interference from unreacted materials. The decrease at high concentration may be due to the formation of side products of the reaction and a bathochromic spectral shift effect [28]. Amine reagent oxidation can occur at too high concentrations of $K_3Fe(CN)_6$ [27].

Moreover, the alkaline medium accelerates the oxidative coupling by deprotonating the anilinium group [26]. Amongst various bases, including sodium hydroxide, ammonium hydroxide, potassium hydroxide, and sodium carbonate, a final concentration of 3 mM potassium hydroxide was selected (Fig. 2) to provide the optimum reaction medium since higher amounts of base led to a decrease in the color intensity of the extracted product (data are given in Supplemental Fig. B for bases other than KOH). PADA concentration was optimized in the range of 0.02–0.6 mM (Fig. 3), and the concentration of 0.3 mM was chosen for the optimum concentration equivalent to 0.2 mM of eugenol. Despite the stoichiometric requirement for PADA:eugenol of 1, excess of the oxidized form of PADA can increase the anilinium attack. In any case, in the method being developed, the eugenol is an unknown, and there must be enough/excess PADA present to react with all of the eugenol expected [29]. Finally, to investigate the behavior of the oxidative coupling reaction of eugenol with PADA, the order of reagent addition was investigated to achieve

the best sequence of the addition of reactants. The order of analyte, coupling reagent, oxidant, and then the base was selected and maintained throughout the experiment (data are given in Supplementary Material Table A). This

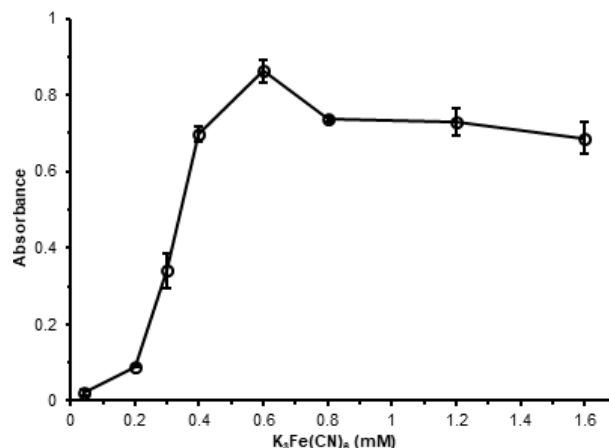


Fig 1. Hexacyanoferrate optimization. Conditions: Eugenol and PADA 0.2 mM, ammonium hydroxide 2 mM

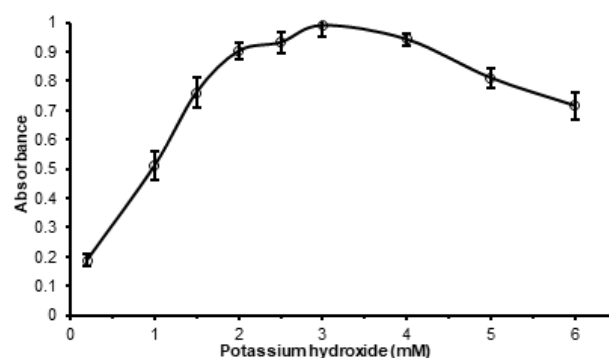


Fig 2. Potassium hydroxide optimization. Conditions: eugenol and PADA 0.2 mM, hexacyanoferrate 0.6 mM

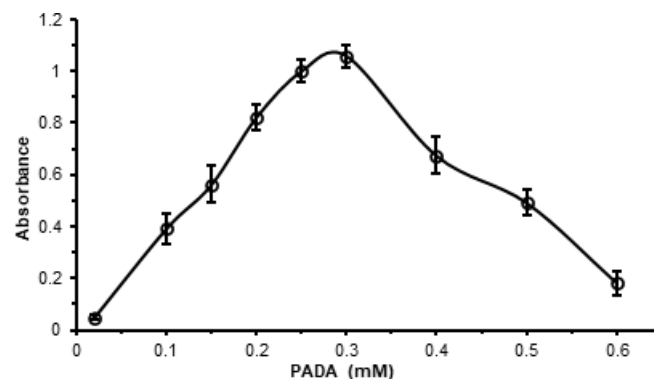


Fig 3. PADA optimization. Conditions: eugenol 0.2 mM, hexacyanoferrate 0.6 mM, potassium hydroxide 3 mM

order confirmed the rapid coupling of the reactants. The chromophore formed shows reasonable stability versus time, no significant change in its absorbance was observed in 1 h after dilution to the final volume.

Optimization of DLLME Method

In comparison to the direct measurement of eugenol, an efficient extraction (with respect to extraction selectivity, sensitivity, and low detection limit) was possible with the derivatized analyte (i.e., its oxidative coupling product). The optimum conditions for the extraction were established by variation of the type and volume of the extraction solvent, dispersive solvent, and the salt used, in addition to the centrifugation time and speed.

A number of water-immiscible organic solvents with different densities than water and good abilities for analyte solvation were tested to achieve the best extraction [30]. The solvents were added to 14 mL of the derivatization reaction mixture from 0.2 mM eugenol. 350 μ L of 1,2-dichloroethane, chloroform, or carbon tetrachloride was tested, using 25 μ L of acetone as the dispersive solvent and 94 μ L of 3 M potassium chloride, i.e., 20 mM final concentration of the salt. Among them, 1,2-dichloroethane was chosen in terms of the distribution ratio "D" since the order in which the D-value decreased was 1,2-dichloroethane > chloroform > carbon tetrachloride (data in Supplementary Material Fig. C). Using this solvent led to a redshift in the value of λ_{\max} of eugenol from 600 nm (in water) to 618 nm (in 1,2-dichloroethane).

The next step was to examine the optimum volume of the organic phase) in the range of 50–950 μ L (with 14 mL of the derivatization reaction mixture from 0.2 mM eugenol) to achieve the highest D-value and a reasonably good enrichment factor (EF). A volume of 550 μ L was chosen (data for 1,2-dichloroethane, Fig. 4) as the best volume in terms of D and EF, and this volume is appropriate for subsequent spectrophotometric analysis or HPLC. The potency of different dispersive solvents towards the extraction efficiency, namely, ethyl acetate, ethanol, methanol, acetone, and acetonitrile, was investigated (data are given in Supplementary Material

Fig. D). The investigation showed that the value of D was in the order of methanol > acetone > ethyl acetate > acetonitrile > ethanol; therefore, methanol was chosen to promote the extraction. Different volumes of CH₃OH (5–500 μ L) were tested (Fig. 5), and a volume of 100 μ L of the dispersive solvent was found to be optimal. Higher volumes tended to decrease the extraction efficiency, which could be attributed to an increase in the dye solubility in the aqueous phase.

Generally, the ionic strength or salt effect tends to decrease the solubility of analytes in the aqueous phase and tends to increase the water immiscibility of organic solvent [30]. Therefore, the ionic strength of the aqueous phase was adjusted to increase the extraction yield. This was accomplished by examining the effect of the presence of the three salts (potassium chloride, sodium

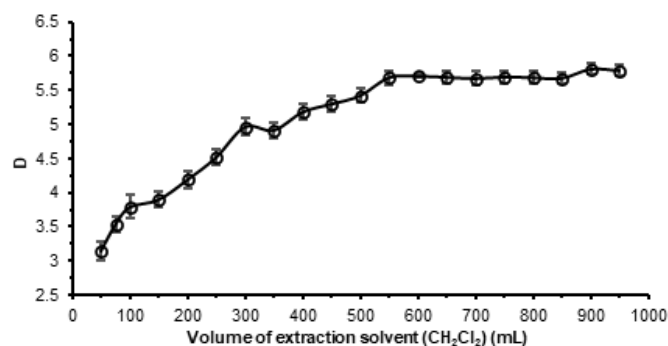


Fig 4. DLLME extraction solvent volume study. Conditions: eugenol 0.2 mM, dispersive solvent (acetone) 25 μ L, aqueous phase (dye) 14 mL, KCl 20 mM, centrifugation 5 min at 1100 rpm

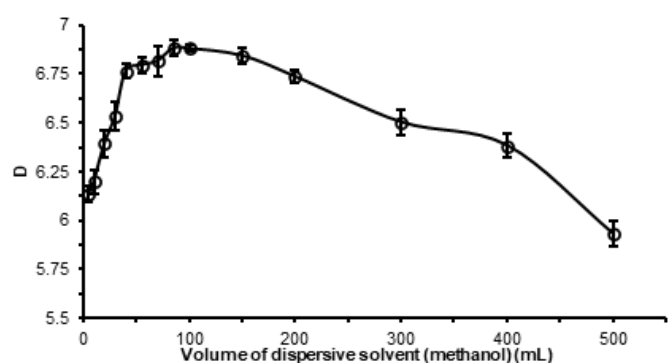


Fig 5. DLLME dispersive solvent volume study. Conditions: eugenol 0.2 mM, extraction solvent 550 μ L, aqueous phase (dye) 14 mL, KCl 20 mM, centrifugation time 5 min and centrifugation speed 1100 rpm

chloride, and ammonium sulfate) on the value of *D* (data are given in Supplementary Material Fig. E). The order of the *D* values was sodium chloride > potassium chloride > ammonium sulfate. Then, sodium chloride at different final concentrations (2–60 mM) was examined. Although the presence of the salt showed no great effect on the value of the distribution ratio (Fig. 6), 28 mM was chosen as the best concentration.

The separation of phases in DLLME is generally carried out by centrifugation. Moreover, the centrifugal force can affect the partitioning of dye between the aqueous and organic phases and the mass transfer activity [13,31]. Both the time needed to attain the best phase separation and the centrifugation speed required for that purpose were studied, Fig. 7, showing that 2500 rpm for 20 min was enough to attain quantitative separation.

Finally, different methods of reagent mixing (i.e., hand mixing, ultrasound mixing, and vortexing) experiments were conducted. The results (data are given in Supplementary Material Fig. F) proved that no difference in extraction efficiency was obtained; hence, hand mixing was preferred for convenience.

Calibration Curve and Validation Study

Table 1 shows a summary of regression parameters and other optical characteristics and statistical data of the developed methods. As expected, the method based on DLLME was applicable to a lower concentration range of eugenol due to the preconcentration of the analyte. Moreover, the liquid-liquid microextraction method shows a higher value of ϵ_{\max} and hence a lower detection limit.

Analytical Application

The application of the method for determining eugenol in commercial personal-care products was tested

(Table 2) using the DLLME procedure because of its selectivity, ability to decrease the matrix effect, and high molar extinction coefficient (Table 1). Although the direct method is simpler and the DLLME method is a longer procedure, Table 1 shows the superiority of the

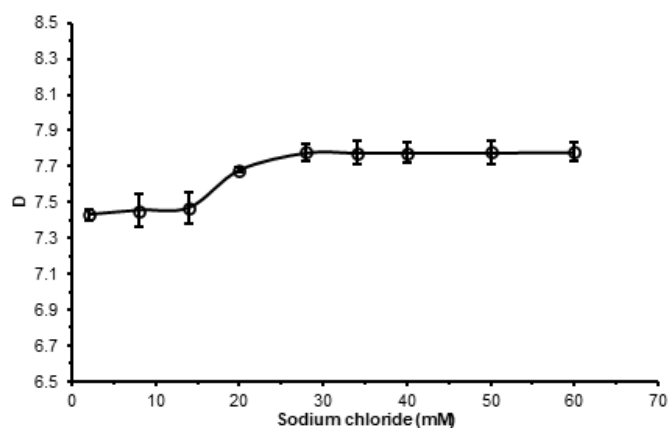


Fig 6. DLLME effect of sodium chloride. Conditions: eugenol 0.2 mM, extraction solvent 550 μ L, dispersive solvent 100 μ L, aqueous phase (dye) was 14 mL, centrifugation time 5 min and centrifugation speed 1100 rpm

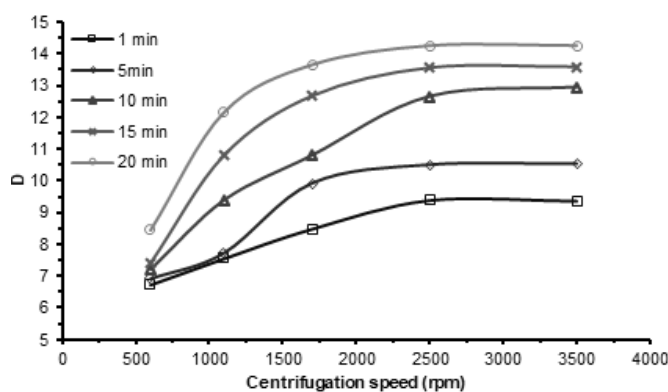


Fig 7. DLLME centrifugation speed and time study. Conditions: eugenol 0.2 mM, sodium chloride 28 mM, extraction solvent 550 μ L, dispersive solvent 100 μ L, aqueous phase (dye) 14 mL

Table 1. Regression equation, correlation coefficient, linear range, LOD, LOQ, and molar absorptivity of the proposed method*

Method	Slope	y-intercept	Correlation coefficient	Linear range ($\mu\text{g}\cdot\text{mL}^{-1}$)	LOD ($\mu\text{g}\cdot\text{mL}^{-1}$)	LOQ ($\mu\text{g}\cdot\text{mL}^{-1}$)	Molar absorptivity ($\text{L}\cdot\text{mol}^{-1}\cdot\text{cm}^{-1}$)
Derivatization reaction	0.0871 ± 0.0010	0.027 ± 0.002	0.9976	0.25–2.5	0.056	0.172	14300 ± 200
DLLME	0.1813 ± 0.002	0.0114 ± 0.002	0.9981	0.05–1.7	0.038	0.117	27800 ± 400

Table 2. Recovery (%) of proposed methods in the determination of eugenol in different products

Product Mouthwash	Proposed methods			
	Direct		DLLME	
	Conc. ($\mu\text{g.mL}^{-1}$)	Recovery (%) ^a	Conc. ($\mu\text{g.mL}^{-1}$)	Recovery (%) ^a
Zak	117	100.1 \pm 0.3	118	99.4 \pm 0.2
Kin	244	100.0 \pm 0.4	244	99.7 \pm 0.3
Paradontax Handwash	74.6	99.2 \pm 0.9	74.1	100.3 \pm 0.6
Lifeboy	17.5	99.8 \pm 0.8	17.6	100.7 \pm 0.7
Cosmetic Lakos	27.6	100.4 \pm 0.7	27.5	100.3 \pm 0.8

^a average of three replicates**Table 3.** Previous methods and proposed methods in the determination of eugenol

Method	Dynamic range ($\mu\text{g.mL}^{-1}$)	LOD ($\mu\text{g.mL}^{-1}$)	LOQ ($\mu\text{g.mL}^{-1}$)	Speed	Cost	Easiness	Application	Reference
HPLC amperometric detection	0.16–16.42	0.052	0.157	Low	High	Low	plants and pharmaceutical form	[17]
HPLC –UV	0.4–10	0.05	0.2	Low	High	Low	methanolic extracts of some spices	[19]
C18-RP-HPLC-PDA	5–1000	0.44	1.34	Low	High	Low	developed nanoemulsion gel and nanoparticles	[21]
HPTLC	200–1200	33.0	46.6	Low	High	Low	herbal extract of <i>Ocimum sanctum</i>	[16]
Voltammetric	2.5–202	0.62	2.1	Medium	High	low	essential oils	[20]
HPLC electrochemical detection	0.01–10	0.0097	0.032	Low	High	Low	aromatic plants	[18]
Oscillating system	0.082–2.052	0.0821		Medium	High	Medium	aq ethanol sample	[22]
Proposed methods								
Derivatization reaction	0.25–2.5	0.056	0.172	High	Low	High	personal-care products	
DLLME	0.05–1.7	0.038	0.117	High	Low	High	personal-care products	

DLLME method; therefore, it was chosen for the purpose of real sample analyses.

Pure samples of eugenol were analyzed, and the precision of the method was calculated. Recoveries were calculated by the spiked sample method. Good precision and recoveries were achieved. Due to the lack of accurate information about the mixture of substances present in personal-care products and the need to know the concentration of eugenol due to the importance of this compound as a biocide, the spiked samples method was used to calculate the accuracy.

Methods found in the literature for comparison are listed in Table 3; the listed information reveals that the proposed method can compete with the previous methods for the determination of eugenol in real samples. The

other methods mentioned in Table 3 are all accurate, but they suffer from disadvantages such as the need for high-cost equipment and the need for those devices for a longer period. By contrast, speed, cost, and ease of use are the advantages of the proposed method in comparison with previous ones Table 3.

■ CONCLUSION

In the proposed derivatization procedure, the concentration of the base used and the reagent were the most sensitive factors in forming the colored product. On the other hand, the speed and time of centrifugation, in addition to the volume of the organic phase, were the most critical factors that determined the value of the distribution ratio in the DLLME of the colored eugenol

derivative. Dispersive liquid-liquid microextraction, followed by spectrophotometric measurement, was successfully applied to determine eugenol in some locally available personal-care products. Because of the method sensitivity and low detection limit, the DLLME method could be applied to trace eugenol in samples, such as pharmaceutical and environmental samples. This method could be readily extended to analytes other than eugenol that can be oxidatively coupled to PADA.

■ ACKNOWLEDGMENTS

The authors extend their thanks and gratitude to the Department of Biology, University of Baghdad-College of Science, for their assistance, including the equipment, chemicals, bench space, and advice. This research did not receive any specific grant from funding agencies in the public, commercial, or not-for-profit sectors.

■ REFERENCES

- [1] Bonilla, J., Poloni, T., Lourenço, R.V., and Sobral, P.J.A., 2018, Antioxidant potential of eugenol and ginger essential oils with gelatin/chitosan films, *Food Biosci.*, 23, 107–114.
- [2] Adefegha, S.A., Okeke, B.M., Oboh, G., Ijomone, O.M., and Oyeleye, S.I., 2018, Modulatory effect of eugenol on arginase, nucleotidase, and adenosine deaminase activities of platelets in a carrageenan-induced arthritis rat model: A possible anti-arthritic mechanism of eugenol, *Biomed. Pharmacother.*, 106, 1616–1623.
- [3] Sakat, M.S., Kilic, K., Akdemir, F.N.E., Yildirim, S., Eser, G., and Kiziltunc, A., 2018, The effectiveness of eugenol against cisplatin-induced ototoxicity, *Braz. J. Otorhinolaryngol.*, 85 (6), 766–773.
- [4] Masghati, S., and Ghoreishi, S.M., 2018, Supercritical CO₂ extraction of cinnamaldehyde and eugenol from cinnamon bark: Optimization of operating conditions via response surface methodology, *J. Supercrit. Fluids*, 140, 62–71.
- [5] Novato, T., Gomes, G.A., Zeringóta, V., Franco, C.T., de Oliveira, D.R., Melo, D., de Carvalho, M.G., Daemon, E., and de Oliveira Monteiro, C.M., 2018, *In vitro* assessment of the acaricidal activity of carvacrol, thymol, eugenol and their acetylated derivatives on *Rhipicephalus microplus* (Acari: Ixodidae), *Vet. Parasitol.*, 260, 1–4.
- [6] Nejad, S.M., Özgüneş, H., and Başaran, N., 2017, Pharmacological and toxicological properties of eugenol, *Turk. J. Pharm. Sci.*, 14 (2), 201–206.
- [7] Filippou, O., Bitas, D., and Samanidou, V., 2017, Green approaches in sample preparation of bioanalytical samples prior to chromatographic analysis, *J. Chromatogr. B*, 1043, 44–62.
- [8] Abedi, G., Talebpour, Z., and Jamechenarboo, F., 2018, The survey of analytical methods for sample preparation and analysis of fragrances in cosmetics and personal care products, *TrAC, Trends Anal. Chem.*, 102, 41–59.
- [9] Kostopoulou, M., and Nikolaou, A., 2008, Analytical problems and the need for sample preparation in the determination of pharmaceuticals and their metabolites in aqueous environmental matrices, *TrAC, Trends Anal. Chem.*, 27 (11), 1023–1035.
- [10] Rundgren, I.M., Bruserud, Ø., Rynningen, A., and Ersvaer, E., 2018, Standardization of sampling and sample preparation for analysis of human monocyte subsets in peripheral blood, *J. Immunol. Methods*, 461, 53–62.
- [11] Nuckowski, Ł., Kaczmarkiewicz, A., and Studzińska, S., 2018, Review on sample preparation methods for oligonucleotides analysis by liquid chromatography, *J. Chromatogr. B*, 1090, 90–100.
- [12] Niu, Z., Zhang, W., Yu, C., Zhang, J., and Wen, Y., 2018, Recent advances in biological sample preparation methods coupled with chromatography, spectrometry and electrochemistry analysis techniques, *TrAC, Trends Anal. Chem.*, 102, 123–146.
- [13] Rykowska, I., Ziemblińska, J., and Nowak, I., 2018, Modern approaches in dispersive liquid-liquid microextraction (DLLME) based on ionic liquids: A review, *J. Mol. Liq.*, 259 (1), 319–339.
- [14] Wang, Q., Chen, R., Shatner, W., Cao, Y., and Bai, Y., 2018, State-of-the-art on the technique of dispersive Liquid-liquid microextraction, *Ultrason. Sonochem.*, 51, 369–377.

- [15] Mansour, F.R., and Danielson, N.D., 2018, Solvent-terminated dispersive liquid-liquid microextraction: A tutorial, *Anal. Chim. Acta*, 1016, 1–11.
- [16] Khan, N., and Ali, S.A., 2014, Quantitative determination of Eugenol in aqueous extract of *Ocimum sanctum* by high performance thin layer chromatography, *J. Pharm. Res.*, 8 (8), 1158–1161.
- [17] Aydoğmuş, Z., Yıldız, G., Yılmaz, E.M., and Aboul-Enein, H.Y., 2018, Determination of eugenol in plants and pharmaceutical form by HPLC with amperometric detection at graphene-modified carbon paste electrode, *Graphene Technol.*, 3 (1), 1–9.
- [18] Cantalapiedra, A., Gismera, M.J., Sevilla, M.T., and Procopio, J.R., 2014, Sensitive and selective determination of phenolic compounds from aromatic plants using an electrochemical detection coupled with HPLC method, *Phytochem. Anal.*, 25 (3), 247–254.
- [19] Inam, F., Deo, S., and Narkhede, N., 2014, HPLC – UV method development and quantification of eugenol from methanolic extracts of some spices, *Int. J. Chem. Phys. Sci.*, 3 (6), 92–102.
- [20] Ziyatdinova, G., Ziganshina, E., and Budnikov, H., 2013, Voltammetric sensing and quantification of eugenol using nonionic surfactant self-organized media, *Anal. Methods*, 5 (18), 4750–4756.
- [21] Pramod, K., Ilyas, U.K., Kamal, Y.T., Ahmad, S., Ansari, S.H., and Ali, J., 2013, Development and validation of RP-HPLC-PDA method for the quantification of eugenol in developed nanoemulsion gel and nanoparticles, *J. Anal. Sci. Technol.*, 4 (1), 16.
- [22] Hu, G., Zeng, Q., Hu, Y., Shen, X., and Song, J., 2014, Determination of eugenol by using a Briggs - Rauscher system catalyzed by a macrocyclic nickel (II) complex, *Electrochim. Acta*, 136, 33–40.
- [23] Marcos, J., and Pozo, O.J., 2015, Derivatization of steroids in biological samples for GC-MS and LC-MS analyses, *Bioanalysis*, 7 (19), 2515–2536.
- [24] Bueno, M., Zapata, J., and Ferreira, V., 2014, Simultaneous determination of free and bonded forms of odor-active carbonyls in wine using a headspace solid phase microextraction strategy, *J. Chromatogr. A*, 1369, 33–42.
- [25] Faust, S.D., and Anderson, P.W., 1968, Factors influencing the condensation of 4-aminoantipyrine with derivatives of hydroxybenzene—III. A study of phenol content in surface waters, *Water Res.*, 2 (7), 515–525.
- [26] Al-Abachi, M.Q., Haddi, H., and Al-Abachi, A.M., 2005, Spectrophotometric determination of amoxicillin by reaction with *N,N*-dimethyl-*p*-phenylenediamine and potassium hexacyanoferrate(III), *Anal. Chim. Acta*, 554, 184–189.
- [27] Fiamegos, Y.C., Stalikas, C.D., Pilidis, G.A., and Karayannis, M.I., 2000, Synthesis and analytical applications of 4-aminopyrazolone derivatives as chromogenic agents for the spectrophotometric determination of phenols, *Anal. Chim. Acta*, 403 (1–3), 315–323.
- [28] Fadhil, G., 2014, Spectrophotometric determination of thymol in pharmaceutical preparations via oxidative coupling reaction with 2,4-dinitrophenylhydrazine in the presence of potassium periodate, *Iraqi J. Sci.*, 55 (1), 27–34.
- [29] Barache, U.B., Shaikh, A.B., Lokhande, T.N., Anuse, M.A., Kamble, G.S., Gurame, V.M., and Gaikwad, S.H., 2017, Acid switched efficient, cost effective, selective separation and determination of selenium(IV), *J. Environ. Chem. Eng.*, 5 (5), 4828–4840.
- [30] Szarka, A., Turková, D., and Hrouzková, S., 2018, Dispersive liquid-liquid microextraction followed by gas chromatography-mass spectrometry for the determination of pesticide residues in nutraceutical drops, *J. Chromatogr. A*, 1570, 126–134.
- [31] Barreto, J.A., dos Santos de Assis, R., Cassella, R.J., and Lemos, V.A., 2019, A novel strategy based on in-syringe dispersive liquid-liquid microextraction for the determination of nickel in chocolate samples, *Talanta*, 193, 23–28.

Design of New Quinazoline Derivative as EGFR (Epidermal Growth Factor Receptor) Inhibitor through Molecular Docking and Dynamics Simulation

Herlina Rasyid¹, Bambang Purwono², and Harno Dwi Pranowo^{1,2,*}

¹Austrian-Indonesian Centre (AIC) for Computational Chemistry, Faculty of Mathematics and Natural Sciences, Universitas Gadjah Mada, Sekip Utara, Yogyakarta 55281, Indonesia

²Department of Chemistry, Faculty of Mathematics and Natural Sciences, Universitas Gadjah Mada, Sekip Utara, Yogyakarta 55281, Indonesia

* **Corresponding author:**

email: harnodp@ugm.ac.id

Received: June 18, 2020

Accepted: September 16, 2020

DOI: 10.22146/ijc.57012

Abstract: Erlotinib, Afatinib, and WZ4002 are quinazoline derivative compounds and classified as first, second, and third-generation EGFR inhibitor. All inhibitors have been given directly to cancer patients for many years but find some resistance. These three compounds are candidates as the lead compound in designing a new inhibitor. This work aims to design a new potential quinazoline derivative as an EGFR inhibitor focused on the molecular docking result of the lead compound. The research method was started in building a pharmacophore model of the lead compound then used to design a new potential inhibitor by employing the AutoDock 4.2 program. Molecular dynamics simulation evaluates the interaction of all complexes using the Amber15 program. There are three new potential compounds (A1, B1, and C1) whose hydrogen bond interaction in the main catalytic area (Met769 residue). The Molecular Mechanics Generalized Born Surface Area (MM-GBSA) binding energy calculation shows that B1 and C1 compounds have lower binding energies than erlotinib as a positive control, which indicates that B1 and C1 are potential as EGFR inhibitor.

Keywords: quinazoline; EGFR; molecular docking; molecular dynamics simulation

■ INTRODUCTION

Epidermal Growth Factor Receptor (EGFR) is a protein receptor that plays an important role in proliferation, angiogenesis, metastasis and inhibits the process of apoptosis in several types of cancer cells [1-2]. Excessive expression of this protein responsible for the growth of cancer cells [3-4]. One of the strategies to inhibit the excessive expression of the EGFR receptor is employing the small molecule tyrosine kinase inhibitors [5].

Quinazoline derivative is the group of compounds that have been widely used as EGFR inhibitor [6], such as erlotinib [7], gefitinib [8], afatinib [9], and WZ4002 [10]. Erlotinib and gefitinib are classified as the first-generation EGFR inhibitor. Both compounds have been given to cancer patients orally and show positive results in inhibiting the growth of cancer cells. However, after giving to patients for two years, resistance was found [11].

Afatinib is a second-generation inhibitor that showed good activity against EGFR T790M, but its activity decreased when given to patients who had previously received treatment with erlotinib and found some side effects such as diarrhea and skin rash [12]. Third-generation inhibitors provide activities around 30 to 100 times better on EGFR T790M mutation. However, this compound also showed resistance in the form of a change in the cysteine amino acid to be serine at position 797 (C797S) [13]. Since many resistances were found to the drug compounds that have been used, then the discovery of new drug candidates is continuously performed. One of the computational methods that can be used to design new drug compounds is molecular docking analysis.

Molecular docking is a method for predicting the orientation and conformation of a molecule when binding to another macromolecule to get a stable

complex structure [14]. Besides, molecular docking is also used to design a new inhibitor by using some molecules as a lead compound. Traxler et al. [15] employed a molecular docking method to design isoflavone and quinolone derivatives based on the pharmacophore model resulting from docking analysis on four lead compounds. The advantage of molecular docking in designing a new inhibitor does not require a large amount of data or only employ some molecules as the lead compounds. Previous research had designed quinazoline derivative compounds by using quantitative structure-activity relationship (QSAR) analysis in large data compounds [16–18] and studied the stability of hydrogen bond formed through compound and protein [19–22]. However, designing a new EGFR inhibitor using a molecular docking approach of the lead compounds such as erlotinib, afatinib, and WZ4002 has never been done. These lead compounds can be used as guidance in designing new compounds by observing the interaction of each compound in EGFR protein and then obtaining the new compounds with better activity. Thereby, this research focused on designing a new quinazoline derivative compound through the docking result of the lead compounds. The interaction stability of new design compounds is then evaluated through molecular dynamics simulation. The new potential compound will have interaction in the main catalytic area of EGFR protein and stable interaction which can be seen in lower binding energy value.

■ COMPUTATIONAL METHODS

Materials

The complex of EGFR protein against erlotinib (PDB ID: 1M17) was downloaded from <http://www.rcsb.org/structure/1M17>, afatinib, and WZ4002 as lead compounds.

Software

The program were used AutoDock 4.2 with the help of AutoDockTools [23], Gaussian 09 [24], GaussView 5.0, Discovery Studio Visualizer [25], UCSF Chimera 1.8.1 [26], and Amber15 with help of AmberTools16 [27], ChemDraw 15.0, and VMD 1.9.2 [28].

Procedure

Molecular docking analysis

There were three compounds used as the lead compound, i.e., erlotinib, afatinib, and WZ4002. These compounds were then prepared to dock by selecting the dock prep menu in Chimera software. The docking procedure was performed by using the AutoDock 4.2 program with the help of AutoDockTools, which started by saving the ligand file as a .pdbqt format. Grid box size was set to be $50 \times 50 \times 50$ Å center to ligand with spacing 0.375 Å. Each docking process was set to produce 10 conformations and then selected the best conformation with the lowest binding energy and correct conformation. A complex of protein and ligand was saved in a .pdb format file and visualized using Discovery Studio Visualizer program. Then, the pharmacophore model complied based on the interaction of the lead compound against EGFR protein to design a new EGFR inhibitor. There were three new compounds resulted (A1, B1, and C1), then modeled and optimized using DFT B3LYP/6-31G(d,p) method in Gaussian 09 software. The new compounds were docked into the EGFR protein active with the same grid size and spacing.

Molecular dynamics simulation

There were three new compounds (A1, B1, and C1) resulted from docking analysis (Fig. 1). These new compounds then evaluated their stability interaction against EGFR protein using the molecular dynamics simulation method. The simulation was proceeded by employing the Amber15 and AmberTools16 software package, applying the ff14SB force field.

Complex protein and ligand charges and other parameters are obtained using the RESP fitting procedure and the general AMBER force field (GAFF) [29]. The system was then solvated with a truncated octahedron box of 50661 water using the TIP3P water model [30] and neutralized by eight of Na⁺ ions as the counterions. The SHAKE algorithm was used to keep water molecules rigid.

Each system then subjected to 1000 steps of steepest descent minimization followed by 4000 steps of

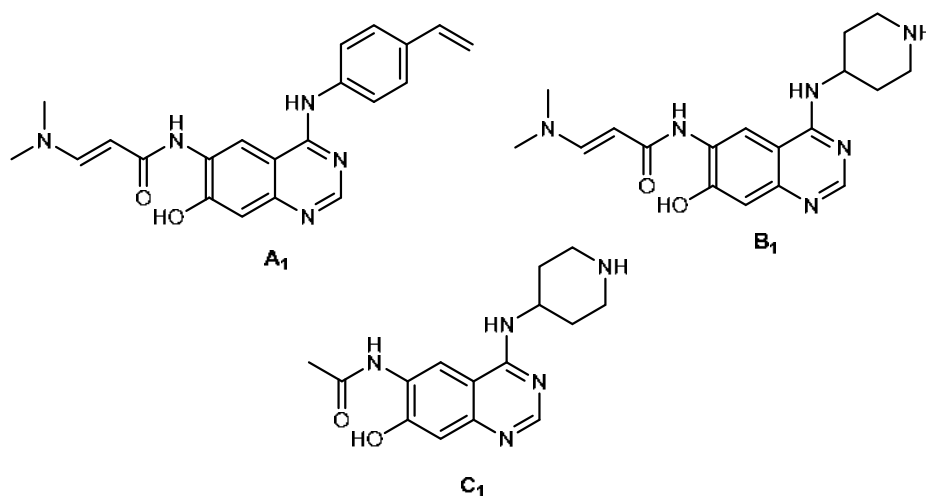


Fig 1. Structures of newly designed compounds A1; B1; and C1

conjugate gradient minimization. Complex protein and ligand were minimized by force constant of 100, 50, 5, and 0 (no constraint) kcal/mol Å⁻². There were 20000 steps in the minimization process.

Following minimization, the heating process was performed. The system was gradually heated from 0 K until 300 K and increase every 50 K in the NVT ensemble for 300 ps. Then continued to density equilibration with time step 2 fs for 300 ps simulation time. The pressure was set at 1 bar applying Berendsen barostat with a relaxation time of 1 ps and temperature was controlled using Langevin thermostat with a collision frequency of 1 ps⁻¹ and kept at 300 K. Then the system was relaxed for 500 ps before production data with time step 2 fs during 13 ns [31-32]. In all simulation steps, Particle Mesh Ewald (PME) [33] was computed with a non-bonded cut off of 12 Å. Binding energies were calculated from the MD trajectories using the PBSA module [34] in AMBER15. Every frame that resulted in the production step was utilized to calculate the binding energy of complex protein and ligand. MM-GBSA is typically used to validate earlier molecular docking and MD simulation result. Parameter descriptor of MM-GBSA, such as salt concentration, was set to be 0.1 M, and igb was set to be 2 in *sander* option. Trajectory analysis was done to confirm hydrogen bond distance, Radial Distribution Function (RDF), Root Mean Square Deviation (RMSD), Root Mean Square Fluctuation (RMSF), and binding energy of each

system. The stability of the complex is indicated by the low value of binding energy and the highest potential inhibitor from the stable complex protein-ligand.

RESULTS AND DISCUSSION

Design of Inhibitors

There are three compounds used as a lead compound in this work to design new EGFR inhibitors, which is erlotinib, afatinib, and WZ4002. These compounds have been proven as the first, second, and third generation of EGFR inhibitors [35]. The docking analysis from all the compounds is used to build a pharmacophore model for the EGFR inhibitors. Fig. 2 shows the 2D and 3D visualization of docking results from the lead compounds. 2D visualization displays that the lead compounds have a hydrogen bond with Met769 or Met793 residue and the additional bond with Cys797 residue for afatinib compound.

Some interactions were identified, such as van der Waals interactions, salt bridge, and pi-sigma stacking. 3D visualization of docking results present that all the compounds have fulfilled the cavity of protein EGFR. Using these docking results, potential inhibitors could be obtained with the following conditions: There is a hydrogen bond to the main catalytic residue that is Met769 or Met793, as well as an additional hydrogen bond to the Cys797 residue. This interaction is obtained from docking analysis of afatinib to the EGFR protein;

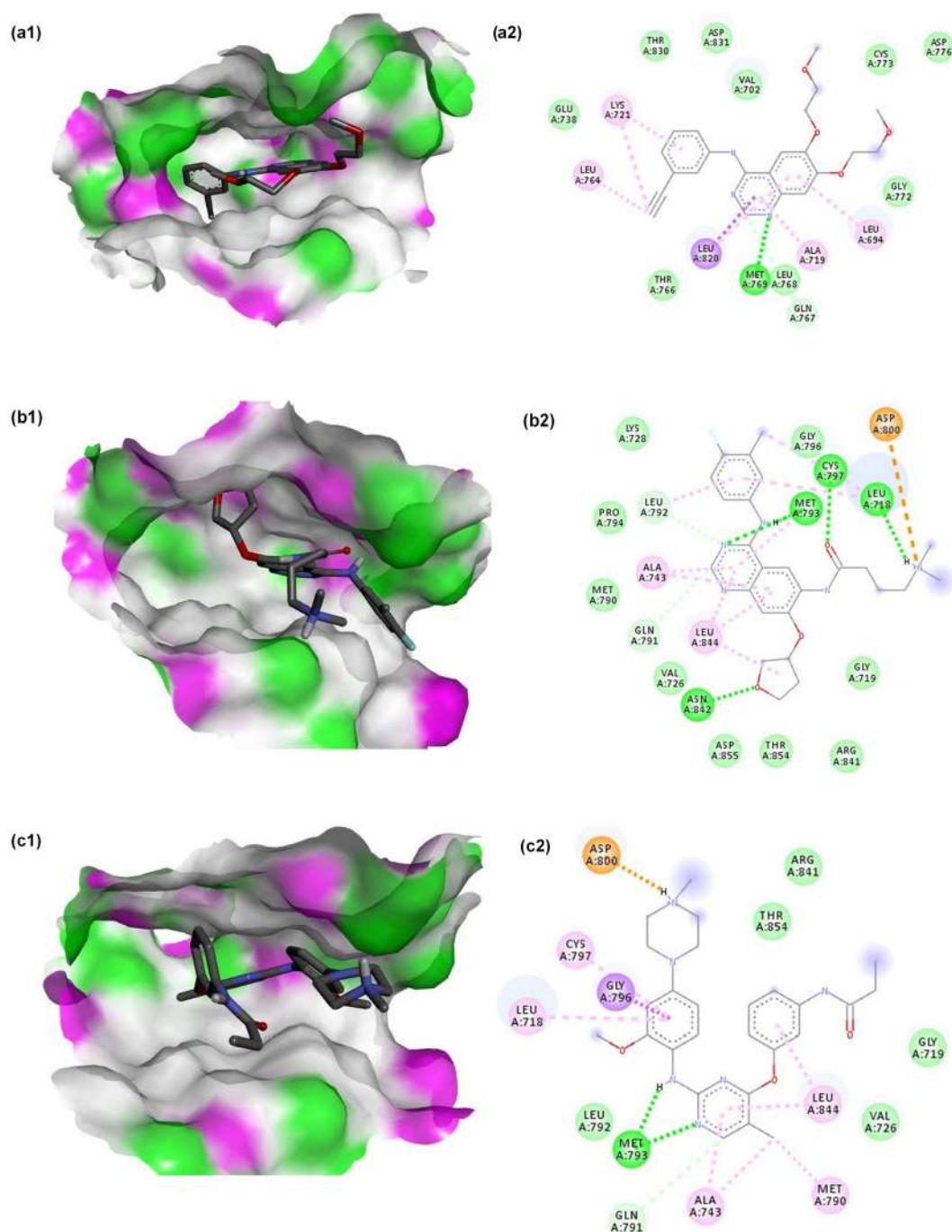


Fig 2. 3D and 2D interactions of (a1) and (a2) erlotinib, (b1) and (b2) afatinib, and also (c1) and (c2) WZ4002 against EGFR protein. Type of interactions: ■ van der Waals, ■ salt bridge, ■ conventional hydrogen bond, ■ carbon hydrogen bond, ■ pi-sigma, and ■ pi-alkyl

there is a -NH linker group and substitute with small groups to avoid steric obstruction. That linker belongs to all lead compounds that influence the accuracy of the lead compound conformations; there are functional groups that can form hydrophobic interactions. All lead

compounds have hydrophobic interactions with some EGFR protein residues, but it should be noted that this interaction should be formed in the hydrophobic region of EGFR protein. All these requirements have been in line with previous research [13,15,35-39].

be used as preliminary indications of whether the design compound better or not. Table 1 shows the docking score of each ligand, and it appears that the new design compound has a lower docking score indicating it has the potential to be a better inhibitor.

Molecular Dynamics Simulation

Hydrogen bond stability

Molecular dynamics simulation had been carried out through 13 ns simulation time for all new compounds against EGFR protein. Fig. 4 showed the hydrogen bond distance plot of compound A1 with some residues of EGFR. Interaction ligand A1 and EGFR before and after simulation showed similar interaction despite different residual numbers due to the renumbering system by the Amber program.

Two hydrogen bond interactions are in Met98 and Cys102 residues. The stable interactions resulting from compound A1(N) and Met98(H), which could be seen through the constant distance during simulation time, were about 2–3 Å. An additional hydrogen bond is also presented from compound A1(O) against Cys102(H) residue, and this belongs to weak interaction due to the distance during simulation time was about 4–5 Å. Fig. 5 showed the snapshot of complex A1 and residue of EGFR protein.

Hydrogen bond stability of compound B1 against EGFR showed a different result between docking results and molecular dynamics simulation. Docking result showed that ligand B1 interacted with Met769, Cys773, and Asp831. However, after simulation, B1 interacted with Met98 (supposed to Met769), Lys50, and Thr95. Fig. 6 presented the graph of hydrogen bond distance of B1 compound against amino acid residues Met98, Lys50, and Thr95. Stable interaction was obtained from B1(N) with

Met98(H) residue, while the other two interactions tend to be unstable. Interaction B1(N3) with Lys50(HZ3) had a high fluctuating distance of about 2 until 6 Å. Furthermore, B1(N1) and Thr95(HG1) interaction had

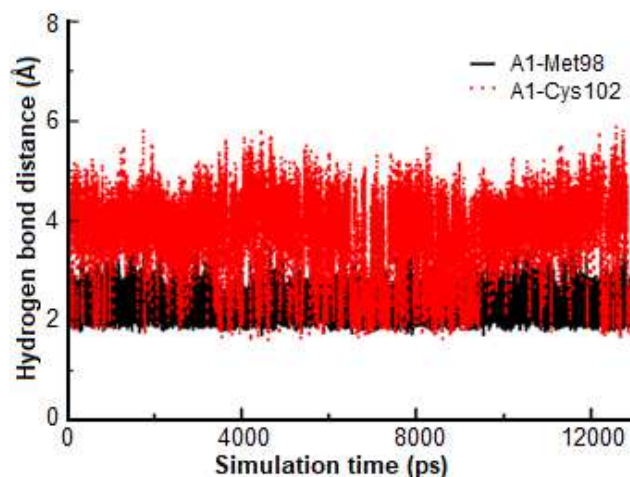


Fig 4. Hydrogen bond distance plot of compound A1 with EGFR protein

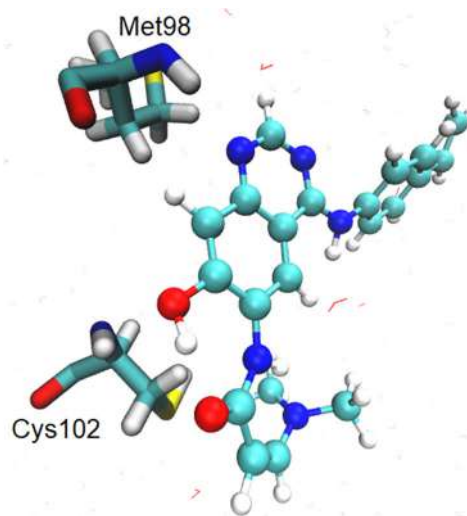


Fig 5. Snapshot of complex A1 and residue of EGFR protein in water

Table 1. Docking score value and hydrogen bond interaction of each ligand

Compound	Docking Score (kJ/mol)	Hydrogen bond interaction residue
Erlotinib	-20.2506	Met769
Afatinib	-25.0622	Met793; Cys797; Leu718; Asn842
WZ4002	-22.2589	Met793
A1	-25.5642	Met769; Cys773
B1	-29.3298	Met769; Cys773; Asp831
C1	-29.2043	Met769; Met769; Cys773; Asp831

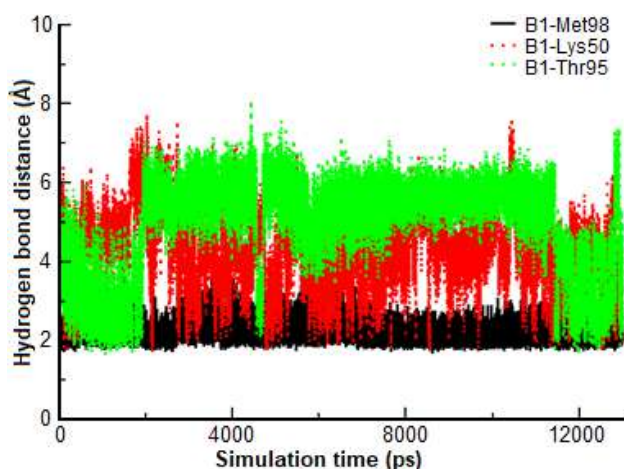


Fig 6. Hydrogen bond distance plot of compound B1 with EGFR protein

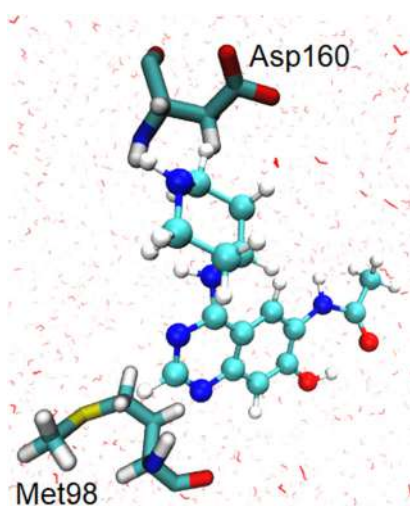


Fig 7. Snapshot of complex B1 and residue of EGFR protein in water

a fluctuating bond distance as well, about 2 until 7 Å. Fig. 7 showed the snapshot of compound B1 and the residue of EGFR protein.

There were four hydrogen bond interactions during simulation time between compound C1 against EGFR protein. One of the residues shown before simulation but disappeared after simulation time, that is Asp831 replaced by Glu67. Fig. 8 depicted the distance graph of each interaction. Hydrogen bond interaction of C1(N) with Met98(H) residue was formed at about 2 Å during the simulation time. Interaction C1(O1) and Cys102(H) appeared at about 4 until 8 Å, while interaction C1(H1) and Glu67(OE2) had a more stable distance about 2 until

4 Å. The other interaction, C1(N1) and Lys50(HZ3) showed a weak hydrogen bond interaction because the distance appeared at 2 until 6 Å. A snapshot of interaction compound C1 and residue of EGFR protein was performed in Fig. 9.

Stability analysis

All the design compounds were then evaluated for stability by RMSD and RMSF analysis for each compound compared with erlotinib as a standard and EGFR protein without any binding ligands.

This analysis was used to identify whether the three design compounds can improve the stability of EGFR protein compared to erlotinib and EGFR without the presence of ligands. Compounds that potential as EGFR

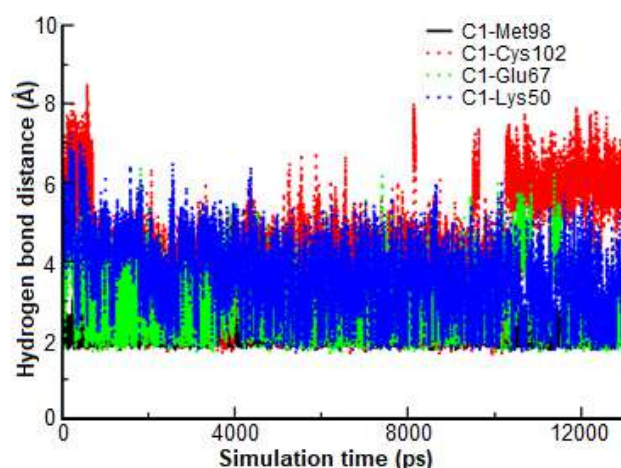


Fig 8. Hydrogen bond distance plot of compound C1 with EGFR protein

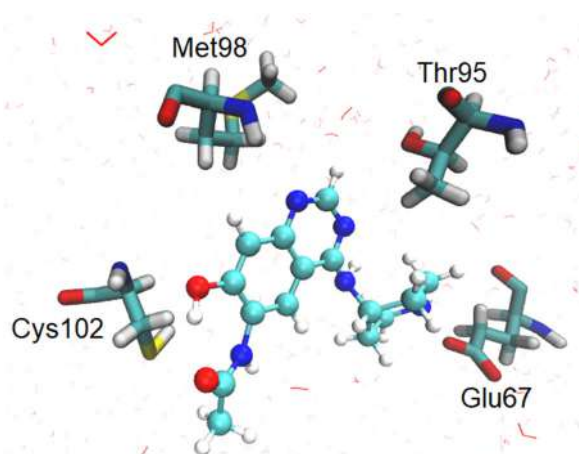


Fig 9. Snapshot of C1 complex and residue of EGFR protein in water

inhibitors are certainly expected to increase the stability of EGFR compared to erlotinib compounds that had been resistant to EGFR.

Fig. 10 represents an RMSD analysis for each complex ligand against EGFR protein. Compounds B1 and C1 showed the lowest RMSD compared to other compounds during simulation time. Both compounds showed increased stability toward the EGFR protein, which can be caused by the number of hydrogen bonds produced during the simulation time, which is greater than the hydrogen bond of compound A1. This result is also supported by RMSF analysis, where the lowest fluctuations based on residual numbers occurred in the complex B1 against EGFR protein (see Fig. 11).

MM-GBSA Binding Energy Calculation

Binding energy calculation of all complexes was exhibited by the MMGBSA method [34] (Eq. (1)). Table 2 showed the calculation result that ligand A1 and C1 have lower binding energy than erlotinib. Furthermore,

compound A1 had the lowest binding energy indicated that compound A1 is the potential to be an EGFR inhibitor.

$$\Delta G_{\text{binding}} = G_{\text{complex}}(i) - G_{\text{protein}}(i) - G_{\text{inhibitor}}(i)_i \quad (1)$$

CONCLUSION

The combination of docking and molecular dynamics simulation had been carried out to design new quinazoline derivatives compounds. Molecular docking was successful in designing new potential compounds using the pharmacophore model of lead compounds. There were three new potential compounds produced (A1; B1; and C1), and their interactions were evaluated via molecular dynamics simulation. The result of the simulation showed a more stable interaction between the A1 and C1 compounds. Furthermore, compound A1 exhibits the lowest binding energy result; about -164.4330 kJ/mol indicated that A1 is a potential compound as an EGFR inhibitor.

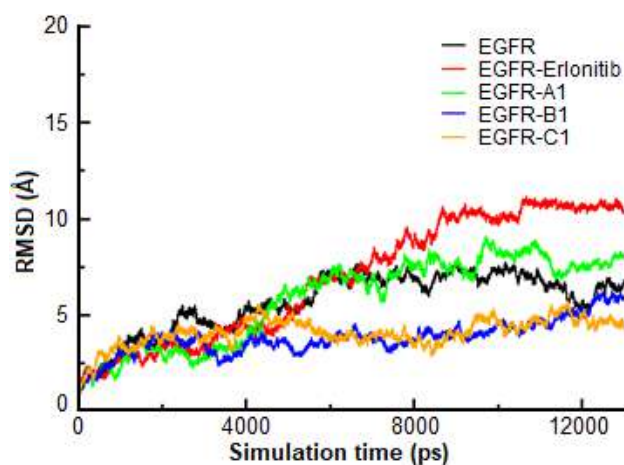


Fig 10. RMSD graph of EGFR and complex EGFR-ligand

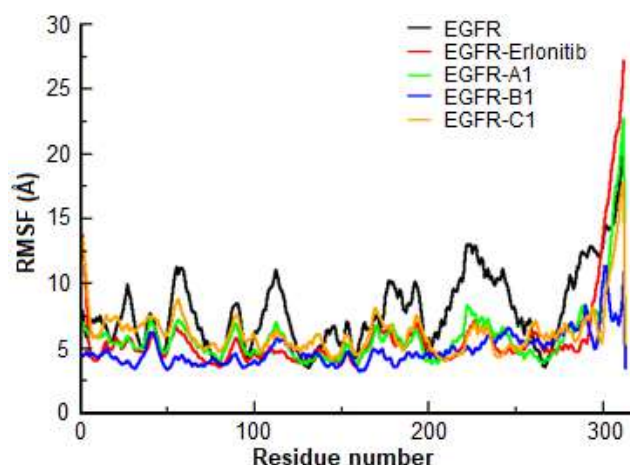


Fig 11. RMSF graph of EGFR and complex EGFR-ligand

Table 2. MMGBSA energy calculation result (kJ/mol)

Energy	A1	B1	C1	Erlotinib
Van der Waals	-208.7230	-171.5590	-189.4682	-209.7849
EEL	-102.9808	-140.8163	-89.6832	-97.6156
EGB	174.6008	189.5344	139.2376	171.8373
ESURF	-27.3190	-22.8948	-23.5304	-25.4303
ΔG_{gas}	-311.7038	-312.3753	-279.1514	-307.4005
ΔG_{solv}	147.2818	166.6396	115.7072	146.4070
$\Delta G_{\text{binding}}$	-164.4220	-145.7357	-163.4442	-160.9935

■ ACKNOWLEDGMENTS

H. Rasyid acknowledges a Ph.D. scholarship issued by the Ministry of Research, Technology, and Higher Education of the Republic of Indonesia (1511/E4.4/2015). Authors also acknowledge the Research Directorate of Universitas Gadjah Mada for research funding under the scheme of *Rekognisi Tugas Akhir* (RTA).

■ REFERENCES

- [1] Herbst, R.S., 2004, Review of epidermal growth factor receptor biology, *Int. J. Radiat. Oncol. Biol. Phys.*, 59 (2), S21–S26.
- [2] Vallbohmer, D., and Lenz, H.J., 2005, Epidermal growth factor receptor as a target for chemotherapy, *Clin. Colorectal Cancer*, 5 (Suppl. 1), S19–27.
- [3] Baselga, J., 2002, Why the epidermal growth factor receptor? The rationale for cancer therapy, *Oncologist*, 7 (Suppl. 4), 2–8.
- [4] Singh, M., and Jadhav, H.R., 2018, Targeting non-small cell lung cancer with small-molecule EGFR tyrosine kinase inhibitors, *Drug Discovery Today*, 23 (3), 745–753.
- [5] Ismail, R.S.M., Ismail, N.S.M., Abuserii, S., and Abou El Ella, D.A., 2016, Recent advances in 4-aminoquinazoline based scaffold derivatives targeting EGFR kinases as anticancer agents, *Future J. Pharm. Sci.*, 2 (1), 9–19.
- [6] Yu, H., Li, Y., Ge, Y., Song, Z., Wang, C., Huang, S., Jin, Y., Han, X., Zhen, Y., Liu, K., Zhou, Y., and Ma, X., 2016, Novel 4-anilinoquinazoline derivatives featuring an 1-adamantyl moiety as potent EGFR inhibitors with enhanced activity against NSCLC cell lines, *Eur. J. Med. Chem.*, 110, 195–203.
- [7] Chen, Y.M., Luo, Y.H., Wu, C., Lee, Y.C., Perng, R.P., and Whang-Peng, J., 2015, Erlotinib or chemotherapy in second-line or later treatment of tumor EGFR wild-type pulmonary adenocarcinoma patients, *J. Cancer Res. Pract.*, 2 (1), 3–11.
- [8] Teraishi, F., Kagawa, S., Watanabe, T., Tango, Y., Kawashima, T., Umeoka, T., Nisizaki, M., Tanaka, N., and Fujiwara, T., 2005, ZD1839 (Gefitinib, 'Iressa'), an epidermal growth factor receptor-tyrosine kinase inhibitor, enhances the anti-cancer effects of TRAIL in human esophageal squamous cell carcinoma, *FEBS Lett.*, 579 (19), 4069–4075.
- [9] Tu, Y., Ouyang, Y., Xu, S., Zhu, Y., Li, G., Sun, C., Zheng, P., and Zhu, W., 2016, Design, synthesis, and docking studies of afatinib analogs bearing cinnamamide moiety as potent EGFR inhibitors, *Bioorg. Med. Chem.*, 24 (7), 1495–1503.
- [10] Cheng, H., Nair, S.K., and Murray, B.W., 2016, Recent progress on third generation covalent EGFR inhibitors, *Bioorg. Med. Chem. Lett.*, 26 (8), 1861–1868.
- [11] Kobayashi, S., Boggon, T.J., Dayaram, T., Jänne, P.A., Kocher, O., Meyerson, M., Johnson, B.E., Eck, M.J., Tenen, D.G., and Halmos, B., 2005, EGFR mutation and resistance of non-small-cell lung cancer to gefitinib, *N. Engl. J. Med.*, 352 (8), 786–792.
- [12] Li, D., Ambrogio, L., Shimamura, T., Kubo, S., Takahashi, M., Chirieac, L.R., Padera, R.F., Shapiro, G.I., Baum, A., Himmelsbach, F., Rettig, W.J., Meyerson, M., Solca, F., Greulich, H., and Wong, K.K., 2008, BIBW2992, an irreversible EGFR/HER2 inhibitor highly effective in preclinical lung cancer models, *Oncogene*, 27 (34), 4702–4711.
- [13] Wang, S., Song, Y., and Liu, D., 2017, EAI045: The fourth-generation EGFR inhibitor overcoming T790M and C797S resistance, *Cancer Lett.*, 385, 51–54.
- [14] Huey, R., Morris, G.M., Olson, A.J., and Goodsell, D.S., 2007, A semiempirical free energy force field with charge-based desolvation, *J. Comput. Chem.*, 28 (6), 1145–1152.
- [15] Traxler, P., Green, J., Mett, H., Séquin, U., and Furet, P., 1999, Use of a pharmacophore model for the design of EGFR tyrosine kinase inhibitors: Isoflavones and 3-phenyl-4(1H)-quinolones, *J. Med. Chem.*, 42, 1018–1026.
- [16] Istyastono, E.P., 2017, Binary quantitative structure-activity relationship analysis to increase the predictive ability of structure-based virtual screening campaigns targeting cyclooxygenase-2, *Indones. J. Chem.*, 17 (2), 322–329.
- [17] Rasyid, H., Purwono, B., and Armunanto, R., 2018, Quantitative structure activity relationship (QSAR)

- based on electronic descriptors and docking studies of quinazoline derivatives for anticancer activity, *Orient. J. Chem.*, 34 (5), 2361–2369.
- [18] Pranowo, H.D., Tahir, I., and Widiatmoko, A., 2007, Quantitative relationship of electronic structure and inhibition activity of curcumin analogs on ethoxyresorufin o-dealkylation (EROD) reaction, *Indones. J. Chem.*, 7 (1), 78–82.
- [19] Rasyid, H., Purwono, B., Hofer, T.S., and Pranowo, H.D., 2019, Hydrogen bond stability of quinazoline derivatives compounds in complex against EGFR using molecular dynamics simulation, *Indones. J. Chem.*, 19 (2), 461–469.
- [20] Pitaloka, D.A.E., Damayanti, S., Artarini, A.A., and Sukandar, E.Y., 2019, Molecular docking, dynamics simulation, and scanning electron microscopy (SEM) examination of clinically isolated *Mycobacterium tuberculosis* by ursolic acid: A pentacyclic triterpenes, *Indones. J. Chem.*, 19 (2), 328–336.
- [21] Dwiastuti, R., Radifar, M., Marchaban, M., Noegrohati, S., and Istyastono, E.P., 2016, Molecular dynamics simulations and empirical observations on soy lecithin liposome preparation, *Indones. J. Chem.*, 16 (2), 222–228.
- [22] Arba, M., Sufriadin, M., and Tjahjono, D.H., 2020, Identification of phosphatidylinositol 3-kinase δ (PI3K δ) Inhibitor: pharmacophore-based virtual screening and molecular dynamics simulation, *Indones. J. Chem.*, 20 (5), 1070–1079.
- [23] Morris, G., and Huey, R., 2009, AutoDock4 and AutoDockTools4: Automated docking with selective receptor flexibility, *J. Comput. Chem.*, 30 (16), 2785–2791.
- [24] Frisch, M.J., Trucks, G.W., Schlegel, H.B., Scuseria, G.E., Robb, M.A., Cheeseman, J.R., Scalmani, G., Barone, V., Petersson, G. A., Nakatsuji, H., Li, X., Caricato, M., Marenich, A.V., Bloino, J., Janesko, B.G., Gomperts, R., Mennucci, B., Hratchian, H.P., Ortiz, J.V., Izmaylov, A.F., Sonnenberg, J.L., Williams-Young, D., Ding, F., Lipparini, F., Egidi, F., Goings, J., Peng, B., Petrone, A., Henderson, T., Ranasinghe, D., Zakrzewski, V.G., Gao, J., Rega, N., Zheng, G., Liang, W., Hada, M., Ehara, M., Toyota, K., Fukuda, R., Hasegawa, J., Ishida, M., Nakajima, T., Honda, Y., Kitao, O., Nakai, H., Vreven, T., Throssell, K., Montgomery, J.A., Jr., Peralta, J.E., Ogliaro, F., Bearpark, M.J., Heyd, J.J., Brothers, E.N., Kudin, K.N., Staroverov, V.N., Keith, T.A., Kobayashi, R., Normand, J., Raghavachari, K., Rendell, A.P., Burant, J.C., Iyengar, S.S., Tomasi, J., Cossi, M., Millam, J.M., Klene, M., Adamo, C., Cammi, R., Ochterski, J.W., Martin, R.L., Morokuma, K., Farkas, O., Foresman, J.B., and Fox, D.J., 2016, *Gaussian 16, Revision C.02*, Gaussian, Inc., Wallingford CT.
- [25] Dassault Systèmes BIOVIA, 2019, *Discovery Studio Visualizer v.20.1.0.19295*, Dassault Systèmes, San Diego, USA.
- [26] Pettersen, E.F., Goddard, T.D., Huang, C.C., Couch, G.S., Greenblatt, D.M., Meng, E.C., and Ferrin, T.E., 2004, UCSF Chimera—a visualization system for exploratory research and analysis, *J Comput Chem.*, 25 (13), 1605–1612.
- [27] Case, D.A., Betz, R.M., Botello-Smith, W., Cerutti, D.S., Cheatham, T.E., Darden, T.A., Duke, R.E., Giese, T.J., Gohlke, H., Goetz, A.W., Homeyer, N., Izadi, S., Janowski, P., Kaus, J., Kovalenko, A., Lee, T.S., LeGrand, S., Li, P., Lin, C., Luchko, T., Luo, R., Madej, B., Mermelstein, D., Merz, K.M., Monard, G., Nguyen, H., Nguyen, H.T., Omelyan, I., Onufriev, A., Roe, D.R., Roitberg, A., Sagui, C., Simmerling, C.L., Swails, J., Walker, R.C., Wang, J., Wolf, R.M., Wu, X., Xiao, L., York, D.M., and Kollman, P.A., 2016, *AMBER 2016*, University of California, San Francisco.
- [28] Humphrey, W., Dalke, A., and Schulten, K., 1996, VMD: Visual molecular dynamics, *J. Mol. Graphics*, 14, 33–38.
- [29] Wang, J., Wolf, R.M., Caldwell, J.W., Kollman, P.A., and Case, D.A., 2004, Development and testing of a general AMBER force field, *J. Comput. Chem.*, 25 (9), 1157–1174.
- [30] Jorgensen, W.L., Chandrasekhar, J., Madura, J.D., Impey, R.W., and Klein, M.L., 1983, Comparison of simple potential functions for simulating liquid water, *J. Chem. Phys.*, 79 (2), 926–935.

- [31] Mustafa, M., Mirza, A., and Kannan, N., 2011, Conformational regulation of the EGFR kinase core by the juxtamembrane and C-terminal tail: A molecular dynamics study, *Proteins Struct. Funct. Bioinf.*, 79 (1), 99–114.
- [32] Liu, B., Bernard, B., and Wu, J.H., 2006, Impact of EGFR point mutations on the sensitivity to gefitinib: Insights from comparative structural analyses and molecular dynamics simulations, *Proteins*, 65 (2), 346, 331–346.
- [33] Darden, T., York, D., and Pedersen, L., 1993, Particle mesh Ewald: An N log (N) method for Ewald sums in large systems, *J. Chem. Phys.*, 98 (12), 10089–10092.
- [34] Miller, B.R., McGee, T.D., Swails, J.M., Homeyer, N., Gohlke, H., and Roitberg, A.E., 2012, *MMPBSA.py*: An efficient program for end-state free energy calculations, *J. Chem. Theory Comput.*, 8 (9), 3314–3321.
- [35] Patel, H., Pawara, R., Ansari, A., and Surana, S., 2017, Recent updates on third generation EGFR inhibitors and emergence of fourth generation EGFR inhibitors to combat C797S resistance, *Eur. J. Med. Chem.*, 142, 32–47.
- [36] Stamos, J., Sliwkowski, M.X., and Eigenbrot, C., 2002, Structure of the epidermal growth factor receptor kinase domain alone and in complex with a 4-anilinoquinazoline inhibitor, *J. Biol. Chem.*, 277 (48), 46265–46272.
- [37] Hou, T., Zhu, L., Chen, L., and Xu, X., 2003, Mapping the binding site of a large set of quinazoline type EGF-R inhibitors using molecular field analyses and molecular docking studies, *J. Chem. Inf. Comput. Sci.*, 43 (1), 273–283.
- [38] Rabindran, S.K., Discafani, C.M., Rosfjord, E.C., Baxter, M., Floyd, M.B., Golas, J., Hallett, W.A., Johnson, B.D., Nilakantan, R., Overbeek, E., Reich, M.F., Shen, R., Shi, X., Tsou, H.R., Wang, Y.F., and Wissner, A., 2004, Antitumor activity of HKI-272, an orally active, irreversible inhibitor of the HER-2 tyrosine kinase, *Cancer Res.*, 64 (11), 3958–3965.
- [39] Eskens, F.A.L.M., Mom, C.H., Planting, A.S.T., Gietema, J.A., Amelsberg, A., Huisman, H., van Doorn, L., Burger, H., Stopfer, P., Verweij, J., and de Vries, E.G.E., 2008, A phase I dose escalation study of BIBW 2992, an irreversible dual inhibitor of epidermal growth factor receptor 1 (EGFR) and 2 (HER2) tyrosine kinase in a 2-week on, 2-week off schedule in patients with advanced solid tumours, *Br. J. Cancer*, 98 (1), 80–85.

Separation of Rhodamine B Dye from Aqueous Media Using Natural Pomegranate Peels

Zainab Mohammad Saigl^{1,*} and Arwa Mohammed Ahmed²

¹Department of Chemistry, Faculty of Science, King Abdulaziz University, P.O. Box 80203, Jeddah 21589, Saudi Arabia

²Department of Chemistry, Faculty of Science, Umm Al Qura University, Makkah, Saudi Arabia

* **Corresponding author:**

tel: +966-12-6952000 ext. 26546

email: zsaigl@kau.edu.sa

Received: August 14, 2020

Accepted: September 16, 2020

DOI: 10.22146/ijc.58592

Abstract: Natural pomegranate peels (PPs) ground powder was proved as effective natural biomass for the separation of RhB from different aqueous media by batch adsorption experiments. Several parameters that affect the maximum adsorption capacity toward RhB dye, e.g., the pH solution, initial dye concentration, adsorbent dosage, shaking time, and solution temperature in the sorption behavior, were studied. Adsorption of RhB dye from aqueous media of pH \approx 5 reached equilibrium in 10 min and was independent of the initial concentration of RhB. RhB dye sorption followed pseudo-second order kinetic with an overall rate constant (k_2) of $0.04 \text{ g mg}^{-1} \text{ min}^{-1}$. Furthermore, the sorption isotherm was found $31.95 \pm 0.02 \text{ mg g}^{-1}$ for the sorption capacity of RhB onto PPs. The thermodynamic parameters (ΔH , ΔS , and ΔG) of RhB retention by the sorbent were calculated. The positive value of ΔH confirms the endothermic behavior of the adsorption of RhB by PPs from aqueous solution. The positive value of entropy ($\Delta S = 42.17 \text{ J mol}^{-1} \text{ K}^{-1}$) of the sorption of RhB onto the sorbent surface may be attributed to the increase in the degree of freedom of the RhB molecules is more restricted in the PPs structure than in solution.

Keywords: adsorption; rhodamine B; natural pomegranate peels; kinetic; thermodynamic

■ INTRODUCTION

In recent years, water pollution is increasing tremendously, so accessing clean water and safe drinking water is important to protect the ecosystem and the health of its organisms. However, one sixth of the world's population needs access to pure water that is free of toxic organic and inorganic substances [1-2]. This situation is threatening the whole ecosystem on earth [3-5]. Furthermore, food additives such as food dyes are toxic, stable, and non-biodegradable [6]. Thus, the elimination of these dyes became a real concern because of their difficulties in the treatment processes, such as the treatment of wastewater by chemical and biological conventional methods [7]. These methods include: layer double oxides and hydroxides [8], sonochemical processes [9], coagulation [10], and adsorption [1,11-13]. However, adsorption process proved to be an effective

technique for the separation of these dyes from different matrices.

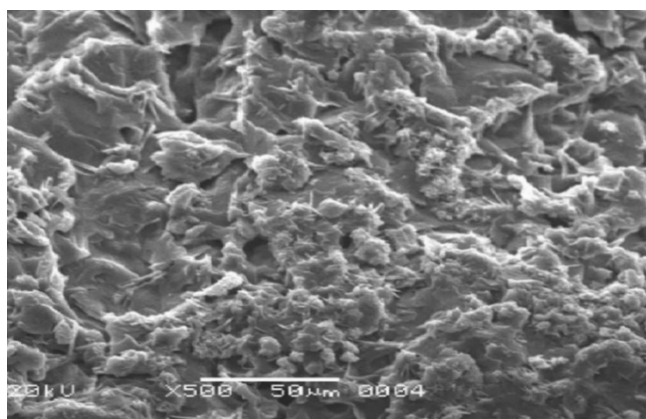
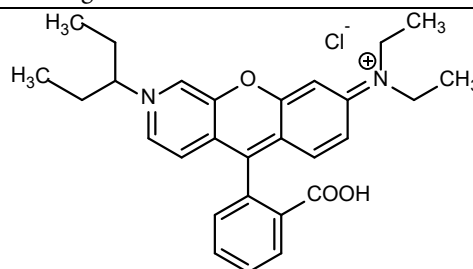
In general, various porous materials are often used to adsorb harmful chemicals and sequentially remove dyes from aqueous environments [14]. There are many examples, including nickel oxide nanoplates [11,15], clays [16], activated carbons [6,17], composites of hydroxyapatite with organic substrates, and graphene oxides [18]. Moreover, non-toxic and completely biodegradable natural fruits, flowers, roots, and leaves are used for removing inorganic dyes and toxic heavy metals [19-20]. The removal of RhB (Table 1), methylene blue, and acidic dye was carried by natural coal, orange peel, and coir pitch [21-22].

Pomegranate peels (PPs) were used as a cheap sorbent for separation of phenols [23], phenolic compounds [24], chromium(VI), nickel, and crude oil

Table 1. Selected properties of RhB dye

Common name	Rhodamine B
Chemical name	[9-(2-carboxyphenyl)-6-diethylamino-3-xanthenylidene]-diethylammonium chloride.
Chemical formula	C ₂₈ H ₃₁ ClN ₂ O ₃
Maximum wavelength	553 nm
Appearance	Red to violet powder
Molecular weight	479.02 g/mol

Structure

**Fig 1.** SEM image of waste PPs

from simulated produced water [25-26]. They have shown great efficiency in remediating polluted water sources by the adsorption of chloride ions [27] and malachite green [28]. Moreover, the raw pomegranate peel bio-sorbent was used for the copper removal [29]. Also, the simulated wastewater was treated by the adsorption of ciprofloxacin using the pomegranate peels and then characterized by different techniques such as Zeta sizer and scanning electron microscopy [30]. SEM image plays a significant role in understanding the key changes in the surface of biomass [31]. To understand the surface morphology via SEM, the morphological features of waste PPs are shown in Fig. 1 [31].

The goal of this quest is the removal of Rhodamine B, RhB, using natural pomegranate peels (PPs), which is

the most widely used in various textile- processing industries. This can be achieved by studying several parameters that affect the maximum adsorption capacity toward RhB dye, such as the pH solution, initial dye concentration, adsorbent dosage, shaking time, and solution temperature in the sorption behavior toward RhB dye. Moreover, the proposed method of adsorption using natural pomegranate peels (PPs) was performed and applied to real environmental samples in order to investigate its capacity for RhB uptake.

■ EXPERIMENTAL SECTION

Materials

All chemical solutions and organic solvents used were of analytical reagent grade quality. Deionizer distilled water (DDW) was used throughout the experiment. Pomegranate peels (PPs) were used as bio sorbent purchased from the local store in Jeddah, KSA. An accurate concentration, equal to 0.1 M, of sodium hydroxide from (NaOH) Merck, Germany, and 0.1 M Hydrochloric acid (HCl) from Fisher Scientific were used to adjust the pH of the RhB solution. RhB is a positive charge dye, purchased from Merck Millipore Corporation, Germany (% purity of RhB is 95%). The stock solution of 1000 mg L⁻¹ RhB (0.1 %w/v) was prepared by dissolving 0.1 g in 100 mL of DDW, then 10 mL of the previous solution was diluted with 100 mL

DDW to produce 100 mg L⁻¹ RhB stock solution. The standard solutions (0.5–80 mg L⁻¹) of the RhB stock solution were prepared with DDW.

Instrumentation

A Perkin Elmer (Lambda EZ-210) double beam spectrophotometer (190–1100 nm) with 1 cm (path width) quartz cell was used for recording the electronic spectrum of RhB and the absorbance measurements. A Corporation Precision Scientific mechanical shaker (Chicago, CH, USA) in which it's shaking rate is in the range 10–300 remand a thermostatically controlled shaker (GFL1083 model, Germany) were used in batch extraction experiments of RhB using PPs as sorbent. The sorbent was crushed with high speed cyclone mill (cT 193 cyclotec TM). DDW was gotten from Milli-Q Waters Plus system (Milford, MA, USA). A Thermo Fisher Scientific Orion model 720 pH Meter (Milford, MA, USA) was -in addition- used to prepare the stock and more diluted solutions of RhB and pH measurements, respectively.

Procedure

Preparation of pomegranate peels powder

The PPs (see Fig. 2) were used as a solid-phase extraction to adsorb RhB dye from water. The PPs were washed thoroughly with running tap water for several times to remove any external dust particles or impurities,

then washed with DDW to remove adhering dirt particles from the surface and dried overnight in a static air oven at 80 °C. Once it was completely dry, an electric grinder (ELEKTA-EFBG-1586 model) was used to crush and to grind the PPs into powder. The sorbent powder was sieved through a 53- μ m electric sieve (Nicomp Z380-USA). The PPs powder was stored for later uses in the experiments.

Recommended batch experiments

The adsorption study performed using 53 μ m particle size of the PPs to determine the effect of different parameters for the removal of RhB from aqueous solution. The experimental procedure was obtained by shaking a known weight (0.1 \pm 0.001 g) of PPS with 50.0 mL of (5.0 mg/L) RhB solution for 60 min on a mechanical shaker at room temperature.

After shaking, the PPs were filtrated by Whatman No. 5 qualitative filter paper. The filtrates were analyzed using a UV-Vis spectrophotometer at λ_{max} of 553 nm. The extraction percentage (% E), the uptake of RhB at equilibrium (q_e) per unit mass of solid sorbent (mg/g), and the distribution ratio (D) of RhB onto the PPs were evaluated using the following equations [32]:

$$\%E = \frac{A_b - A_a}{A_{fa}} \times 100 \quad (1)$$

$$q_e = (A_b - A_a) \times \frac{V(L)}{m(g)} \quad (2)$$



Fig 2. Dried PPs (a) and PPs powder (53 μ m) (b)

$$D = \left(\frac{\%E}{100} - \%E \right) \times \frac{V_{(mL)}}{m_{(g)}} \quad (3)$$

where; V represents the volume of the solution (mL), A_b and A_a are the absorbance before and after the extraction, respectively. The parameter (m) represents the mass of the sorbent (g). The extraction percentage (%E) and the distribution ratio (D) are the mean of three independent measurements. In addition, the precision in most cases was $\pm 0.2\%$.

To study the effect of pH, a series of solutions (50 mL) of 5 mg L^{-1} of RhB with an accurate weight ($0.1 \pm 0.001 \text{ g}$) of the PPs were adjusted to different pH values (1–10) in the presence of 0.1 M HCl and 0.1 M NaOH. The standard solutions of RhB were individually mechanically shaken for 60 min using a mechanical shaker at room temperature. The amount of RhB dye adsorbed per gram of the adsorbent at equilibrium (q_e , mg g^{-1}) and at pH values can be calculated, as previous from Eq. (2).

To examine the influence of PPs dose on sorption of RhB, series of aqueous solutions (50 mL) containing RhB at 5 mg L^{-1} level at optimum pH were also shaken for 60 min at room temperature with different weights ($0.1 - 0.8 \pm 0.001 \text{ g}$) of PPs. After shaking, the percent extraction of RhB that retained onto PPs was then determined from the absorbance at 553 nm before and after extraction using Eq. (1).

To study the effect of contact time on uptake of RhB from aqueous solution using the PPs, an accurate weight of the PPs ($0.1 \pm 0.001 \text{ g}$) was shaken with 5 mg L^{-1} of RhB concentration (50 mL) at the optimized pH for various time intervals up to 60 min at room temperature. After shaking, the amount of RhB retained onto PPs was then determined from the absorbance at 553 nm as before.

To investigate the effect of temperature on the RhB uptake onto PPs, 50 mL of RhB at 5 mg L^{-1} were shaken with PPs ($0.1 \pm 0.001 \text{ g}$) for 10 min at different temperatures (15–65 °C) in a mechanical shaker. Then adsorbents were filtrated, and the percent extraction of RhB that retained onto PPs solution was measured at 553 nm using Eq. (1).

To study the adsorption capacity of prepared adsorbent PPs under batch conditions, various

concentrations ($0.5 - 80 \text{ mg L}^{-1}$) of RhB in 50 mL aqueous solution at optimum parameters were individually mixed with the PPs ($0.1 \pm 0.001 \text{ g}$) and shaken for 10 min at room temperature. After shaking, the adsorption capacity (q_e , mg g^{-1}) was calculated from Eq. (2). The experimental adsorption isotherms data were calculated by classical adsorption isotherms.

Analytical applications

The environmental samples of water collected from Jeddah City, KSA, including tap water, drink water, seawater, and well water. The samples of tap water were acquired from the chemistry laboratory at King Fahd Medical Research Center, and the drink water samples were purchased from a local store, seawater sample collected from North beach in Jeddah.

The application was performed by filtrating the given 50 mL of each type of water through $0.45 \mu\text{m}$ cellulose membrane filter prior to analysis. A concentration of 5 mg L^{-1} RhB was then introduced to each type of water. The pH was adjusted again to 5 in the presence of an appropriate amount of natural sorbent and then was shaken separately for 10 min. All samples were analyzed using the standard addition method under the same batch conditions as described before, and the RhB dye amount retained was measured as described before.

RESULTS AND DISCUSSION

Retention Profile of RhB Dye onto PPs

Effect of different pH of the adsorption of RhB onto PPs

The most critical parameter that affects the RhB adsorption onto PPs ($53 \mu\text{m}$) surface is the pH of the solution where it controls the PPs surface charge. To investigate the pH effect on the PPs ($53 \mu\text{m}$) affinity toward RhB, different pH of samples solutions was studied through ranging from 2.00 to 9.00 (Fig. 3). Fig. 3 showed that the percentage of extraction depends on the pH of the solution. The value of pH from 2.00 to 5.00 increased the removal percentage of RhB dye from 67.4 to 89.8%, which indicates that PPs was most selective toward RhB at $\text{pH} \approx 5$. The extraction percentage of RhB onto PPs was calculated by Eq. 1.

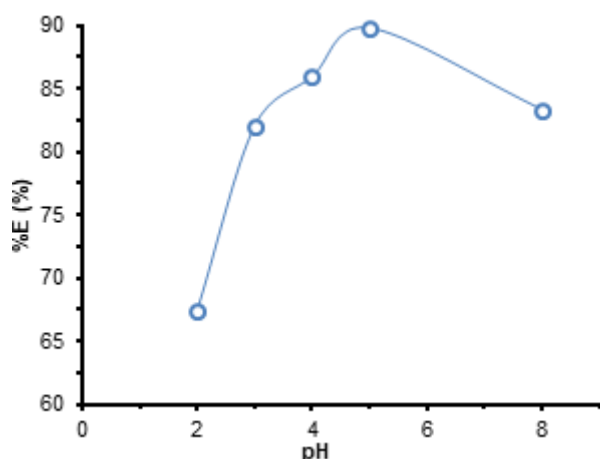
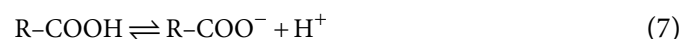


Fig 3. pH effect on the extraction percentage of RhB dye from aqueous solution using PPs after 60 min shaking at 25 °C

The low adsorption capacity at low pH values is the result of a competition between the cationic dye and hydrogen ions for the same active adsorption sites [33]. pH effect on the RhB interaction with the surface functional groups onto PPs has been clarified as follows:



where R represents the PPs surface; R-OH_2^+ , R-OH and R-O^- represent protonated, neutral, and ionized surface hydroxyl functional groups; R-O-RhB and R-COO-RhB are the formation of the bonding complexes. At $\text{pH} < 5$, the adsorption is unfavorable because of repulsive electrostatic interactions between cationic dye and positively charged functional groups [33]. At $\text{pH} \approx 5$, ion association has taken place between the negative charged surface of PPs and positive charge RhB molecules [34]. This shows that RhB molecules bind to hydroxyl and carboxyl groups that are found on the surface of PPs (Eq. (6), (8)). This proves that the principal adsorption mechanism for the removal of RhB dye could be the chemical ion exchange process [34-35].

Effect of different sorbent masses

The study of sorbent mass is necessary and very

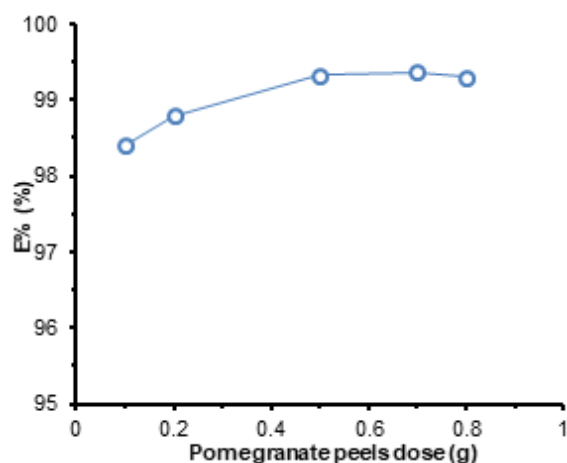


Fig 4. PPs dose effect on the sorption distribution of RhB dye (5 mg L^{-1}) from aqueous solution after 60 min shaking at $\text{pH} \approx 5$ and 25 °C

useful to find the optimum amount of sorbent required. The data represented in Fig. 4 indicated the sorption percentage of RhB slightly increased from 98.39 to 99.32% with increasing natural sorbent mass from 0.1 to $0.8 \pm 0.001 \text{ g}$ with 5 mg L^{-1} of RhB at $\text{pH} \approx 5$. This behavior belongs to the increasing of adsorption with increasing the mass of adsorbent can be attributed to higher adsorbent surface area and the obtainability of more adsorption sites [32]. In fact, Fig. 4 showed there is no significant difference. Therefore, 0.1 g was chosen for later removal studies. The extraction percentage of RhB was calculated by Eq. (1).

Effect of contact time

The influence of shaking time (0.0–75 min) on the retention of RhB (5 mg L^{-1}) from the aqueous media at $\text{pH} \approx 5$ by PPs was carried out at room temperature. The results are demonstrated in Fig. 5 in which the sorption of tested RhB onto PPs sorbent was fast and reached its maximum adsorption after 10 min of shaking time. Consequently, a 10 min shaking period was adopted in the subsequent experiments. In the primary stages, the separation of the RhB by PPs increased rapidly due to the presence of a large number of available surface sites for adsorption. By increasing time in the post-stage (plateau portion), the residual available surface sites are hard to be taken as a result of the repulsive forces between the RhB molecules on the sorbent and bulk phases [33].

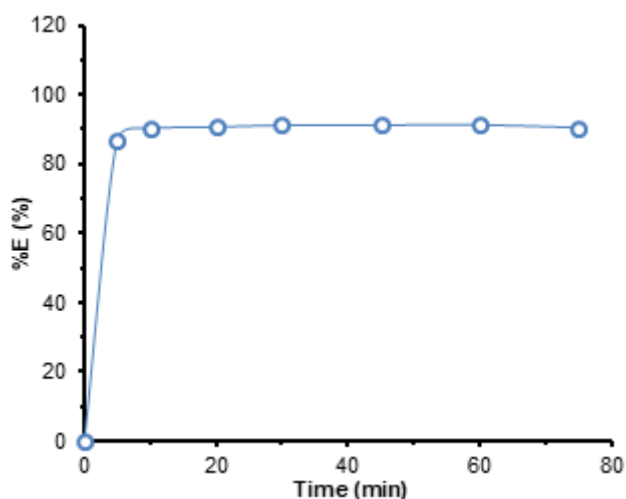


Fig 5. Time contact effect on the removal of RhB dye (5 mg L^{-1}) by 0.1 g PPs at $\text{pH} \approx 5$ and 25°C

Effect of different temperatures on the sorption of RhB dye onto PPs

The enthalpy and the entropy changes during adsorption were informatively studied as temperature dependence reactions [1,36]. The effect of solution temperature on the distribution ratio of RhB from aqueous solution using PPs observed in Fig. 6, which shows an increase of removal efficiency of RhB from 25 to 55°C due to the high mobility of RhB toward available binding sites onto PPs but the percentage extraction of RhB (5 mg L^{-1}) increased from 94.5 to 98.18% at $\text{pH} \approx 5$ that mean the adsorption process is an endothermic process in nature.

Effect of different concentrations of RhB dye

The effect of initial concentration on the extraction percentage of RhB by studied adsorbents was showed in Fig. 7. The experimental results showed that increasing the dye ion concentration from 0.5 mg to 80 mg L^{-1} causes decreasing in the removal percentage of RhB from 97.62 to 30.17%. The decrease of adsorption capacity with raising the initial RhB dye concentration is due to the competing of dye ions for available binding sites of adsorption and because of the possible aggregation of RhB molecules onto the solid phase extractor. At lower RhB dye concentration, the active sites more ability to saturate, and adsorption capacity approaches higher value [33]. Therefore, 5 mg L^{-1} of RhB was chosen for all later other experiments.

Sorption Isotherms of RhB Dye onto PPs

The mechanism of the interaction of RhB dye on the PPs surface was described by the sorption isotherms. The equilibrium studies contingent upon the nature of the sorption system is beneficial for calculating the maximum sorption capacity of the PPs toward RhB dye. They are also beneficial for determining some significant surface properties of the selected biomass [37-38]. At a wide range of concentrations RhB dye ($0.5\text{--}80 \text{ mg/L}$), the sorption behavior of RhB dye at $\text{pH} \approx 5$ onto PPs were investigated. At the perfect parameters, the plot of the amount of RhB retained (q_e) onto PPs versus their

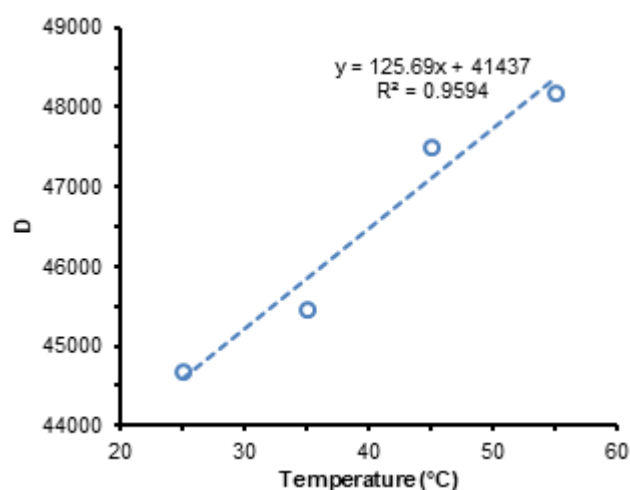


Fig 6. Various temperatures effect on the sorption of RhB dye (5 mg L^{-1}) at $\text{pH} \approx 5$ using 0.1 g of PPs after 10 min shaking

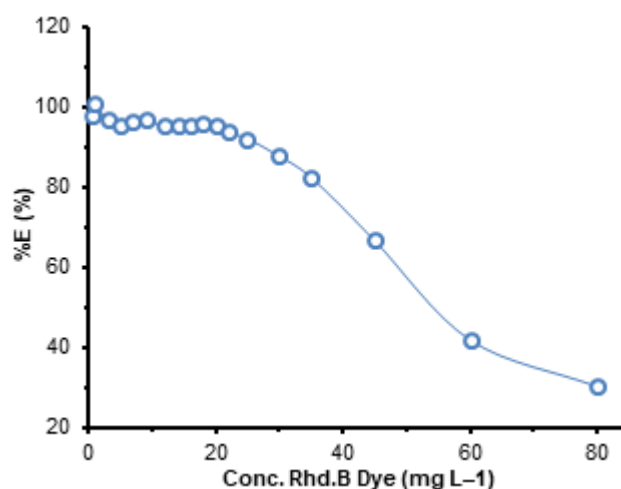


Fig 7. Initial concentration effect on the uptake of RhB dye at $\text{pH} \approx 5$ using 0.1 g of PPs after 10 min shaking

equilibrium concentrations in the bulk aqueous solution is shown in Fig. 8. The isotherm showed a strong RhB–PPs interaction. At low concentrations ($0.1\text{--}6\text{ mg L}^{-1}$) of RhB, a sharp rise in the RhB retained, followed by a slight increase at a concentration higher than 15 mg L^{-1} . This is due to the surface coverage of the PPs could be low, and the vacant vigorous sites of PPs are not completely occupied by RhB. On increasing analyte concentration, the linearity of the plot decreases because the surface coverage increases, and the available active sites of the PPs for RhB are limited. The sorption isotherm was found $31.95 \pm 0.02\text{ mg g}^{-1}$ for the sorption capacity of RhB onto PPs.

The equilibrium data were subjected to the adsorption isotherm models, e.g., Langmuir, Freundlich, and Dubinin–Radushkevich (D-R) over a wide range of equilibrium concentration through linear regression at optimum conditions [37–38]. Adsorption equilibrium is found when RhB contacted with the PPs for adequate time. The perfect close-fitting model is subjected to its agreeability to the experimental data with the correlation coefficient that is close to unity. The parameters data of the three isotherms studied models are represented in Table 2.

The uptake behavior of RhB dye from the aqueous solution onto PPs was subjected to the Langmuir model, which shows that a single layer of molecules on the PPs surface is adsorbed, so adsorption is restricted to a monolayer only. Since PPs surface is homogeneous, the adsorption energy is uniform for all sites. As a result, RhB doesn't transmigrate in the plane of the PPs surface. As an RhB dye occupies a site, no more adsorption can take place in that site, the intermolecular attractive forces a rapid decrease as distance increases. There is no interaction between RhB molecules adsorbed on adjacent sites, in which the adsorption is localized on the surface. Langmuir model is expressed by the following equation [39]:

$$C_e/q_e = C_e/q_m + 1/K_L q_m \quad (9)$$

where C_e is the concentration of adsorbate at equilibrium (mg L^{-1}), q_e is the equilibrium quantity of adsorbate per unit mass of the sorbent (mg g^{-1}), q_m is the monolayer maximum adsorption capacity of RhB per unit mass of sorbent (mg g^{-1}), and K_L is Langmuir constant related to the binding energy of RhB sorption (L mg^{-1}), which determined from the slope and intercept of linear plot

respectively, K_L can be correlated with the variation of the suitable area and porosity of the sorbent which indicates that large surface area and high pore volume will give a higher adsorption capacity.

The dimensionless constant separation factor R_L is expressing the essential characteristics of the Langmuir isotherm [40].

$$R_L = 1/1 + K_L C_0 \quad (10)$$

where K_L is Langmuir constant (mg g^{-1}), and C_0 is the initial concentration of adsorbate (mg g^{-1}). R_L values show the adsorption to be disapproving at $R_L > 1$, linear when $R_L = 1$, favorable when $0 < R_L < 1$, and irreversible when $R_L = 0$.

The plot of C_e/q_e versus C_e over the entire RhB concentration range, as seen in Fig. 9. The plot was linear with a good correlation factor ($R^2 = 0.994$), which indicates favorable adsorption. Moreover, the previous

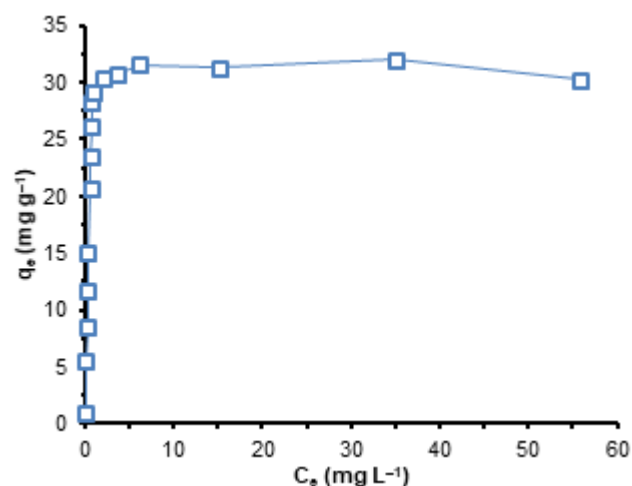


Fig 8. Sorption isotherm of RhB dye amount onto 0.1 g PPs at $\text{pH} \approx 5$ after 10 min shaking

Table 2. Isotherm models and their parameters for RhB dye sorption from model solution onto natural sorbent

Isotherm model	Parameter	Value
Langmuir	q_m (mg g^{-1})	7.37
	k_L (L g^{-1})	1.369
	R^2	0.994
Freundlich	k_f (L g^{-1})	25.22
	$1/n$	0.6766
D-R	R^2	0.9127
	E (kJ mol^{-1})	15.80
	R^2	0.9998

relation confirms that the characteristics of analyte adsorption onto the sorbent followed the Langmuir adsorption model. The Langmuir parameters q_m and K_L were calculated from the slope and intercept were found equal $7.37 \pm 1.0 \text{ mg g}^{-1}$ and 1.369 L mg^{-1} , respectively, the low value of K_L obtained indicated that PPs has a high affinity for RhB. Thus, PPs are most likely to contain fixed individual sites, each of which equally adsorbs only one RhB molecule forming a monolayer [29]. These data confirm that an added component for "surface adsorption" participated in RhB dye uptake. The dimensionless constant equilibrium parameter R_L of Langmuir isotherm is given by the Eq. (10), the adsorption of RhB on PPs is favorable adsorption as the R_L values obtained (0.09) at all initial concentrations lie between 0 and 1. This proposes the applicability of this PPs for RhB removal.

The Freundlich isotherm model is an empirical equation and another form of Langmuir that can be useful to multilayer adsorption. This model indicates that the surface of the adsorbent is heterogeneous in which the active sites and their energies distribute exponentially. Firstly, the stronger binding sites are occupied continuously up to the adsorption energy is exponentially decreased upon the completion of the adsorption process [35]. The linear form of the Freundlich model is expressed by the following equation:

$$\log q_e = \log K_F + 1/n \log C_e \quad (11)$$

where K_F is adsorption capacity (L mg^{-1}) and $1/n$ is adsorption intensity; it also shows the relative distribution of the energy and the heterogeneity of the adsorbate sites.

The value of slope ($1/n$) ranges between 0 and 1. If the value of ($1/n$) gets close to zero, the surface of the adsorbent becomes more heterogeneous, while a value of

($1/n$) that is above unity indicates unfavorable adsorption isotherms. Since the value of ($1/n$) is found to be 0.6766, which is more than 0.1, so the adsorption isotherm approaches irreversible isotherm. This isotherm did not much fit the experimental data ($R^2 = 0.9127$). The constants $1/n$ and K_F were attained from the slope and intercept of the linear plot were found equal 0.6766 and $25.22 \text{ mg g}^{-1} (\text{L mg}^{-1})^{1/n}$, respectively (Table 2). Moreover, the value of $1/n < 1$ indicates favorable adsorption isotherm for the sorption of RhB onto PPs sorbent. The value of n obtained (1.5) lies within this range, which implies that PPs have a high affinity for RhB in solution.

Moreover, the adsorption capacity of PPs for removal RhB dye was compared with many adsorbents peels that are summarized in Table 3. These data revealed that the natural PPs is an excellent extractor for selective separation of RhB at trace concentration levels from aqueous solutions.

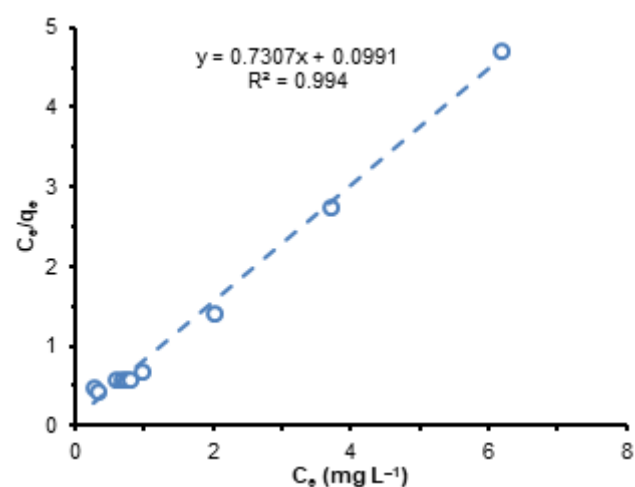


Fig 9. Langmuir sorption isotherm of RhB dye uptake onto 0.1 g PPs at $\text{pH} \approx 5$ after 10 min shaking

Table 3. Adsorption Capacity of natural adsorbents peels for removal RhB dye

Adsorbent	Conc. RhB, mg/L	q_m , mg/g (Langmuir)	Reference
Acid treated banana peel	20	9.52	[37]
Banana peel powder	25	3.8	[41]
Chestnut peel	20	2.97	[42]
Orange peel	10	3.23	[21]
Pomegranate peel	15	7.37	Present work

Kinetic Behavior of RhB Dye Adsorption onto PPs

Predicting the rate at which the sorption of pollutants occurs in a given system is one of the essential factors in the sorption system. Thus, determining the most probable kinetic mode for describing the analyte retention is subjected to pseudo-first-order and pseudo-second-order, which are the most common models to assign the retention step [37-38]. The data were subjected to the Lagergren model (pseudo-first-order) expressed by the following Lagergren model [43]:

$$\ln(q_e - q_t) = \log q_e - k_1 t \quad (12)$$

where q_e and q_t (mg g^{-1}) are the sorption capacities at equilibrium and at time t , respectively, and k_1 (min^{-1}) is the pseudo-first-order adsorption rate constant for RhB uptake per min by the PPs extractor. The values of k_1 and q_e are determined from the slope. The parameters K_L and q_e can be determined from the linear plot of $\ln(q_e - q_t)$ versus t . A nonlinear plot of $\ln(q_e - q_t)$ versus t was obtained low correlation value ($R^2 = 0.9422$). As a result, RhB uptake by PPs does not fit well with the pseudo-first-order rate equation.

Hence, the data were further subjected to pseudo-second-order that expressed by the equation [37-38]:

$$t/q_t = 1/k_2 q_e^2 + t/q_e \quad (13)$$

where k_2 ($\text{g mg}^{-1} \text{min}^{-1}$) is the pseudo-second-order rate constant.

The plot of t/q_t versus t was found linear with an excellent correlation value ($R^2 = 0.998$) (Fig. 10). The calculated value of k_2 was found equal to $0.04 \text{ g mg}^{-1} \text{min}^{-1}$. Thus, it can be concluded that RhB retention by the used PPs fitted well with the second-order model. Good agreement between the experimental value of q_e (175.86 mg g^{-1}) and the calculated value of q_e (152.73 mg g^{-1}) for the pseudo-second-order kinetic model. These findings confirm the suitability of the pseudo-second-order rate equation for the RhB adsorption using PPs from aqueous solutions.

Thermodynamic Behavior of RhB Dye Retention onto PPs

The sorption behavior of RhB by PPs was investigated at different temperatures (298–328 K) to determine the nature of RhB dye uptake onto PPs at

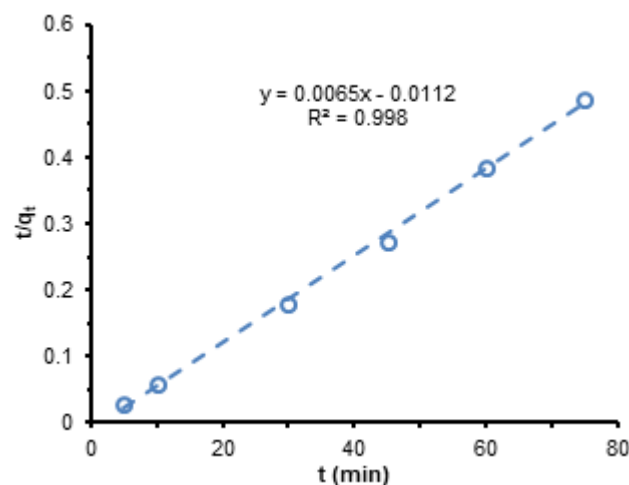


Fig 10. Pseudo-second-order plot of RhB dye uptake by 0.1 g PPs at $\text{pH} \approx 5$ after 10 min shaking

optimum conditions [44]. The thermodynamic activation parameters of the process, such as activation enthalpy (ΔH), Gibbs free energy (ΔG), which is the fundamental criterion to determine if a process occurs spontaneously, and the entropy (ΔS) were calculated from the equations below [26,45-46]:

$$\ln K_c = \frac{-\Delta H}{RT} + \frac{\Delta S}{R} \quad (14)$$

$$\Delta G = \Delta H - T\Delta S \quad (15)$$

$$\Delta G = -RT \ln K_c \quad (16)$$

The K_c values of RhB sorption by the PPs are dependent on the fractional attainment (F_e) of the sorption process, and the values of K_c can be calculated using the following equation:

$$K_c = \frac{F_e}{1 - F_e} \quad (17)$$

ΔH and ΔS determined from the slope and intercept (Eq. (14)), respectively, of plotting $\ln K_c$ against $1/T$.

The distribution ratio (D) of PPs according to Van't Hoff equation, using the following expression [45]:

$$\log D = \frac{-\Delta H}{2.303 RT} + C \quad (18)$$

where, C is a constant. RhB uptake from aqueous media of $\text{pH} \approx 5$ onto PPs shows decreased D values on increasing temperature. The plot of $\log D$ against $1000/T$ (K^{-1}) was linear (Fig. 11). The evaluated ΔH data for RhB

sorption onto PPs is equal to $30.15 \pm 1.01 \text{ kJ mol}^{-1}$.

The positive value of ΔH confirms the endothermic behavior of the adsorption of RhB by PPs from aqueous solution [44]. The adsorption capacity of adsorbent increased with an increase in temperature from 298 to 328 K. The positive value of entropy ($\Delta S = 42.17 \text{ J mol}^{-1} \text{ K}^{-1}$) of the sorption of RhB onto the sorbent surface may be attributed to the increase in the degree of freedom of the RhB molecules is more restricted in the PPs structure than in solution [44]. The negative value of ΔG at all studied temperatures indicated the feasibility and spontaneous nature of RhB sorption onto PPs.

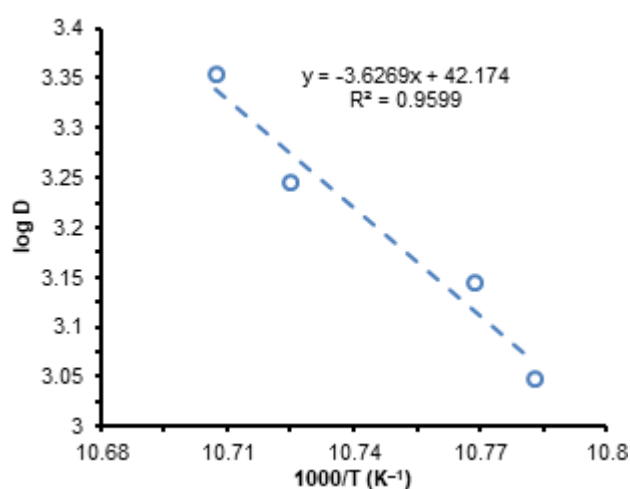


Fig 11. Vant- Hoff plot of RhB dye retention onto 0.1 g PPs at pH \approx 5 after 10 min shaking

Table 4. Extraction percentage of RhB dye at different concentrations in real water samples using 0.1 g of PPs at pH \approx 5

Samples	Concentration (mg L ⁻¹)	% Extraction*
Well water	5	89.8 \pm 9.85
	10	87.75 \pm 10.0
	15	87.63 \pm 9.45
Tap water	5	92.23 \pm 7.65
	10	86.23 \pm 9.88
	15	89.84 \pm 9.43
Bottle water	5	93.45 \pm 5.85
	10	93.78 \pm 6.05
	15	92.92 \pm 6.85
Sea water	5	97.86 \pm 1.88
	10	89.37 \pm 9.85
	15	94.97 \pm 4.45

*Average (n = 3)

The increase in the ΔG values $-1024.19 \text{ kJ mol}^{-1}$ at 298 K, $-1445.93 \text{ kJ mol}^{-1}$ at 308 K, and $-1356.94 \text{ kJ mol}^{-1}$ at 318 K with increasing temperature because of the spontaneous nature of sorption [44]. It implies that is more favorable at higher temperatures confirming the endothermic sorption process.

Environmental Application

To examine the applicability of the suggested method for RhB detection, it was implemented to extract RhB dye from real water samples. Therefore, different environmental samples of well water, tap water, bottled water, and seawater were collected from Jeddah, Saudi Arabia. Then, the suggested procedure was applied to analyze the samples by above-proposed batch conditions (Table 4). The percentage of RhB dye extraction, using PPs from the real environmental samples, was ranging from 92.82–98.15%. Thus, the proposed method is accurate and applicable to RhB removal from real water samples.

CONCLUSION

The current approach demonstrates the efficacy of the natural PPs as a solid phase extractor for selective separation of RhB at trace concentration levels from aqueous solutions. PPs adsorbent also provided high adsorption capacity for RhB dye at pH \approx 5 at 10 min. Isotherm models such as Langmuir adsorption fitted with the experimental data of RhB adsorption onto PPs sorbent, indicating the adsorption process mainly by a monolayer of RhB onto a homogenous surface of PPs.

The results of kinetics of the RhB retention from the aqueous media towards PPs fitting well with pseudo second order rate equation. The thermodynamic study showed that the sorption process was spontaneous and endothermic in nature, associated with positive entropy value. Overall, the results were reliable, feasible and suitable. Therefore, the proposed method can be successfully used for a selective separation of organic dyes from the real water samples.

REFERENCES

- [1] Tahir, M.A., Bhatti, H.N., Hussain, I., Bhatti, I.A., and Asghar, M., 2020, Sol-gel synthesis of

- mesoporous silica-iron composite: Kinetics, equilibrium and thermodynamics studies for the adsorption of Turquoise-Blue X-GB dye, *Z. Phys. Chem.*, 234 (2), 233–253.
- [2] Shannon, M.A., Bohn, P.W., Elimelech, M., Georgiadis, J.G., Mariñas, B.J., and Mayes, A.M., 2008, Science and technology for water purification in the coming decades, *Nature*, 452 (7185), 301–310.
- [3] Kurniawan, T.A., Sillanpää, M.E.T., and Sillanpää, M., 2012, Nanoadsorbents for remediation of aquatic environment: Local and practical solutions for global water pollution problems, *Crit. Rev. Env. Sci. Technol.*, 42 (12), 1233–1295.
- [4] Alcamo, J., Henrichs, T., and Rösch, T., 2017, *World Water in 2025: Global Modeling and Scenario Analysis for the World Commission on Water for the 21st Century*, Center for Environmental Systems Research, University of Kassel, Germany.
- [5] Cosgrove, W.J., and Rijsberman, F.R., 2014, *World Water Vision: Making Water Everybody's Business*, Routledge, United Kingdom.
- [6] Maneerung, T., Liew, J., Dai, Y., Kawi, S., Chong, C., and Wang, C.H., 2016, Activated carbon derived from carbon residue from biomass gasification and its application for dye adsorption: Kinetics, isotherms and thermodynamic studies, *Bioresour. Technol.*, 200, 350–359.
- [7] Namasivayam, C., Radhika, R., and Suba, S., 2001, Uptake of dyes by a promising locally available agricultural solid waste: Coir pith, *Waste Manage.*, 21 (4), 381–387.
- [8] Kulyukhin, S.A., Krasavina, E.P., Rumer, I.A., and Gordeev, A.V., 2019, Use of layered double oxides and hydroxides of Mg and Al for removing dyes from aqueous solutions containing 137Cs, 90Sr, 90Y, and U(VI), *Radiochemistry*, 61 (5), 585–591.
- [9] Eslami, A., Yazdanbakhsh, A.R., and Momayyezi, M.H., 2015, Removal of reactive dyes from textile wastewater using sonochemical process: effective parameters study, *JRH*, 5 (2), 184–192.
- [10] Mahmoudabadi, T.Z., Talebi, P., and Jalili, M., 2019, Removing disperse red 60 and reactive blue 19 dyes removal by using *Alcea rosea* root mucilage as a natural coagulant, *AMB Express*, 9 (1), 113.
- [11] Zhou, Y., Lu, J., Zhou, Y., and Liu, Y., 2019, Recent advances for dyes removal using novel adsorbents: A review, *Environ. Pollut.*, 252, 352–365.
- [12] Bhatti, H.N., Safa, Y., Yakout, S.M., Shair, O.H., Iqbal, M., and Nazir, A., 2020, Efficient removal of dyes using carboxymethyl cellulose/alginate/polyvinyl alcohol/rice husk composite: Adsorption/desorption, kinetics and recycling studies, *Int. J. Biol. Macromol.*, 150, 861–870.
- [13] Noreen, S., Bhatti, H.N., Iqbal, M., Hussain, F., and Sarim, F.M., 2020, Chitosan, starch, polyaniline and polypyrrole biocomposite with sugarcane bagasse for the efficient removal of Acid Black dye, *Int. J. Biol. Macromol.*, 147, 439–452.
- [14] Gupta, V.K., and Suhas, 2009, Application of low-cost adsorbents for dye removal – A review, *J. Environ. Manage.*, 90 (8), 2313–2342.
- [15] Forgacs, E., Cserhádi, T., and Oros, G., 2004, Removal of synthetic dyes from wastewaters: A review, *Environ. Int.*, 30 (7), 953–971.
- [16] Aguiar, J.E., Cecilia, J.A., Tavares, P.A.S., Azevedo, D.C.S., Castellón, E.R., Lucena, S.M.P., and Silva Junior, I.J., 2017, Adsorption study of reactive dyes onto porous clay heterostructures, *Appl. Clay Sci.*, 135, 35–44.
- [17] Senthilkumar, T., Chattopadhyay, S.K., and Miranda, L.R., 2017, Optimization of activated carbon preparation from pomegranate peel (*Punica granatum* peel) using RSM, *Chem. Eng. Commun.*, 204 (2), 238–248.
- [18] Yu, S., Wang, X., Ai, Y., Tan, X., Hayat, T., Hu, W., and Wang, X., 2016, Experimental and theoretical studies on competitive adsorption of aromatic compounds on reduced graphene oxides, *J. Mater. Chem. A*, 4 (15), 5654–5662.
- [19] Maurya, I.C., Singh, S., Srivastava, P., Maiti, B., and Bahadur, L., 2019, Natural dye extract from *Cassia fistula* and its application in dye-sensitized solar cell: Experimental and density functional theory studies, *Opt. Mater.*, 90, 273–280.

- [20] Mozafarjalali, M., Hajiani, M., and Haji, A., 2020, Efficiency of *Aptenia cordifolia* mucilage in removal of anion dyes from aqueous solution, *IJNC*, 7 (2), 111–124.
- [21] Namasivayam, C., Muniasamy, N., Gayatri, K., Rani, M., and Ranganathan, K., 1996, Removal of dyes from aqueous solutions by cellulosic waste orange peel, *Bioresour. Technol.*, 57 (1), 37–43.
- [22] Hage, R., and Lienke, A., 2006, Applications of transition-metal catalysts to textile and wood-pulp bleaching, *Angew. Chem. Int. Ed.*, 45 (2), 206–222.
- [23] Afsharnia, M., Saedi, M., Zarei, A., Narooie, M.R., and Biglari, H., 2016, Phenol removal from aqueous environment by adsorption onto pomegranate peel carbon, *Electron. Physician*, 8 (11), 3248–3256.
- [24] Ververi, M., and Goula, A.M., 2019, Pomegranate peel and orange juice by-product as new biosorbents of phenolic compounds from olive mill wastewaters, *Chem. Eng. Process. Process Intensif.*, 138, 86–96.
- [25] Saadi, R., Saadi, Z., Fazaeli, R., and Fard, N.E., 2015, Monolayer and multilayer adsorption isotherm models for sorption from aqueous media, *Korean J. Chem. Eng.*, 32 (5), 787–799.
- [26] Liu, Y., and Liu, Y.J., 2008, Biosorption isotherms, kinetics and thermodynamics, *Sep. Purif. Technol.*, 61 (3), 229–242.
- [27] Al Jaaf, H.J.M., 2020, Adsorption of chloride ion from polluted water using pomegranate peels powder and tea leaves, *J. Eng. Sustainable Dev.*, 24 (1), 70–78.
- [28] Gündüz, F., and Bayrak, B., 2017, Biosorption of malachite green from an aqueous solution using pomegranate peel: Equilibrium modelling, kinetic and thermodynamic studies, *J. Mol. Liq.*, 243, 790–798.
- [29] Ben-Ali, S., Souissi-Najar, S., and Ouederni, A., 2017, Comments on “Characterization and adsorption capacity of raw pomegranate peel biosorbent for copper removal”, *J. Cleaner Prod.*, 154, 269–275.
- [30] Mekhamer, W., and Al-Tamimi, S., 2019, Removal of ciprofloxacin from simulated wastewater by pomegranate peels, *Environ. Sci. Pollut. Res.*, 26 (3), 2297–2304.
- [31] Siddiqui, M., Nizamuddin, S., Mubarak, N.M., Shirin, K., Aijaz, M., Hussain, M., and Baloch, H.A., 2019, Characterization and process optimization of biochar produced using novel biomass, waste pomegranate peel: a response surface methodology approach, *Waste Biomass Valorization*, 10 (3), 521–532.
- [32] Ghaneian, M.T., Jamshidi, B., Dehviri, M., and Amrollahi, M., 2015, Pomegranate seed powder as a new biosorbent of reactive red 198 dye from aqueous solutions: Adsorption equilibrium and kinetic studies, *Res. Chem. Intermed.*, 41 (5), 3223–3234.
- [33] Ben-Ali, S., Jaouali, I., Souissi-Najar, S., and Ouederni, A., 2017, Characterization and adsorption capacity of raw pomegranate peel biosorbent for copper removal, *J. Clean. Prod.*, 142, 3809–3821.
- [34] Shen, K., and Gondal, M.A., 2017, Removal of hazardous Rhodamine dye from water by adsorption onto exhausted coffee ground, *J. Saudi Chem. Soc.*, 21 (Suppl. 1), S120–S127.
- [35] Boparai, H.K., Joseph, M., and O’Carroll, D.M., 2011, Kinetics and thermodynamics of cadmium ion removal by adsorption onto nano zerovalent iron particles, *J. Hazard. Mater.*, 186 (1), 458–465.
- [36] Saha, P., and Chowdhury, S., 2011, “Insight into adsorption thermodynamics” in *Thermodynamics*, Eds. Tadashi, M., IntechOpen, Rijeka, 349–364.
- [37] Oyekanmi, A.A., Ahmad, A., Hossain, K., and Rafatullah, M., 2019, Adsorption of Rhodamine B dye from aqueous solution onto acid treated banana peel: Response surface methodology, kinetics and isotherm studies, *PLoS One*, 14 (5), e0216878.
- [38] Chin, M., Cisneros, C., Araiza, S.M., Vargas, K.M., Ishihara, K.M., and Tian, F., 2018, Rhodamine B degradation by nanosized zeolitic imidazolate framework-8 (ZIF-8), *RSC Adv.*, 8 (47), 26987–26997.
- [39] Dąbrowski, A., 2001, Adsorption – From theory to practice, *Adv. Colloid Interface Sci.*, 93 (1-3), 135–224.
- [40] Nimibofa, A., Angaye, S.S., Wankasi, D., and Dikio, E.D., 2015, Synthesis, characterization and application of Mg/Al layered double hydroxide for

- the degradation of Congo Red in aqueous solution, *Open J. Phys. Chem.*, 5 (3), 56–70.
- [41] Singh, S., Parveen, N., and Gupta, H., 2018, Adsorptive decontamination of rhodamine-B from water using banana peel powder: A biosorbent, *Environ. Technol. Innovation*, 12, 189–195.
- [42] Khan, T.A., Nazir, M., and Khan, E.A., 2013, Adsorptive removal of rhodamine B from textile wastewater using water chestnut (*Trapa natans* L.) peel: Adsorption dynamics and kinetic studies, *Toxicol. Environ. Chem.*, 95 (6), 919–931.
- [43] Lagergren, S.K., 1898, About the theory of so-called adsorption of soluble substances, *Kungl. Svenska Vetenskapsakad. Handl.*, 24 (4), 1–39.
- [44] Bello, O.S., Alabi, E.O., Adegoke, K.A., Adegboyega, S.A., Inyinbor, A.A., and Dada, A.O., 2020, Rhodamine B dye sequestration using *Gmelina aborea* leaf powder, *Heliyon*, 6 (1), e02872.
- [45] Chakraborty, S., Chowdhury, S., and Saha, P.D., 2011, Adsorption of crystal violet from aqueous solution onto NaOH-modified rice husk, *Carbohydr. Polym.*, 86 (4), 1533–1541.
- [46] El-Shahawi, M., Othman, M.A., and Abdel-Fadeel, M.A., 2005, Kinetics, thermodynamic and chromatographic behaviour of the uranyl ions sorption from aqueous thiocyanate media onto polyurethane foams, *Anal. Chim. Acta*, 546 (2), 221–228.